Statistical Approaches to the Estimation of Missing Values Arising in Remotely Sensed Data

Thelma Krug

A thesis presented in candidature for the degree of
Doctor of Philosophy at the University of Sheffield

Department of Probability and Statistics

February, 1992

Statistical Approaches to the Estimation of Missing Values Arising in Remotely Sensed Data

Abstract

This dissertation concerns the estimation of missing values arising in remotely sensed from optical systems. Missing values in this kind of data usually arise from the failure of one, or more, of the system detectors, or from the presence of thick clouds at the time of imaging. A through investigation of all the known existing methods to estimate missing remotely sensed data is carried out, and new approaches, and methods, are suggested. The estimates obtained from simple methods, which can be implemented on a routine basis to replace missing values on the imagery, are contrasted with those from more complex methods, to see if the implementation of more sophisticated methods is warranted. The methods are applied to real TM Landsat 5 data, from two distinct areas in Brazil, and their performances evaluated for a set of statistical measures, and visually. These results give a good insight into where the methods fail to perform well, which may be useful in the development of other methods. The estimation of missing values arising from the presence of thick clouds has received very little attention in the literature. Several methods are proposed and evaluated in the estimation of a clumped set of missing sites, such as occurs with thick, small, cloud cover in remote sensing with optical sensor systems. The results here might be useful to clarify the extent to which good estimates of the missing values occurring in clusters, can be expected. The loss of information on the parameters for a Gaussian univariate process on a rectangular lattice is also discussed, and exact and approximate formulae for this loss given for some spatial processes.

To my parents, from whom I have learnt to face the hardships of life.

To my son, whom I have not really seen become a man.

To José, with whom I have shared the journey.

Acknowledgements

Every author has many debts to acknowledge. First of all, I am grateful to the Conselho Nacional de Desenvolvimento Científico e Tecnológico, CNPq, for the grant for this research, and to the Instituto Nacional de Pesquisas Espaciais, INPE, for granting me a 4 years leave, and for providing the data sets for this research. I would especially like to thank Dr. Richard Martin, who supervised this Ph.D., for introducing me into the knowledge of spatial statistics, for the many hours he has spent reading the drafts of this dissertation, and for his constructive suggestions. My special thanks to Moacir Godoy Jr., from INPE, for his endless patience in selecting, recording, and sending the data used in this research, and to my INPE's colleagues Bernardo F. T. Rudorff, Dr. Getúlio T. Batista, Dr. Evlyn M. L. L. Novo, Claudia C. Z. F. Braga, Dr. Luciano V. Dutra, and Dr. Paulo Renato de Morais. To my friends Corina, Forchech, Fosam, Nedret, and Aiporê, I offer my heartiest thanks. Finally, and most importantly, I owe my greatest debt of gratitude to my husband José for his help, good humour, understanding, patience, and love at all times. He has been a constant source of inspiration and encouragement, which gave me the strength to reach the end of the journey.

Contents

List of Figures

List of Tables

Chapter 1

Introduction

This investigation addresses the estimation of missing values arising in remotely sensed data from optical systems. In particular, this study uses real data from the satellite Landsat 5, which is one of the remote sensing satellites presently in operation.

Broadly speaking, there are two main reasons for the occurrence of missing values in this kind of data. The first one is related to a fault in one (or more) components of the imaging system (detector failure), and the other is the presence of clouds, at the time of image acquisition.

The two causes have different effects on the image. The failure of one, or more detectors, for instance, causes the image to have systematically missing scan lines, which show as black horizontal lines across the image. An example of simulated detector failure is given in Figure 5.2, in Chapter 5. The presence of these missing lines on the imagery disrupts the visual observation (and interpretation) of the imaged objects, and leads to unreliable statistics of the image, if these are based on pixel values. Considering that most agencies that receive, and process, remotely sensed data, normally use them for commercial purposes, it is important that these imperfections be corrected, and that the user be provided with as good data as possible. In other words, it is important that good estimates of the missing values be obtained.

Commonly, the missing values arising in remotely sensed data are estimated using linear interpolation, or by replacing the missing values with those in the line immediately above. Since Landsat 5 provides multispectral data, some more sophisticated methods have been developed, exploring this additional available

information, to improve the estimation of missing values arising from detector failure, or other causes that may have the same result on the image.

The effect of the presence of cloud cover in the imagery varies according to the cloud extent, its shape, and thickness. Most discussion in the literature concerns the 'correction' of the data distorted by the presence of thin clouds. In this case, some information from the objects on the ground is still available, but needs to be corrected (usually by the application of some sort of filter), to remove the interference (noise) of the cloud.

The presence of thick clouds has a much more profound effect on the image. Since clouds are highly reflective, they show in the image as bright areas, which are normally scattered across the image. Moreover, clouds '*usually have an associated congruent darker area at a certain specific distance and orientation - their shadows*' (Haralick & Fu, 1983), which can cause as much 'damage' to the image as the clouds themselves. As an example, Figure 1.1 displays a colour composite (bands 3, 4, and 5) TM Landsat 5 image of Phuket Malaya (Thailand), acquired in August 1989, where the effects of clouds (shown in white) and their shadows (shown in black), can be clearly seen.

Few approaches exist for the estimation of missing values arising from the presence of thick clouds (or their shadows). For some types of applications of remotely sensed data, such as classification and mapping, it may be important that accurate estimates of the missing values be obtained. At present, the only known approach for replacing missing values arising from the presence of thick clouds, suggests their replacement by the corresponding values in another passage (Hord, 1982).

In this investigation, the estimation of missing values arising from detector failure, and from the presence of thick, small clouds, is considered, using real Landsat 5 data from two distinct areas in Brazil. Due to the specific characteristics of this kind of data, some generalities about Landsat 5 remotely sensed data are presented in Chapter 2. Details about the data used in this research, and the two test sites, are given in Chapter 3.

In Chapter 4, all the existing methods suggested in the literature for estimating missing values arising from detector failure, are evaluated. Other new approaches are also proposed in that chapter. All the methods in the chapter are relatively simple ones, which can be implemented on a routine basis, to re-

place missing scan lines on the imagery. Considering the large amount of remotely sensed data that needs to be processed, it is important that the proposed methods be easily implemented, and relatively fast.

In Chapter 5, more complex methods, which use spatial modelling, are evaluated in the estimation of missing values occurring from detector failure. Due to the fact that the implementation of these methods is more difficult, and much more computing demanding than the simple methods in Chapter 4, it is important to see if they give significantly better estimates of the missing values than the simple approaches, to warrant their routine implementation.

In Chapter 6, the estimation of missing values occurring in small clusters, as if arising from the presence of thick, small clouds, is addressed. Simple methods, as well as more complex ones using spatial modelling, are considered in the estimation of the missing values, and their performance evaluated when applied to some simulated 'clouded' areas in images from both data sets.

Chapter 7 is of a more theoretical nature, and addresses the loss of information on the mean, and on the dependence parameter, for some of the spatial processes introduced in Chapter 5. Exact, as well as approximate formulae for the loss on the mean are given, and evaluated, for some of the processes. From the approximate formulae, a good insight into how the loss on the mean varies over the different configuration of the missing values is obtained.

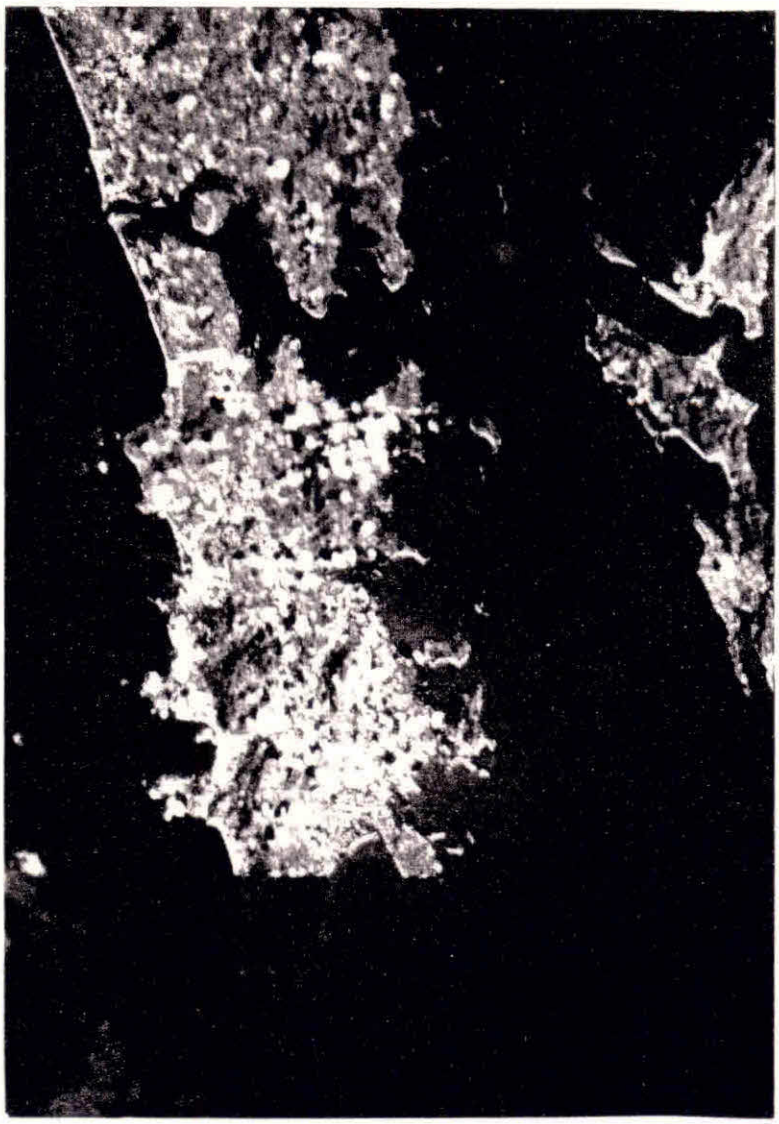

Figure 1.1: An example of the effect of clouds (and their shadows) on a TM Landsat 5 image (Courtesy of Dr. Chris Clark, Geography Department, The University of Sheffield).

Chapter 2

Some Principles of Remote Sensing

Since this research is concerned with remotely sensed data from a satellite, and in view of the specific characteristics of this kind of data, a general introduction of remote sensing is given in this chapter, emphasizing only those aspects which seem relevant to this study.

2.1 Introduction

Amongst definitions of remote sensing, the one given by Rees (1990) seems to be the most appropriate:

> 'Remote sensing is, broadly but logically speaking, the collection of information about an object without coming into physical contact with it. This definition is too wide to be useful, so we shall impose a number of restrictions. The first is that the object is located on or near the Earth's surface, and the sensor is more or less above the object, and at a 'substantial' distance from it. The second restriction is that the information is carried by electromagnetic radiation, some property of which is affected by the remotely sensed object.'

This research uses data from the sensor that is currently being operated from the Landsat 5 satellite, which is one of a series of satellites devised to provide information about the Earth's surface. Landsat 5 carries a Thematic Mapper (TM)

sensor that provides multispectral data, which are recorded 'simultaneously' in seven regions of the electromagnetic spectrum. These regions are usually referred to as bands.

The recorded data correspond to the average 'brightness' or radiance measured electronically over an area on the ground. This area, which is usually referred to as a ground cell resolution, corresponds to a pixel (picture element) in the image, and is equal to 30 metres by 30 metres for six of the TM bands (1-5,7) and 120 metres by 120 metres for the thermal band (band 6). Table 2.1 (from Curran, 1985) shows the spectral bands recorded by the TM Landsat 5, and gives a brief summary of the principal characteristics of each band, for remote sensing applications.

Table 2.1: The wavebands recorded by the Thematic Mapper sensor carried by Landsat 5.

Band number	Band name	Band width(μm)	Points
1	Blue/Green	$0.45 - 0.52$	Good water penetration strong vegetation absorbance
2	Green	$0.52 - 0.60$	Strong vegetation reflectance
3	Red	$0.63 - 0.69$	Very strong vegetation absorbance
4	Near infrared	$0.76 - 0.90$	High land/water contrast very strong vegetation reflectance
5	Near-middle infrared	$1.55 - 1.75$	Very moisture sensitive
6	Thermal infrared	$10.4 - 12.5$	Very sensitive to soil moisture and vegetation
7	Middle infrared	$2.08 - 2.35$	Good geological discrimination

From Curran (1985).

The availability of multispectral data can aid in the identification of the objects on the ground, since different materials have a specific reflectance in each

band.

The radiation from objects on the ground is sensed by the detectors, which are defined by Harris (1980) as:

> 'devices formed from substances known to respond to energy over a defined wavelength interval, generating a weak electrical signal with a strength related to the radiance of the features in the field of view[a] of the sensor. The electrical current is then amplified, then used to generate a digital signal that can be used to form a pictorial image.'

The TM uses 16 detectors for all nonthermal bands and four detectors for the thermal band (100 detectors in all). Thus, 16 lines of each nonthermal band and four lines of the thermal data are acquired with each sweep of an oscillating scan mirror, which collects data in its forward (west-east) and reverse (east-west) motion – see Figure 2.1, which shows the projection of the detector's instantaneous field of view (IFOV) on Earth surface.

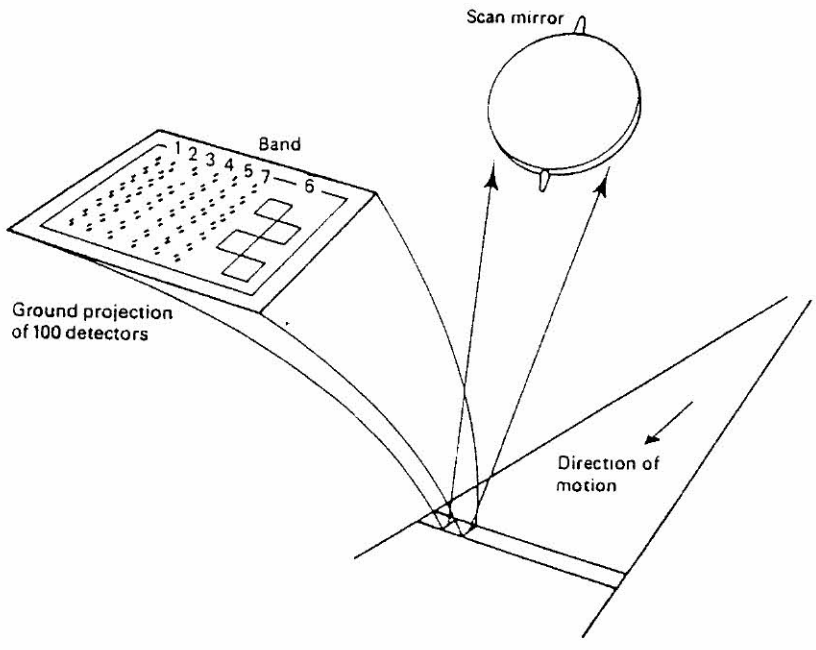

Figure 2.1: Projection of detector IFOVs on Earth surface. (Adapted from Lillesand & Kiefer, 1987).

[a]The smallest solid angle through which a detector is sensitive to radiation (Thomas, 1987).

Landsat 5 generates data in digital form, with each element in the image representing the radiation of an area on the surface. This radiation is expressed by a non-negative integer (*digital number* or *grey level*), which for the TM ranges from 0 to 255. A definition of digital data is given in Bernstein (1983) as

> '... a sampled and quantized numeric representation of a scene. The scene is spatially partitioned by the sensing device into a regular array of numbers whose values represent the radiance or brightness of the sampled region in one or more spectral bands.'

All the TM Landsat data are transmitted to Earth through a ground receiving station. The analog signal from each detector is converted to digital form by an onboard converter, and recorded on high density tapes at the receiving station. Each Landsat scene is 'framed' from the continuous TM data so that it covers an area of approximately 185 km by 185 km. The data is processed, transferred to a CCT (computer compatible tape), and then distributed amongst the users. Figure 2.2 illustrates the Landsat TM operating configuration, showing the square instantaneous field of view of the scanner, which results in a ground resolution cell of side approximately 30 metres.

The choice of the orbit for Landsat 5 allows for multitemporal sensing, where data about the same area on the ground are collected at every 16 days. According to Lillesand & Kiefer (1987):

> 'each Landsat satellite passes over the same area on the Earth's surface during daylight hours about 20 times per year. The actual number of times a given ground area is imaged depends on amount of cloud cover, the Sun angle, and whether or not the satellite is in operation on any specific pass.'

The availability of multitemporal imagery usually improves classification of ground cover, '*as single-date images rarely possess sufficient spectral differentiation between crop types for accurate classification*' (Jewell, 1989).

The use of multispectral and/or multitemporal remotely sensed data requires the proper registration [b] of the data recorded in different bands, or at different

[b] The process of geometrically aligning two or more sets of image data so that the resolution cell for a single ground area can be digitally or visually superposed (Curran, 1985).

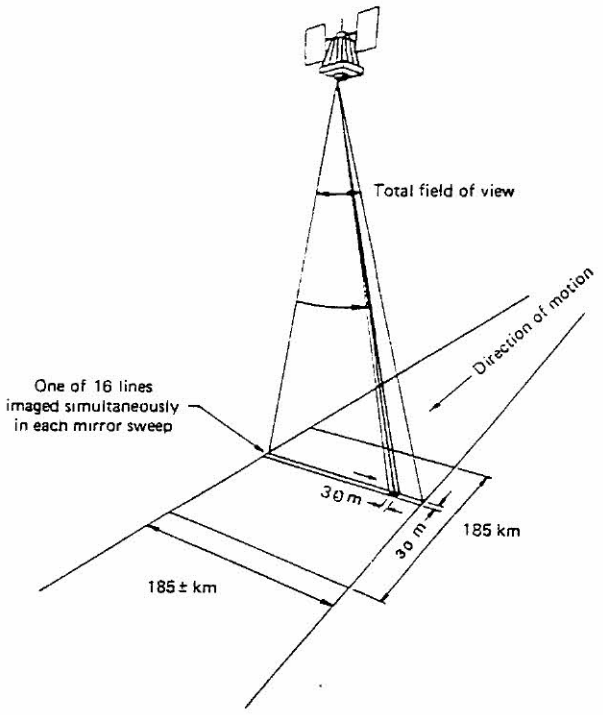

Figure 2.2: Landsat TM operating configuration. (Adapted from Lillesand & Kiefer, 1987).

times. From the analysis of 8 TM images, Wrigley *et al.* (1985) reported that the band-to-band registration of the TM was within the satellite specification (less than 6 metres). In contrast to band-to-band specification, which is a pre-launch specification of the imaging system, registration of multi-date imagery, to correct for any spatial displacement between passages, is usually carried out as part of the data preprocessing manipulations performed at the ground receiving station. The registration process usually consists of superimposing the different images, to make geographic control points (e.g. rivers, roads, lakes, etc.) coincide.

2.2 Data Quality

Many factors may limit the quality of the remotely sensed data, for example, the imaging system itself, the performance of the recording equipment, and errors in the transmission of the data to the ground receiving station. Other factors, such

as the rough topography of the area being imaged, may also introduce distortions in the image data. These distortions need to be removed before the data can be effectively used. The 'raw' remotely sensed data is usually corrected for certain random geometric distortions, and for the effects of variations in radiation caused by changes in atmospheric conditions, scene illumination, and viewing geometry. Data from different dates, for instance, are corrected to account for the different solar illumination at the different times of data acquisition, a procedure which is important when joining images from adjacent tracks, or when comparing annual changes in land cover.

Besides the geometric and radiometric corrections applied to the data, other manipulations may also be necessary to account for the presence of systematic and/or random noise which may be present in the image data. These unwanted fluctuations may either degrade or totally mask the true radiometric information content of the digital image, and are caused by such factors as malfunction of a detector, interference between sensor components, and errors in the transmission and reception of the data (Lillesand & Kiefer, 1987). If the pattern of the noise is known, then appropriate modifications can be made at the receiving station to diminish its effect.

Several types of noise can be identified in an image, some of them of known origin. For the TM, which sweeps 16 scan lines at the same time in six of its spectral bands, variations in the response of an individual detector within a given band may result in relatively higher or lower values every 16^{th} line in the image data, causing *striping* effects. To correct for this defect, data in the defective lines are usually *normalized* with respect to their neighbouring observations.

Noise may also be introduced in the digital data when a detector partially (or entirely) fails. This causes a number of adjacent pixels along a line (or an entire line) to contain spurious digital numbers, which shows as systematic black stripes across the digital image. This problem is usually referred to as *line dropout* or *line drop*. The defective lines are usually replaced by those immediately above it. However, some types of application, such as classification and mapping, require a more refined analysis of the data, and in this case more sophisticated methods than adjacent line replacement may be warranted.

For the images degraded by noise, the usual approach for noise removal consists of postulating a model for the data, where noise is usually introduced as

an additive component. Approaches to remove striping effects can be found in Mather (1987), Horn & Woodham (1979), and Moik (1980), whilst for the removal of noise using data modelling see, for instance, Woods *et al.* (1987), Combettes & Trussel (1989), Liu & Caelli (1988), and Frieden (1980).

The quality of remotely sensed data from optical systems may also be affected by the presence of clouds, which do not allow the 'true' information on the Earth's surface to reach the sensor. Thick clouds completely block the radiation from the objects on the ground, and show in the image as bright areas. Their shadows may also appear on the image, but as darker areas, which '*are often harder to identify since the observed reflectance depends both upon the extent to which the ground is obscured and on the nature of the ground surface*' (Gurney, 1982). Since grey levels within and between shadows may vary considerably, they are also easily confounded with other classes of ground cover.

Few efforts have been made to recover the information distorted, or blocked by the presence of clouds. Hord (1982), for instance, suggests the simple replacement of the missing values in the image, due to the presence of clouds, by the corresponding values in another passage. There are obvious limitations to this approach, for even if the proper corrections to account for the different atmospheric conditions and the varying behaviour of the sensors at the times of data acquisition are made, there is still the problem of changes in land cover which Hord (1982) completely ignores.

It has been suggested that data from other remote sensing systems, such as radar, can be used to improve the recovery of the missing data in the TM imagery, due to clouds. Radars are not optical systems, and can in fact 'see' through clouds. However, because of the different spatial and spectral specification of each system, data are not readily comparable. In order to account for the different spatial resolution of different sensors, for instance, it may be necessary to resample data from one system, to register with data from another. In this process, the 'original' information from one of the systems is completely lost.

The use of data from SPOT 1, the French satellite operating since 1986, can also be used to improve the recovery of missing TM data. SPOT 1 revisits the same area on the ground more frequently than Landsat 5, and this increases its potential for providing cloud-free imagery. However, Landsat and SPOT 1 record data in different bands, besides having incompatible spatial resolutions. SPOT

1 has different spatial resolutions (pixel) for the panchromatic (0.5 - 0.9 μm), and the multispectral bands (10 and 20 metres, respectively), whereas the TM Landsat has a spatial resolution of 30 metres for all but the thermal band.

Although in this investigation only TM Landsat 5 data are used, the methods proposed in the next chapters are not restricted to this kind of data, and can be applied to data from other remote sensing systems which provide multispectral, multipolarised, and/or multitemporal data (e.g. SPOT 1, ERS-1, airborne platforms, systems on the Space Shuttle, etc.).

Chapter 3

Data Sets

3.1 Introduction

The investigation carried out on missing values in this dissertation uses TM Landsat data from two distinct areas in São Paulo State, Brazil. The images have been provided by the Instituto de Pesquisas Espaciais, INPE, a Brazilian government agency that receives, digitally processes, and makes available commercially Landsat data for Brazil, and other parts of South America.

In view of the high demand for remotely sensed data in agriculture, data from a previous study over an area of high wheat production, by Rudorff & Batista (1989), were made available in the most informative bands for agricultural purposes (bands 3, 4, and 5 – refer to Table 2.1).

In order to investigate the consistency of the methods to different image contents, data from another area were also used. The data have been used previously by Novo & Braga (1991), in a project on aquatic systems, and were available in bands 4 and 5.

The data have been submitted to the usual radiometric and geometric corrections at INPE, and any defective scan line, if detected, has been automatically replaced by the line immediately above. This is the current practice adopted by INPE, when confronted with any spurious data from detector failure, or from errors associated with the transmission and reception of remotely sensed data.

In view of the impracticality of working with data from a whole image, a sub-area comprising different patterns was selected from each image, to allow the evaluation of the replacement methods under a number of different situations.

Because the images were available at different dates, data from corresponding areas in images acquired at different times were registered using several control points in one image and finding the equivalent points in the others. This was done manually as well as digitally, using the facilities provided at a SUN workstation. The results from both procedures were very similar.

In section 3.2 some notation is introduced. Section 3.3 presents the data sets, providing descriptive statistics of the data, as well as visual interpretation of the corresponding sub-images.

3.2 Notation

Remotely sensed data in band k, acquired at time t, can be thought of as observations $u_t^k(i,j)$, on an n_1 by n_2 rectangular lattice, where rows are indexed by $i = 1, \ldots, n_1$ and columns by $j = 1, \ldots, n_2$. Let $\mho$ be the set of all sites (i,j) in the lattice.

Let the sample autocorrelations at lags g, h, for the data in band k, acquired at time t, $r_t^k(g,h)$, be defined here as $C_t^k(g,h)/C_{0,0}^k$ where, for $gh \geq 0$,

$$C_t^k(g,h) = \{(n_1 - \mid g \mid)(n_2 - \mid h \mid)\}^{-1} \sum [u_t^k(i,j) - \bar{u}_t^k][u_t^k(i+g, j+h) - \bar{u}_t^k];$$

$$C_t^k(g,-h) = \{(n_1 - \mid g \mid)(n_2 - \mid h \mid)\}^{-1} \sum [u_t^k(i,j+h) - \bar{u}_t^k][u_t^k(i+g, j) - \bar{u}_t^k]$$

and $\bar{u}_t^k$ is the mean of the data.

The correlation between data in different bands (say, k and l), acquired at time t, is henceforth denoted by rb_t^{kl} (or simply rb_{kl}), and is the usual bivariate correlation. Similarly, the correlation between the data in band k, acquired at different times (say t_1 and t_2), is the usual bivariate correlation, and is henceforth referred to as $rd_{t_1 t_2}^k$ (or simply $rd_{t_1 t_2}$).

3.3 Descriptive Statistics of the Data and Visual Interpretation

In this section some descriptive statistics are provided for both data sets. The discussion of these statistics is usually followed by visual interpretation of the corresponding sub-images.

3.3.1 First Data Set

3.3.1.1 Introduction

Data for the first data set, henceforth referred to as D_1, were made available in bands 3, 4 and 5 of the TM Landsat, on three consecutive passages (08/06/86, 24/06/86, and 10/07/86), over an area in São Paulo State, Brazil. The data in each band and date correspond to an area of 92 × 92 pixels mainly cultivated with wheat, which is usually planted between the end of April and the beginning of May. The average cycle between sowing and harvesting for the different varieties planted in this region is 110 days (Rudorff & Batista, 1989).

Unfortunately, due to the fact that the data correspond to an area selected from a much larger image, the details about the exact location of the area, and the type of ground cover present, could not be precisely identified. However, from the technical report by Rudorff and Batista (1989), who used data over the whole image, and the visual interpretation of the sub-images in bands 3, 4 and 5, many details could be deduced about the area.

Figure 3.1 indicates the approximate location of the test site on the map of Brazil.

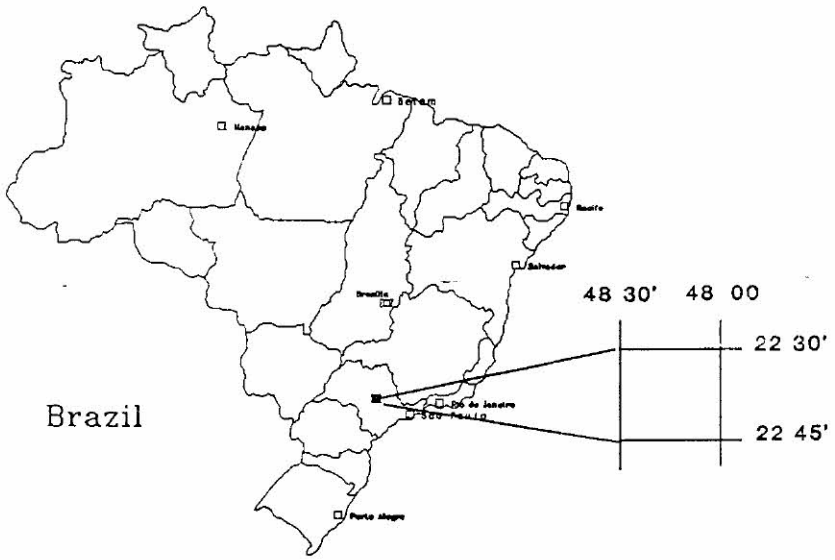

Figure 3.1: Approximate location of the test site for the first data set.

3.3.1.2 Descriptive statistics of the data

Descriptive statistics for each of the nine sub-images in D_1 are now provided. Each image is coded, to facilitate its identification in the text. Let $D_1(tb)$ refer to the sub-image acquired at time t in band b, where the subscript $t = 1, 2, 3$ refers to dates 10/07/86, 24/06/86, and 08/06/86, respectively, and $b = 3, 4, 5$ refers to bands 3, 4 and 5, respectively. Henceforth, the relevant information about the sub-images in either data set, are always presented in order of increasing band, and decreasing date.

Table 3.1 gives the mean, median, standard deviation (stdev), minimum and maximum [(m,M)], and the range of the data in each sub-image in D_1.

Table 3.1: Summary statistics of the sub-images in D_1.

Code	Mean	Median	Stdev	(m,M)	Range
$D_1(13)$	25.2	26	5.3	(10, 46)	36
$D_1(23)$	24.2	24	5.0	(11, 43)	32
$D_1(33)$	23.1	22	4.9	(11, 45)	34
$D_1(14)$	43.2	42	10.6	(6, 76)	70
$D_1(24)$	46.9	45	10.8	(8, 82)	74
$D_1(34)$	48.9	48	10.3	(8, 76)	68
$D_1(15)$	60.0	58	17.7	(5, 106)	101
$D_1(25)$	56.6	54	16.0	(7, 100)	93
$D_1(35)$	55.9	52	15.9	(7, 101)	94

From the standard deviations and the ranges in Table 3.1 it is noted that data in band 3 are much more homogeneous than data in either bands 4 or 5. This characteristic is also evidenced in the sub-images corresponding to data in band 3, shown in row (a) of Figure 3.2. Rows (a), (b) and (c) of Figure 3.2 display the sub-images in D_1 in bands 3, 4 and 5, respectively. Each column in Figure 3.2, from left to right, gives the sub-images acquired at dates 10/07, 24/06 and 08/06, respectively. This figure, and all others to follow, show the sub-images in false colour. The histogram shown below the range of colours, at the right hand side of the figure, corresponds to the data over all nine sub-images displayed. A

compact version of the entire frame is shown above the range of colours. Most of the photographs in this dissertation include the compact version, the colour range, and the histogram, at the right hand side.

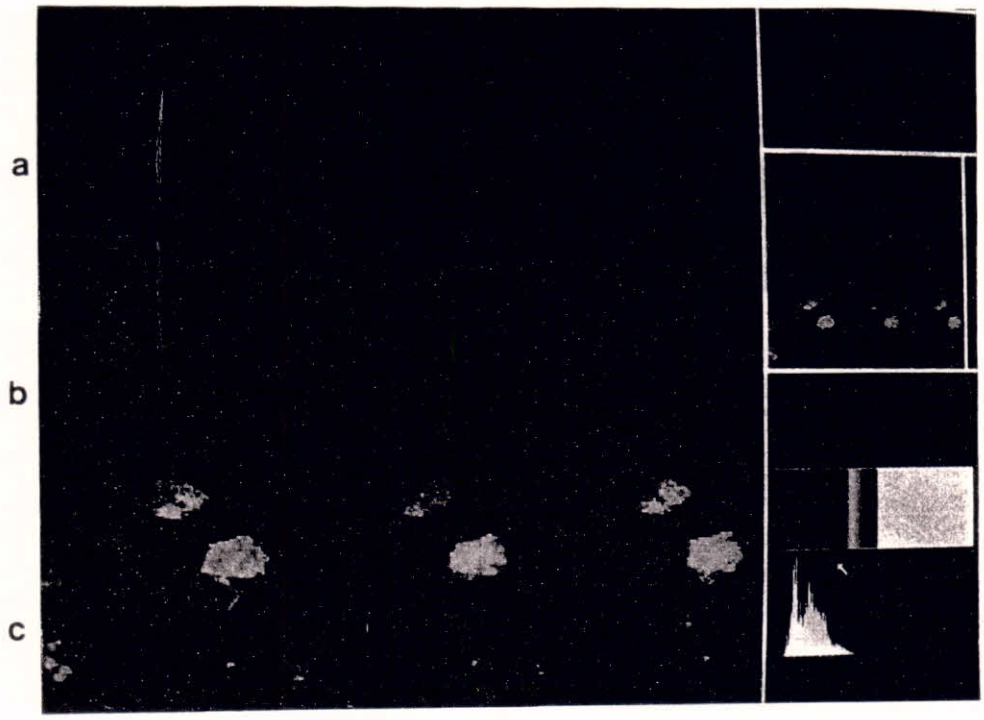

Figure 3.2: From left to right: frame with sub-images acquired at 10/07/86, 24/06/86, and 08/06/86, respectively, in bands (a) 3; (b) 4; and (c) 5.

Note that the colours in any sub-image, depend both on the range of the data, and on the compression adopted for the range of the colours. The maximum range of the colours is 256 [0,255], and comprises varying intensities of the colours magenta, blue (cyan), green, yellow, orange, and red, which are associated, in this order, with increasingly higher digital numbers (radiance values). The range of each individual colour can be observed in Figure 3.3 (a). An example of a compressed range of colours (from 64 to 208) is shown in (b).

By compressing the range of the colours, the images can be displayed with more contrast, thus being more informative. For example, the range of colours in Figure 3.2, has been compressed to 128 [0,127], which is essentially the range of the data over all sub-images displayed in the figure (see the corresponding histogram). If the range of colours is smaller than the range of the data, the

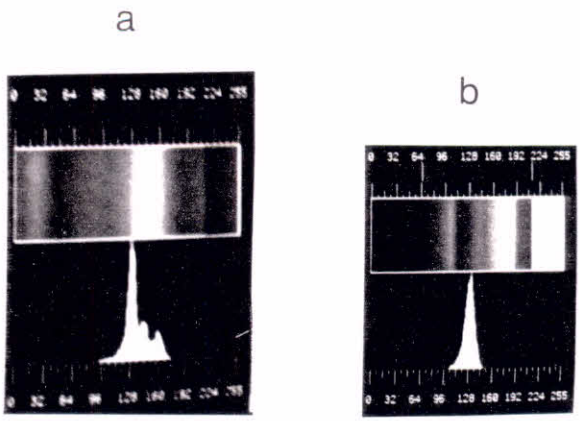

Figure 3.3: (a) Full range of the colours; (b) Compressed range of colours (from 64 to 208).

pixels at the tails of the distribution shown in the histogram are displayed in black (left tail), or white (right tail). Thus, the compression of the range of colours needs to be controlled, to be approximately the same as the range of the data, if the images are to be displayed with the maximum informative content possible. If the range of colours is approximately the same as the range of the data, then the colour red is associated with the highest values of the data, whilst the colour magenta indicates the lowest ones. If the range of colours is greater than the range of data, then the contrast is reduced, and the observed colour will only be a subset of those possible. For instance, the range of colours in the image corresponding to the Figure 3.3 (a) would be from blue to orange. A similar effect is observed in Figure 3.2 (a),where only magenta and cyan are used. These sub-images can be displayed in a different contrast, if the range of the colours is compressed to [0,63], for example, since the range of the values encompass a large number of colours. The sub-images shown in Figure 3.4 correspond to those in Figure 3.2 (a), when the range is compressed to the interval [0,63].

The sub-images displayed in Figure 3.2, especially those acquired in different bands, give valuable information about the main features of the test site, which are indicated in Figure 3.5, on the sub-image acquired at 10/07/86 in band 5. Light intensities of the grey levels in this figure correspond to high digital values on the corresponding sub-image shown in Figure 3.2 (c), whereas the dark ones are associated with low digital values.

Since the original image is over an area of intense wheat cultivation, it has been inferred that the areas above and below the road correspond to two wheat

fields (**A**), which are bordered, at the left, by areas of greater moisture (**B**). At the bottom of the sub-image, two areas of intense moisture (**C**) can be observed. Part of the remaining area is bare soil (**D**), and soil covered with low density vegetation (**E**).

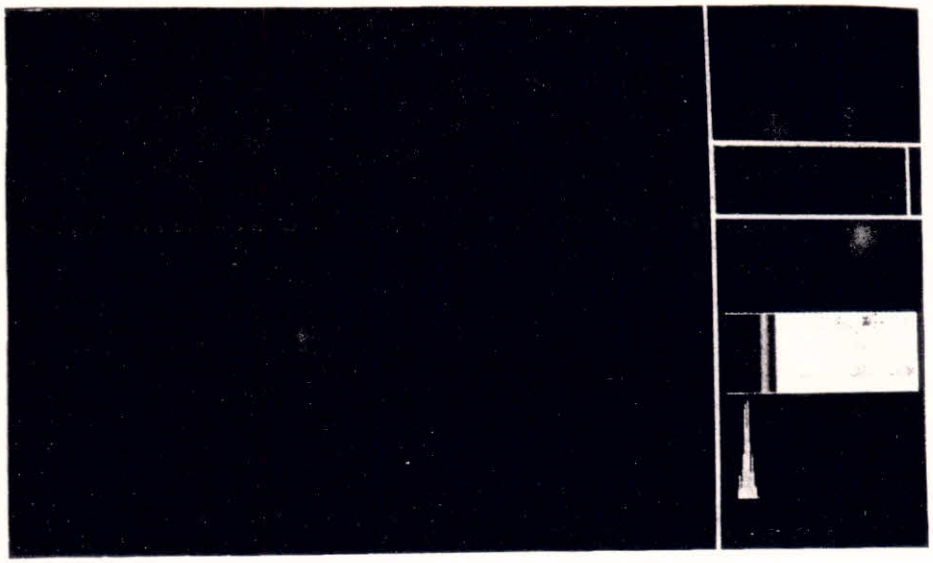

Figure 3.4: From left to right: sub-images in band 3 acquired at 10/07, 24/06, and 08/06, shown in a different contrast.

The most heterogenous area in all sub-images in D_1 is that delimited by lines 76 and 90, which contains the regions of intense moisture, as indicated by **C** in Figure 3.5. The sub-images in band 5 are the most heterogeneous ones. For example, the minimum and maximum values [(m,M)] of the data in each of columns 33 to 36, which intersect lines 77 and 85, in sub-image $D_1(15)$, are (8,51), (5,59), (7,63), and (7,62), respectively. The minimum values are the radiance from the portion of the diagonal moisture stripe that is contained in the area delimited by these lines and columns.

It is especially in the sub-images in band 5 that large variations are observed between pixel values at sites which are geographically close. Figure 3.6 displays the plot of the data in lines 76, 77, and 78, in sub-image $D_1(15)$, from where the decrease in the pixel values between sites (76,14) [value 78] and (76,15) [value 52] can be observed. Another example is the difference between the pixel values between sites (76,33) [value 39] and (77,33) [value 8]. Note that a constant, shown in the legend of the figure, has been added to the data in lines 77 and 78, to better discriminate the data in the different lines. Other examples for D_1 are given in

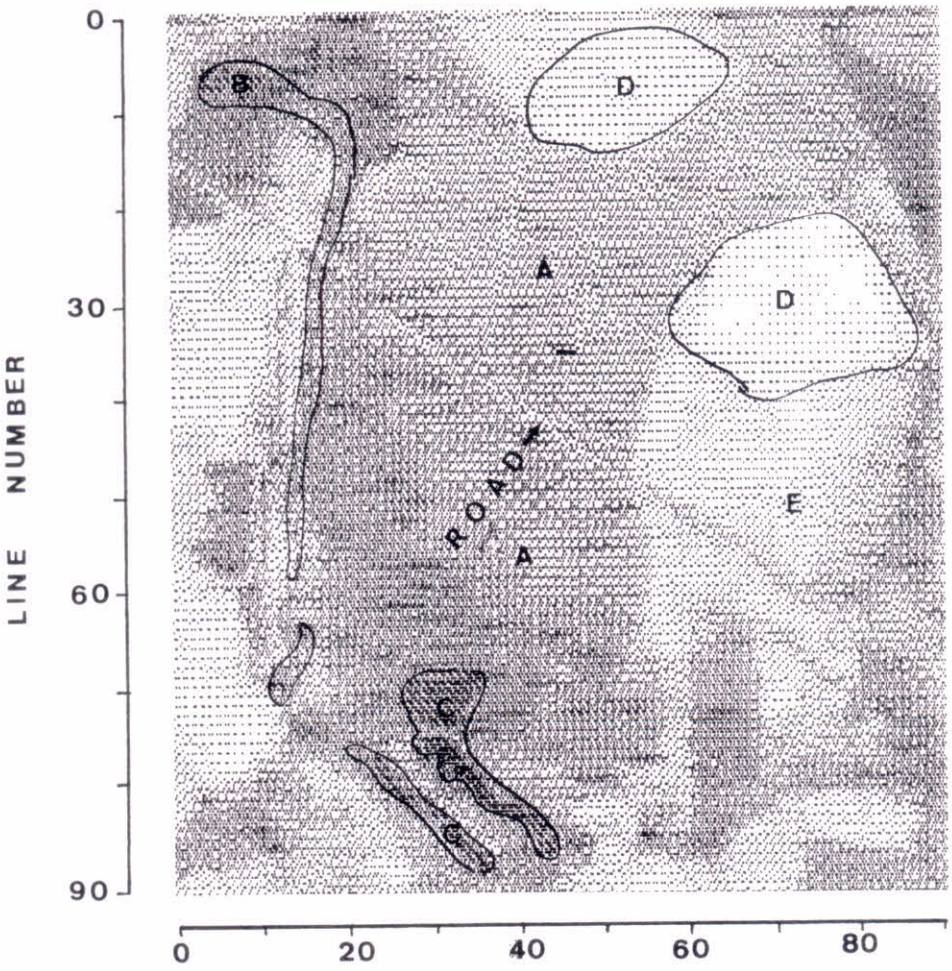

Figure 3.5: Representation of the sub-image acquired at 10/07/86 in band 5.

Figures 5.8, 5.9, and 5.10, in Chapter 5.

The large variations in the pixel values at sites that are close geographically can also be deduced from visual observation of sub-images, and the corresponding histogram. For example, in Figure 3.2 (c), the area shown in yellow and orange, at the top right of the sub-image acquired at 10/07, is contiguous to an area shown in cyan. From the range of colours, it can be inferred that the difference between the values of the pixels shown in cyan, and those shown in yellow, is approximately 25 to 40 grey levels. In fact, the pixel values in sub-image $D_1(15)$, in lines 22 and 23, intersected by columns 79 to 84, are:

	Column					
Line	79	80	81	82	83	84
Line 22 :	60	66	74	77	71	57
Line 23 :	87	92	101	101	103	97

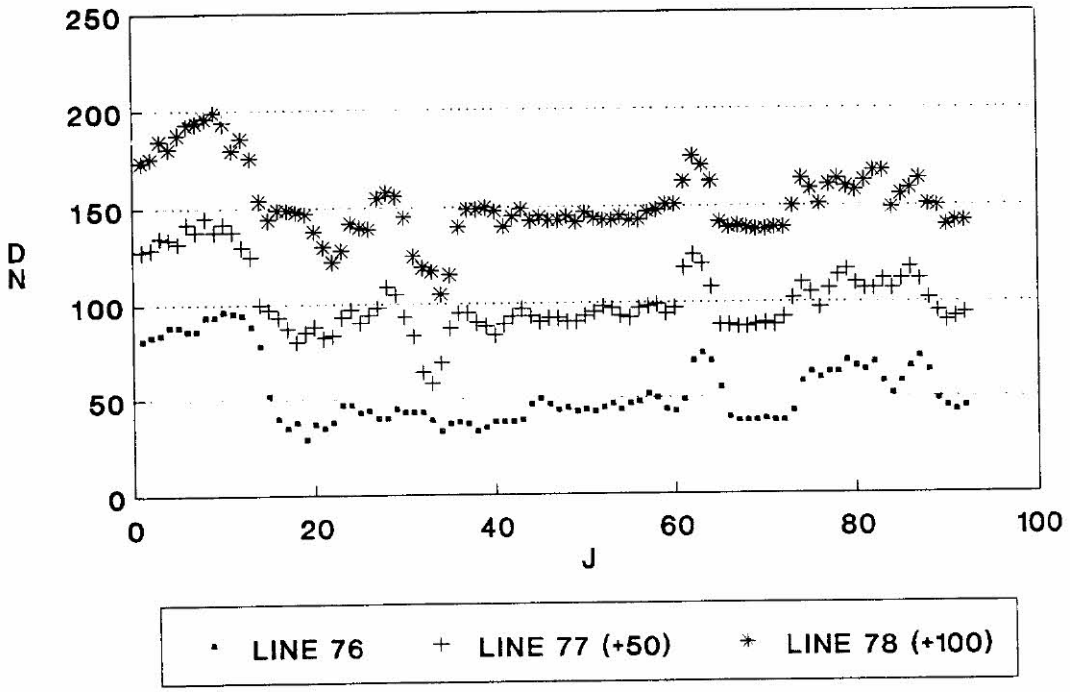

Figure 3.6: Plot of the data in lines 76, 77 and 78, in the sub-image acquired in band 5, at 10/07.

and variations, from 24 to 40 grey levels, occur.

Note that even larger variations than the ones given above, may occur. For example, in sub-image $D_1(15)$, the pixel values in the intersection of lines 26 and 27, with column 88, are 43 and 102, respectively, corresponding to a variation of 59 grey levels.

The small variation amongst the means and standard deviations of the sub-images acquired at different dates, for any fixed band, as shown in Table 3.1, suggests that few changes in ground cover have occurred between the dates of imaging. However, the larger variation amongst the means and standard deviations of data in the three bands, for any fixed date, indicates a significant difference in brightness, from the same objects on the ground, to distinct wavelengths.

These variations can be also be seen in Figures 3.7 and 3.8, which display the difference images for sub-images acquired at different times, and in different bands, respectively. The difference image for two images is obtained by subtracting corresponding pixel values, and adding a constant value of 128, to ensure

values are non-negative.

Note, from the range of values in the histogram displayed in Figures 3.7 and 3.8, that larger differences are observed between the data acquired in different bands, than between those acquired at different times. Although the histogram in these figures correspond to the data over all difference images displayed, it is nevertheless useful and informative. From the histogram it can be seen that the largest differences are associated with the colour red, and the smallest with dark magenta [note that although magenta shows very distinctively in the frame displayed in Figure 3.8, suggesting large changes between bands 4 and 5, the colour is associated with pixels with small differences, as is cyan (both colours are near dark blue, which is associated with differences of approximately zero)].

The differencing process on images acquired on different dates, and in different bands, allows an evaluation of the degree of change in land cover that has taken place between different passages, and the difference in response from the same targets to different wavelengths, respectively. For instance, from the presence of red and yellow in the difference images in Figure 3.7 (b) (corresponding to band 4), it can be inferred that significant differences have occurred in the areas that display these colours, between passages acquired at 10/07 and 24/06, and 10/07 and 08/06. As band 4 has high land/water contrast (refer to Table 2.1), these changes may have been caused by the occurrence of rainfall, or the application of irrigation on, or shortly before 10/07. Note that these changes do not show as pronouncedly in the sub-images in either bands 3 or 5.

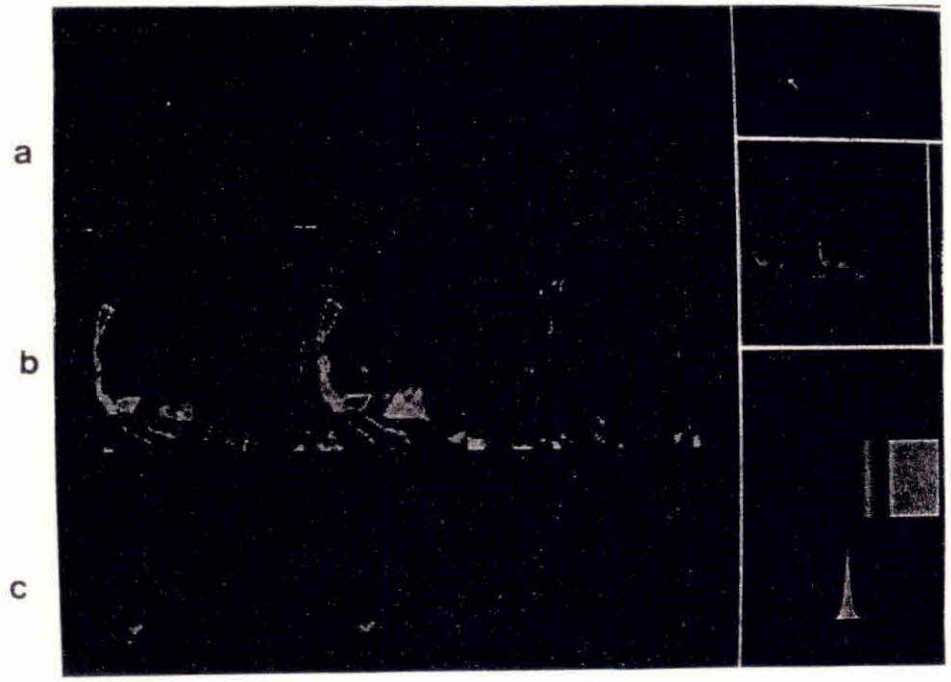

Figure 3.7: Difference images for data acquired at different times in bands (a) 3 (b) 4 (c) 5. From left to right: 24/06 data from 10/07 data (+128); 08/06 data from 10/07 data (+128); 08/06 data from 24/06 data (+128).

Figure 3.8: Difference images for data acquired in different bands at (a) 10/07; (b) 24/06; and (c) 08/06. From left to right: band 3 data - band 4 data (+128); band 3 data - band 5 data (+128); and band 4 data - band 5 data (+128).

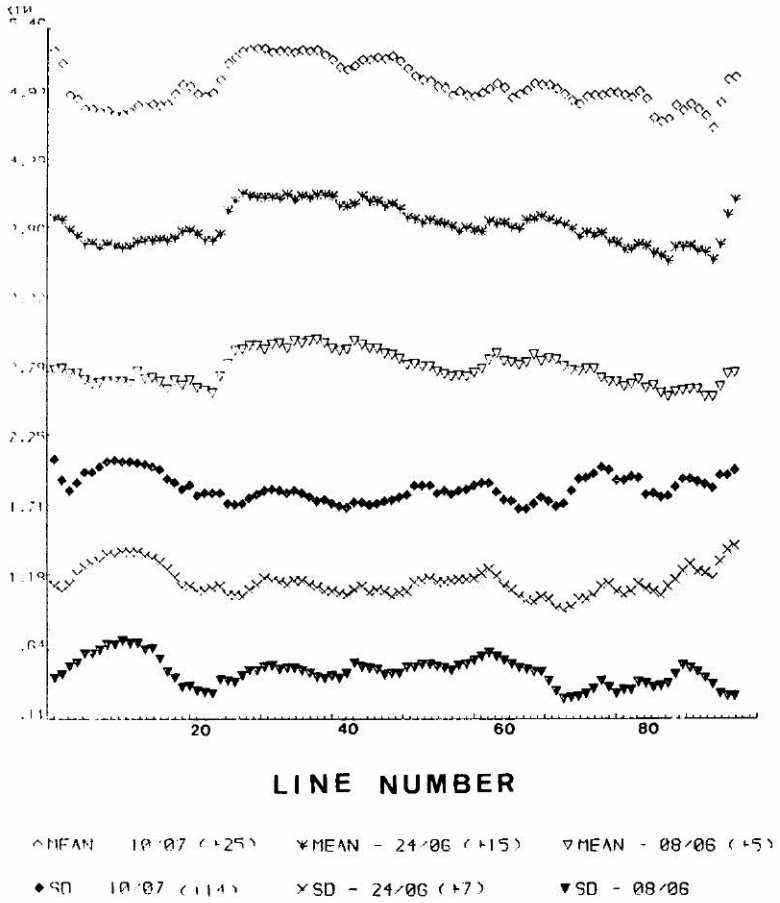

Figure 3.9: Plot of the line means and line standard deviations for the sub-images in band 3, acquired at dates 08/06, 24/06 and 10/07.

The plots of line means and line standard deviations for images acquired in different bands and the same date, and for images acquired at different times in the same band (Figures 3.9, 3.10, and 3.11), may also provide valuable information about the differences in response, and changes in land cover, respectively.

Figures 3.9, 3.10, and 3.11 display the plots of line means and line standard deviations of the sub-images acquired at the three dates, in bands 3, 4 and 5, respectively. A constant has been added to each set of line means and line standard deviations, to better discriminate these plots. The constant, if added, is shown in parenthesis in the legend of each figure, alongside the symbol used to represent the corresponding means, or standard deviations. The notation SD in Figures 3.9, 3.10, 3.11, 3.18, and 3.19 stands for standard deviation.

The uniform behaviour of the line means and line standard deviations in sub-images at different dates in all bands, displayed in Figures 3.9, 3.10, and 3.11,

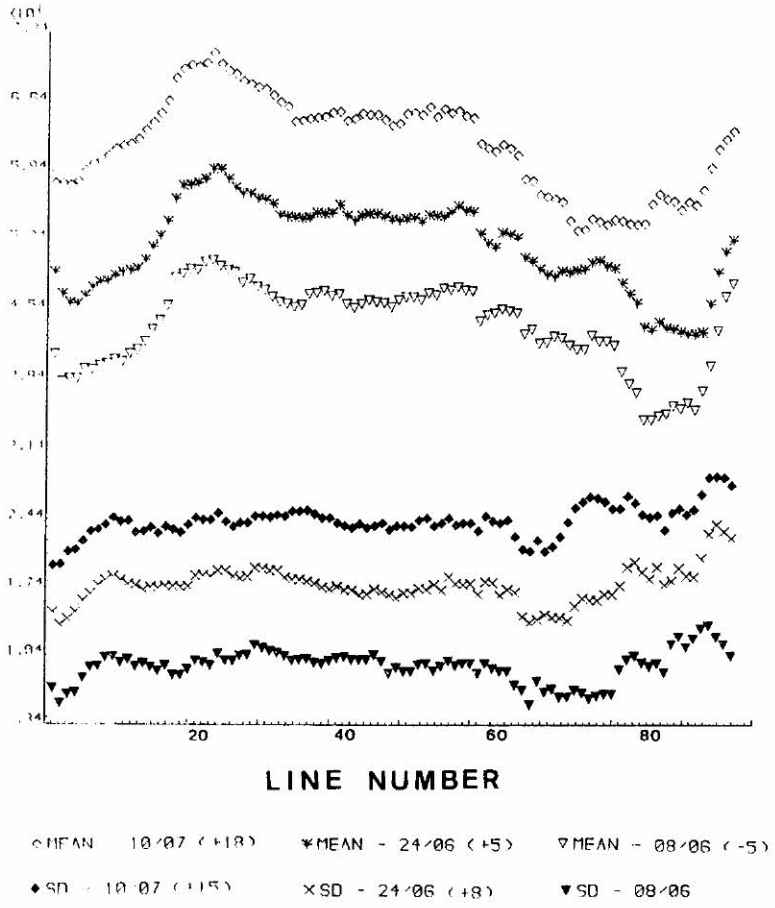

Figure 3.10: Plot of the line means and line standard deviations for the sub-images in band 4, acquired at dates 08/06, 24/06 and 10/07.

suggests that few changes in land cover have occurred between the different dates of imaging. The progressive decrease in homogeneity from band 3, to band 5, can also be inferred from these figures.

The increase in the means, in the first 15 lines of Figure 3.10, for band 4, corresponding to a decrease in the corresponding lines in Figure 3.11, for band 5, suggests a progressive replacement of bare soil by vegetation, since bands 4 and 5 are respectively sensitive to vegetation and soil reflectance.

From the plots in Figures 3.9, 3.10, and 3.11, and also from Figures 3.7 and 3.8 it is expected that data on sub-images acquired at different dates but in the same band have a stronger correlation than data in sub-images in different bands but at the same date. This is confirmed by the correlations given in Tables 3.2 and 3.3, respectively. Table 3.2 gives the correlation rd_{ij} between data acquired at different dates for each band. The subscripts i and j, $i, j = 1, 2, 3$ refer to the

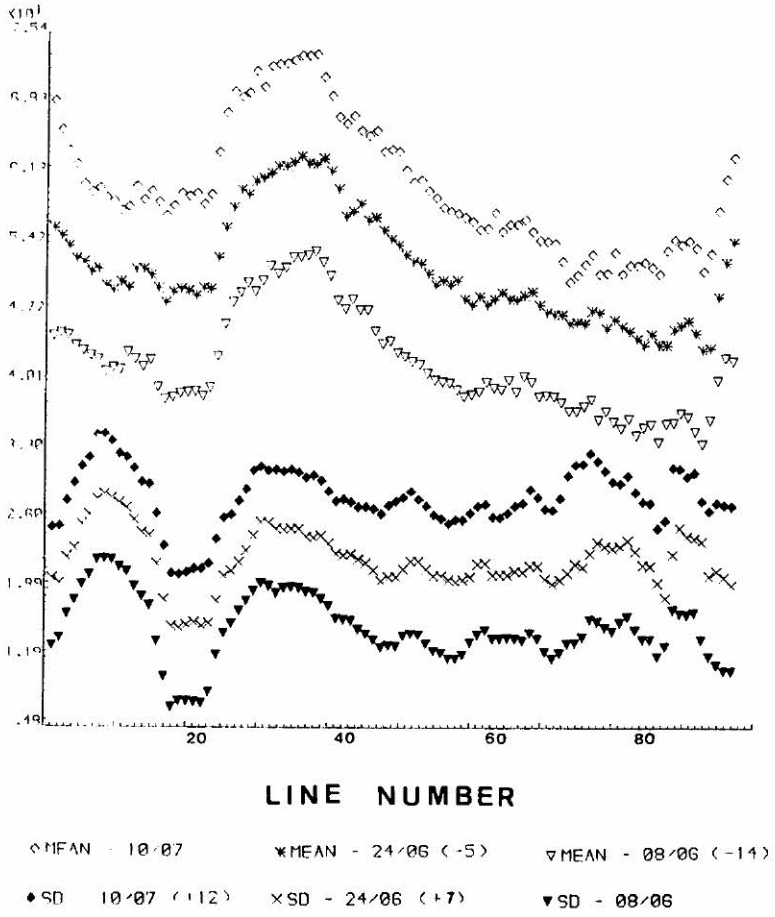

Figure 3.11: Plot of the line means and line standard deviations for the sub-images in band 5, acquired at dates 08/06, 24/06 and 10/07.

dates 10/07/86, 24/06/86, and 08/06/86, respectively.

These correlations show that the data at the different times are all well correlated, especially those in band 5, due to the greater heterogeneity of data in this band. This greater heterogeneity is explained by the presence of different types of ground cover which respond very distinctively in this wavelength.

The correlation between bands, for each date, is given in Table 3.3, where rb_{kl}, $k, l = 3, 4, 5$ refers to bands 3, 4 and 5, respectively.

Table 3.3 indicates that data in bands 3 and 5 are well correlated, and that data in band 4 are poorly correlated with data in both bands 3 and 5. The higher correlation between bands 3 and 5 in this data set may be justified on the grounds that these bands are more sensitive to soil reflectance, whereas band 4 is more sensitive to soil absorbance.

Table 3.2: Correlation between data acquired at different dates in bands 3, 4, and 5.

rd_{ij}	Band 3	Band 4	Band 5
rd_{12}	0.864	0.834	0.937
rd_{13}	0.764	0.710	0.913
rd_{23}	0.817	0.853	0.920

Table 3.3: Correlation between data in different bands on the 3 dates.

rb_{kl}	DATES		
	10/07	24/06	08/06
rb_{34}	0.081	0.012	−0.126
rb_{35}	0.719	0.705	0.760
rb_{45}	0.146	−0.016	−0.122

The fact that pixels in TM imagery are spatially autocorrelated, i.e., sites closer in geographical space tend to have similar reflectance values, has been reported before (e.g. Labovitz *et al.*, 1982; Ulaby, 1986; Mather, 1987). The plots of the sample autocorrelations, which are now presented, confirm this observation.

The sample autocorrelations at lags g, h, where $g = -3, \ldots 3$, and $h = 0, \ldots, 19$ for the data acquired at 10/07/86 in bands 3, 4 and 5 are displayed in Figure 3.12 (a), (b) and (c), respectively. Tables A.1, A.2, and A.3 in Appendix A give these autocorrelation values, and some additional ones, for data in bands 3, 4 and 5, respectively. Values for $h < 0$ are not provided since $r_{g,h} = r_{-g,-h}$ for all g, h.

The sample autocorrelation values for the data acquired at other dates in bands 3, 4 and 5, are very similar to the ones presented in Figure 3.12, and so are not given here.

From Figure 3.12 it can be seen that the sample autocorrelations are slow decaying in all bands. However, the autocorrelations in the most homogeneous band 3 decay faster than those in the more heterogenous bands 4 and 5. Although

the autocorrelations in band 3 decay more rapidly than those in band 4, this role is reversed at larger lags. Figure 3.13 shows the plot of $r_{-1,h}, r_{-h,1}, r_{-2,h}$ and $r_{-h,2}$, for $h = 0, \ldots, 19$, for the data acquired on 10/07/86 in bands 3, 4 and 5. From the figure it can be observed that the sample autocorrelations at small lags are approximately symmetric about both axes, that is, $r_{g,h} \approx r_{g,-h} \approx r_{-g,h} \approx r_{-g,-h}$. This is also observed on the data acquired at the other two passages.

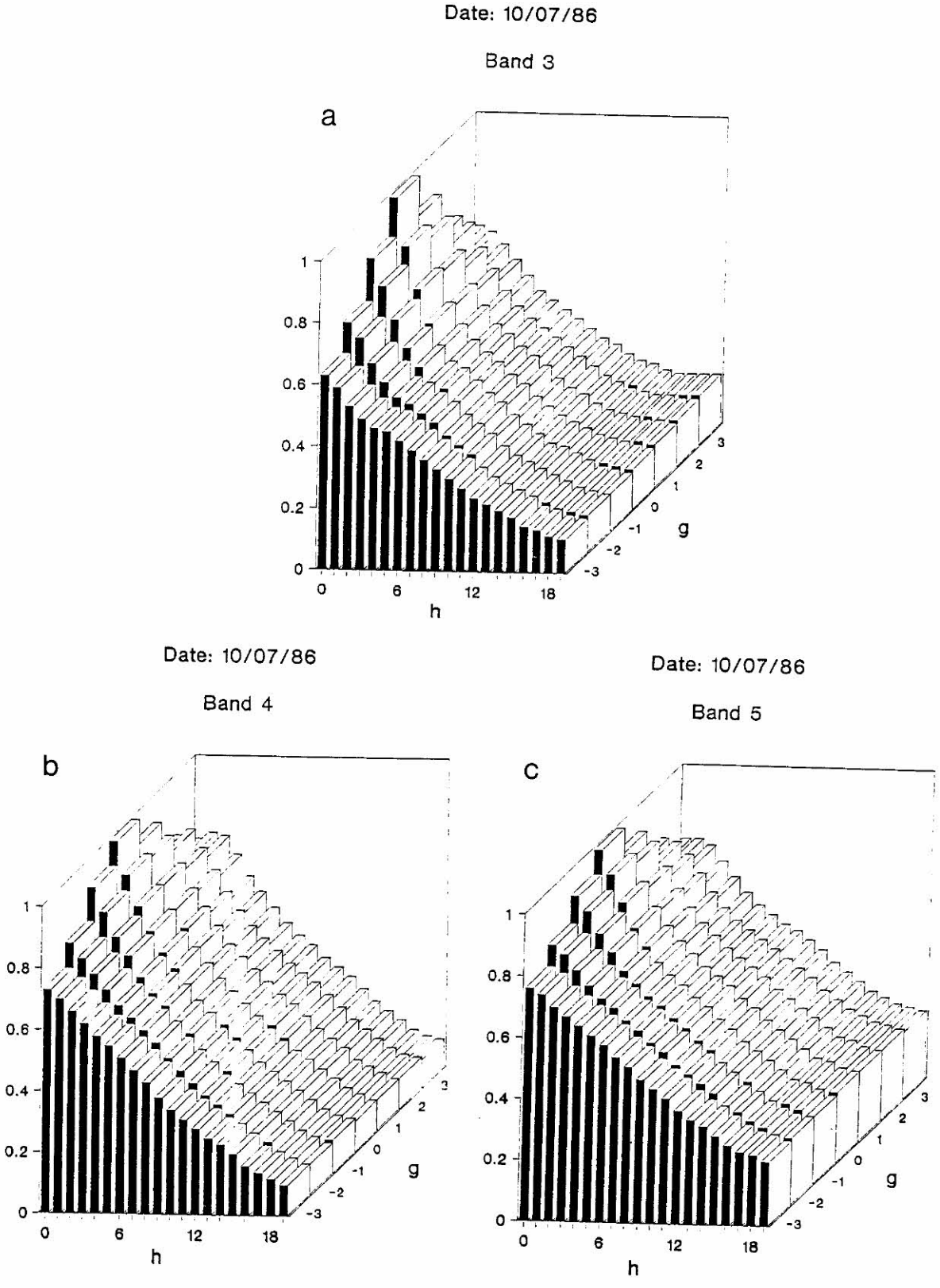

Figure 3.12: Sample autocorrelations, $r_{g,h}$, $g = -3, \ldots, 3$ and $h = 0, \ldots, 19$, for the data in the sub-images acquired at 10/07/86 in bands (a) 3; (b) 4; and (c) 5.

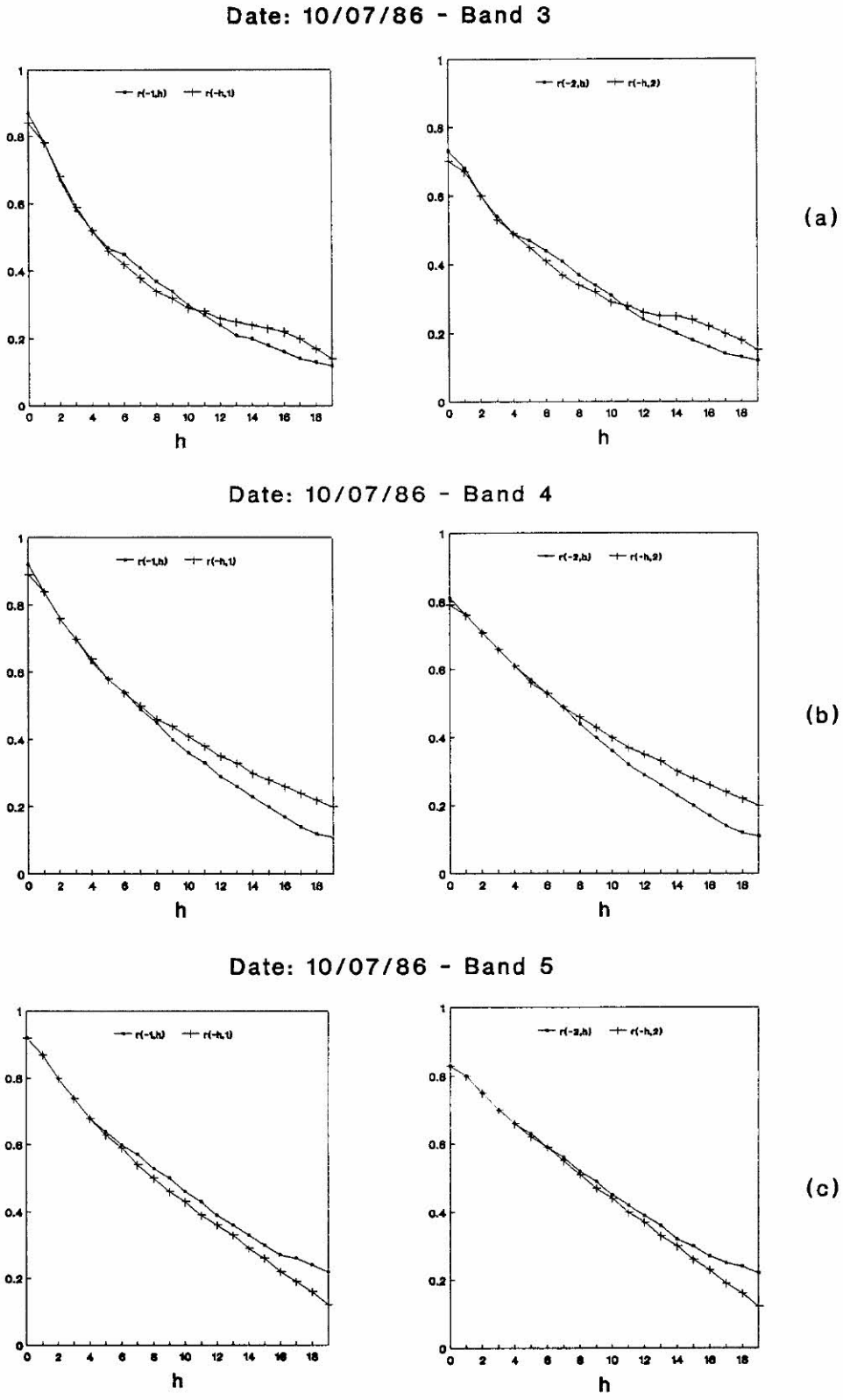

Figure 3.13: Plot of sample autocorrelations for the data on the sub-images acquired at 10/07/86 in bands (a) 3; (b) 4; and (c) 5. Left: $r_{-1,h}$ and $r_{-h,1}$; Right: $r_{-2,h}$ and $r_{-h,2}$, $h = 0, \ldots, 19$.

3.3.2 Second Data Set

3.3.2.1 Introduction

Data for the second data set, herewith referred to as D_2, were made available in bands 4 and 5 of TM Landsat 5 on thirteen dates of imaging between 1984 and 1990. The area is in São Paulo State, Brazil. Its approximate location on the map of Brazil is given in Figure 3.14.

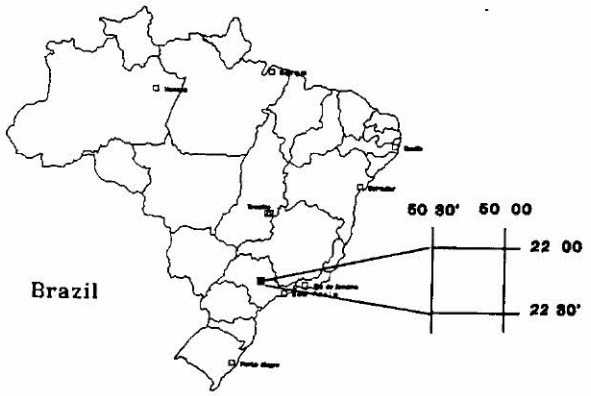

Figure 3.14: Approximate location of the test site for the second data set.

As for D_1, the impracticality of working with data from a whole image made the selection of a sub-area necessary. In this case one was chosen, corresponding to a sub-image of 100 by 100 pixels. The land cover was identified from a classification map of the area, provided by INPE, and consists mainly of reforestation and low density vegetation. The classification map was produced using the sub-images acquired at 04/07/89 and 20/07/89.

Despite the availability of a large number (13) of images, most of them are months, or even years apart. Since some of the methods proposed in Chapter 4 for the replacement of defective scan lines in an image require information over corresponding areas on images acquired at close passages, only the 6 images in D_2 that fulfill this requirement are considered. Each sub-image in D_2 is henceforth coded $D_2(ij)$, where $i = 1, 2, 3, 4, 5, 6$ refers to dates 09/09/90, 08/08/90, 20/07/89, 04/07/89, 17/07/88, 01/07/88, respectively, and $j = 4, 5$, refers to bands 4 and 5, respectively. The relevant pairs of sub-images, for $j = 4, 5$, are

$i = 1$ and $i = 2$, $i = 3$ and $i = 4$, and $i = 5$ and $i = 6$, which are respectively 32, 16 and 16 days apart.

The statistics for the selected sub-images from D_2 are now given. As for D_1, these statistics are usually followed by visual interpretation of the corresponding sub-images.

3.3.2.2 Descriptive statistics of the data

Table 3.4 gives the mean, median, standard deviation (stdev), minimum and maximum [(m,M)], and the range of the data on the selected sub-images.

Table 3.4: Summary statistics of the selected sub-images from D_2.

Code	Mean	Median	Stdev	(m,M)	Range
$D_2(14)$	53.4	54	6.3	(28, 79)	51
$D_2(24)$	42.8	43	5.4	(17, 65)	48
$D_2(34)$	39.8	40	5.4	(17, 59)	42
$D_2(44)$	36.6	36	5.2	(21, 62)	41
$D_2(54)$	41.6	42	6.2	(22, 64)	42
$D_2(64)$	38.5	38	6.1	(15, 61)	46
$D_2(15)$	96.6	104	27.2	(32, 192)	160
$D_2(25)$	76.5	85	24.8	(18, 138)	120
$D_2(35)$	74.7	84	25.4	(18, 129)	111
$D_2(45)$	63.0	70	20.8	(14, 115)	101
$D_2(55)$	66.3	72	21.9	(15, 131)	116
$D_2(65)$	62.8	68	20.6	(14, 126)	112

From the ranges and the standard deviations given in Table 3.4, it is seen that data in band 4 are more homogenous than those in band 5, and that with the exception of $D_2(15)$ and $D_2(25)$, all the statistics displayed in Table 3.4 do not change significantly from passage to passage. The sub-images in band 4 and band 5, at the different dates, are displayed in Figures 3.15 and 3.16, respectively.

Large variations between the values of pixels that are geographically close also occur in the sub-images in D_2, especially those in band 5. For instance, the values

of the pixels in sub-image $D_2(15)$, in lines 59 and 60, intersected by column 1, are 100 and 49, respectively; those in the same lines, intersected by column 2, are 86 and 37. Other examples are given in Chapter 5, in Figures 5.19, 5.20, and 5.21.

The greater homogeneity of data in band 4, in contrast to those in band 5, is clear from the sub-images displayed in Figure 3.15 for band 4, and Figure 3.16 for band 5. Note that the range of the colours, in Figure 3.15, has been compressed to approximately 16-88, to enhance the contrast of the sub-images.

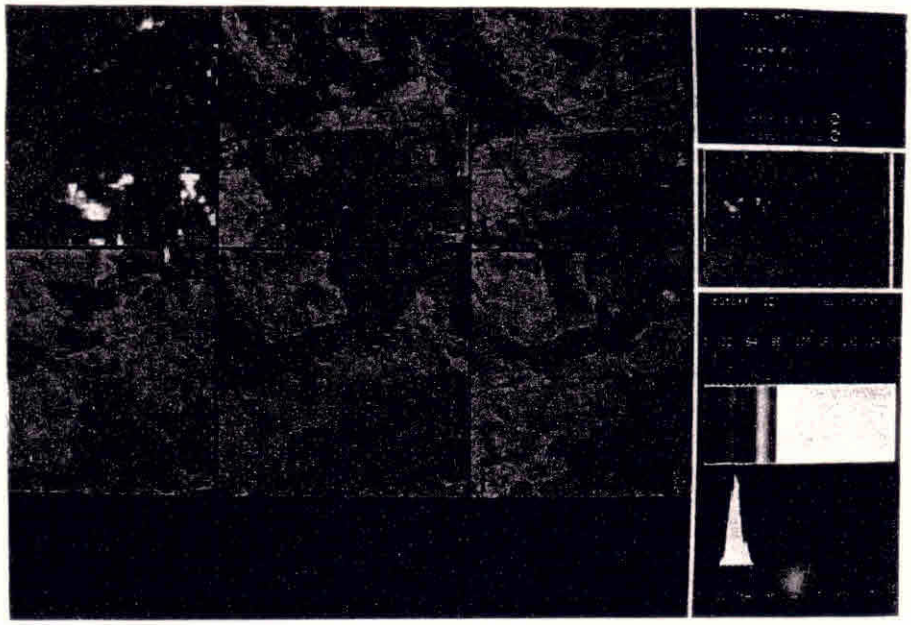

Figure 3.15: Frame of the selected sub-images in band 4, at different times of acquisition: 1. $D_2(14)$ 2. $D_2(24)$ 3. $D_2(34)$ 4. $D_2(44)$ 5. $D_2(54)$ 6. $D_2(64)$.

From Figure 3.15 it is seen that the colours cyan and magenta dominate in all sub-images, except $D_2(14)$. In band 4, the reforested areas show as magenta, thus being associated with low grey levels. The cyan colour indicates either the presence of bare soil, or soil covered with low density vegetation.

On the other hand, the greater sensitivity of band 5 to soil reflectance associates relatively high grey levels with bare soil. Thus, the presence of yellow in the sub-images shown in Figure 3.16 indicates bare soil whereas cyan also suggests soil with low density vegetation. Magenta in this band indicates the areas of reforestation, with predominance of green biomass (vegetation absorbance).

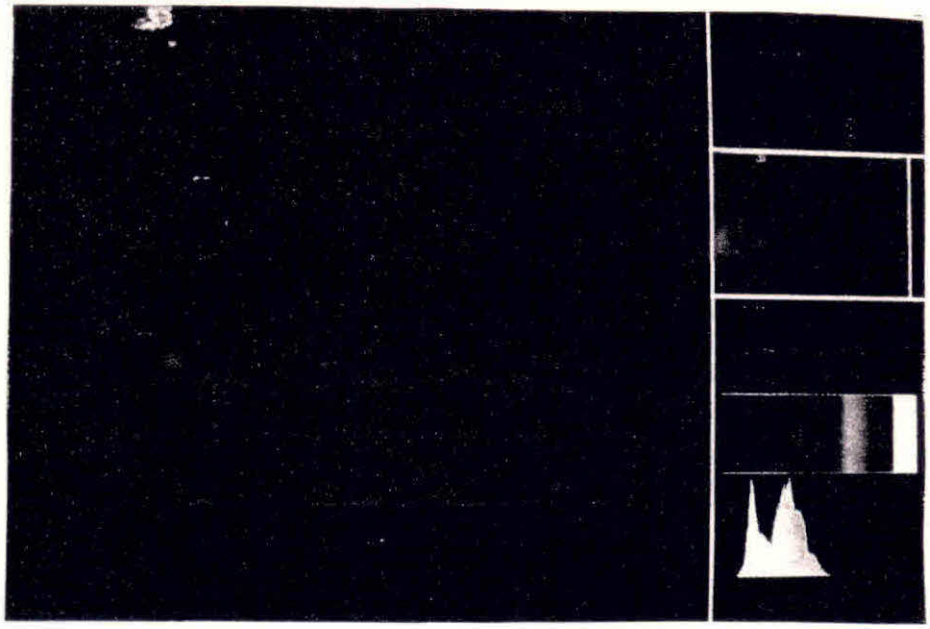

Figure 3.16: Frame of the selected sub-images in band 5, at different times of acquisition: 1. $D_2(15)$ 2. $D_2(25)$ 3. $D_2(35)$ 4. $D_2(45)$ 5. $D_2(55)$ 6. $D_2(65)$.

The contrast between the amount of biomass in the areas of reforestation and the areas of low density vegetation (grass) explains the bimodal distribution of the grey levels in this band.

Figure 3.17 is a representation of the sub-image in band 5, acquired at 09/09/90, and indicates the land use described above. Both letters **A** and **B** correspond to reforested areas, but **B** is associated with reforestation in an early stage; **C** denotes areas of soil covered with low density vegetation, whilst **D** represents the areas of very low coverage. **E** indicates bare soil.

The difference in mean grey level in sub-images $D_2(14)$ and $D_2(24)$, and $D_2(15)$ and $D_2(25)$, is possibly due to differences in soil moisture between the two dates of imaging. A possible explanation based on changes in land cover between the two passages is rejected when the sub-images from the two passages are compared visually. The plots of line means and line standard deviations for all selected sub-images also agree with the explanation of differences in soil moisture, rather than changes in land cover. These plots are given in Figures 3.18 and 3.19 for the six sub-images in band 4, and the six sub-images in band 5,

respectively. A constant has sometimes been added to a set of line means or line standard deviations, to better discriminate the plots corresponding to different passages. The constant, if added, is shown in parenthesis in the legend of Figures 3.18 and 3.19, alongside the symbol used to represent the corresponding mean, or standard deviation.

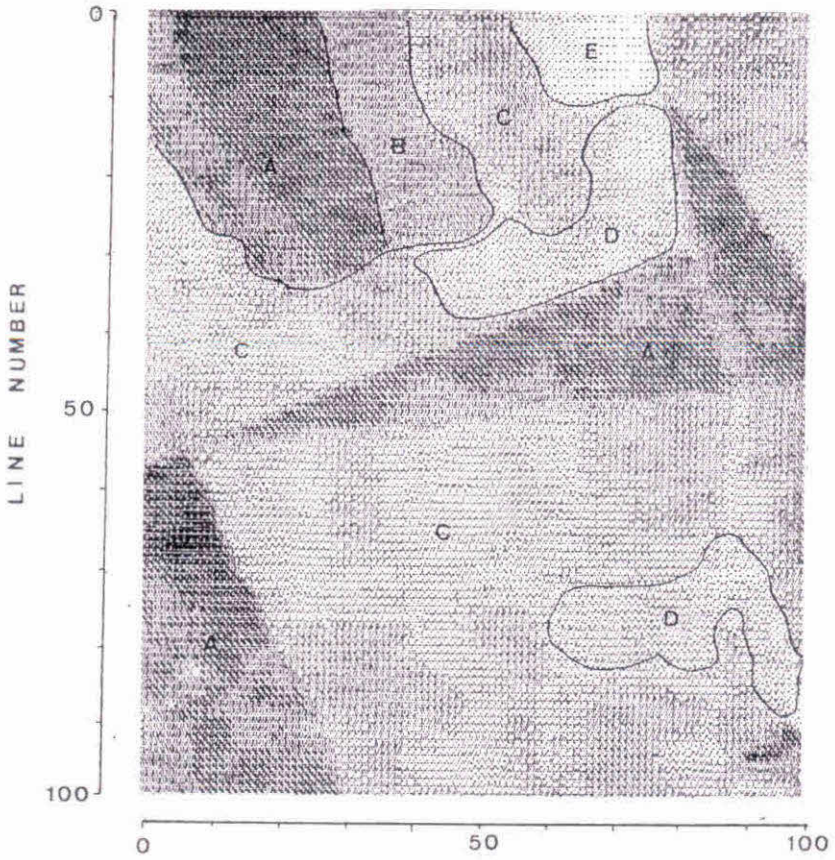

Figure 3.17: Representation of the sub-image acquired at 09/09/90 in band 5.

The plots in Figures 3.18 and 3.19 suggest that few changes in land cover occurred between the passages acquired at close dates (16/32 days apart).

The different response of the land cover, in different wavelengths, is also clear from these plots. The similar pattern displayed by all curves, for each band, indicates that the area has been used for the same purpose for at least the last 6 years, and that its main features have been preserved throughout these years. Visual inspection of the sub-images acquired at 10/08/85 in bands 4 and 5 (Figure 3.20), and those gathered at 08/08/90 in these bands [$D_2(24)$, $D_2(25)$ – see

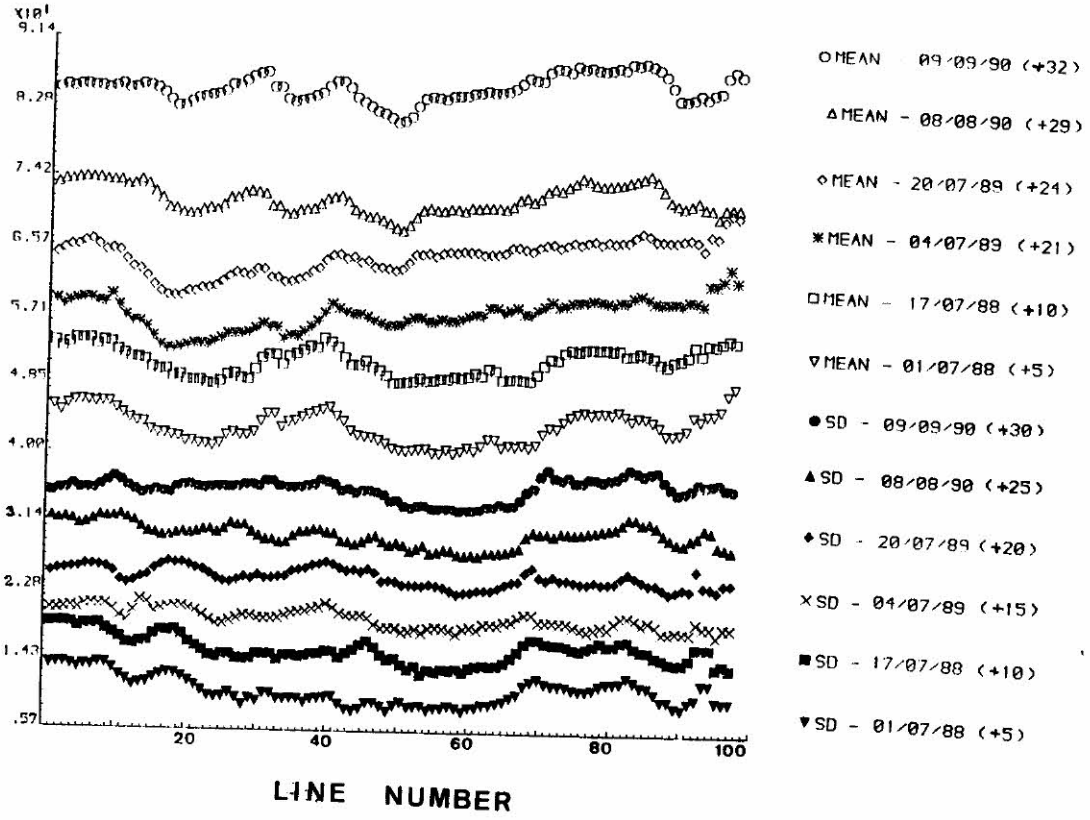

Figure 3.18: Plot of the line means and line standard deviations for the six sub-images in band 4.

Figures 3.15 and 3.16] shows that the main differences between these sub-images, are probably due to the process of deforestation. For instance, the top half of the sub-image in Figure 3.20 (b), corresponding to band 5, is dominated by the reforestation (shown in magenta), whereas the corresponding area on the sub-image in the same band, acquired at 08/08/90, has reduced areas with reforestation, low density vegetation, and small patches of bare soil (shown in magenta, cyan, and green, respectively). However, it is interesting to note that the structures on the ground are reasonably preserved, despite the 5 year gap between the two sub-images. The man-made features, stressed by the linear geometry of the patterns on the ground, change very little between all the images made available, and especially on those selected for this study.

The difference images obtained from sub-images acquired at close dates (16/32 days apart), in bands 4 and 5, are given in Figure 3.21 (a) and (b), respectively.

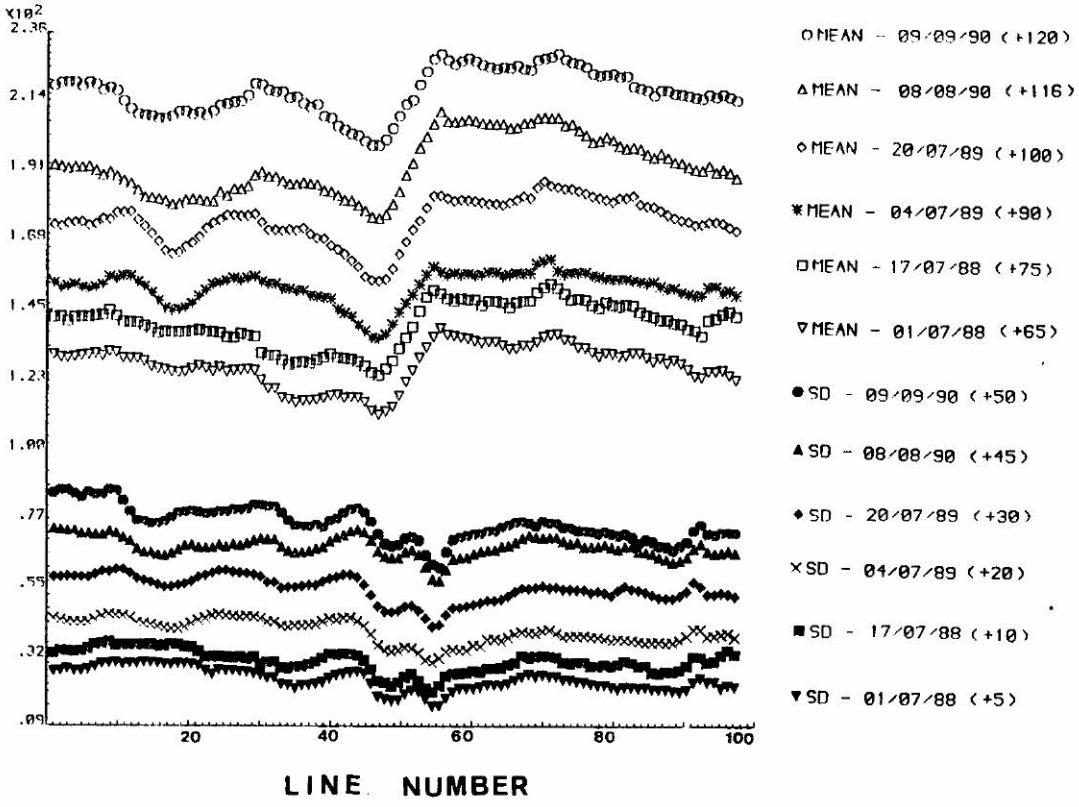

Figure 3.19: Plot of the line means and line standard deviations for the six sub-images in band 5.

Figure 3.22 shows the difference images obtained for each of the relevant pairs of sub-images acquired in different bands, on all six dates of acquisition.

From the difference images displayed in Figure 3.21 it is observed that few changes in land cover occurred between the passages at close dates (16/32 days apart). However, the distinct response of the same targets on the ground, to the different wavelengths, is very clear in the difference images shown in Figure 3.22.

The correlations, rd_{ij}, between data in sub-images acquired at different dates, given in Table 3.5, also indicate the close association between the data in the sub-images acquired at different dates. The subscripts $i, j = 1, 2, 3, 4, 5, 6$ refer to the dates as given previously.

From Table 3.5 it is noted that data in sub-images from consecutive passages ($i = 1$ and $i = 2$; $i = 3$ and $i = 4$; $i = 5$ and $i = 6$) are well correlated, and that the correlation is still good between data on sub-images 32 days apart [$D_2(14)$ &

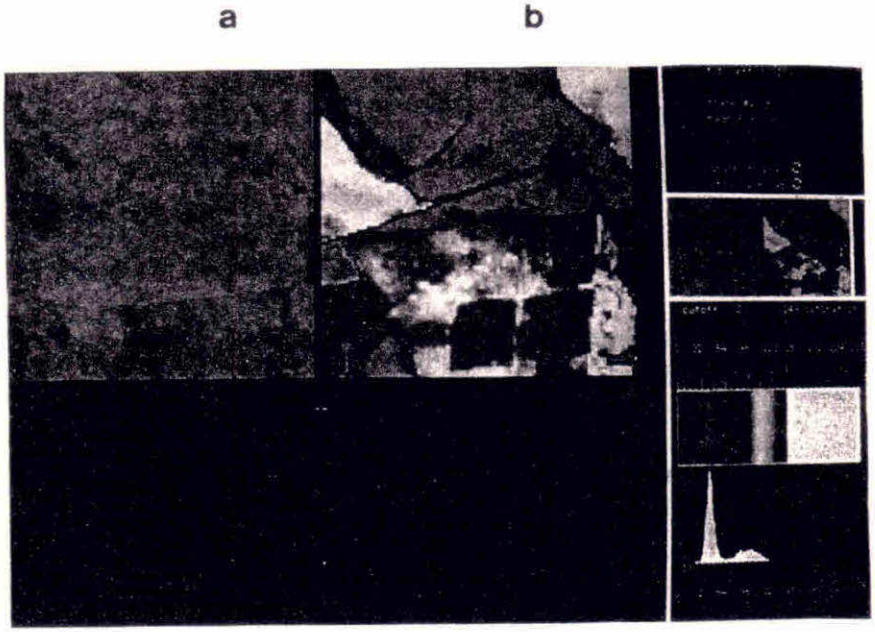

Figure 3.20: Sub-images acquired at 10/08/85 in bands (a) 4 (b) 5.

$D_2(24)$; $D_2(15)$ & $D_2(25)$]. The correlations are always higher for data in band 5 than in band 4. Even images which are one year apart [$D_2(25)$ & $D_2(35)$] are fairly well correlated ($rd_{23} = 0.81$). This may be justified by both the fairly constant type of land cover, and the greater heterogeneity of data in band 5.

The correlations, rb_{kl}, between data in bands 4 and 5 are given in Table 3.6, for all six chosen dates of imaging. The subscripts $k, l = 4, 5$ refer to bands 4 and 5, respectively. From these correlations it is seen that there is a moderate correlation between data in bands 4 and 5 at all passages, and that for any given passage the highest correlation between bands occurs between data in $D_2(14)$ and $D_2(15)$ ($rb_{45} = 0.58$). Comparison of the correlations displayed in Tables 3.5 and 3.6 shows that temporal information may provide a relevant source of knowledge when considering methods for the estimation of missing values in remotely sensed data.

The similarity of the sample autocorrelation functions of sub-images acquired at consecutive passages also supports this suggestion. The sample autocorrelations $r_{g,0}$, $g = 0, \ldots, 19$, for all sub-images in D_2 are shown in Figure 3.23.

Table 3.5: Correlation between data acquired at different dates in bands 4 and 5.

rd_{ij}	i											
	D_2	24	34	44	54	64	D_2	25	35	45	55	65
	14	0.81	0.54	0.45	0.54	0.50	15	0.96	0.77	0.74	0.70	0.69
	24		0.44	0.38	0.39	0.38	25		0.81	0.77	0.74	0.73
j	34			0.90	0.65	0.56	35			0.97	0.85	0.84
	44				0.62	0.57	45				0.81	0.81
	54					0.89	55					0.95

Table 3.6: Correlation between data in bands 4 and 5, at all passages.

rb_{kl}	l						
	D_2	14	24	34	44	54	64
	15	0.58	0.62	0.60	0.58	0.47	0.49
	25	0.39	0.44	0.55	0.53	0.43	0.46
	35	0.44	0.52	0.32	0.29	0.34	0.31
k	45	0.36	0.42	0.21	0.17	0.24	0.21
	55	0.56	0.56	0.40	0.37	0.30	0.30
	65	0.44	0.43	0.28	0.25	0.15	0.14

The similarity between pairs of consecutive sub-images, or sub-images acquired a month apart, is very clear in this figure. This similarity is also observed at lags $r_{0,h}$, $h = 0, \ldots, 19$.

As for D_1, the sample autocorrelations for all sub-images in D_2 are slow decaying, with those for sub-images in band 4 decaying faster than those in band 5. The sample autocorrelations at lags (g,h), $g = -3, \ldots, 3$ and $h = 0, \ldots, 19$ are presented in Figure 3.24 (a) and (b) for the sub-images acquired at 09/09/90 in bands 4 and 5, respectively. The values are given in Tables A.4 and A.5 in Appendix A. These tables also include correlations at greater lags. It is interesting to note that for the sub-images in this data set, the sample autocorrelations in the south east direction decay faster than those in the north east direction, especially for the data in band 5. Thus, $r_{g,h} \not\approx r_{-g,h}$ for all g, h.

For some of the sub-images in band 4 [$D_2(14)$ and $D_2(24)$], $r_{g,h} \approx r_{h,g}$ for

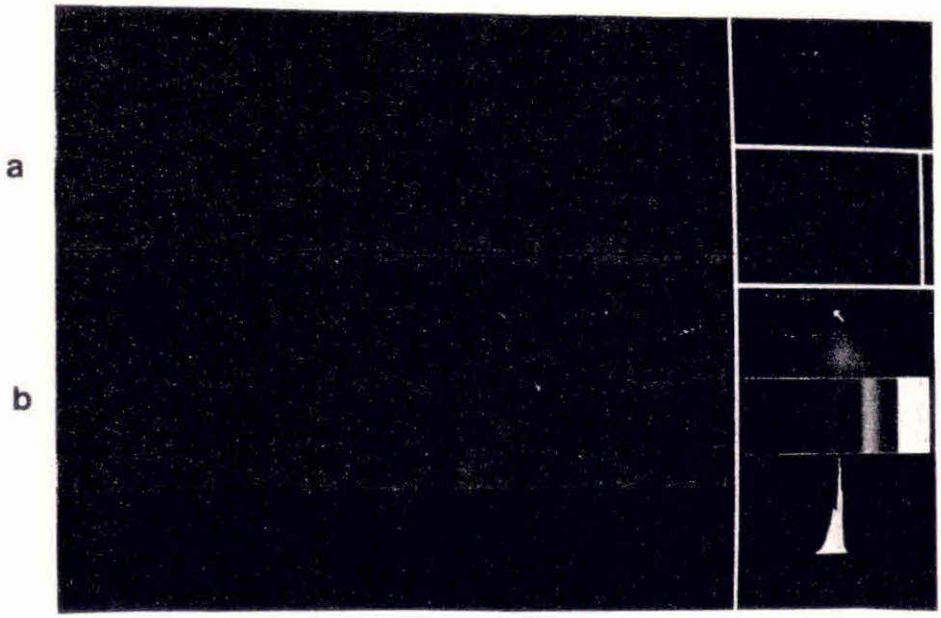

Figure 3.21: Difference images for the relevant pairs of sub-images acquired at different dates in bands (a) 4 (b) 5.
1. $D_2(14) - D_2(24)(+128)$; 2. $D_2(34) - D_2(44)(+128)$; 3. $D_2(54) - D_2(64)(+128)$;
4. $D_2(15) - D_2(25)(+128)$; 5. $D_2(35) - D_2(45)(+128)$; 6. $D_2(55) - D_2(65)(+128)$.

$0 \leq g \leq 19$ and $0 < h < 8$. The plots of the sample autocorrelations, $r_{g,h}$, at some selected lags ($g = -2, -1$ and $h = 0, \ldots, 19$), are presented in Figure 3.25 for the sub-images acquired at 09/09/90 in bands 4 and 5, respectively. For all other sub-images in band 4, and all sub-images in band 5, $r_{g,h}$ is not similar to $r_{h,g}$.

All sub-images in D_2 have been corrected at INPE for a systematic defect that affected lines 33, 65 and 97 of the TM images in all bands. The cause of the defect has not yet been discovered. The intriguing fact is that it affects data in all bands, and exactly the same lines on all six sub-images available between 1988 and 1990. In some of these sub-images the defect shows as a whole sequence of spurious values, which have been replaced at INPE by the values in the line immediately above. In others the defect shows as intermittent sequences of spurious values, and in this case only the spurious pixel values have been replaced by the corresponding ones in the line immediately above.

Unfortunately, this problem was identified very late in the course of this re-

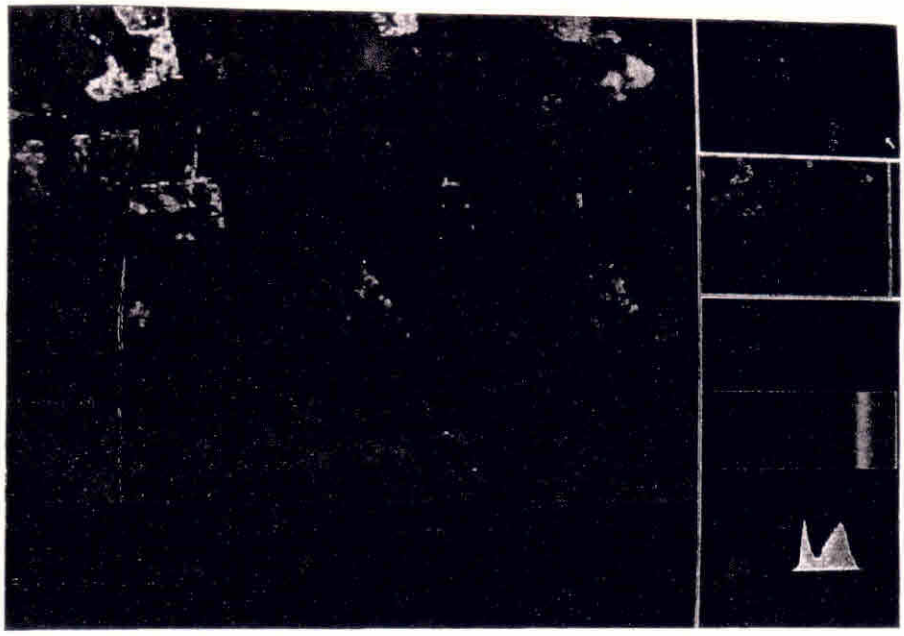

Figure 3.22: Difference images for the relevant pairs of sub-images, acquired in different bands. 1. $D_2(14) - D_2(15)(+128)$; 2. $D_2(24) - D_2(25)(+128)$; 3. $D_2(34) - D_2(35)(+128)$; 4. $D_2(44) - D_2(45)(+128)$; 5. $D_2(54) - D_2(55)(+128)$; 6. $D_2(64) - D_2(65)(+128)$.

search, preventing the possibility of a more sensible treatment of the data on these 'defective' lines. Throughout this dissertation these data have been treated as correct, and all the analysis of the data include them as such. However, it is not expected that these repeated lines will introduce too much bias in the results in Chapters 4 and 5, for the following reasons: in Chapter 4 the results are the average performance of the methods using all lines in the sub-images (a total of 10000 pixel values), and 300 values represent too small a fraction of values to have any significant role in the overall results; in Chapter 5, when a different approach is used to evaluate the perfomance of the methods, data in line 33 are never used, whereas those in lines 65, or 97, are included with data from 9 more lines. Moreover, in most sub-images, line 97 is not entirely 'defective', and only a few pixel values are replaced by those in the line immediately above.

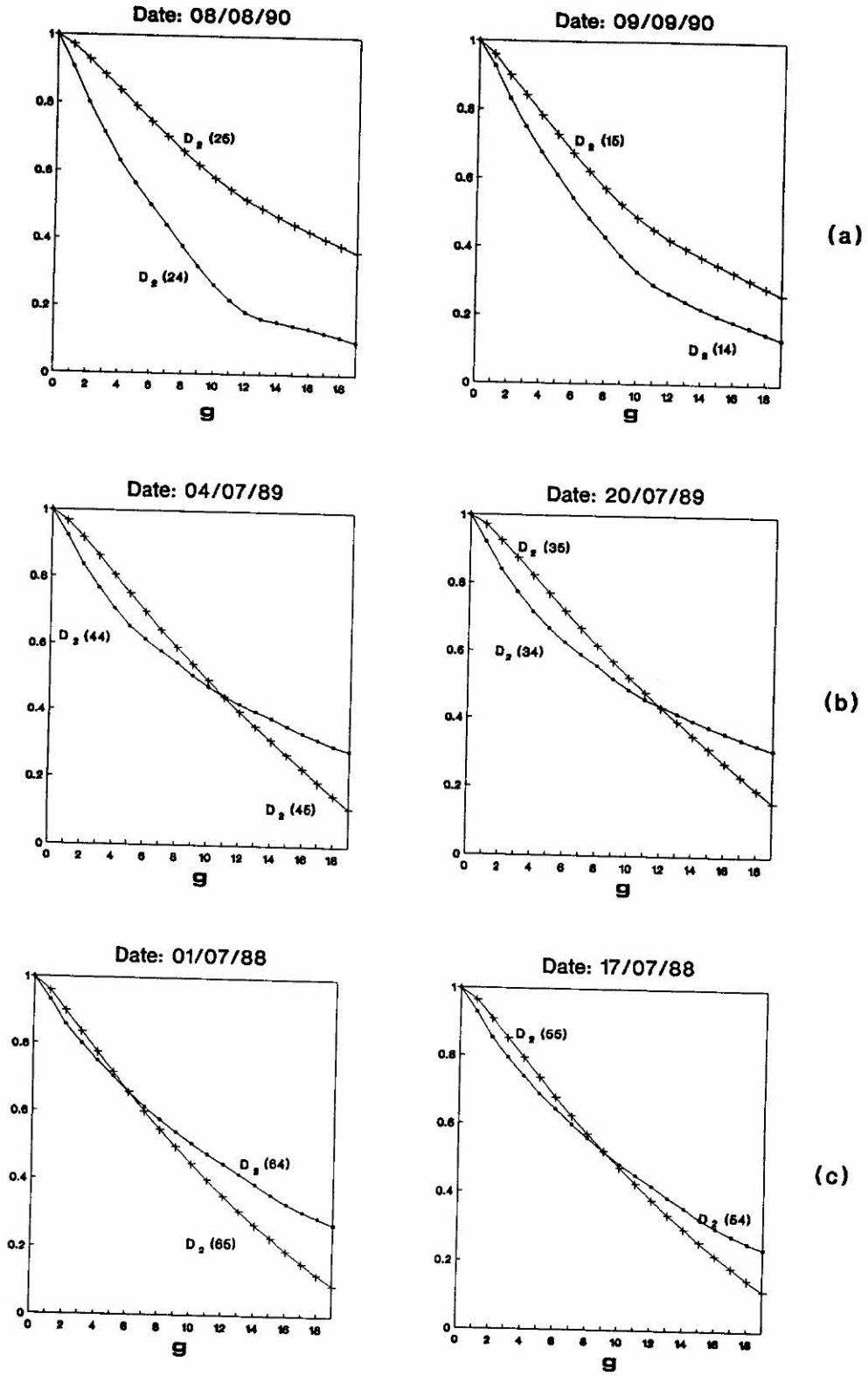

Figure 3.23: Sample autocorrelations, $r_{g,0}$, $g = 0, \ldots, 19$, for the data in the relevant pairs of sub-images from D_2, in bands 4 and 5, acquired at (from left to right): (a) 08/08/90 and 09/09/90; (b) 04/07/89 and 20/07/89; and (c) 01/07/88 and 17/07/88.

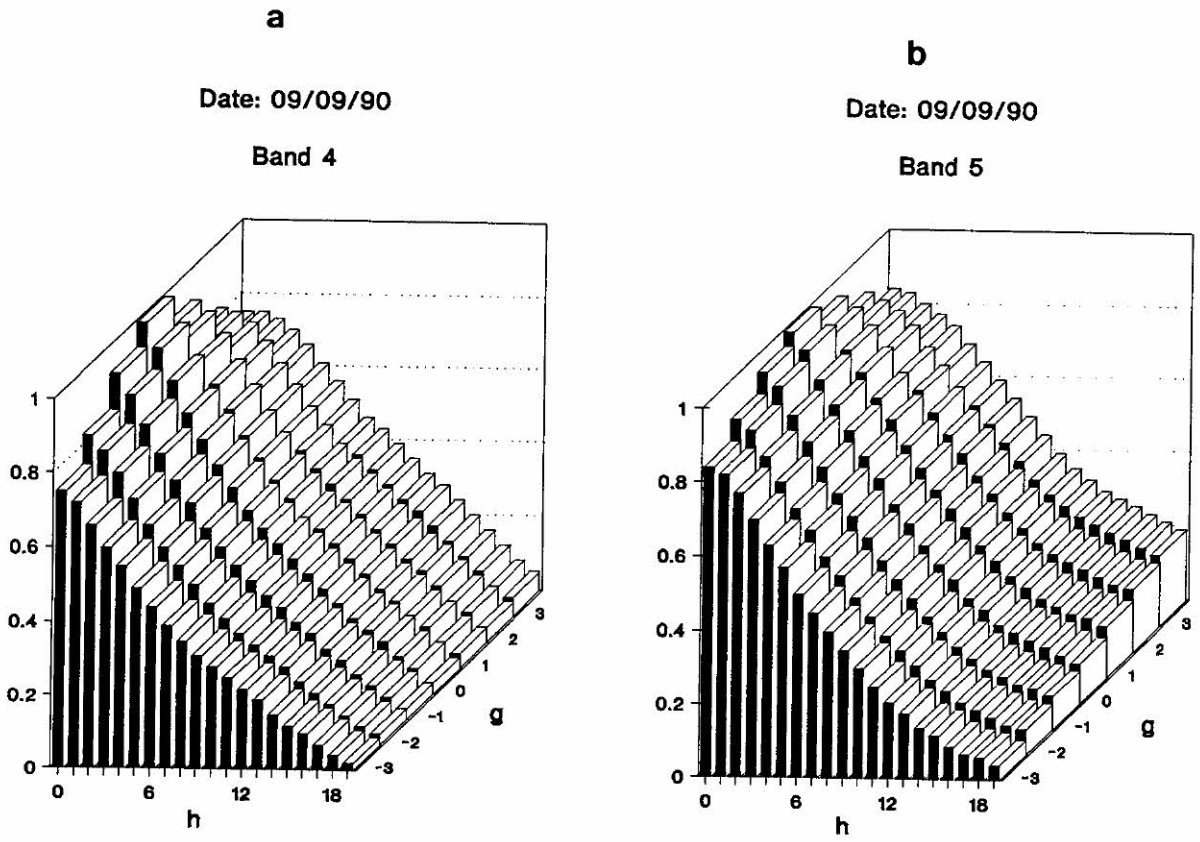

Figure 3.24: Sample autocorrelations $r_{g,h}$, $g = -3, \ldots, 3$ and $h = 0, \ldots, 19$, for the data in the sub-image acquired at 09/09/90 in bands (a) 4 and (b) 5.

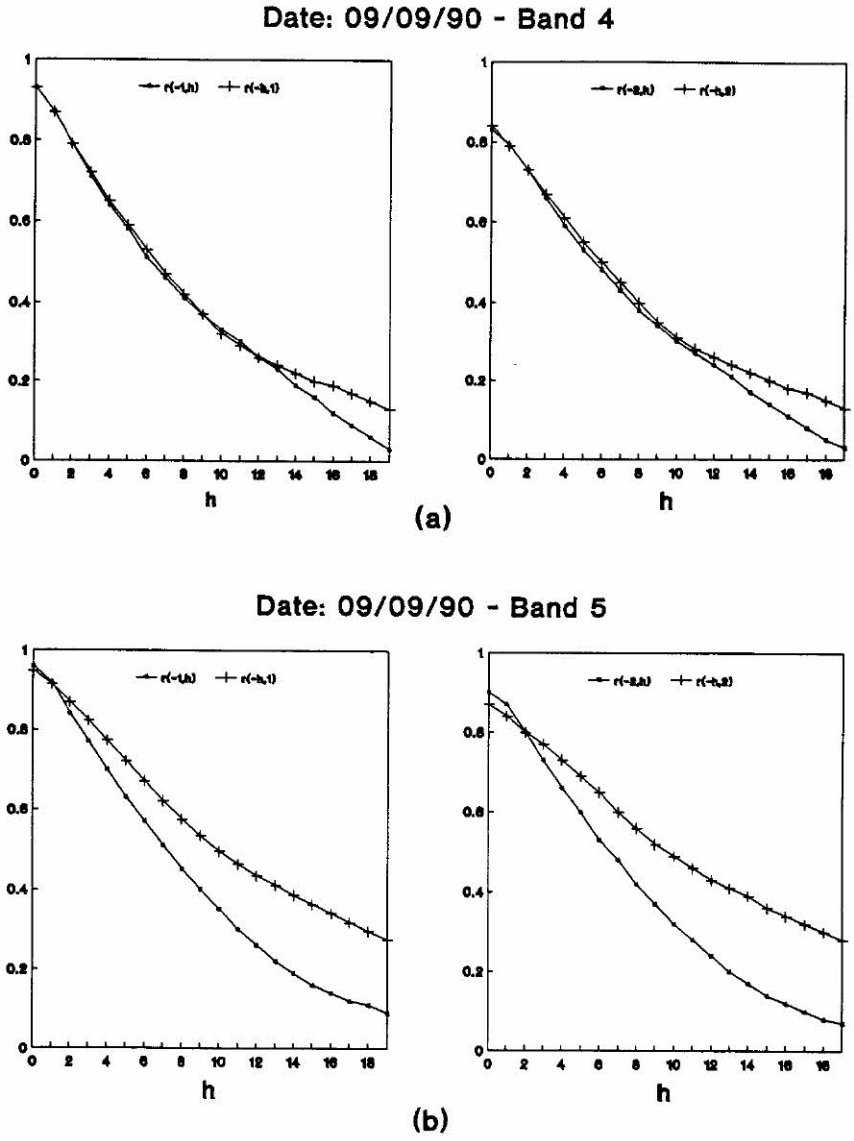

Figure 3.25: Plot of sample autocorrelations for the data on the sub-images acquired at 09/09/90 in bands (a) 4 and (b) 5. Left: $r_{-1,h}$ and $r_{-h,1}$; Right: $r_{-2,h}$ and $r_{-h,2}$, $h = 0, \ldots, 19$.

Chapter 4

Estimation of Missing Values from Line dropout

4.1 Introduction

In this chapter the estimation of missing values due to detector failure is addressed using relatively simple methods. As already described in Chapter 2, noise can be introduced in the digital data when a detector partially (or entirely) fails, causing a number of adjacent pixels along a line (or an entire line) to contain sequences of spurious values of zero, which show as systematic black stripes across the digital image. The problem is commonly referred to as line dropout (or line drop), and may also arise due to errors associated with the transmission and reception of data, or in the reproduction of compatible computer tapes (CCT's).

As the TM Landsat has 16 detectors in each of its spectral bands, which record data simultaneously for 16 scan lines, the failure of one detector causes the TM imagery to have a systematic defect every 16^{th} line, until the detector is fixed.

If caused by other types of error, data from the affected scan lines may contain intermittent sequences of spurious values, which show as segments of black stripes on the digital image.

Whatever the cause, line dropout disturbs the visual examination and interpretation of the image, and leads to unreliable statistics of the image, if these are based on pixel values. The inclusion of spurious values of zero in the computation of the image statistics causes the overall mean to be underestimated, and

the overall variance to be overestimated. This is less evident in images over areas of low radiance ground cover, in view of their low pixel values.

The estimation of missing values from line dropout is usually addressed by replacing the missing values in the faulty line with the values from the line immediately above it. This practice was adopted at NASA, and is currently in use at INPE. Although computationally simple, the duplication of the line above the 'faulty' one may not be the most appropriate method, and '*can cause very observable distortions in the final image products, especially images of high contrast cultural features*' (Bernstein *et al.*, 1984).

In this chapter the performances of this, and other methods for the replacement of the missing scan lines on an image are evaluated. Some of these methods have already been proposed in the literature, and are introduced in section 4.2. Other new approaches are presented in section 4.3. They are all computationally simple methods that can be implemented on a routine basis, during the preprocessing stage of digital image processing. In Chapter 5 other approaches are proposed, which use spatial statistical models.

For certain types of application, accurate estimation of the missing values may be important. However, factors such as computational complexity, easiness of implementation, and speed cannot be overlooked, in view of the large quantities of remotely sensed data that need to be processed. Also, some methods might require information that is not readily available, as when multitemporal information is used. In any case, it seems important to contrast the estimates obtained from relatively simple methods with those obtained from more complex, statistical methods, to see if more complicated methods are significantly better.

There has not been a thorough investigation of all the existing methods on the same image. Bernstein *et al.* (1984), for instance, carried out an investigation using TM data in bands 1 and 2 from two Landsat-4 subimages, one that includes a stadium, and the second an airport. They show the replacements obtained from duplication of the line above a failed detector in band 2, in a 16 by 16 pixels subscene comprising the stadium, and note that the 'donut-shaped' stadium appeared as a 'horseshoe'. They report the observation of similar distortions on the airport subimages.

They also note that:

'It has been suggested that the ground processing, instead of merely

> replacing the failed detector with the line above, should linearly interpolate between the line above and the line below to calculate the failed detector line. This does not solve the problem... Even interpolation with higher order curves, such as quadratic fit, are of no help.'

In view of the unsatisfactory results obtained from the single band methods of adjacent line replacement and linear interpolation, Bernstein *et al.* (1984) suggested three methods that use information from another band. They implemented the algorithms on the sub-images containing the stadium, and the airport, and reported that excellent results were obtained. In their paper, only the visual replacements obtained from line replacement, linear interpolation, and their three methods are presented for the sub-image containing the stadium. Bernstein *et al.* (1984) do report that a detailed examination of the replacement of the failed detector lines still showed some defects with the template algorithms, but that they are not as extreme as the defects observable with adjacent line replacement. Finally, they conclude that:

> 'if you wish to replace a failed detector with another detector's output and are concerned with maintaining the shape of geometric features, you are better off using the same detector's output from a nearby band than a nearby detector's output from the same band.'

Fusco & Trevese (1985) discuss the effects of the application of line replacement, linear interpolation, and one of the methods proposed by Bernstein *et al.* (1984) (algorithm 2) in the replacement of missing scan lines in several 64 by 64 sub-scenes extracted from two Landsat-4 TM images: one containing fields and a portion of river, and another of the centre of Rome. They also proposed two alternatives to algorithm 2, which were applied to reconstruct entire sub-scenes, where every line was sequentially replaced by the values estimated from their methods. The root mean square residual was used as a performance indicator for these methods, although Fusco & Trevese (1985) note that their conclusions were not drawn solely on the results obtained for this measure. One of other measures investigated was the correlation between the data in the entirely reconstructed sub-scenes, and those in the original sub-scenes.

With respect to the methods of line replacement, linear interpolation, and algorithm 2 of Bernstein *et al.* (1984), Fusco & Trevese (1985) note that:

- 'the replacement of the missing line with the contiguous line ... destroys some geometric structures';
- 'the average of two contiguous pixels improves the radiometry but still destroys some structures';
- 'the addition of a second (correlated) band reduces the error and preserves the geometric structures present'.

One of the methods they propose is only slightly different, in form, from algorithm 1 in Bernstein *et al.* (1984), and uses the slope (P) of the straight line regression of corresponding values on the sub-image and on the template band (a band that is fairly well correlated with the defective band). They concluded that the use of P, as defined in their method, 'always gives an error closer to the minimum', based on the values they have obtained for the root mean square residual, and the correlation between the reconstructed sub-scenes, and the original ones.

Their second method uses the slope (p) of the straight line regression of the 3 values above and the 3 values below the 'missing one', on corresponding values in a template band. If the local variance of the values on the template band are close to zero, this slope is set equal to P. They investigated the effect, on the root mean square measure, of the use of different thresholds for the local variations of the values in the template band, below which p was set equal to P. In one of the thresholds defined by Fusco & Trevese (1985) the difference between the pixel values in the template band, which are above and below the one corresponding to the missing value, was set equal to zero; in another, this difference was set equal to 8. They concluded that the values of the root mean square residual, under both assumptions, did not differ much.

Fusco & Trevese (1985) reported that this algorithm generally reduces the error with respect to their previous method, but that:

> 'in the presence of uniform terrain, the local calculation of the inclination p does not improve the error with respect to the case in which the inclination of P is appropriately fixed, while it could significantly reduce the error where large local variances occur. Therefore, by choosing an appropriate threshold, also function of the signal/ noise ratio of the band, we can obtain an improvement in reconstruction

with respect to the methods until now proposed, still limiting the computing resources.'

Finally, Guindon (1984), in a little known publication, considers two classes of algorithms for the estimation of missing data: the first one involves interpolation, whose principal disadvantage, as he points out, '*is the potential distortion of the image spatial frequency spectrum introduced by the interpolation process*'. The second class utilizes the observed grey level modulation in adjacent bands, to aid the estimation process. Guindon (1984) notes that the success of these techniques depends on the level of interband correlation.

Besides using linear interpolation, Guindon (1984) also examined interpolation using a 4-point cubic spline, and the method of line replacement. His investigation was carried out on three Landsat-4 TM images and on two simulated TM images (by degrading an airborne MSS scanner), and the test areas included a range of surface types (forest, ocean, mountains, agriculture, and urban coverage). The images were of much larger size than those used by Fusco & Trevese (1985), with an approximate size of 400 by 400 pixels. Data for the three Landsat-4 TM images were available in all six non-thermal bands, and in 4, and 5 bands for each of the simulated TM images. Guindon (1984) used the mean residual, residual standard deviation, and the largest absolute residual as performance indicators to evaluate the methods, and concluded that his method, in general, outperformed all other methods except in band 4, which is a band that is not strongly correlated with either of its adjacent bands.

He noted that although computationally simple, the methods of linear interpolation and interpolation using cubic splines have spatial smoothing effects.

In this chapter, all the existing methods proposed for the replacement of missing scan lines are evaluated using the sub-images from data sets D_1 and D_2. Other new, similar, methods are also investigated. The study is limited to bands 3, 4 and 5 of the TM, and the data sets include only areas of agricultural use, reforestation and low density vegetation (pasture, grass).

In order to evaluate each of the methods, the failure of detectors is simulated, thus allowing the true values to be contrasted with those estimated from the various methods proposed. This is discussed in detail in section 4.4. The performance of each method is evaluated using several measures that are computed for some sub-images from D_1 and D_2. Numerical results are presented in §4.5, and

are discussed in §4.6. In section 4.7, a visual evaluation of the methods is carried out. In view of the results in sections 4.5 and 4.7, other alternative methods for the estimation of missing scan lines on the imagery are proposed, and evaluated in §4.8. The conclusion follows in §4.9.

4.2 Existing Approaches

In this and the next section it is assumed that any information required by a method is both available and non defective. The methods given here can be applied to the cases of partially, or entirely missing scan lines.

Assume that the missing values on the i^{th} line of an n_1 by n_2 sub-image correspond to pixels (i,j), $j \in A_i \subseteq \{1,2,\ldots,n_2\}$. If all values are missing in line i, then $A_i = \{1,\ldots,n_2\}$. Note that this notation extends to the case of several missing scan lines, say $i_1, i_2, \ldots$. Let $\hat{u}_t^k(i,j)$ denote the estimated value of pixel (i,j) on the image acquired in band k, at time t, for $j \in A_i$.

The formulae given below, for the existing, and the proposed methods, apply for the estimation of individual missing pixel values occurring in isolated missing scan lines on the imagery.

The usual and simplest approach for estimating a missing value in a line consists of replacing its value by that of the corresponding pixel on the line immediately above it. If the line above is not available, or if its values are also missing, then the usual practice consists of replacing the missing values in the 'faulty' line by those in the line immediately below it.

The method, usually referred to as *adjacent line replacement* and henceforth addressed to as LR, is simply

$$\hat{u}_t^k(i,j) = u_t^k(i-1,j) \ , \quad j \in A_i.$$

Another simple procedure, which only utilizes data from neighbouring detectors of the band containing the failed detector is linear interpolation, herewith referred to as LI. The method consists of replacing the missing values on a defective line by the average of the corresponding pixel values in the lines immediately above and below the defective one, that is

$$\hat{u}_t^k(i,j) = [u_t^k(i-1,j) + u_t^k(i+1,j)]/2 \ , \quad j \in A_i.$$

Another single band method, henceforth referred to as CSP, is the 4-point cubic spline interpolation defined in Guindon (1984) as

$$\hat{u}_t^k(i,j) = \frac{11}{16}[u_t^k(i,j-1) + u_t^k(i,j+1)] - \frac{3}{16}[u_t^k(i,j-2) + u_t^k(i,j+2)], \quad j \in A_i. \quad (4.1)$$

Although Guindon (1984) refers to CSP as a 4-point cubic spline interpolation, it is questionable that this is really what the method is. Cubic splines require at least 5 points for fitting, whereas the method in equation 4.1 uses only 4.

It is not clear from Guindon (1984) how the coefficients of the cubic spline in equation 4.1 have been found. He only points out that:

> 'It should be noted that the coefficients of the cubic spline algorithm have been derived based on the assumption that a gap of two lines exists between samples $u_t^k(i,j-1)$ and $u_t^k(i,j+1)$.'

It might be worth mentioning that the coefficients for interpolating the mid-point using a third-order polynomial fit to 4 points (2 above, and 2 below the missing one) are the same as those for a quadratic fit, and approximately the same as those given in equation 4.1 ($\frac{2}{3}$ and $-\frac{1}{6}$, instead of $\frac{11}{16}$ and $-\frac{3}{16}$).

Since the purely spatial methods, LR and LI, proved to be inefficient when applied to an area of high contrast, Bernstein *et al.* (1984) suggested three methods that incorporate information from a 'template' band – a band that is fairly well correlated with the defective band, with no failed detectors.

Their first method, *template replacement*, henceforth referred to as TB-1, replaces the failed line with the corresponding scaled line (after mean adjustment) from another band. The adjustment of the mean and the scaling are performed on each value in the line corresponding to the defective one in a template band, say l, through the simple linear equation

$$\hat{u}_t^k(i,j) = A\,\{u_t^l(i,j) - \bar{u}_t^l\} + \bar{u}_t^k\ , \quad j \in A_i \qquad (4.2)$$

where $A = s_t^k / s_t^l$.

Here, $\bar{u}_t^k$ and s_t^k are the mean and standard deviation, respectively, of the values in the image acquired at time t in band k, except those on the defective lines $i_f, f = 1, \ldots, F$; while $\bar{u}_t^l$ and s_t^l are the mean and standard deviation of all values in the template band acquired at time t, in band l.

This approach is very similar to that used to correct the images for radiometric mismatches among the sensor detectors, causing the *banding* effect discussed in Chapter 2. Algorithms to correct for this defect usually assume that the output from a detector is a linear function of the input (or received radiance value) according to the expression: $\text{value}_{\text{out}} = \text{offset} + \text{gain value}_{\text{in}}$. The standard deviation (s) and the mean for the whole image ($\bar{u}$) are usually considered to be equivalent to the gain and offset characteristics of the sensor system. The values for an unbalanced detector d are adjusted so that its mean, $\bar{u}_d$, and its standard deviation, s_d, are equal to the overall mean and overall standard deviation. This is usually achieved by means of the expression

$$u'_d(i,j) = a_d\{u_d(i,j) - \bar{u}_d\} + \bar{u}$$

where $u'_d(i,j)$ and $u_d(i,j)$ refer to the corrected and the 'unadjusted' values for the unbalanced detector d, and $a_d = s/s_d$.

The unsatisfactory destriping results sometimes obtained from the use of the above expression are justified in the observation by Horn & Woodham (1979) that '... *it appears that different gains and offsets are appropriate for different scene radiance* [value_{in}] *ranges, i.e., the sensor transfer curves are somewhat non-linear*'.

Method TB-1 is based on the assumption that the output from a detector in any given band is approximately a linear function of the output from the corresponding detector in a neighbouring band. If *every* pixel value on the sub-image is replaced by the value obtained from TB-1, the mean and variance of the sample distribution of these replaced values correspond to those over the entire original sub-image.

The second method proposed by Bernstein *et al.* (1984), *template replacement with error adjustment*, herein referred to as TB-2, differs from the previous method by the inclusion of an adjustment term, ζ, which gives a measure of the difference between the faulty and the template images in a neighbourhood of the failed line. This adjustment term is the average of the difference between each mean corrected and scaled value in the template band and the value in the defective image, in the lines above and below the faulty one. The method is expressed as

$$\hat{u}_i^k(i,j) = A\ u_t^l(i,j) + \zeta(i,j)\ , j \in A_i \qquad (4.3)$$

where

$$\zeta(i,j) = [\{u_t^k(i-1,j) + u_t^k(i+1,j)\} - A\ \{u_t^l(i-1,j) + u_t^l(i+1,j)\}]/2,$$

and A is as defined for TB-1.

Equation 4.3 can also be expressed as

$$\hat{u}_t^k(i,j) = \frac{1}{2}[u_t^k(i-1,j)+u_t^k(i+1,j)] + A\{u_t^l(i,j) - \frac{1}{2}[u_t^l(i-1,j)+u_t^l(i+1,j)]\}\ , j \in A_i. \tag{4.4}$$

Thus, method TB-2 is simply linear interpolation with an additional component to adjust for possible non-homogeneity in band l.

Their last method, *quadratic vertical fit with template data*, here referred to as TB-3, consists of fitting a quadratic equation to a vertical slice consisting of 5 pixels (2 above and 2 below the failed one), after the replacement of the central pixel value by the value estimated from TB-1, say $\dot{u}_t^k(i,j)$.

Although Bernstein *et al.* (1984) note that '*new coefficients must be calculated for each pixel that needs to be replaced*', and that '*algorithm 3 requires per pixel multiplications and divisions (to perform the least squares fit)*', it is not really necessary. The missing values can be estimated from

$$\hat{u}_t^k(i,j) = \{34\ \dot{u}_t^k(i,j)+24[u_t^k(i-1,j)+u_t^k(i+1,j)]-6[u_t^k(i-2,j)+u_t^k(i+2,j)]\}/70\ ,\ j \in A_i. \tag{4.5}$$

Note that the coefficients in equation 4.5 are the same as those for a cubic fit.

Subsequently, Fusco & Trevese (1985) proposed some possible improvements to TB-2, as this method had been noted to yield '*slightly off-colour pixels near or on the man-made features*' in flat, low contrasted regions (Bernstein *et al.*, 1984).

Their first suggestion is to replace TB-2 by a method which estimates the missing values from the regression line of the values in the entire 'defective' image in band k, on the corresponding values in a template band, say l. The method, herein referred to as TB-4, is

$$\hat{u}_t^k(i,j) = P\ \{u_t^l(i,j) - \bar{u}_t^l\} + \bar{u}_t^k\ ,\quad j \in A_i \tag{4.6}$$

where $P = rb_t^{k,l} s_t^k / s_t^l$; and $rb_t^{k,l}$ is the correlation between the values in the 'faulty' image acquired at time t in band k, except those on the 'defective' lines, and the corresponding values on a template band l, acquired at time t.

Note that the sample distribution of the values estimated from equation 4.6, when *all* the values in the original sub-image are replaced, has the same mean as the original sub-image, but a smaller standard deviation, unless $rb_t^{kl} = 1$. The standard deviation of the image obtained from equation 4.6 is $rb_t^{kl}s_t^k$. Hence, when the correlation between the original and the template images is poor, the variance of the sample distribution of the estimated values is very small, and the estimates of the missing values are very close to the mean of the distribution of the original sub-image.

The second method proposed by Fusco & Trevese (1985) is again based on linear regression of the values on the 'defective' image on the values on a template band, but now using only a 'local' neighbourhood of the 'faulty' pixel, instead of the whole image, as in their first method.

The method, as interpreted here, replaces the value of P in equation 4.6 by the slope p of the linear regression of u_t^k on u_t^l, using data in a neighbourhood of the failed line, consisting of 3 lines above and 3 lines below. However, their description is unclear, and it was realised at a late stage that the neighbourhood can be interpreted differently, as a 'local' neighbourhood of the 'missing' pixel (consisting of the 3 pixel values above, and 3 below).

The method, as applied in this study, and henceforth referred to as TB-5, is

$$\hat{u}_t^k(i,j) = p\{u_t^l(i,j) - u_t^l\} + u_t^k \quad , \quad j \in A_i. \tag{4.7}$$

Here, u_t^k and u_t^l are the means in the neighbourhood of the 'faulty' line in the defective image, and in the corresponding neighbourhood on a template image, respectively. The neighbourhood consists of three lines above and three lines below the 'missing' one. In the computation of u_t^l, the values in the line corresponding to the faulty one in a template image are also included.

Earlier indications by Bernstein & Lotspiech (1983) that the grey levels in an adjacent band could be used as additional information to improve the recovery of missing values in remotely sensed data led Guindon (1984) to develop his *adjacent band modulation* method, of the form:

$$\begin{aligned} \hat{u}_t^k(i,j) \;=\; & b_0 + u_t^l(i,j)\left\{p_1\left[\frac{u_t^k(i-1,j)-b_0}{u_t^l(i-1,j)} + \frac{u_t^k(i+1,j)-b_0}{u_t^l(i+1,j)}\right]\right. \\ & \left. +\; p_2\left[\frac{u_t^k(i-2,j)-b_0}{u_t^l(i-2,j)} + \frac{u_t^k(i+2,j)-b_0}{u_t^l(i+2,j)}\right]\right\}/2), \quad j \in A_i \end{aligned} \tag{4.8}$$

where p_1 is a weighting factor for the pixel values in the lines immediately above and below the 'defective' scan line, and $p_2 = 1 - p_1$ is a weighting factor for the pixels values two lines above and two lines below the 'missing' one; and b_0 allows for a possible difference in offset between bands k and l, which can be estimated from a linear least squares fit to grey levels from both bands, after deletion of the values in the template image in band l, corresponding to the missing ones in the sub-image in band k.

The method is based '*on the assumption that the correlation between adjacent band grey levels can be expressed in a simple multiplicative sense and that this correlation is stationary over distances of the scale of the interpolation window (i.e. 3 to 5 lines)*' (Guindon, 1984).

Guindon (1984) used his algorithm with two sets of weighting factors: one involving only adjacent lines ($p_1 = 1$ and $p_2 = 0$), henceforth referred to as method TB-6, and another involving the nearest 4 lines (two above and two below the missing line), equally weighted ($p_1 = p_2 = \frac{1}{2}$), to be referred to here as method TB-7. He noted, however, that the results from the two sets of weighting factors were not significantly different, and that '*accurate estimations ... can be achieved using adjacent detector data only* ' (Guindon, 1984).

4.3 New Approaches

This section introduces other simple methods that can be used to estimate missing scan lines in remotely sensed imagery. Most of them are analogous to the ones presented in the previous section, but incorporate information from another passage, instead of information from another band.

4.3.1 Methods using a Template Band

The first method herein proposed, to be referred to as TB-8, is a combination of methods TB-2 and TB-6. A method similar to TB-6 had been developed before knowledge of the method proposed by Guindon (1984). It was giving better results than those proposed by Bernstein *et al.* (1984), or by Fusco & Trevese (1985), on isolated lines (see §5.9). Since the results from method TB-2 were usually better than those given by the other methods using a template

band, the method has been incorporated with the original one (similar to TB-6), to investigate if further improvements could be achieved.

The method involves two steps. Firstly, the values on the missing scan line are replaced by those estimated using TB-2. Then, using these estimated values, the lines above and below the defective one are replaced by those estimated from TB-2. At the end of this step, the defective line and those adjacent to it carry information from both the 'faulty', and the template images.

In the second step, each value in the 'missing' line is estimated similarly to method TB-6, using the pixel values above and below the 'defective' one, in the 'defective' and the template sub-images.

The method is

$$\hat{u}_t^k(i,j) = u_t^l(i,j) \left\{ \frac{u_t^{k^*}(i-1,j)}{u_t^l(i-1,j)} + \frac{u_t^{k^*}(i+1,j)}{u_t^l(i+1,j)} \right\} /2, \quad j \in A_i. \tag{4.9}$$

where $u_t^{k^*}$ refers to the estimates obtained from method TB-2.

Two further methods use a linear regression of the values in the 'defective' image acquired at time t in band k, on the corresponding values in the same passage, but from two other neighbouring bands, say l and h. The methods use

$$\hat{u}_t^k(i,j) = b_0 + b_1 u_t^l(i,j) + b_2 u_t^h(i,j), \quad j \in A_i \tag{4.10}$$

where b_0, b_1 and b_2 in equation 4.10 are the least squares estimates of β_0, β_1, and β_2 in the general linear model

$$U_t^k = \beta_0 + \beta_1 U_t^l + \beta_2 U_t^h + \varepsilon_t^k \,, \tag{4.11}$$

where ε_t^k is white noise.

Two cases are considered. For the method henceforth referred to as TB-9, data from the entire sub-image, with the exception of those on the missing scan lines, are used. For the method henceforth referred to as TB-10, the values of b_0, b_1 and b_2 in equation 4.10 are the 'local' least squares estimates, using data from 2 lines above and 2 lines below the missing one. Results have also been obtained when data from 3 lines, instead of 2, are used. As they are consistently inferior than those obtained when using only 2 lines above and 2 lines above, they are not presented here.

4.3.2 Methods using a Template Date

All the previous methods, with the exception of *adjacent line replacement*, *linear interpolation*, and *interpolation using cubic splines* make use of the multispectral characteristic of the TM, but do not explore its multitemporal potential. Since the TM records information over the same area every 16 days, it seems natural to explore this multitemporal potential in the estimation of missing scan lines. The methods proposed in this subsection are essentially the same as those introduced in section 4.2 and subsection 4.3.1, but incorporate the information contained on another passage, instead of the information in another band. It is necessary for the method to be reasonable, that no significant changes in land cover have occurred between the two acquisitions. The passage used is referred to as a *template date* – a passage that is well correlated with the defective one and that has no corresponding defective detectors. Note also that the methods using a template date need that the data from the different passages be well registered – refer to §2.1.

These methods are henceforth referred to as TD-1 to TD-10, and correspond to the temporal versions of methods TB-1 to TB-10, respectively. Thus, the equations corresponding to methods TD-1 to TD-10 are the same as those given for methods TB-1 to TB-10, for u_t^k and u_t^l replaced by $u_{t_1}^k$ and $u_{t_2}^k$, respectively. Here, t_1 and t_2 are the respective dates of acquisition of the 'defective' image, and the template image.

A brief summary of all the methods is presented in Table 4.1.

Table 4.1: Summary of the methods.

Method	Description of method
LR	Replaces the values in the missing scan line by those in the line immediately above.
LI	Replaces the value in the missing scan line by the average of the corresponding values in the lines above and below.
CSP	Estimates the missing values using cubic spline interpolation.
$TB/D-1$	Bernstein *et al.* (1984) algorithm 1: replaces the missing line with the corresponding scaled line (after mean adjustment) from another band (date).
$TB/D-2$	Bernstein *et al.* (1984) algorithm 2: as TB/D-1, but includes an adjustment term that uses information from the line above and the line below the defective one, in both the 'faulty' image and the template band (date).
$TB/D-3$	Bernstein *et al.* (1984) algorithm 3: estimates the missing value by fitting a quadratic equation to a vertical slice of 5 pixels, after replacement of the central pixel in the slice by the values estimated using TB/D-1.
$TB/D-4$	Fusco & Trevese (1985) equation 4: straight line regression of the values in the entire image on the corresponding values in another band (date).
$TB/D-5$	Fusco & Trevese (1985) equation 6: as TB/D-4, but uses data from 3 lines above and 3 lines below the missing one.
$TB/D-6$	Guindon (1984) algorithm ABM(1,0): estimates the missing value using information in the lines above and below the missing one, in both the 'defective' and a template band (date) images.
$TB/D-7$	Guindon (1984) algorithm ABM(1,1): as TB/D-6, but uses information from up to 2 lines above and 2 lines below the 'defective' line
$TB/D-8$	Estimates the missing line, and the lines above and below the 'faulty' one using method TB/D-2, and then uses this information, and the information in the lines above and below the corresponding one in a template band (date).
$TB/D-9$	Uses regression on two bands (dates), using data from the entire image (excluding those corresponding to the missing scan line).
$TB/D-10$	As TB/D-9, but uses data from two lines above and two lines below the 'defective' one.

4.4 Test Images and Measures

This section introduces the sub-images on which the methods proposed in the previous section are to be used, and the set of measures proposed to evaluate the quality of the estimates of the missing values, obtained from each method.

To evaluate the replacement of the missing scan lines by each method, it is necessary to simulate the failure of detectors in order to know the true pixel values and to contrast them with the estimated values.

All sub-images from D_1 and D_2 are considered, and instead of using only the lines corresponding to a particular failed detector, the approach adopted here is to individually estimate each line, as in Fusco & Trevese (1985). Because each line on the sub-image is replaced, the final product from this procedure is a completely new image, herein referred to as the *test image*, which, ideally, should resemble very closely the original sub-image. This procedure makes it easier to visually detect the properties of the methods.

For each sub-image from D_1 and D_2, and a particular template (band or date), three test images are generated from purely spatial methods (LR, LI, and CSP), eight are obtained from methods using a template band (TB-1 to TB-8), and eight from methods using a template date (TD-1 to TD-8). When necessary, adjustments were made to methods on the first and last few lines, but these adjustments will only slightly affect the results.

Test images are also obtained for sub-images from D_1 from methods TB/D-9 and TB/D-10. Due to the unavailability of data from two other bands, and the lack of two 'reasonable' template dates (two images acquired at close dates), these methods are not applied to the sub-images from D_2.

The use of sub-images from two distinct data sets provides the opportunity to investigate the consistency of the methods when applied to different types of land cover, which may form distinct geometric patterns on the image. The sub-images in band 5, from D_2, for example, have several well-defined, strong, linear features, whereas those in band 5, from D_1, have less pronounced characteristics, which are reasonably consistent over the entire image.

The set of measures introduced in §4.4.2 is used to evaluate the test images from each method.

4.4.1 Sub-images and Templates

4.4.1.1 Using D_1

As described in Chapter 3 (§3.3.1), the first data set comprises nine sub-images, corresponding to data on three consecutive passages, in three neighbouring bands. All nine sub-images are estimated from single band methods, methods using information contained in other bands (template band methods), and from methods using the information provided by one, or more images acquired at other dates (template date methods). For the methods using a template band, each sub-image is estimated using information from either remaining band, whereas for the methods using a template date, the information usually comes from the template with the higher correlation with the sub-image. Thus, for each sub-image in D_1, there are two test images from each method using a template band (except for methods TB-9 and TB-10), and one from each method using a template date. The template date may have been acquired prior to, or after the acquisition of the sub-image.

In just one situation, test images are obtained using a less correlated template date. As sub-images from 24/06 in bands 3 and 5 are better correlated with data from the sub-image acquired at 10/07, then the sub-image acquired at 10/07 has also been used as template date for band 4, although data in sub-image $D_1(24)$ is better correlated with data in sub-image $D_1(34)$. Thus, the test images obtained for sub-image $D_1(24)$, using $D_1(34)$ as template, may be superior to those obtained from $D_1(14)$, not only because of the higher correlation between $D_1(24)$ and $D_1(34)$ [$rd_{23} = 0.853$] but also due to the smaller amount of changes in land cover that took place between dates 08/06 and 24/06, than between dates 24/06 and 10/07 – see Figure 3.7(b).

It is important to note, however, that the use of a template date acquired after the acquisition of the sub-image is only viable if the estimation of the missing values is not carried out routinely, during the preprocessing stage of digital image processing. Also, if data from previous passages are to be used during this stage, they need to be well registered with data on the image being processed. This care is unnecessary if data from other bands, but the same passage, are used, since the band-to-band registration accuracy of the TM has been reported to be within the satellite specifications (Wrigley *et al.*, 1985).

For each sub-image in D_1, one test image is also obtained from each method that uses two bands (dates) [TB/D-9 and TB/D-10].

For the template band and template date methods, assume that the test images are obtained for particular pairs of images, consisting of the original sub-image and the template (band or date) considered with the methods. Henceforth, denote this pair by OT (original/template). Let each pair of sub-images from D_1 be coded $D_1(ij)(kl)$, where i and k refer to the date of acquisition of the original sub-image and the template image, respectively, and j and l refer to the band of the sub-image and the template image, respectively. For methods using a template band, $i = k$, whereas for those using a template date, $j = l$.

Table 4.2 gives the list of all pairs of sub-images from D_1, and their code. Depending on the template used with the methods, the pairs are listed under *Template Band Methods*, or *Template Date Methods* for template band, or template date, respectively. A number is also assigned to each pair, for easier identification. The table also gives the correlations between the sub-images in each pair, that is, between the original sub-image and the template. These correlations come from Tables 3.2 and 3.3 for the template date and the template band, respectively.

Table 4.2: Numbers and codes for the pairs of sub-images from D_1, and the correlations between the sub-images in each pair.

TEMPLATE BAND METHODS						
OT Number	OT Code	Sub-Image		Template Band		rb_{jl}
		Date	Band	Date	Band	
1	$D_1(13)(14)$	10/07	3	10/07	4	0.081
2	$D_1(23)(24)$	24/06	3	24/06	4	0.012
3	$D_1(33)(34)$	08/06	3	08/06	4	−0.126
4	$D_1(13)(15)$	10/07	3	10/07	5	0.719
5	$D_1(23)(25)$	24/06	3	24/06	5	0.705
6	$D_1(33)(35)$	08/06	3	08/06	5	0.760
7	$D_1(14)(13)$	10/07	4	10/07	3	0.081
8	$D_1(24)(23)$	24/06	4	24/06	3	0.012
9	$D_1(34)(33)$	08/06	4	08/06	3	−0.126
10	$D_1(14)(15)$	10/07	4	10/07	5	0.146
11	$D_1(24)(25)$	24/06	4	24/06	5	−0.016
12	$D_1(34)(35)$	08/06	4	08/06	5	−0.122
13	$D_1(15)(13)$	10/07	5	10/07	3	0.719
14	$D_1(25)(23)$	24/06	5	24/06	3	0.705
15	$D_1(35)(33)$	08/06	5	08/06	3	0.760
16	$D_1(15)(14)$	10/07	5	10/07	4	0.146
17	$D_1(25)(24)$	24/06	5	24/06	4	−0.016
18	$D_1(35)(34)$	08/06	5	08/06	4	−0.122
TEMPLATE DATE METHODS						
OT Number	OT Code	Sub-Image		Template Date		rd_{ik}
		Date	Band	Date	Band	
19	$D_1(13)(23)$	10/07	3	24/06	3	0.864
20	$D_1(23)(13)$	24/06	3	10/07	3	0.864
21	$D_1(33)(23)$	08/06	3	24/06	3	0.817
22	$D_1(14)(24)$	10/07	4	24/06	4	0.834
23	$D_1(24)(14)$	24/06	4	10/07	4	0.834
24	$D_1(34)(24)$	08/06	4	24/06	4	0.853
25	$D_1(15)(25)$	10/07	5	24/06	5	0.937
26	$D_1(25)(15)$	24/06	5	10/07	5	0.937
27	$D_1(35)(25)$	08/06	5	24/06	5	0.920

4.4.1.2 Using D_2

As mentioned in Chapter 3 (§3.3.2), the second data set contains only sub-images in bands 4 and 5, thus leaving no choice for the template band to be used with the methods proposed by Bernstein *et al.* (1984), Fusco & Trevese (1985), and Guindon (1984). The fact that data in bands 4 and 5 are always poorly correlated in this data set, and the unavailability of data in other bands, stresses the importance of the development of other methods that do not require a well correlated template band.

The selection of the six passages from D_2 in Chapter 3 was to ensure the existence of a reasonable template date. All sub-images from D_2 are estimated from single band, template band, and template date methods.

Table 4.3 gives a list of the pairs of sub-images from D_2. A number and a code similar to those used for D_1 are assigned to each pair, which are listed under *Template Band Methods*, or *Template Date Methods*, depending on the template used with the methods (band or date, respectively). The correlations between the original sub-image and the template are also provided in Table 4.3, as well as in Tables 3.5 and 3.6 in Chapter 3.

Table 4.3: Numbers and codes for the pairs of sub-images from D_2, and the correlations between the sub-images in each pair.

TEMPLATE BAND METHODS						
OT Number	OT Code	Sub-Image		Template Band		rb_{jl}
		Date	Band	Date	Band	
1	$D_2(14)(15)$	09/09/90	4	09/09/90	5	0.579
2	$D_2(24)(25)$	08/08/90	4	08/08/90	5	0.441
3	$D_2(34)(35)$	20/07/89	4	20/07/89	5	0.322
4	$D_2(44)(45)$	04/07/89	4	04/07/89	5	0.172
5	$D_2(54)(55)$	17/07/88	4	17/07/88	5	0.298
6	$D_2(64)(65)$	01/07/88	4	01/07/88	5	0.138
7	$D_2(15)(14)$	09/09/90	5	09/09/90	4	0.579
8	$D_2(25)(24)$	08/08/90	5	08/08/90	4	0.441
9	$D_2(35)(34)$	20/07/89	5	20/07/89	4	0.322
10	$D_2(45)(44)$	04/07/89	5	04/07/89	4	0.172
11	$D_2(55)(54)$	17/07/88	5	17/07/88	4	0.298
12	$D_2(65)(64)$	01/07/88	5	01/07/88	4	0.138
TEMPLATE DATE METHODS						
OT Number	OT Code	Sub-Image		Template Date		rd_{ik}
		Date	Band	Date	Band	
13	$D_2(14)(24)$	09/09/90	4	08/08/90	4	0.810
14	$D_2(24)(14)$	08/08/90	4	09/09/90	4	0.810
15	$D_2(34)(44)$	20/07/89	4	04/07/89	4	0.903
16	$D_2(44)(34)$	04/07/89	4	20/07/89	4	0.903
17	$D_2(54)(64)$	17/07/88	4	01/07/88	4	0.887
18	$D_2(64)(54)$	01/07/88	4	17/07/88	4	0.887
19	$D_2(15)(25)$	09/09/90	5	08/08/90	5	0.956
20	$D_2(25)(15)$	08/08/90	5	09/09/90	5	0.956
21	$D_2(35)(45)$	20/07/89	5	04/07/89	5	0.968
22	$D_2(45)(35)$	04/07/89	5	20/07/89	5	0.968
23	$D_2(55)(65)$	17/07/88	5	01/07/88	5	0.951
24	$D_2(65)(55)$	01/07/88	5	17/07/88	5	0.951

4.4.2 Evaluation of the Performance of the Methods

The methods are evaluated based on their performance on a set of measures, and visually. Let the residuals for the sub-image of size n_1 by n_2, $e(i,j), i = 1,\ldots,n_1, j = 1,\ldots,n_2$, be defined as the difference between the values in the original image, $u(i,j)$, and the corresponding values in the test image, $\hat{u}(i,j)$, that is, $e(i,j) = u(i,j) - \hat{u}(i,j)$. The measures are now described.

The first is the scaled root mean square residual (SRMS), given by

$$SRMS = (s_t^k)^{-1} \left\{ \sum_{i=1}^{n_1} \sum_{j=1}^{n_2} e^2(i,j)/(n_1 n_2) \right\}^{1/2} \tag{4.12}$$

where s_t^k is the standard deviation of the original sub-image acquired at time t, in band k.

The use of a scaled root mean square residual here, instead of the root mean square residual used by Fusco & Trevese (1985), is to contrast the values obtained for this measure, for test images in different bands, or in different data sets.

Note that if the mean value of the residuals is zero, that is,

$$\bar{e} = \sum_{i=1}^{n_1} \sum_{j=1}^{n_2} e(i,j)/(n_1 n_2) = 0.0 \ ,$$

then the mean square residual is equal to the residual variance, s_e^2, if the divisor of the residual variance is $n_1 n_2$. As previously mentioned, the residual standard deviation has been used by Guindon (1984) as a measure of the performance of some methods. In the present investigation, the values for the residual variance and the mean square residual are very close.

The second measure used to evaluate the methods is the complementary correlation (CCOR), $1 - r_{u,\hat{u}}$, where $r_{u,\hat{u}}$ is the correlation between the original image and the test image.

Finally, the third measure, SRAN, is the range of the residuals divided by the standard deviation of the original sub-image. Note that since SRAN is a measure that uses only the range of the residuals, a large value for this measure may only indicate the occurrance of a few large residuals, and may not reflect the actual overall performance of the methods. This stresses the importance of the visual evaluation of the methods, as a complement to the numerical evaluation.

The methods are evaluated by their ability to give consistently small values of SRMS, CCOR, and SRAN.

Initially, all the methods are evaluated for the sub-images from D_1. As in this data set there are two possible pairs of original and template band sub-images to be used with methods TB-1 to TB-8, let TB-mL, $m = 1, \ldots, 8$ designate the method that uses a poorly correlated template, and TB-mH the method that uses a well correlated template. Hence, the test image obtained for the pair $D_1(13)(14)$ from method TB-1, for instance, is designated by TB-1L, whereas that obtained for the pair $D_1(13)(15)$ is designated by TB-1H.

For each original sub-image from D_1, 31 test images are obtained, as follows: 3 from single band methods (LR, LI, CSP), 8 from template band methods that use a poorly correlated template (TB-1L to TB-8L), 8 from template band methods that use a well correlated template (TB-1H to TB-8H), 8 from template date methods (TD-1 to TD-8), and 4 from methods that use 2 template band, or 2 template date sub-images (TB-9 and TB-10, TD-9 and TD-10, respectively).

In order to aid the evaluation of the methods, ranks 1 to 31 are formed for each method, in each original sub-image from D_1. For each measure, the ranks are assigned in order of increasing SRMS, CCOR, and SRAN. By averaging the individual ranks assigned in each of the 9 original sub-images from D_1, an average rank (AR) is also obtained for each method.

A similar procedure is adopted for the sub-images from D_2. However, as there is no choice of a template to be used with the template band/date methods, and as methods TB/D-9 and TB/D-10 cannot be 'reasonably' used with the sub-images in the second data set, then only 19 test images are obtained for each OT. From the results obtained for each method, in each of the 12 OT's from D_2, the methods are assigned a rank from 1 to 19, in order of increasing SRMS, CCOR, and SRAN.

Fusco & Trevese (1985) have noted that:

> 'From the statistical point of view, *linear interpolation* improves both *SRMS* and $r_{u,\hat{u}}$ in respect to *adjacent line replacement.* However, the improvement in respect to *adjacent line replacement* is not as strong as indicated by the statistical parameters; some structure could be altered even more by *linear interpolation* than by *adjacent line replacement'*.

This suggests that the evaluation of the methods should not be based only on

statistical measures, but also on the visual results obtained from each method. The visual evaluation of the methods is carried out using the following images:

- the test image obtained for each method;
- the residual image obtained as the difference between the original sub-image and the test image, plus 128; and
- the 'cut' image, which highlights, in the residual image, the values estimated exactly.

Note that as the grey levels are integers ranging from 0 to 255, the estimates obtained from all methods have been rounded to the nearest integer, for the visual evaluation. No estimates obtained here for any method exceeded 255, or were below 0.

Visual inspection of each test image provides an assessment of the performances of the methods, by showing the deformations they introduce on the particular structures present in the image. The difference image indicates the distribution of the residuals, showing the size of the residual in relation to the original image. Finally, the 'cut' image provides the spatial distribution of the pixels estimated exactly, allowing identification of the areas on the image that are more accurately estimated.

4.5 Numerical Results and Discussion

Before the results from the application of the methods to the sub-images from D_1, and D_2 are given, it is interesting to note that, for some of the methods, the values for SRMS and CCOR are known either exactly, or approximately. From this knowledge, it is possible to indicate which methods perform better than others, and under what conditions. These theoretical results are now presented.

4.5.1 Some Theoretical Considerations

Let $u(i,j)$, $\hat{u}(i,j)$, and $v(i,j)$ denote the pixel value at site (i,j) in the original sub-image, in the test image, and in the template image, respectively. Let $\bar{u}$, $\bar{v}$, and $\bar{\hat{u}}$, denote their respective means, and s_u, $s_{\hat{u}}$, and s_v their respective standard deviations.

Here, define the sample autocorrelations at lags g and h, $r_{g,h}$, as

$$r_{gh} = \{ns_u^2\}^{-1} \sum_{(i,j)\in\Omega} [u(i,j) - \bar{u}][u(i+g, j+h) - \bar{u}]. \tag{4.13}$$

where Ω is the set of sites (i,j), $i = 1, \ldots, n_1 - g$, $j = 1, \ldots, n_2 - h$.

Let rt_{uv} denote the correlation between the data in the original sub-image, and those in the template (band or date).

- For **LR**:

  For LR, the estimate of the pixel at site (i,j) is $\hat{u}(i,j) = u(i-1,j)$, and $\bar{\hat{u}} \approx \bar{u}$, $s_{\hat{u}} \approx s_u$. The correlation between the values in the original sub-image, and those in the test image corresponding to LR, $r_{u,\hat{u}}$, can be found by substituting $\hat{u}(i,j)$ and $\bar{\hat{u}}$ into the formulae for this correlation, giving:

$$r_{u,\hat{u}} \approx \frac{\sum_{(i,j)\in v}[u(i,j) - \bar{u}][u(i-1,j) - \bar{u}]}{ns_u^2} \approx r_{10}. \tag{4.14}$$

  The approximate expression for SRMS, for LR, can be found by substituting $\hat{u}(i,j)$ into equation 4.12, which gives:

$$\begin{aligned} SRMS &\approx \left\{ \frac{\sum[u(i,j)-\bar{u}]^2}{ns_u^2} + \frac{\sum[u(i-1,j)-\bar{u}]^2}{ns_u^2} - 2r_{10} \right\}^{1/2} \\ &\approx \{2(1 - r_{10})\}^{1/2}. \end{aligned} \tag{4.15}$$

- For **LI**:

  Using the same approach as for LR, the approximate expressions for $r_{u,\hat{u}}$, and SRMS, for the method of linear interpolation can also be found. For LI, the estimate of the value at site (i,j) is

$$\hat{u}(i,j) = [u(i-1,j) + u(i+1,j)]/2 \tag{4.16}$$

  and $\bar{\hat{u}} \approx \bar{u}$ and $s_{\hat{u}} \approx s_u$.

  The approximate expressions for $r_{u,\hat{u}}$ and SRMS, for LI, are as follows:

$$r_{u,\hat{u}} \approx \frac{r_{10}}{\sqrt{(1 + r_{20})/2}} \tag{4.17}$$

and

$$SRMS \approx \{(3 - 4r_{10} + r_{20})/2\}^{1/2}. \tag{4.18}$$

- For **CSP**:

Using the same approach as for LR and LI, the following approximate equations are obtained for $r_{u,\hat{u}}$ and SRMS, for method CSP.

$$r_{u,\hat{u}} \approx \frac{11r_{10} - 3r_{20}}{\{(130 - 66r_{10} + 121r_{20} - 66r_{30} + 9r_{40})/2\}^{1/2}} \tag{4.19}$$

and

$$SRMS \approx \{(258 - 418r_{10} + 217r_{20} - 66r_{30} + 9r_{40})/128\}^{1/2}. \tag{4.20}$$

- For **TB/D-1**:

The estimate of the pixel value at site (i, j), for method TB/D-1, is $\hat{u}(i, j) = \bar{u} + \frac{s_u}{s_v}[v(i, j) - \bar{v}]$, and $\bar{\hat{u}} = \bar{u}$ and $s_{\hat{u}} = s_u$.

By substituting these values into the expression for the correlation between the values in the original image and those in the test image obtained for method TB-1, *viz.*

$$r_{u,\hat{u}} = \frac{\sum_{(i,j)\in\Omega}[u(i, j) - \bar{u}][\hat{u}(i, j) - \bar{\hat{u}}]}{n\ s_u s_{\hat{u}}} \tag{4.21}$$

gives

$$r_{u,\hat{u}} = rt_{uv}. \tag{4.22}$$

The value of SRMS for method TB/D-1 can also be easily found, by replacing the value of $\hat{u}(i, j)$ into 4.12. The equation is as follows:

$$SRMS = s_u^{-1}\left\{\left[2s_u^2 - 2s_u \sum_{(i,j)\in\Omega} \frac{[u(i, j) - \bar{u}][v(i, j) - \bar{v}]}{s_v n}\right]\right\}^{1/2}. \tag{4.23}$$

By using the correlation between the values in the original sub-image, and those in the template image, equation 4.23 simplifies to

$$SRMS = \{2[1 - rt_{uv}]\}^{1/2}. \tag{4.24}$$

Note that equations 4.22 and 4.24 are exact if the estimates are exact, and approximate if the estimates are rounded .

- For **TB/D-2**:

  For method TB/D-2, the expression for SRMS involves the cross-covariances, c^{uv}, between the data in the original sub-image and those in the template.

  The equation is as follows:

$$\begin{aligned}(SRMS)^2 &\approx \tfrac{1}{2}(3-4r_{10}^{u}+r_{20}^{u})+\tfrac{1}{2}(3-4r_{10}^{v}+r_{20}^{v}) \\ &- \tfrac{1}{s_u s_v}\{3c_{00}^{uv}-2(c_{10}^{uv}+c_{-10}^{uv})+\tfrac{1}{2}(c_{20}^{uv}+c_{-20}^{uv})\}.\end{aligned} \tag{4.25}$$

- For **TB/D-4**:

  The values for SRMS and $r_{u,\hat{u}}$ can be also obtained theoretically for method TB/D-4, in a fashion similar to that used for TB/D-1. Note that for TB/D-4, $\bar{\hat{u}} = \bar{u}^k$ and $s_{\hat{u}} = \mid rt_{uv} \mid \frac{s_u}{s_v}$.

  The following expressiong are obtained for $r_{u,\hat{u}}$ and SRMS:

$$r_{u,\hat{u}} = \mid rt_{uv} \mid . \tag{4.26}$$

  and

$$SRMS = \{1 - rt_{uv}^2\}^{1/2}. \tag{4.27}$$

  As for method TB/D-1, expressions 4.26 and 4.27 are exact if the estimates are exact, and approximate if the estimates are rounded.

- For **TB/D-9**:

  For method TB/D-9, it can be easily shown that

$$r_{u,\hat{u}} = \{R^2_{uv_1v_2}\}^{1/2} \tag{4.28}$$

  and

$$SRMS = \{1 - R^2_{uv_1v_2}\}^{1/2} \tag{4.29}$$

where $R^2_{uv_1v_2}$ is the coefficient of multiple determination.

From the expressions given above for SRMS and CCOR, for some of the methods, the following conclusions can be drawn:

- From equations 4.14 and 4.15 (for LR), and equations 4.17 and 4.18 (for LI): that LI always has smaller values for SRMS and CCOR than LR.

- From equations 4.14 and 4.15 (for LR), and equations 4.22 and 4.24 (for TB/D-1): that LR has smaller values for SRMS and CCOR than TB-1, if $r_{10} > rt_{uv}$.

- From equations 4.17 and 4.18 (for LI) and equations 4.19 and 4.20 (for CSP): that CSP has smaller SRMS and CCOR than LI if $22 - 54r_{10} + 51r_{20} - 22r_{30} + 9r_{40} < 0$ (which can happen if $r_{10} - r_{20} > 1 - r_{10}$).

- From equation 4.22 (for TB/D-1): that the correlation between the data in the original sub-image, and those in the test image is the same as that between the data in the original sub-image and the template (band or date).

- From equation 4.25 (for TB/D-2): that if u and v are similar, and separable, SRMS $\approx \{2(1 - rt_{uv})\}^{\frac{1}{2}}\{\frac{1}{2}(3 - 4r_{10} + r_{20})\}^{\frac{1}{2}}$.

- From equations 4.26 and 4.27 (for TB/D-4) and equations 4.28 and 4.29 (for TB/D-9): that method TB/D-9 is better than the better TB/D-4, but not by much, unless the second regressor contributes a large amount extra.

Note also, from equations 4.22 (for TB/D-1) and 4.26 (for TB/D-4), that the correlation between the data in the original sub-image and the test image, obtained for methods TB/D-1 and TB/D-4 are the same, in absolute value. Hence, from equations 4.24 and 4.27 it can be concluded that TB/D-4 always has smaller SRMS than TB/D-1, and that TB/D-1 is approximately $\sqrt{2}$ bigger, for low $\mid rt_{uv} \mid$.

For all methods, the numerical results for SRMS, and CCOR, in the next section, are obtained by running the corresponding programs, instead of using the formulae presented in this section.

4.5.2 Numerical Results for D_1, for SRMS, CCOR, and SRAN.

The numerical results are now presented for D_1, for each of the measures introduced in §4.2.2. When discussing these results, emphasis is placed on the methods that perform well in general.

Besides the interest in detecting which of the methods usually gives the best results, several other questions also seem relevant to be investigated. For instance,

the consistency of the methods when applied to the same TM band in different sub-images, or their consistency when applied to different bands of the same original sub-image. Also of interest is the consistency of the methods over the different measures introduced in §4.4.2.

The values for SRMS, CCOR, and SRAN, obtained from the application of the 31 methods to the sub-images from D_1, are given in Tables B.1, B.2, and B.3, in Appendix B, respectively. These results are presented in two separate parts in the tables, one for the template band, and another for the template date methods. Note also that results for the template band methods that use a poor, or a well correlated template, are presented separately [e.g. results for sub-image $D_1(13)$, using a poorly correlated template are shown for the pair $D_1(13)(14)$, whereas those obtained when using a well correlated template are presented for $D_1(13)(15)$].

Each of the 31 methods is assigned a rank from 1 to 31, for each measure, in each of the 9 sub-images from D_1. These ranks are then averaged, to give the average rank of each method (AR), to two decimal places, for each of the measures. These are presented in Table 4.4. The table also includes the absolute value of the difference, to one decimal place, between the average ranks of each method for: (1) SRMS & CCOR; (2) SRMS & SRAN; and (3) CCOR & SRAN.

To clarify the overall performance of the methods for the three measures, new ranks from 1 to 31 are assigned to each method in Table 4.4, according to its position in the table (rank 1 for the method at the top). Thus, three new ranks are formed for each method, one for each of the measures, SRMS, CCOR, and SRAN. These new ranks are subsequently averaged (resulting in new average ranks, NAR), to give the results in Table 4.5 (under D_1), where $\bar{r}_a$ and s_{r_a} are the mean and standard deviation of the new ranks, respectively. The minimum and maximum values of the new ranks [(m,M)], for each method, are also presented.

From the differences between the average ranks of each method, for SRMS and CCOR, given under difference (1) in Table 4.4, it can be seen that all methods are reasonably consistent for measures SRMS nad CCOR. However, only a few methods are consistent for SRMS and SRAN (18 of the differences in (2) exceed 3, the maximum difference being 10.9), or for CCOR and SRAN (19 of the differences in (3) exceed 3, the maximum difference being 11.9).

From Table 4.4 it can be noted that LI has the smallest values for SRMS,

and CCOR, whereas CSP performs best for SRAN. It can also be seen from the table that smaller values for SRMS, and CCOR, are first obtained for some of the template date methods (TD-7, TD-6, TD-3, TD-2, TD-8), than for template band methods. Amongst the template band methods, those which perform better, for SRMS, and CCOR, are TB-6H, TB-6L, TB-2H, and TB-7H. Since most methods are not reasonably consistent for SRMS and SRAN, or for CCOR and SRAN, a different performance of the methods, for SRAN, is expected. Note that the template date methods which performed well for SRMS, and CCOR, are outperformed by other template methods, for SRAN. Contrast, for instance, the average ranks of methods TD-7, TD-6, and TD-8, for SRMS and CCOR, and for SRAN. This is also observed amongst the template band methods - see, for example, the average ranks of methods TB-6H and TB-6L, for SRMS, CCOR, and SRAN. Since SRAN is a measure that uses the range for the residuals, it penalizes the methods for which some few, but large, residuals occur. Hence, for a method that performs well for SRMS, and CCOR, a large value for SRAN may only indicate the occurrance of a few, large, residuals.

Table 4.4: Average rank (AR) of each method, for SRMS, CCOR, and SRAN, and differences between AR's for (1) SRMS-CCOR; (2) SRMS-SRAN; (3) CCOR-SRAN.

SRMS		CCOR		SRAN		DIFFERENCES			
Method	AR	Method	AR	Method	AR	Method	(1)	(2)	(3)
LI	2.44	LI	3.11	CSP	3.11	LR	0.2	0.3	0.5
$TD-7$	3.67	$TD-7$	3.67	LI	3.50	LI	0.7	1.1	0.4
CSP	4.11	CSP	3.89	$TD-3$	3.72	CSP	0.2	1.0	0.8
$TD-6$	5.28	$TD-6$	5.06	$TB-2H$	9.89	$TB-1L$	0.6	0.4	0.2
$TD-3$	6.33	$TD-3$	6.67	$TD-2$	10.11	$TB-2L$	0.3	7.0	7.3
$TD-8$	7.39	$TD-2$	6.83	$TD-9$	11.22	$TB-3L$	1.3	9.0	7.7
$TD-2$	7.89	$TD-8$	6.83	$TD-5$	11.61	$TB-4L$	1.9	6.9	8.9
$TB-6H$	7.94	$TB-6H$	8.00	$TD-10$	11.67	$TB-5L$	0.0	3.8	3.8
$TD-10$	8.89	$TD-10$	8.72	$TB-3H$	12.56	$TB-6L$	0.2	9.4	9.3
$TB-6L$	9.22	$TB-6L$	9.39	$TD-7$	12.83	$TB-7L$	0.1	7.8	7.8
$TB-2H$	11.67	$TB-2H$	11.78	$TD-6$	13.56	$TB-8L$	0.6	1.6	2.1
$TD-5$	12.72	$TB-7H$	12.17	$TB-9$	14.89	$TB-9$	0.1	10.9	11.0
$TD-9$	12.83	$TD-9$	13.44	$TB-5H$	14.94	$TB-10$	0.3	4.8	5.1
$TB-7H$	12.89	$TD-5$	13.44	$TB-4H$	15.33	$TB-1H$	0.9	6.7	5.8
$TB-7L$	14.50	$TB-7L$	14.56	$TD-8$	15.61	$TB-2H$	0.1	1.8	1.9
$TD-4$	15.67	$TB-2L$	16.11	$TD-4$	16.39	$TB-3H$	0.8	10.7	9.9
$TB-2L$	16.44	LR	16.33	$TB-6H$	16.50	$TB-4H$	1.4	10.5	11.9
LR	16.56	$TB-8H$	16.44	LR	16.83	$TB-5H$	0.5	8.2	8.7
$TB-8H$	16.67	$TD-1$	17.22	$TB-10$	17.50	$TB-6H$	0.1	8.6	8.5
$TD-1$	17.89	$TD-4$	17.22	$TB-7H$	18.44	$TB-7H$	0.7	5.6	6.3
$TB-8L$	21.44	$TB-8L$	20.89	$TB-6L$	18.67	$TB-8H$	0.2	4.5	4.7
$TB-10$	22.28	$TB-3H$	22.44	$TB-3L$	20.22	$TD-1$	0.7	2.9	3.6
$TB-5H$	23.17	$TB-10$	22.56	$TD-1$	20.78	$TD-2$	1.1	2.2	3.3
$TB-3H$	23.28	$TB-5H$	23.67	$TB-8H$	21.17	$TD-3$	0.3	2.6	2.9
$TB-9$	25.78	$TB-9$	25.89	$TB-4L$	21.39	$TD-4$	1.6	0.7	0.8
$TB-4H$	25.83	$TB-5L$	26.67	$TB-1H$	21.50	$TD-5$	0.7	1.1	1.8
$TB-5L$	26.67	$TB-4H$	27.28	$TB-7L$	22.33	$TD-6$	0.2	8.3	8.5
$TB-1H$	28.17	$TB-1H$	27.28	$TB-5L$	22.89	$TD-7$	0.0	9.2	9.2
$TB-4L$	28.33	$TB-3L$	27.89	$TB-8L$	23.00	$TD-8$	0.6	8.2	8.8
$TB-3L$	29.22	$TB-4L$	30.28	$TB-2L$	23.39	$TD-9$	0.6	1.6	2.2
$TB-1L$	30.83	$TB-1L$	30.28	$TB-1L$	30.44	$TD-10$	0.2	2.8	3.0

Table 4.5: Mean and standard deviation of the new ranks assigned to each method, for D_1 and D_2.

D_1				D_2			
Method	$\bar{r}_a$	s_{r_a}	(m,M)	Method	$\bar{r}_a$	s_{r_a}	(m,M)
LI	1.33	0.58	(1,2)	LI	1.17	0.41	(1,2)
CSP	2.33	1.16	(1,3)	CSP	2.17	0.75	(1,3)
$TD-3$	4.33	1.16	(3,5)	$TD-7$	4.00	1.67	(2,6)
$TD-7$	4.67	4.62	(2,10)	$TD-6$	4.33	1.51	(3,7)
$TD-2$	6.00	1.00	(5,7)	$TD-2$	5.33	1.51	(3,7)
$TD-6$	6.33	4.04	(4,11)	$TD-3$	5.83	1.94	(3,8)
$TD-10$	8.67	0.58	(8,9)	$TB-6$	7.17	2.71	(4,11)
$TB-2H$	8.67	4.04	(4,11)	$TD-8$	7.33	1.37	(6,10)
$TD-8$	9.33	4.93	(6,15)	$TD-5$	8.83	1.94	(5,10)
$TD-9$	10.67	4.04	(6,13)	$TB-7$	10.33	2.34	(9,15)
$TB-6H$	11.00	5.20	(8,17)	$TD-4$	11.75	2.14	(8,14)
$TD-5$	11.00	3.61	(7,14)	LR	12.00	1.79	(9,14)
$TB-6L$	13.67	6.35	(10,21)	$TB-2$	12.17	1.94	(11,16)
$TB-7H$	15.33	4.16	(12,20)	$TD-1$	13.42	0.49	(13,14)
$TD-4$	17.17	2.02	(16,19.5)	$TB-8$	15.83	1.33	(15,18)
LR	17.67	0.58	(17,18)	$TB-3$	15.83	2.14	(12,18)
$TB-3H$	18.33	8.14	(9,24)	$TB-5$	16.67	0.82	(16,18)
$TB-7L$	19.00	6.93	(15,27)	$TB-4$	17.00	1.76	(14,18.5)
$TB-5H$	20.00	6.08	(13,24)	$TB-1$	18.83	0.26	(18.5,19)
$TB-8H$	20.33	3.21	(18,24)				
$TB-9$	20.67	7.51	(12,25)				
$TD-1$	20.83	1.89	(19.5,23)				
$TB-2L$	21.00	7.81	(16,30)				
$TB-10$	21.33	2.08	(19,23)				
$TB-4H$	22.50	7.40	(14,27.5)				
$TB-8L$	23.67	4.62	(21,29)				
$TB-5L$	27.00	1.00	(26,28)				
$TB-3L$	27.00	4.36	(22,30)				
$TB-1H$	27.17	1.04	(26,28)				
$TB-4L$	28.17	2.84	(25,30.5)				
$TB-1L$	30.83	0.29	(30.5,31)				

4.5.3 Numerical results for D_2, and comparison with the results for D_1

Results for the sub-images from D_2 are obtained for 19 methods only, (3 single band, 8 using a template band, and 8 using a template date), since the template band methods only have available templates that are poorly correlated with the original sub-images, and since methods TB/D-9 and TB/D-10 cannot be sensibly applied to the sub-images in this data set.

The values for SRMS, CCOR, and SRAN, for the sub-images in D_2 are given in Tables B.6, B.7, and B.8, in Appendix B. As for D_1, the results in these tables are presented in two separate parts, one for the template band, and another for the template date methods.

Each of the 19 methods is assigned a rank from 1 to 19, for each measure, in each of the 12 sub-images in D_2. These ranks are then averaged, to give the average rank of each method (AR), to two decimal places, for each of the measures. These results are presented in Table 4.6. The table also includes the absolute value of the difference, to one decimal place, between the average ranks of each method for: (1) SRMS & CCOR; (2) SRMS & SRAN; and (3) CCOR & SRAN. From these differences, the methods that are reasonably consistent for the different measures are readily identified (those for which the difference between their average ranks, for both measures, is small).

In order to see if the methods are consistent using sub-images in different data sets, only the results in Tables B.1, B.2, and B.3, for D_1, corresponding to the methods that are applied to the sub-images in D_2, are examined. Hence, the results for methods that use a well correlated template, and for methods TB/D-9 and TB/D-10 are excluded from the investigation. The methods are assigned a rank, from 1 to 19, and their average rank, for the 9 sub-images in D_1, is obtained. The consistency of the methods, for different data sets, is examined by contrasting the average ranks of each method, in D_1, and in D_2.

The average ranks of the 19 methods, in each data set, are presented in Table 4.6. The absolute value of the differences between the average ranks of each method are also presented for: (1) SRMS-CCOR; (2) SRMS-SRAN; and (3) CCOR-SRAN. As before, these differences indicate the methods that are reasonably consistent for the different measures.

Table 4.6: Average rank (AR) of each method, for SRMS, CCOR, and SRAN, and differences between AR's for (1) SRMS-CCOR; (2) SRMS-SRAN; (3) CCOR-SRAN: D_1 and D_2.

D_2									
SRMS		CCOR		SRAN		DIFFERENCES			
Method	AR	Method	AR	Method	AR	Method	(1)	(2)	(3)
LI	2.46	LI	2.38	LI	3.54	LR	0.2	2.0	2.1
CSP	2.50	CSP	2.58	CSP	3.83	LI	0.1	1.1	1.2
$TD-6$	3.71	$TD-6$	3.29	$TD-2$	4.54	CSP	0.1	1.3	1.3
$TB-6$	4.50	$TB-6$	4.67	$TD-7$	5.54	$TB-1$	0.5	0.8	1.4
$TD-7$	4.96	$TD-7$	4.79	$TD-6$	5.63	$TB-2$	0.7	0.1	0.8
$TD-2$	5.25	$TD-2$	4.88	$TD-3$	6.08	$TB-3$	0.4	2.2	1.8
$TD-8$	6.75	$TD-8$	6.54	$TD-8$	6.25	$TB-4$	0.5	3.3	3.8
$TD-3$	8.08	$TD-3$	8.33	$TB-6$	7.79	$TB-5$	0.3	0.0	0.4
$TB-7$	9.21	$TB-7$	9.33	$TB-7$	9.62	$TB-6$	0.2	3.3	3.1
$TD-5$	10.29	$TD-5$	10.25	$TD-5$	9.96	$TB-7$	0.1	0.4	0.3
$TB-2$	10.83	$TB-2$	11.54	$TB-2$	10.75	$TB-8$	0.0	2.4	2.3
$TD-4$	12.25	LR	12.08	$TD-4$	10.96	$TD-1$	0.2	0.7	0.5
LR	12.25	$TD-1$	12.54	$TD-1$	12.04	$TD-2$	0.4	0.7	0.3
$TD-1$	12.75	$TD-4$	12.54	LR	14.21	$TD-3$	0.3	2.0	2.3
$TB-8$	14.21	$TB-8$	14.25	$TB-3$	14.54	$TD-4$	0.3	1.3	1.6
$TB-5$	16.33	$TB-3$	16.33	$TB-4$	14.71	$TD-5$	0.0	0.3	0.3
$TB-3$	16.71	$TB-5$	16.67	$TB-5$	16.29	$TD-6$	0.4	1.9	2.3
$TB-4$	17.19	$TB-1$	18.50	$TB-8$	16.58	$TD-7$	0.2	0.6	0.8
$TB-1$	17.96	$TB-4$	18.50	$TB-1$	17.13	$TD-8$	0.2	0.5	0.3
D_1									
SRMS		CCOR		SRAN		DIFFERENCES			
Method	AR	Method	AR	Method	AR	Method	(1)	(2)	(3)
LI	2.22	LI	2.89	CSP	2.17	LR	0.2	2.1	1.8
$TD-7$	3.06	$TD-7$	3.06	LI	2.44	LI	0.7	0.2	0.4
CSP	3.33	CSP	3.11	$TD-3$	2.72	CSP	0.2	1.2	0.9
$TD-6$	4.22	$TD-6$	4.00	$TD-2$	6.00	$TB-1$	0.5	0.2	0.3
$TD-3$	5.00	$TD-3$	5.22	$TD-5$	6.89	$TB-2$	0.2	1.9	2.1
$TD-8$	6.00	$TD-2$	5.50	$TD-7$	7.50	$TB-3$	0.8	5.9	5.1
$TD-2$	6.28	$TD-8$	5.61	$TD-6$	8.11	$TB-4$	1.3	3.7	5.0
$TB-6$	7.22	$TB-6$	7.39	$TD-4$	9.83	$TB-5$	0.0	1.8	1.8
$TD-5$	9.17	$TD-5$	9.78	LR	9.94	$TB-6$	0.2	4.6	4.4
$TB-7$	10.67	$TB-7$	10.67	$TD-8$	10.33	$TB-7$	0.0	2.9	2.9
$TD-4$	11.39	LR	11.78	$TB-6$	11.78	$TB-8$	0.0	0.9	0.9
$TB-2$	11.94	$TB-2$	11.78	$TB-3$	11.94	$TD-1$	0.5	0.2	0.3
LR	12.00	$TD-1$	12.22	$TD-1$	12.50	$TD-2$	0.8	0.3	0.5
$TD-1$	12.72	$TD-4$	12.22	$TB-4$	13.50	$TD-3$	0.2	2.3	2.5
$TB-8$	14.78	$TB-8$	14.78	$TB-7$	13.61	$TD-4$	0.8	1.6	2.4
$TB-5$	16.00	$TB-5$	16.00	$TB-2$	13.83	$TD-5$	0.6	2.3	2.9
$TB-4$	17.17	$TB-3$	17.00	$TB-8$	13.89	$TD-6$	0.2	3.8	4.1
$TB-3$	17.83	$TB-4$	18.50	$TB-5$	14.22	$TD-7$	0.0	4.4	4.4
$TB-1$	19.00	$TB-1$	18.50	$TB-1$	18.78	$TD-8$	0.4	4.3	4.7

Similarly to the procedure adopted for D_1, and in order to clarify the overall performance of the methods, new ranks are formed from 1 to 19, for each of the measures, according to the the position of the methods in Table 4.6 (rank 1 for the method at the top). Here, 6 new ranks are formed (2 for each measure, one for D_1 and another for D_2). These new ranks are averaged, to produce new average ranks, which are presented in Table 4.5, under D_2, where $\bar{r}_a$ and s_{r_a} are the mean and standard deviation of the 6 new ranks, respectively. The minimum and maximum values of the new ranks [(m,M)] are also presented for each method.

From the differences under (1) and (2), in Table 4.6, given for D_1 and D_2, it can be seen that all methods are reasonably consistent for SRMS and CCOR (the maximum difference between the average ranks of the methods, for SRMS and CCOR is 1.3, for D_1, and 0.7, for D_2). However, for some of the methods, larger differences between their average ranks for SRMS and SRAN, or CCOR and SRAN may be observed. In D_1, for instance, 6 methods have average ranks for SRMS and SRAN (or for CCOR and SRAN) which differ by more than 3; in D_2, the number of methods for which the difference between their average ranks, for SRMS and SRAN, exceeds 3, is 2. This number is also 2, for CCOR and SRAN.

From Table 4.6 it can be noted that LI, on average, performs better than the other methods, for SRMS, CCOR, and SRAN, in D_1. However, although LI has the best average performance for SRMS and CCOR, in D_2, method CSP performs best for SRAN, in this data set.

The absolute value of the differences between the average ranks of the methods (DAR), for SRMS, CCOR, and SRAN, in D_1, and D_2, are given in Table 4.7. From the differences for SRMS and CCOR, it can be seen that most methods are reasonably consistent between data sets, for these two measures (only for method TD-3 the difference between the average ranks for SRMS (and CCOR), in one data set, and another, exceeds 3). However, most methods are not reasonably consistent for SRAN, in one data set and another.

Table 4.7: Differences between the average ranks of the methods in D_1 and in D_2, for SRMS, CCOR, and SRAN.

Method	DAR		
	SRMS	CCOR	SRAN
LR	0.25	0.31	4.27
LI	0.24	0.51	1.10
CSP	0.83	0.53	1.67
$TB-1$	0.00	0.00	1.65
$TB-2$	1.11	0.24	3.08
$TB-3$	1.13	0.67	2.60
$TB-4$	0.79	0.00	1.21
$TB-5$	0.33	0.67	2.07
$TB-6$	2.72	2.72	3.99
$TB-7$	1.46	1.33	3.99
$TB-8$	0.57	0.53	2.69
$TD-1$	0.03	0.32	0.46
$TD-2$	1.03	0.63	1.46
$TD-3$	3.08	3.11	3.36
$TD-4$	0.86	0.32	1.13
$TD-5$	1.13	0.47	3.07
$TD-6$	0.51	0.71	2.48
$TD-7$	1.90	1.73	1.96
$TD-8$	0.75	0.93	4.08

4.5.4 Results for Single Band and Template Band Methods

Since information from the different bands reaches the Earth almost simultaneously, and as the multispectral data are reasonably registered, template band methods can be implemented routinely to replace missing scan lines in the imagery. This is not as simple using template date methods, since data from different passages may not be readily available, and may need to be registered before they can be effectively used. Thus, it seems interesting to investigate the sort of results that only the template band methods give, in contrast to the results obtained for the single band methods. An evaluation of the results obtained only for the single band methods, and the template date methods, is also carried out.

In this subsection, only the single band, and the template band methods are evaluated for each of the measures in §4.2.2. To accomplish this evaluation using the sub-images in D_1, the results from the 21 methods (3 single band methods, 8

from the template band methods that use a poor correlated template (TB-mL), 8 from the template band methods that use a well correlated template (TB-mH) and 2 using two template bands) are independently grouped, for each measure. Recall that the results for these methods are given in Tables B.1, B.2, and B.3, in Appendix B, under *Template Band*, for SRMS, CCOR, and SRAN, respectively.

For the OT's from D_2, only 11 methods are evaluated, since the original sub-images in this data set are always poorly correlated with the template band (which excludes investigation of methods $TB-\mathrm{m}H$), and as data from two template bands are not available (which excludes investigation of methods TB-9 and TB-10). The values for SRMS, CCOR, and SRAN, for D_2, are given in Tables B.6, B.7, and B.8, in Appendix B, respectively.

In order to investigate the consistency of the methods for sub-images from different data sets, results are also obtained for D_1, only for the methods that are applied to the sub-images from D_2, and using only the sub-images in corresponding bands (bands 4 and 5), which are poorly correlated with the template [OT's (7,8,9),(16,17,18) in Table 4.1].

The results for SRMS, CCOR, and SRAN are first presented for D_1, and then for D_2. Since the methods have a similar performance for SRMS and CCOR, as indicated in §4.5.2 and §4.5.3, the results for these two measures are presented together. Although the average performances of the methods are presented for SRMS, those obtained for CCOR are only slightly different, and do not warrant being presented separately.

4.5.4.1 Results for SRMS and CCOR, using D_1

Since the performances of the methods, for SRMS and CCOR, are similar, their results are presented in a single section.

To provide more readily an evaluation of the performances of the methods for SRMS, the plot for this measure is given in Figure 4.1, for some of the methods, for OT's 1 to 18 in Table 4.2. From the figure, the results for methods TB-mL and TB-mH can be easily contrasted. Also, as the results are first given for the sub-images in band 3 (OT's 1 to 6), followed by those in band 4 (OT's 7 to 12), and finally by those in band 5 (OT's 13 to 18), the results for SRMS, for sub-images in different bands can also be contrasted. The results for some of the methods have been deliberately omitted from the plot, due to their similarity

with those for other methods (e.g., LI and CSP, TB-6 and TB-7), or to their consistent inferior performance (e.g., TB-1, TB-4).

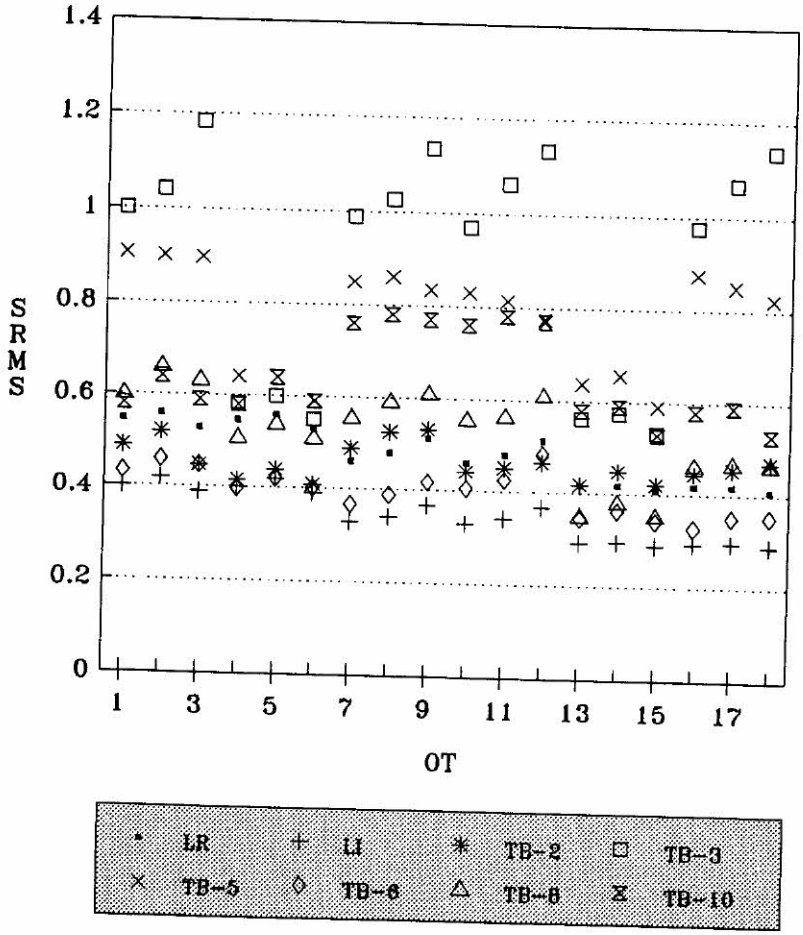

Figure 4.1: Plot for SRMS for single band methods, and the methods using a template band: D_1.

From Figure 4.1 it can be seen that, in general, the methods perform better (have lower values for SRMS and CCOR), when the original sub-image, and the template, are well correlated [e.g. OT's (4,5,6) and (13,14,15)]. However, it seems that some of the methods are more affected than others by a low correlation between the two sub-images. Note, for instance, the small difference between the values for SRMS for methods TB-2, TB-6, and TB-8, and TB-10, in OT's (13,14,15) and (16,17,18). For these OT's, the correlations between the original sub-image and the template are, respectively, (0.719, 0.705, 0.760) and (0.146, -0.016, -0.122).

The average rankings of the single band, and the template band methods, for

SRMS, are as follows:

LI	*CSP*	*TB − 6H*	*TB − 6L*	*TB − 2H*	*TB − 7H*	*TB − 7L*	*TB − 8H*	*LR*	*TB − 2L*	*TB − 8L*
1.3	2.5	3.3	4.3	5.8	6.7	6.8	8.1	8.1	8.4	11.6
TB − 10	*TB − 5H*	*TB − 3H*	*TB − 9*	*TB − 4H*	*TB − 5L*	*TB − 1H*	*TB − 4L*	*TB − 3L*	*TB − 1L*	
12.4	13.3	13.6	15.8	15.8	16.7	18.2	18.3	19.2	20.8	

Note that, on average, the single band methods LI and CSP perform better than the template band methods, even when there is a good correlation between the original sub-image and the template. Although LI performs better than the other methods in almost all sub-images (has rank 1 or 1.5 in 7 out of 9 cases, and rank 2 in the remaining 2), CSP works well for the sub-images in bands 4 and 5, while it is consistently outperformed by method TB-6H in the sub-images in band 3. Methods CSP and TB-7H perform similarly in the sub-images in this band.

A closer observation of the residuals obtained for methods CSP and TB-7H, and for TB-6H, using OT 1 $[D_1(13)(14)]$ shows that large residuals occur for all these methods in the areas of intense moisture shown in Figure 3.5 (**C**), and that these residuals are larger for methods CSP and TB-7H, than for TB-6H.

The observation that the purely spatial methods, LI and CSP, perform better than methods TB-6H or TB-7H, in sub-images in more heterogeneous bands (bands 4 and 5) can possibly be explained from the following: since varying degrees of moisture can be observed even within small areas, and since different bands respond differently to the presence of moisture on the ground, the basic assumption of Guindon (1984), that '*the correlation between adjacent band grey levels can be expressed in a simple multiplicative sense and that this correlation is stationary over distances of the scale of the interpolation window (i.e. 3 to 5 lines)*' fails, and the methods do not perform well (especially in more heterogenous bands). Since the areas of intense moisture indicated by C in Figure 3.5 cross diagonally the area delimited by lines 78 and 92, and columns 27 and 44, in all sub-images, and as they are narrow (±3 pixels), $\frac{u_t^k(i-1,j)}{u_t^l(i-1,j)} \approx \frac{u_t^k(i,j)}{u_t^l(i,j)} \not\approx \frac{u_t^k(i+1,j)}{u_t^l(i+1,j)}$, which may explain the 'poor' performance of methods TB-6 and TB-7 in the area. For instance, the ratios between the pixel values in the original sub-image and the template, in line 88, 89 and 90, intersected by column 41 are 1.27, 0.84, and 0.49, indicating the variation in the response of the same area in the ground, in different bands.

Note also the similar performance of methods TB-6L and TB-6H. A closer

investigation of the results for these two methods shows that TB-6L performs better than TB-6H in the sub-images in band 4, and similarly in the sub-images in band 5, whilst for the sub-images in band 3, method TB-6H (which uses band 5 as template) performs significantly better than TB-6L (which uses band 4 as template). The average rank of methods TB-6L and TB-6H for sub-images in bands 3, 4 and 5 are respectively 6.2 and 1.6; 3 and 4.5; and 3.7 and 3.7.

By contrasting the difference images displayed in the first and second columns of the frame displayed in Figure 3.8, corresponding to bands 3 and 4, and 3 and 5, respectively, it can be seen that more gradual shifts in colour are observed in the difference images for bands 3 and 5, than between bands 3 and 4, which explains the superior performance of Guindon's method using band 5, rather than band 4. For instance, the estimates of the pixel values along the road, from method TB-6H, are much better than those obtained for method TB-6L, as are those in the areas of intense moisture. Note that not only are the areas of intense moisture in the difference images for bands 3 and 5 narrower than those for bands 3 and 4, but also smaller variations in the grey levels of the neighbouring pixels occur in the area.

Despite the fact that more differences are observed in Figure 3.8 between the sub-images in bands 4 and 5, than between those in either bands 3 and 4, or 3 and 5, note that they concentrate in reasonably large, homogenous areas, where no great variations are expected to occur between neighbouring pixels. Although $u_t^k(i-1,j) - u_t^l(i-1,j) \approx u_t^k(i+1,j) - u_t^l(i+1,j)$ does not imply that $\frac{u_t^k(i-1,j)}{u_t^l(i-1,j)} \approx \frac{u_t^k(i+1,j)}{u_t^l(i+1,j)}$, it may be an indicator that Guindon's assumption holds, in which case good estimates from methods TB/D-6, and TB/D-7 would be expected.

Note that despite the poor correlation between the sub-images in band 5 and those in band 4 (maximum correlation is 0.146), method TB-6B performs similarly to TB-6H, for which the minimum correlation between the original sub-image and the template is 0.705. Thus, it seems that Guindon's methods are not as sensitive to a poor correlation between the sub-image and the template, as they are to 'local', contrasting, differences in response of the objects, in the two bands (original and template).

As mentioned at the beginning of this section, the methods have a similar performance for SRMS, and CCOR. To give an idea of how consistent the methods

are, for the two measures, the differences between the ranks assigned to each of the 21 methods, for SMRS and for CCOR, were computed for the 9 sub-images in D_1. The mean and standard deviation of these differences are 0.59 and 0.79, respectively, which clearly shows the similarity of the results obtained for the methods, for both measures.

4.5.4.2 Results for SRAN using D_1.

Results for SRAN have been obtained in a manner similar to that used for SRMS and CCOR. Recall that the values for this measure are given in Table B.3 in Appendix B. The minimum and maximum [(m,M)] values for the residuals are also presented in Table B.5, in Appendix B.

The methods are in general not consistent for SRAN and SRMS, or SRAN and CCOR. Hence, methods which have small values for SRMS and CCOR, may have large values for SRAN, indicating the presence of some 'localized' large residuals in the corresponding test image.

The average rankings of the single band, and the template band methods, for SRAN, are given below.

LI	*CSP*	*TB − 6L*	*TB − 2H*	*TB − 3H*	*TB − 9*	*TB − 7L*	*TB − 5L*	*LR*	*TB − 10*	*TB − 4H*
2.3	2.4	6.5	7.3	7.3	9.1	9.5	9.8	10.4	10.7	10.8
TB − 4L	*TB − 3L*	*TB − 8L*	*TB − 5H*	*TB − 2L*	*TB − 1H*	*TB − 6H*	*TB − 8H*	*TB − 7H*	*TB − 1L*	
11.1	12.0	12.9	13.1	13.9	14.6	15.3	15.4	16.7	19.8	

It is interesting to note that in the list above, some of the methods that use a better correlated template have an inferior performance than others using a poor correlated template. In particular, methods TB-6H, TB-7H, and TB-8H have, on average, larger values for SRAN than most single band, and template band methods.

4.5.4.3 Results for SRMS and CCOR, using D_2.

The similar performance of the methods, for SRMS, and CCOR, observed in D_1 (§4.5.4.1), is also observed in D_2. Hence, these two measures are also treated together here.

Figure 4.2 gives the plot for SRMS, for some of the methods, for OT's 1 to 12 in Table 4.3.

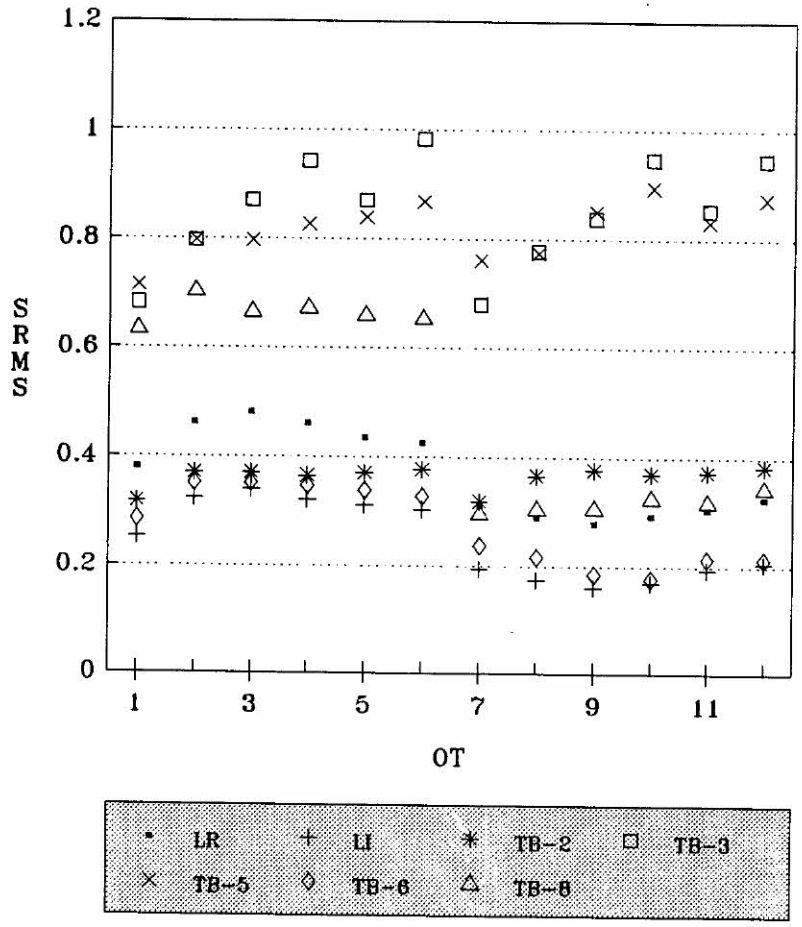

Figure 4.2: Plot for SRMS for the single band methods, and the methods using a template band: D_2.

Figure 4.2 shows the similar performances of the methods, in the different OT's. Recall that the sub-images in D_2 are, in general, not well correlated with the template (the minimum correlation is 0.138, and the maximum is 0.579). Note, as for D_1, that methods TB-2, TB-6, and TB-8, seem to be less affected by the correlation between the original sub-image and the template than others (TB-3, TB-5). Note also that method TB-8 performs consistently better than method TB-2, in OT's 7 to 12 (when all original sub-images are in band 5). A possible explanation for this is the fact that method TB-8 first applies method TB-2 to the data in the lines above and below, and then uses an approach similar to TB-6. In the first step, method TB-2 'smooths' the data in the lines above

and below, making them more similar to the data in the template. Hence, after this first operation, the data at the boundaries between the reforested area, and soil with low density vegetation, are not as contrasting as they are in the original sub-image (note that the boundaries between these two types of land cover, in the sub-images in band 4, are not as well defined as in band 5).

The difference between the ranks assigned to each method, in each of the 12 OT's from D_2, are always less than 1.5, except for methods TB-2 and TB-8, and even for these two methods, the difference is not large (3 for TB-2, and 2.5 for TB-8). This indicates that the methods are reasonably consistent for this measure.

The average ranks of the methods, for SRMS, are given below:

LI	CSP	$TB-6$	$TB-7$	$TB-2$	LR	$TB-8$	$TB-5$	$TB-3$	$TB-4$	$TB-1$
1.5	1.6	2.9	4.5	5.5	5.6	6.4	8.3	8.7	9.9	11.0

For methods LI and CSP, the minimum and maximum [(m,M)] ranks in the 12 OT's are (1,2), indicating the consistently better performance of these single band methods, in contrast to the methods using a template band. Due to the usually poor correlation between the original sub-images and the templates, in OT's 1 to 12, and from the different response of the objects on the ground, in bands 4 and 5, (see Figure 3.22), it was not expected that the template band methods would perform better than LI or CSP.

The performances of the methods, for SRMS, are also consistent in OT's (7,8,9) [band 4] and (16,17,18) [band 5], from D_1. In these 6 OT's, the range of the ranks of any of the methods never exceeds 1. As for D_2, the minimum and maximum [(m,M)] ranks of methods LI and CSP, in all 6 OT's are (1,2), indicating the consistent superior performance of these single band methods, in contrast to the methods that use a template band. Note that the maximum correlation between the original sub-images and the templates, in OT's (7,8,9) and (16,17,18), is 0.146, and this might explain the failure of the template band methods.

When contrasting the average ranks of the 11 methods, for SRMS, using OT's 1 to 12 in Table 4.3 (for D_2), and OT's (7,8,9) and (16,17,18) in Table 4.2 (for D_1), it is observed that the maximum difference between these average ranks, for each method, never exceeds 1.1, thus indicating that the methods are consistent between both data sets.

The similar performance of the methods, for SRMS and CCOR, is indicated by the small difference between the average ranks of the methods, for both measures. For D_2, the maximum difference between the average ranks of the 11 methods, for SRMS and CCOR is 1 (using OT's 1 to 12 in Table 4.3); and it is 1.4 for D_1 [using OT's (7,8,9,16,17,18) in Table 4.2].

4.5.4.4 Results for SRAN using D_2.

Although it has been observed that more methods are reasonably consistent for any combination of any two of the three measures, using the sub-images from D_2, than using those from D_1, their performance is not as consistent as for SRMS, or CCOR. For instance, the minimum and maximum ranks of methods LR and TB-7, using the 12 OT's from D_2, are (3,10) and (4,10), respectively, whilst they are (7,11) and (3,6.5) for SRMS, and (7,11) and (2.5,5.5) for CCOR.

The average ranks of the methods, for SRAN, using OT's 1 to 12 from D_2 are:

LI	*CSP*	*TB−6*	*TB−7*	*TB−2*	*LR*	*TB−4*	*TB−3*	*TB−5*	*TB−8*	*TB−1*
1.5	1.9	3.8	5.1	5.2	6.9	7.2	7.5	8.4	8.8	9.6

and using OT's (6,7,8,16,17,18) from D_1:

LI	*CSP*	*LR*	*TB−3*	*TB−4*	*TB−6*	*TB−8*	*TB−5*	*TB−2*	*TB−7*	*TB−1*
1.0	2.0	4.0	5.1	6.4	6.4	6.5	7.7	7.8	8.3	10.9

Contrasting the average ranks of the methods, using OT's 1 to 12 in Table 4.3, with those obtained for OT's (7,8,9,16,17,18) in Table 4.2 indicates that the largest differences between the average ranks (DAR) for SRAN, in both data sets, occur for methods TB-2 (DAR=2.6), TB-6 (DAR=2.6), LR (DAR=2.9), and TB-7 (DAR=3.2).

4.5.5 Results for Single Band and Template Date Methods

In this section, the single band, and the template date methods are evaluated, using OT's 19 to 27 in Table 4.2, and OT's 13 to 24 in Table 4.3.

The fact the original sub-images, and the template date, are always well correlated, leaves only 13 methods to be investigated (3 single band, 8 using a template

date, and two using two template dates). Recall that the results for these methods, for SRMS, CCOR, and SRAN, are respectively given in Tables B.1, B.2, and B.3, in Appendix B, under *Template Date.* In Table B.5, in Appendix B, the minimum and maximum values [(m,M)] for the residuals are also presented.

As two reasonable template dates are not available for the sub-images in D_2, methods TD-9 and TD-10 are excluded from the investigation for this data set, leaving only 11 methods to be examined. The values for SRMS, CCOR, and SRAN, for these methods, are respectively presented in Tables B.6, B.7, and B.8, in Appendix B. Table B.10, in Appendix B, gives the minimum and maximum [(m,M)] values for the residuals.

In order to evaluate the performances of the methods for sub-images in different data sets, the results for the 11 methods, using OT's 13 to 24 in Table 4.2, are independently considered.

The methods are now evaluated for each of the measures.

4.5.5.1 Results for SRMS and CCOR, using D_1

Figure 4.3 gives the plot for SRMS for some of the single band, and the template date methods. As in §4.5.4.1, some of the results have been deliberately deleted from the plot, due to their similarity with the results from other methods (LI and CSP, TD-6 and TD-7), or their consistent inferior performance (TD-1, TD-4).

The fact that in OT's (25,26,27) [band 5], the original sub-images and the template date are highly correlated (the minimum correlation is 0.920), might explain the better performance of all methods in these OT's, as can be seen from Figure 4.3.

The average performances of the template date methods, for SRMS, is indicated by their average rank using all OT's from D_1. These average ranks are given below.

LI	$TD-7$	CSP	$TD-6$	$TD-3$	$TD-8$	$TD-2$	$TD-10$	$TD-5$	$TD-9$	$TD-4$	LR	$TD-1$
2.3	3.2	3.4	4.4	4.7	6.1	6.4	6.8	9.3	9.3	11.3	11.4	12.4

Note that, on average, method TD-7 performs better than method TD-6. A closer investigation of the results obtained from these two methods reveals that TD-7 is better than TD-6 in all OT's, except those in band 4 [(22,23,24)].

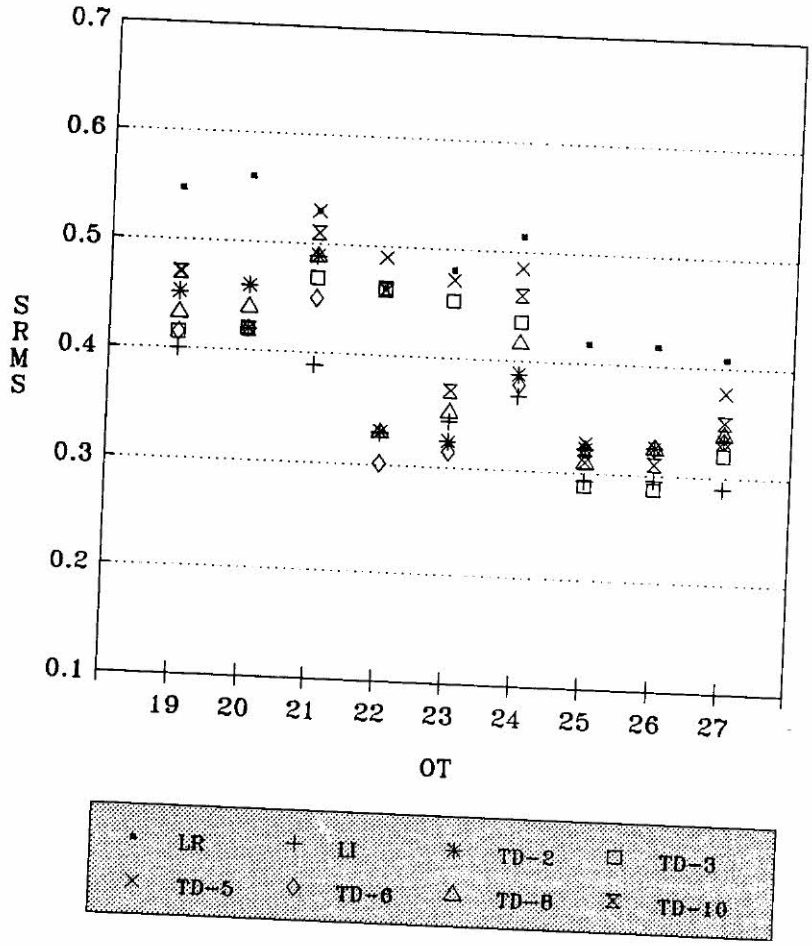

Figure 4.3: Plot for SRMS for the single band methods, and the methods using a template date: D_1.

The average ranks of these two methods, using these 3 OT's are 1.8 and 2.7, respectively.

It has been observed that method TD-6 has an inferior performance in OT's (25,26,27) [band 5], than in OT's (19,20,21) [band 3], or OT's (22,23,24) [band 4]. The average ranks of this method, for OT's in bands 3, 4, and 5, are respectively 3.8, 1.8, and 7.5. A closer investigation of the results for method TD-6, for sub-images in band 5, indicates that the method has some few, extremely large residuals, which also increases the values for SRMS, in OT's (25,26,27).

The occurrence of these large residuals can be predicted from the difference images in Figure 3.7 (c). Consider, for instance, the difference image for the

24/06 data from 10/07 data (+128). The residuals obtained from method TD-6, for the pixels which show as yellow spots in the difference image, are all large. For each of the pixels shown as yellow spots, note the large range of colours that separates them from their neighbouring pixels (the one above, and the one below). This indicates a large difference between the corresponding pixel values (in the difference image), which suggests that Guindon's assumption does not hold. The largest residual (54) observed for method TD-6, corresponds to one of the pixels shown as a yellow spot, at the top left of the difference image.

A sequence of large residuals (values between 14 and 27) is also observed at the top left of the test image obtained from TD-6, corresponding to the narrow strip shown in dark magenta in the difference image (line 1, between columns 9 and 19).

It is interesting to note that even when the original sub-images are highly correlated with the template (as is the case in OT's 25 to 27), methods TD-1 and TD-4 are usually outperformed by the other methods. These methods, in particular, give poor estimates of the pixels in areas of change (for instance, for sub-images in band 4, in the areas shown in red, yellow, or magenta, in Figure 3.7). These are also the areas where method TD-3 usually fails. However, as this method uses, besides the estimate from TD-1, the information from the neighbouring sites of the one that is missing, it is expected to have, at least, a better performance than method TD-1.

As the template date methods usually perform better than the template band methods (due to the higher correlation between the original sub-images and the template date), note the difference between the average performance of the method of adjacent line replacement (AR=11.4), amongst the template date methods, and in §4.5.4.1 (AR=8.6), amongst the template band methods.

In just a few instances, a method using a template band performed better than its corresponding method using a template date. Smaller values for SRMS have been obtained for methods TB-2H and TB-6H, than for TD-2 and TD-6, respectively. This has only been observed for original sub-images in band 3.

The similar performance of the methods, for SRMS, and CCOR, can be deduced from the value of the maximum difference between their average ranks, for each of these measures, which does not exceed 0.8.

4.5.5.2 Results for SRAN, using D_1.

The rankings of the single band, and template date methods, for SRAN, are given below.

CSP	*LI*	*TD − 3*	*TD − 2*	*TD − 9*	*TD − 5*	*TD − 10*	*TD − 7*	*TD − 6*	*LR*	*TD − 8*	*TD − 4*	*TD − 1*
2.4	2.5	2.8	6.2	7.1	7.3	7.4	7.4	7.5	9.4	9.7	9.9	11.2

By contrasting the average ranks above, with those for SRMS, in §4.5.5.1, it can be seen that seen that the largest differences between these average ranks (DAR) occur for methods TD-6 (DAR=3.1), TD-8 (DAR=3.6), and TD-7 (DAR=4.2). This may indicate these methods have some few, large, residuals. For all the other methods, the maximum difference between their average ranks, for both measures, does not exceed 2.6.

4.5.5.3 Results for SRMS and CCOR, using D_2.

The plot for SRMS, for some of the methods, for OT's 13 to 24 in Table 4.3, is given in Figure 4.4. Recall that the values for SRMS and CCOR, for D_2, are given in Tables B.6 and B.7, in Appendix B.

Note that despite the high correlation between the original sub-images and the template date in OT's 19 to 24 (the minimum correlation is 0.951), the template date methods do not consistently have better results than the purely spatial methods of LI and CSP. This might be justified by the particular structures present on the sub-image, characterized by well defined, man-made linear features. Within the regions delimited by the sharp boundaries that separate the two types of land cover, the data are reasonably homogeneous, and the spatial methods perform well. Obviously, these methods will perform very poorly on those portions of the line that lie on the boundary between different types of land cover. As the template date methods rely on few changes in land cover occurring between the passages, they may perform better on the boundaries between the regions (if these are permanent), but poorer than LI and CSP in the homogeneous areas.

The rankings of the methods, for SRMS, using OT's 12 to 24 are as follows:

LI	*CSP*	*TD − 6*	*TD − 7*	*TD − 2*	*TD − 8*	*TD − 3*	*TD − 5*	*LR*	*TD − 4*	*TD − 1*
1.6	2.5	2.9	3.9	5.0	6.2	6.3	8.5	8.9	9.6	10.5

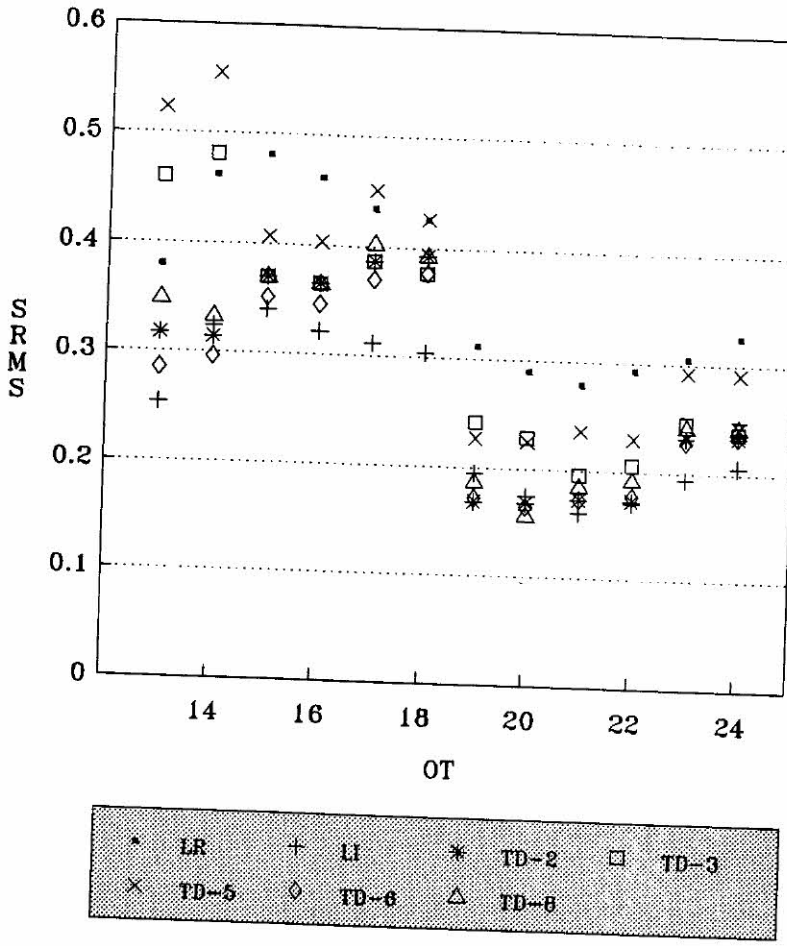

Figure 4.4: Plot for SRMS for the single band methods, and the methods using a template date: D_2.

The rankings of the methods, for D_1 are similar to those given above for D_2. For all methods, except TD-3, the difference between their average ranks, for both data sets, does not exceed 1.5. For method TD-3 this difference is 2.1. This also appplies for CCOR.

It might be interesting to point out that method TD-6 performs better in OT's (16,17,18) (its average rank is 1.8) than in OT's (19,20,21) (its average rank is 6.3). From the uniform range of colours on the difference images in Figure 3.21 (1, 2, and 3) (corresponding to band 4), Guindon's method can be expected to give good estimates. However, the greater contrast of colours in the difference images in Figure 3.21 (4, 5, and 6) (corresponding to sub-images in band 5) indicates

that large residuals can occur, increasing the value for SRMS.

4.5.5.4 Results for SRAN using D_2.

The average rankings of the methods, for SRAN, are given below, for D_2, and D_1.

LI	*CSP*	*TD − 2*	*TD − 7*	*TD − 6*	*TD − 3*	*TD − 8*	*TD − 5*	*TD − 4*	*TD − 1*	*LR*
3.4	3.5	3.9	4.5	4.7	4.7	5.1	7.9	8.7	9.4	10.3

and for D_1:

LI	*CSP*	*TD − 3*	*TD − 2*	*TD − 7*	*TD − 6*	*TD − 5*	*LR*	*TD − 4*	*TD − 8*	*TD − 1*
1.2	2.3	3.3	5.3	6.5	6.8	7.3	7.4	8.2	8.9	9.0

By contrasting the average ranks of the methods, for SRAN, and SRMS (given in §4.5.5.3), it can be observed that, for D_2, most methods are reasonably consistent (the maximum difference between the average ranks of the methods, for both measures, does not exceed 1.8), whereas for D_1, larger differences are observed, in particular for methods TD-6 (DAR=2.7), TD-7 (DAR=2.8), and TD-8 (DAR=3.3).

Similarly to the template band methods, most template date methods are also not consistent for SRAN, and large ranges for the ranks assigned to the methods, in OT's 13 to 24, are usually observed.

4.6 Summary of Numerical Results and Discussion

From the results presented in §4.5, the following conclusions can be drawn:

Since all methods are consistent for SRMS and CCOR, in both data sets, it is possible that only one of these measures suffices as an indicator of the performances of the methods. The fact that most methods are not consistent for SRMS and SRAN (and consequently, for CCOR and SRAN) indicates that possibly an evaluation based solely on SRMS (or CCOR) may not be enough to characterize the overall performance of the methods. It is important to realize that better estimates of the missing values may be obtained for methods that have large SRAN

(which may only indicate the presence of some 'outlier' residual). Some methods, in particular methods TB/D-6 and TB/D-7, are very sensitive to changes in response from the objects in the 'local' neighbourhood of the missing pixel, in one band and another, or to 'local' changes, from one passage to another, and some 'local', large residuals are likely to be observed. The occurrence of these large residuals is highly dependent on the type of structures that appear on the image, and their nature ('dynamic', or permanent).

The observation that the purely spatial methods LI and CSP in general outperform the template band methods can be possibly explained by the low correlation between the sub-images and the template band, in both data sets. However, to find an explanation for the fact that these methods usually perform well, even amongst the template date methods, is a more difficult task. For D_2, the structure of the features on the sub-images may have benefited the purely spatial methods. For D_1, the fact that differences in land cover may have occurred between the passages, as indicated in the difference images in Figure 3.7, may have contributed to the inferior performance of the template date methods, in contrast to the purely spatial methods of LI and CSP.

Since methods LI, TB/D-2, TB/D-3, TB/D-6, TB/D-7, and TB/D-8 estimate each pixel value in the original sub-image incorporating the information from a 'local' neighbourhood (1 pixel above and 1 pixel below, except method TB/D-7, which uses 2 pixels above and 2 below), they in general perform better than methods TB/D-1, TB/D-4, or TB/D-5. Note, however, that the estimates of the pixel values in 'dynamic' areas, where 'local' differences are more likely to occur (for instance, pixels which are close geographically may belong to distinct types of land cover, or may be associated to different degrees of soil moisture), can be poorer from the methods that incorporate 'local' information, than from other methods (TB/D-1, TB/D-4, and TB/D-5, for instance). Good estimates of the pixel values over 'dynamic' areas are obtained using LI, if the objects in their 'local' neighbourhood have a similar response in the band under consideration. The extent to which this method performs well depends on the similarity of the information in the 'local' neighbourhood of the pixels being estimated. For methods TB/D-2, TB/D-6, TB/D-7, and TB/D-8, the condition is that the relative

changes in the local neighbourhood of the missing pixel be approximately the same, in both the original, and the template sub-images.

Amongst the template band/date methods, Guindon's methods TB/D-6 and TB/D-7 usually perform better than the other methods. However, Guindon (1984) reported that his methods, in general, performed better than LI, or CSP. The fact that his results do not agree with the results found in this study may have two explanations: firstly, as the sub-images used by Guindon (1984) are not displayed in his paper, it is impossible to know the kind of structures present on the image, and their impact on the methods he has investigated; secondly, with his methods, Guindon (1984) always used information from neighbouring bands, noting that because data in band 4 were not well correlated with data from either bands 3, or 5, better results were observed for single band interpolation. Unfortunately, data from other bands are not available for D_1, or D_2. It is possible that by using information from band 2, for instance, better results would be obtained for the template band methods, than by using the information from band 5, as here (despite the fact that the sub-images in bands 3 and 5 used here are well correlated, and that this is the condition for the methods to work well). However, observation of the difference images in Figure 3.8 show that the objects on the ground respond similarly only in bands 3 and 5, but possibly not similar enough to allow methods TB-6/7 to have better results than LI or CSP alone.

Since for the template band methods the sub-images are usually poorly correlated with template, this may have favoured the template date methods which, in general, perform better than the template band methods. It has been noted that methods TB-2 and TB-6 are the least sensitive to the degree of correlation between the sub-image and the template. In some instances, better results (smaller SRMS, CCOR) have been obtained for these template band methods, than for their corresponding methods using a template date, despite the lower correlation between the original sub-images and the template band. This suggests that besides a high correlation between the sub-image and the template, it is also important (if not essential) that few 'local' variations occur, between the original sub-image and the template (band or date).

4.7 Visual Evaluation of the Methods

To evaluate the methods visually, photographs of the test images, residual images, and 'cut' images have been obtained for all methods (except TB/D-7 and TB/D-10, due to their similarity with methods TB/D-6 and TB/D-9, respectively). The photographs of the test images, residual images, and 'cut' images are presented separately. However, each of these photographs display the results for several methods, which are presented in the following order:

LI	LR	T$\star-1$
T$\star-2$	T$\star-3$	T$\star-4$
T$\star-5$	T$\star-6$	T$\star-8$

where $\star$ is either only B, or only D, depending on the template used (band or date, respectively).

The test images, residual images, and 'cut' images obtained for method TD-9, for OT's 19 to 27 in Table 4.2, are presented separately in Figures 4.38, 4.39, and 4.40.

In order to avoid unnecessary repetition, the visual results (test image, residual image, and 'cut' image) are given here only for some of the OT's from D_1, and D_2. Note, however, that results have been observed for all OT's, in both data sets. The comments below, drawn on the basis of the results presented in Figures 4.5 to 4.40, are valid for all OT's. The methods are evaluated by their ability to reproduce, as closely as possible, the original sub-image, as indicated by both the test, and the residual images.

Since the approach adopted in this chapter is to replace all the lines in the original sub-images, the test images from LR are simply a one line shifted version of the original sub-image, and can thus be used as a 'reference' to contrast the results for the other methods. Hence, the real effect of LR cannot be properly appreciated from simple observation of its test images. However, the residual images clearly show the deformations introduced by this method on particular image structures, especially linear ones, and in more heterogeneous bands – see, for instance, Figures 4.6, 4.9, 4.27, 4.30, and 4.36.

From the 'cut' images for the LR method, the systematic and consistent defect on all sub-images in the second data set, mentioned in Chapter 3 (§3.3), can be

clearly appreciated – refer to Figures 4.22, 4.25, 4.28, 4.31, 4.34, and 4.37. As lines 33, 65, and 97 are simply duplicates of lines 32, 64, and 96, all estimates obtained from LR, for those lines, have zero residual. This explains the continuous green lines on the 'cut' images, on the former lines. Note that the third defective line, corresponding to line 97, usually contains intermittent sequences of values which have been replaced by the corresponding values on the line immediately above – see Figures 4.22, 4.34, and 4.37.

The method of linear interpolation, which in general performs well for the numerical evaluations carried out in the previous sections, consistently has a 'blurred' test image, with consequent reduction in resolution – see, for instance, Figures 4.5, 4.8, 4.11, 4.14, 4.17, and 4.32. Because LI is just a linear filter, it tends to have spatial smoothing effects, which especially affects the linear features on the image. Fusco & Trevese (1985) have noted that

> 'From the statistical point of view, *linear interpolation* improves both *SRMS* and *CCOR* in respect to *adjacent line replacement.* However, the improvement in respect to *adjacent line replacement* is not as strong as indicated by the statistical parameters; some structure could be altered even more by *linear interpolation* than by *adjacent line replacement.*'
>
> Note: Contents in *italics* adapted here, from the original text.

However, for the particular structures on the sub-images investigated here, adjacent line replacement has consistently introduced more distortions on the image than the method of linear interpolation.

Note from Figures 4.6, 4.9, 4.27, 4.30, 4.33, and 4.36 (and the corresponding 'cut' images) that LI estimates with larger error the pixel values at the boundaries between regions of contrasting response, such as those corresponding to the road that crosses the two wheat fields, on the sub-images in band 5, from D_1, or those at the boundaries between the reforested area and the areas of low density vegetation, on the sub-images in band 5, from D_2.

Note, however, that because different bands respond differently to the same objects on the ground, the pixel values associated to the road are better estimated in the sub-images in bands 3 and 5, than in band 4. Note, from Figure 3.2 that

the responses from the road, and the wheat fields, are most different in band 4, than in either band 3, or 5, explaining the poorer performance of LI along the road, in all OT's in band 4 (photographs not provided).

Note from the residual images displayed in Figure 4.9, for LI and TD-6, that method TD-6 does not distort the pixels values at the boundaries between the different types of ground cover, in the same extent that LI does. From the figure, the close correspondence between the occurrence of large residuals from Guindon's method and the areas of contrasting 'local' differences shown in Figure 3.7 (c) can be appreciated. Observe that the pixel values on the road are estimated well using TD-6 [no contrasting 'local' differences are noticed on Figure 3.7 (c) for the majority of the pixels along the road], but not LI. However, due to the homogeneity of sub-images in band 3, note that LI estimates well the pixels in this feature on the sub-images in this band [$D_1(33)$, for instance], as can be noted on the residual image for this method, in Figure 4.12, and the corresponding 'cut' image in Figure 4.13. This figure also shows that method TB-6 does not perform well along the road, essentially because of the contrasting difference in response of this target, in bands 3 and 4 (used as the template band). As the road is narrow, and due to the fact that it crosses the sub- image diagonally, 'local' differences are more likely to occur, explaining the failure of Guindon's method in this particular image, and feature. Note, however, the superior performance of method TD-6 in the corresponding residual image in Figure 4.30, for OT 20 [$D_2(25)(15)$]. Due to the heterogeneity of the sub-images in band 5, LI does not perform well at the boundaries between the different types of land cover, when more significant 'local' differences occur. The use of information from a template date, if no significant changes in land cover occur between the passages, can improve the estimation of these pixels, as can be seen in the 'cut' image in Figure 4.31.

Whenever there is a poor correlation between the original sub-image and the template, methods TB/D-1 and TB/D-4 tend to reproduce the features in the template, completely masking the true features in the original sub-image. This can be observed in the test images obtained for these methods, in OT 14 [$D_1(25)(23)$, in Figure 4.5], and in OT 3 [$D_1(33)(34)$, in Figure 4.11]. The correlations between the original sub-image and the template band in OT 14, and OT

3, are 0.705 and -0.126, respectively. Note, by contrasting Figures 4.5 and 3.4 (for OT 14), and Figures 4.11 and 3.2 (for OT 3), how closely the test images obtained for methods TB-1 and TB-4 resemble the template band. For the second data set, the 'poor' results from methods TB-1 and TB-4 can also be observed in Figures 4.20, 4.26, and 4.32, for OT's 2, 8, and 10, in Table 4.3. The correlations between the original sub-image and the template band, for each of these OT's are 0.441, 0.441, and 0.172, respectively.

To a lesser extent, the test images for methods TB/D-3 and TB/D-5 show the same effect as that observed for methods TB/D-1 and TB/D-4. Note, however, the improved results obtained for methods TD-1, TD-3, TD-4, and TD-5, in contrast to those obtained for the corresponding template band methods, in the following sequence of figures:

1. 4.5 $[D_1(25)(23), rb_{35} = 0.705]$ and 4.8 $[D_1(25)(15), rd_{12} = 0.937]$;
2. 4.11 $[D_1(33)(34), rb_{34} = -0.126]$ and 4.17 $[D_1(33)(23), rd_{23} = 0.817]$;
3. 4.20 $[D_2(24)(25), rb_{45} = 0.441]$ and 4.23 $[D_2(24)(14), rd_{12} = 0.810]$;
4. 4.26 $[D_2(25)(24), rb_{45} = 0.441]$ and 4.29 $[D_2(25)(15), rd_{12} = 0.956]$; and
5. 4.32 $[D_2(45)(44), rb_{45} = 0.172]$ and 4.35 $[D_2(45)(35), rd_{34} = 0.968]$.

The improved results obtained from the template date methods can be possibly explained by the higher correlation between the data in the original sub-images and the template date, and by the fact that there are fewer differences between the sub-images and the template date, than between the sub-images and the template band (see difference images in Figures 3.7 and 3.8, for D_1, and in Figures 3.21 and 3.22, for D_2). Note that despite the small difference in the degree of correlation between the original sub-image and the template, in OT 6 $[D_1(33)(35), rb_{35} = 0.760]$ and in OT 21 $[D_1(33)(23), rd_{23} = 0.817]$, the results for methods TD-1, TD-3, TD-4, and TD-5, using OT 21, are much better than those obtained for methods TB-1, TB-3, TB-4, and TB-5, using OT 6 - see Figures 4.14 (for OT 6) and 4.17 (for OT 21). By observing the test images obtained for these methods (template band and template date), and the difference images $D_1(33) - D_1(35)$, in Figure 3.8 (c) (second column in the photograph), and

$D_1(33) - D_1(23)$, in Figure 3.7 (c) (third column in the photograph), it can be seen that the test images fail to resamble the original sub-image mainly in the areas of change, as indicated in the difference images. Thus, the quality of the estimates obtained for methods TB/D-1, TB/D-3, TB/D-4, and TB/D-5, depends both on the degree of correlation between the original sub-image and template, as well as on the amount (and degree) of changes between them.

From the same sequence of figures indicated above for methods TB/D-1, TB/D-3, TB/D-4, and TB/D-5, it can be seen that the results for methods TB/D-2, TB/D-6, and TB/D-8, improve as the correlation between the original sub-image and the template increases, but that the improvement is not as pronounced as that observed for those methods. Note, for instance, in Figures 4.26 and 4.29, the small difference between the test images for methods TB-6 and TD-6, using OT 8 [$D_2(25)(24)$ ($rb_{45} = 0.441$)] and OT 20 [$D_2(25)(15)$ ($rd_{12} = 0.956$)].

The different colours in the 'cut' images corresponding to methods TB-1, TB-3, TB-4, and TB-5 in Figures 4.28 [$D_2(25)(24)$, OT 8] and 4.34 [$D_2(45)(44)$, OT 10] are associated with those pixels at the tails of the distribution of the residuals (or, equivalently, of the 'cut' image). Note, in Table B.10, in Appendix B, the large residuals obtained for these methods, in OT 8 [$D_2(25)(24)$]. For instance, the minimum and maximum values of the residuals for method TB-1, using OT 8, are -121 and 100, respectively, corresponding to values 7 (-121+128) and 228 (100+128) in the residual image. These values are respectively associated to the colours black, and white, as indicated in the range of colours in Figure 4.28. Large residuals are also observed for method TB-1, in OT 10 [$D_2(45)(44)$]. The minimum and maximum values of the residuals for this method, using OT 10, are -102 and 60, corresponding to values 26 (-102+128) and 188 (60 +128) in the residual image. In the 'cut' image for this method, values 26 and 188 show as black and grey, respectively. Note that the colour grey, in the 'cut' image in Figure 4.34, is associated with the large residuals shown in yellow and orange, in Figure 4.33.

Since the variance of the test images obtained for method TB/D-4 depends on the correlation between the original sub-image and the template (refer to page 54), very 'poor' test images are generated for this method if the sub-image and

the template (band or date) are poorly correlated. In this case, the variance of the data in the test image is low, and the test image image shows very uniformly, with a colour matching that of the mean of the original sub-image. An example for the first data set is displayed in Figure 4.11 [$D_1(33)(34), rb_{3,4} = -0.126$], whereas Figures 4.20 [$D_2(24)(25), rb_{4,5} = 0.441$], and 4.32 [$D_2(45)(44), rb_{3,4} = 0.172$] constitute examples for the second data set.

Since method TB/D-5 estimates the missing values in each line, using the data in the region delimited by 3 lines above, and 3 lines below (to compute the values of rb_{kl} (or rd_{kl}), s_k, s_l, $\bar{u}_k$, and $\bar{u}_l$), an interesting effect can be observed in some of the test images. Due to the variability of the correlation between the data in the original sub-image, and those in the template, from region to region, some lines of the original sub-image may be estimated well if this correlation is high, whereas other may show the uniform effect described above for method TB/D-4, if the correlation is poor. This effect can be observed in the test images displayed for this method, in Figures 4.11 [$D_1(33)(34)$], 4.26 [$D_2(25)(24)$], and 4.32 [$D_2(45)(44)$].

All the test images obtained from template date methods are visually superior to those obtained from template band methods. The methods which seem to be least affected by the correlation between the test image and the template are TB/D-2, TB/D-6, TB/D-7, and TB/D-8. Contrast, for instance, the test images corresponding to methods TB-2, TB-6, and TB-8, with those corresponding to TB-1, TB-3, TB-4, and TB-5, in Figures 4.11 [$D_1(33)(34), rb_{34} = -0.126$], 4.20 [$D_1(24)(25), rb_{45} = 0.441$], and 4.26 [$D_2(25)(24), rb_{45} = 0.041$].

Regardless of the correlation between the original sub-images, and the template, note that methods TB/D-1, TB/D-3, TB/D-4, and TB/D-5, fail to estimate well the pixel values corresponding to areas where changes occur. The areas of changes in the response of the different objects on the ground, in different bands, can be observed in Figure 3.8, whereas the areas of change, between different dates of imaging, can be seen in Figure 3.7. Note, for instance, the association between the occurrance of the black (or grey) patches in the 'cut' images in Figure 4.7 [$D_1(25)(23)$, $rb_{35} = 0.705$], and the areas of change depicted in the

difference image in Figure 3.8. Another example can be seen in the 'cut' image in Figure 4.31 [$D_2(25)(15)$]. The grey patches at the top of the 'cut' images for methods TD-1, TD-3, TD-4, and TD-5, correspond to the pixels displayed in magenta, in the difference image in Figure 3.21 (b) (first column in the photograph).

Although, in general, method TB/D-2 performs numerically better than method TB/D-8, the test images for the former method are, in general, visually inferior to those obtained for method TB/D-8, especially in more heterogenous bands. The test images for method TB/D-2 usually have an 'speckled' appearance, which is not observed in the test images for method TB/D-8 – see, for instance, Figures 4.5, 4.8, 4.26, and 4.32. However, method TB/D-8 usually enhances the boundaries between the different features in the image (see, for instance, Figures 4.11 and 4.20). Note that the test images in Figure 4.11, correspond to an original sub-image in band 3, using a template in band 4 [$D_1(33)(34)$], whereas those in Figure 4.20 correspond to an original sub-image in band 4, and a template in band 5 [$D_2(24)(25)$]. As already noted in Chapter 3 (§3.3) bands 3 and 5 are both sensitive to vegetation reflectance, whereas band 4 is soil reflectance. Therefore, a sharp contrast in response is expected from bands 3 and 4, and 4 and 5, at the boundaries between vegetation and soil.

The residual images in Figure 4.39, and the 'cut' images in Figure 4.40, for method TD-9 (for OT's 19 to 27 in Table 4.2) show very clearly the strong association between the areas where this method fails to perform well, and the areas of changes shown in the difference images in Figure 3.7 (a), (b), (c) [for OT's (19,20,21), (22,23,24) and (25,26,27)], respectively. Better estimates for this method are obtained for the sub-images in band 3, which are more homogeneous (recall the uniform difference images for sub-images in this band, acquired at different dates), and for the sub-images which have a template acquired prior, and another acquired after their acquisition (e.g. the sub-images acquired at 24/06, i.e., $D_1(23)$, $D_1(24)$, and $D_1(25)$, for which there is a template acquired at 08/06, and another at 10/07). The improved performance of the method can be observed in Figures 4.39 and 4.40, by contrasting the sub-images in the second column of the photograph (which correspond to the sub-images acquired at 24/06), with those in either the first, or third columns (which correspond to the

sub-images acquired at 10/07, and 08/06, respectively).

From the residual images it can be seen that method TB/D-6 usually performs better than the other methods, except, in general, LI. However, the smoothing effect caused by method of linear interpolation has not been observed on the test images for TB/D-6.

4.7.1 Some Additional Comments

Observation of the 'cut' images may give an idea of the number of pixel values estimated with no error, and the areas, on the image, which are better estimated from each method.

Not only can the exact number of pixel values estimated with no error be used as an indicator of the performance of the methods, but also the number that are estimated within an small error. The proportion of pixel values estimated within a small error has also been observed for all methods, usually assuming an error of ± 4 grey levels for the original sub-images in the more homogenous bands 3 and 4, and ± 10 grey levels for those in band 5. The values for the complimentary proportion of pixels estimated within a small error, ACC, are given in Table B.4, in Appendix B, for all methods, using OT's 1 to 27 in Table 4.2, and in Table B.9 in Appendix B, using OT's 1 to 24 in Table 4.3.

The same procedure used to evaluate the performance of the methods for SRMS, CCOR, and SRAN, in §4.5, is used here to investigate their performance for ACC. The average ranks of the 31 methods, using D_1, and the 19 methods, using D_2, are presented in Table 4.8. From the results in this table it can be seen that, on average, methods LI, TD-6, and TD-7, estimate a larger number of values within a small error, than the other methods.

Table 4.8: Average ranks (AR) of the single band, template band, and template date methods, for ACC, using D_1, and D_2.

D_1		D_2	
Method	AR	Method	AR
$TD-7$	3.6	LI	2.0
LI	3.9	$TD-6$	3.5
$TD-8$	5.7	$TD-7$	4.3
$TD-6$	5.7	$TB-6$	4.4
$TD-2$	5.9	$TD-2$	4.9
$TD-10$	7.4	$TD-8$	5.4
$TB-6L$	8.7	CSP	6.1
CSP	9.8	$TD-3$	8.7
$TB-6H$	10.9	$TD-5$	9.9
$TB-7L$	11.6	$TB-7$	9.9
$TD-3$	11.6	$TB-2$	10.7
$TD-9$	11.7	LR	11.9
$TD-5$	11.9	$TD-4$	12.0
$TB-8H$	12.1	$TD-1$	12.7
$TB-2H$	12.7	$TB-8$	13.6
$TD-4$	14.8	$TB-3$	16.5
$TD-1$	15.6	$TB-5$	16.9
$TB-7H$	15.6	$TB-4$	18.1
$TB-2L$	16.3	$TB-1$	18.6
LR	16.6		
$TB-8L$	20.1		
$TB-10$	21.6		
$TB-5H$	23.2		
$TB-3H$	24.9		
$TB-9$	25.4		
$TB-4H$	25.8		
$TB-5L$	26.8		
$TB-4L$	27.7		
$TD-1H$	28.4		
$TB-3L$	29.4		
$TB-1L$	30.7		

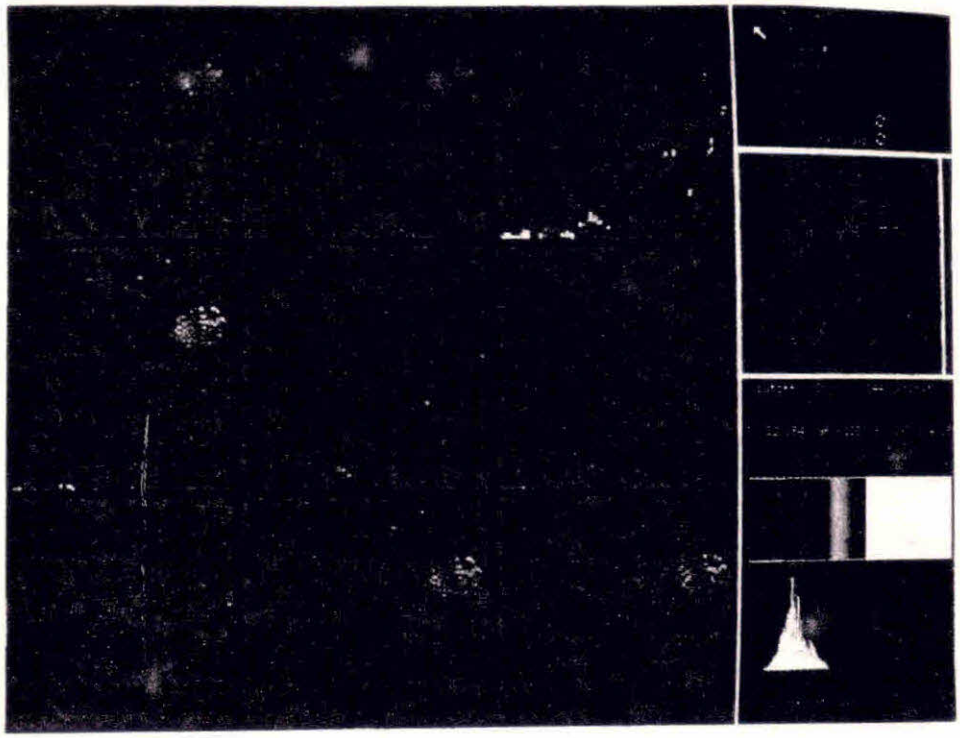

Figure 4.5: Test images for $D_1(25)(23)$, for methods: 1. LR 2. LI 3. TB-1 4. TB-2 5.TB-3 6.TB-4 7.TB-5 8. TB-6 9. TB-8.

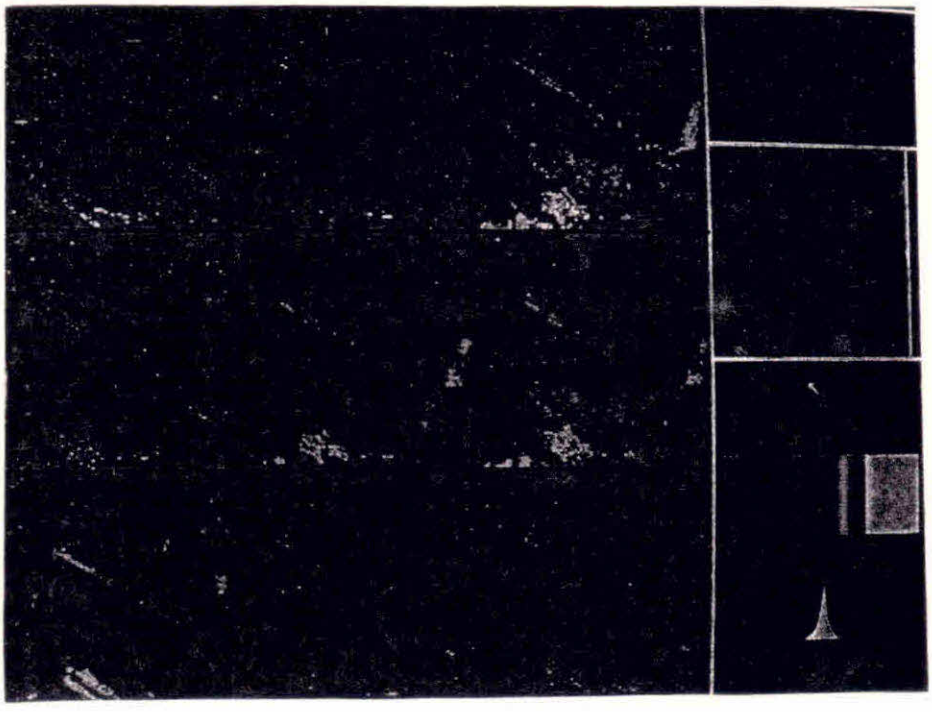

Figure 4.6: Residual images for $D_1(25)(23)$, for methods: 1. LR 2. LI 3. TB-1 4. TB-2 5. TB-3 6. TB-4 7. TB-5 8. TB-6 9. TB-8.

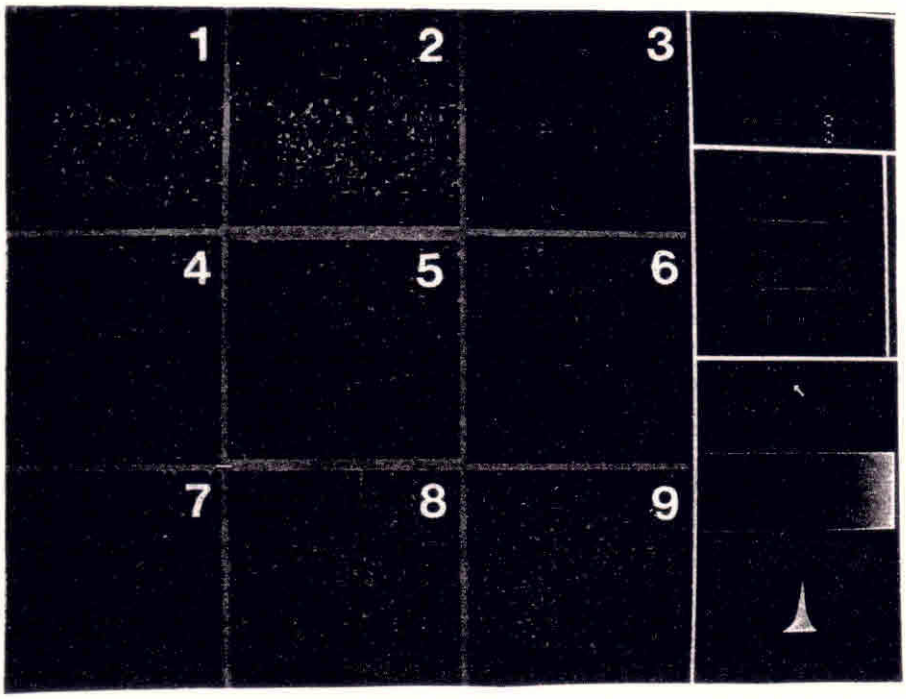

Figure 4.7: 'Cut' images for $D_1(25)(23)$ for methods 1. LR 2. LI 3. TB-1 4. TB-2 5. TB-3 6. TB-4 7. TB-5 8. TB-6 9. TB-8.

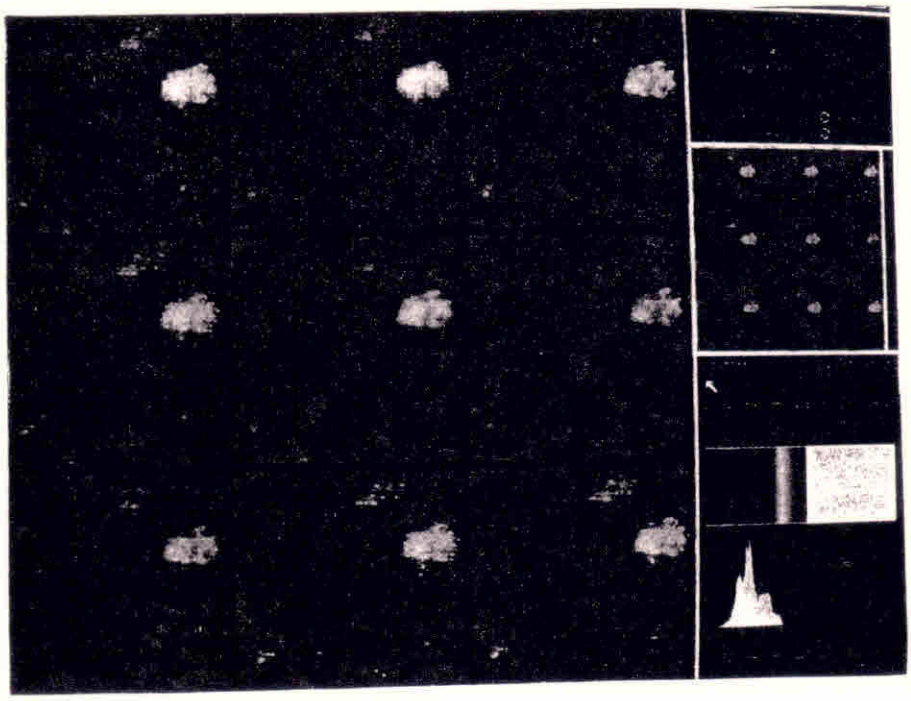

Figure 4.8: Test images for $D_1(25)(15)$, for methods: 1. LR 2. LI 3. TD-1 4. TD-2 5. TD-3 6. TD-4 7. TD-5 8. TD-6 9. TD-8.

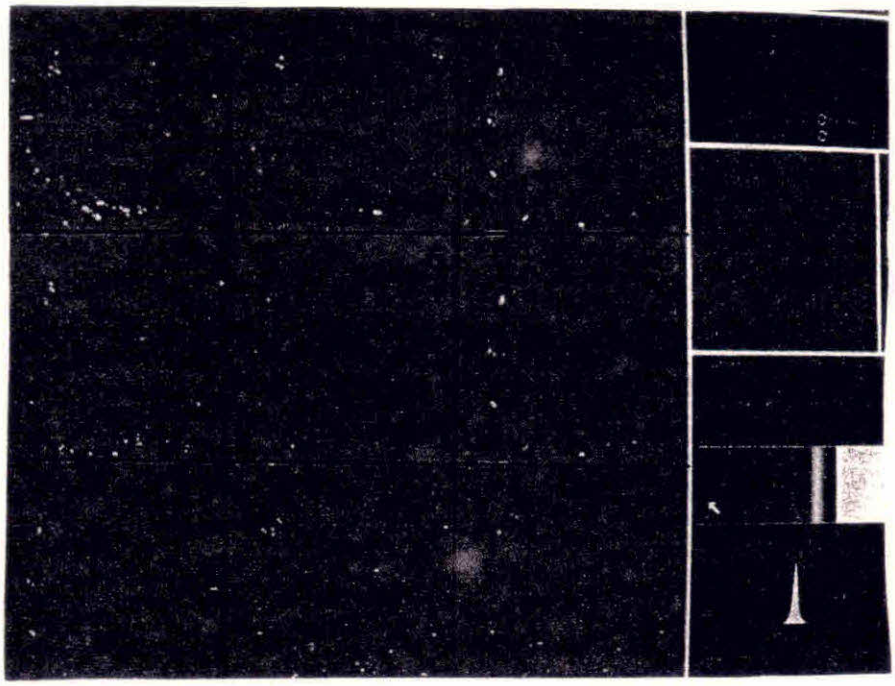

Figure 4.9: Residual images for $D_1(25)(15)$ for methods: 1. LR 2. LI 3. TD-1 4. TD-2 5. TD-3 6. TD-4 7. TD-5 8. TD-6 9. TD-8.

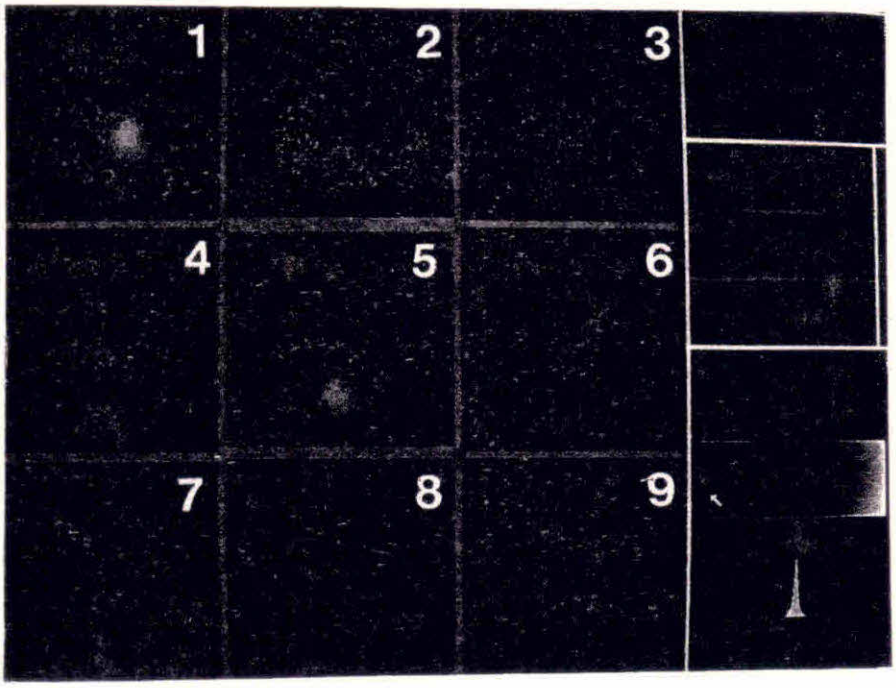

Figure 4.10: 'Cut' images for $D_1(25)(15)$ for methods: 1. LR 2. LI 3. TD-1 4. TD-2 5. TD-3 6. TD-4 7. TD-5 8. TD-6 9. TD-8.

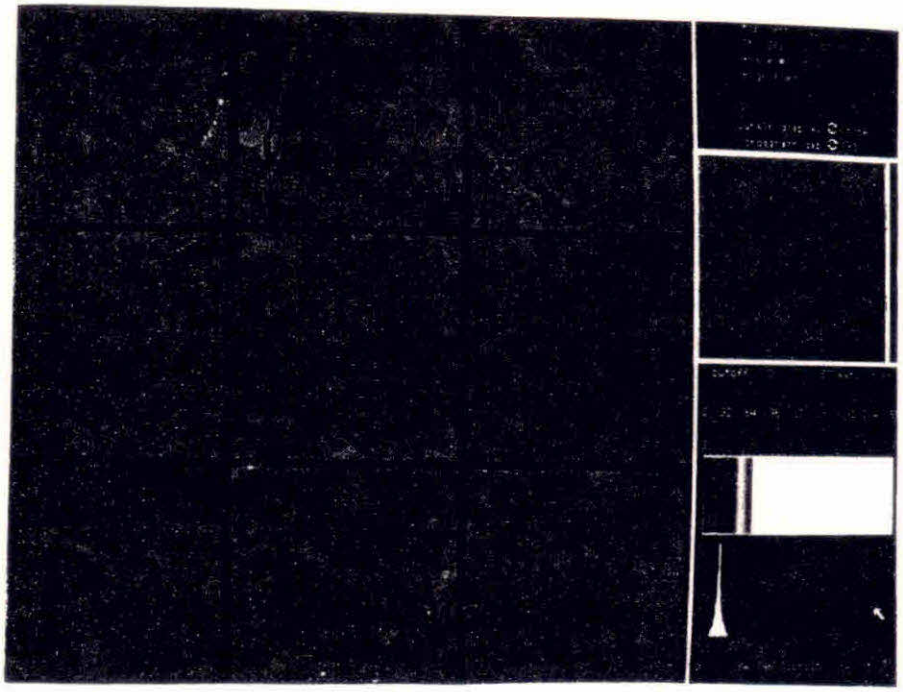

Figure 4.11: Test images for $D_1(33)(34)$.
(Displayed in the same sequence as in Figure 4.5).

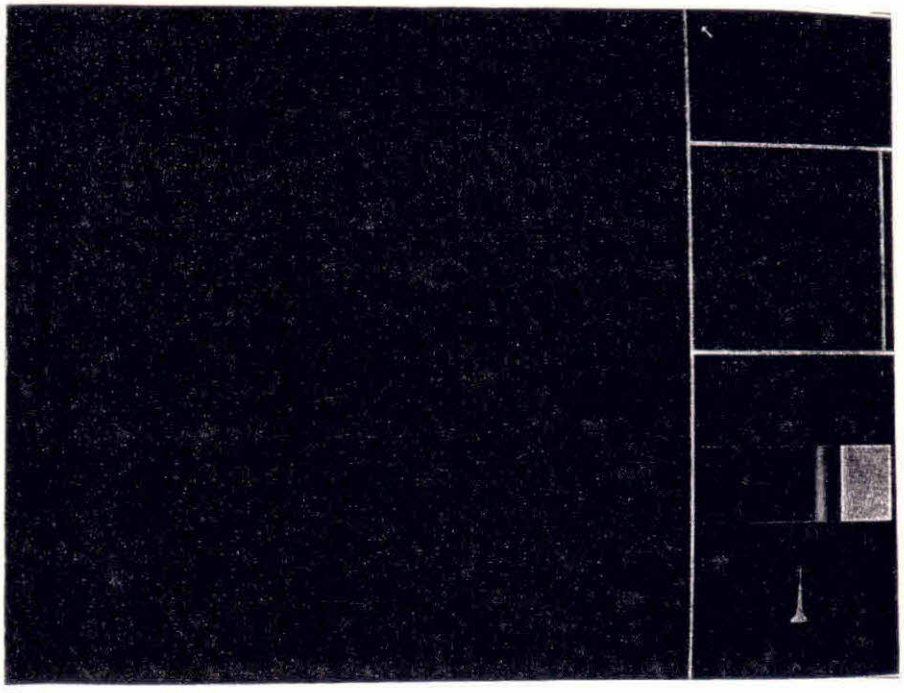

Figure 4.12: Residual images for $D_1(33)(34)$.
(Displayed in the same sequence as in Figure 4.6).

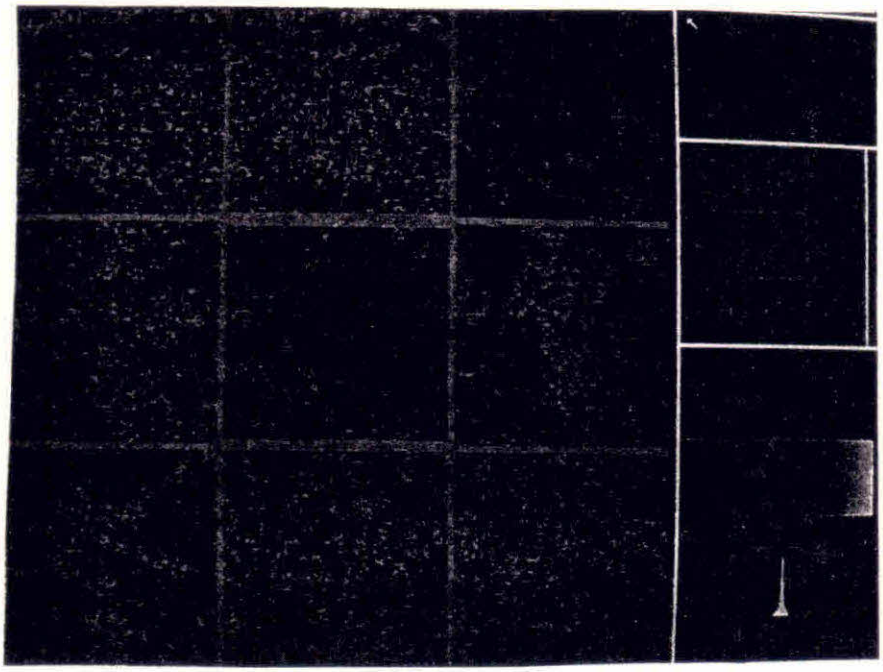

Figure 4.13: 'Cut' images for $D_1(33)(34)$.
(Displayed in the same sequence as in Figure 4.7).

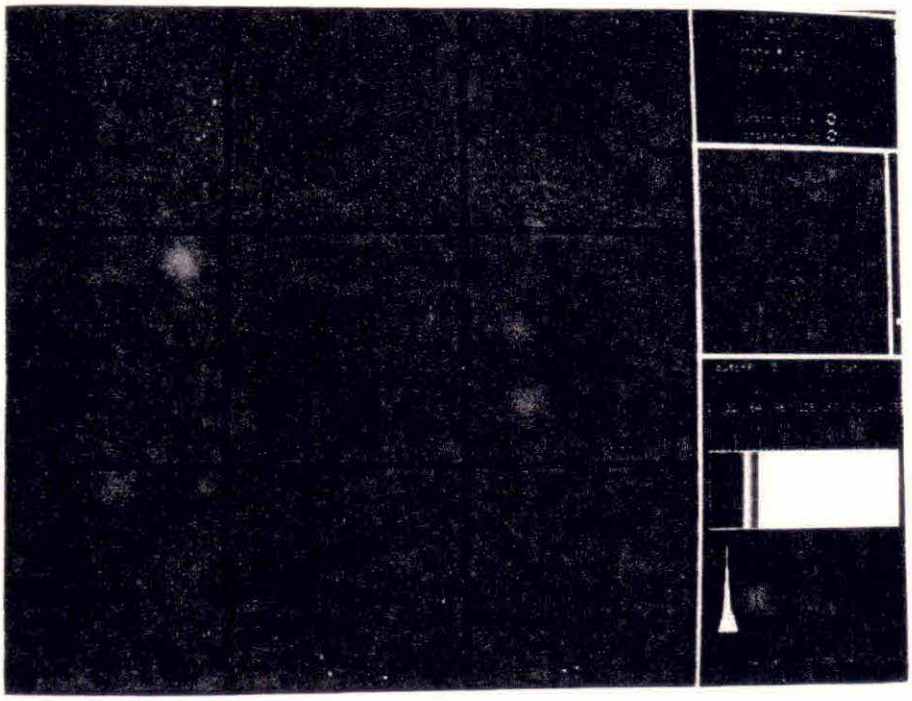

Figure 4.14: Test images for $D_1(33)(35)$.
(Displayed in the same sequence as in Figure 4.5).

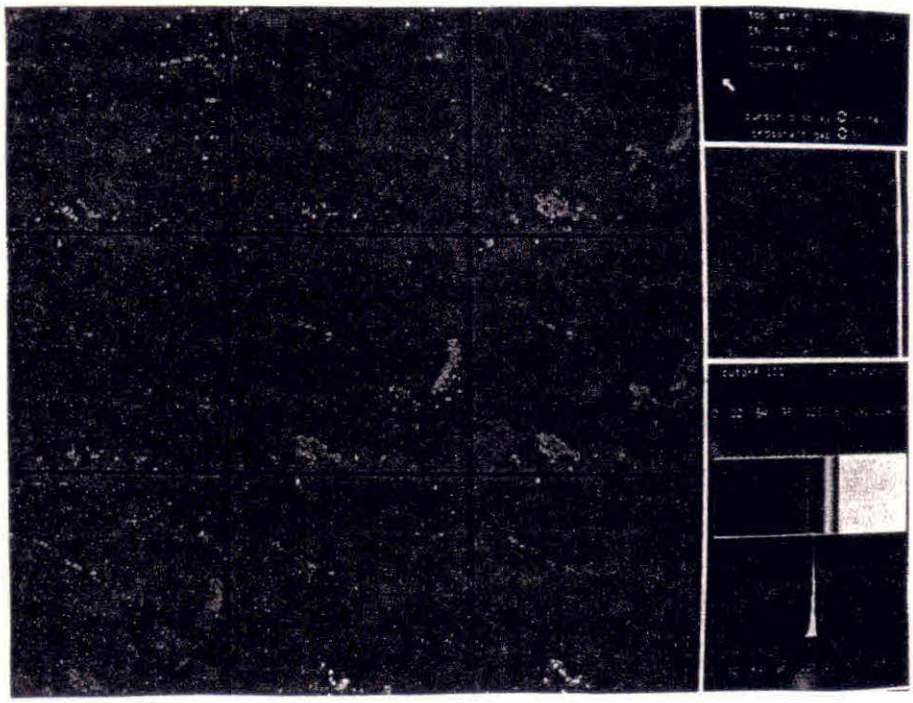

Figure 4.15: Residual images for $D_1(33)(35)$.
(Displayed in the same sequence as in Figure 4.6).

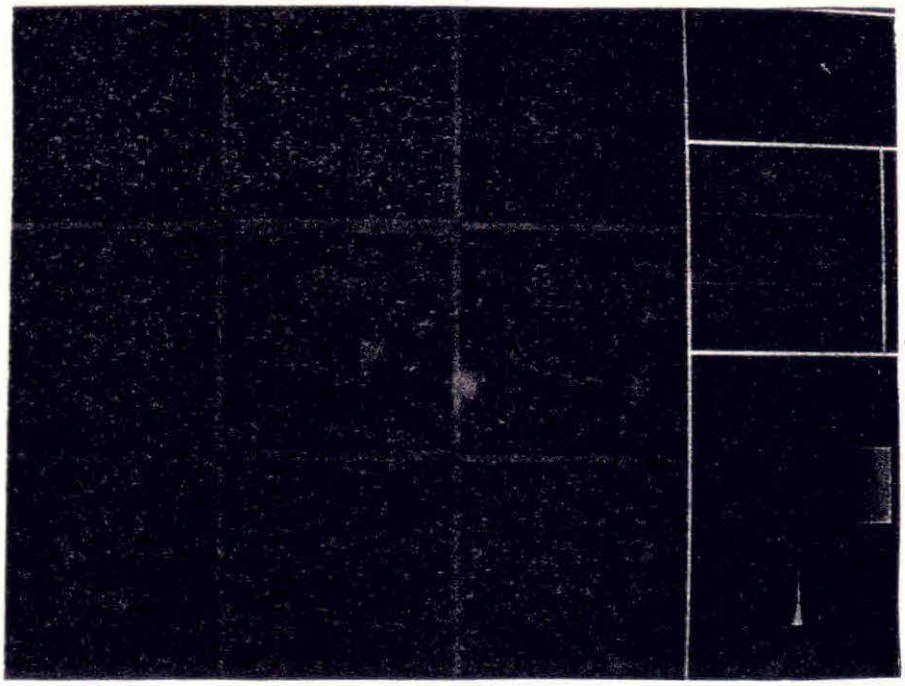

Figure 4.16: 'Cut' images for $D_1(33)(35)$.
(Displayed in the same sequence as in Figure 4.7).

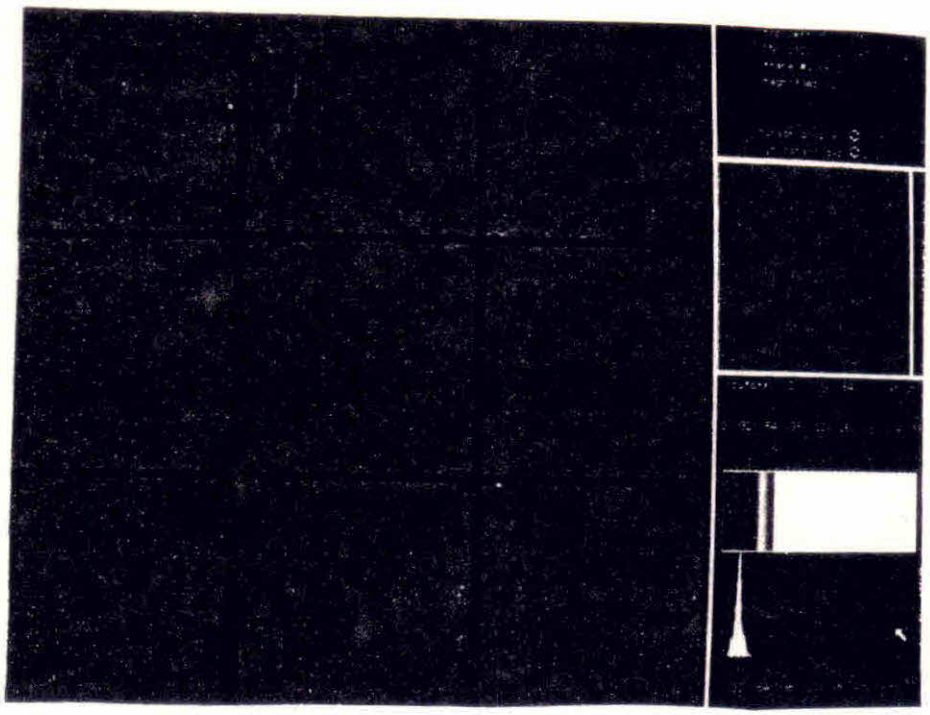

Figure 4.17: Test images for $D_1(33)(23)$.
(Displayed in the same sequence as in Figure 4.8).

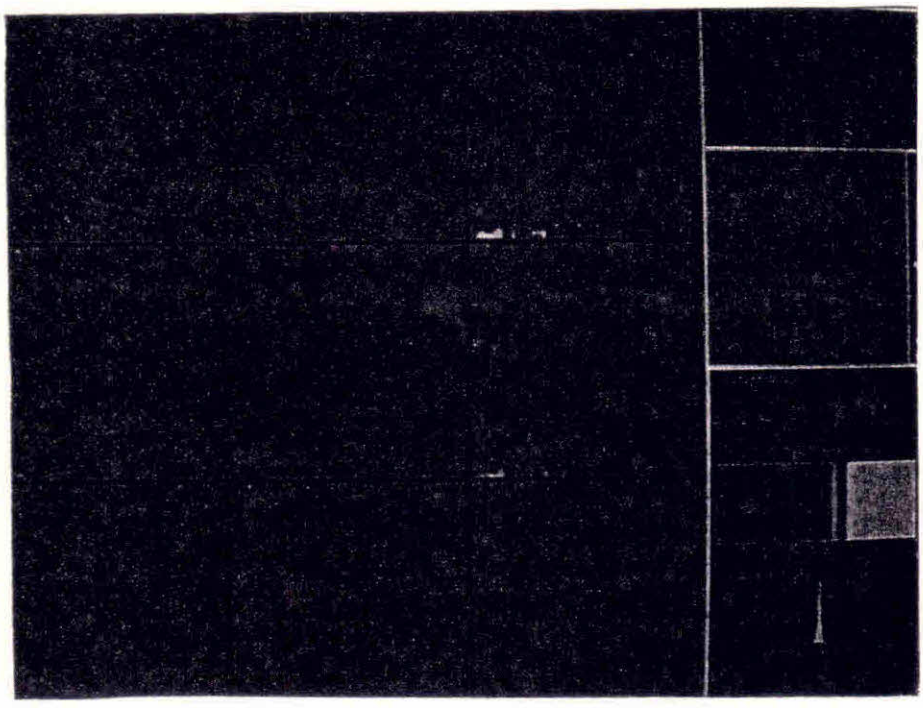

Figure 4.18: Residual images for $D_1(33)(23)$.
(Displayed in the same sequence as in Figure 4.9).

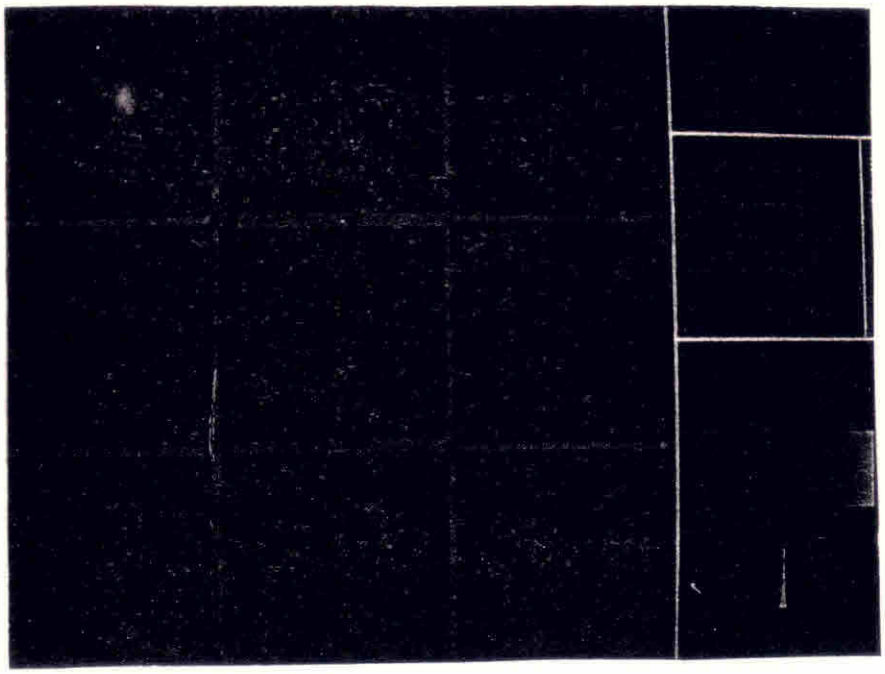

Figure 4.19: 'Cut' images for $D_1(33)(23)$.
(Displayed in the same sequence as in Figure 4.10).

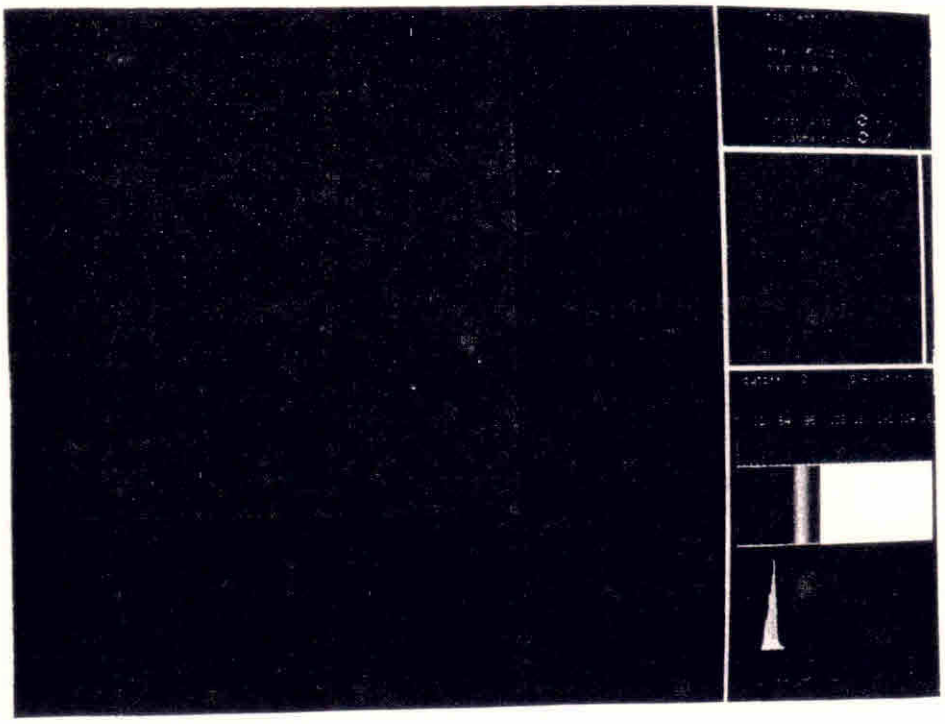

Figure 4.20: Test images for $D_2(24)(25)$.
(Displayed in the same sequence as in Figure 4.5).

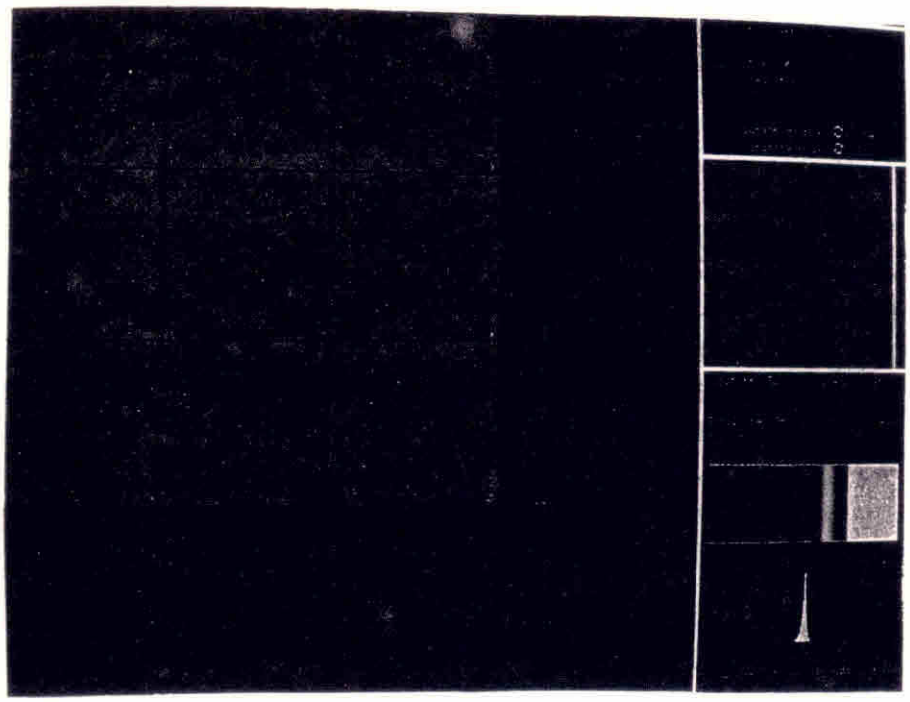

Figure 4.21: Residual images for $D_2(24)(25)$.
(Displayed in the same sequence as in Figure 4.6).

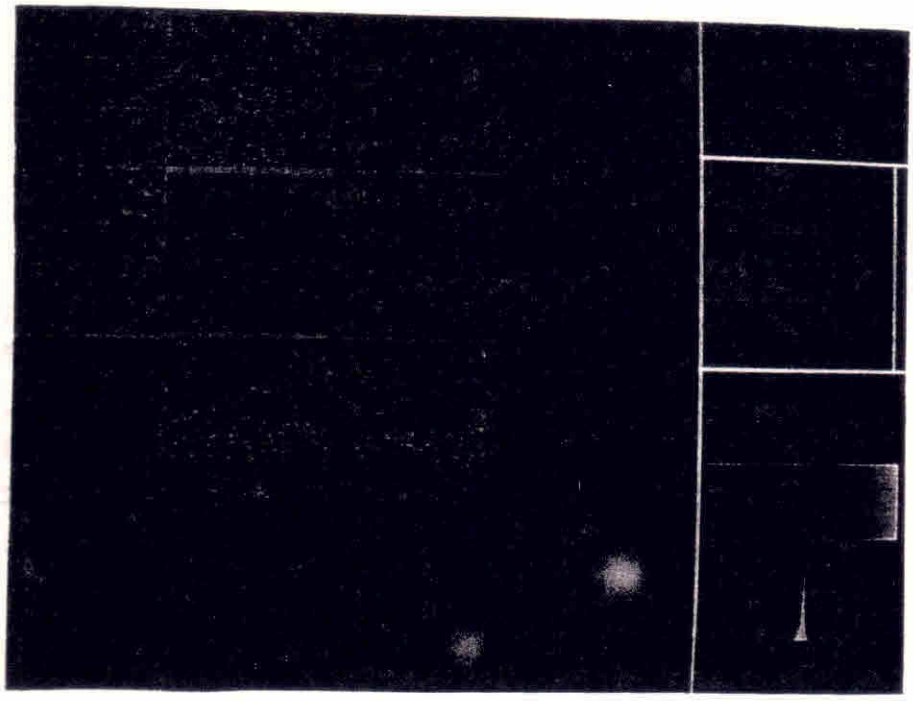

Figure 4.22: 'Cut' images for $D_2(24)(25)$.
(Displayed in the same sequence as in Figure 4.7).

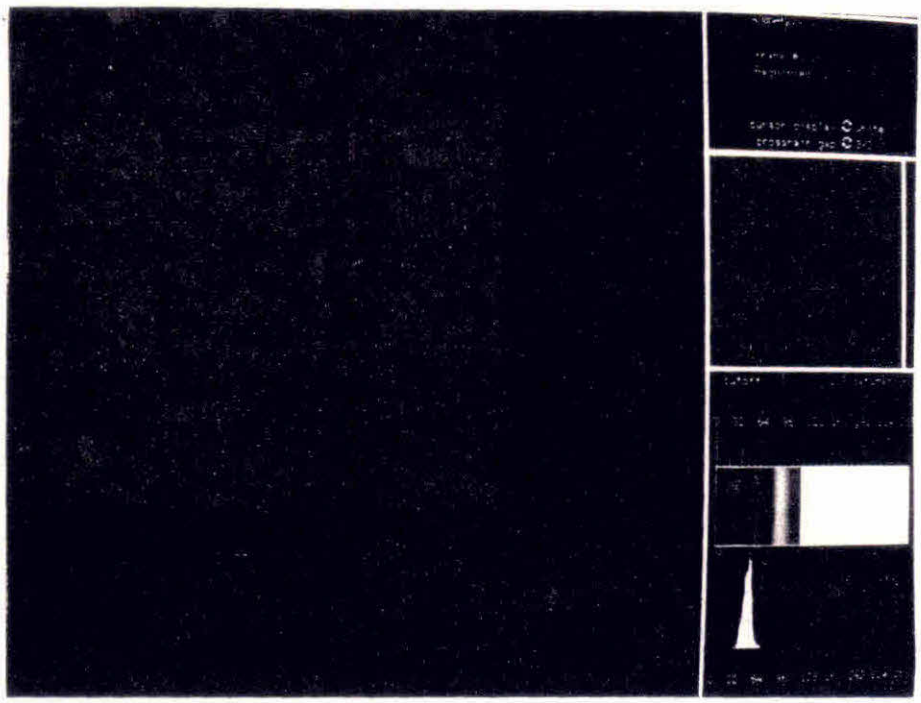

Figure 4.23: Test images for $D_2(24)(14)$.
(Displayed in the same sequence as in Figure 4.8).

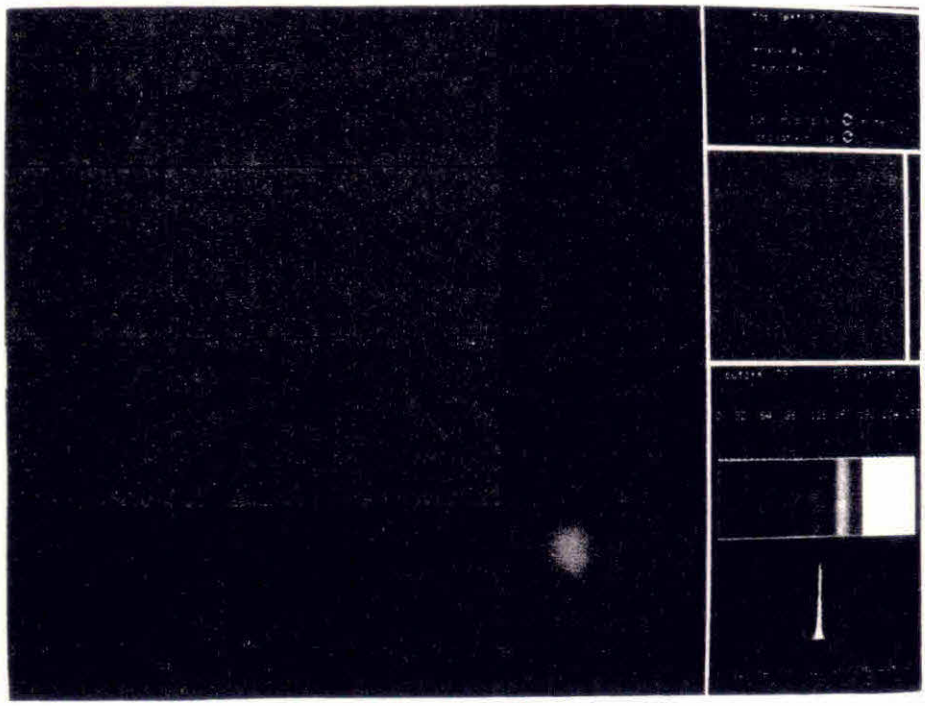

Figure 4.24: Residual images for $D_2(24)(14)$.
(Displayed in the same sequence as in Figure 4.9).

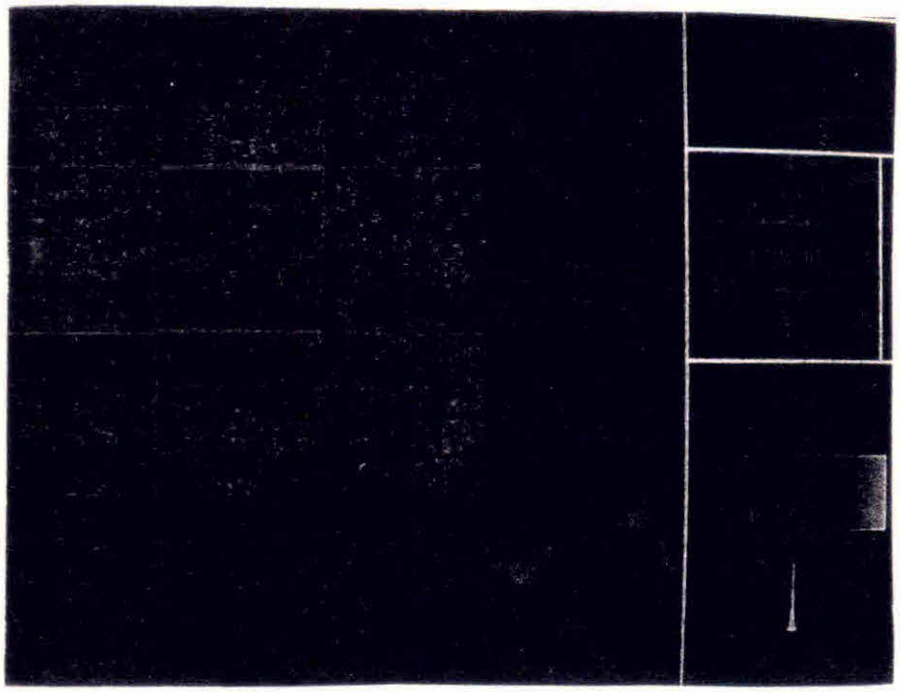

Figure 4.25: 'Cut' images for $D_2(24)(14)$.
(Displayed in the same sequence as in Figure 4.10).

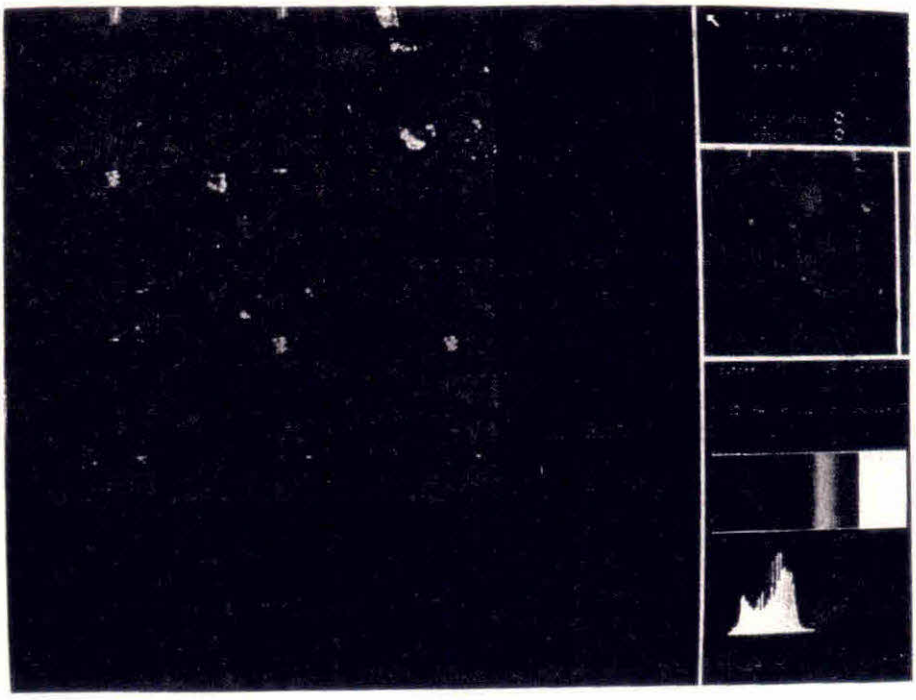

Figure 4.26: Test images for $D_2(25)(24)$.
(Displayed in the same sequence as in Figure 4.5).

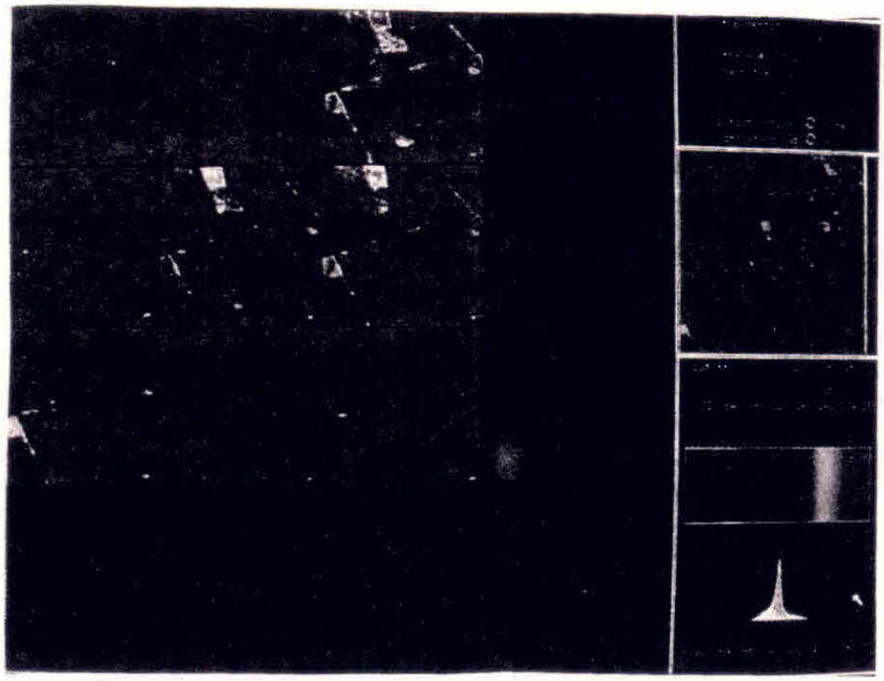

Figure 4.27: Residual images for $D_2(25)(24)$.
(Displayed in the same sequence as in Figure 4.6).

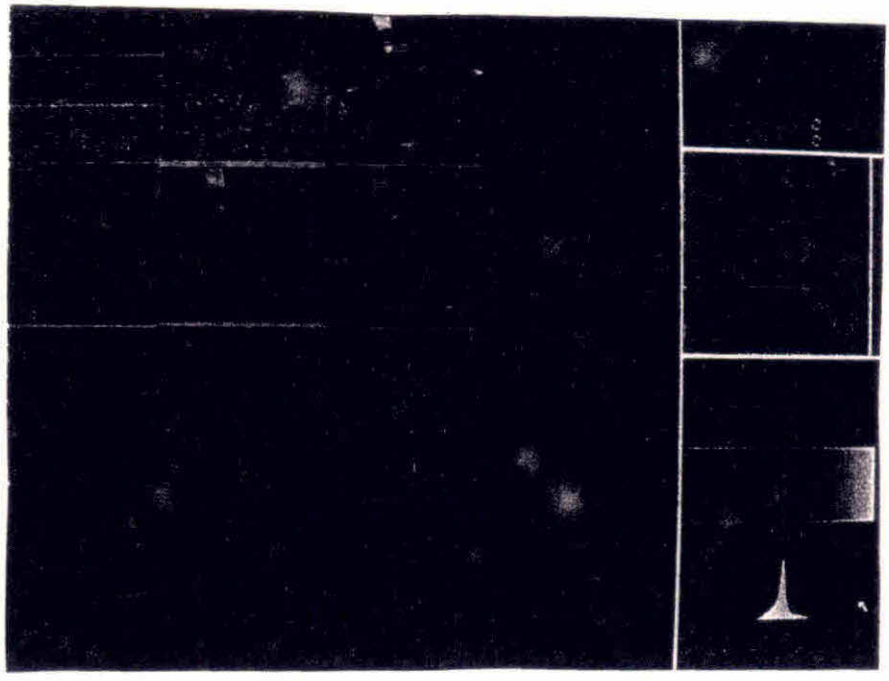

Figure 4.28: 'Cut' images for $D_2(25)(24)$.
(Displayed in the same sequence as in Figure 4.7).

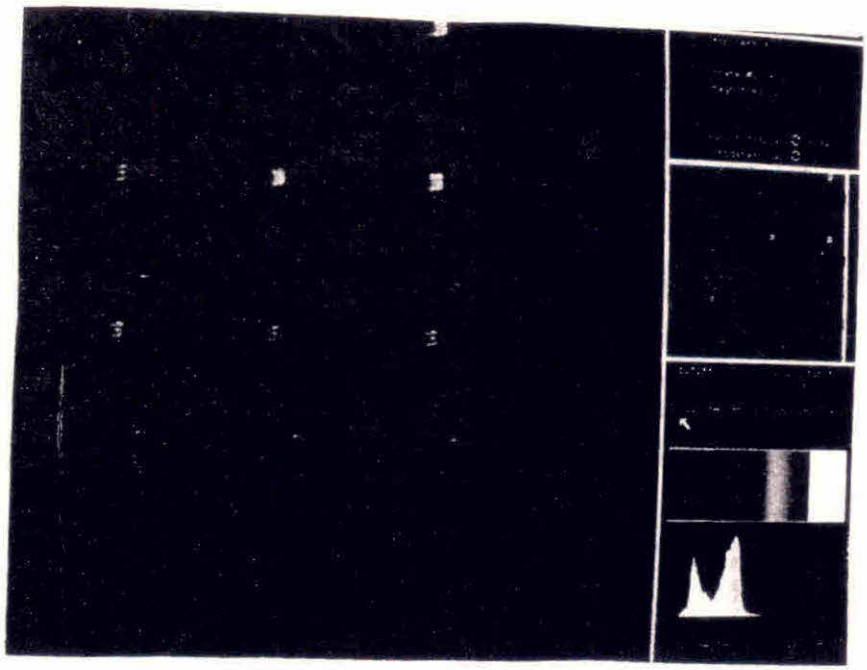

Figure 4.29: Test images for $D_2(25)(15)$.
(Displayed in the same sequence as in Figure 4.8).

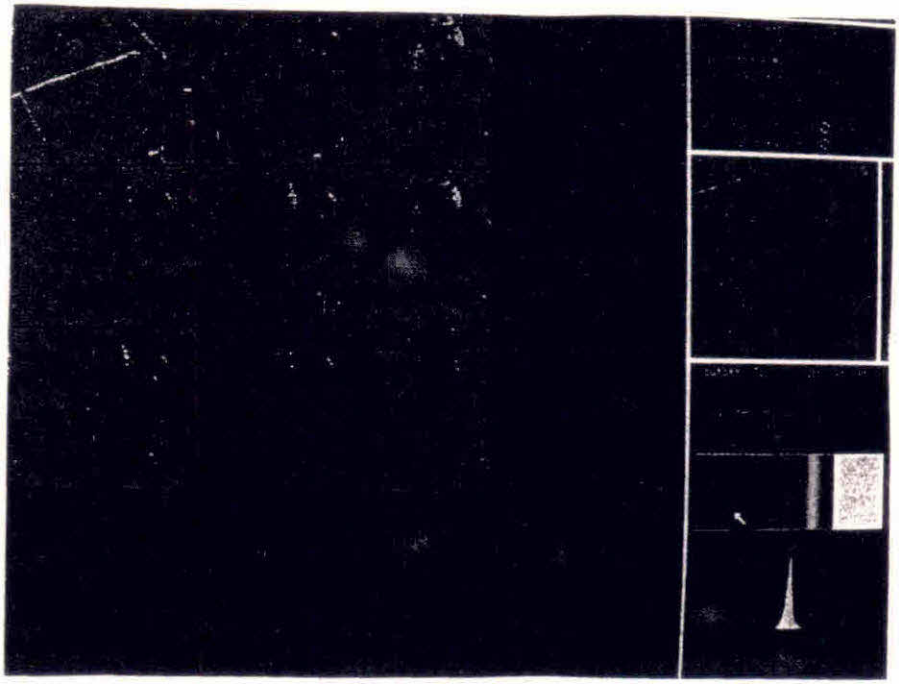

Figure 4.30: Residual images for $D_2(25)(15)$.
(Displayed in the same sequence as in Figure 4.9).

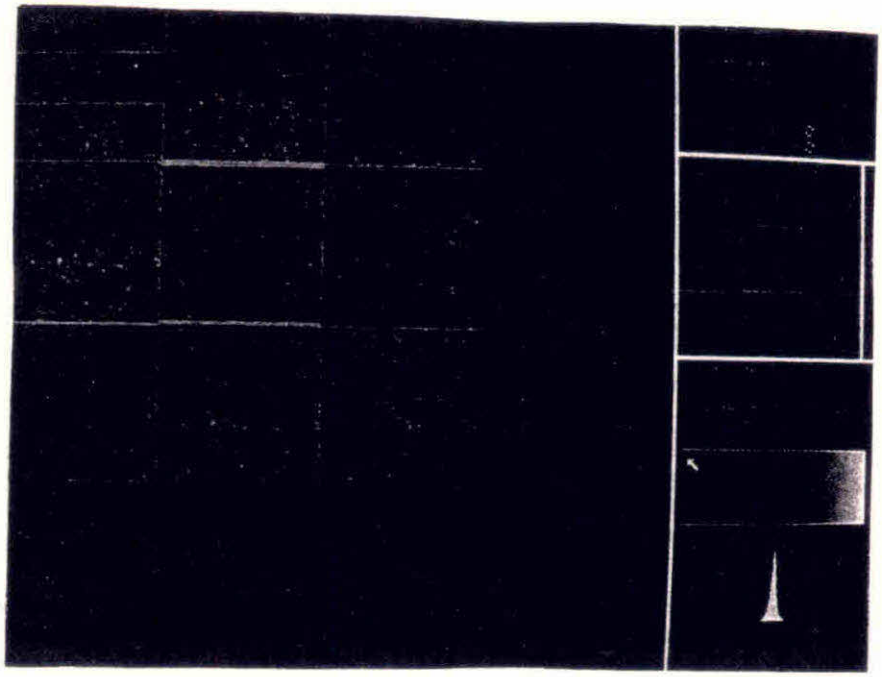

Figure 4.31: 'Cut' images for $D_2(25)(15)$.
(Displayed in the same sequence as in Figure 4.10).

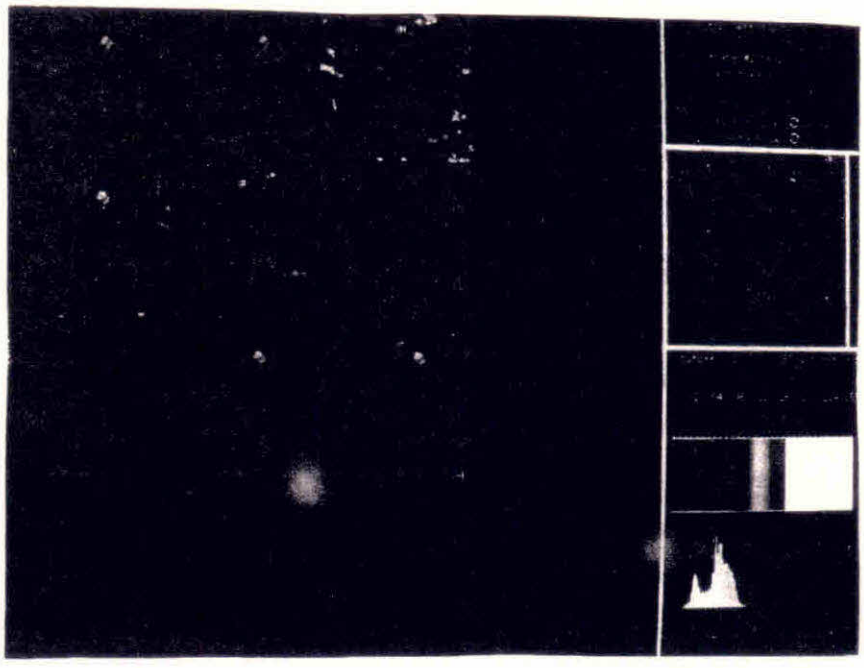

Figure 4.32: Test images for $D_2(45)(44)$.
(Displayed in the same sequence as in Figure 4.5).

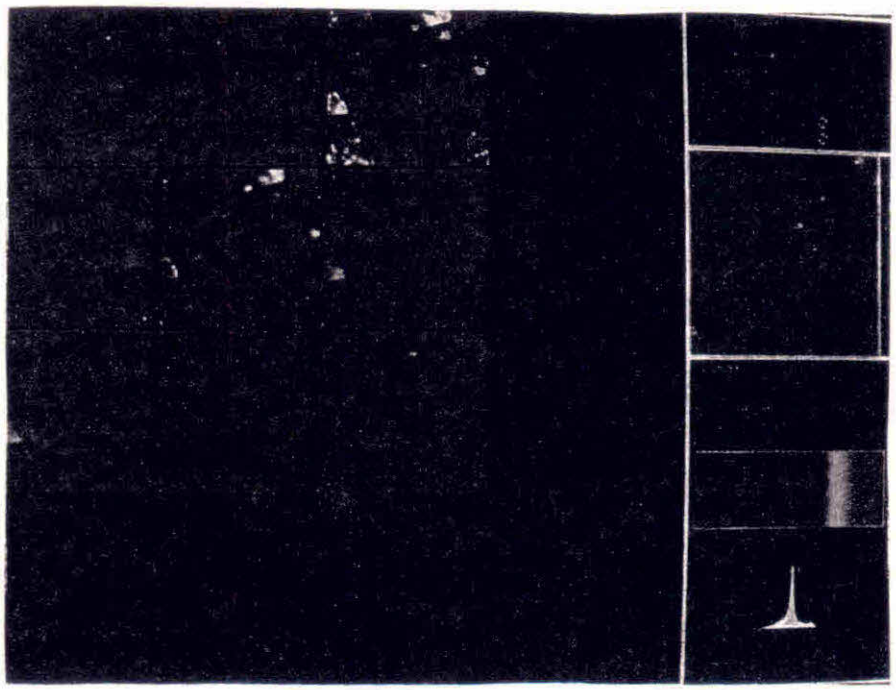

Figure 4.33: Residual images for $D_2(45)(44)$.
(Displayed in the same sequence as in Figure 4.6).

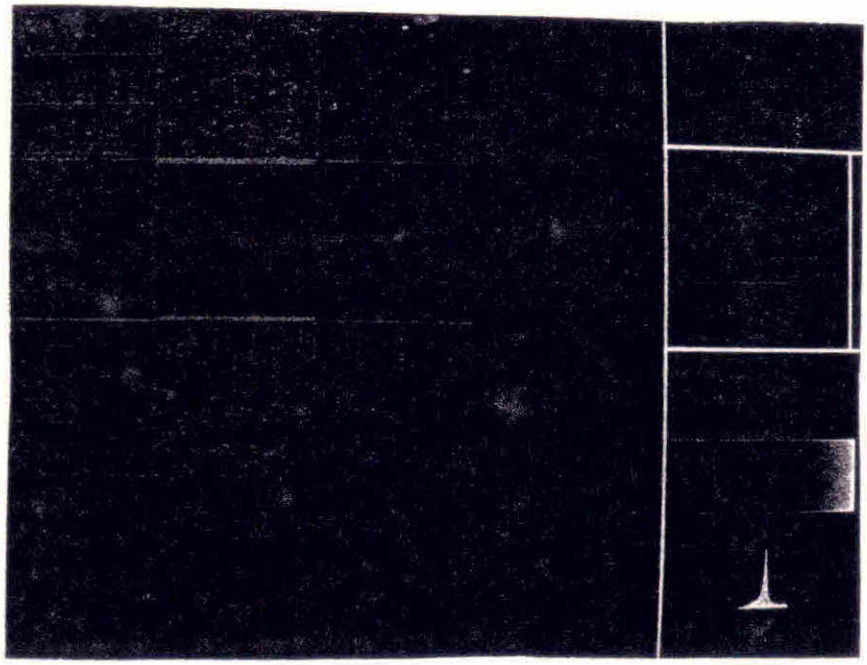

Figure 4.34: 'Cut' images for $D_2(45)(44)$.
(Displayed in the same sequence as in Figure 4.7).

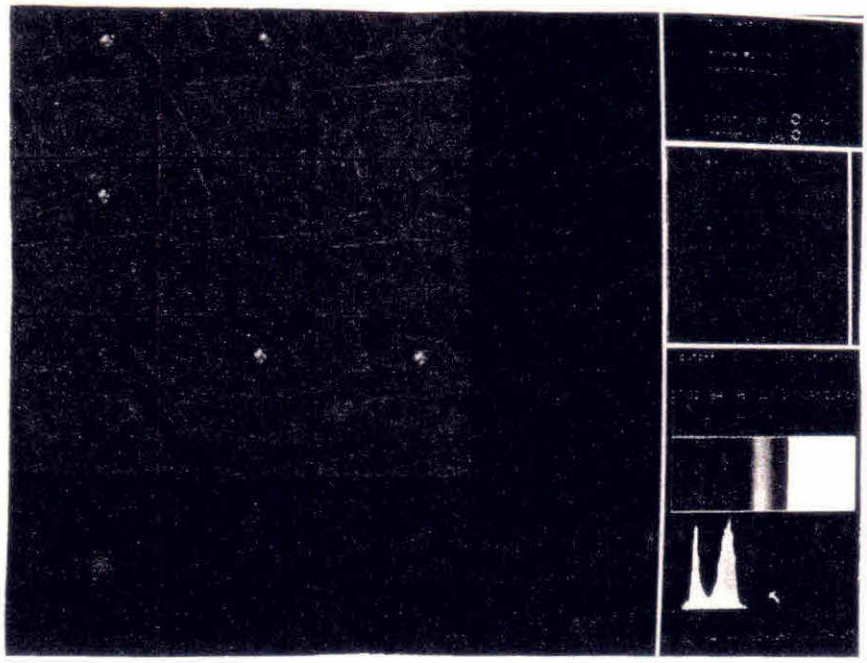

Figure 4.35: Test images for $D_2(45)(35)$.
(Displayed in the same sequence as in Figure 4.8).

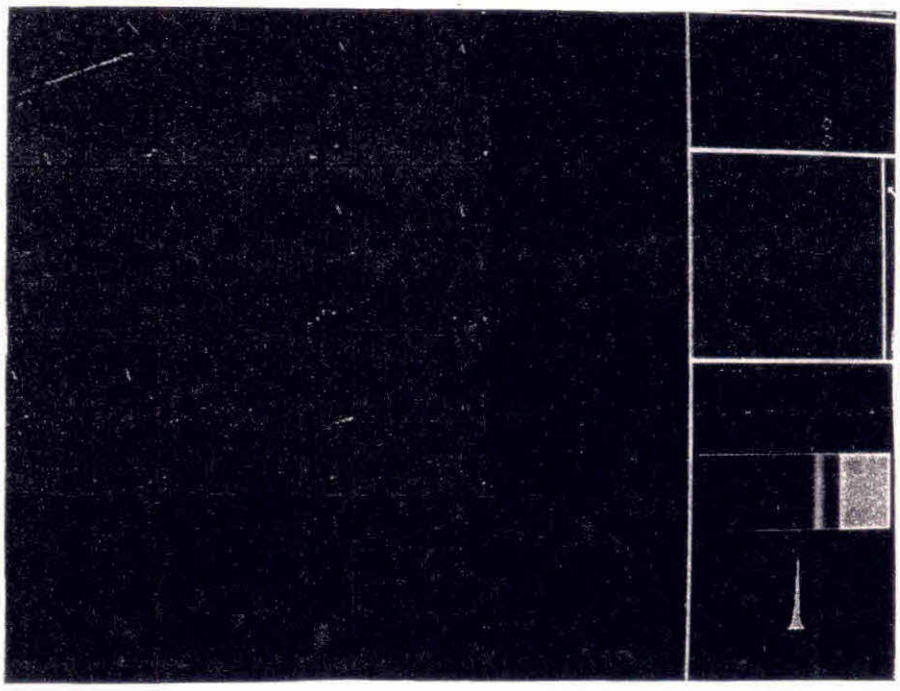

Figure 4.36: Residual images for $D_2(45)(35)$.
(Displayed in the same sequence as in Figure 4.9).

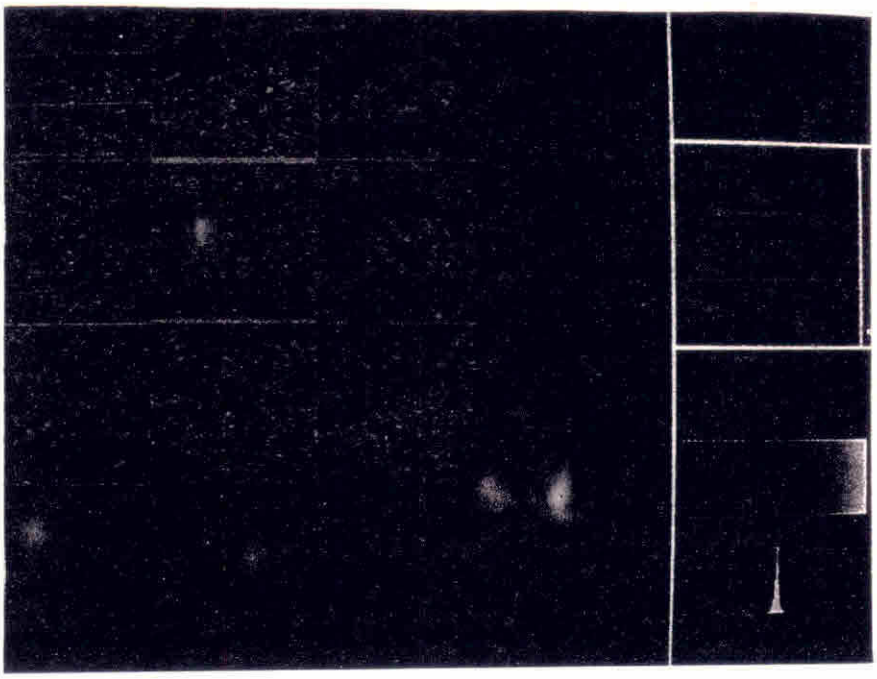

Figure 4.37: 'Cut' images for $D_2(45)(35)$.
(Displayed in the same sequence as in Figure 4.10).

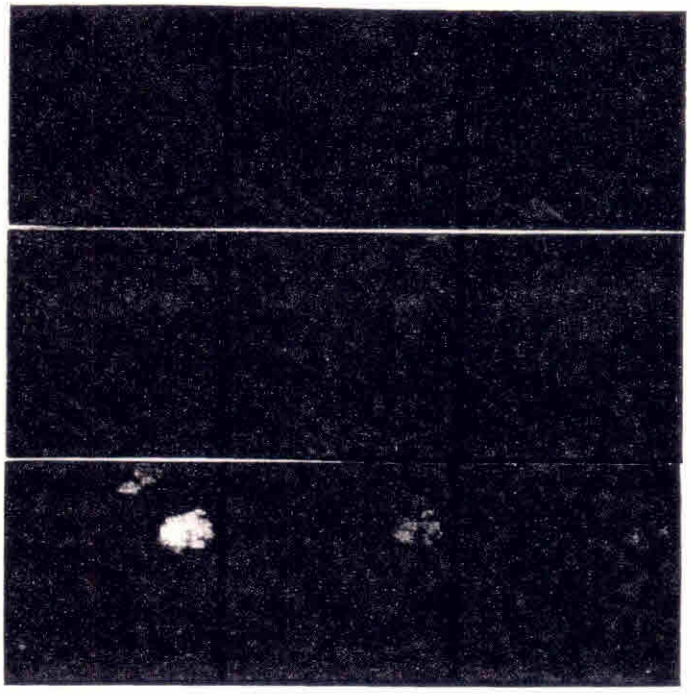

Figure 4.38: Test images for method TD-9: 1. OT 19 2. OT 20 3. OT 21 4. OT 22 5. OT 23 6. OT 24 7. OT 25 8. OT 26 9. OT 27.

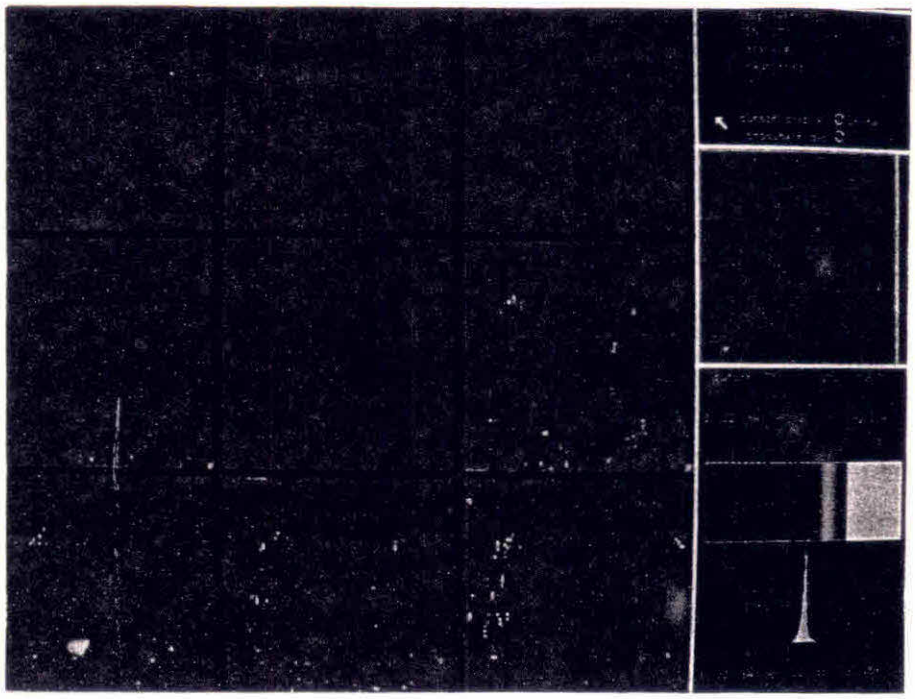

Figure 4.39: Residual images for method TD-9: 1. OT 19 2. OT 20 3. OT 21 4. OT 22 5. OT 23 6. OT 24 7. OT 25 8. OT 26 9. OT 27.

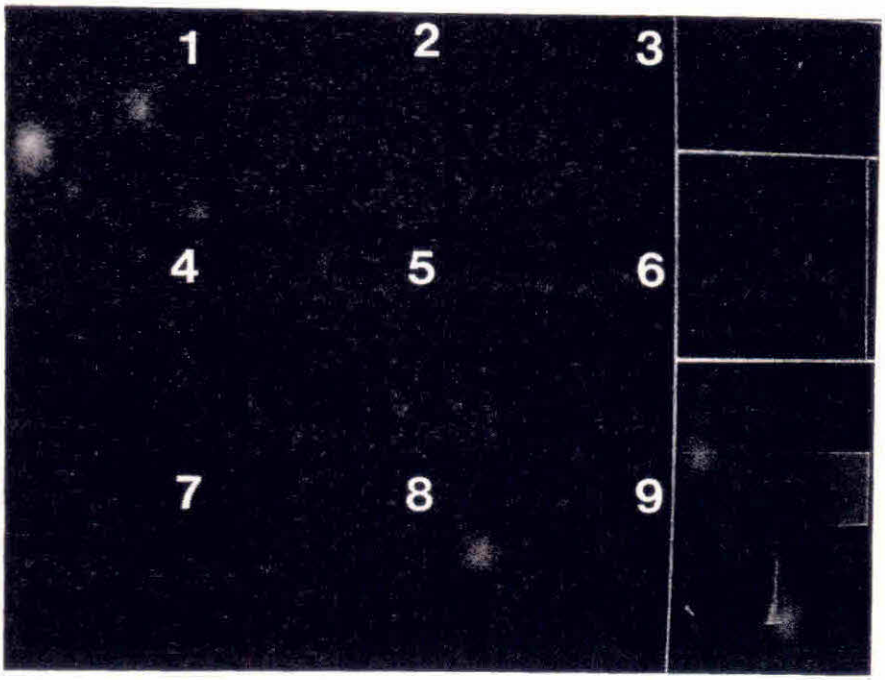

Figure 4.40: 'Cut' images for method TD-9: 1. OT 19 2. OT 20 3. OT 21 4. OT 22 5. OT 23 6. OT 24 7. OT 25 8. OT 26 9. OT 27.

4.8 Some Alternative Approaches

From the numerical, and visual, results presented in §4.5 and in §4.7, respectively, it is clear that none of the methods is consistently better than others. From the observation that some of the methods perform better than others (for instance, LI, TB/D-6, TB/D-7), but not necessarily over the entire sub-image, an alternative method has, at a late stage been explored, which would preserve the features of a good method, whilst trying to compensate for its drawbacks. A 'switching' method was tried, as follows:

1. computation of the 'local' variations of the data in the template image, expressed by:

$$a^l(i,j) = u^l(i,j) - \frac{[u^l(i-1,j) + u^l(i+1,j)]}{2} \tag{4.30}$$

2. application of a switching rule, consisting of the following:

$$\hat{u}^k(i,j) = \begin{cases} \text{as for LI, if } a^l(i,j) < cs^l \\ \\ \text{as for method TB/D-6, otherwise.} \end{cases}$$

Hence, the method uses linear interpolation whenever the template date is 'locally' homogeneous, and applies Guindon's method TB/D-6, otherwise. The method has been applied to the sub-images in D_1, and D_2, using c=1, 1.5, and 2. Let the method be referred to as TB/D-11, TB/D-12, and TB/D-13, when c=1, 1.5, and 2, respectively.

The values for SRMS, CCOR, and SRAN, for OT's 1 to 18, and OT's 19 to 27 in Table 4.2 are given in Tables B.11 and B.12, in Appendix B, under *Template Band* and *Template Date*, respectively. The values for these measures, for OT's 1 to 12, and OT's 13 to 24 in Table 4.3 are given in Tables B.13 and B.14 in Appendix B, under *Template Band* and *Template Date*, respectively.

The results in Tables B.11 to B.14 show that the 'switching' method, if sometimes better than LI, is only marginally so. Also, it has been noticed that the use of method TB/D-6 is possibly not the best alternative, as this method can have large residuals, as pointed out previously. In the analysis of the residuals obtained for method TD-11 (which is the method that applies the switching rule

most frequently), using OT $D_1(25)(35)$, it has been observed that only 100 pixel values were estimated using Guindon's method, and only half of these estimates were in fact better than the estimates for LI. Therefore, method TD-11 (as well as TD-12 and TD-13) will definitely not improve the visual deficiencies of LI.

The 'failure' of these methods can possibly be explained by the switching rule that has been used, which does not take into account the 'local' variations in the original sub-image *and* in the template image. Other alternative methods using different switching rules (and different switching methods) have also been experimented. However, at present, better results than LI alone have not yet been obtained from any of these new, alternative, methods.

More encouraging results, however, have at a late stage been obtained for two variations of method TB/D-2, which originated from theoretical considerations. The first and second alternative methods use, instead of A, in equation 4.3, the values of P, and p, as defined in §4.2. These methods, which are henceforth referred to as TB/D-14 and TB/D-15, respectively, have also been applied to all sub-images in D_1 and D_2. The values for SRMS, CCOR, and SRAN, obtained for these methods, using OT's 1 to 27 in Table 4.2, are presented in Tables B.11 (for SRMS and CCOR), and B.12 (for SRAN), in Appendix B; the corresponding results, using OT's 1 to 24 in Table 4.3, are given in Tables B.13 and B.14, in Appendix B.

Methods TB/D-14 and TB/D-15 perform consistently better than method TB/D-2, for all measures. In general, the results for method TB/D-14 are better than those for TB/D-15, and similar to those for LI, as can be seen from the plot for SRMS, CCOR, and SRAN given in Figure 4.41 for the two methods.

Recall that the original sub-images and the template band in OT's (1,2,3), (7,8,9,10,11,12), and (16,17,18) are poorly correlated. However, the good performance of method TB-14 in these OT's seems to indicate that the method is not sensitive to the degree of correlation between the sub-image and the template. The results for method TD-14, in OT's 19 to 27, are also similar to those for LI. However, even if only marginally, the numerical results for LI are generally better than those for TD-14.

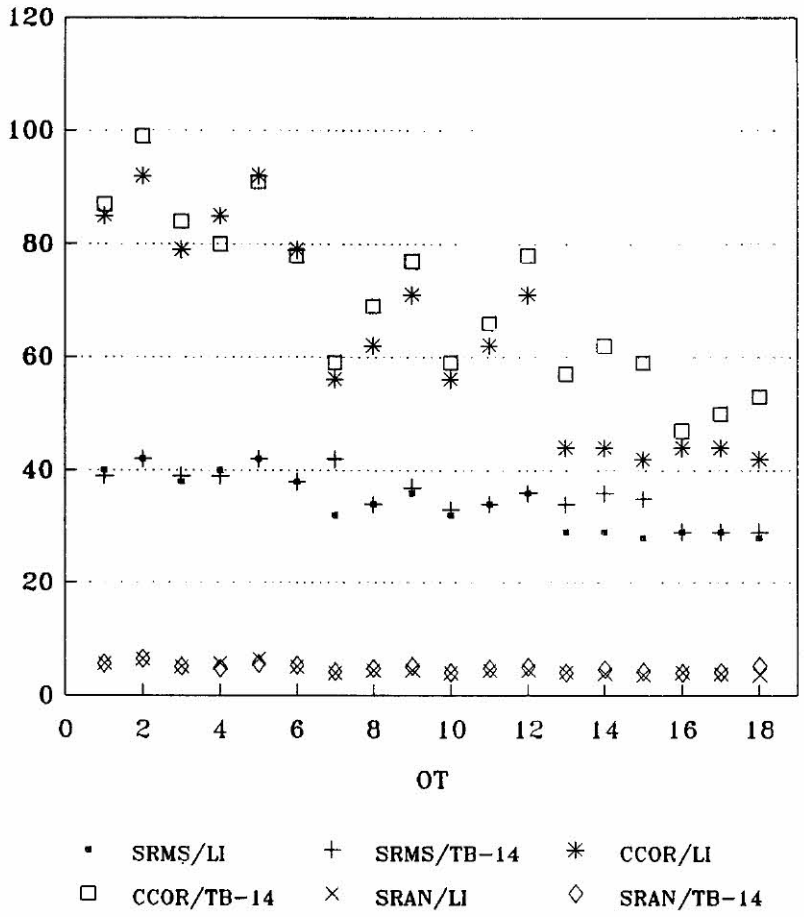

Figure 4.41: Plot of SRMS, CCOR, and SRAN for OT's 1 to 18 in Table 4.2, for methods LI and TB-14.

Figure 4.42 (a), (b), and (c) respectively display the test images, the residual images, and the 'cut' images for methods LI, TB-2, and TB-14, using OT 3 $[D_1(33)(34)]$, in Table 4.2.

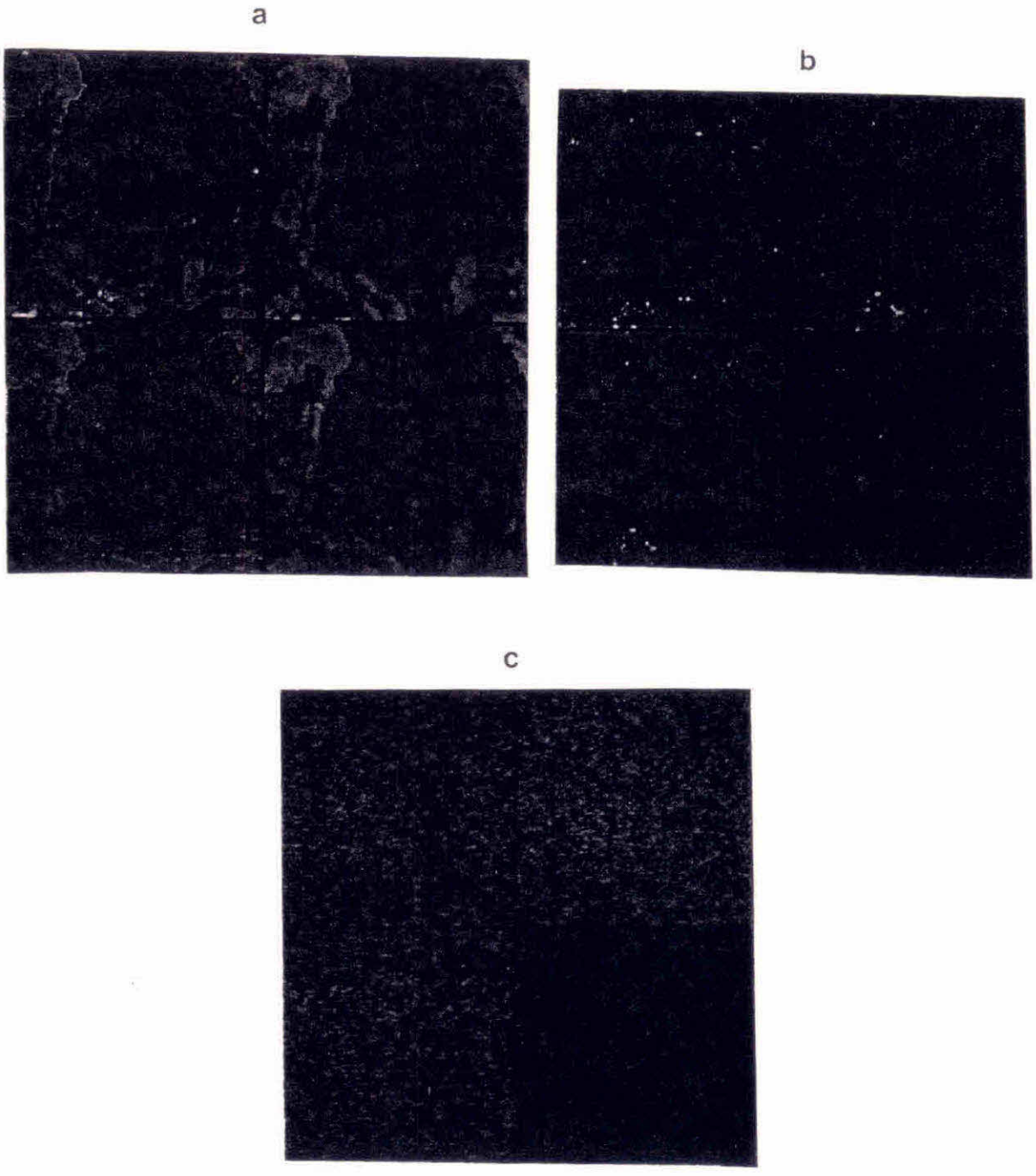

Figure 4.42: (a) 1. Original sub-image $D_1(33)$; 2. Test image for LI, using $D_1(33)(34)$; 3. Test image for TB-2, using $D_1(33)(34)$; 4. Test image for TB-14, using $D_1(33)(34)$; (b) 1. Residual image for LI; 2. Residual image for TB-2; 3. Residual image for TB-14; (c) 1. 'Cut' image for LI; 2. 'Cut' image for TB-2; 3. 'Cut' image for TB-14.

From the test images displayed in Figure 4.42 (a), it can be noted that method TB-14 has better visual results than LI, or TB-2 (see also Figure 4.11). Note, for instance, the estimates of the pixel values along the road, obtained for the three methods. Those for LI are 'smoother' than they should be [and as expected, from a linear filter], whilst some of the estimates for TB-2 have large residuals [recall that band 4 has been used as the template, and that the response from the road, in this band, and in band 3, are very distinct – refer to Figures 3.2 (b) and 3.4 (a)]. This is not observed in the test image for method TB-14. Although this method also has some smoothing effect, which causes the test image to appear slightly blurred, this effect is not as pronounced as that observed for LI. Method TB-14 also smoothes the 'speckled' appearence of the test image for TB-2. However, there is only a slight difference between the residual images for these two methods.

4.9 Conclusions

In this chapter, the performances of several relatively simple methods proposed to estimate missing values arising from line dropout have been evaluated. All the methods suggested as alternatives to single band methods, such as linear interpolation, and interpolation using cubic splines, use the multispectral potential of the TM, by incorporating information from another neighbouring, well correlated, band to the one where the missing values occur. The use of these methods, incorporating information from another passage, instead of information from another band, have been experimented here. The results indicate that multitemporal data can be a valuable source of information to aid the accurate estimation of missing values arising from detector failure, especially over areas where small changs, from passage to passage, occur.

One of the drawbacks of the use of methods that incorporate information from another passage is the fact that, at present, they cannot be implemented routinely to replace missing scan lines on the imagery. Unlike multispectral data, the information from other, close, passages may not be readily available. Another disadvantage of the template date methods is that they require that the data from the different passages be well registered, before they can be effectively used.

Despite these deficiencies, the template date methods have been shown to be particularly useful in the estimation of missing values occurring on 'fixed'

features on the ground, such as roads, agricultural plots, and reforested areas, as this information is more likely to be similar, from one passage to another, than from one band to another. It is probable that better estimates of missing values occurring in urban areas will be obtained from template date methods, than from template band methods, although this could not be investigate here, due to the non-availability of suitable data. Also, the estimates of the missing values on the image used by Bernstein *et al.* (1984), which featured a stadium, and an airport, would certainly be estimated well from template date methods. Note that in the case of missing values occurring over 'fixed' features, it is not necessary that information be from a close passage to the one in which the missing values occur.

Although the results in this chapter have indicated a superior performance of the template date methods, relative to the template band methods, it is important to note that the data from the different passages were consistently better correlated than the data from the other bands available. All the methods proposed to estimate missing values arising from line dropout assume that data from a well correlated template is used. This study has demonstrated that although, in general, better estimates are obtained from all methods, from the use of a better correlated template, some of the methods are less sensitive to the degree of correlation between the 'defective' image and the template, than others. The methods which seem to be the least affected by this correlation are the *template replacement with error adjustment* method of Bernstein *et al.* (1984) (referred to here as method TB/D-2), and the *adjacent band modulation* methods of Guindon (1984) (denoted here as methods TB/D-6, and TB/D-7).

The performances of the methods, evaluated for a set of numerical measures, consisting of the scaled root mean square residual (SRMS), the complimentary correlation between the original sub-image and the test image (CCOR), and the scaled range of the residuals (SRAN), were in general consistent for the two data sets investigated here. All methods had a similar performance for SRMS, and CCOR, suggesting that only one of these measures needs to be used as a performance indicator. On the other hand, the performances of the methods were usually not consistent for SRMS (and CCOR), and SRAN. Methods which had low values for SRMS, and CCOR, sometimes had large values for SRAN. As SRAN uses only the range of the residuals, large values may only indicate the presence of a few, large residuals. In particular, methods TB/D-6 and TB/D-7

usually had low values for SRMS and CCOR, but large values for SRAN (refer to Table 4.4), indicating the occurrence of some large residuals for these methods. Note that these few, large residuals, also increase the value of SRMS. Hence, it is important to realize that an evaluation of the performances of the methods, based solely on numerical measures, may be misleading. This stresses the importance of a visual evaluation of the methods, as a complement to the numerical evaluation. From the residual images, for instance, it is possibly to identify the spatial distribution of the residuals, and their size, in relation to the original image. Methods with low values for SRMS, CCOR, and SRAN, may show visually as introducing more distortions in the original image than others for which the values for these measures are larger. These methods may only introduced some 'local' distortions in the image, while performing well elsewhere, whereas the methods with a better numerical performance may introduce more subtle, but more frequent, distortions on the image.

If based solely on the numerical evaluations carried out here, the method of linear interpolation would be indicated as the 'best' method to estimate missing values arising from line dropout. However, considering that this method has spatial smoothing effects, with consequent reduction in resolution (which explains the usually 'blurred' test images for this method), and that it can introduce considerable distortions, especially at the boundaries between regions of contrasting response, the indication of other methods may be justified. Methods TD-6, and TD-7, for instance, perform particularly well on D_2, since the features in the sub-images in this data set are more 'permanent', causing an improved performance of template date methods. However, in 'dynamic' areas, where changes from one passage to another are more likely to be observed, or where the objects on the ground are more likely to have contrasting responses, in different bands, these methods are not expected to work well in general.

In summary, none of the methods, including linear interpolation, and the adjacent band modulation methods estimate well the missing values occurring in 'dynamic' areas, especially in images in more heterogenous bands. However, over areas where the features are more permanent, methods TD-6, and TD-7 are expected to perform better than their corresponding methods using a template band, and better than the method of linear interpolation. The latter may, in general, perform better than the template band, or the template date methods, over

areas which are reasonably homogeneous, and where large 'local' variations are not likely to occur. Since the template band, and the template date methods rely on the existance of a good association between the data on the 'defective' image, and the template image, in order to perform well, their use, over homogenous areas, is certainly not justified.

Since none of the single band, template band, or template band methods alone perform consistently well in all situations, but each has its own individual potential to estimate missing values on the imagery, it is suggested that the development of 'switching' methods, which explore, and incorporate, the individual potentialities of some of the single band, template band, and template date methods, be further explored. Despite the logic of the use of such methods, it has been observed that the identification of the appropriate switching rule to apply, or what methods to use, may present undue difficulties. Although some 'switching' methods have been experimented with here, the results have not been encouraging, and further work in this respect is still warranted.

Amongst the several new methods proposed in this chapter, methods TB/D-14, and TB/D-15 (which are variations on method TB/D-2) have a similar numerical performance to the method of linear interpolation, and a better visual performance than the latter, although method TB-14 still has some spatial smoothing effects. Regardless of the degree of correlation between the original sub-image and the template considered, the results obtained for methods TB/D-14 and TB/D-15 were consistently similar to those obtained for LI, and consistently superior to those obtained for method TB/D-2.

Due to the similarity of the numerical results obtained for these methods, with those for LI, and their visual superiority with respect to the latter, their incorportation into the 'switching' methods above, may be warranted, and should be further investigated.

Chapter 5

Estimation of Missing Values using Spatial Modelling

5.1 Introduction

All methods investigated in the previous chapter, except line replacement, linear interpolation, and interpolation using cubic splines, require either information in adjacent, well correlated bands, or information from other, close, passages. For the template date methods to perform well generally, they require that few changes between the sub-image and the template occur.

Although, in general, linear interpolation performed better numerically than other single band, template band, or template date methods investigated in the previous chapter, it has the undesirable smoothing effect. In that chapter it was also mentioned that a single method that performs consistently better than others, for all measures (numerical and visual), could not be identified. Besides, the performances of the methods depend upon the geometry of the features present in the image, in which case template date methods, or template band methods may estimate the missing values better than single band methods.

Recall that the methods in Chapter 4 were all relatively simple ones, which could warrant their implementation on a routine basis, to replace missing scan lines on the imagery.

Since certain classes of spatial models have been shown to fit remotely sensed data well, they are investigated in this chapter as methods to replace missing values arising in this particular kind of data. These spatial methods take into

account the fact the remotely sensed data are usually spatially autocorrelated.

An approach to account for the spatial dependence of the observations is its removal before the main analysis of the data is initiated, so that conventional methods may then be applied. The use of polynomials has been suggested to eliminate spurious correlation due to the position of the observation in space. The technique, nowadays referred to as *trend surface analysis*, has already been investigated in connection with remotely sensed data (Haining *et al.*, 1989). Another alternative to remove the spatial dependence between the observations consists of spatial differencing, analogous to the differencing used in time series to remove non-stationarity (Cliff & Ord, 1975; Gleeson and McGilchrist, 1980).

Two classes of spatial models seem to have received most attention in connection with remotely sensed data: the conditional autoregressive (CAR) and the simultaneous autoregressive (SAR). Künsch (1987), for instance, fitted an intrinsic CAR model with constant mean to Switzer's 16 by 25 Landsat data of three rock-types in one of four spectral bands, and compared the results with those from an ordinary CAR with up to third- order neighbours, whilst Haining *et al.* (1989) fit a trend surface model with first-order CAR errors to an 11 by 11 subset of reflectance values from an aerial survey monitoring marine pollution levels off the south coast of England. In their investigation, Haining *et al.* (1989) deliberately and artificially deleted some values from the centre of the image, analyzing two situations: one consisting of the complete deletion of the values in line 5 of their original data, and another consisting of the deletion of a cluster of size 3 by 3 from the centre of the lattice. They compare the results obtained by averaging neighbouring observed values, and by the fit of a sequence of trend surface models of successively higher order. Estimates based on a stationary form for the covariance matrix have also been obtained. Haining *et al.* (1989) used the root mean square error as a measure for evaluate the results from the different models. The results from averaging, and from the use of a second-order trend surface with 1p-CAR(1) errors (fixed border values, and stationary form) were very similar, both in the case of the sequentially missing values, as well in the clustered case. The larger values for the root mean square error were obtained for the methods that assumed a stationary form for the covariance matrix.

Before data from D_1 and D_2 became available, the fit of several spatial models

to the original 11 by 11 data of Haining *et.al* (1989) has been investigated. As the data showed some trend on the mean, some exploratory data analyses have been applied to the data, consisting of a method proposed by Tukey (1977) (*line median polishing* and *row median polishing*), and *line differencing*. CAR and SAR processes of several orders have been fitted to their data, the results of which are included in Appendix D. From these results it can be seen that there is only a slight gain in using higher-order processes.

Krug & Martin (1990) reported the results from the use of a method using spatial modelling, and the methods of adjacent line replacement, linear interpolation, and TB/D-4, and TB/D-5, which were used to estimate some simulated missing lines in one sub-image from D_1 [$D_1(15)$]. The results from that preliminary investigation suggested further exploration of methods using spatial modelling.

Subsequently, Krug & Martin (1991a), applied the same methods to a larger number of simulated missing lines, using some sub-images from D_1, acquired at different dates, and in different bands. Results were obtained for 10 simulated missing lines [3 in sub-image $D_1(15)$, 2 in $D_1(14)$, 1 in $D_1(25)$, 3 in $D_1(24)$, and 1 in $D_1(35)$], and for eight hypothetical configurations of missing values. As for the results for the missing lines, Krug & Martin (1991a) concluded that the results using spatial modelling were better than those for methods TB/D-4, or TB/D-5, although only slightly better than those obtained for LI.

The application of methods that use spatial modelling has been investigated in other contexts than remote sensing. For instance, Mead (1967) reported the use of a one-parameter first-order CAR in a study involving the estimation of inter-plant competition, to describe competition effects between neighbouring plants.

In this chapter, the results from the use of CAR and SAR models, as methods to estimate missing values in remotely sensed data, are evaluated. A general introduction to CAR and SAR processes is given in §5.3 and §5.4, whilst in §5.5 some particular classes of these processes are examined. Although the material presented in these sections covers more than is necessary for the aims of this chapter, it is relevant to Chapter 7. The notation introduced in §5.2, and the contents in §5.3 to §5.5 are essentially verbatim from Krug & Martin (1991b). Details of CAR and SAR processes can also be found in §5.2 in Ripley (1981).

The main objective in this chapter is to contrast the results obtained from the application of methods that use spatial modelling with those obtained from the

simple methods introduced in Chapter 4. As in that chapter, the missing values are assumed here to arise from line-dropout. In Chapter 6 the methods proposed here, which are presented in §5.6, as well as some of the methods presented in Chapter 4, are evaluated in the estimation of missing values occurring in small clusters, as if arising from the presence of small, thick, clouds.

The model parameters are estimated using maximum likelihood, since the least square estimators for SAR models are inconsistent (Whittle, 1954). Although the least squares procedure leads to consistent estimators for a CAR scheme, these estimators are nonetheless inefficient. Some problems encountered with the use of the method of maximum likelihood are described in §5.7.

As the application of methods that use spatial modelling to estimate a large number of missing values can be so computer demanding as to become prohibitive, only the failure of a few detectors is simulated in this chapter, generating systematically missing scan lines (every 16^{th} line) in one selected sub-image from D_1 [$D_1(15)$], and in another from D_2 [$D_2(15)$]. The simulated missing lines, and some descriptive statistics, are presented in §5.8, for some sub-images from both data sets.

Results for the methods proposed in §5.6, and for those introduced in Chapter 4 are given in §5.9; a discussion of the results in §5.9 is presented in §5.10. The conclusion follows in §5.11.

5.2 Notation

In this section, some notation is introduced. For convenience assume in this section that the n sites in the n_1 by n_2 lattice are labelled by the first n positive integers, in lexicographic order [that is, in the ordering, site (i, j) precedes $(i, j+1)$ for $j < n_2$ and (i, n_2) precedes $(i+1, 1)$].

Two sites i and j on the lattice are said to be lag k neighbours if $i - j = \pm k$. Thus, if $d = 3$, for instance, and $k' = (k_1, k_2, k_3)$ then the lag k neighbours of $i' = (i_1, i_2, i_3)$ are $(i_1 + k_1,\ i_2 + k_2, i_3 + k_3)$ and $(i_1 - k_1,\ i_2 - k_2, i_3 - k_3)$.

Let the n by n lag k neighbour matrix $\mathbf{W}_k$ be such that $W_k[i, j]$ is 1 if i and j are lag k neighbours, and 0 otherwise, where $W_k[i, j]$ is the value in matrix $\mathbf{W}_k$ for the row corresponding to site i and the column corresponding to site j.

Define also the n by n directed lag k neighbour matrix $\mathbf{T}_k$ by $T_k[i, j]$ is 1 if

$j - i = k$, and 0 otherwise, and note that $\mathbf{W}_k = \mathbf{T}_k + \mathbf{T}_k'$, and that $\mathbf{T}_k' = \mathbf{T}_{-k}$.

5.3 CAR processes

Assume that K_c is a set of vectors $k \neq 0$ for which $\beta_k = \beta_{-k}$ is non-zero, and exactly one of $\pm k$ is in K_c. The CAR process is then defined here through its inverse covariance matrix

$$\mathbf{V}^{-1} = \mathbf{I} - \sum_{k \in K_c} \beta_k \mathbf{W}_k. \tag{5.1}$$

All subsequent sums in this section are over K_c. For $k \neq 0$ and $\pm k \notin K_c$, define $\beta_k = 0$. Note that $\mathbf{V}^{-1}$ must be positive definite, and that in general this process is not stationary - for example, the diagonal elements of $\mathbf{V}$ are not constant, so that $\text{var}(x_i)$ is not constant, and covariances are also a function of location.

Equation 5.1 implies that the conditional mean and variance are

$$\text{E}(x_i \mid \bullet) = \mu + \sum \beta_k (x_{i-k} + x_{i+k} - 2\mu) \ , \text{ and } \text{var}(x_i \mid \bullet) = \sigma^2 \ , \tag{5.2}$$

where the notation $\bullet$ stands for all other values x_j in the lattice, i.e. $\{x_j \mid j \neq i \ , \ j \in \mathcal{U}\}$. If $j \notin \mathcal{U}$ then it is assumed in (5.2) that $x_j = \mu$.

The stationary process can be defined by equation 5.2 when $\mathcal{U}$ is extended to the infinite lattice $\mathbf{Z}^d$, provided the β_k satisfy $\sum \beta_k \cos(\omega' k) < \frac{1}{2}$, for all ω. For a finite $\mathcal{U}$, $\mathbf{V}^{-1}$ in 5.1 is always positive definite under this condition, but slightly larger values of the $\mid \beta_k \mid$ may be possible.

Site i is said to be an interior site of $\mathcal{U}$ if its corresponding row in $\mathbf{V}^{-1}$ has sum equal to $1 - 2\sum \beta_k$, i.e. if i has both neighbours at all lags $k \in K_c$. Otherwise i is referred to as a boundary site. If $\mathbf{V}_s^{-1}$ denotes the inverse covariance matrix for a realization on $\mathcal{U}$ of the stationary process, then the (i,j)- elements of $\mathbf{V}^{-1}$ and $\mathbf{V}_s^{-1}$ only differ if i and j are boundary sites. Thus, for the stationary process on $\mathcal{U}$ equation 5.2 holds for interior sites i, but not for boundary sites.

Sites i and j are isolated if $\beta_{i-j} = 0$ (or $\pm \ (i-j) \notin K_c$). Thus x_j does not occur in expression 5.2 for $\text{E}(x_i \mid \bullet)$. Two groups of sites are isolated if all sites in one group are isolated from all sites in the other group.

5.4 SAR processes

The simultaneous autoregressive (SAR) process is defined here by its inverse covariance matrix $\mathbf{V}^{-1} =$

$$(\mathbf{I} - \sum \beta_k \mathbf{T}_k)'(\mathbf{I} - \sum \beta_k \mathbf{T}_k) = \mathbf{I} - \sum \beta_k \mathbf{W}_k + \sum\sum \beta_k \beta_l \mathbf{T}_k' \mathbf{T}_l \qquad (5.3)$$

where all sums are over K_s, the set of all vectors $k \neq 0$ for which $\beta_k \neq 0$. Again $\beta_k = 0$ if $k \neq 0$ and $k \notin \mathbf{K}_s$. Note that the matrix $\mathbf{I} - \sum \beta_k \mathbf{T}_k$ must be non-singular, and that in general β_k is different from β_{-k}. As for the CAR process of §2.2, this process is in general not stationary.

Equation 5.3 implies that

$$x_i = \mu + \sum_{k \in K_s} \beta_k (x_{i-k} - \mu) + \epsilon_i \qquad (5.4)$$

where the ϵ_i are white noise, and $x_j = \mu$ when $j \notin \mathcal{U}$.

The stationary process can be defined by equation 5.4 when $\mathcal{U}$ is extended to the infinite lattice $\mathbf{Z}^d$ provided the β_k satisfy the stationarity condition $\sum_{k \in K_s} \beta_k \cos(\omega' k) < 1$, $\forall w$. For a finite $\mathcal{U}$, large values of the $\mid \beta_k \mid$ may also be possible.

Every stationary SAR process has a corresponding CAR formulation. For a SAR process a site i is said to be an interior one if it is interior in its corresponding CAR formulation, which can be found by equating equations 5.11 and 5.12 in Besag (1974).

Assume here that the generating function for the SAR process is $(1 - \sum_{k \in K_s} \beta_k z^k)$, where z^k denotes $\prod z_i^{k_i}$ (for instance, if $d = 2$ and $k = (1, -1)$ then $z^k = z_1^1 z_2^{-1}$), then that for the corresponding CAR is

$$b^{-1}(1 - \sum_{k \in K_s} \beta_k z^k)(1 - \sum_{k \in K_s} \beta_k z^{-k}) = b^{-1} \sum_{k \in K_s^*} z^k \sum_{r \in K_s^+} \beta_r \beta_{r+k} \qquad (5.5)$$

with $K_s^+ = K_s \cup \{0\}$, $K_s^* = \{k \mid k = k_1 - k_2 \text{ for all } k_1, k_2 \in K_s^+\}$,
$\beta_0 = -1$ and $b = \sum_{k \in K_s^+} \beta_k^2$.

Then equation 5.5 shows that the corresponding CAR is defined by

$$\mathrm{E}(x_i \mid \bullet) = \mu + \sum_{k \in K_c^*} \beta_k^* (x_{i-k} + x_{i+k} - 2\mu)$$

for $\beta_k^* = -b^{-1} \sum_{r \in K_s^+} \beta_r \beta_{r+k}$. The appropriate $\mathbf{K}_c^*$ for which the β_k^* are non-zero contains one of each pair $\pm k$ for $k \neq 0$, $k \in K_s^*$.

Consider, for instance, the CAR formulation corresponding to the two-parameter first-order SAR referred to in subsection 5.5.4 This has

$K_s = \{(0,1),(0,-1),(1,0),(-1,0)\}$ and $\beta_k = \alpha$ for $k = (\pm 1, 0)$ and $\beta_k = \beta$ for $k = (0, \pm 1)$. The corresponding K_c^* is $\{(1,0),(0,1),(1,1),(1,-1),(2,0),(0,2)\}$, and the corresponding CAR is

$$\begin{aligned}(1 + 2\alpha^2 + 2\beta^2) \quad & \mathrm{E}(x_{ij} \mid \bullet) = 2\alpha(x_{i-1,j} + x_{i+1,j}) + 2\beta(x_{i,j-1} + x_{i,j+1}) \\ & -2\alpha\beta(x_{i-1,j-1} + x_{i-1,j+1} + x_{i+1,j-1} + x_{i+1,j+1}) \\ & -\alpha^2(x_{i-2,j} + x_{i+2,j}) - \beta^2(x_{i,j-2} + x_{i,j+2}),\end{aligned} \tag{5.6}$$

where i and j are scalars here.

For the CAR corresponding to the general four-parameter first-order SAR see equations 5.7 and 5.8 in Besag (1974).

Under the assumption that $\beta_k = \beta_{-k}$ for all $k \in K_s$, the process is referred to here as the symmetric SAR. Then $\mathbf{V}^{-1}$ can be written as $(\mathbf{I} - \sum_{k \in K_c} \beta_k \mathbf{W}_k)^2$.

5.5 Some classes of two-dimensional CAR and SAR processes

For simplicity define now the following matrices:
$\mathbf{U}_{1h} = \mathbf{W}_k$ for $k = (1,0)$, the adjacent horizontal neighbours matrix;
$\mathbf{U}_{1v} = \mathbf{W}_k$ for $k = (0,1)$, the adjacent vertical neighbours matrix;
$\mathbf{U}_1 = \mathbf{U}_{1h} + \mathbf{U}_{1v}$, the adjacent neighbours matrix;
$\mathbf{U}_2 = \mathbf{W}_k + \mathbf{W}_l$ for $k = (1,1)$ and $l = (-1,1)$, the adjacent diagonal neighbours matrix.

Note that for the first- and second-order CAR processes discussed here a site i is interior if it is not in the outer layer of the rectangular lattice, i.e. if it is not in the first or last row, or in the first or last column of the lattice.

5.5.1 One-parameter first-order CAR

The one-parameter first-order CAR has one parameter for its horizontally and vertically adjacent neighbours. It is defined by $\mathbf{V}^{-1} = \mathbf{I}_n - \beta\mathbf{U}_1$. The stationarity condition is $|\beta| < \frac{1}{4}$.

For a first-order CAR, two sites i and j are isolated if j is not an adjacent horizontal or vertical neighbour of i.

5.5.2 Two-parameter first-order CAR

The two-parameter first-order CAR has one parameter for horizontal neighbours and one for vertical neighbours. Its inverse covariance matrix is $\mathbf{V}^{-1} = \mathbf{I}_n - \alpha\mathbf{U}_{1h} - \beta\mathbf{U}_{1v}$. The stationarity condition is $\mid \alpha \mid + \mid \beta \mid < \frac{1}{2}$. For an n_1 by n_1 lattice, $\mathbf{V}^{-1}$ is positive definite when $\mid \alpha \mid + \mid \beta \mid < [2cos\{\pi/(n_1+1)\}]^{-1}$. When $\alpha = \beta$ the one-parameter first-order CAR of subsection 5.2.1 results. The condition for two sites to be isolated is the same as in 5.5.1.

Higher order models can be extended from first-order models by incorporating more elements in the set K_c. Thus, a second-order model, for instance, includes the diagonal neighbours in the specification of $\mathbf{V}^{-1}$, and a third-order includes sites which lie at lags $(0,2)$ and $(2,0)$.

5.5.3 Two-parameter second-order CAR

For the second-order process $K_c = \{(0,1),(1,0),(1,1),(-1,1)\}$. Assume here that $\beta_k = \begin{cases} \alpha & \text{if } k = (0,1) \text{ or } k = (1,0) \\ \beta & \text{if } k = (1,1) \text{ or } k = (-1,1) \end{cases}$. Thus, this two-parameter second-order CAR has one parameter for horizontally and vertically adjacent neighbours, and one for diagonally adjacent neighbours. The inverse covariance matrix is $\mathbf{V}^{-1} = \mathbf{I}_n - \alpha\mathbf{U}_1 - \beta\mathbf{U}_2$. The stationarity conditions are $\beta > -\frac{1}{4}$ and $\mid \alpha \mid + \beta < \frac{1}{4}$. When $\beta = 0$, the one-parameter first-order CAR of subsection 5.5.1 is obtained.

For the second-order CAR two sites i and j in $\mho$ are isolated if j is not an adjacent horizontal, vertical, or diagonal neighbour of i.

5.5.4 First-order symmetric SAR

The two-parameter first-order symmetric SAR has one parameter for horizontal neighbours and one parameter for vertical neighbours. It is defined by $\mathbf{V}^{-1} = (\mathbf{I}_n - \alpha\mathbf{U}_{1h} - \beta\mathbf{U}_{1v})^2$. The stationarity condition for this process is $\mid \alpha \mid + \mid \beta \mid < \frac{1}{2}$. The corresponding CAR formulation is given in equation 5.6. The first-order SAR is a special case of a third-order CAR.

Two sites i and j are isolated for a first-order SAR if j is not an adjacent horizontal, vertical, or diagonal neighbour of i, and also not its lag $(0,2)$ or $(2,0)$ neighbour.

For all SAR processes discussed here a site i is interior if it does not lie in the two outer layers of the rectangular lattice, i.e., if it is not a site in the first or last two rows or first or last two columns of the lattice.

The one-parameter first-order SAR has $\alpha = \beta$.

5.5.5 Two-parameter second-order symmetric SAR

For the second-order symmetric SAR $K_c = \{(0,1),(1,0),(1,1),(1,-1)\}$. Here it is assumed that $\beta_k = \begin{cases} \alpha & \text{if } k = (0,1) \text{ or } k = (1,0) \\ \beta & \text{if } k = (1,1) \text{ or } k = (1,-1) \end{cases}$.
Thus $\mathbf{V}^{-1} = (\mathbf{I}_n - \alpha\mathbf{U}_1 - \beta\mathbf{U}_2)^2$. The stationarity conditions are $\beta > -\frac{1}{4}$ and $\mid \alpha \mid + \beta < \frac{1}{4}$. The one-parameter first-order SAR of subsection 5.5.4 results when $\beta = 0$.

5.6 Proposed Methods using Spatial Modelling

The methods proposed in this section, for the estimation of missing values arising in remotely sensed data, use the spatial models introduced in §5.5.

The following methods are proposed:

- the one-parameter first-order CAR (1p-CAR) of §5.5.1;
- the one-parameter first-order SAR (1p-SAR) of §5.5.4;
- the two-parameter first-order SAR (2p-SAR) of §5.5.4.

Results have also been obtained for a two-parameter first-order CAR of §5.5.2, a two-parameter second-order CAR of §5.5.3, and for a two-parameter second-order SAR of §5.5.5. The maximum likelihood estimate of the parameter α, for the methods using second-order models, were similar to the estimate obtained for the corresponding methods using first-order models, and the estimate of β was always close to zero. Hence, the estimates of the variance, and the function value for the methods using second-order models were similar to those obtained for the corresponding methods using first-order models. The results for a method that uses a two-parameter first-order CAR were consistently worse than those obtained for the other methods proposed here, and hence are not included.

For the case of missing values occurring sequentially on a line, as in this chapter, the estimates for a first-order CAR incorporate the information from all sites in the lines above and below the one where the missing values occur. For example, consider the case of the 5 by 5 lattice given below, where the missing values occur sequentially in line 3. The sites are labelled by the first integers, in lexicographic order, and those corresponding to the missing values are indicated in bold.

1	2	3	4	5
6	7	8	9	10
11	**12**	**13**	**14**	**15**
16	17	18	19	20
21	22	23	24	25

The estimate of the missing value at site **13**, for instance, for the method using a 1p-CAR(1) (assuming constant mean) is a linear combination of the values in the lines above, and below, as follows:

$$\hat{u}_{13} = a(u_8 + u_{18}) + b(u_7 + u_9 + u_{17} + u_{19}) + c(u_6 + u_{10} + u_{16} + u_{20})$$

where u_v is the pixel value at site v. The values of a, b and c are a function of the size of the lattice, and of the value of the dependence parameter β. Assuming $\beta = 0.25$, the approximate values of a, b, and c are 0.288, 0.077, and 0.019, respectively.

The method that uses a 1p-SAR(1) estimates the missing values by incorporating information from a larger number of sites than the 1p-CAR. For instance, the estimate of the missing value at site **13** is given by

$$\begin{aligned}\hat{u}_{13} &= a(u_8 + u_{18}) + b(u_7 + u_9 + u_{17} + u_{19}) + c(u_3 + u_{23}) \\ &+ d(u_2 + u_4 + u_{22} + u_{24}) + ed(u_6 + u_{10} + u_{16} + u_{20}) + f(u_1 + u_5 + u_{21} + u_{25})\end{aligned}$$

The approximate values of a, b, c, d, e and f, assuming $\beta = 0.25$, are 0.672, 0.277, -0.192, -0.095, 0.086, and -0.033.

All the methods proposed above assume that the corresponding process has a constant mean, that is, $\mu_{i,j} = \mu, \forall (i,j) \in \mho$. Two other methods, which assume stationarity in covariance structure, but not in the mean, are also proposed, which use trend surface analysis.

The two additional methods proposed here are:

- second-order trend surface with 1p-CAR(1) errors (1p-CART);
- second-order trend surface with 1p-SAR(1) errors (1p-SART).

Results have also been obtained for a third-order trend surface with 1p-CAR(1) errors, but as they are similar to those obtained for the method using a second-order trend surface, they are not included.

In trend surface analysis, which is a particular case of regression analysis, the regressor variables refer to the spatial coordinates of the sites. The mean at a site (i,j), say $\mu(i,j)$, is expressed in the linear form

$$\mu(i,j) = \sum_{s=0}^{p}\sum_{r=0}^{q} \alpha_{sr} i^s j^r \tag{5.7}$$

where $p+q \leq k$, and k is the order of the polynomial trend.

In matrix notation, the mean vector is $\mu = \mathbf{A}\theta$, where $\mathbf{A}$ is an n by p design matrix, and $\theta = [\alpha_{00}, \alpha_{01}, \alpha_{10}, \alpha_{11}, \alpha_{02}, \alpha_{20}]'$, for the second-order surface ($k = 2$).

5.7 Maximum Likelihood Estimation

All the methods proposed in this chapter require the estimation of the parameter vector φ ($\varphi = \beta$ for the one parameter methods, and $\varphi = [\alpha \quad \beta]^t$ for the two-parameter methods).

As mentioned in the introduction, the least squares method provides inconsistent estimates of the parameters for a SAR model, and consistent, but inefficient, estimates for a CAR. In this section the method of maximum likelihood is discussed, assuming the vector of observations, u_t^k, is jointly normally distributed with mean $\mu = \mathbf{A}\theta$ and covariance matrix $\mathbf{V}\sigma^2$, where:

- the design matrix $\mathbf{A}$ is n by p with rank p;
- θ is a p by 1 vector of parameters for the mean of u_t^k;
- $\mathbf{V}$ is proportional to a correlation matrix, and is assumed here to be a function of a q by 1 parameter vector φ; and
- σ^2 is a scaling factor.

Henceforth, the vector of observations, u_i^k, is simply denoted by u.

In the maximum likelihood approach, under the above assumptions, the estimates of the unknown parameter σ^2 and parameter vector φ are such that $f(u, \sigma^2, \varphi)$, the likelihood function of $\Phi = [\sigma^2 \quad \varphi]'$ for u fixed at the observed values, is maximized.

Martin (1984) gives the log likelihood for the full data as:

$$L(\theta, \varphi, \sigma^2 \mid u) = -\frac{n}{2} ln 2\pi - \frac{n}{2} ln\sigma^2 - \frac{1}{2} ln \mid \mathbf{V} \mid -\frac{1}{2\sigma^2}(u - \mathbf{A}\theta)'\mathbf{V}^{-1}(u - \mathbf{A}\theta). \quad (5.8)$$

The maximum likelihood estimates of θ and σ^2, $\hat{\theta}$ and $\hat{\sigma^2}$, are obtained from 5.8, and are simply

$$\hat{\theta} = (\mathbf{A}'\hat{\mathbf{V}}^{-1}\mathbf{A})^{-1}\mathbf{A}'\hat{\mathbf{V}}^{-1}u \quad \text{and} \quad \hat{\sigma^2} = n^{-1}(u - \mathbf{A}\hat{\theta})'\hat{\mathbf{V}}^{-1}(u - \mathbf{A}\hat{\theta})$$

The maximum likelihood estimate of the vector of parameters, $\hat{\varphi}$,is obtained from 5.8 by minimizing

$$\mid \hat{\mathbf{V}}^{-1} \mid^{-\frac{1}{n}} (u - \mathbf{A}\hat{\theta})'\hat{\mathbf{V}}^{-1}(u - \mathbf{A}\hat{\theta}) = \mid \hat{\mathbf{V}}^{-1} \mid^{-\frac{1}{n}} e'\mathbf{V}^{-1}e \,, \quad (5.9)$$

for $e = u - \mathbf{A}\hat{\theta}$, and assuming $\mathbf{A}'\hat{\mathbf{V}}^{-1}\mathbf{A}$ is of rank p.

For first- and second-order CAR and SAR processes defined on rectangular lattices, the term $\mid \mathbf{V} \mid$, and the quadratic form $e'\mathbf{V}^{-1}e$ in equation 5.9, are easily found for a given φ.

Ord (1975) proposed a procedure for the evaluation of $\mid \mathbf{V} \mid$ based on the fact that the determinant of a matrix may be computed as the product of its eigenvalues. For example, for the 1p-CAR(1) process, whose inverse covariance matrix is $\mathbf{V}^{-1} = \mathbf{I}_n - \beta\mathbf{U}_1$ (refer to §5.5.1),

$$\mid \mathbf{V}^{-1} \mid = \mid \mathbf{I}_n - \beta\mathbf{U}_1 \mid = \prod_{i=1}^{n}(1 - \beta\lambda_i) \quad (5.10)$$

where λ_i, $i = 1, \ldots, n$ are the eigenvalues of $\mathbf{U}_1$. As the λ_i's need to be evaluated only once, then the problem reduces to finding that value of β, $\hat{\beta}$, which minimizes

$$\{\prod_{i=1}^{n}(1 - \beta\lambda_i)\}^{(-\frac{1}{n})}(\mathbf{e}'\mathbf{e} - \beta\mathbf{e}'\mathbf{U}_1\mathbf{e}). \quad (5.11)$$

Ord (1975) stresses that for irregularly spaced points analytic simplification of the equation for the eigenvalues is usually impossible. However, when the lattice has a regular grid structure, some analytic progress is possible.

Note that for processes of order higher than two, defined on rectangular lattices, the computation of $|\mathbf{V}|$ is not as simple as for the first- and second-order processes, since they require higher-order neighbourhood matrices which no longer commute with the lower-order ones. If all the matrices commute, there exists an orthogonal transformation that diagonalizes these matrices simultaneously (the diagonal elements being their respective characteristic roots) (Ali, 1979), and it is very simple to calculate $|\mathbf{V}|$.

One way to ensure that all neighbourhood matrices commute is by defining the process on a torus lattice, instead of on a rectangular one. For details on such processes see, for instance, Kiiveri & Campbell (1989), and Mardia (1990). Hence, for processes defined on a torus lattice, the computation of $|\mathbf{V}|$ is always simple, regardless of the order of the process under consideration. However, the periodic boundaries defined by such processes do not seem to be very realistic, especially in the case of remotely sensed data, when the size of the lattice is large.

The computation of $|\mathbf{V}|$ is also easily carried out for separable processes. These processes have many desirable properties which may make them suitable for representing autocorrelated variables in practical situations. For details, see Martin (1979, 1990a).

When fitting different spatial models to the 11 by 11 data set used by Haining *et al.* (1989), the processes were assumed to occur on a rectangular lattice, as well as on a torus lattice. However, the fits of the models, under the torus assumption, were in general inferior (based on the function values – refer to Appendix D) than those obtained under the rectangular assumption. Considering also the unrealistic assumption of periodic boundaries mentioned above, then only models defined on a rectangular lattice have been assumed.

In order to ensure that $\mathbf{V^{-1}}$ is a valid covariance matrix it needs to be positive definite, which from theorem 12.2.2 in Graybill (1969) is ensured if the eigenvalues of $\mathbf{V}$ are all positive.

Consider again the case of a 1p-CAR(1) process, which has $\mathbf{V^{-1}} = \mathbf{I}_n - \beta\mathbf{U}_1 = \mathbf{I}_n - \beta(\mathbf{U}_h + \mathbf{U}_v)$. To ascertain that $\mathbf{V^{-1}}$ is positive definite it is necessary that the i^{th} eigenvalue of $\mathbf{V^{-1}}$, $1 - \beta(\eta_i + \xi_i)$, be positive for $i = 1, 2, \ldots, n$. Let $\eta_{max} > 0$ and $\eta_{min} < 0$ be the maximum and minimum eigenvalues of $\mathbf{U}_h$, respectively. Similarly, define $\xi_{max} > 0$ and $\xi_{min} < 0$ as the maximum and minimum eigenvalues of $\mathbf{U}_v$, respectively. The conditions for the covariance matrix to be positive

definite are:

- $1 - \beta(\eta_{max} + \xi_{max}) > 0 \Rightarrow \beta(\eta_{max} + \xi_{max}) < 1 \Rightarrow \beta < (\eta_{max} + \xi_{max})^{-1}$;
- $1 - \beta(\eta_{min} + \xi_{min}) > 0 \Rightarrow \beta(\eta_{min} + \xi_{min}) < 1 \Rightarrow \beta > (\eta_{min} + \xi_{min})^{-1}$.

Therefore, the search for β is confined to the range

$$(\eta_{min} + \xi_{min})^{-1} < \beta < (\eta_{max} + \xi_{max})^{-1}.$$

5.7.1 Maximum Likelihood Estimation with Missing Values

Suppose now that m out of the n observations are missing at random, and assume that the vector u can be reordered into $x = (y' \quad z')$, where y corresponds to the first $n-m$ elements of x, and z to the last m elements, which are associated with the missing values.

Let $var(x)/\sigma^2 = \mathbf{V}_{xx}$ be partitioned as $\begin{pmatrix} \mathbf{V}_{yy} & \mathbf{V}_{yz} \\ \mathbf{V}_{zy} & \mathbf{V}_{zz} \end{pmatrix}$, and $(\mathbf{V}_{xx})^{-1}$ as $\begin{pmatrix} \mathbf{V}^{yy} & \mathbf{V}^{yz} \\ \mathbf{V}^{zy} & \mathbf{V}^{zz} \end{pmatrix} = \begin{pmatrix} \mathbf{V}^{yx} \\ \mathbf{V}^{zx} \end{pmatrix}$.

The estimates of the missing values using spatial modelling can be obtained simultaneously with the parameters estimates, in several iterations, until convergence of the model parameters is achieved. This has been the approach adopted here.

In the first iteration, all the missing values are replaced by the mean of the remaining values (that is, by $\bar{y} = (n-m)^{-1}1'y$), and the vector of observations is treated as if complete. At the end of each iteration, the parameters of the model are used to estimate the missing values. From Martin (1984) it is known that the minimum mean square estimator of the unobserved vector z, for known θ and φ is the conditional mean $E[z \mid y]$. The maximum likelihood estimator of the vector of missing observations, z, is given by

$$E(z \mid y, \hat{\theta}, \hat{\varphi}, \hat{\sigma^2}) = \mathbf{A}_z\hat{\theta} + \hat{\mathbf{V}}_{zy}\hat{\mathbf{V}}_{yy}^{-1}(y - \mathbf{A}_y\hat{\theta}) = \mathbf{A}_z\hat{\theta} + (\hat{\mathbf{V}}^{zz})^{-1}\hat{\mathbf{V}}^{zy}(y - \mathbf{A}_y\hat{\theta}) \quad (5.12)$$

A schematic representation of the method is given in Figure 5.1. The estimate of $\varphi^{(0)}$ is that of no spatial dependence, that is, 0, and p refers to the iteration number (initial p is 0).

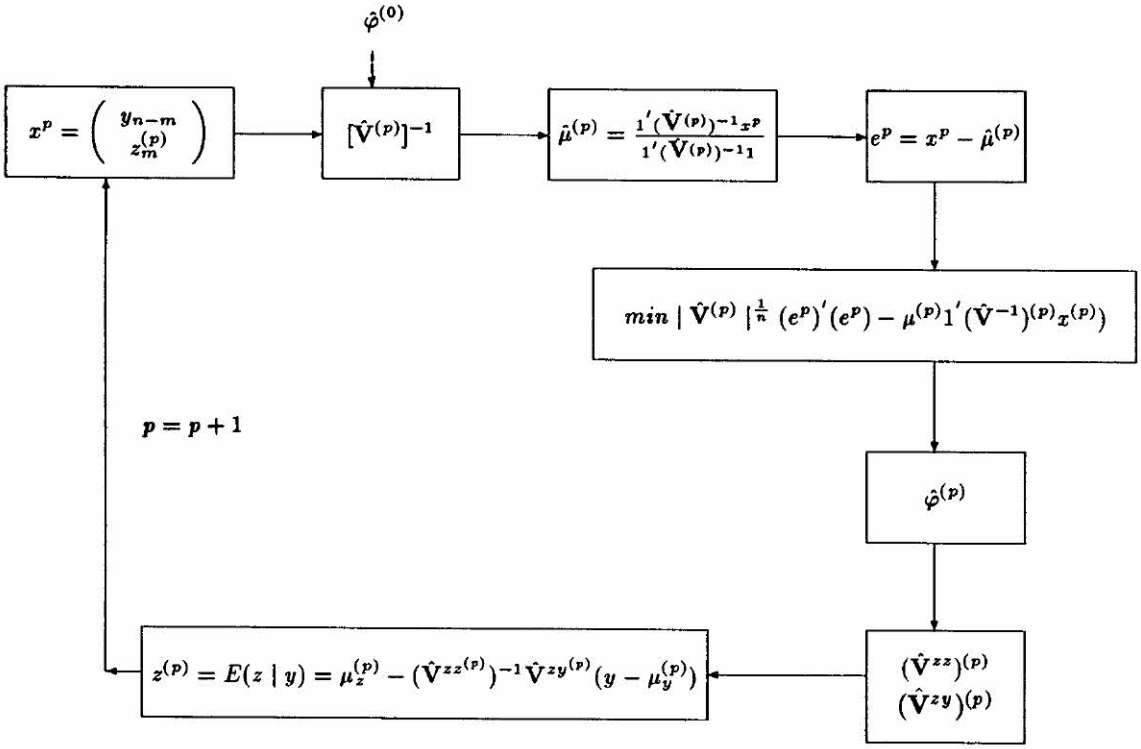

Figure 5.1: Diagram for a method of estimating missing values using maximum likelihood.

As mentioned in §5.1, the use of the method of maximum likelihood has some drawbacks, the first associated with the need for a minimization routine, and the second related to the easiness of implementation of the method, particularly in the case of large lattices, as is the case with remotely sensed data. It is difficult to guarantee that the minimization routine is not converging to a local minimum, instead of to a global minimum. Moreover, if the covariance matrix is specified using the $\mathbf{U}$ matrices in §5.5, then large matrices need to be stored in the case of large lattices, which the computer may not be able to handle. Even for lattices of size 11 by 92, or 11 by 100, as the ones used here, the number of bites necessary to store the $\mathbf{U}$ matrices for a 2p-CAR(1) process, for instance, is prohibitive. If the inverse covariance matrix for this process is written as $\mathbf{I}_n - \alpha(\mathbf{U}_h + \mathbf{U}_v) - \beta\mathbf{U}_2$ then there are at least three matrices of dimension 1100 by 1100 to be stored, viz., $\mathbf{V}^{-1}$, $\mathbf{U}_h + \mathbf{U}_v$, and $\mathbf{U}_2$. The solution to this problem is to write the programs in such a way that only one matrix, viz, $\mathbf{V}^{zz}$, needs to be stored. All the programs used in this dissertation, for the methods using spatial modelling, have been written in both forms. However, only the ones requiring less

storage were able to handle data from the entire neighbourhood of the missing line, defined as the sub-region consisting of 5 lines above, and 5 lines below the missing one. When using the more memory demanding programs, results could only be obtained (for up to a second-order SAR) for lattices of dimension less than 11 by 40. For the results obtained in this chapter, the programs were run at a SUN workstation. However, although the computer memory problem has been overcome by appropriately writing the programs, another problem had to be faced, regarding the speed at which the results were obtained, especially for higher order processes. For example, to obtain the estimates of the 92 pixel values in a line, for a 2p-SAR(1), more than 90 min of CPU time were required (at a SUN workstation). By increasing the order of the process under consideration, especially SAR, the programs become very inefficient, and extremely slow. This is an important factor that needs to be taken into account, when applying methods that use spatial modelling.

The method for function minimization used here was the *downhill simplex method* due to Nelder & Mead (1965), using a sub routine based on the algorithm given by O'Neill (1971), incorporating remarks ASR11, ASR15, and ASR28 in vols. 23, 25, and 27, respectively, of Applied Statistics. Before use of the *downhill method*, another function minimization routine has been considered (routine E04KAF, from the NAG library, which uses only function values), but as convergence problems were encountered, it was abandoned. For a detailed description of the *downhill simplex method*, see also §10.4 in Press *et al.* (1988).

5.8 Simulated line dropout, and some descriptive statistics

5.8.1 Introduction

The fact that, for large lattices, the methods that use spatial modelling can be very computer demanding, made it difficult to apply here the same approach used in Chapter 4, i.e., that of estimating each line in all sub-images in D_1, and D_2. Hence, besides simulating the failure of a few detectors, only one sub-image from each data set has been selected to be used with the methods.

The selected sub-images from D_1, and from D_2, are $D_1(15)$ (acquired at 10/07)

and $D_2(15)$ (acquired at 09/09), respectively. The simulation of detector failure generated entirely missing lines, which occurred systematically at every 16^{th} line on these sub-images. The simulated 'defective' lines on sub-image $D_1(15)$ are 11, 27, 43, 59, 75, and 91, whilst those in $D_2(15)$ are 7, 23, 39, 45, 61, 77, and 93. Note that for the second data set the failure of two different detectors has been simulated. The 'defective' lines 7, 23, and 39 arise from the failure of one detector, whilst the 'faulty' lines 45, 61, 77 and 93 arise from the failure of another.

The simulated 'defective' sub-images, $D_1(15)$ and $D_2(15)$, are displayed in Figure 5.2 (a) and (b), respectively.

In order to estimate the missing values occurring in the simulated 'defective' lines, data from 5 lines above, and 5 lines below the 'faulty' one are used with the spatial methods. This neighbourhood around each missing line (except line 91, in sub-image $D_1(15)$) ensures that most missing values on each 'defective' line, occur at interior sites, and hence have information from all neighbours. The neighbours of any interior site, for a first-order CAR process, consist of its adjacent horizontal and vertical sites (see §5.5.1). For the first-order SAR, the neighbours of an interior site consist of its adjacent horizontal, vertical and diagonal sites, and those at lags $(0, \pm 2)$ and $(\pm 2, 0)$.

5.8.2 Description of the neighbourhood of each missing line in sub-image $D_1(15)$

The mean and standard deviation (stdev) of the data in the neighourhood of each 'defective' line, in the 'faulty' sub-image and in all possible templates (band or date), are presented in Table 5.1. The minimum and maximum values [(m,M)], the range, and the correlation (r) between data in the neighbourhood of the missing line, and the corresponding data in the template, are also included. In the computation of the means and the standard deviations of the template, data from the line corresponding to the missing one in the 'defective' sub-image and in its neighbourhood are all used (i.e., data in the entire 11 by 92 area), whilst for the 'defective' sub-image, only data in the neighbourhood of the 'faulty' line are considered.

a

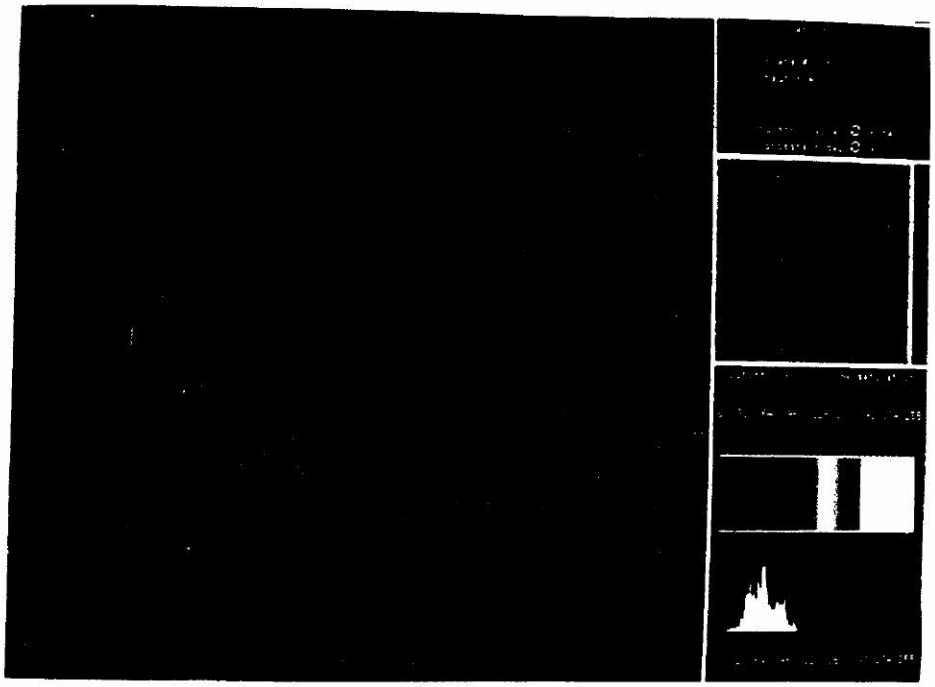

b

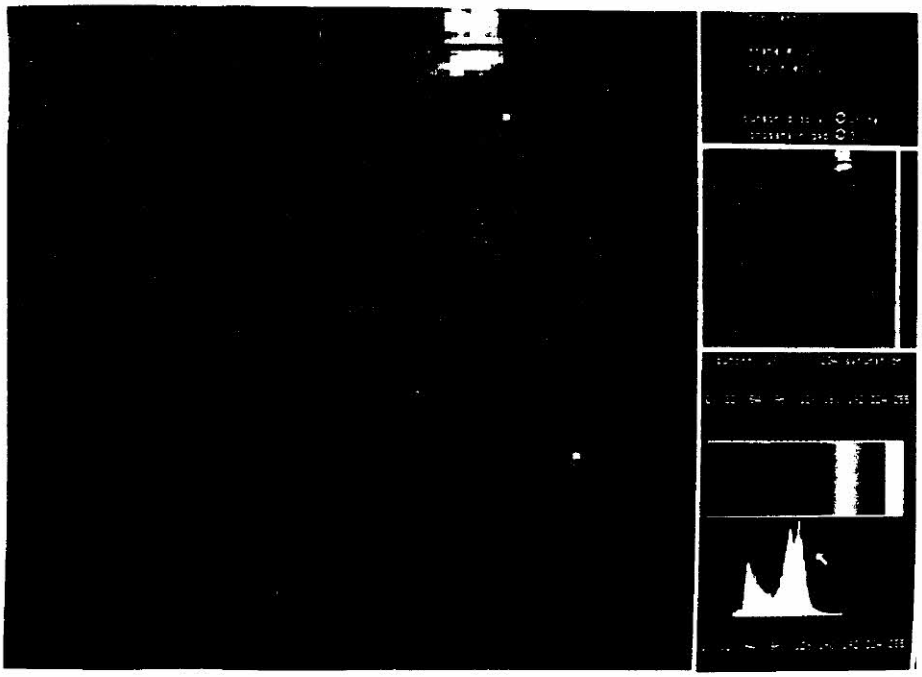

Figure 5.2: Simulated defective sub-images: (a) $D_1(15)$; (b) $D_2(15)$.

Table 5.1: Descriptive statistics of the data in the neighbourhood of each 'defective' line in sub-image $D_1(15)$, and of the data in corresponding areas in the possible templates (band and date), including those corresponding to the missing line, in sub-image $D_1(15)$.

Sub-Image					Template					
Line	Mean	Stdev	(m,M)	Range	Sub-Image	Mean	Stdev	(m,M)	Range	r
11	58.73	19.13	(21,99)	78	$D_1(13)$	23.32	6.55	(11,35)	24	0.896
					$D_1(14)$	43.73	8.84	(27,65)	38	−0.008
					$D_1(25)$	55.39	18.73	(20,94)	74	0.978
					$D_1(35)$	55.45	19.07	(19,98)	79	0.959
27	68.77	16.93	(24,106)	82	$D_1(13)$	27.29	4.44	(14,40)	26	0.762
					$D_1(14)$	49.45	9.60	(18,65)	47	−0.355
					$D_1(25)$	63.37	16.02	(23,100)	77	0.943
					$D_1(35)$	62.28	17.09	(24,101)	77	0.939
43	65.40	15.82	(32,97)	65	$D_1(13)$	27.01	3.82	(14,38)	24	0.682
					$D_1(14)$	45.94	8.84	(19,64)	45	−0.289
					$D_1(25)$	61.83	14.69	(31,94)	63	0.956
					$D_1(35)$	60.38	14.90	(32,95)	63	0.919
59	56.57	14.55	(22,93)	71	$D_1(13)$	24.64	4.46	(11,37)	26	0.670
					$D_1(14)$	43.76	9.04	(18,62)	44	0.035
					$D_1(25)$	53.92	13.47	(20,84)	64	0.927
					$D_1(35)$	53.53	13.42	(22,90)	72	0.830
75	51.94	18.52	(5,99)	94	$D_1(13)$	24.30	5.61	(11,40)	29	0.603
					$D_1(14)$	35.21	10.91	(7,65)	58	0.425
					$D_1(25)$	50.88	15.49	(7,93)	86	0.885
					$D_1(35)$	50.44	14.78	(7,92)	85	0.881
91	55.64	16.94	(11,89)	78	$D_1(13)$	23.83	5.75	(11,39)	28	0.650
					$D_1(14)$	40.75	12.79	(11,76)	65	0.298
					$D_1(25)$	52.75	15.44	(9,90)	81	0.857
					$D_1(35)$	52.08	13.54	(11,80)	69	0.847

Since the methods using spatial modelling estimate the missing values in each 'defective' line using the information from its neighbours, a brief discussion is now carried out about the main features of the data in the neighbourhood of each missing line.

Let the set of sites that are adjacent vertical, or diagonal, to any site (i, j) in a 'missing' line on the lattice, be referred to as the adjacent neighbourhood of site (i, j). Each site in this neighbourhood is an adjacent neighbour of site (i, j).

The first simulated missing line in sub-image $D_1(15)$ (line 11, i_1=11) comprises diverse types of land cover, but most of the pixel values at the boundaries between them are not contrastingly different. The greatest fluctuation between the data in the adjacent neighbourhood of any pixel in this line is 36, which occurs at column 30 ($j = 30$), (boundary between wheat field and soil with low density vegetation); other large variation occurs at column 86, which is a boundary pixel separating the wheat field from the moisture soil shown in magenta in Figure 5.2 (a). The range of the data in the adjacent neighbourhood of the site at column 86 is 28.

Sharper contrasts between the values of adjacent neighbours are observed for the missing sites in line 27, between columns 15 and 21, inclusive. The ranges of the data in the adjacent neighbourhood of these pixels are 40, 35, 35, 45, 45, 51, and 45, respectively. These pixels are associated to the area near the road that crosses the sub-image from top left to bottom right. The ranges of the adjacent neighbours of the pixels at columns 68 and 69, which correspond to the boundary between the wheat field and the bare soil area (shown in green) are also relatively high (40 and 32, respectively). However, even higher variations are observed for the data in the adjacent neighbourhood of the pixels at columns 87, 88, and 89, which correspond to the boundary between the bare soil and the soil with low density vegetation. The ranges are 63, 58, and 59.

The range of the data in the adjacent neighbourhood of the missing pixels, in line 43, is larger for the pixels at columns 14 to 17, inclusive (ranges are 26, 26, 35 and 25), and at column 60 (range is 30).

From Figure 5.2 (a), it is very clear the sharp contrast between the adjacent neighbours of the pixels at columns 4 to 10, in line 59 [note that the pixels in these columns are boundary pixels between an area of intense moisture (shown above the missing line, in dark magenta) and the area of low density vegetation (shown

below the missing line, in medium blue)]. The ranges of data in the adjacent neighbourhood of these pixels are respectively 49, 54, 47, 46, 34, 36, and 36. Also contrasting are the data in the adjacent neighbourhood of the pixels at columns 73 and 74, near the intersection of the missing line with the road the crosses the sub-image. Note that as the road is narrow, and crosses the sub-image diagonally, then it is expected that the lines above and below the missing one carry different information (one corresponding to the road, and another to the land cover). This can be observed in Figure 5.2 (the point where the missing line crosses the road). The ranges of the data in the adjacent neighbourhood of the pixels at columns 73 and 74 are respectively 25 and 19. Note from the figure that there should not exist (as there does not) a too contrasting difference between the pixel values in the adjacent neighbourhood of the pixel corresponding to the road, in line 43. This occurs because there exists less contrast between the response of this feature and the wheat fields, than between the road and the soil with low density vegetation.

From observation of Figure 5.2 (a), some variation between the pixels in the adjacent neighbourhood of the sites in line 75, at columns 31, 32, and 33 can be expected. Note the difference in the colour of the adjacent neighbours of these sites, above and below the road (dark magenta above, and light magenta below), and at columns 85 to 89 (magenta above, and cyan below). For the missing values occurring at columns 31, 32, and 33, the ranges of the data in their adjacent neighbourhood are respectively 24, 26, and 26, whereas for those occurring between columns 84 and 88 inclusive, are 37, 34, 39, 23, and 32.

Finally, data in the adjacent neighbourhood of line 91 is most contrasting between columns 38 and 41 (ranges are respectively 41, 37, 42, and 36), and between columns 47 and 53 (ranges are 35, 43, 31, 27, 28, 29, and 25).

In order to evaluate the changes between the data in the neighbourhood of each missing line in sub-image $D_1(15)$, and the corresponding data in the sub-images in other bands [$D_1(13)$ and $D_1(14)$], 'difference' images are obtained and presented in Figure 5.3, for $D_1(15) - D_1(13)$ and $D_1(15) - D_1(14)$. Note that the figure also gives the difference for the 'missing' lines, which are marked, for their easier identification, at the right hand side of the figure. As before, a constant (128) is added to each pixel in the 'difference' image.

Similarly, difference images are also presented in Figure 5.4 for the data in

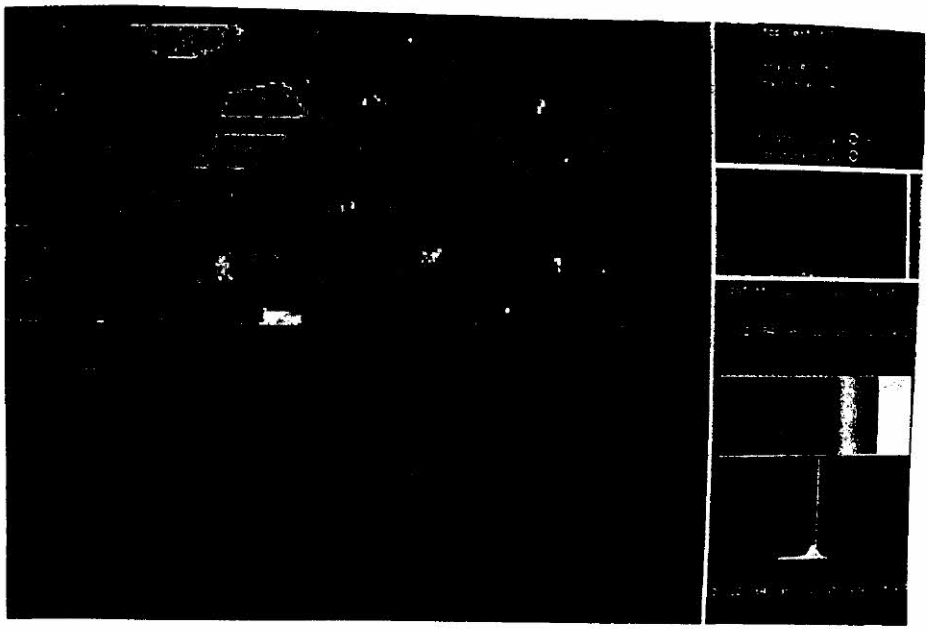

Figure 5.3: Difference images for the data in the neighbourhood of each 'defective' line, in different bands: (a) $D_1(15) - D_1(14)(+128)$; (b) $D_1(15) - D_1(13)(+128)$.

the neighbourhood of each missing line, in images acquired at different passages, that is, for $D_1(15) - D_1(25)$, and $D_1(15) - D_1(35)$. The difference data in the line corresponding to the missing one is also included, and is marked at the right hand side of the figure.

Although the information in Figures 5.3 and 5.4 is of no relevance for the purely spatial methods, they are nonetheless important for the methods that use information from a template band, or a template date. As results from these methods are also included in this chapter, it seems pertinent to include the difference images here.

Of greater relevance to the methods using spatial modelling are the plots of the sample autocorrelations. Figure 5.5 (a) to (e) gives the plot of $r_{1,g}$, $r_{-1,g}$, $r_{2,g}$, and $r_{-2,g}$, for $g = 0, \ldots, 7$, for the data in the neighbourhood of lines 11, 27, 43, 59, and 75, respectively.

From the sample autocorrelations given in Figure 5.5 (a) to (e) it can be seen that the data in the neighbourhood of each missing line (and including the data corresponding to the 'missing' line), are highly spatially correlated. The sample autocorrelations are approximately symmetric about both axes, that is $r_{g,h} \approx r_{g,-h} \approx r_{-g,h} \approx r_{-g,-h}$, which suggests that the application of methods that use one-parameter models may be adequate.

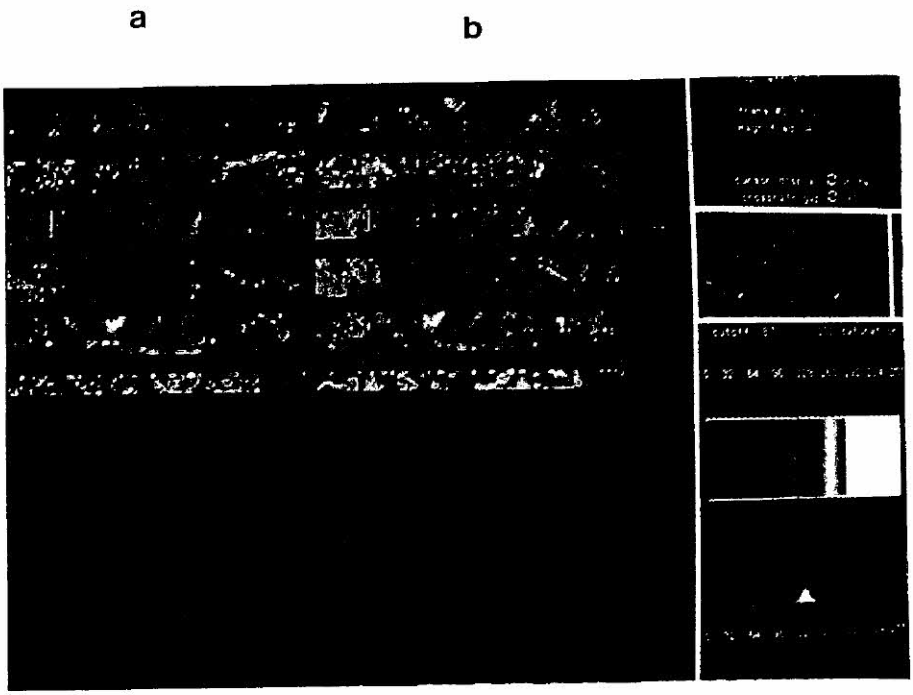

Figure 5.4: Difference images for the data in the neighbourhood of each 'defective' line, acquired at different passages: (a) $D_1(15) - D_1(25)(+128)$; (b) $D_1(15) - D_1(35)(+128)$.

5.8.3 Description of the neighbourhood of each missing line in sub-image $D_2(15)$

The summary statistics for the data in the neighbourhood of each simulated missing line in sub-image $D_2(15)$, and in the corresponding areas in the reasonable templates are presented in Table 5.2. The information provided in the table is that given for sub-image $D_1(15)$, in the previous section, except that now the area is of size 11 by 100, instead of 11 by 92.

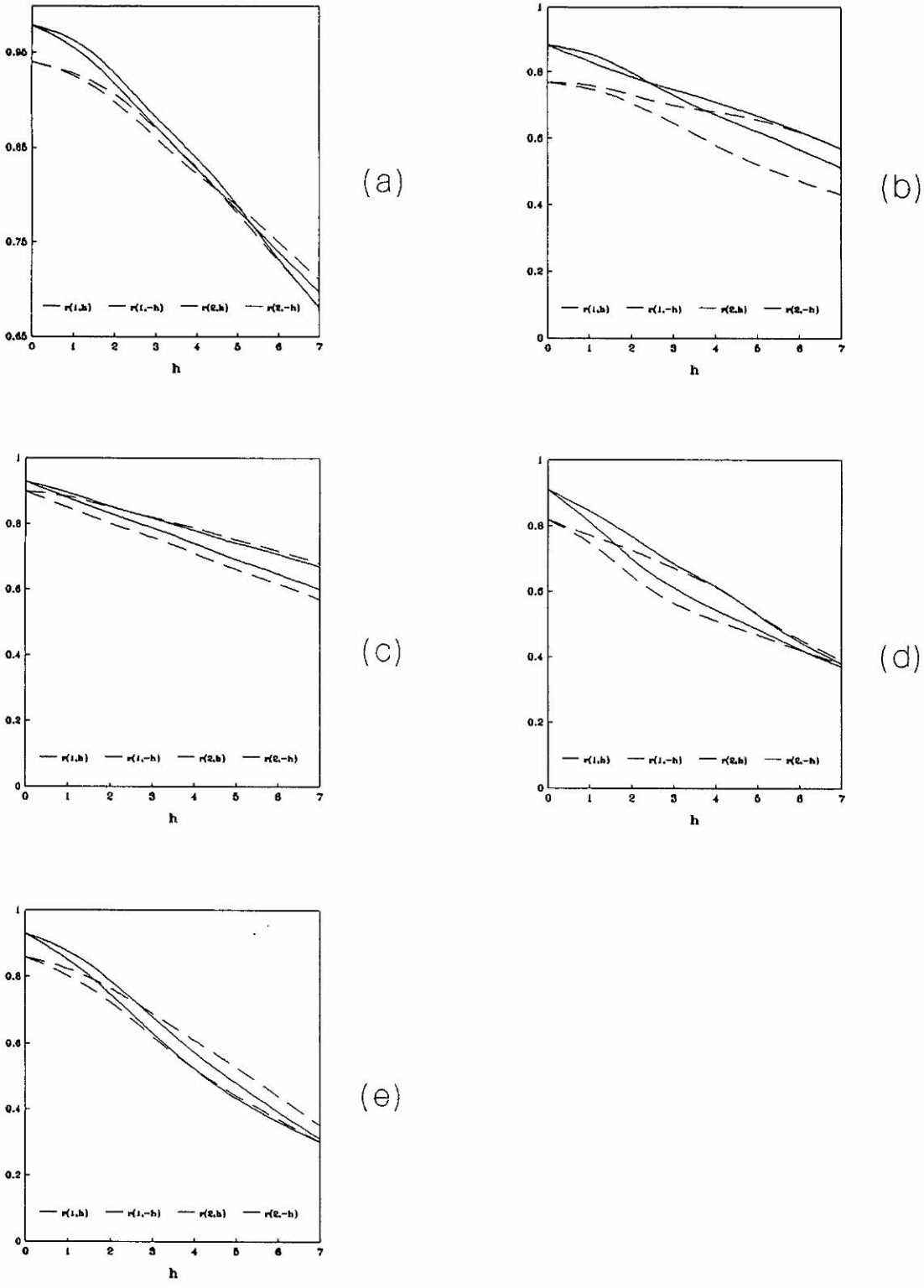

Figure 5.5: Sample autocorrelations, $r_{1,h}$, $r_{-1,h}$, $r_{2,h}$, and $r_{-2,h}$, $h = 0, \ldots, 7$ for the data in the neighbourhood of lines (a) 11; (b) 27; (c) 43; (d) 59; and (e) 75.

Table 5.2: Descriptive statistics of the data in the neighbourhood of each 'defective' line in sub-image $D_2(15)$, and of the data in corresponding areas in the possible templates (band and date), including those corresponding to the missing line, in sub-image $D_2(15)$.

Sub-Image					Template					
Line	Mean	Stdev	(m,M)	Range	Sub-Image	Mean	Stdev	(m,M)	Range	r
7	97.30	35.34	(45,192)	147	$D_2(13)$	53.21	5.85	(28,70)	42	0.425
					$D_2(14)$	74.18	27.03	(27,138)	111	0.986
23	90.86	29.57	(46,166)	120	$D_2(13)$	52.38	5.91	(38,67)	29	0.603
					$D_2(14)$	65.88	22.59	(31,112)	81	0.967
39	89.92	27.25	(49,139)	90	$D_2(13)$	52.72	6.23	(37,66)	29	0.580
					$D_2(14)$	68.78	23.42	(31,113)	82	0.970
45	83.27	25.79	(49,131)	82	$D_2(13)$	51.83	6.02	(38,66)	28	0.680
					$D_2(14)$	63.83	24.67	(34,114)	80	0.978
61	106.64	20.11	(35,133)	98	$D_2(13)$	52.79	3.55	(41,67)	26	0.397
					$D_2(14)$	90.97	18.91	(24,111)	87	0.971
77	105.80	24.33	(40,167)	127	$D_2(13)$	56.12	7.49	(40,79)	39	0.715
					$D_2(14)$	88.33	24.34	(26,134)	108	0.965
93	96.02	20.79	(39,158)	119	$D_2(13)$	53.76	7.12	(35,78)	43	0.783
					$D_2(14)$	77.20	20.41	(22,124)	102	0.951

A brief discussion of the data in the neighbourhood of each missing line in sub-image $D_2(15)$ is now presented, since this information is relevant to the discussion of the results for the methods using spatial modelling, in §5.9.

From the standard deviation, and the range of the data in line 7, in Table 5.2, and also from Figure 5.2 (b), it can be seen that amongst all the simulated missing lines, this is the most heterogeneous one, comprising several different types of land cover: reforested areas (at early and late stages), grass, and bare soil. However, it is for the pixels at columns 78 and 79, that the data in the adjacent neighbourhood are most contrasting. For the pixel at column 78, the range of the values in the adjacent neighbourhood is 45, and for that at column 79, it is 26. These pixels are located at the boundary between bare soil (shown in yellow) and grass (show in cyan). On this line, contrasting values can also be found in the adjacent neighbourhood of the pixels at columns 27 and 28 (42 and 36, respectively). For the pixels at the boundary between the areas shown in cyan and green, at columns 39 and 40, the ranges of the values in the adjacent neighbourhood are also reasonably large (30 and 44, respectively).

On line 23, the ranges of the values in the adjacent neighbourhood of the pixels at columns 6, 7, and 8 are very large. The ranges of the values in the adjacent neighbourhood of these pixels are 69, 69 and 42, respectively. Large variation of the data in the adjacent neighbourhood also occurs for the pixels at columns 89 and 90 (57 and 69). These pixels are located at the boundary between the reforested area and soil with low density vegetation

Figure 5.2 (b) shows very clearly where large variations of the data in the adjacent neighbourhood of the pixels in line 39 are expected to occur. Note that the pixels in this missing line, between columns 48 and 61 delimit the boundary between two distinct responses of soil with low density vegetation, which may be related to differences in soil moisture. Above the missing line, the pixels in this area are displayed in light green, whereas below the line they are displayed in dark blue [note the range of the values associated to these two colours, in the histogram in Figure 5.2 (b)]. For the pixels between columns 48 to 54, the minimum range of the values in their adjacent neighbourhood is 31; however, from column 55 to 61, the ranges of the data in the adjacent neighbourhood of each of these sites are very large, and are respectively 60, 76, 74, 76 75, 73, and 52.

The large variation of the data in the adjacent neighbourhood of the pixels in line 45, between columns 38 and 43, is also clear from Figure 5.2 (b). These pixels mark the limit between the reforested area and grass, which are shown in the colours magenta and blue, respectively. The ranges of the data in the adjacent neighbourhood of the pixels between columns 38 and 43 are 58, 54, 51, 51, 44, and 42.

Data in the neighbourhood of line 61 are relatively homogeneous. The greater contrast between the values in the adjacent neighborhood occurs for the pixels at columns 9, 10, and 11, which mark the limit between the reforested area and grass. The ranges of the data in the adjacent neighbourhood of these pixels are respectively 75, 77, and 32.

It is essentially for the pixels at the boundary between the reforested area and grass (at columns 18 and 19), in line 77, that the largest variation between the data in their adjacent neighbourhood occurs (69 and 54, respectively).

As for lines 61 and 77, the greatest variation between the data, in line 93, occurs for the pixels at columns 28 and 29, which delimit the boundary between the reforested area and grass. The ranges of the data in the neighbourhood of the missing values at these columns are respectively 48 and 49. Large differences are also observed for the data in the adjacent neighbourhood of the missing values at columns 93 to 98 (ranges are 37, 44, 55, 51, 39, and 38, respectively).

Figure 5.6 (a) shows the 'difference' image for the data in the neighbourhood of each missing line, using sub-images in different bands [$D_2(15)$ and $D_2(14)$]; and (b) displays the 'difference' image corresponding to the data in the neighbourhood of each missing line, using sub-images acquired at different passages [$D_2(15) - D_2(25)$].

The plots of the sample autocorrelations, $r_{1,g}$, $r_{-1,g}$, $r_{2,g}$, and $r_{-2,g}$, for $g = 0, \ldots, 7$, for the data in the neighbourhood of lines 7, 23, 39, 45, 61, and 77 are given in Figure 5.7.

From the sample autocorrelations in Figure 5.7 it can be noted that the data in the neighbourhood of each missing line (and including those corresponding to the 'missing' line) are highly spatially correlated. The 'atypical' behaviour of the sample autocorrelations for the data in the neighbourhood of lines 39 and 45 can be possibly explained by the diagonally oriented features in the area, which are more pronounced in the south-east direction.

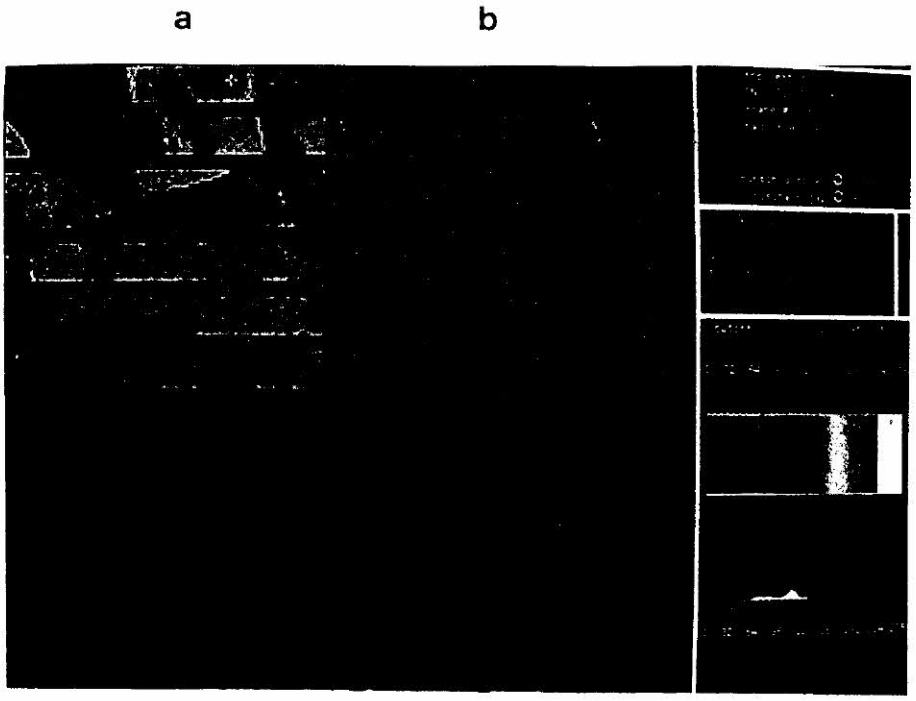

Figure 5.6: Difference images obtained for the data in the neighbourhood of each 'defective' line in sub-image $D_2(15)$ and in the templates. (a) $D_2(15) - D_2(14)(+128)$; (b) $D_2(15) - D_2(25)(+128)$.

The sample autocorrelations for the data in lines 7, 23, 61, and 77 are approximately symmetric about both axes, that is $r_{g,h} \approx r_{g,-h} \approx r_{-g,h} \approx r_{-g,-h}$.

5.9 Results from Methods using Spatial Modelling and from Simpler Methods

The results obtained for the methods using spatial modelling, and the methods introduced in Chapter 4, using the simulated scan lines in sub-images $D_1(15)$, and $D_2(15)$. are now presented.

The estimates of the missing pixel values in the simulated lines in $D_1(15)$, from template methods (band or date), are obtained using all possible templates. Hence, there are two sets of results for each method using a template band [one using sub-image $D_1(13)$, and other using sub-image $D_1(14)$], and two sets for each method using a template date [one using sub-image $D_1(25)$, and another using $D_1(35)$].

For sub-image $D_2(15)$, results are obtained using sub-image $D_2(14)$ as the template band, and sub-image $D_2(25)$ as the template date. Recall that the

descriptive statistics for the data in all possible templates are given in Table 5.1 for sub-image $D_1(15)$, and in Table 5.2 for sub-image $D_2(15)$.

The same set of numerical measures used in Chapter 4 (§4.4.2) (SRMS, CCOR, and SRAN) is also applied here to evaluate the performances of the methods. As in that chapter, the methods are evaluated by their ability to give small values for SRMS, CCOR, and SRAN. Since here only some lines in the sub-images are estimated, the visual results do not have the same significance as they did in Chapter 4, when all lines in the image were estimated, thus showing the deformations introduced in the image by each of the methods. Only a few of the visual results obtained from the replacement of the missing values by the estimates obtained for some methods are presented in this chapter. In this case, the photograph displaying the residuals is also included. The residuals in these figures correspond to the difference between the estimate obtained for a given method, and the true pixel value.

5.9.1 Results using $D_1(15)$

The results for the methods using spatial modelling, when applied to the simulated missing lines in sub-image $D_1(15)$, are presented in Table 5.3. The table gives the values for SRMS, CCOR, SRAN, and the minimum and maximum values for the residuals. The fit statistics for the spatial methods [estimates of the model parameters ($\hat{\alpha}$ and $\hat{\beta}$), and of the standard deviation ($\hat{\sigma}$), and the function value, divided by 100 (L)], are also given in the table.

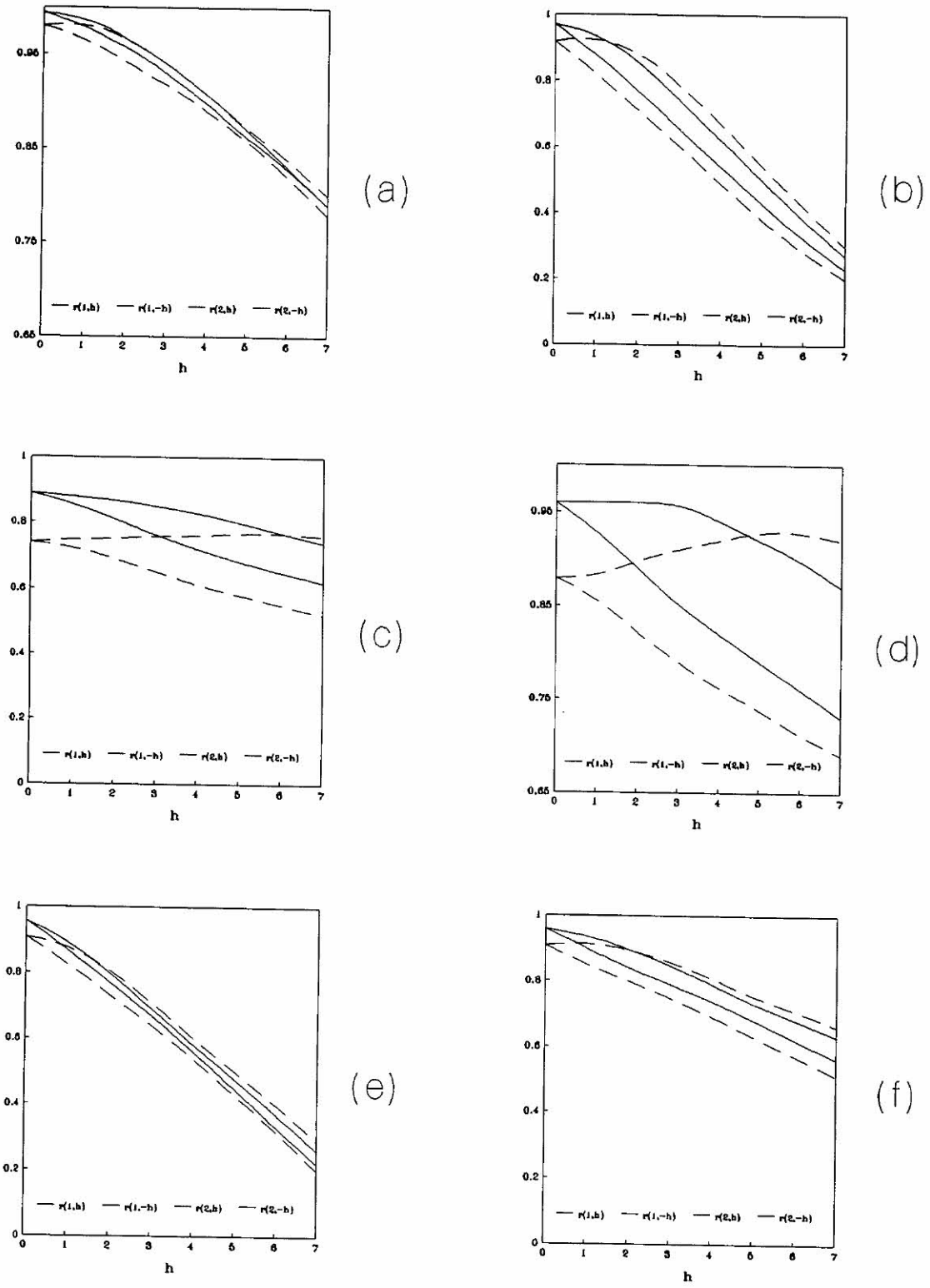

Figure 5.7: Sample autocorrelations, $r_{1,h}$, $r_{-1,h}$, $r_{2,h}$, and $r_{-2,h}$, $h = 0, \ldots, 7$ for the data in the neighbourhood of lines (a) 7; (b) 23; (c) 39; (d) 45; (e) 61; and (f) 77.

Table 5.3: Values for SRMS (×100), CCOR (×1000), SRAN, and the fit statistics for the methods using spatial modelling: $D_1(15)$.

Line	Method	SRMS	CCOR	SRAN	(m,M)	$\hat{\alpha}$	$\hat{\beta}$	L	$\hat{\sigma}$
11	$1p-CAR$	16	11	0.7	$(-9,5)$	0.254	--	10.37	4.7
	$1p-CART$	16	11	0.7	$(-8,5)$	0.254	--	10.29	4.5
	$1p-SAR$	16	11	0.7	$(-7,6)$	0.251	--	10.03	3.9
	$2p-SAR$	15	11	0.7	$(-7,6)$	0.316	0.183	10.02	3.8
	$1p-SART$	16	11	0.7	$(-7,6)$	0.250	--	10.01	3.7
27	$1p-CAR$	40	80	3.2	$(-25,29)$	0.254	--	10.84	6.0
	$1p-CART$	40	80	3.1	$(-24,29)$	0.254	--	10.72	5.6
	$1p-SAR$	40	84	3.4	$(-25,33)$	0.250	--	10.63	5.2
	$2p-SAR$	41	82	3.4	$(-25,32)$	0.293	0.196	10.61	5.1
	$1p-SART$	41	84	3.5	$(-25,34)$	0.242	--	10.60	5.0
43	$1p-CAR$	24	31	1.5	$(-13,11)$	0.254	--	10.43	4.9
	$1p-CART$	24	30	1.5	$(-13,11)$	0.254	--	10.30	4.6
	$1p-SAR$	23	29	1.3	$(-9,12)$	0.248	--	10.10	4.0
	$2p-SAR$	23	29	1.3	$(-10,12)$	0.302	0.193	10.08	3.9
	$1p-SART$	23	29	1.3	$(-9,12)$	0.247	--	10.06	3.8
59	$1p-CAR$	38	61	2.5	$(-24,13)$	0.254	--	10.58	5.2
	$1p-CART$	38	60	2.5	$(-24,13)$	0.254	--	10.52	5.1
	$1p-SAR$	36	59	2.6	$(-24,14)$	0.248	--	10.29	4.5
	$2p-SAR$	36	59	2.6	$(-24,14)$	0.253	0.241	10.28	4.4
	$1p-SART$	37	59	2.6	$(-24,14)$	0.250	--	10.26	4.2
75	$1p-CAR$	27	23	1.9	$(-21,14)$	0.254	--	10.86	6.0
	$1p-CART$	26	23	1.9	$(-22,14)$	0.254	--	10.77	5.8
	$1p-SAR$	24	23	1.5	$(-16,11)$	0.250	--	10.45	4.8
	$2p-SAR$	25	23	1.7	$(-18,13)$	0.323	0.176	10.42	4.7
	$1p-SART$	24	23	1.5	$(-16,11)$	0.248	--	10.40	4.5

The results for the methods introduced in Chapter 4 are now given. The values for SRMS, CCOR, and SRAN, for the single band methods (LR, LI, and CSP), for the methods using a template band (TB-1 to TB-10), and for the methods using a template date (TD-1 to TD-10) are given in Tables C.1, C.2, and C.3, in Appendix C, respectively. In these tables, the code L, alongside the line number, denotes the results obtained for the template methods that use a less correlated template, whereas the code H denotes the results using the better correlated template (band or date). The correlations between data in sub-image $D_1(15)$ and the template are given in the last column of Table 5.1.

In order to evaluate the performances of the methods for the missing lines in sub-image $D_1(15)$, a procedure similar to that used in Chapter 4, where ranks were formed for each method, for each measure, is also adopted here. Since, in general, the methods using a less correlated template (band or date) have an inferior performance than those using a better correlated one, then the investigation is carried out only for the methods that use a better correlated template, that is, using only the results coded H, in Tables C.1, C.2, and C.3, in Appendix C. Results for method TB/D-14 are also included in the analysis, since this method performed well amongst the alternative methods introduced in §4.8. The values for SRMS, CCOR, and SRAN, for method TB/D-14 are presented in Table C.7, in Appendix C.

Ranks are formed for each of the 30 methods (3 single band, 10 using a template band, 10 using a template date, 5 using spatial modelling, and TB/D-14), for each measure, according to their performance when applied to each simulated missing line. The results for line 91 are not included in the investigation, since they are not available for the methods that use spatial modelling. The ranks assigned to the methods, in each line, are subsequently averaged, individually for each measure, giving the results in Table 5.4. The table also includes the absolute value of the differences between the average ranks for: (1) SRMS and CCOR; (2) SRMS and SRAN; and (3) CCOR and SRAN.

New ranks, from 1 to 30, are now assigned to each method, according to its position in Table 5.4 (rank 1 to the method at the top), for each measure. Hence, each method has 3 new ranks, indicating its performance for SRMS, CCOR, and SRAN. By averaging the 3 new ranks assigned to each method, the overall performances of the methods can be evaluated. These new average ranks are

given in Table 5.5 (under D_1), where $\bar{r}_a$ and s_{r_a} are the mean and the standard deviation of the new ranks, respectively. The table also gives the minimum and maximum [(m,M)] values of the new ranks assigned to each method.

The true 'missing' values, and the corresponding estimates for LI and the method using a 1p-SAR, are given in Figures 5.8 (a) and (b), 5.9 (a) and (b), and 5.10 for lines 11 and 27, 43 and 59, and 75, respectively.

Table 5.4: Average ranks of the methods, for SRMS, CCOR, and SRAN, and the absolute value of the differences between the average ranks for: (1) SRMS and CCOR; (2) SRMS and SRAN; (3) CCOR and SRAN.

SRMS		CCOR		SRAN		DIFFERENCES			
Method	AR	Method	AR	Method	AR	Method	(1)	(2)	(3)
$TD-8$	5.3	$TD-8$	5.2	$TD-8$	5.3	LR	1.6	1.2	0.4
$TD-6$	5.8	$TD-14$	6.3	$TD-6$	5.6	LI	0.2	3.3	3.1
$TD-14$	6.1	$TD-7$	7.4	$TD-14$	5.8	CSP	1.5	2.0	0.5
$TD-7$	6.5	$TD-6$	8.1	$TD-2$	6.1	$TB-1$	1.2	2.9	1.7
$TD-2$	7.6	$TD-2$	8.1	$TD-7$	6.7	$TB-2$	0.3	1.0	0.7
LI	8.2	LI	8.4	LI	11.5	$TB-3$	0.1	0.4	0.5
$1p-SAR$	8.5	$1p-SAR$	8.4	CSP	12.3	$TB-4$	0.2	4.1	3.9
$2p-SAR$	9.2	$2p-SAR$	8.4	$TD-10$	12.4	$TB-5$	1.1	3.5	4.6
$TD-10$	9.6	$1P-SART$	8.4	$TD-9$	12.5	$TB-6$	1.0	2.5	1.5
$1p-SART$	9.9	$TD-3$	11.5	$TD-3$	13.0	$TB-7$	0.5	1.6	1.1
$1p-CART$	12.4	$1P-CAR$	11.9	$TD-5$	13.5	$TB-8$	2.1	1.4	0.7
$1p-CAR$	12.7	$1P-CART$	11.9	$1P-SAR$	13.8	$TB-9$	0.3	5.3	5.0
$TD-9$	13.5	CSP	12.8	$TD-4$	13.9	$TB-10$	0.7	1.4	2.1
$TD-3$	14.3	$TD-10$	14.3	$1P-SART$	14.2	$TD-1$	3.7	2.6	1.1
CSP	14.3	$TD-9$	14.7	$TB-6$	14.3	$TD-2$	0.5	1.5	2.0
$TB-7$	14.7	$TD-5$	14.7	$2P-SAR$	14.4	$TD-3$	2.8	1.3	1.5
$TD-5$	15.3	$TD-4$	14.7	$TD-1$	15.8	$TD-4$	1.3	2.1	0.8
$TD-4$	16.0	$TD-1$	14.7	$1P-CART$	15.9	$TD-5$	0.6	1.8	1.2
$TB-14$	16.4	$TB-7$	15.2	$1P-CAR$	16.3	$TD-6$	2.3	0.2	2.5
$TB-6$	16.8	$TB-6$	15.8	$TB-7$	16.3	$TD-7$	0.9	0.2	0.7
$TB-8$	17.6	$TB-14$	17.2	$TB-14$	17.1	$TD-8$	0.1	0.0	0.1
LR	17.9	LR	19.5	$TB-8$	19.0	$TD-9$	1.2	1.0	2.2
$TD-1$	18.4	$TB-8$	19.7	LR	19.1	$TD-10$	4.7	2.8	1.9
$TB-2$	23.4	$TB-2$	23.1	$TB-2$	22.4	$1P-CAR$	0.8	3.6	4.4
$TB-3$	25.2	$TB-3$	25.1	$TB-5$	23.5	$1P-CART$	0.5	3.5	4.0
$TB-10$	25.6	$TB-10$	26.3	$TB-8$	23.9	$1P-SAR$	0.1	5.3	5.4
$TB-5$	27.0	$TB-5$	28.1	$TB-10$	24.2	$2P-SAR$	0.8	5.2	6.0
$TB-4$	28.3	$TB-4$	28.1	$TB-4$	24.2	$1P-SART$	1.5	4.3	5.8
$TB-9$	29.2	$TB-1$	28.1	$TB-3$	25.6	$TB-14$	0.8	0.7	0.1
$TB-1$	29.3	$TB-9$	28.9	$TB-1$	26.4	$TD-14$	0.2	0.3	0.5

Table 5.5: Average of the new ranks assigned to the methods: $D_1(15)$ and $D_2(15)$.

D_1				D_2			
Method	$\bar{r}_a$	s_{r_a}	(m,M)	Method	$\bar{r}_a$	s_{r_a}	(m,M)
$TD-8$	1.0	0.00	(1,1)	$TD-7$	1.0	0.00	(1,1)
$TD-14$	2.7	0.58	(2,3)	$TD-14$	3.0	1.73	(2,5)
$TD-6$	2.8	1.44	(2,4.5)	$TD-2$	3.0	0.00	(3,3)
$TD-7$	4.0	1.00	(3,5)	$1P-SAR$	4.0	2.00	(2,6)
$TD-2$	4.5	0.50	(4,5)	$1P-SART$	4.3	0.58	(4,5)
LI	6.5	0.87	(6,7.5)	CSP	6.0	1.00	(5,7)
$1P-SAR$	8.8	2.75	(7,12)	$2P-SAR$	6.6	0.58	(6,7)
$TD-10$	10.3	3.21	(8,14)	$TD-8$	8.3	0.58	(8,9)
$2P-SAR$	10.5	4.77	(7.5,16)	LI	8.7	0.58	(8,9)
$1P-SART$	10.5	3.28	(7.5,14)	$TD-3$	12.0	2.65	(10,15)
$TD-3$	11.3	2.31	(10,14)	$TB-14$	12.7	2.08	(11,15)
CSP	11.7	4.16	(7,15)	$1P-CART$	13.0	3.61	(10,17)
$TD-9$	12.8	3.75	(9,16.5)	$1P-CART$	13.0	4.36	(10,18)
$1P-CART$	13.5	3.91	(11,18)	$TD-6$	13.0	0.00	(13,13)
$1P-CAR$	14.3	4.48	(11.5,19.5)	$TB-6$	14.0	0.00	(14,14)
$TD-5$	14.8	3.33	(11,17)	$TD-5$	15.3	2.89	(12,17)
$TD-4$	15.8	2.57	(13,18)	$TD-4$	17.3	1.15	(16,18)
$TB-7$	18.2	1.89	(16,19.5)	LR	17.8	2.89	(16,21)
$TB-6$	18.3	2.89	(15,20)	$TD-1$	18.3	3.06	(15,21)
$TD-1$	18.8	3.62	(16.5,23)	$TB-7$	19.7	1.16	(19,21)
$TB-14$	20.3	1.16	(19,21)	$TB-8$	20.7	1.15	(20,22)
$TB-8$	22.0	1.00	(21,23)	$TB-2$	21.3	1.15	(20,22)
LR	22.3	0.58	(22,23)	$TB-3$	23.0	0.00	(23,23)
$TB-2$	24.0	0.00	(24,24)	$TB-5$	24.0	0.00	(24,24)
$TB-3$	26.3	2.31	(25,29)	$TB-4$	25.0	0.00	(25,25)
$TB-10$	26.5	0.87	(26,27.5)	$TB-1$	26.0	0.00	(26,26)
$TB-5$	26.7	1.53	(25,28)				
$TB-4$	27.8	0.29	(27.5,28)				
$TB-9$	28.3	2.08	(26,30)				
$TB-1$	29.3	1.15	(28,30)				

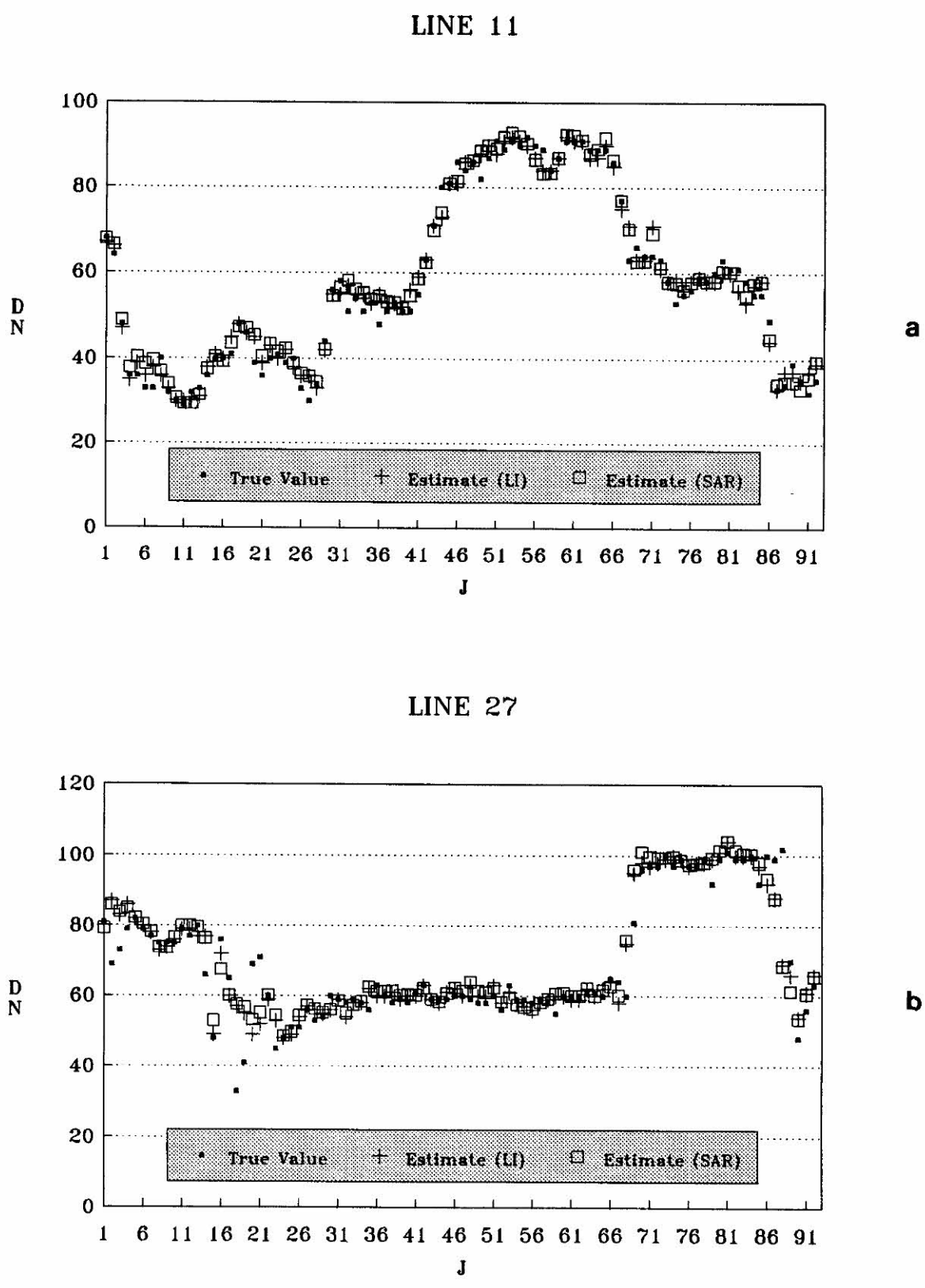

Figure 5.8: Plot of the true values, and the estimates obtained for LI and 1p-SAR on: (a) line 11; (b) line 27.

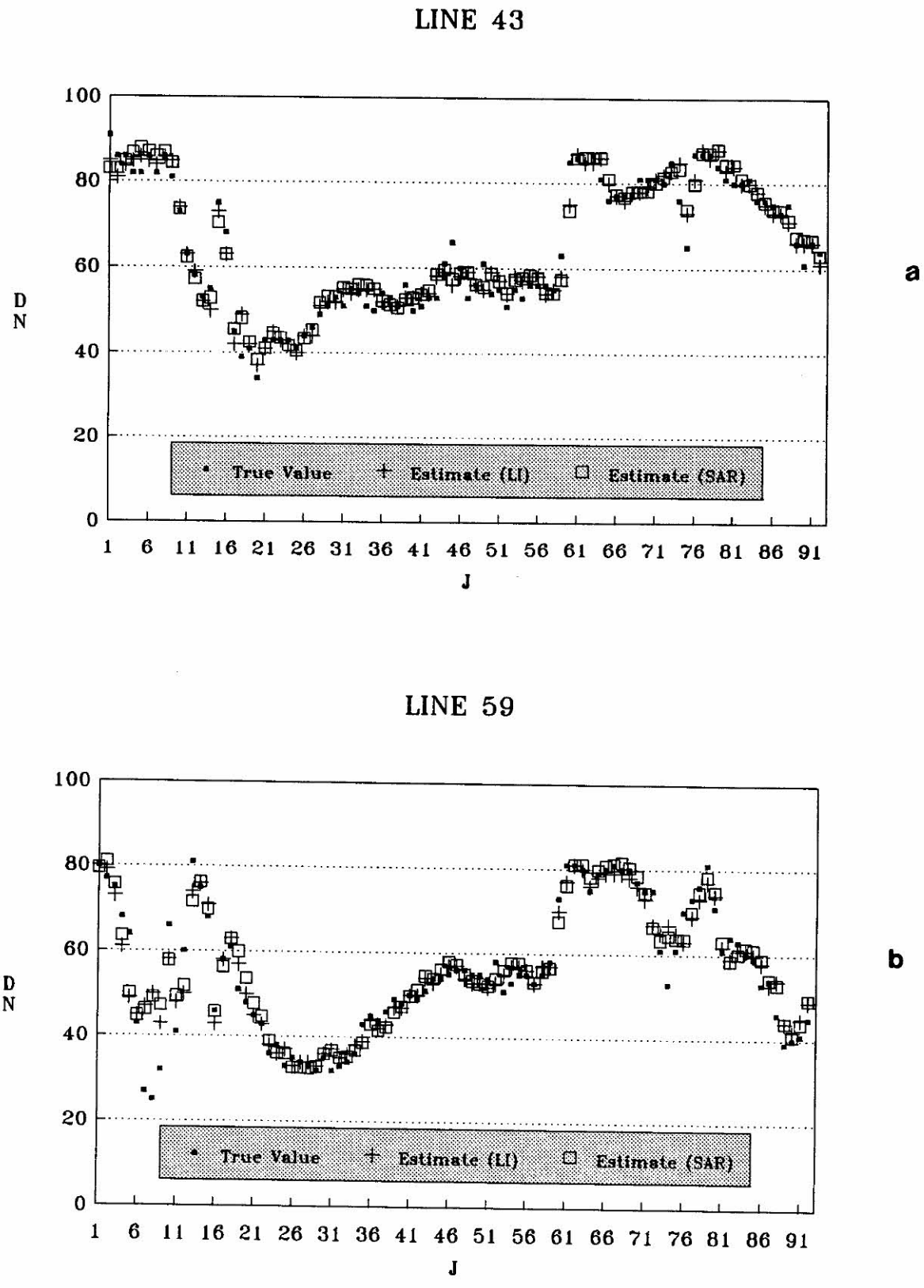

Figure 5.9: Plot of the true values, and the estimates obtained for LI and 1p-SAR on: (a) line 43; (b) line 59.

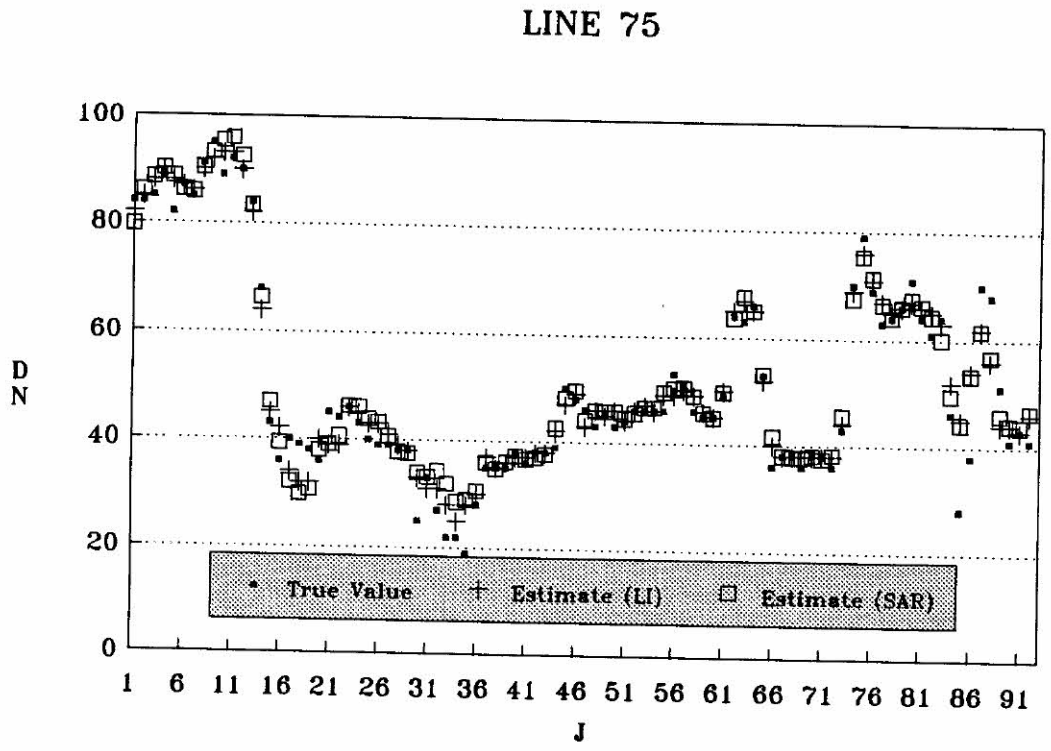

Figure 5.10: Plot of the true values, and the estimates obtained for LI and 1p-SAR, line 75.

Figure 5.11 (a) shows the simulated sub-image $D_1(15)$, after the replacement of the simulated missing lines with the estimates obtained for the method using a 1p-SAR. Figure 5.11 (b) displays the residuals obtained for this method, in each of the 'missing' lines, which indicates the occurrence of large residuals particularly at lines 27 and 59, and at the boundaries between contrasting types of land cover (for line 27, for instance, this occurs between columns 18 and 21, and at column 88, as expected from §5.8.2). In this 'residual' image, the largest negative, and the largest positive residuals show in the colours red and blue, respectively.

Figures 5.12 (a) and (b), 5.13 (a) and (b), and 5.14 display the true 'missing' values, and the estimates obtained for method TD-6H, for lines 11 and 27, 43 and 59, and 75, respectively.

a

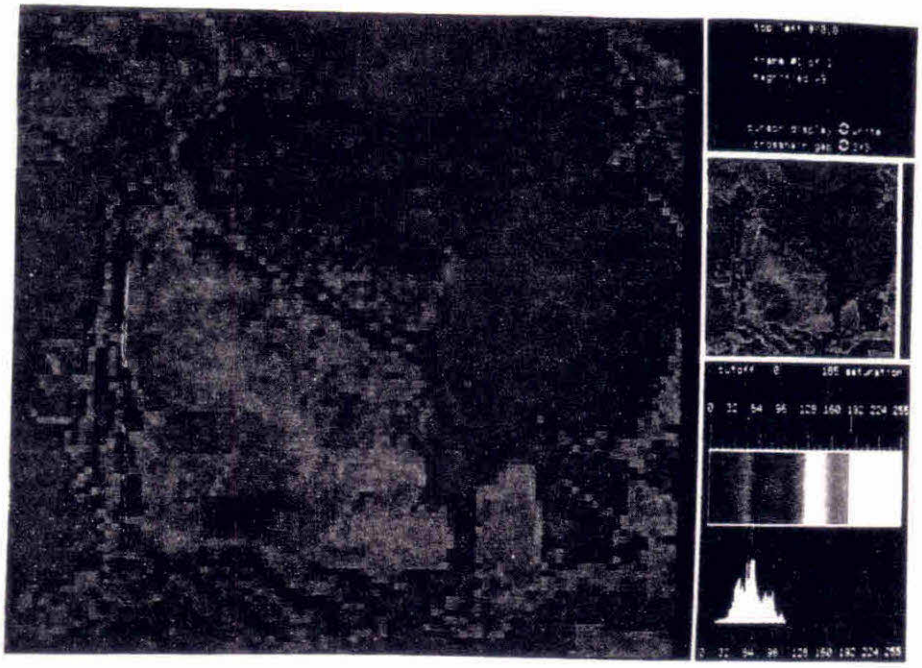

b

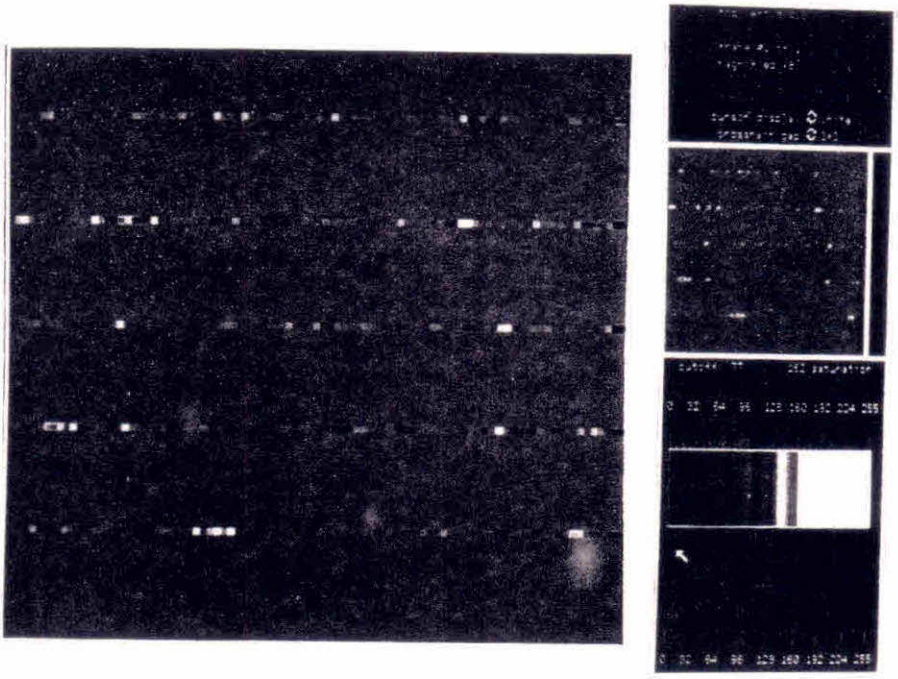

Figure 5.11: (a) Simulated sub-image $D_1(15)$, after the replacement of the simulated missing lines by the estimates for 1p-SAR; (b) residuals obtained for a 1p-SAR, for the simulated missing lines in sub-image $D_1(15)$.

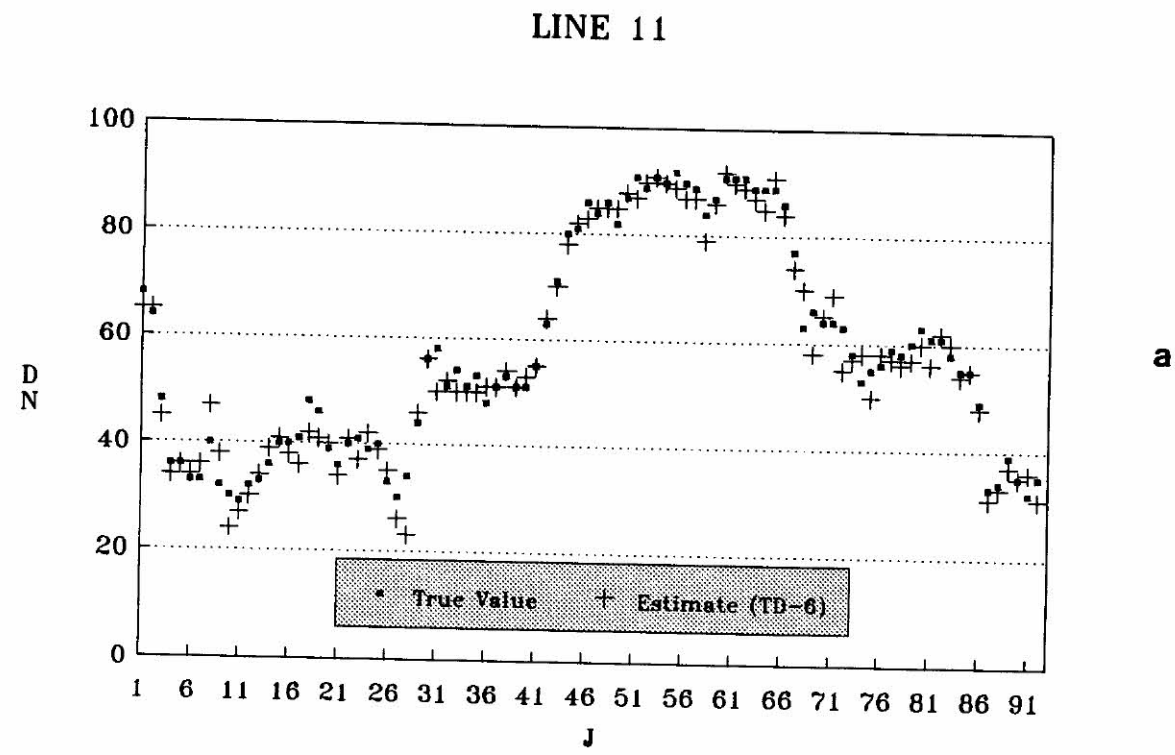

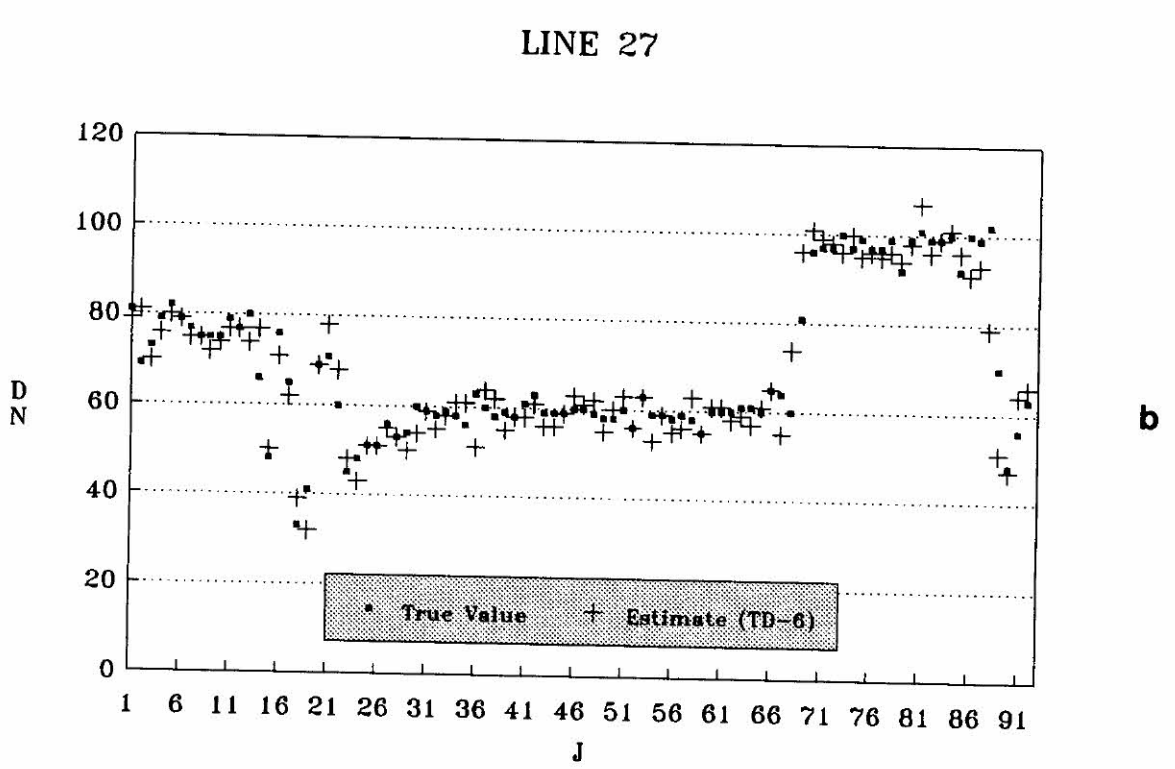

Figure 5.12: Plot of the true values, and the estimates obtained for method TD-6H, on lines (a) 11 and (b) 27.

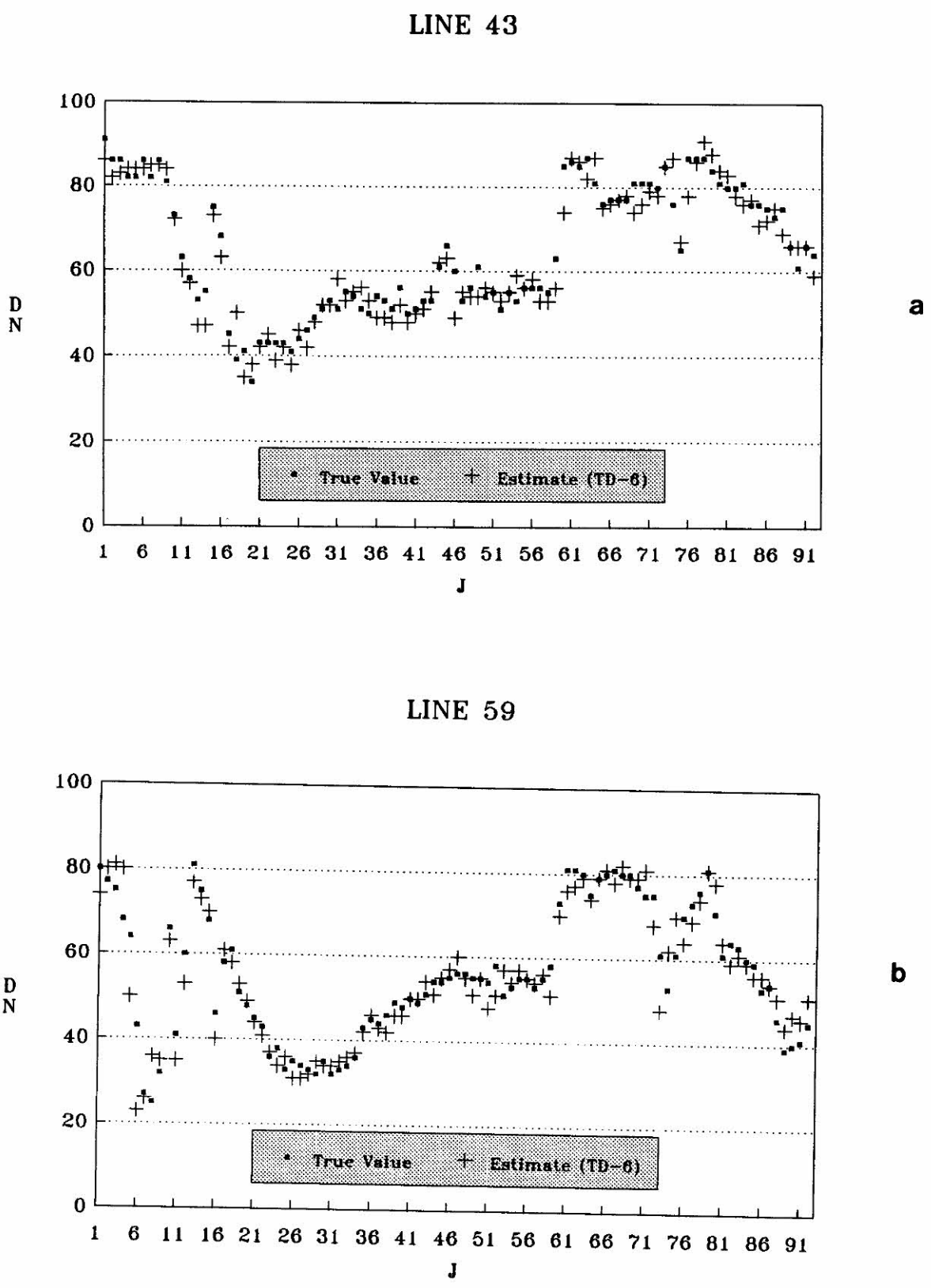

Figure 5.13: Plot of the true values, and the estimates obtained for method TD-6H, on lines (a) 43 and (b) 59.

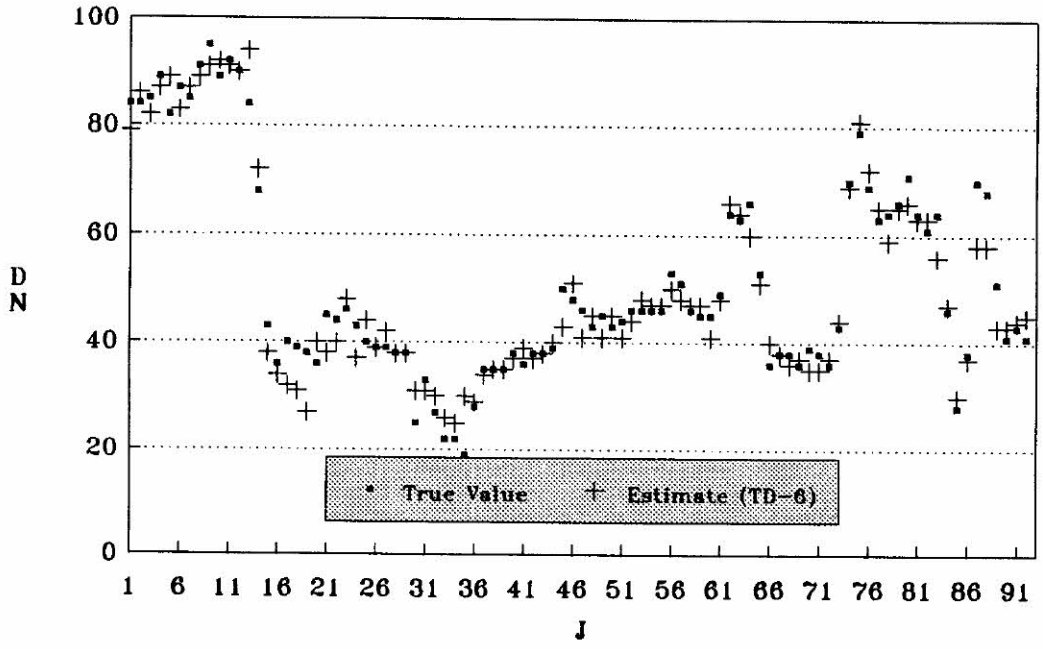

Figure 5.14: Plot of the true values, and the estimates obtained for method TD-6H, on line 75.

5.9.2 Results using $D_2(15)$

The results for the methods using spatial modelling, using the simulated missing scan lines in sub-image $D_2(15)$, are presented in Table 5.6. The table gives the values for SRMS, CCOR, SRAN, and the minimum and maximum values for the residuals. The fit statistics for the spatial methods [estimates of the model parameters ($\hat{\alpha}$ and $\hat{\beta}$), of the standard deviation ($\hat{\sigma}$), and the function value (L)] are also included in the table.

Table 5.6: Values for SRMS (×100), CCOR (×1000), and SRAN, and the fit statistics for the methods using spatial modelling: $D_2(15)$.

LINE	METHOD	SRMS	CCOR	SRAN	(m,M)	$\hat{\alpha}$	$\hat{\beta}$	L	$\hat{\sigma}$
07	$1p-CAR$	9	5	0.45	$(-8,8)$	0.254	--	12.36	7.5
	$1p-CART$	10	5	0.45	$(-8,8)$	0.254	--	11.86	6.0
	$1p-SAR$	8	4	0.42	$(-7,8)$	0.252	--	11.72	5.1
	$2p-SAR$	9	4	0.42	$(-7,7)$	0.343	0.160	11.59	4.6
	$1p-SART$	8	4	0.42	$(-7,8)$	0.252	--	10.45	4.5
23	$1p-CAR$	19	19	1.08	$(-16,16)$	0.254	--	12.60	8.3
	$1p-CART$	19	19	1.05	$(-16,15)$	0.254	--	12.42	7.7
	$1p-SAR$	14	10	0.81	$(-12,12)$	0.251	--	11.94	5.6
	$2p-SAR$	15	13	1.29	$(-20,18)$	0.329	0.173	11.89	5.4
	$1p-SART$	14	10	0.81	$(-12,12)$	0.251	--	10.65	4.9
39	$1p-CAR$	28	40	1.65	$(-21,24)$	0.254	--	12.71	8.7
	$1p-CART$	27	40	1.65	$(-21,24)$	0.254	--	12.42	7.6
	$1p-SAR$	25	33	1.39	$(-18,20)$	0.250	--	12.12	6.1
	$2p-SAR$	25	33	1.39	$(-18,20)$	0.382	0.117	11.85	5.2
	$1p-SART$	25	33	1.39	$(-18,20)$	0.251	--	10.67	5.1
45	$1p-CAR$	18	11	1.28	$(-18,15)$	0.254	--	12.10	6.6
	$1p-CART$	18	11	1.28	$(-18,15)$	0.254		11.87	5.8
	$1p-SAR$	17	11	1.32	$(-18,16)$	0.251	--	11.54	4.7
	$2p-SAR$	17	9	1.16	$(-16,14)$	0.364	0.137	11.35	4.6
	$1p-SART$	17	11	1.32	$(-18,16)$	0.251		10.06	4.5
61	$1p-CAR$	19	15	1.84	$(-16,21)$	0.254	--	11.96	6.1
	$1p-CART$	18	16	1.84	$(-14,23)$			11.46	4.9
	$1p-SAR$	14	9	0.94	$(-5,14)$	0.251	--	11.39	4.4
	$2p-SAR$	16	12	1.19	$(-8,16)$	0.312	0.189	11.37	4.3
	$1p-SART$	13	8	0.94	$(-5,14)$	0.250		10.18	4.0
77	$1p-CAR$	19	20	1.11	$(-16,11)$	0.254	--	12.14	6.5
	$1p-CART$	19	21	1.11	$(-15,12)$	0.254		11.70	5.5
	$1p-SAR$	15	13	0.78	$(-10,9)$	0.250	--	11.63	4.9
	$2p-SAR$	16	15	0.90	$(-12,10)$	0.335	0.165	11.56	4.7
	$1p-SART$	15	12	0.78	$(-10,9)$	0.247		10.47	4.6
93	$1p-CAR$	26	39	2.02	$(-22,20)$	0.254	--	12.13	6.5
	$1p-CART$	26	40	2.07	$(-23,20)$	0.254	--	11.86	5.9
	$1p-SAR$	23	30	1.78	$(-14,23)$	0.250	--	11.71	5.1
	$2p-SAR$	24	32	1.97	$(-16,25)$	0.330	0.167	11.62	4.9
	$1p-SART$	24	32	2.02	$(-19,23)$	0.251	--	10.57	4.8

The results for the methods in Chapter 4 are now presented. The values for SRMS, CCOR, and SRAN, for the single band methods (LR, LI, CSP), for the methods using a template band (TB-1 to TB-8), and for the methods using a template date (TD-1 to TD-8) are given in Tables C.4, C.5, and C.6, in Appendix C, respectively.

Similarly to the procedure adopted in §5.9.1, ranks from 1 to 26 are formed for 26 methods (3 single band, 8 using a template band, 8 using a template date, 5 using spatial modelling, and TB/D-14), to evaluate the methods, using $D_2(15)$. The ranks thus assigned are averaged, individually for each measure, giving the results in Table 5.7, which also includes the absolute value of the differences between the average ranks of the methods for: (1) SRMS and CCOR; (2) SRMS and SRAN; and (3) CCOR and SRAN.

New ranks, from 1 to 26, are now assigned to each method, according to its position in Table 5.7 (rank 1 to the method at the top), for each measure. By averaging the 3 new ranks assigned to each method, the overall performances of the methods can be evaluated. These averages are given in Table 5.5 (under D_2), where $\bar{r}_a$ and s_{r_a} are the mean and the standard deviation of the new ranks, respectively. The table also gives the minimum and maximum [(m,M)] values of the new ranks assigned to each method.

Figure 5.15 (a) shows the simulated sub-image $D_2(15)$, after the replacement of the values on the simulated missing lines with the estimates obtained for linear interpolation. Figure 5.15 (b) shows the residuals obtained for this method, which indicates the occurrence of large residuals at the boundaries between regions of contrasting response, as indicated in §5.8.3.

The plots in Figures 5.16 (a) and (b), 5.17 (a) and (b), and 5.18 (a) and (b), display the true 'missing' value, and the estimates obtained for lines 7 and 23, 39 and 45, and 61 and 77, respectively, using method 1p-SAR. These figures may give an idea of where the method fails to estimate the missing values well. This can also be verified for method TD-6, from the plots of the true 'missing' values and the estimates obtained for this method, given in Figures 5.19 (a) and (b), 5.20 (a) and (b), 5.21 (a) and (b), for lines 7 and 23, 39 and 45, 61 and 77, respectively.

Table 5.7: Average ranks of the methods, for SRMS, CCOR, and SRAN, and the absolute value of the differences between the average ranks for: (1) SRMS and CCOR; (2) SRMS and SRAN; (3) CCOR and SRAN.

SRMS		CCOR		SRAN		DIFFERENCES			
Method	AR	Method	AR	Method	AR	Method	(1)	(2)	(3)
$TD-7$	5.14	$TD-7$	4.79	$TD-7$	5.14	LR	1.0	3.4	2.4
$1p-SAR$	5.21	$TD-14$	5.07	$TD-14$	5.86	LI	0.1	1.0	0.9
$TD-2$	5.36	$TD-2$	5.64	$TD-2$	6.43	CSP	0.9	1.2	2.1
$1p-SART$	5.43	$1P-SART$	6.07	$1P-SAR$	6.93	$TB-1$	0.7	0.2	1.0
$TD-14$	6.29	CSP	6.07	$1P-SART$	8.00	$TB-2$	0.5	0.3	0.9
CSP	7.00	$1p-SAR$	6.29	$2P-SAR$	8.21	$TB-3$	0.2	0.3	0.5
$2P-SAR$	7.43	$2P-SAR$	6.79	CSP	8.21	$TB-4$	0.2	0.3	0.5
$TD-8$	7.64	LI	8.14	$TD-8$	9.00	$TB-5$	0.7	0.2	1.0
LI	8.00	$TD-8$	10.36	LI	9.07	$TB-6$	0.2	0.1	0.4
$1P-CART$	10.93	$1p-CAR$	10.50	$TD-3$	9.71	$TB-7$	0.5	0.4	0.9
$1P-CAR$	11.00	$TD-3$	10.64	$TB-14$	12.51	$TB-8$	0.2	0.3	0.1
$TB-14$	12.07	$1P-CART$	10.93	$TD-5$	12.64	$TD-1$	1.8	5.4	3.5
$TD-6$	12.79	$TD-6$	12.64	$TD-6$	12.93	$TD-2$	0.2	1.0	0.7
$TB-6$	13.07	$TB-6$	13.36	$TB-6$	12.93	$TD-3$	3.5	4.5	0.9
$TD-3$	14.21	$TB-14$	13.71	$TD-1$	13.00	$TD-4$	1.3	4.9	3.5
LR	15.00	LR	16.00	$TD-4$	13.00	$TD-5$	1.5	2.4	3.9
$TD-5$	15.07	$TD-5$	16.57	$1P-CART$	13.14	$TD-6$	0.1	0.1	0.2
$TD-4$	17.93	$TD-4$	16.57	$1P-CAR$	13.29	$TD-7$	0.3	0.0	0.3
$TB-7$	18.07	$TD-1$	16.57	$TB-7$	17.64	$TD-8$	2.7	1.3	1.3
$TB-8$	18.21	$TB-8$	18.43	$TB-2$	18.36	$1P-CAR$	0.5	2.2	2.7
$TD-1$	18.43	$TB-7$	18.57	LR	18.43	$1P-CART$	0.0	2.2	2.2
$TB-2$	18.71	$TB-2$	19.29	$TB-8$	18.57	$1P-SAR$	1.0	1.7	0.6
$TB-3$	23.21	$TB-3$	23.00	$TB-3$	23.57	$2P-SAR$	0.6	0.7	1.4
$TB-5$	24.21	$TB-5$	25.00	$TB-5$	24.00	$1P-SART$	0.6	2.5	1.9
$TB-4$	24.79	$TB-4$	25.00	$TB-4$	24.43	$TB-14$	1.6	0.4	1.2
$TB-1$	25.79	$TB-1$	25.00	$TB-1$	26.00	$TD-14$	1.2	0.4	0.7

a

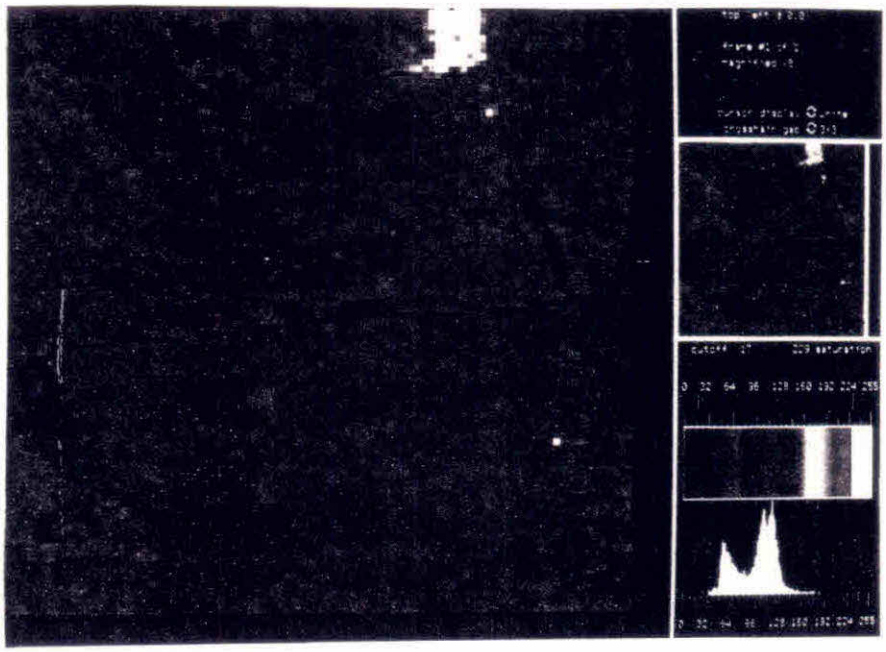

b

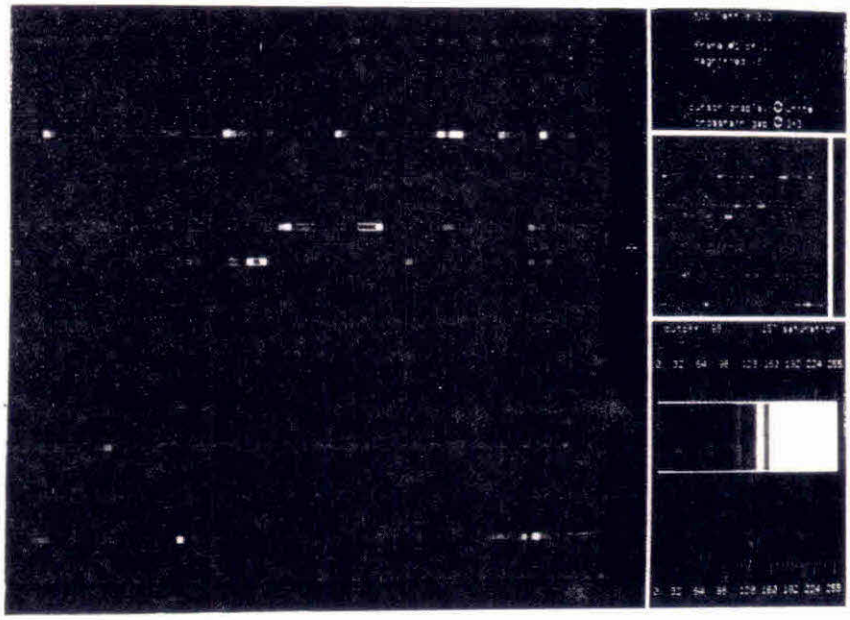

Figure 5.15: (a) Simulated sub-image $D_2(15)$, after the replacement of the simulated missing lines by the estimates obtained for LI; (b) residuals obtained for LI, for the simulated missing lines in sub-image $D_2(15)$.

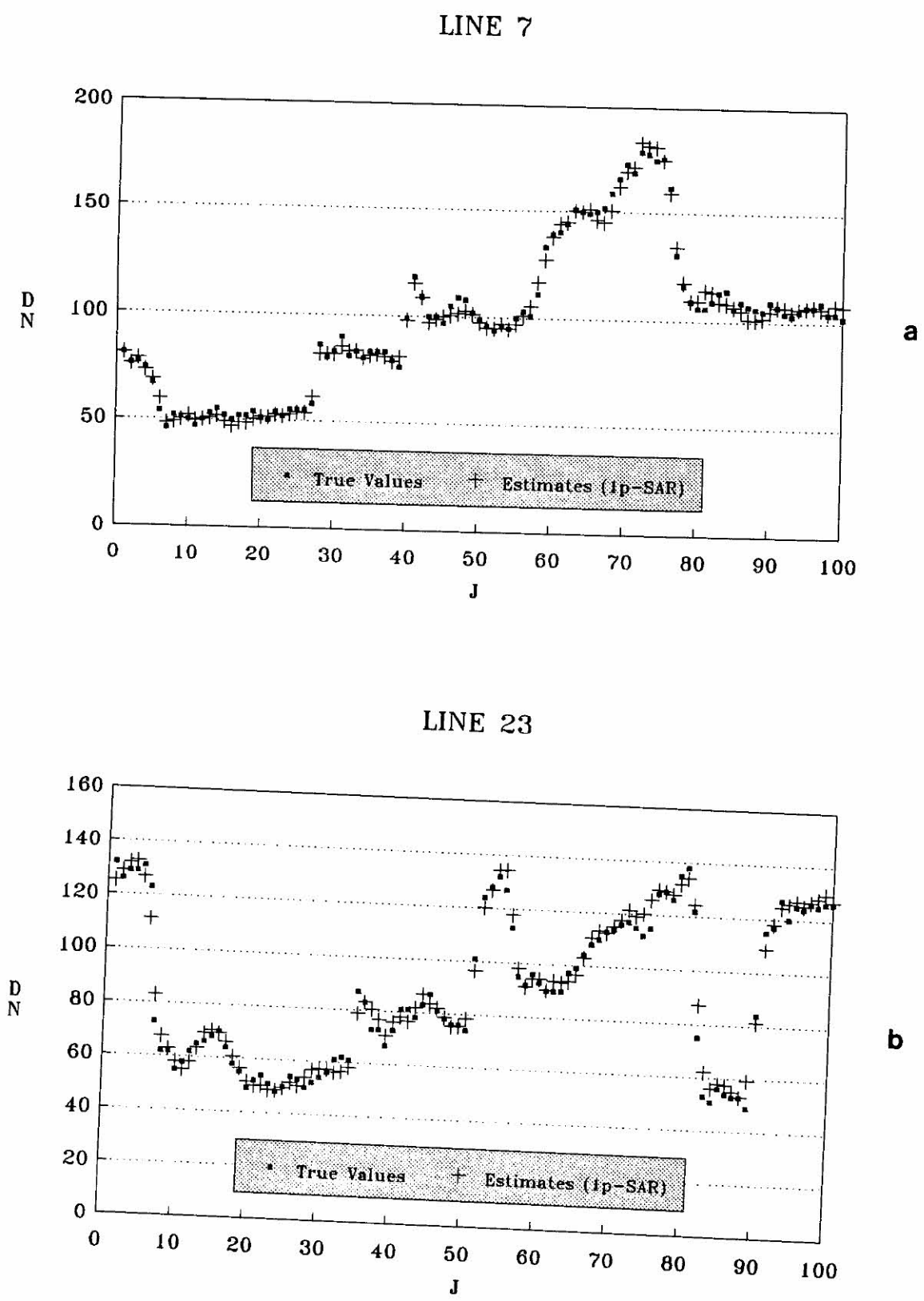

Figure 5.16: Plot of the true values, and the estimates for a 1p-SAR on: (a) line 7; (b) line 23.

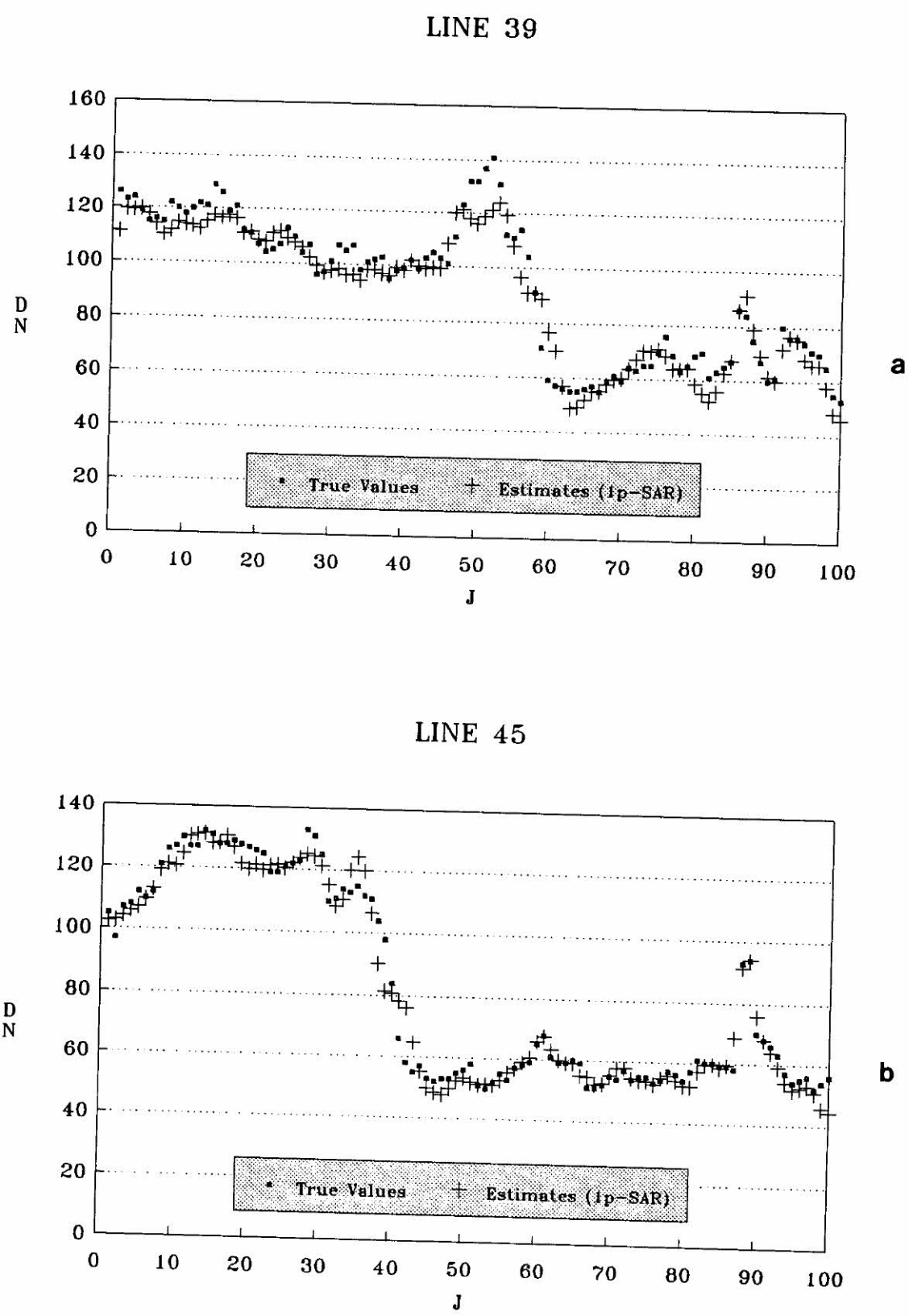

Figure 5.17: Plot of the true values, and the estimates for a 1p-SAR on: (a) line 39; (b) line 45.

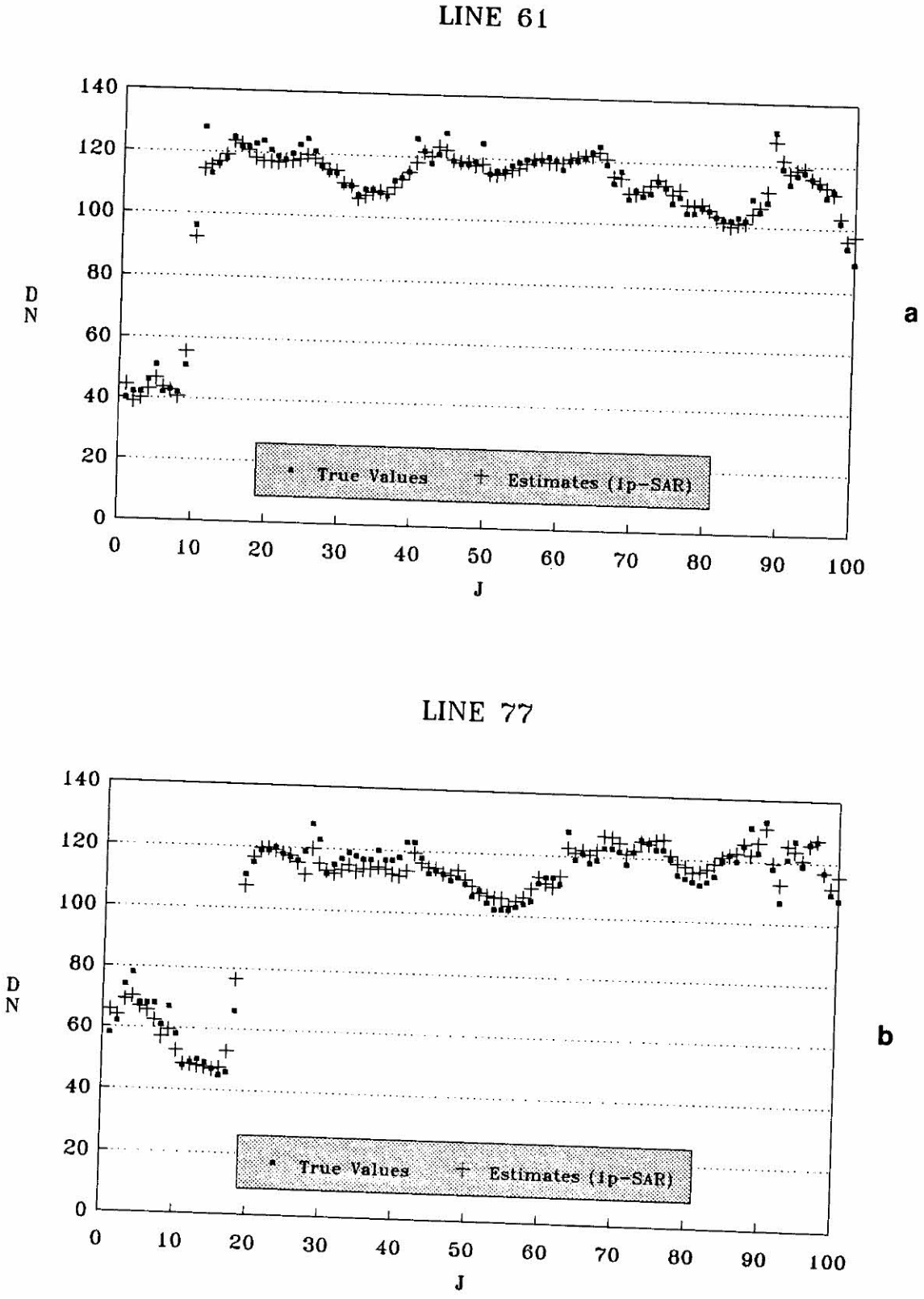

Figure 5.18: Plot of the true values, and the estimates for a 1p-SAR on: (a) line 61; (b) line 77.

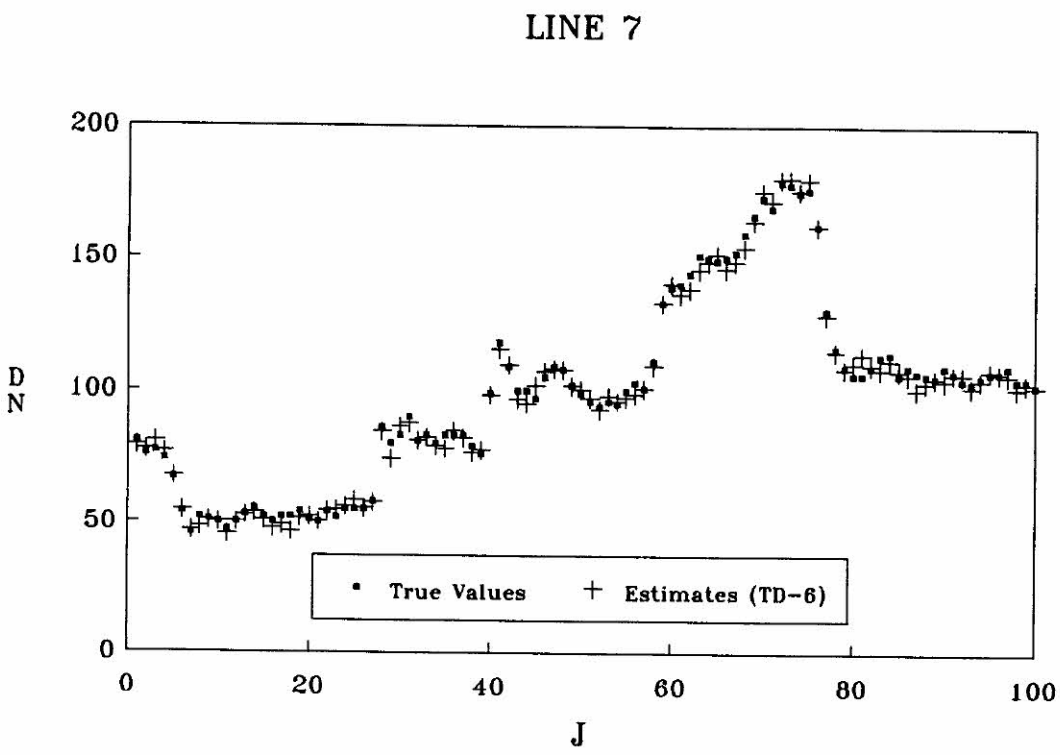

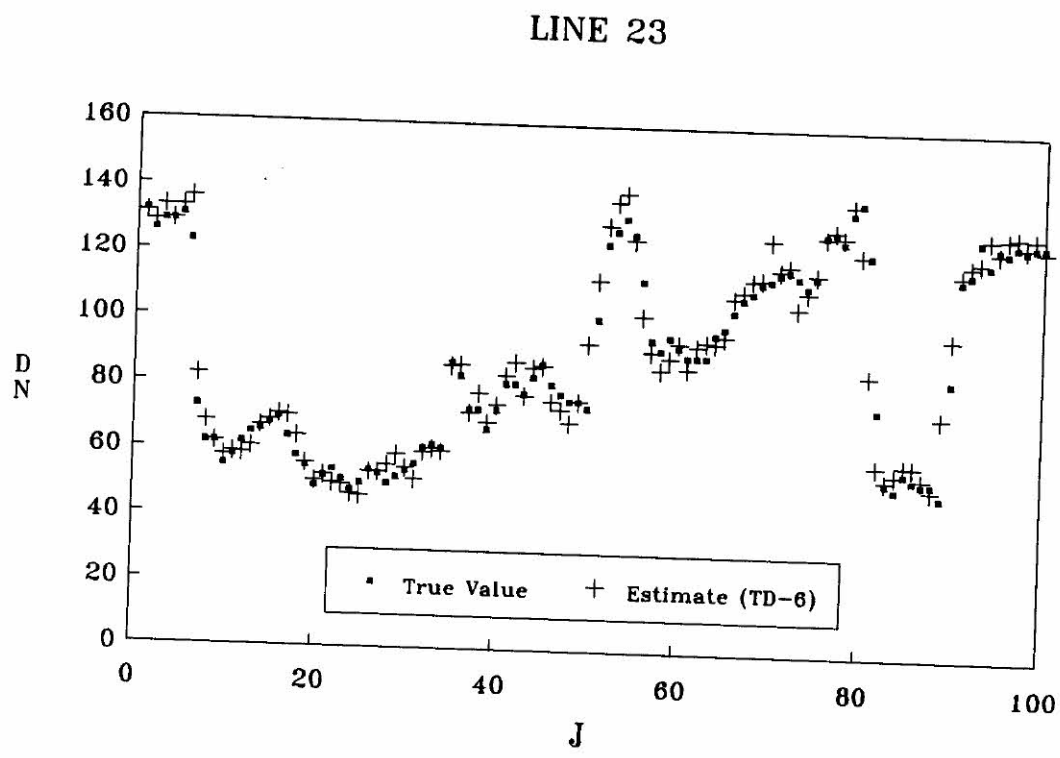

Figure 5.19: Plot of the true values, and the estimates for method TD-6 on: (a) line 7; (b) line 23.

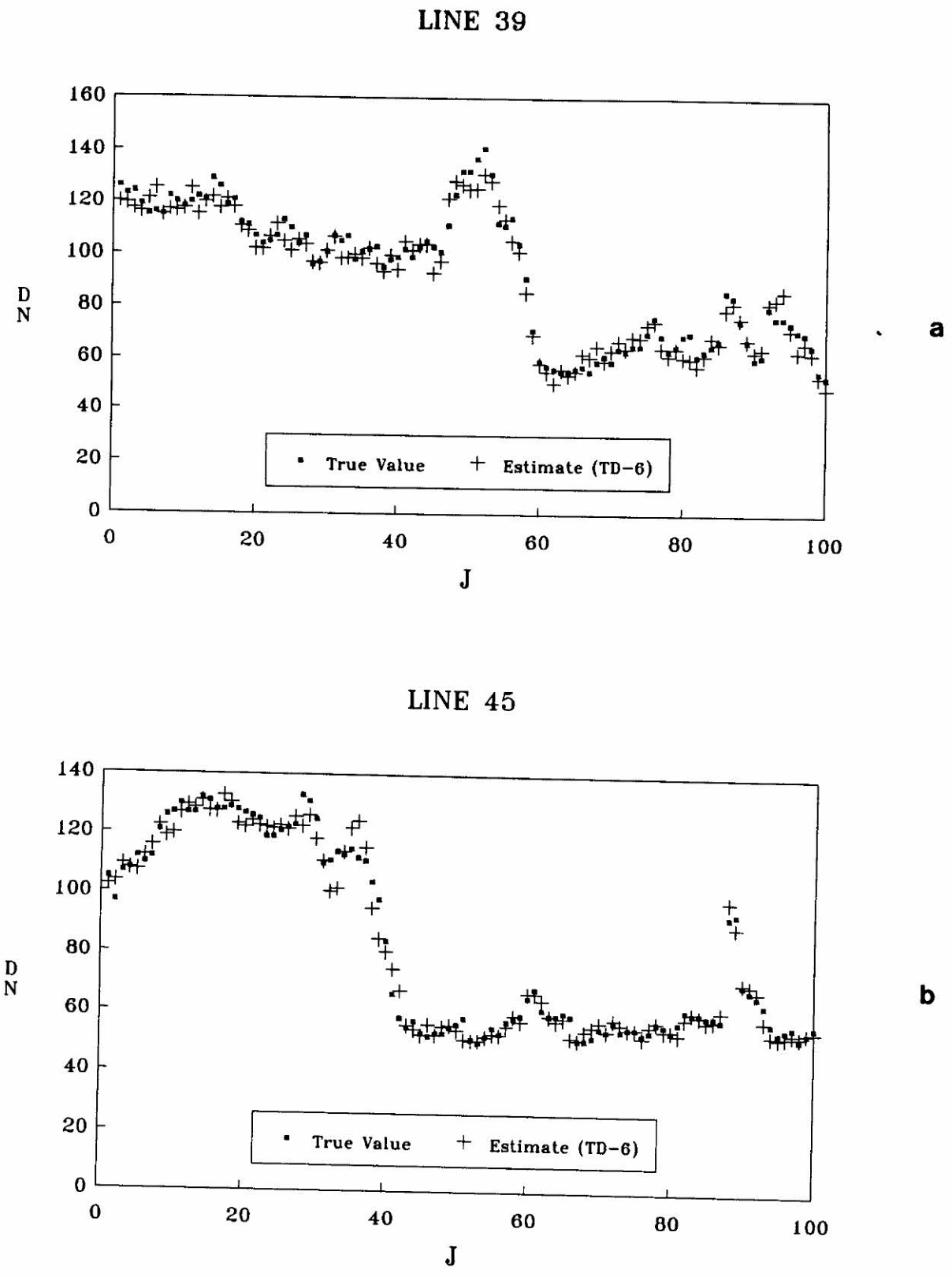

Figure 5.20: Plot of the true values, and the estimates for method TD-6 on: (a) line 39 (b) line 45.

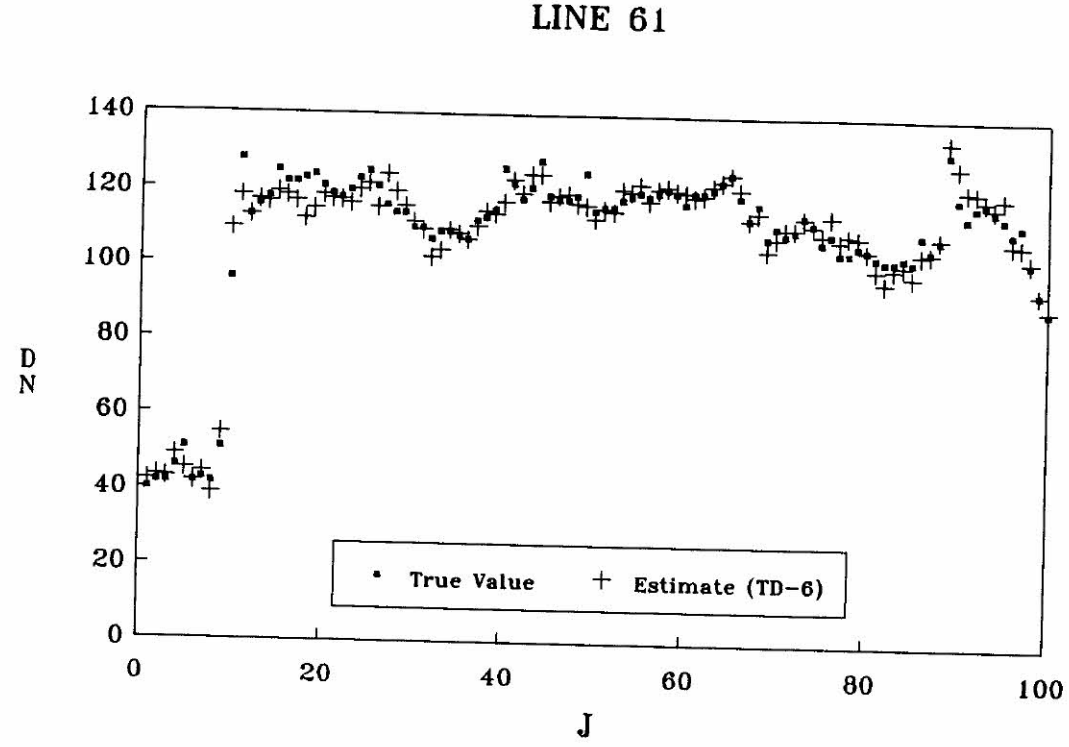

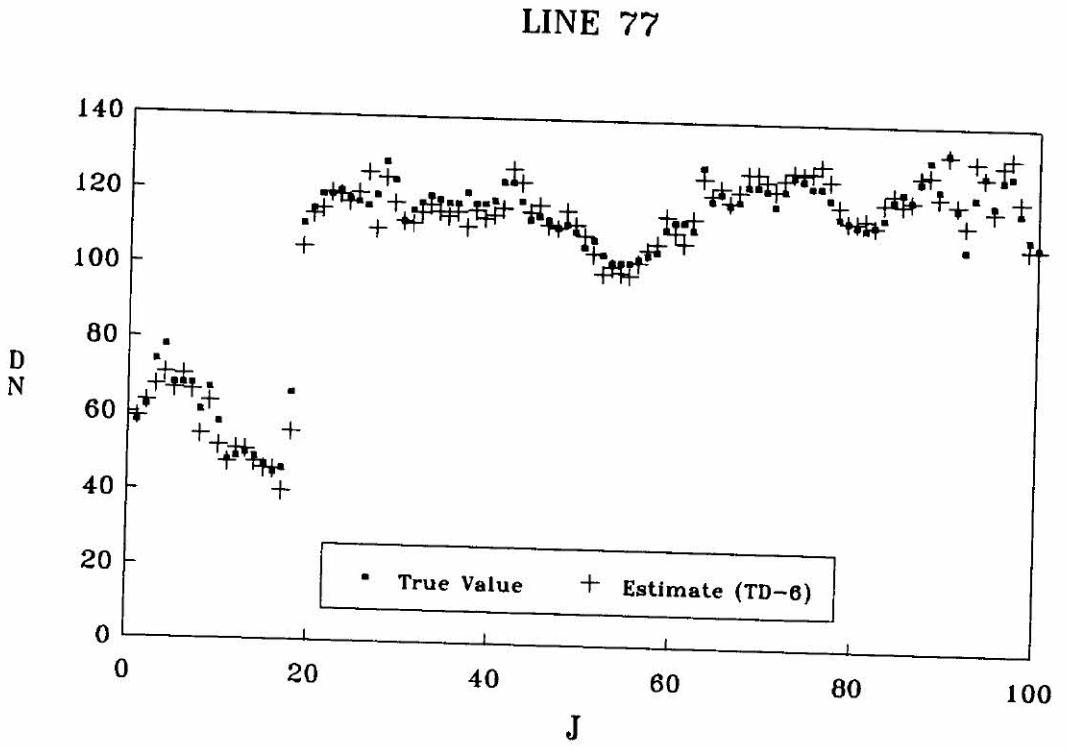

Figure 5.21: Plot of the true values, and the estimates for method TD-6, on line 77.

5.10 Discussion of Results

The results presented in section §5.9 are now discussed, firstly for the simulated lines in $D_1(15)$, and then for those in $D_2(15)$. The discussion concentrates on the methods that usually perform well.

5.10.1 Results using the simulated lines in sub-image $D_1(15)$

From the results in Table 5.4, it can be seen that, unlike in Chapter 4, when linear interpolation usually performed numerically better than the other methods (smaller SRMS, CCOR and SRAN), it does not do so here. However, since the results in Chapter 4 correspond to the average performance of the methods, using several sub-images, (in which case a poor performance in one sub-image, may be shadowed by a good performance in another), and as in this chapter the methods are evaluated using only one sub-image, and 5 missing lines, some contrasting results may be expected. For instance, the performance of method TD-8 is much better here than in Chapter 4. However, a closer investigation of the results for this method, in that chapter, indicates that method TD-8 performs particularly well in sub-image $D_1(15)$ (in fact, its ranks were similar to those for TD-7, which usually performed well, in that chapter).

It has been the good performance of this method, for the missing lines in $D_1(15)$, that motivated its application to other sub-images. Recall that method TB/D-8 had been developed before knowledge of Guindon's methods, and hence its results were being compared only with those obtained for method TB/D-2. From Table 5.5 it can be seen that, in general, method TB/D-8 performed better than TB/D-2.

Note, from Table 5.5, that the good performances of Guindon's methods, observed in Chapter 4, are still maintained here. The same applies to method TB/D-14.

From the absolute value of the differences between the average ranks of methods, for the different measures, given in Tables 5.4 and 5.7 under (1), (2), and (3) (for SRMS and CCOR, SRMS and SRAN, and CCOR and SRAN, respectively), it can be noted that most methods are reasonably consistent for all measures.

Since the missing lines are simulated in a sub-image in the most heterogeneous band 5, where more 'local' variations of the data are expected to occur, the method of linear interpolation does not perform as well as in sub-images in more homogeneous bands. However, for some of the simulated lines, good estimates of the missing values are still obtained for LI. For example, the estimates of the missing values in line 11, for LI, are in general good, with 82 percent of the absolute value of the residuals not exceeding 5 grey levels [the largest residual (in absolute value) is 8]. However, as may be expected from the brief description of the neighbourhood of each missing line, in §5.8.3, large residuals are obtained for LI at the boundaries between different types of land cover, as detailed in that section. Henceforth, unless otherwise stated, the discussion is carried out using the absolute value of the residuals.

Although a large percentage of the missing values in line 27 is estimated within an error of less than 5 grey levels (78 percent), some large residuals are obtained for LI, particularly for the values which are associated to the pixels near the intersection of the missing line with the road that crosses the sub-image (between columns 18 and 21). The residuals are 24, 14, 20, and 19, for the pixels at columns 18 to 21, respectively. The largest residual (33) occurs at the boundary between bare soil, and soil with low density vegetation (column 88).

The missing values in line 43 are reasonably well estimated using linear interpolation. The largest residual is 10, and 82 percent of the residuals do not exceed 5 grey levels. Most the missing values in line 59 are also well estimated from LI (78 percent); the largest residuals are associated to the pixels at the boundary between the area with moisture, and the area covered with low density vegetation (between columns 4 and 10).

In line 75, the largest residuals occur for the pixels between columns 85 and 89 (17, 16, 8, 12, and 7); 82 percent of the residuals are less than 5 grey levels.

Due to the greater heterogeneity of the data in the neighbourhood of line 91, only 45 percent of the residuals do not exceed 5 grey levels. The largest residuals are associated to the pixels between columns 48 and 54, and are 18, 12, 20, 17, 16, 11, and 12.

From Figures 5.8, 5.9, and 5.10, the similar performances of the purely spatial methods, LI and 1p-SAR, can be appreciated. Note that the pixels that are not estimated well using LI, are usually not estimated well using a 1p-SAR. In certain

cases, the estimates from a 1p-SAR can be worse than those for LI, particularly when the data in the neighbourhood of the missing pixel are heterogeneous. As an example, consider the missing values in line 75 (shown in bold), at columns 32 and 33. The data in lines 73 to 77, between columns 30 and 35 are given below:

	Column					
	30	31	32	33	34	35
Line 73	22	20	21	17	17	15
Line 74	23	19	19	17	18	19
Line 75	**25**	**33**	**27**	**22**	**22**	**19**
Line 76	43	43	43	39	33	37
Line 77	43	33	14	8	19	37

The missing values at the sites at columns 32 and 33, for instance, are not estimated well from LI (the rounded estimates are 31 and 28). However, even worse estimates of these missing values are obtained for the method that uses a 1p-SAR, since the data in the 'local' neighbourhood of these pixels (consisting of the 2 pixels above, and the 2 pixels below the missing ones) are heterogeneous. Although the estimates for the method that uses a 1p-SAR incorporate information from all sites in the 2 lines above and the 2 lines below the missing one, more weight is placed on the pixel values in the 'local' neighbourhood of the pixel where the missing observation occurs. The respective estimates for the 1p-SAR method, for sites 32 and 33 are 34 and 32. Since the method that uses a 1p-CAR incorporates information only from the sites on the lines above and below the missing one, better estimates of the missing values can be obtained from this method than from a 1p-SAR, since the data in this neighbourhood is more homogeneous than those in the enlarged neighbourhood of the 1p-SAR. The rounded estimates of the missing values in the sites at columns 32 and 33, for the method that uses a 1p-CAR, are similar to those obtained for LI (and hence better than those obtained for the 1p-SAR), and are respectively equal to 30 and 28.

In §5.8.2 it was mentioned that the range of the data in the adjacent neighbourhood of each of the pixels between columns 85 and 89, in line 75, was reasonably large. In fact, the pixels at these columns delimit the boundary between a moisture patch and soil with low density vegetation. The values of the pixels at lines 73 to 77, between columns 84 and 90 inclusive, are given below. The values

for the 'defective' line 75 are shown in bold.

	Column						
	84	85	86	87	88	89	90
Line 73	65	47	49	48	47	42	46
Line 74	52	32	43	53	48	39	43
Line 75	**46**	**28**	**38**	**70**	**68**	**51**	**41**
Line 76	52	58	66	71	64	49	45
Line 77	57	62	68	62	52	45	40

Note that the range of the data above and below the pixels in line 75, between columns 85 and 88 is large, particularly for the pixels at columns 85 and 86 (the ranges are 26 and 23, respectively). Since the one-parameter methods assign equal weights to the pixel values above and below the missing one, and due to the relatively large variation of the data in this 'local' neighbourhood, the purely spatial methods do not perform well. The residuals (in absolute value) using a 1p-CAR method are 21, 16, 12, 14, and 4, for the sites at columns 85 and 89, respectively; the corresponding residuals for a 1p-SAR are 16, 15, 8, 11, and 5; and finally those for LI are 45, 53, 62, 56, and 44.

The estimates obtained from the methods using spatial modelling are all similar, as can be seen from Table 5.3. For all the simulated missing lines in sub-image $D_1(15)$, the estimates of the parameter β, for the methods using first-order models, are close to 0.25, that is, close to the upper limit allowed for this parameter, to ensure the covariance matrix is positive definite.

For some lines, estimates of the missing values have been obtained using $\hat{\beta} = 0.25$, and are almost always identical to those obtained using the maximum likelihood estimate of the dependence parameter β. The maximum difference between the estimates (rounded up to the nearest integer) obtained from both approaches (maximum likelihood, and fixed at 0.25) is 1 grey level.

If a fixed value for the dependence parameter β (say $\beta = 0.25$) is assumed, great simplification may be achieved in the computation of the estimates of the missing values occurring sequentially in a line, from methods that use spatial modelling. If all the values are assumed to be missing in each 'defective' scan line on the imagery, then the product $(\hat{\mathbf{V}}^{zz})^{-1}\hat{\mathbf{V}}^{zy}$ (refer to equation 5.12) is fixed for a given value of β, and needs to be calculated only once. Only the vector of

observations in the neighbourhood of each missing line changes, from one missing line to another.

From Table 5.3 it can be noted that all the methods using spatial modelling have a very similar performance, suggesting that the trend surface may be reasonably flat. The estimates of the vector θ, $\hat{\theta} = [\hat{\alpha}_{00}, \hat{\alpha}_{01}, \hat{\alpha}_{10}, \hat{\alpha}_{02}, \hat{\alpha}_{20}, \hat{\alpha}_{11}]'$, for the second-order trend surface methods are given in Table 5.8, for each simulated missing line.

Table 5.8: Estimates of the parameters of the second-order trend surface with 1p-CAR(1) and 1p-SAR(1) errors, using the data in the neighbourhood of each simulated missing line: $D_1(15)$.

1p-CART						
Line	$\hat{\alpha}_{00}$	$\hat{\alpha}_{01}$	$\hat{\alpha}_{10}$	$\hat{\alpha}_{02}$	$\hat{\alpha}_{20}$	$\hat{\alpha}_{11}$
11	38.98	4.64	1.09	−0.01	−0.37	−0.01
27	58.32	1.06	−0.29	0.01	−0.04	0.00
43	79.43	−4.26	−0.72	0.01	0.24	0.00
59	65.75	−1.54	−0.73	−0.02	0.19	0.01
75	66.65	1.01	−0.90	−0.02	−0.01	0.01
1p-SART						
Line	$\hat{\alpha}_{00}$	$\hat{\alpha}_{01}$	$\hat{\alpha}_{10}$	$\hat{\alpha}_{02}$	$\hat{\alpha}_{20}$	$\hat{\alpha}_{11}$
11	41.49	4.45	0.95	−0.01	−0.36	−0.01
27	52.05	2.58	−0.06	0.02	−0.16	0.00
43	76.20	−3.19	−0.55	0.01	0.15	0.00
59	62.97	−0.15	−0.63	−0.01	0.07	0.01
75	62.98	1.27	−0.78	−0.02	−0.02	0.00

From Figure 5.4 (a), which shows the difference image for the data in the neighbourhood of each simulated missing line, it is possible to have an idea of where method TD-6 is expected to fail. Recall, from Chapter 4, that the difference image can aid the identification of the pixels where Guindon's method may fail. Essentially, observation of the contrast between the pixels in the difference image, above and below the one corresponding to the missing value, may suggest if the

assumption under which Guindon's methods are based, is satisfied. Note, for instance, that method TD-6 does not estimate well most of the missing values in line 59, between columns 1 and 8 – refer to Figure 5.13 (b). It can be seen, in Figure 5.4 (a), that the pixels between columns 1 and 8, in the lines above and below the 'defective' one, are displayed in different colours (magenta for the pixels above, and cyan for the pixels below), which suggest a possible failure of Guindon's assumption.

5.10.2 Results using the simulated missing lines in sub-image $D_2(15)$

The results obtained using sub-image $D_2(15)$ are, in general, similar to those using $D_1(15)$. Note that methods TD-2, TD-7, and TD-14, perform better than LI, for all measures. Poor estimates of the missing values using LI usually occur at the boundaries between distinct types of land cover, as for the simulated lines in $D_1(15)$. However, if there is no large variation of the data in the 'local' neighbourhood of the missing one (1 pixel above and 1 below), good estimates from LI can still be obtained, even at the boundaries. This occurs particularly in line 7, despite the heterogeneity of the data in the neighbourhood of this line. Note, in Figure 5.2 (b), that the boundary between the bare soil (shown in yellow) and the soil with low density vegetation (shown in cyan) is a vertical feature, which ensures small variations of the data in the 'local' neighbourhood of the missing values occurring at columns 76 and 77. The pixel values in lines 5, 6, 7, 8, and 9, for the sites between columns 76 to 79 are as follows:

	Column			
	76	77	78	79
Line 5	147	123	119	109
Line 6	162	132	117	107
Line 7	**162**	**130**	**116**	**109**
Line 8	158	135	120	112
Line 9	165	151	131	114

The pixels in lines 5 to 9, at column 76, are displayed in yellow, in Figure 5.2 (b), whilst those at column 77 are displayed in green. Finally, those at columns 78

and 79 are displayed in cyan. Note that the variations of the data occur between pixels that are horizontally adjacent, and not between the vertically adjacent pixels. Hence, good estimates of these missing pixels are obtained using linear interpolation, although the data in the area are reasonably heterogeneous. The estimates of the missing values for the sites between columns 75 and 78, from the methods that use spatial modelling are also good. The estimates for the values at sites between columns 75 to 78, using LI, are 160, 134, 119, and 110, respectively; whilst those for the method using a 1p-CAR the corresponding estimates are 159, 138, 123, and 133; and finally, for the method that uses a 1p-SAR the estimates are 160, 134, 118, and 109. Note the similarity between the estimates obtained for these three purely spatial methods.

The fact that line 23 intersects the boundaries of several types of land cover characterized by linear features, but that transverse the image diagonally, explains the large number of residuals greater than 4 grey levels (32 percent), using LI. For instance, the pixel values in the lines above and below the missing one, at columns 5, 6, and 7, are respectively 118 and 130; 90 and 131; 62 and 104, and delimit the boundaries between the soil with low density vegetation and the reforested area. The lower values are associated with the pixels in the reforested area (shown in magenta) in Figure 5.2 (b), whereas the larger ones are associated with the pixels corresponding to low density vegetation (shown in cyan). The missing values at columns 5, 6, and 7 are respectively 131, 123, and 73, and the residuals from LI are 7, 13, and 10. The residuals obtained for the method using a 1p-CAR are 9, 16, and 13, whilst those for the method using a 1p-SAR are 4, 12, and 10.

A higher percentage (46 percent) of the residuals obtained for LI, in line 39, are usually associated to the pixels at the boundary between the area with low density vegetation [shown in green, in Figure 5.2 (b)], and reforestation (shown in magenta). Note that the boundary between these two areas, in line 39, is a horizontal feature that comprises approximately 8 pixels (from column 55 to 62). Note also from Figure 5.2 (b) that even before line 39 intersects the boundary between these two areas, a contrasting response from the area covered with low vegetation, above, and below, the missing line is observed, as mentioned in §5.8.3. Hence, a sequence of poor estimates are expected from LI, for the missing values at the sites delimited by columns 55 and 62, in line 39. The largest residual in this line is 25.

The comments drawn above for line 39, also apply for line 45. However, only 22 percent of the residuals are larger than 4 grey levels. The largest residual is 21.

From the greater homogeneity of the area intersected by missing line 61, as can be noted in Figure 5.2 (b), a good performance of LI is expected. Only 9 percent of the residuals are larger than 4 grey levels, and the largest residual, associated with the pixel at the boundary between the reforested area, and soil with low density vegetation, is 15. All other residuals in this line do not exceed 8 grey levels.

Only 25 percent of the residuals in line 77 exceed 4 grey levels [note, in Figure 5.2 (b), the homogeneity of the data in the entire neighbourhood of this line (5 lines above and 5 below)]. The largest residual is 11.

Finally, and as expected from the comments in §5.8.3, small residuals are obtained for LI, in line 93 [only 22 percent of the residuals exceed 4 grey levels]. The largest residual (23) is associated with the pixel at the bottom right of the sub-image, where the missing line intersects a small reforested area.

As mentioned in the previous section, the methods using spatial modelling have a similar performance to the method of linear interpolation, and perform similarly amongst themselves. As in the case of the simulated lines in $D_1(15)$, this suggests that the second-order surfaces (in methods 1p-CART and 1p-SART) are reasonably flat. The estimates of the parameters of the vector θ are given in Table 5.9.

In general, the missing values in the simulated lines in sub-image D_2 are better estimated from method TD-6, than LI. For instance, only 5 percent of the residuals obtained for this method, in line 7, are greater than 4 grey levels. The largest residual is 8. Although, in line 23, a smaller number of the residuals are greater than 4 grey levels, using TD-6 (27 percent), than LI (32 percent), the range of the residuals obtained for TD-6 (58) is much larger than that for LI (26).

In the previous chapter it was suggested that the occurrence of large residuals, from method TD-6, can be deduced from observation of the difference image. It seems plausible to assume that if large differences occur between the difference pixel values above and below the missing one, then the assumption on which Guindon's method are based is not a reasonable one. Examination of the pixel

Table 5.9: Estimates of the parameters of the second-order trend surface with 1p-CAR(1) and 1p-SAR(1) errors, using the data in the neighbourhood of each simulated missing line: $D_2(15)$.

1p-CART						
Line	$\hat{\alpha}_{00}$	$\hat{\alpha}_{01}$	$\hat{\alpha}_{10}$	$\hat{\alpha}_{02}$	$\hat{\alpha}_{20}$	$\hat{\alpha}_{11}$
7	38.52	7.27	2.05	−0.01	−0.61	−0.01
23	64.41	6.37	0.43	−0.03	−1.43	0.00
39	90.03	−0.26	−0.19	−0.05	0.12	0.00
45	71.23	−1.54	−1.48	0.07	0.70	0.01
61	83.47	−6.87	1.58	0.04	0.37	−0.02
77	64.48	−1.46	1.55	0.00	0.06	−0.01
93	59.52	6.08	1.03	−0.01	−0.47	0.00

1p-SART						
Line	$\hat{\alpha}_{00}$	$\hat{\alpha}_{01}$	$\hat{\alpha}_{10}$	$\hat{\alpha}_{02}$	$\hat{\alpha}_{20}$	$\hat{\alpha}_{11}$
7	40.97	6.01	1.94	−0.01	−0.52	−0.01
23	62.23	4.27	0.21	0.00	−0.02	−0.98
39	92.44	−0.50	−0.17	0.00	−0.03	0.05
45	89.01	−0.15	−0.63	−0.01	0.07	0.01
61	76.16	−3.70	1.81	0.04	0.13	−0.02
77	64.46	−0.95	1.51	0.02	0.04	−0.01
93	52.84	10.82	1.20	−0.01	−0.84	0.00

values above and below the missing one, in the difference image obtained from $D_1(15)$ and $D_1(25)$, that is, $[u^k_{t_1}(i_p-1,j)-u^k_{t_2}(i_p-1)]$ and $[u^k_{t_1}(i_p+1,j)-u^k_{t_2}(i_p+1)]$ where t_1 refers to date 10/07 (date of acquisition of sub-image $D_1(15)$), t_2 refers to date 24/06 (date of acquisition of the template), and i_p refers to the p^{th} simulated missing line, p=7, 23, 39, 45, 61, 77, and 93, indicates the following:

1. that the largest residual for method TD-6 (33), in line 23, is observed for the pixel at column 81 ($j = 81$), for which the above differences are respectively 40 and 43 (suggesting that the assumption for the method holds). The reason why the method fails to estimate the missing value well is the fact

that the difference $[u_{t_1}^k(27,81) - u_{t_2}^k(27,81)] = 67$, is significantly larger than those for the lines above and below, indicating the Guindon's assumption may not be a reasonable one.

Note that because the value of $u_{t_1}^k(27,81)$ corresponds to the missing one, the difference $[u_{t_1}^k(27,81) - u_{t_2}^k(27,81)]$ is not available, and the observation of a large residual for this pixel value, for TD-6, would not be predicted.

2. for the second largest residual (21) obtained for method, in line 23 (at column 89), the following differences are observed: 8 for the pixel above the missing one and 17 for the pixel below. The values of the pixel corresponding to the missing one, in the difference image is -9.

3. for the third largest residual (17) observed in line 27 (at column 50), the above differences are, respectively, 22, 6, and 23.

4. for the residual of 15, observed in line 27, at column 80, the values of the pixels above and below the missing one, in the difference image, are 44 and 42, respectively. The one corresponding to the missing value is 56.

For all other simulated missing lines, method TD-6 performs better than LI. For instance, the largest residuals in each of lines 39, 45, 61, 77 and 93, for LI, are 25, 21, 15, 11, and 23, whilst for method TD-6 they are 13, 13, 12, 11, and 13, respectively. And whereas the percentages of residuals greater than 4 grey levels, for LI, are 17, 32, 46, 22, 9, 25, and 22, for lines 7, 23, 39, 45, 61, 77, and 93, respectively, they are equal to 5, 27, 30, 17, 15, 19, and 20, for method TD-6.

5.11 Conclusions

This chapter concerned the application of methods that use spatial modelling to estimate missing lines in the imagery, arising from line dropout. The two classes of spatial models most commonly applied to remotely sensed data, *viz.*, the conditional autoregressive, and the simultaneous autoregressive models, have been investigated here, using data from a sub-image in D_1, and from another from D_2.

The main interest was to evaluate the results obtained from the methods using spatial modelling, with those obtained for the simpler methods in Chapter 4

(other single band, or template band/date methods), to decide if the implementation of more complex, and time consuming, methods would be warranted.

The advantage of the purely spatial methods, is that they do not require that information from another band(s), or date(s) be available. Also, for the methods that use a template band to work generally well, it is essential that the objects on the ground respond similarly in the different bands (in other words, that their transfer functions be somewhat linear); and the methods using information from a template date require that few changes occur between the passages. In general, for these methods to work well, it is not the amount of changes that occur between these passages that matters, but how contrastingly different the areas of change are in the specific band under study, from one passage, to another.

The results in this chapter indicate that the linear interpolation method, and the methods using spatial modelling have a very similar performance. However, over relatively homogeneous regions, the methods using spatial modelling should perform better than linear interpolation alone, since they incorporate information from a larger number of pixels, and may not be as affected by some 'local' variations of the data (data in the lines above and below), as LI.

From the visual observation of the data in the adjacent neighbourhood of the missing line, it is possible to have a general idea of how the purely spatial methods will perform; and from observation of the difference images (for sub-images in different bands, or different dates), the performances of the template band, or template date methods can, in general, be reasonably deduced.

Although, as mentioned above, it might be reasonable to expect that over relatively homogeneous regions, the methods that use spatial modelling should perform better than linear interpolation, it is questionable if the estimates thus obtained are significantly better than those obtained for LI. Considering that the methods that use spatial modelling are far more demanding, in terms of computing, than linear interpolation, and considering that they still do not provide 'reasonable' estimates of the missing values at the boundaries of regions of contrasting response, or over dynamic areas, their use does not seem to be justified in the estimation of missing values arising from line dropout, especially considering the large amount of missing values that may need to be estimated.

If the missing values occur over reasonably homogeneous areas, and if a fixed value for the dependence parameter β is assumed for the one-parameter methods

(1p-CAR, 1p-SAR, 1p-CART, 1p-SART), then the computational effort is greatly reduced, and these methods may be preferable to linear interpolation, if the number of missing values is not too large.

Also, the application of methods that use higher-order models does not seem to be justified in the estimation of missing values occurring in heterogeneous areas, as they are unable to improve significantly the estimates of the missing values occurring at the boundaries between regions of contrasting responses, which are usually poorly estimated from the methods that use low-order models.

If few changes occur in the particular area where the missing values occur, between two close passages, then better estimates of the missing values may be obtained from the use of template date methods, then from purely spatial methods. Incorporation of the data from a neighbouring band to the one where the missing values occur may also prove to be useful, especially when the data in the neighbourhood of the missing values is very heterogeneous, and where large 'local' variations of the data may be expected.

It has been shown that even when the data is heterogeneous, good estimates from LI can still be obtained. However, this depends essentially on the structures of the objects on the scene, on the location of the missing line on the imagery, and how contrastingly different is the information in the neighbourhood of the missing line.

Without a visual examination of the 'defective' image, and of the difference images (for different bands, and different dates) it is not possible to predict if better estimates will be obtained from single band methods, or from methods that use a template band, or a template date. Depending on the structures present on the image, and on the location of the missing line, it may also be possible to foresee if the results from the use of methods based on spatial modelling will be better than those for the method of linear interpolation.

Chapter 6

Estimation of Clusters of Missing Values

6.1 Introduction

Landsat images are very frequently affected by the presence of clouds, which may either completely block any information on the Earth's surface, or else produce values that are distorted, and do not represent the true radiance (brightness) of the objects on the ground.

In order to recover the ground radiance information that does not reach the sensor due to the presence of thick clouds, Hord (1982) suggests the replacement of the affected pixel values by the values of the corresponding pixels on another passage. This has been the only approach found in the literature.

Approaches for recovering the radiance values distorted by the presence of thin clouds are more frequent, and usually consist of modelling the distortion (noise) introduced by the cloud. Chanda & Majumder (1991), for instance, note that:

> 'According to Mitchell *et al.* (1977), the 'noise' effects of cloud are not a strictly additive or multiplicative process alone, but are a combination of both. A simple transformation, such as 'logarithm', can then be applied to make the signal and noise additive. Finally, a filtering technique is to be applied to separate out signal from noise, followed by an appropriate inverse transformation which returns the filtered

signal to the picture domain.'

Unfortunately, as thick clouds prevent any information from the ground reaching the sensor, the recovery of the 'true' radiance values from the objects on the ground cannot be approached in the same manner as that described above for thin clouds.

Clouds, being highly reflective, generally show in the image as bright areas, '*which usually have an associated congruent darker area at a specific distance and orientation - their shadows*' (Haralick & Fu, 1983). Unlike most clouds, which can usually be identified by visual inspection, '*areas of shadows are harder to identify since the observed reflectance depends both upon the extent to which the ground is obscured and on the nature of the ground surface*' (Gurney, 1982). Grey levels within and between shadows may vary considerably, and can be easily confounded with other classes of ground cover.

A pixel value may also be 'contaminated' by cloud, if cloud is present within the field of view of the sensor.

Although not actually missing, pixel values from areas covered by thin clouds, shadows, or those contaminated by cloud, can be deliberately deleted from the image data, and treated as missing. The approaches suggested in this chapter for the estimation of missing values arising from thick clouds can also be considered in the estimation of these 'missing' values.

The acquisition of cloud-free imagery varies depending on the location of the region of interest, and the time of the year. In Britain, for instance, coastal districts are relatively less cloudy than upland areas, while the south-east and the western coast have the highest percentages of useful imagery (Legg, 1991). Nevertheless, a review of Landsat Multispectral Scanner 'Quicklook' images in the National Remote Sensing Centre archive by Legg (1991) indicates that, on average, only one satellite pass in six over the United Kingdom results in cloud-free imagery - see also Legg (1988).

Because of the frequent occurrence of cloud covered Landsat images, and in view of the fact that the most demanding potential of remotely sensed data is the mapping, or monitoring, of agricultural crops, then the estimation of missing values due to cloud cover is an important task. However, as the methods proposed for the estimation of missing values from cloud cover must either rely on the spatial information available, and/or on data acquired at other passages, es-

timates of missing values in extensive clouded areas are not expected to be good, unless the clouded area is very homogeneous, or that few changes occur between passages.

In this chapter, the performances of some of the methods introduced in Chapter 4 (§4.2 and §4.3), and Chapter 5 (§5.6), are evaluated in the estimation of missing values occurring in clusters, as if arising from the presence of small, thick, clouds. Some new methods that use temporal information are also proposed, and evaluated. As the presence of thick clouds prevents the acquisition of information on the ground in all bands of the TM (except the thermal), none of the template band methods introduced in Chapter 4 can be used.

Some of the template date methods in Chapter 4 are also not studied in this chapter, since the information they require is not available in the case of clusters of missing values. These methods are TD-2, TD-3, TD-6, TD-7, and TD-8 – refer to Table 4.1 in §4.3.

To evaluate the methods, small clusters of missing values are simulated in some sub-images from D_1, and D_2, and the true values contrasted with those obtained from each method.

The missing values have been simulated in two configurations: in one, they occur as an oblong clump with 'holes' – see Figure 6.1, over selected areas in some sub-images in D_1; and in another they occur as a diagonal, compact patch – refer to Figure 6.13, over selected areas in some sub-images in D_2.

However unrealistic these simulated configurations may appear, they do allow the identification of the situations where particular methods fail to produce good estimates, which can then be generalized to the case of larger clouds, and/or possibly more realistic configurations. Also, the simulation of 'holes' provides the opportunity to investigate the kind of spatial information that the purely spatial methods require, to produce good estimates of the missing values.

As in Chapter 4, and Chapter 5, the performances of the methods are evaluated for their ability to consistently give small values for the SRMS, CCOR, and SRAN.

For the visual evaluation of the methods, the images obtained by replacing the missing values with those estimated from the various methods (test images), and the residual images, are observed for each method. From these images, the distortions introduced by each method, on the particular features present on the

image can be detected, and the methods thus evaluated. Note that the test images only differ from the original sub-image in the sites where observations are missing.

The chapter is set out as follows: section 6.2 introduces the proposed methods for the estimation of clusters of missing values; section 6.3 introduces the simulated 'cloudy' areas, and sections 6.4 and 6.5 presents and discusses the results obtained for each method, respectively. Conclusions are drawn in section 6.6.

6.2 Proposed Methods for the Estimation of Clusters of Missing Values

6.2.1 Notation

Suppose that observations are gathered on an n_1 by n_2 rectangular lattice, and that m out of $n = n_1\, n_2$ observations are missing. Assume that these observations are missing on sites that form a clump or cluster, in the interior of which some observations may still be available. Assume also that none of the missing values occur in the first or last row, or first or last column, of the rectangular lattice. Let $\mho$ be the set of sites in a n_1 by n_2 rectangular lattice, chosen so as to enclose the missing cluster, and let Υ be the set of missing sites.

Assume that the missing values correspond to pixels $(i,j) \in \Upsilon$, and that they occur on the sub-image acquired at time t_1 in band k, and that other images, acquired at times $t_2, t_3, \ldots$, in band k are available. Assume also that if missing values occur in these other passages, they do not occur at sites for which information is not available at time t_1 (that is, $\Upsilon_{t_1} \cap \Upsilon_{t_d} = \emptyset,\ d \neq 1$, where Υ_{t_d} denotes the set of missing sites in the passage acquired at time t_d).

As previously, let $\hat{u}_i^k(i,j)$ denote the estimate of the missing pixel (i,j), on the image acquired in band k, at time t.

6.2.2 Proposed methods

Most of the methods proposed here are the same as some of those introduced in Chapter 4 (§4.2 and §4.3), and in Chapter 5 (§5.5). However, unlike in those chapters, where the missing values correspond to pixels (i,j), $j \in A_i \subseteq \{1,2,\ldots,n_2\}$,

the missing values here correspond to pixels $(i,j) \in \Upsilon$.

The first method, to be referred to as CL-1, consists of estimating the missing values sequentially, from top left to bottom right, lexicographically, by averaging the values at sites $(i-1,j)$ and $(i,j-1)$. Then, the estimate of the missing value at site $(i,j) \in \Upsilon$, if $(i-1,j)$ and $(i,j-1) \notin \Upsilon$ is

$$\hat{u}^k_{t_1}(i,j) = \frac{u^k_{t_1}(i-1,j) + u^k_{t_1}(i,j-1)}{2}.$$

If $(i-1,j) \in \Upsilon$, then $u(i-1,j)$ is replaced by $\hat{u}(i-1,j)$, and similarly if $(i,j-1) \in \Upsilon$, then $u(i,j-1)$ is replaced by $\hat{u}(i,j-1)$.

Note that several variations of this method are possible. For instance, the method may include information from more than two sites, if this information is available; or, instead of estimating the missing values from a single starting point (top left), the method may allow different starting points (say, top left, top right, bottom left, and bottom right), in which case the estimation process converges to the centre of the lattice. The method proposed here (CL-1) may be preferable to these variations, due to its computational simplicity, and possibly speed. Since these variations have not been experimented with here, it is not possible to evaluate if they perform significantly better than the method proposed, and at what cost (diminished speed, computational complexity, etc).

The second method, herein referred to as CL-2, is analogous to method TD-1 in Chapter 4 (§4.3.2), that is

$$\hat{u}^k_{t_1}(i,j) = A\,\{u^k_{t_2}(i,j) - \bar{u}^k_{t_2}\} + \bar{u}^k_{t_1}\ , \quad (i,j) \in \Upsilon \tag{6.1}$$

where $A = s^k_{t_1}/s^k_{t_2}$. Here, $\bar{u}^k_{t_1}$ and $s^k_{t_1}$ are the mean and the standard deviation of the data corresponding to the sites in $\mho - \Upsilon$, at time t_1, respectively; and $\bar{u}^k_{t_2}$ and $s^k_{t_2}$ are the mean and standard deviation of the data corresponding to the sites in $\mho$, at time t_2, respectively.

The third method, to be referred to as CL-3, is analogous to method TD-4 in Chapter 4 (§4.3.2). The method uses information from the sites in $\mho - \Upsilon$ at time t_1, and from the sites in $\mho$, at time t_2. Note that depending on the size of the lattice that encloses the missing cluster, the results for method CL-3 and for a method analogous to TD-5 (in Chapter 4), are similar.

Method CL-3 is

$$\hat{u}^k_{t_1}(i,j) = p\{u^k_{t_2}(i,j) - \bar{u}^k_{t_2}\} + \bar{u}^k_{t_1}, \quad (i,j) \in \Upsilon \tag{6.2}$$

where p is the slope of the straight line regression of $u^k_{t_1}$ on $u^k_{t_2}$, using the data corresponding to the sites in $\mho - \Upsilon$, acquired at times t_1 and t_2; and $\bar{u}^k_{t_1}$ and $\bar{u}^k_{t_2}$ are the means of the data corresponding to the sites in $\mho - \Upsilon$, at time t_1, and to the sites in $\mho$, at time t_2, respectively.

The fourth method, henceforth referred to as CL-4, is similar to method TD-8, in Chapter 4. Unlike that method, which in the first step replaces the missing values from line drop by those estimated from TD-2, this method replaces the missing values by those estimated from CL-3, say $\hat{u}^{k^*}_{t_1}$, and then estimates the missing values using:

$$\hat{u}^k_{t_1}(i,j) = u^k_{t_2}(i,j)\left\{\frac{u^{k^*}_{t_1}(i-1,j)}{u^k_{t_2}(i-1,j)} + \frac{u^{k^*}_{t_1}(i+1,j)}{u^k_{t_2}(i+1,j)}\right\}/2, \quad (i,j) \in \Upsilon. \tag{6.3}$$

Note that CL-2, instead of CL-3, could also be used to replace the missing values in the first step of method CL-4. However, as better estimates of the missing values are expected for method TD-4, than for TD-1 (refer to §4.5.1), then only the use of the former method has been considered with method CL-4.

The fifth method, herewith referred to as CL-5, incorporates temporal information from more than one passage, using a straight linear regression of the form:

$$\hat{u}^k_{t_1}(i,j) = a_1\{u^k_{t_2}(i,j) - \bar{u}^k_{t_2}\} + a_2\{u^k_{t_3}(i,j) - \bar{u}^k_{t_3}\} + \bar{u}^k_{t_1} \tag{6.4}$$

where a_1 and a_2 are the least squares estimates of the α_1 and α_2 in the linear regression model

$$u^k_{t_1} = \alpha_0 + \alpha_1 u^k_{t_2} + \alpha_2 u^k_{t_3} + \epsilon^k_{t_1}$$

and ϵ represents uncorrelated error terms with mean zero and common variance σ^2. This method is similar to method TD-9 in Chapter 4, and uses information from all sites in $\mho - \Upsilon$ at times t_1, t_2 and t_3. Note that depending on the size of the lattice that encloses the missing cluster, the results using method TD-9, or method TD-10, are similar.

The sixth method, herewith referred to as CL-6, expresses the missing value at site (i,j) as a linear combination of the corresponding pixel value and its first-order neighbours on a template date, acquired at time t_2. The method can be formally expressed as:

$$\hat{u}^k_{t_1}(i,j) = b_0 + b_1 u^k_{t_2}(i,j) + b_2 u^k_{t_2}(i,j)_N + \epsilon^k_{t_d}(i,j), \quad (i,j) \in \Upsilon. \tag{6.5}$$

for ϵ as defined for CL-5; and

$$u^k_{t_2}(i,j)_N = u^k_{t_2}(i-1,j) + u^k_{t_2}(i+1,j) + u^k_{t_2}(i,j-1) + u^k_{t_2}(i,j+1).$$

The values of b_0, b_1 and b_2 in 6.5 are the least squares estimates of β_0, β_1, and β_2, in the linear model

$$u^k_{t_1}(i,j) = \beta_0 + \beta_1 u^k_{t_2}(i,j) + \beta_2 u^k_{t_2}(i,j)_N + \varepsilon^k_{t_1}(i,j). \tag{6.6}$$

A different definition from the one given above, for $u^k_{t_2}(i,j)_N$, has also been considered, which includes the information from higher-order neighbours of site (i,j) (consisting of the values at sites at lags $g, h = -2, -1, 0, 1, 2$, g and h not simultaneously equal to -2 or 2). Since the results thus obtained did not improve the the estimates of the missing values obtained when using only the information on the sites that are adjacent horizontal and vertical to site (i,j), they are not included.

Since the results in Chapter 5 indicate that the application of methods using spatial modelling of higher-order does not improve the accuracy of the estimates of the missing values, then only methods 1p-CAR, 1p-SAR, and 1p-CART of §5.6 are considered here. These methods are henceforth referred to as CL-7, CL-8, and CL-9, respectively. Results for a method using third-order trend surface with 1p-CAR errors, henceforth referred to as CL-10, are also obtained.

In order to clarify the way the estimates of the missing values occurring in clusters are obtained, using the spatial modelling methods proposed here, some considerations are drawn below.

For the case of a missing value corresponding to an isolated site, using a 1p-CAR method (refer to §5.5.1), the estimate is found using the values of its first-order neighbours. If β is assumed to be 0.25, then the estimate of the missing value is simply the average of the values of its four first-order neighbours (that is, its adjacent horizontal and vertical sites).

If using a 1p-SAR method, the estimate of the missing value corresponding to an isolated site (see §5.5.4) is a linear combination of the pixel values at the sites that are adjacent horizontal, vertical, and diagonal to it, and at lags 0 and ± 2, and ± 2 and 0, with weights as shown below (the missing value is represented

by a '+'):

			s_c			
		s_b	s_a	s_b		
	s_c	s_a	+	s_a	s_c	
		s_b	s_a	s_b		
			s_c			

where s_a, s_b, and s_c are respectively equal to $\frac{2\beta}{1+4\beta^2}$, $-\frac{\beta^2}{1+4\beta^2}$ and $-\frac{2\beta^2}{1+4\beta^2}$.

If the missing values occur in a compact cluster (as in (a) below, with the missing sites indicated in bold), then the estimate of a missing value using a 1p-CAR, is an average of the values of its first-order neighbours, and of the first-order neighbours of the other missing sites. The estimate of the missing value at site 15, for instance, is found by averaging the values at sites 9, 10, 14, 17, 20, 23, 27 and 28, with weights as indicated in (b). For missing site 15, the values of c_a, c_b, and c_c are 1.17, 0.33, and 0.17, respectively.

(a)

1	2	3	4	5	6
7	8	9	10	11	12
13	14	**15**	**16**	17	18
19	20	**21**	**22**	23	24
25	26	27	28	29	30
31	32	33	34	35	36

(b)

		c_a	c_b		
	c_a			c_b	
	c_b			c_c	
		c_b	c_c		

The estimate of a missing value at site (i, j), in a compact cluster, using a 1p-SAR (refer to §5.5.4), is found in a manner similar to that for a 1p-CAR, but includes the information from the sites that are its first- and second-order neigbhours (that is, those which are adjacent horizontal, vertical and diagonal, and those at lags 0 and ± 2, and ± 2 and 0), and the information from the first- and second-order neighbours of the other sites in the compact cluster.

6.3 Simulated 'Clouded' Areas

6.3.1 Introduction

In order to evaluate the performances of the methods presented in §6.2.2, missing values are simulated in areas selected from some sub-images in the first, and in the second data sets, respectively. Two different configurations, shown in §6.3.2 and §6.3.3, are simulated.

Estimates of the missing values occurring in each simulated 'clouded' area are obtained for each method. By replacing the missing values with the estimates for any given method, a test image is generated for that method.

For the selected areas from D_1, estimates for methods CL-2, CL-3, CL-4 are obtained using the two possible template dates, whilst for those selected from D_2, only the nearest passage is used as the template. Method CL-5 is not applied to the sub-images in D_2, since in this data set there is only one template date that can be reasonably used with the methods.

6.3.2 Selected areas from D_1

Missing clumps of values with the configuration displayed in Figure 6.1, have been simulated in six sub-images from D_1. A '+', in the figure, indicates a missing value. On four of these sub-images [($D_1(13)$, $D_1(14)$, $D_1(15)$, and $D_1(25)$ - refer to Table 3.1 in Chapter 3], an area of 23 by 15 pixels containing the missing values was extracted, as shown in Figure 6.1, and treated independently from the rest of the sub-image. The area, A_1, is bounded by lines 29 and 51, and columns 33 and 47 on the original sub-image. It is shown in Figures 6.2 to 6.5 (marked as **1**), for $D_1(13)$, $D_1(14)$, $D_1(15)$, and $D_1(25)$, respectively. Let $A_1(dk)$ denote the area limited by these lines and columns on sub-images from D_1, acquired at time d, in band k.

On two of the sub-images [$D_1(14)$ and $D_1(15)$], missing values with the configuration shown in Figure 6.1 have also been simulated in another area (A_2), also of size 23 by 15, which is bounded by lines 70 and 92, and by columns 25 and 39 on the original sub-images. This area is marked as **2** in Figures 6.2 to 6.5. Denote by $A_2(dk)$ the area delimited by these lines and columns on sub-images in D_1, acquired at time d, in band k.

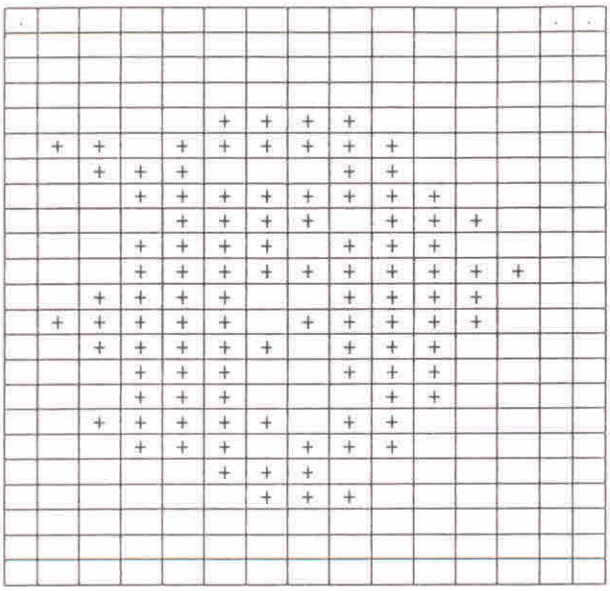

Figure 6.1: Configuration of the missing sites in areas A_1 and A_2.

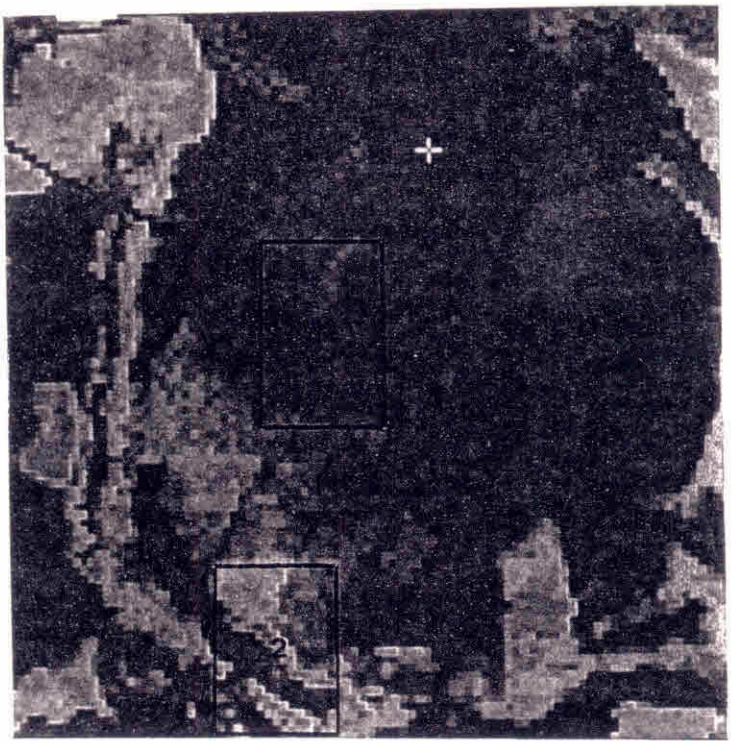

Figure 6.2: Location of areas A_1 and A_2 in sub-image $D_1(13)$.

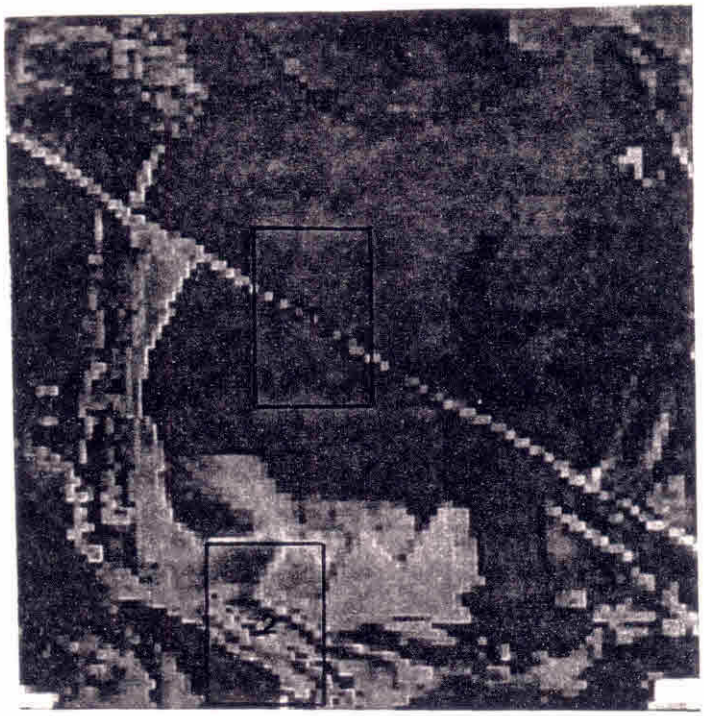

Figure 6.3: Location of areas A_1 and A_2 on sub-image $D_1(14)$.

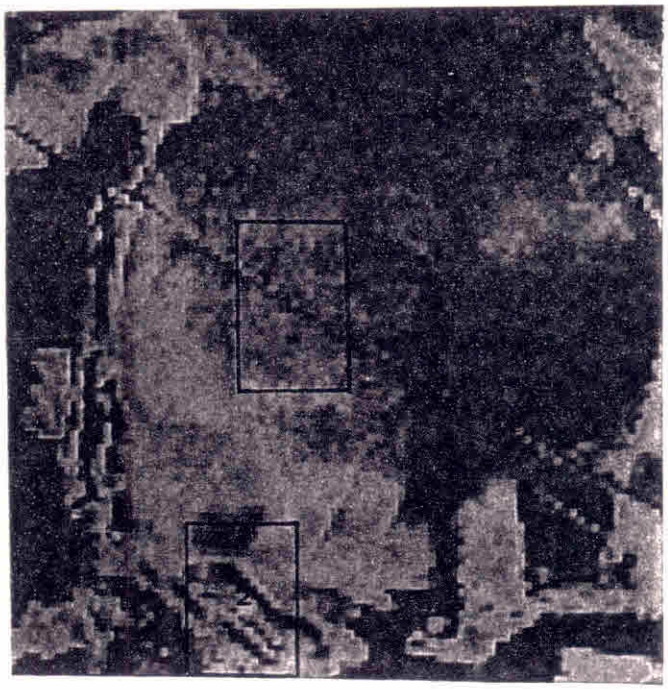

Figure 6.4: Location of areas A_1 and A_2 on sub-image $D_1(15)$.

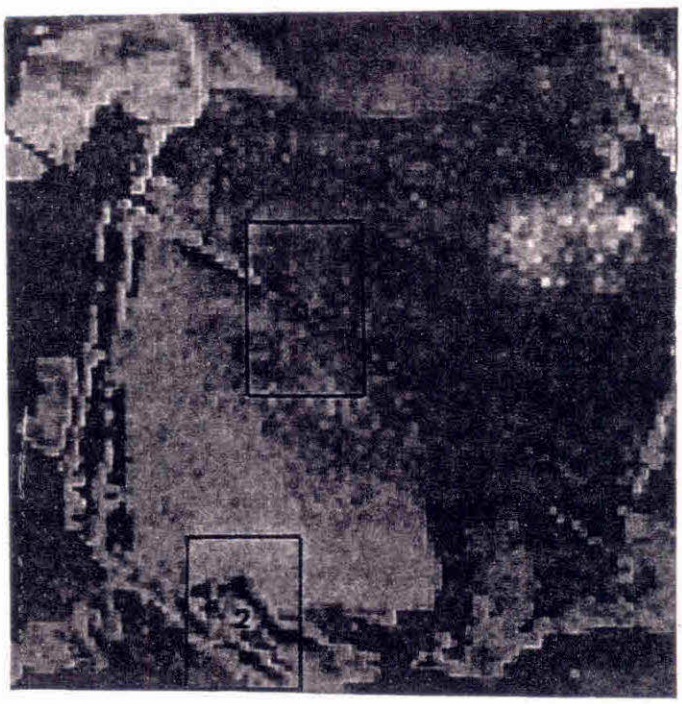

Figure 6.5: Location of areas A_1 and A_2 on sub-image $D_1(25)$.

Figure 6.6 shows a 3-dimensional representation of the data in area $A_1(14)$. The 'valley' across the figure is associated with the road that crosses sub-image $D_1(14)$, from top left to bottom right – see Figure 3.5. The areas above and below the road, in A_1, are relatively homogeneous, and are cultivated with wheat.

In Figure 6.7 a three dimensional representation of the data in area $A_2(15)$ is given. The two depressions across the figure are associated with the areas of intense moisture indicated by C in Figure 3.5. The area is heterogeneous, and includes soil with varying degrees of moisture.

The number of missing sites in either area A_1, or A_2, is 105, corresponding to approximately 30% of the total number of sites in each area.

Let $d = 1, 2, 3$ refer to dates 10/07/86, 24/06/86, and 08/06/86, respectively, and $k = 3, 4, 5$ to bands 3, 4, and 5, in this order.

The mean, standard deviation (stdev), minimum and maximum [(m,M)], and the range of the data in areas $A_1(dk)$ and $A_2(dk)$, $d = 1, 2, 3$, $k = 3, 4, 5$, are given in Table 6.1. These statistics are given for the data in the entire 23 by 15 area (complete data), that is, to the data corresponding to the sites in $\mho$. Since the statistics for the data corresponding to the sites in $\mho - \Upsilon$ (incomplete data) are similar to the ones presented in Table 6.1, they are not included.

The correlations, $r\dot{d}^l_{db,eb}$, between the complete data in areas $A_l(db)$ and $A_l(eb)$, $l = 1, 2$, acquired at different passages, are given below. These correlations, for

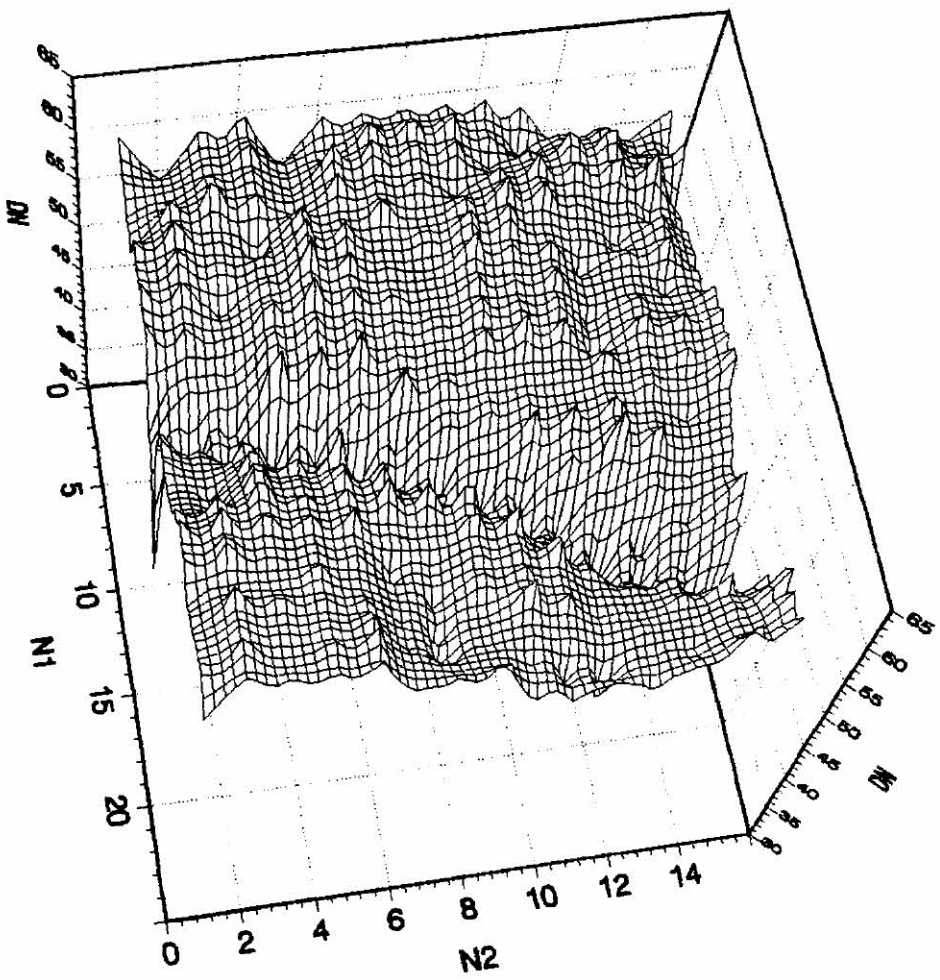

Figure 6.6: 3-dimensional representation of the data in area $A_1(14)$.

the incomplete data, are similar to the ones presented for the complete data (the maximum difference between these correlations is 0.052).

$$rd^1_{13,23} = 0.635; \quad rd^1_{13,33} = 0.671; \quad rd^1_{14,24} = 0.907;$$
$$rd^1_{14,34} = 0.859; \quad rd^1_{15,25} = 0.649; \quad rd^1_{15,35} = 0.610;$$
$$rd^1_{25,35} = 0.590; \quad rd^2_{14,24} = 0.548; \quad rd^2_{14,34} = 0.476;$$
$$rd^2_{15,25} = 0.799; \quad rd^2_{15,35} = 0.806.$$

Figure E.1 (a) and (b), in Appendix E, gives the plots for the complete data in areas $A_1(13)$ and $A_1(23)$, and $A_1(13)$ and $A_1(33)$, In these plots, the digital numbers (DN) correspond to the sites in the n_1 by n_2 lattice, labelled by the first n positive integers, in lexicographic order [that is, in the ordering, site (i,j) precedes $(i,j+1)$ for $j < n_2$ and (i,n_2) precedes $(i+1,1)$]. Hence, site number 31 corresponds to site (3,1) (line 3 and column 1), in the lattice. The periodicity

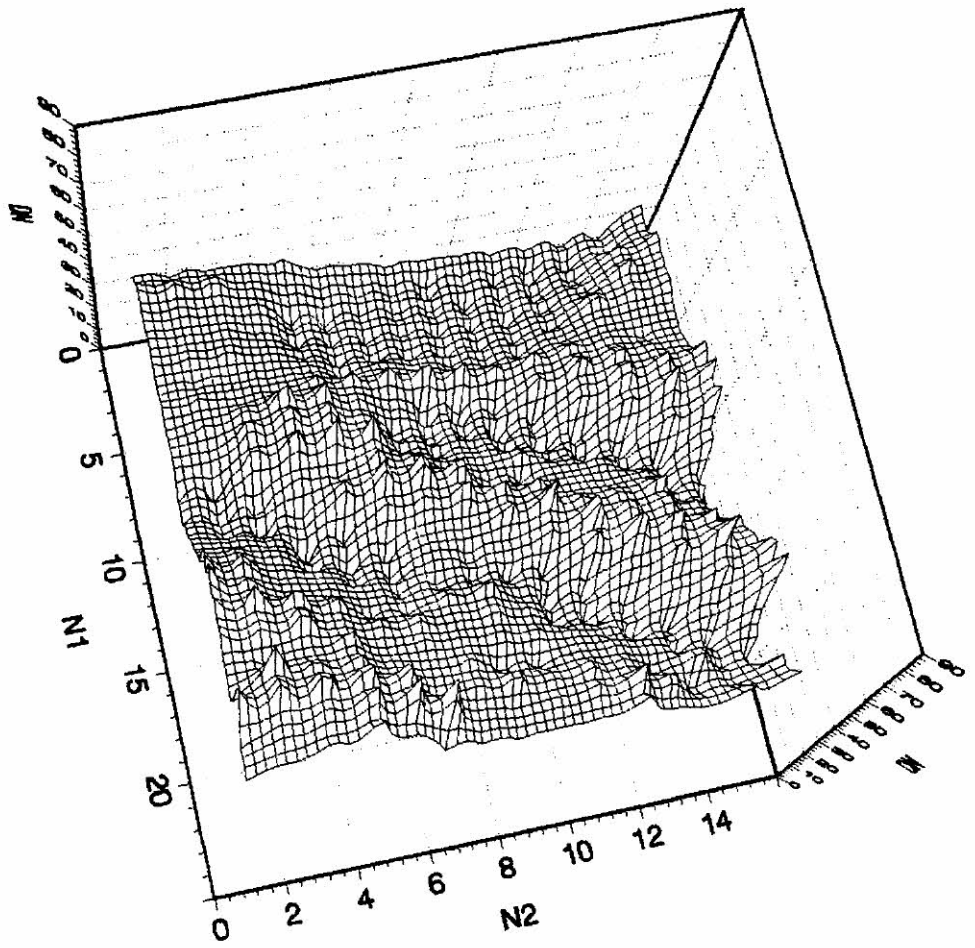

Figure 6.7: 3-dimensional representation of the data in area $A_2(15)$.

sometimes observed in these plots occurs due to the similarity of the pixel values at sites that are geographically close. For instance, the pixel value at site 31 ($i = 3, j = 1$) is more likely to be similar to the pixel value at site 46 ($i = 4, j = 1$), than to the value at site 45 (i=3,j=15).

Similar plots to those displayed in Figure E.1 (a) and (b) are given in Appendix E for the following data:

in areas $A_1(14)$ and $A_1(24)$, and $A_1(14)$ and $A_1(34)$ – Figure E.2 (a) and (b), respectively;

in areas $A_1(15)$ and $A_1(25)$, and $A_1(15)$ and $A_1(35)$ – Figure E.3 (a) and (b), respectively;

in areas $A_1(25)$ and $A_1(15)$, and $A_1(25)$ and $A_1(35)$ – Figure E.4 (a) and (b),

Table 6.1: Descriptive statistics of the data in areas A_1 and A_2, in all sub-images in D_1.

Area	Mean	Stdev	(m,M)	Range
$A_1(13)$	26.24	2.24	(22,35)	13
$A_1(23)$	26.18	2.24	(22,35)	13
$A_1(33)$	22.96	2.31	(19,33)	14
$A_1(14)$	55.54	6.38	(32,63)	31
$A_1(24)$	59.00	7.23	(33,68)	35
$A_1(34)$	58.53	7.23	(34,69)	35
$A_1(15)$	55.85	3.71	(48,69)	21
$A_1(25)$	52.44	3.19	(44,64)	20
$A_1(35)$	50.73	3.81	(43,63)	20
$A_2(14)$	28.25	12.34	(6,70)	63
$A_2(24)$	35.68	12.50	(8,76)	68
$A_2(34)$	39.26	13.68	(8,64)	56
$A_2(15)$	40.36	17.44	(5,89)	84
$A_2(25)$	41.35	14.66	(7,90)	83
$A_2(35)$	40.89	13.00	(7,73)	66

respectively;

Note, however, that these plots are more useful in the detection of global changes that may have occurred between different passages, rather than in the detection of local changes, which affect small areas.

From Table 6.1, it is noted that the data in area A_1 are most homogeneous in sub-images in band 3. This is evident from both the narrower range, and the lower standard deviation of the data in A_1, in this band. Area A_1 comprises the portion of the wheat fields that is crossed by the road – refer to Figure 3.5. The largest variations between the values of the pixels that are geographically close occur at the boundary between the road and the fields (the largest variation is 6).

The variation of the data at the boundary between the road and the fields, in area $A_1(14)$ can be clearly seen in Figure E.2 (a) and (b). The lower values, between sites 120 and 285 are associated with the road. Note, from the plot,

that the data in the wheat fields are reasonably homogenous. In this band, there are usually 2 or 3 pixels in each column, which correspond to the road (and contaminated neighbouring pixels).

Data in areas $A_1(15)$ and $A_1(25)$ are also reasonably homogeneous. The pixel values corresponding to the road are, in this band, higher than those associated to the fields, but large variations between the pixel values associated to the road, or those associated to the wheat fields, do no occur [the largest variation, in either area $A_1(15)$ or $A_1(25)$ is 13].

From Figures E.1, E.2, E.3, and E.4, in Appendix E, it can be seen that the objects on the ground respond similarly in band 3, from one passage to another. This similarity is also observed in bands 4, and 5, from which it can be inferred that no major changes occurred in A_1, between the different passages.

The similarity of the sample autocorrelations, for the data in $A_1(d3)$, $d = 1, 2, 3$, shown in Figure 6.8 to some selected lags, also suggests that few relative changes on the ground may have occurred between these passages. Figure 6.8 (e) and (f) shows that a mild anisotropy is observed on the data in $A_1(d3)$, for $d = 1, 2, 3$.

The plots of the sample autocorrelations to some selected lags, for data in $A_1(d4)$, and $A_1(d5)$ $d = 1, 2, 3$, are given in Figures 6.9 and 6.10, respectively. Again, note the similarity of the sample autocorrelation to these lags, for the data on all passages, which, as for $A_1(d3)$, might suggest that few relative changes on the ground may have occurred between all passages.

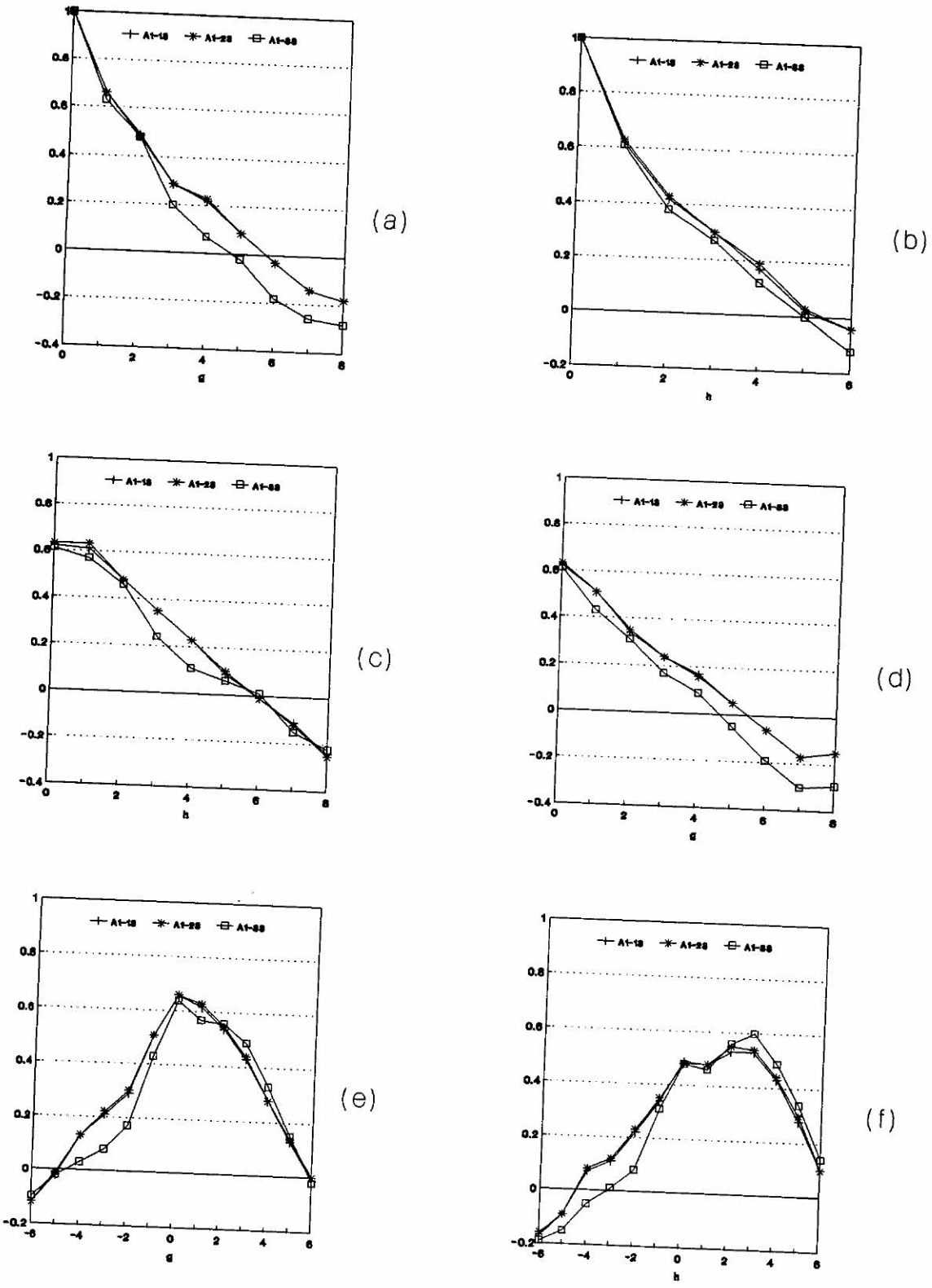

Figure 6.8: Sample autocorrelations for the data in area A_1, in band 3, acquired at the different passages: (a) $r_{g,0}$, (b) $r_{0,h}$, (c) $r_{g,1}$, (d) $r_{g,-1}$, (e) $r_{1,h}$, (f) $r_{2,h}$, $g = 0, \ldots 8$, $h = 0, \ldots, 6$.

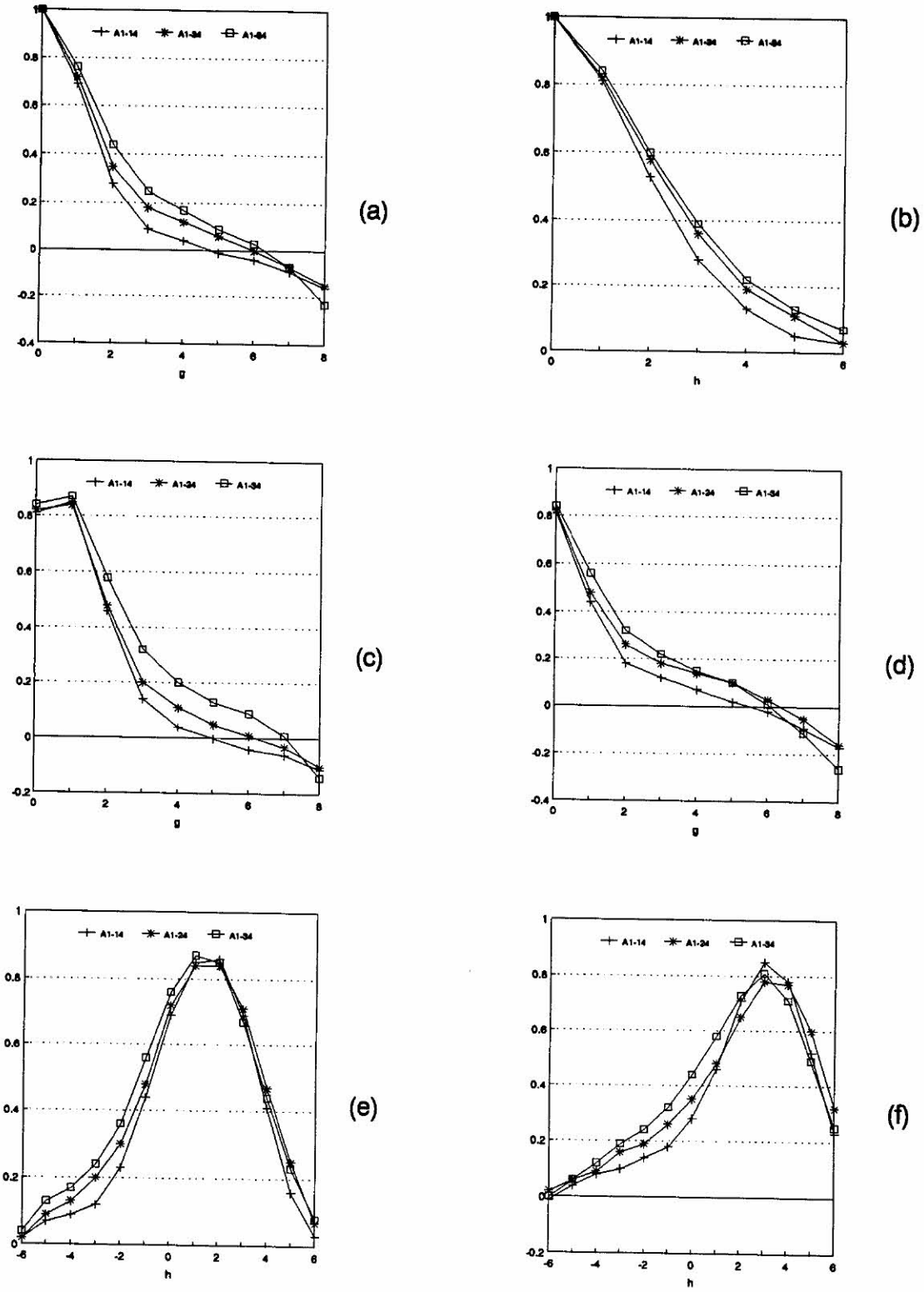

Figure 6.9: Sample autocorrelations for the data in area A_1, in band 4, acquired at the different passages: (a) $r_{g,0}$, (b) $r_{0,h}$, (c) $r_{g,1}$, (d) $r_{g,-1}$, (e) $r_{1,h}$, (f) $r_{2,h}$, $g = 0, \ldots 8$, $h = 0, \ldots, 6$.

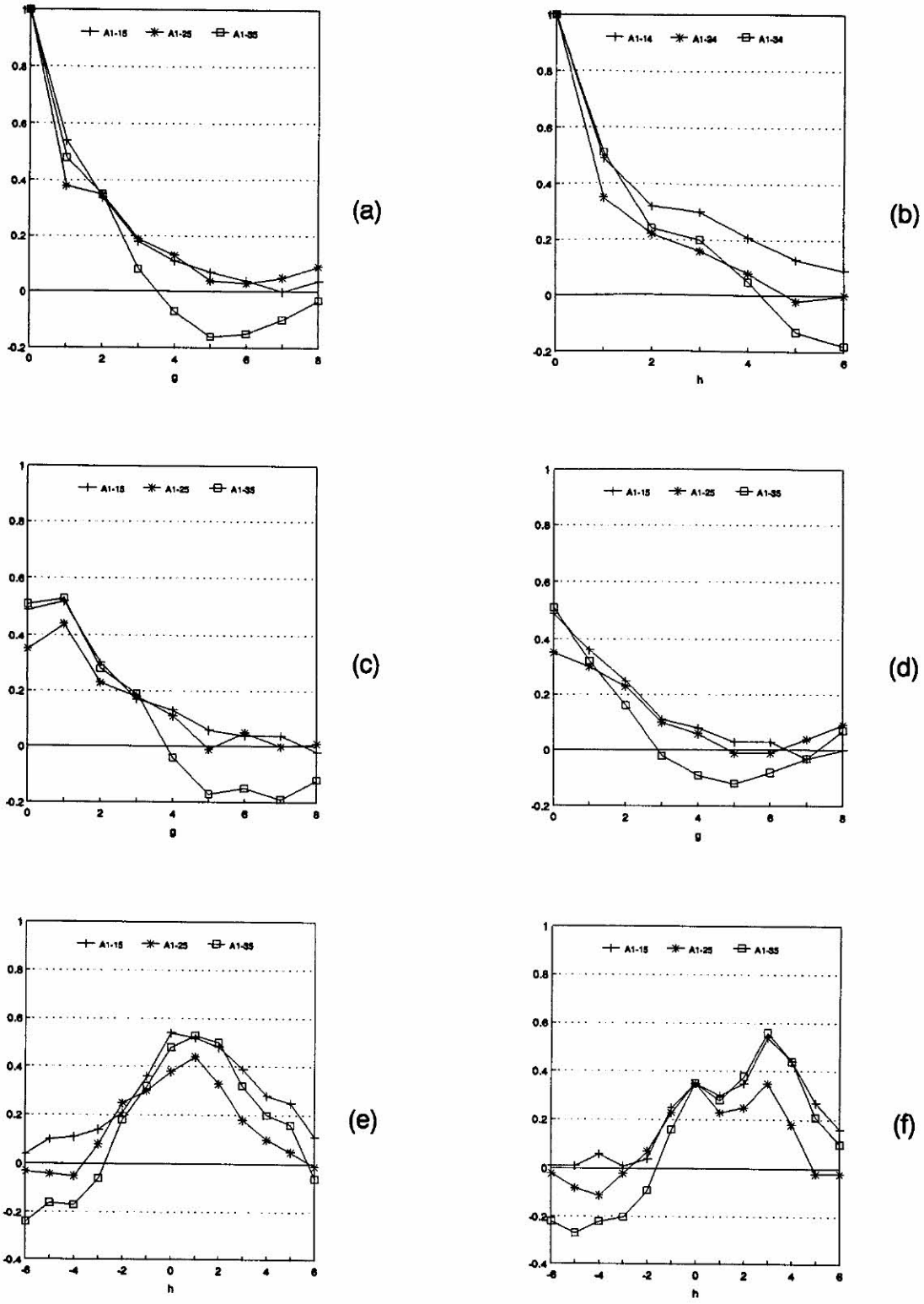

Figure 6.10: Sample autocorrelations for the data in area A_1, in band 5, acquired at the different passages: (a) $r_{g,0}$, (b) $r_{0,h}$, (c) $r_{g,1}$, (d) $r_{g,-1}$, (e) $r_{1,h}$, (f) $r_{2,h}$, $g = 0, \ldots 8$, $h = 0, \ldots, 6$.

As for the data in bands 3 and 4, the data in area A_1, in band 5, display some sort of anisotropy, characterized by larger values of the autocorrelations at lags (g, h) than at lags $(g, -h)$.

Area A_2 is very heterogeneous, and comprises mainly soil with intense moisture, and soil with low density vegetation.

The plots for the data in $A_2(14)$ and $A_2(24)$, and in $A_2(14)$ and $A_2(34)$, are given in Figure E.5 (a) and (b) in Appendix E, respectively. The figure shows that data in the top third of $A_2(24)$, and $A_2(34)$ are homogeneous, [especially those in $A_2(34)$], and that there are significant differences between the data in the six first lines of areas $A_2(34)$ [and $A_2(24)$, to a lesser extent], and $A_2(14)$.

The plots of the data in areas $A_2(15)$ and $A_2(25)$, and in $A_2(15)$ and $A_2(35)$ are given in Figure E.6 (a) and (b), respectively, in Appendix E. From the plot it can be observed that in area $A_2(25)$, the data in sites 1 to 90 are very homogeneous, but that from site 90 onwards, large variations occur between the values of the pixels that are geographically close.The pixel values in the areas of intense moisture are very low (vary from 7 to 19), whilst the pixel values corresponding to soil with low density vegetation (shown in cyan, in Figure 6.5) vary from approximately 48 to 69. At the bottom left of the area, higher pixel values, associated with a small patch of bare soil (shown in green), vary from 74 to 90.

The main differences between the data in areas $A_2(15)$ and $A_2(25)$ occur in the first six lines (from sites 1 to 90). From Figures 6.4 and 6.5 it can be seen that part of the area delimited by these lines, in area $A_2(15)$ has more moisture than the corresponding area in $A_2(25)$. This explains the lower pixel values observed in Figure E.6, in Appendix E, between sites 1 to 90. Note that in the rest of the area the data in $A_2(15)$ and $A_2(25)$ are similar.

Since the features in area A_2 are more pronounced in the north east direction – see Figure 6.7, this causes the sample autocorrelations to decay slower at lags (g, h), than at lags $(g, -h)$. This is also noticed in Figures 6.11 and 6.12 [(a and b), (c and d)], which display the plots of the sample autocorrelations for data in $A_2(d4)$ and $A_2(d5)$, $d = 1, 2, 3$, respectively, to some selected lags.

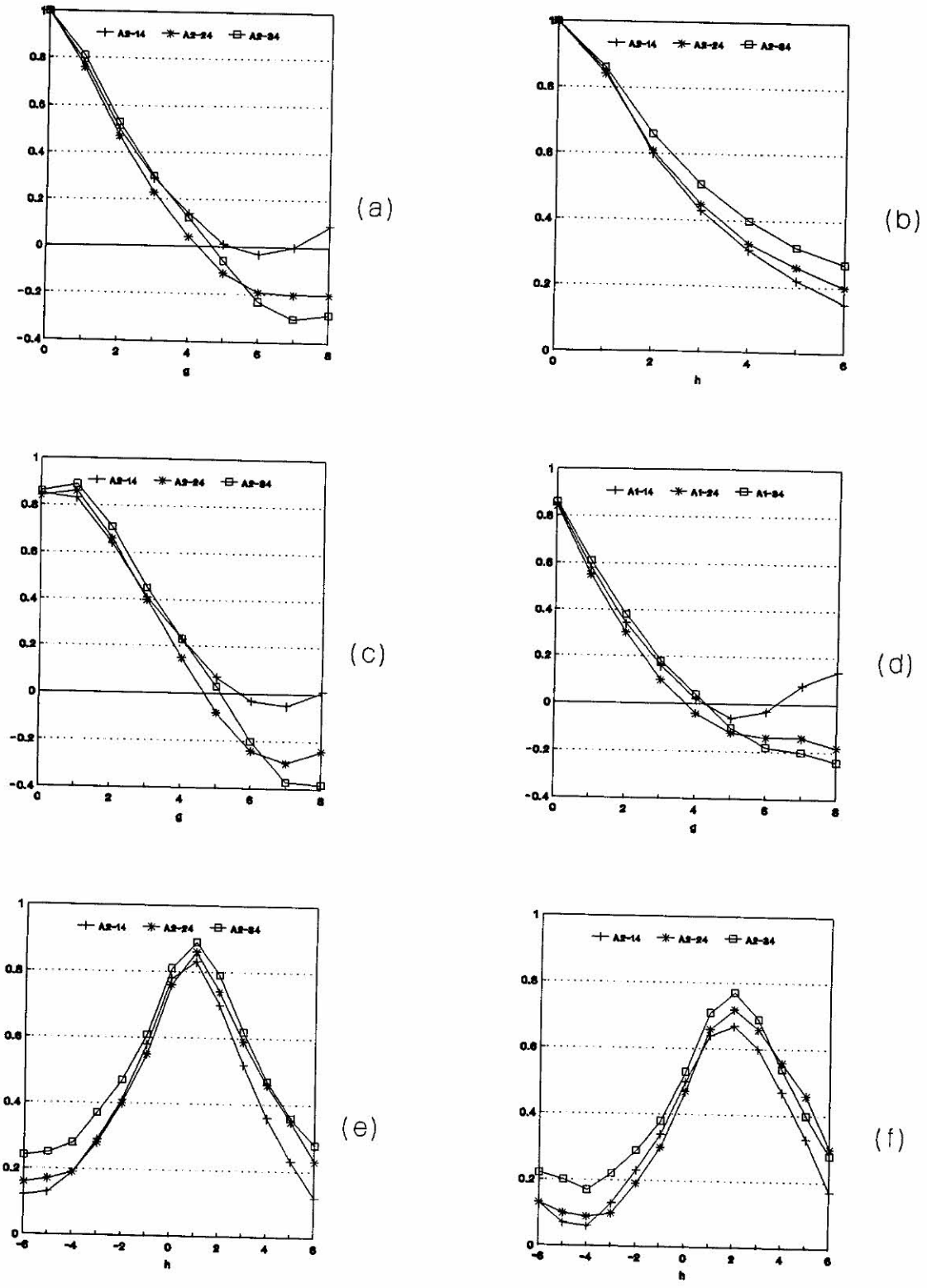

Figure 6.11: Sample autocorrelations for the data in area A_2, in band 4, acquired at the different passages: (a) $r_{g,0}$, (b) $r_{0,h}$, (c) $r_{g,1}$, (d) $r_{g,-1}$, (e) $r_{1,h}$, (f) $r_{2,h}$, $g = 0, \ldots 8$, $h = 0, \ldots, 6$.

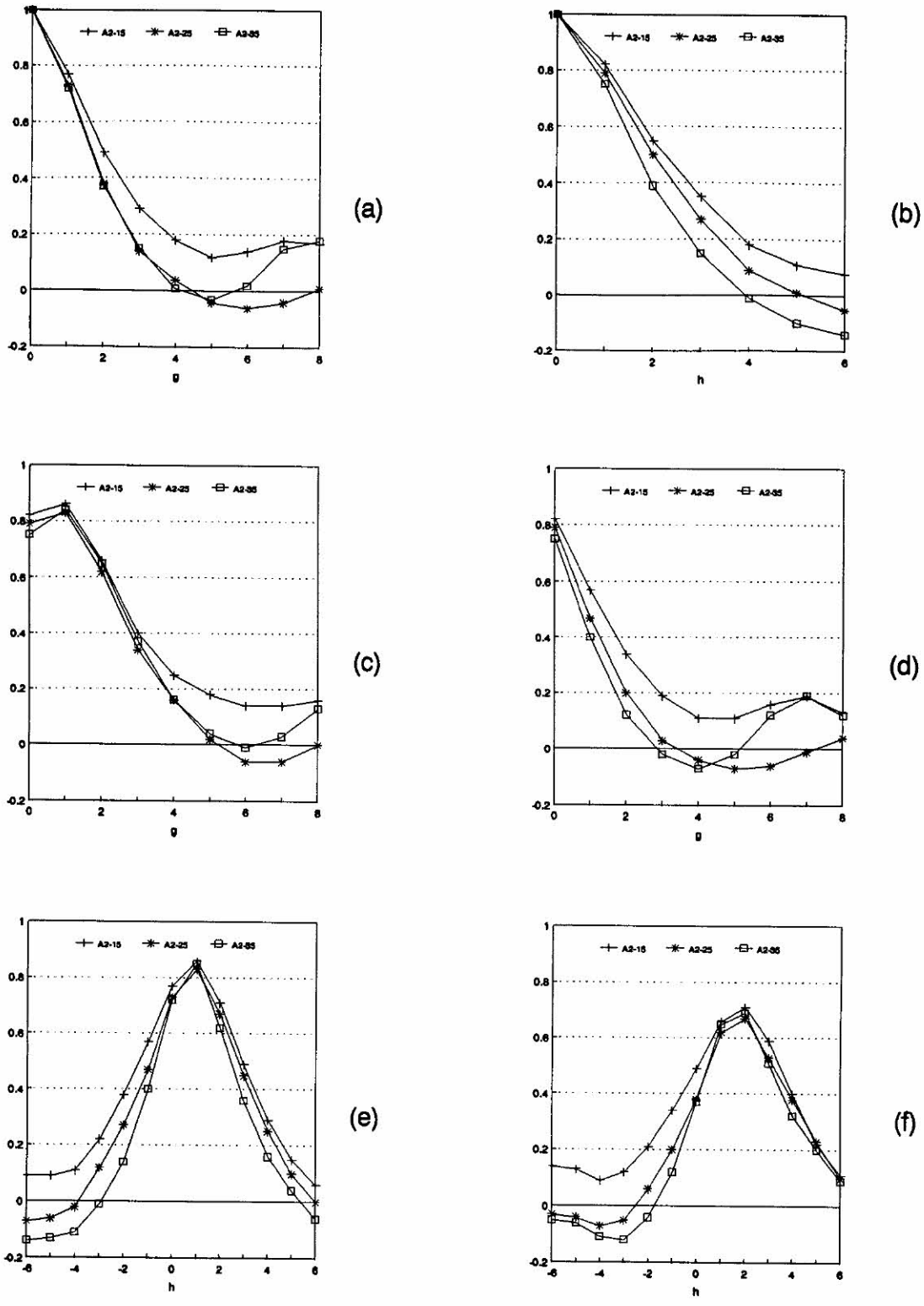

Figure 6.12: Sample autocorrelations for the data in area A_2, in band 5, acquired at the different passages: (a) $r_{g,0}$, (b) $r_{0,h}$, (c) $r_{g,1}$, (d) $r_{g,-1}$, (e) $r_{1,h}$, (f) $r_{2,h}$, $g = 0, \ldots 8$, $h = 0, \ldots, 6$.

6.3.3 Selected Areas from D_2

The configuration of the missing values displayed in Figure 6.13, has been simulated in three sub-images from D_2. In each of the three sub-images, an area of 25 by 25 pixels containing the missing values was extracted, as shown in Figure 6.13, and treated independently from the rest of the sub-image.

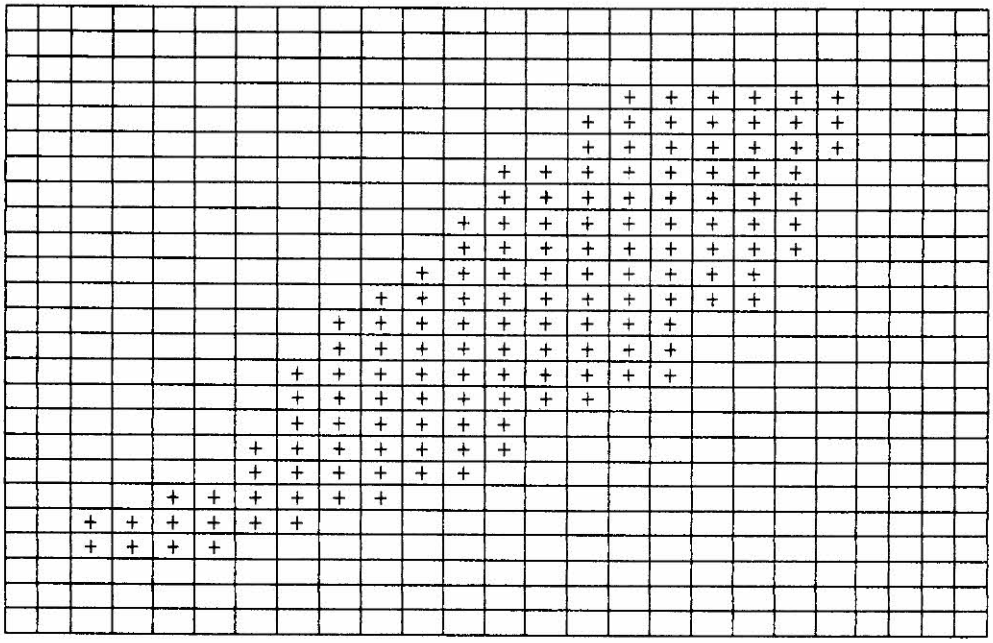

Figure 6.13: Configuration of the missing sites in areas A_3 and A_4.

On two sub-images [$D_2(25)$ and $D_2(45)$], the area surrounding the missing sites, A_3, is bounded by lines 53 and 77, and columns 61 and 85 on the original sub-images. The area is shown in sub-images $D_2(25)$ and $D_2(45)$ in Figures 6.14 and 6.15 , respectively.

From these figures it can be seen that area A_3 is fairly homogeneous in both sub-images, consisting only of low density vegetation (indicated as **C**, in Figure 3.17).

In another sub-image [$D_2(64)$], the missing sites are enclosed in the area delimited by lines 17 and 41, and columns 1 and 25 (A_4) on the original sub-image. The area is shown in Figure 6.16.

Area A_4 consists of low density vegetation (marked as **1** in Figure 6.16) and reforestation (marked as **2** in Figure 6.16). The boundary between the two types of land cover is drawn in the figure.

Let $A_3(db)$ and $A_4(db)$ denote the areas in sub-images from D_2 acquired at time d, in band b, which are bounded by lines 53 and 77, and columns 61 and 85, and by lines 17 and 41, and columns 1 and 25, respectively, where $d = 1,2,3,4,5,6$ refers to the dates 09/09/90, 08/08/90, 20/07/89, 04/07/89, 17/07/88, and 01/07/88, respectively, and $b = 4,5$ refers to bands 4 and 5, respectively.

The number of missing values in areas A_3 and A_4 is 144, corresponding to approximately 23% of the total number of sites in each area.

Descriptive statistics of the data in areas A_3 and A_4, in the sub-images acquired at close passages, are given in Table 6.2. The statistics are given for the complete data, and include the mean, standard deviation (stdev), the minimum and maximum [(m,M)], and the range.

Table 6.2: Descriptive statistics of the data in areas A_3 and A_4, in sub-images acquired at a close passage, in the same band.

Area	Mean	Stdev	(m,M)	Range
$A_3(15)$	112.81	8.44	(97,140)	43
$A_3(25)$	99.39	5.68	(85,117)	32
$A_3(35)$	90.67	7.84	(75,123)	48
$A_3(45)$	73.61	6.41	(60,97)	37
$A_4(54)$	41.12	5.27	(30,53)	23
$A_4(64)$	36.89	3.35	(29,45)	16

The correlations, $rd^l_{db,eb}$, between the complete data in areas $A_l(db)$ and $A_l(eb)$, $l = 3,4$, acquired at different passages are: $rd^3_{15,25} = 0.724; rd^3_{35,45} = 0.858$; and $rd^4_{54,64} = 0.808$. As for the selected areas in D_1, the statistics for the complete, and the incomplete data, are similar. The maximum difference between the correlations for the complete, and the incomplete data is 0.014.

The plots of the data in areas $A_3(15)$ and $A_3(25)$, and $A_3(35)$ and $A_3(45)$ are given in Figures E.7 and E.8, respectively, in Appendix E.

Data in areas $A_3(25)$ are very homogeneous, as can be seen from Figure E.7. The largest variation between the values of the pixels in the immediate neighbourhood of any site in the area (consisting of the sites that are adjacent horizontal,

vertical, and diagonal) is 9.

Area $A_3(45)$ is reasonably homogeneous, but larger variations between neighbouring pixels occur. For instance, in the intersection of lines 22 and 23, with columns 1 to 5, the pixel values are as follows:

	Column				
Line	1	2	3	4	5
Line 22	90	97	84	83	81
Line 23	80	74	67	69	72

Because area A_3 comprises only one type of ground cover, the differences in the data, observed at different passages, are possibly due to the different degrees of soil moisture. Note for instance, the similar pattern of the data in Figure E.8, and the consistently higher radiance values in $A_3(35)$, rather than in $A_3(45)$, suggesting greater soil moisture on the passage at 20/07/89, than at 04/07/89.

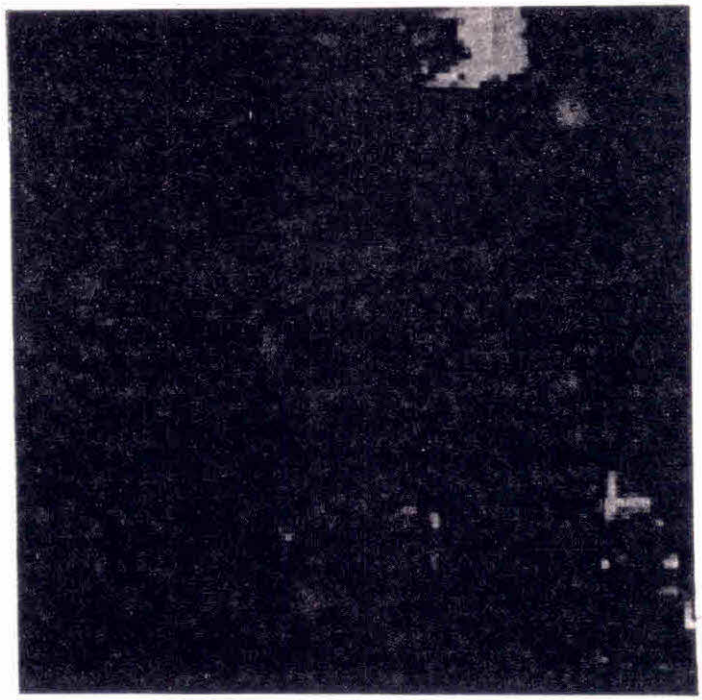

Figure 6.14: Location of area A_3 in sub-image $D_2(25)$.

Plots of the sample autocorrelations at some selected lags for data in $A_3(15)$ and $A_3(25)$, and $A_3(35)$ and $A_3(45)$ are given in Figures 6.17 and 6.18, respectively. From Figures 6.17 and 6.18 it can be seen that $r_{g,h} \approx r_{g,-h}$, which suggests that data in A_3, is approximately isotropic, on both passages.

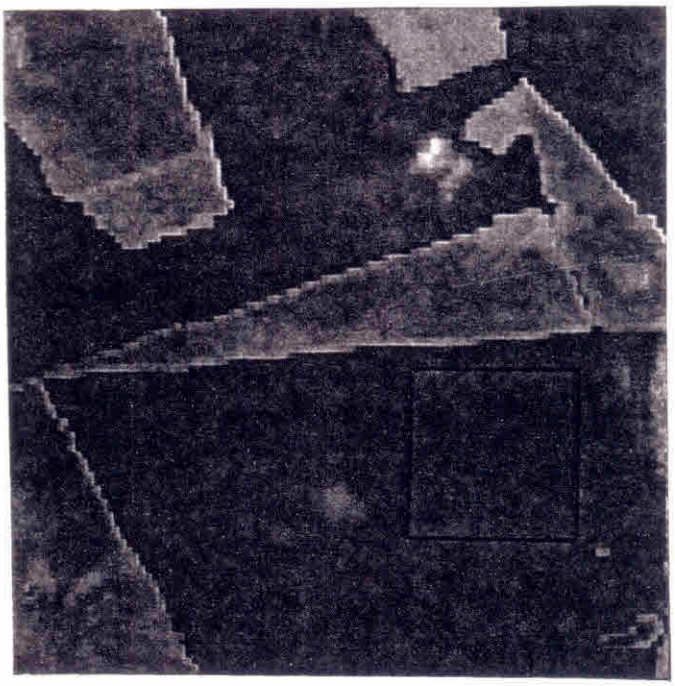

Figure 6.15: Location of area A_3 in sub-image $D_2(45)$.

Figure 6.16: Location of area A_4 in sub-image $D_2(64)$.

Figure 6.15: Location of area A_3 in sub-image $D_2(45)$.

Figure 6.16: Location of area A_4 in sub-image $D_2(64)$.

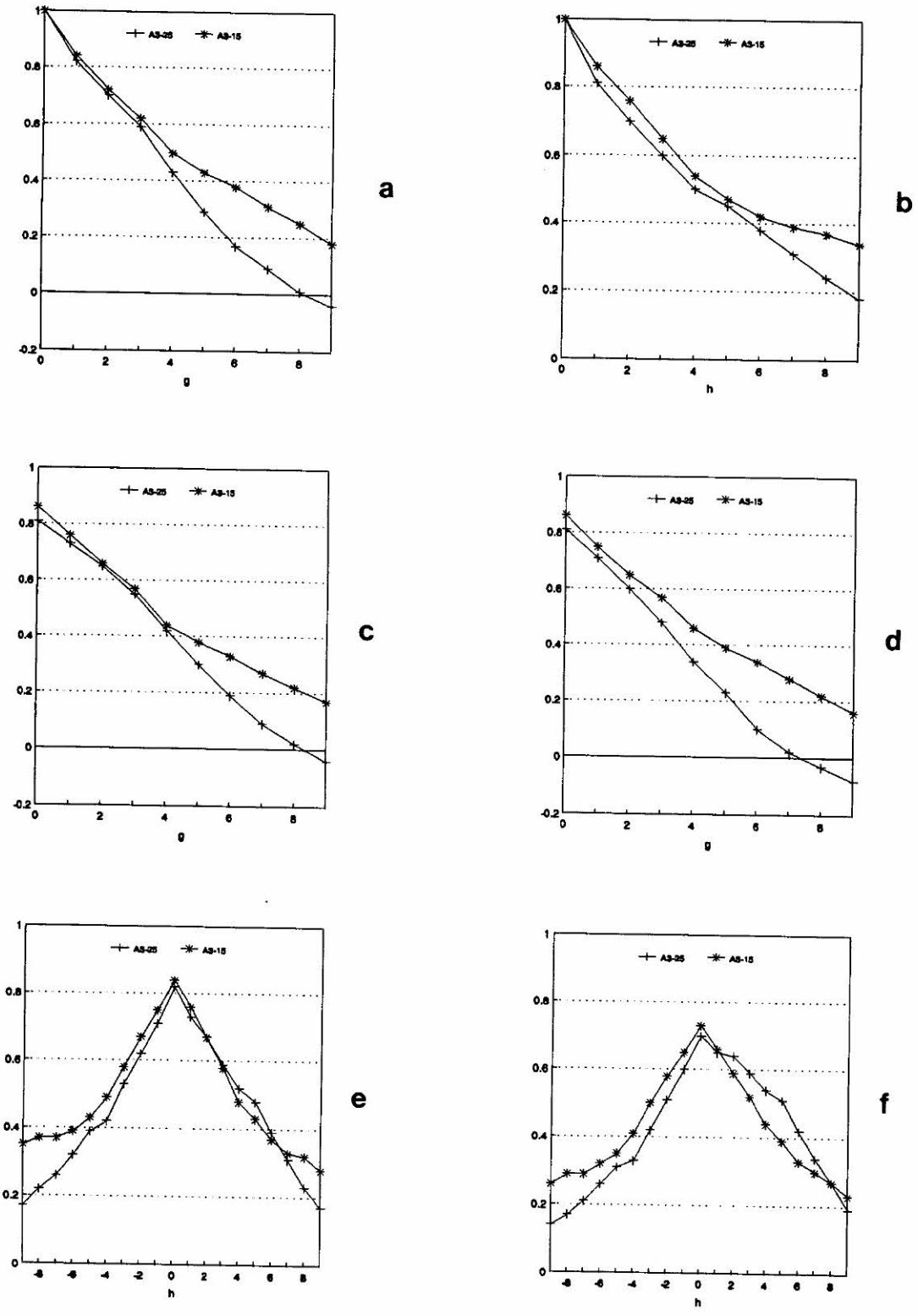

Figure 6.17: Sample autocorrelations for the data in areas $A_3(15)$ and $A_3(25)$: (a) $r_{g,0}$, (b) $r_{0,h}$, (c) $r_{g,1}$, (d) $r_{g,-1}$, (e) $r_{1,h}$, (f) $r_{2,h}$, $g = 0, \ldots 8$, $h = 0, \ldots, 8$.

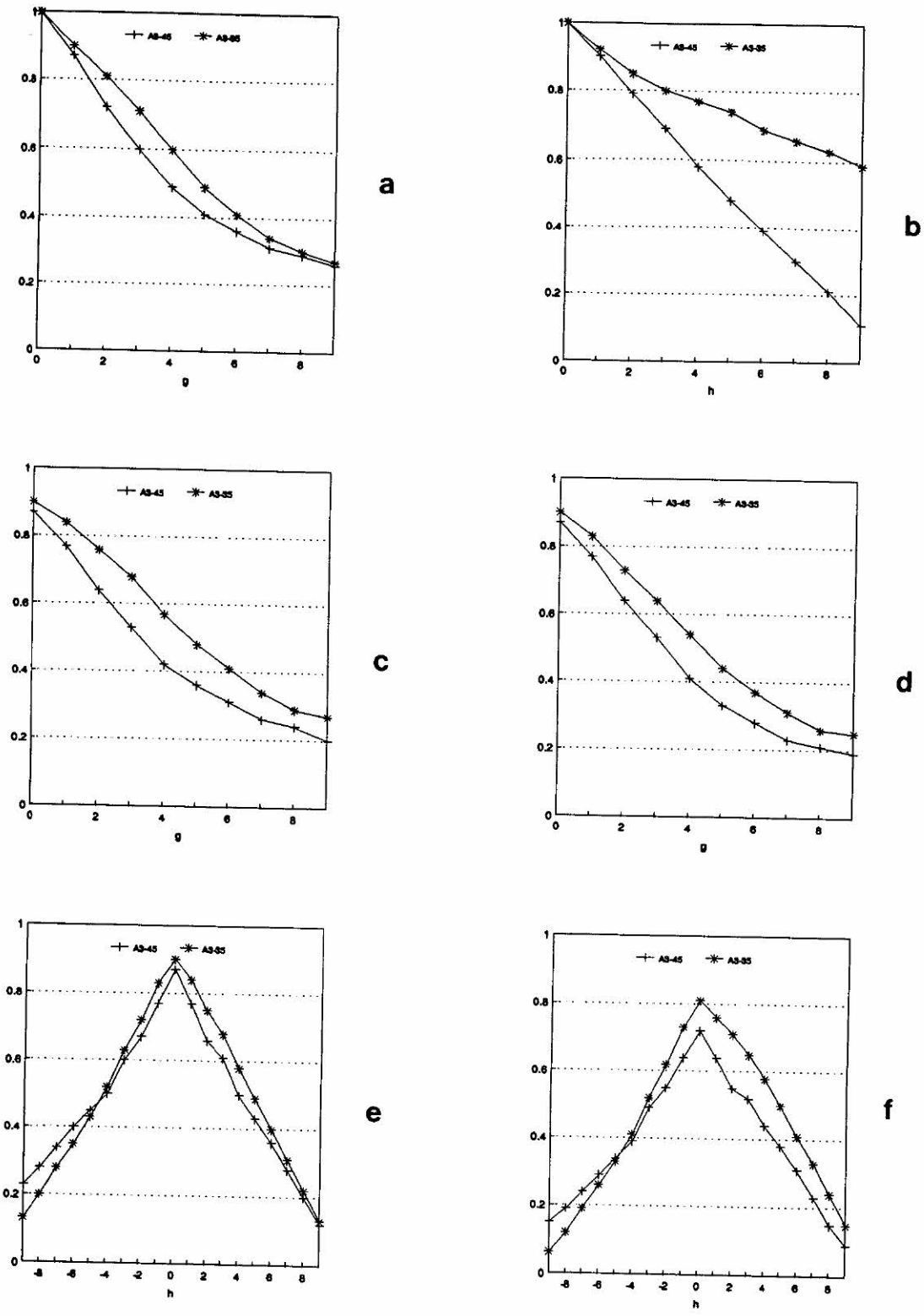

Figure 6.18: Sample autocorrelations for the data in areas $A_3(35)$ and $A_3(45)$: (a) $r_{g,0}$, (b) $r_{0,h}$, (c) $r_{g,1}$, (d) $r_{g,-1}$, (e) $r_{1,h}$, (f) $r_{2,h}$, $g = 0, \ldots 8$, $h = 0, \ldots, 8$.

The plot of the data in areas $A_4(54)$ and $A_4(64)$ is given in Figure E.9, in Appendix E.

Data in area $A_4(64)$ are very homogeneous, and despite the boundary between the reforested area and the soil with low density vegetation, no contrasting variations between the pixel values occur in band 4. The largest variation between a pixel value associated with soil, and another associated with reforestation is 6.

Figure E.9 also shows that data in areas $A_4(54)$ and $A_4(64)$ are most dissimilar in the last seven rows (from site 451 onward).

The plot of the sample autocorrelations for the data in areas $A_4(54)$ and $A_4(64)$, is given in Figure 6.19.

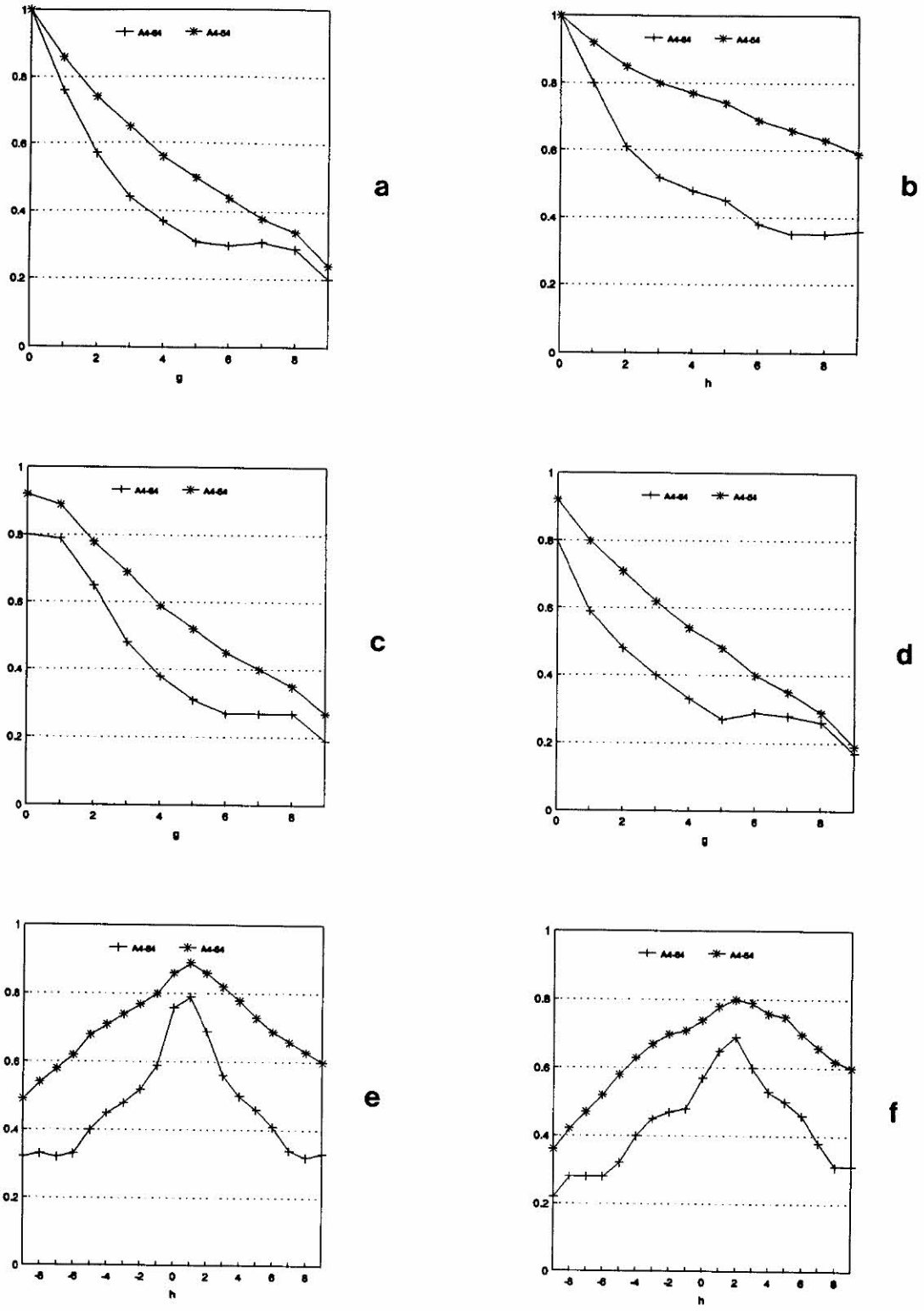

Figure 6.19: Sample autocorrelations for the data in areas $A_4(54)$ and $A_4(64)$: (a) $r_{g,0}$, (b) $r_{0,h}$, (c) $r_{g,1}$, (d) $r_{g,-1}$, (e) $r_{1,h}$, (f) $r_{2,h}$, $g = 0, \ldots 8$, $h = 0, \ldots, 8$.

6.4 Results for D_1 and D_2.

In this section, the results (numerical and visual) for all methods are presented and discussed, for each simulated area from D_1 and D_2.

Whenever there is a choice of the template date to be used with the methods, let CL-kH denote the method that uses the higher correlated template, and CL-kL, the method that uses the less correlated template date, $k = 2, 3, 4$.

In order to visually evaluate the methods, the following information is given in Figures 6.20 to 6.25:

1. (a) a frame containing: 1. the original area; 2. simulated area; test images for the following methods: 3. CL-1; 4. CL-2; 5. CL-3; 6. CL-4; 7. CL-5; 8. CL-6; and 9. CL-8.

2. (b) a frame containing the residual images for methods: 1. CL-1; 2. CL-2; 3. CL-3; 4. CL-4; 5. CL-5; 6. CL-6; and 7. CL-8; and

3. (c) the frame with the difference images, using data from corresponding areas, in sub-images acquired in the same band, at different passages.

Since the test images, and the residual images, are displayed in the same contrast, the properties of each of the methods can be examined. The visual results obtained for methods CL-7, CL-9, and CL-10 are not presented, due to their similarity with those for method CL-8.

Although none of the photographs in this chapter include the histogram and the range of colours, note that yellow, in the residual images, indicate the largest positive residual, whereas magenta is associated with the largest negative residual. The range of colours is usually compressed to enhance the differences. Thus, yellow in one image may be associated with residuals of approximately 12 [e.g., those in Figure 6.21 (b)], whilst in another image it may be associated with residuals of approximately 30 [e.g., those in Figure 6.25 (b)].

6.4.1 Results for area A_1.

Table 6.3 gives the values for SRMS, CCOR, and SRAN, for each method, in area A_1.

The values for ACC, the proportion of pixels estimated within a small error, are also included in the table, although not used when evaluating the overall performance of the methods. The error is usually assumed to be ± 2 grey levels, in area $A_1(13)$, and ± 4 grey levels in areas $A_1(14)$, $A_1(15)$ and $A_1(25)$.

Table 6.3: Values for SRMS ($\times 100$), CCOR ($\times 100$), ACC ($\times 100$), and SRAN, on $A_1(13)$,$A_1(14)$,$A_1(15)$, and $A_1(25)$.

Methods	$A_1(13)$					$A_1(14)$				
	SRMS	CCOR	ACC	SRAN	(m,M)	SRMS	CCOR	ACC	SRAN	(m,M)
$CL-1$	70	30	30	3.57	$(-4,4)$	70	25	32	4.08	$(-13,13)$
$CL-2H$	84	32	38	5.36	$(-4,8)$	43	08	19	2.98	$(-9,10)$
$CL-2L$	80	31	40	3.57	$(-3,5)$	64	18	34	3.61	$(-9,14)$
$CL-3H$	78	32	44	4.46	$(-4,6)$	43	08	20	2.82	$(-7,11)$
$CL-3L$	75	31	43	3.12	$(-4,3)$	62	18	32	3.29	$(-7,14)$
$CL-4H$	94	43	52	7.14	$(-5,11)$	45	09	20	3.45	$(-11,11)$
$CL-4L$	91	46	52	4.02	$(-5,4)$	67	20	28	4.23	$(-12,15)$
$CL-5$	67	22	30	3.13	$(-4,3)$	43	08	21	3.14	$(-8,12)$
$CL-6$	74	26	33	3.57	$(-3,5)$	47	08	23	3.14	$(-10,10)$
$CL-7$	62	22	29	3.57	$(-4,4)$	65	18	37	3.92	$(-10,15)$
$CL-8$	62	22	31	3.13	$(-4,3)$	58	15	26	4.23	$(-12,15)$
$CL-9$	64	23	30	3.57	$(-4,4)$	65	18	36	3.92	$(-10,15)$
$CL-10$	64	23	30	3.57	$(-4,4)$	65	18	36	3.92	$(-10,15)$
Method	$A_1(15)$					$A_1(25)$				
$CL-1$	86	61	35	4.58	$(-8,9)$	87	56	20	4.08	$(-8,5)$
$CL-2H$	93	47	33	6.47	$(-7,17)$	92	47	21	6.58	$(-14,7)$
$CL-2L$	97	47	31	6.47	$(-13,11)$	96	45	33	5.33	$(-9,8)$
$CL-3H$	82	47	39	5.39	$(-7,13)$	82	47	19	5.96	$(-13,6)$
$CL-3L$	82	47	30	5.12	$(-8,11)$	81	45	31	4.39	$(-8,6)$
$CL-4H$	90	47	38	5.93	$(-8,14)$	95	47	30	6.27	$(-12,8)$
$CL-4L$	112	58	36	6.74	$(-11,14)$	107	53	33	6.27	$(-10,10)$
$CL-5$	77	40	24	5.12	$(-7,12)$	76	39	18	5.33	$(-11,6)$
$CL-6$	85	45	22	5.12	$(-7,12)$	93	47	30	6.27	$(-14,6)$
$CL-7$	81	54	29	4.31	$(-11,5)$	85	52	30[a]	4.08	$(-9,4)$
$CL-8$	92	66	37	5.93	$(-13,9)$	97	57	39[a]	3.76	$(-8,4)$
$CL-9$	82	56	30	4.31	$(-11,5)$	85	51	28[a]	4.08	$(-9,4)$
$CL-10$	82	55	29	4.31	$(-11,5)$	85	51	28[a]	4.08	$(-9,4)$

[a] ± 3 grey levels

Table 6.4 gives the maximum likelihood estimates of β, of the standard deviation, and the function value divided by 100, which are respectively denoted by $\hat{\beta}$, $\hat{\sigma}$, and L.

Table 6.4: $L, \hat{\beta}$, and $\hat{\sigma}$ for methods CL-7 to CL-10, in area A_1.

	$A_1(13)$			$A_1(14)$		
Method	L	$\hat{\beta}$	$\hat{\sigma}$	L	$\hat{\beta}$	$\hat{\sigma}$
CL-7	22.18	0.2527	1.21	28.24	0.2531	2.90
CL-8	19.77	0.2535	2.20	27.13	0.2416	2.65
CL-9	22.01	0.2526	1.18	28.14	0.2529	2.86
CL-10	21.84	0.2528	1.15	27.99	0.2526	2.83
Method	A1(15)			A1(25)		
CL-7	26.20	0.2519	2.17	26.08	0.2462	2.16
CL-8	24.55	0.2243	1.90	24.00	0.2134	1.85
CL-9	25.72	0.2376	2.07	25.75	0.2244	2.13
CL-10	25.70	0.2307	2.06	25.70	0.2300	2.11

From Table 6.4 it can be noted that the results from the different methods are very similar, and that the value of β is near the boundary, possibly due to the presence of some features on the areas (road), which makes the data non homogeneous. The maximum likelihood estimates of the parameters of the second-order surface [that is, $\hat{\alpha}_{00}$, $\hat{\alpha}_{01}$, $\hat{\alpha}_{10}$, $\hat{\alpha}_{02}$, $\hat{\alpha}_{20}$, and $\hat{\alpha}_{11}$] are given below.

1p-CART						
Area	$\hat{\alpha}_{00}$	$\hat{\alpha}_{01}$	$\hat{\alpha}_{10}$	$\hat{\alpha}_{02}$	$\hat{\alpha}_{20}$	$\hat{\alpha}_{11}$
$A_1(13)$	26.30	−0.09	−0.10	0.00	0.00	0.02
$A_1(14)$	59.67	−0.72	−0.07	−0.01	0.01	−0.01
$A_1(15)$	57.23	−0.33	0.07	−0.01	0.01	−0.01
$A_1(25)$	53.71	−0.23	−0.13	−0.05	0.00	0.03

The estimates of the parameters of a third-order trend surface, using $A_1(13)$, $[\hat{\alpha_{00}}, \hat{\alpha_{01}}, \hat{\alpha_{11}}, \hat{\alpha_{02}}, \hat{\alpha_{20}}, \hat{\alpha_{12}}, \hat{\alpha_{21}}, \hat{\alpha_{03}}, \hat{\alpha_{30}}]'$ are 25.45, 0.33, -0.14, -0.07, 0.02, -0.00, 0.04, 0.00, and 0.00. These estimates, and those for the second-order surface

given above indicate that the fitted surfaces are very smooth (that is, the means are approximately constant).

The test images, residual images, and 'cut' images for methods CL-1, CL-kH, $k = 2,\ldots,6$, and CL-8, for areas $A_1(13)$, $A_1(14)$, $A_1(15)$ and $A_1(25)$, are displayed in Figures 6.20 to 6.23, respectively. In Figure 6.20 the numbers associated with each image (original, simulated, and the test images for each method) are displayed. The residual images in this figure are also numbered according to their corresponding methods. The same sequence of presentation is maintained in the other figures.

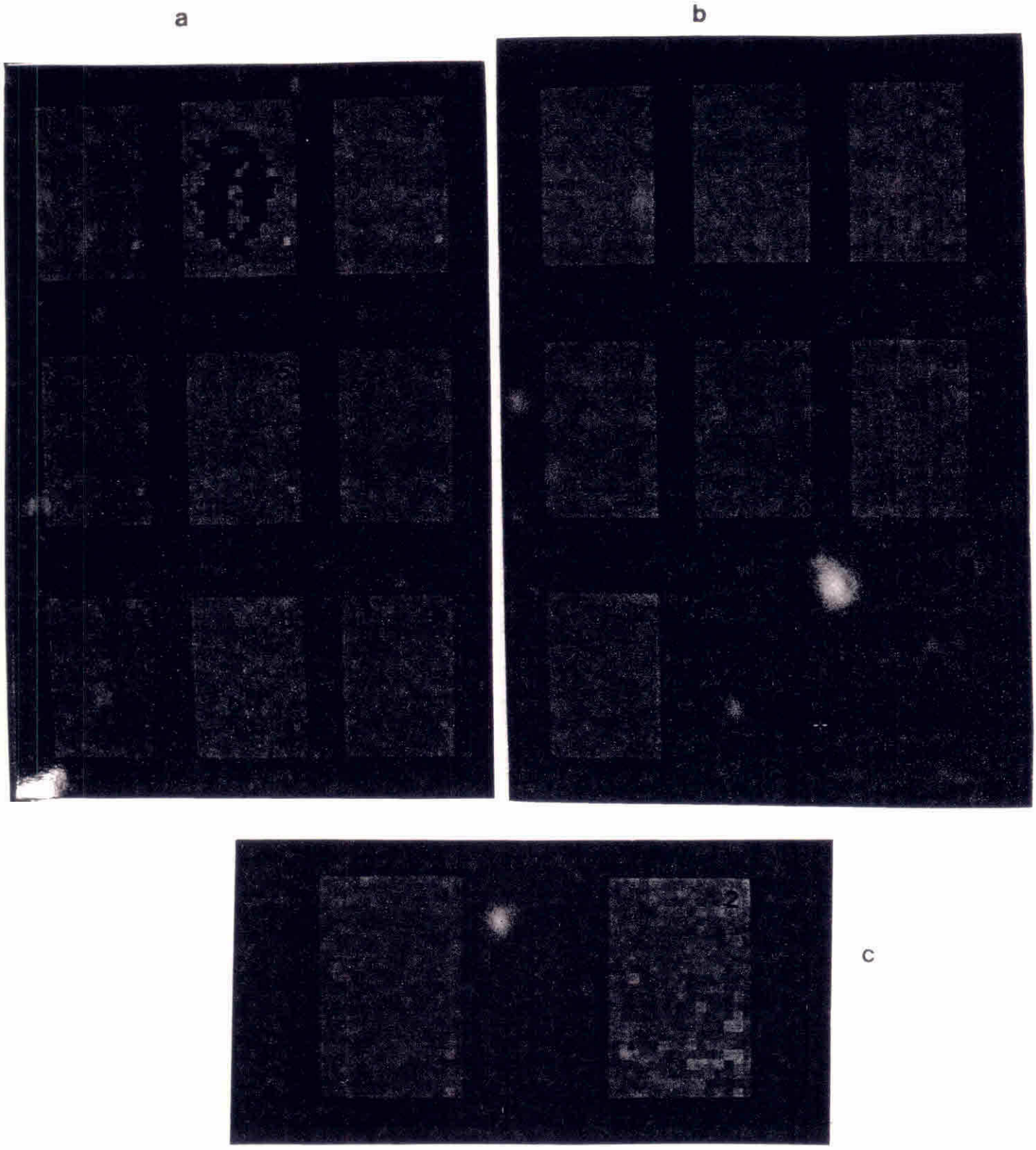

Figure 6.20: (a) 1. Original area $A_1(13)$; 2. Simulated 'clouded' area; Test images for methods: 3. CL-1; 4. CL-2H; 5. CL-3H; 6. CL-4H; 7. CL-5; 8. CL-6H; 9. CL-8; (b) Residual images for: 1. CL-1; 2. CL-2H; 3. CL-3H; 4. CL-4H; 5. CL-5; 6. CL-6H; 7. CL-8; (c) Difference images: 1. $A_1(13) - A_1(23)$ (+128); 2. $A_1(13) - A_1(33)$ (+128).

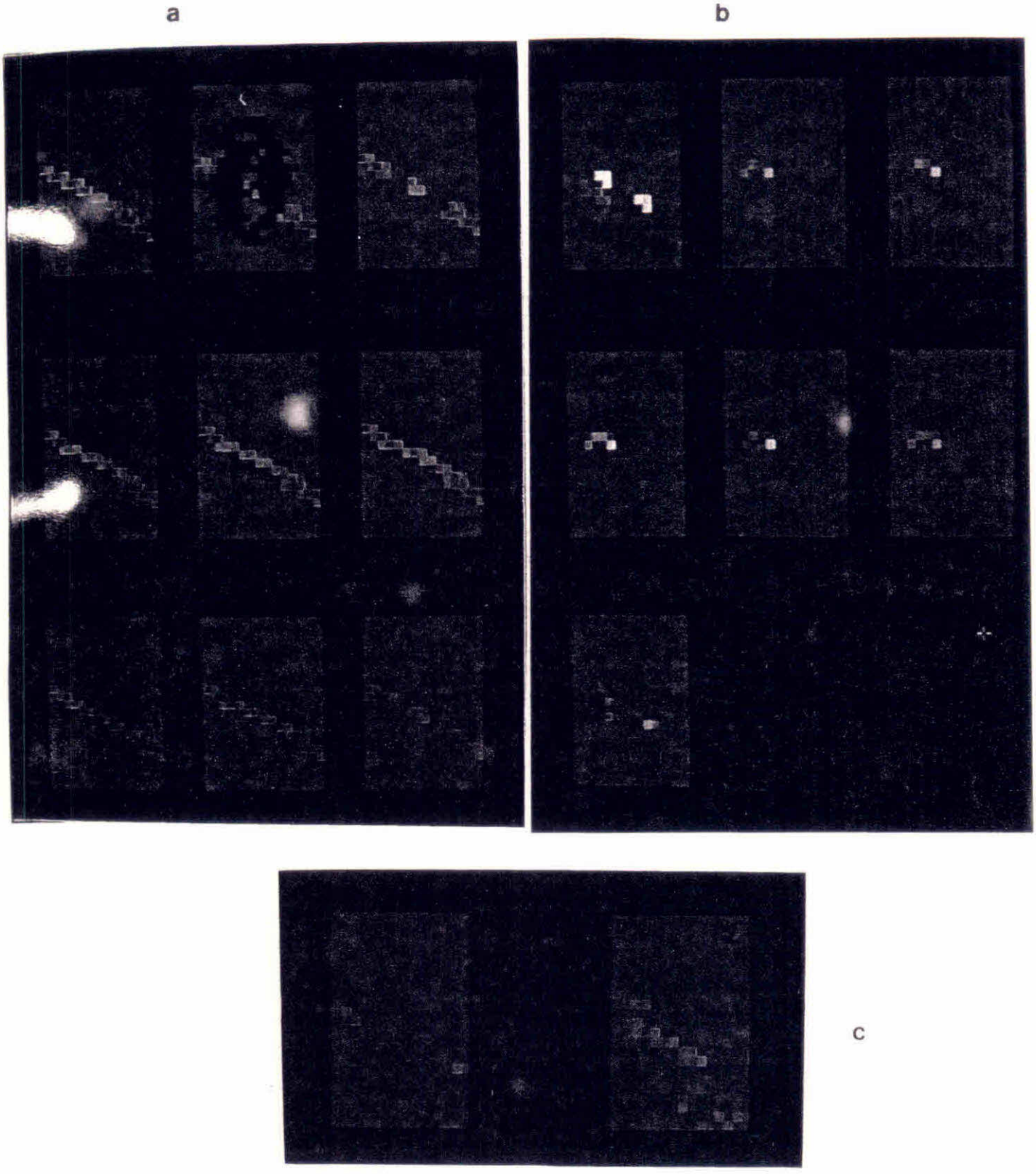

Figure 6.21: (a) Area $A_1(14)$, simulated 'clouded' area, and the test images for area $A_1(14)$, displayed in the same order as in Figure 6.20 (a); (b) Residual images, displayed in the same order as in Figure 6.20 (b); (c) Difference images: 1. $A_1(14) - A_1(24)$ (+128); 2. $A_1(14) - A_1(34)$ (+128).

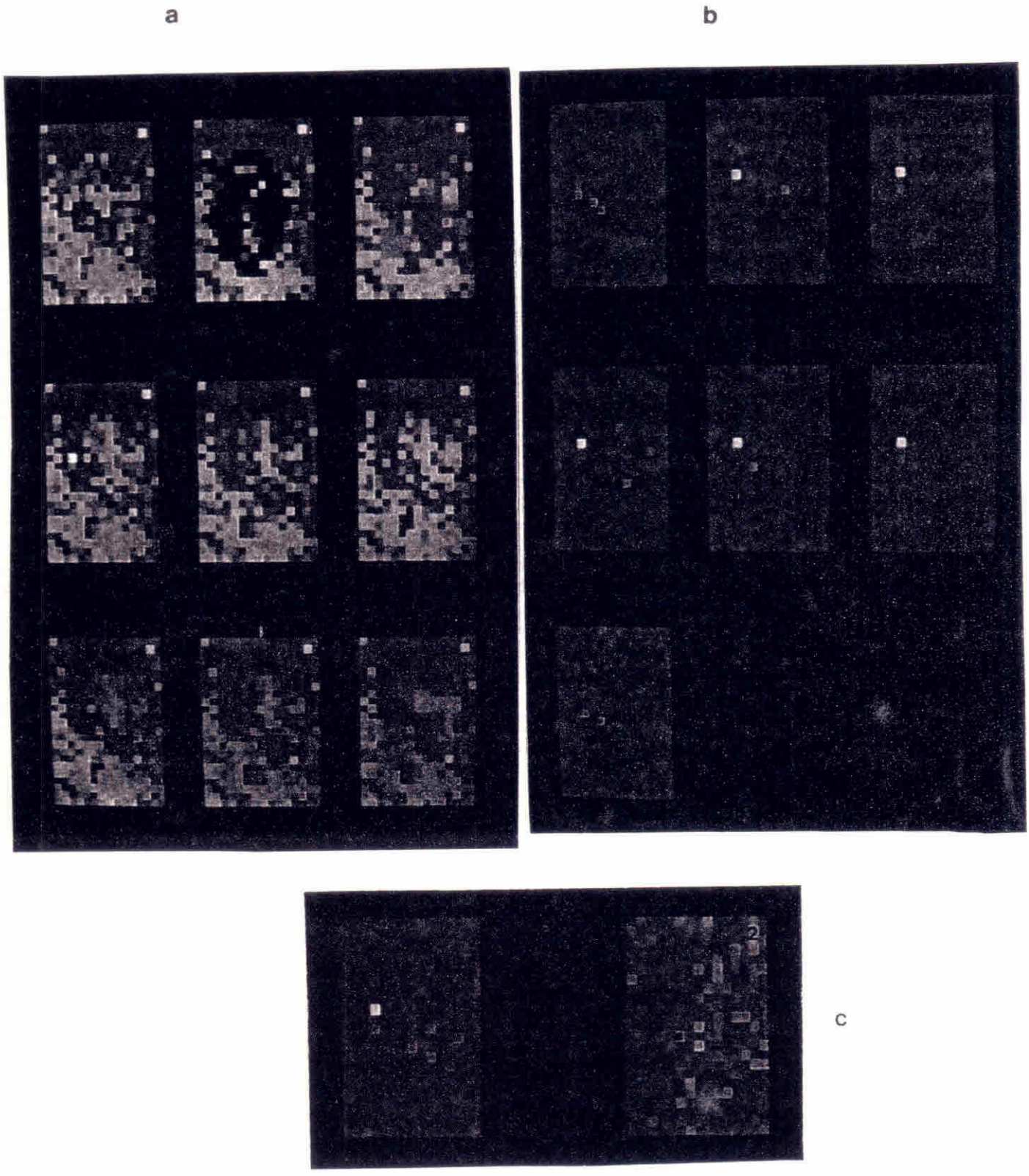

Figure 6.22: (a) Area $A_1(15)$, simulated 'clouded' area, and the test images for area $A_1(15)$, displayed in the same order as in Figure 6.20 (a); (b) Residual images, displayed in the same order as in Figure 6.20 (b); (c) Difference images: 1. $A_1(15) - A_1(25)$ (+128); 2. $A_1(15) - A_1(35)$ (+128).

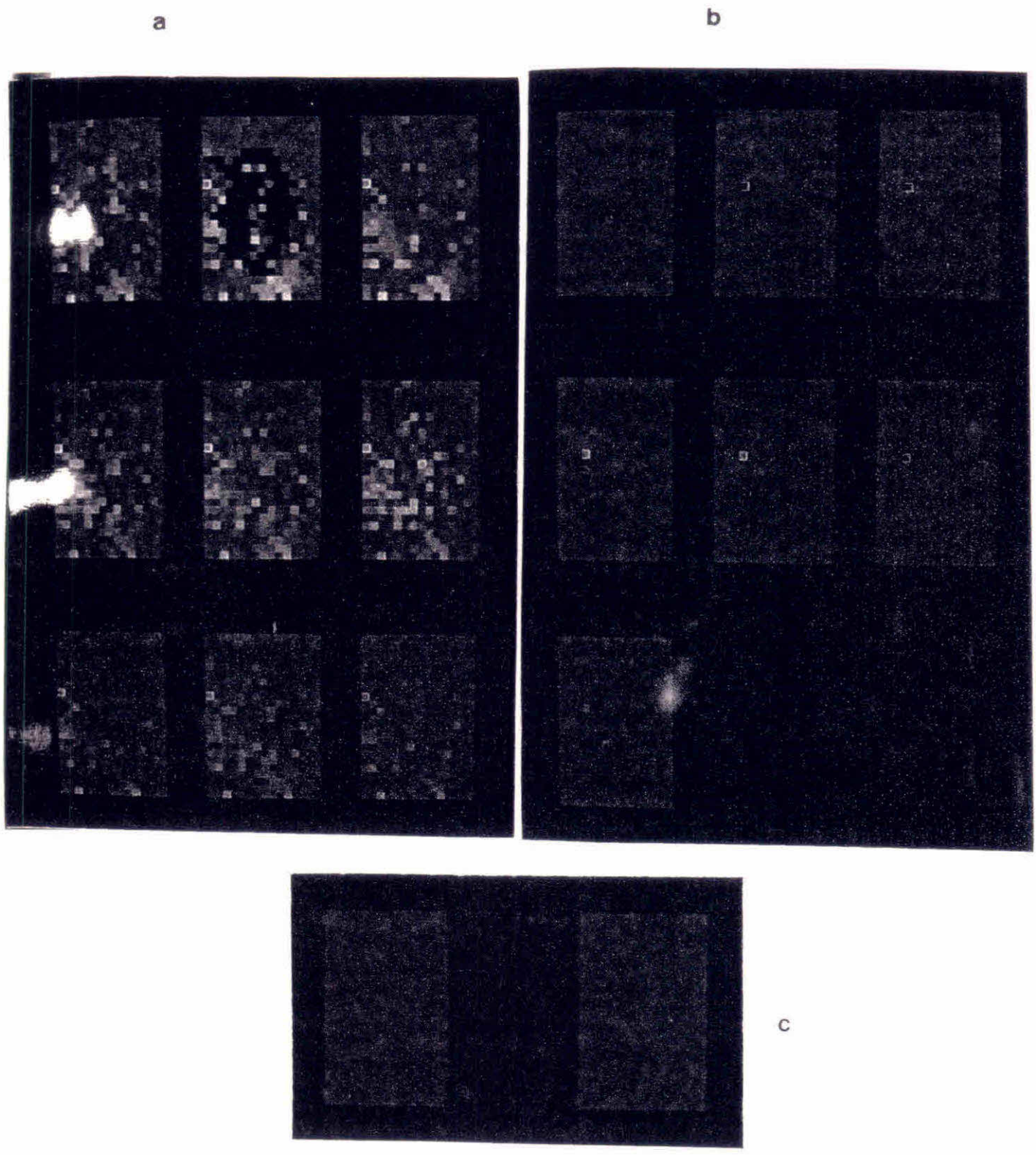

Figure 6.23: (a) Area $A_1(25)$, simulated 'clouded' area, and the test images for area $A_1(25)$, displayed in the same order as in Figure 6.20 (a); (b) Residual images, displayed in the same order as in Figure 6.20 (b); (c) Difference images: 1. $A_1(25) - A_1(15)$ (+128); 2. $A_1(25) - A_1(35)$ (+128).

The greater homogeneity of the data in the difference image in Figure 6.20 c (1), relative to c (2), suggests that fewer relative changes in land cover took place between the passages acquired at 10/07 and 24/06, than between those gathered at 10/07 and 08/06 This explains why the results are usually better (smaller SRMS, CCOR, and SRAN) for methods CL-2L, CL-3L, and CL-4L than for methods CL-2H, CL-3H, and CL-4H, respectively, in area $A_1(13)$.

In $A_1(14)$, the high range of the residuals obtained for method CL-1 and for the purely spatial methods is due to the inability of these methods to estimate well the missing values occurring along the road, and neighbouring areas.

From the sample autocorrelations for the data in $A_1(14)$, given in Figure 6.9 (a) and (b), it is noted that the autocorrelations decay slower in the vertical direction than in the horizontal direction, which might suggest that the use of a method that takes into account this particular behaviour of the data, (by weighting differently the pixel values in the horizontal, and in vertical direction, for instance), may be more appropriate.

From the homogeneity of the difference images in Figure 6.21 c (1) [$A_1(14)$-$A_1(24)$], and c (2) [$A_1(14)$-$A_1(34)$], it can be inferred that few changes occurred between these passages, and especially between those acquired at 10/07 and 24/06. Note that although there exists little difference between $rd^1_{14,24}$ (0.907) and $rd^1_{14,34}$ (0.859), the results obtained for methods CL-2H, CL-3H, and CL-4H are much better than those obtained for CL-2L, CL-3L, and CL-4L, respectively. This is probably due to the greater 'degree' of change that took place between the passages acquired at 10/07 and 08/06, than between those gathered at 10/07 and 24/06. The estimates of the missing values in sites above the road are usually better using CL-3L than CL-3H (note the more uniform difference image in Figure 6.21 c (2), than in c (1), in the area above the road), but are poorer elsewhere. Note that although the road is a permanent feature on this area, the difference image in Figure 6.21 c (2) indicates that changes in response from this particular feature seem to have occurred, between the two passages. As previously mentioned, there are usually 2 to 3 pixels which correspond to the road, in each column of the lattice representing area $A_1(14)$ – see Figure 6.3.2 (area A_1 in band 4), and Figures 6.2 (area A_1 in band 3), and 6.4 and 6.5 (area A_1 in band 5). In fact, the pixels shown in magenta, in Figure 6.3.2 are pixels associated to the road, whilst those neighbouring the road, shown in cyan, represent contaminated

pixels (road and wheat fields). The differences shown in Figure 6.21 c (2) are associated to differences in response from these contaminated pixels, from one passage to another.

The missing values occurring on permanent features in the area (such as roads, streams, etc.) are usually better estimated from methods that incorporate spatial-temporal information, than from purely spatial methods alone. Note, for instance, the estimates of the missing values in $A_1(14)$, from purely spatial methods, and from methods using a template date. Observation of the test images in Figure 6.21 (a) shows very clearly that the single band methods cannot estimate well the missing values occurring along the road, due to the lack of the 'reasonable' spatial information that these methods require. The distortions introduced by these methods, on this particular feature in the image, are readily observed in the figure.

In both areas $A_1(15)$ and $A_1(25)$, the purely spatial methods do not estimate well the missing values occurring along the road (shown in faint yellow, crossing the area from top left to bottom right). Note, especially in $A_1(25)$, that the estimates of the missing values on the narrow strip corresponding to the road, obtained for methods CL-1 and CL-8 are smoothed, causing the corresponding test images to appear 'blurred', as shown in Figures 6.22 (a) and 6.23 (a).

6.4.2 Results for area A_2.

The values of SRMS, CCOR, ACC, and SRAN, for areas $A_2(14)$ and $A_2(15)$ are given in Table 6.5. In the computation of ACC, the error is usually assumed to be ± 8 grey levels for $A_2(14)$, and ± 10 grey levels for $A_2(15)$.

Table 6.5: Values of SRMS (×100), CCOR (×100), ACC (×100), and SRAN in area A_2.

Method	$A_2(14)$					$A_2(15)$				
	SRMS	CCOR	ACC	SRAN	(m,M)	SRMS	CCOR	ACC	SRAN	(m,M)
$CL-1$	49	28	32[a]	2.43	$(-15,15)$	61	29	40	3.09	$(-24,30)$
$CL-2H$	87	51	48	3.16	$(-13,26)$	58	21	43	3.15	$(-28,27)$
$CL-2L$	89	50	46	3.56	$(-17,27)$	54	13	39	2.75	$(-25,23)$
$CL-3H$	67	51	37[a]	2.67	$(-12,21)$	53	21	36	3.03	$(-26,27)$
$CL-3L$	65	50	38[a]	2.67	$(-11,22)$	44	13	25	2.35	$(-19,22)$
$CL-4H$	60	36	23	2.91	$(-10,26)$	50	18	37	3.32	$(-24,34)$
$CL-4L$	59	33	25	2.91	$(-10,26)$	40	11	26	2.40	$(-19,23)$
$CL-5$	68	52	39[a]	2.67	$(-12,21)$	43	13	25	2.29	$(-19,21)$
$CL-6$	70	50	37	2.83	$(-12,23)$	49	15	34	2.58	$(-21,24)$
$CL-7$	53	31	44[a]	2.43	$(-12,18)$	62	28	47	3.09	$(-21,33)$
$CL-8$	48	23	28[a]	2.51	$(-14,17)$	57	24	41	3.04	$(-25,28)$
$CL-9$	57	36	36[a]	2.83	$(-12,23)$	61	26	47	3.04	$(-21,32)$
$CL-10$	58	36	29	3.07	$(-12,26)$	61	27	46	3.04	$(-21,32)$

[a] ±8 grey levels

Table 6.6 gives the maximum likelihood estimates of β and the standard deviation, and the function value divided by 100, respectively denoted by $\hat{\beta}$, $\hat{\sigma}$, and L.

Table 6.6: $L, \hat{\beta}$, and$\hat{\sigma}$ for methods CL-7 to CL-10, in area A_2.

Method	$A_2(14)$			$A_2(15)$		
	L	$\hat{\beta}$	$\hat{\sigma}$	L	$\hat{\beta}$	$\hat{\sigma}$
CL-7	32.00	0.2534	5.00	34.52	0.2533	7.21
CL-8	29.30	0.2501	4.17	31.04	0.2455	6.12
CL-9	31.38	0.2534	4.57	33.94	0.2525	6.65
CL-10	31.33	0.2533	4.53	33.93	0.2525	6.64

Note, from Table 6.6, that there is only a slight gain in applying methods that use a trend surface with 1p-CAR(1) errors (CL-9 and CL-10), than applying method 1p-CAR, which has a constant mean. Note that due to the heterogeneity of the data in area A_2, the estimate of the parameter β, is close to the boundary (upper limit). The estimate of β (near the boundary), for methods CL-9 and CL-10, indicate that the data are still heterogeneous, and that the trend in the

data was not properly removed.

The maximum likelihood estimates of the parameters of the second-order surface are given below, for areas $A_2(14)$ and $A_2(15)$.

1p-CART						
Area	$\hat{\alpha}_{00}$	$\hat{\alpha}_{01}$	$\hat{\alpha}_{10}$	$\hat{\alpha}_{02}$	$\hat{\alpha}_{20}$	$\hat{\alpha}_{11}$
$A_2(14)$	14.50	1.98	3.31	−0.01	−0.01	−0.16
$A_2(15)$	38.39	1.23	−2.79	−0.07	0.01	0.15

The test images and the residual images, for methods CL-1, CL-kH, $k = 2, \ldots, 6$ and CL-8, in areas $A_2(14)$ and $A_2(15)$ are given in Figures 6.24 and 6.25, respectively. The test images and the residual images in these figures are displayed in the same order as in Figure 6.20. Note that the test images in Figure 6.25 correspond to the template date methods that use a lower correlated template (methods CL-kL, $k = 2$ to 6). The range of the colours in Figure 6.24 has been compressed to [0,80] (the minimum and maximum values of the data in area $A_2(14)$ is 6 and 70, respectively); whilst the range of the colours in Figure 6.25 has been compressed to [0,112] (the minimum and maximum values of the data in area $A_2(15)$ is 5 and 89, respectively).

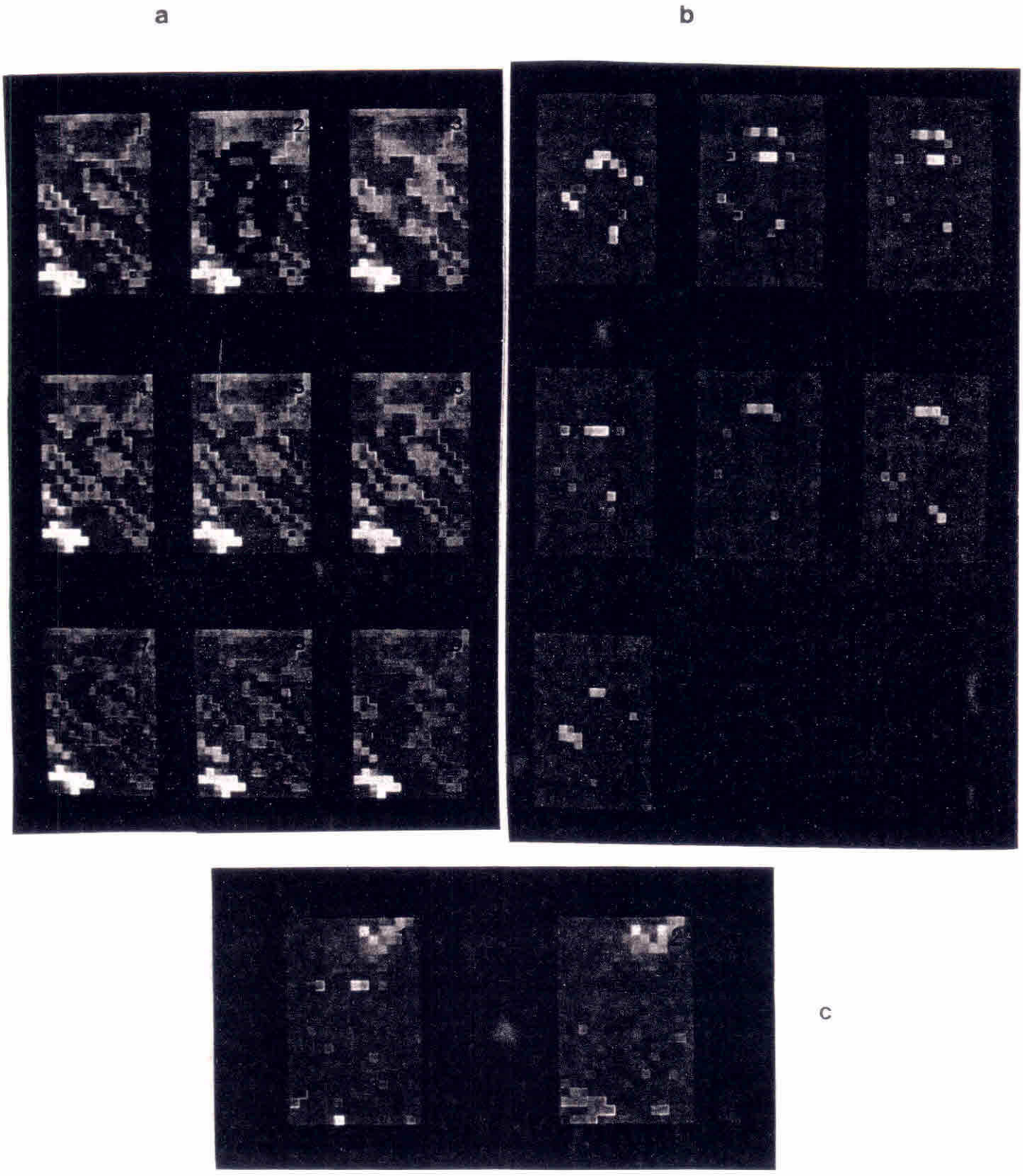

Figure 6.24: (a) Area $A_2(14)$, simulated 'clouded' area, and the test images for area $A_2(14)$, displayed in the same order as in Figure 6.20 (a); (b) Residual images for area $A_2(14)$, displayed in the same order as in Figure 6.20 (b); (c) Difference images: 1. $A_2(14) - A_2(24)$ (+128); 2. $A_2(14) - A_1(34)$ (+128).

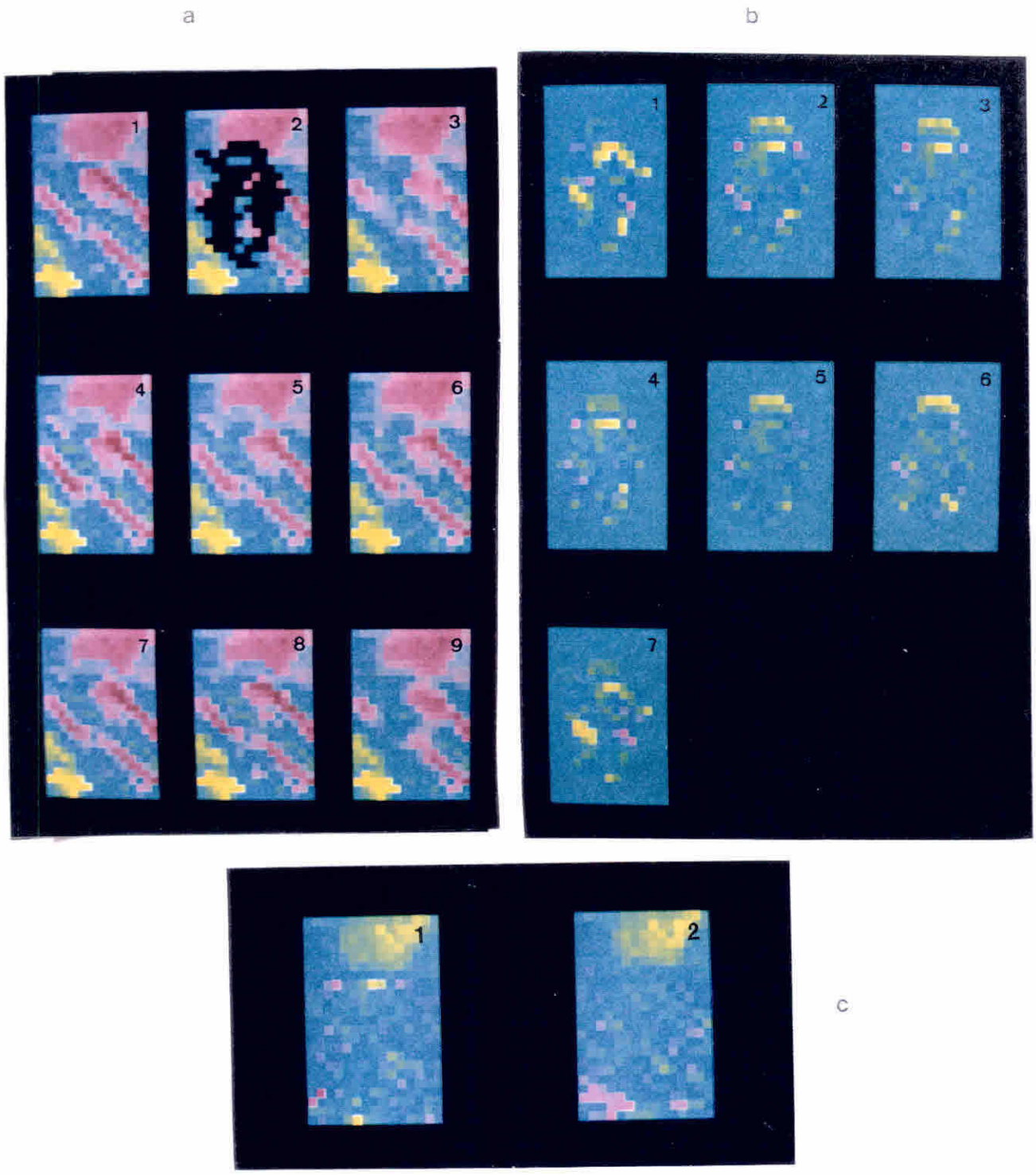

Figure 6.25: (a) 1. Area $A_2(15)$; 2. Simulated 'clouded' area; Test images for methods: 3. CL-1; 4. CL-2L; 5. CL-3L; 6. CL-4L; 7. CL-5; 8. CL-6L; 9. CL-8; (b) Residual images for: 1. CL-1; 2. CL-2L; 3. CL-3L; 4. CL-4L; 5. CL-5; 6. CL-6L; 7. CL-8; (c) Difference images: 1. $A_2(15) - A_2(25)$ (+128); 2. $A_2(15) - A_1(35)$ (+128).

Due to the heterogeneity of the data in A_2, the purely spatial methods CL-1, CL-7 to CL-10 were not expected to estimate well the missing values occurring in this area. However, due to the changes that occurred in area $A_2(14)$ and $A_2(24)$, between the two passages, the estimates for the methods using a template date are in general poorer than those obtained for the single band methods.

The test images in Figure 6.25 (a), from template date methods, are obtained using $A_2(25)$ as the template, to show the high association between the areas where the template date methods fail, and the areas of change [as indicated in the difference image in Figure 6.25 c (1)]), from one passage to another. Note, in this diference image, that changes occurred in the area mainly on the first 6 lines (area of change shown in yellow), between the passages acquired at 10/07 and 24/06 [$A_2(15)$ and $A_2(25)$], and also between those at 10/07 and 08/06. In this area of change, better estimates of the missing values are obtained for the purely spatial methods, than for the methods using a template date, as can be seen in the residual images in Figure 6.25 (b). However, the single band methods fail to estimate well the pixel values corresponding to the areas of intense moisture. Since the difference images in Figure 6.25 (c) indicate that these boundaries are reasonably unchanged, from one passage and another, this explains the better estimates obtained for the missing values occurring in this area using template date methods, than using single band methods.

Obviously, in a real situation, the difference image is not available over the areas where the missing values occur, and the decision of which template to use must rely solely on the observation of the difference images in the neighbourhood of the missing cluster. There is no certainty of which template will give the best estimates of the missing values, as sometimes a less correlated template may give better estimates than a better correlated one.

Since method CL-5 uses information from two template dates, it may estimate better the missing values associated to areas of change in one template, but which are not associated to change, in another. For example, the pixels shown in yellow and magenta, in line 8 of the difference image displayed in Figure 6.25 c (1), which indicate change, from one passage to another [$A_2(15)$ and $A_2(25)$], are not observed in Figure 6.25 c (2). As in this area the values of a_1 and a_2, in equation 6.4, are 0.567 and 0.556, respectively, the information from a second template helps to improve the accuracy of the estimates of the missing values which occur

over areas of change in one of the templates, but not over areas of change, in the other – see Figure 6.25 b (5).

Because data in $A_2(14)$ are more homogeneous than those in $A_2(15)$, the purely spatial methods perform better in $A_2(14)$ than in $A_2(15)$. The residual images in Figure 6.24 (b) indicate, again, the high correspondence between the areas in the image where the template date methods fail, and the areas of change, between one passage and another.

6.4.3 Results for area A_3.

The values for SRMS, CCOR, ACC, SRAN, and the range for the residuals are given in Table 6.7, for all methods, on area A_3. In the computation of ACC, the error is usually assumed to be ± 4 and ± 3 grey levels, in areas $A_3(25)$ and $A_3(45)$, respectively.

Table 6.8 gives the maximum likelihood estimates of β and the standard deviation, and the function value, respectively denoted by $\hat{\beta}$, $\hat{\sigma}$, and L.

Table 6.7: Values of SRMS (×100), CCOR (×100), ACC (×100), and SRAN in area A_3.

Method	$A_3(25)$					$A_3(45)$				
	SRMS	CCOR	ACC	SRAN	(m,M)	SRMS	CCOR	ACC	SRAN	(m,M)
$CL-1$	58	13	31	2.46	$(-8,6)$	33	7	24	2.02	$(-7,6)$
$CL-2$	68	23	38	3.52	$(-10,10)$	36	7	25	2.02	$(-7,6)$
$CL-3$	66	23	43	2.81	$(-10,6)$	32	7	21	1.71	$(-6,5)$
$CL-4$	70	30	43	4.04	$(-10,13)$	32	6	20	1.71	$(-7,4)$
$CL-6$	64	19	43	2.81	$(-10,6)$	31	6	22	1.56	$(-6,4)$
$CL-7$	48	13	15	1.76	$(-5,5)$	34	5	22	1.56	$(-5,5)$
$CL-8$	51	15	25	2.11	$(-8,4)$	34	7	24	1.87	$(-8,4)$
$CL-9$	49	13	25	2.28	$(-8,3)$	35	6	20	1.71	$(-8,3)$
$CL-10$	49	12	25	2.28	$(-8,3)$	35	6	20	1.71	$(-8,3)$

Table 6.8: $L, \hat{\beta}, \text{and} \hat{\sigma}$ for methods CL-7 to CL-10, in area A_3.

Method	$A_3(25)$			$A_3(45)$		
	L	$\hat{\beta}$	$\hat{\sigma}$	L	$\hat{\beta}$	$\hat{\sigma}$
CL-7	52.80	0.2517	2.45	53.42	0.2517	2.58
CL-8	51.02	0.2368	2.19	50.01	0.2486	1.80
CL-9	52.24	0.2516	2.35	50.17	0.2516	1.99
CL-10	51.47	0.2517	2.30	50.14	0.2517	1.98

The estimates of the parameters of the second-order surface, using data in $A_3(25)$ and $A_3(45)$ are given below.

1p-CART						
Area	$\hat{\alpha}_{00}$	$\hat{\alpha}_{01}$	$\hat{\alpha}_{10}$	$\hat{\alpha}_{02}$	$\hat{\alpha}_{20}$	$\hat{\alpha}_{11}$
$A_3(25)$	98.93	0.83	−0.49	0.01	−0.03	0.01
$A_3(45)$	83.39	0.85	−2.21	0.01	−0.04	0.06

As for areas A_1, the estimates given above for the second-order surface indicate that the surfaces are very flat, and hence the results obtained for methods CL-7, CL-9, and CL-10 are all similar (there is only a slight improvement from the use of a third-order surface). The estimates of the parameter β, all near the boundary, indicate a possible trend in the data, which could not be properly removed using trend surface analysis. The results in Table 6.8 also indicate that the methods are very similar, with a slight gain from the use of a 1p-SAR.

The test images and the residual images, for methods CL-1 to CL-4, CL-6, and CL-8, are given in Figures 6.26 and 6.27, for $A_3(25)$ and $A_3(45)$, respectively.

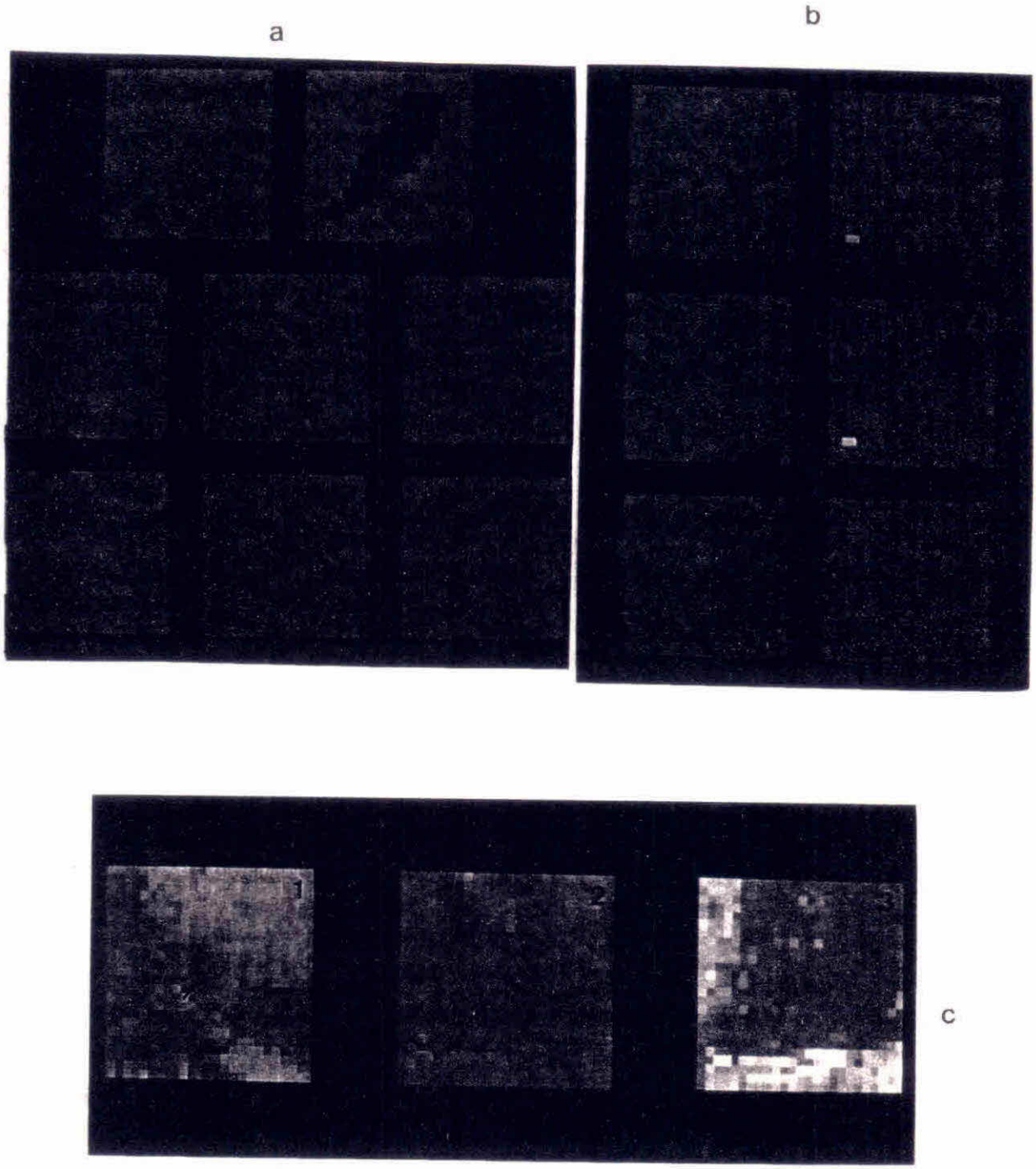

Figure 6.26: (a) 1. Original area $A_3(25)$; 2. Simulated 'clouded' area; Test images for methods: 3. CL-1; 4. CL-2; 5. CL-3; 6. CL-4; 7. CL-6; and 8. CL-8; (b) Residual images for: 1. CL-1; 2. CL-2; 3. CL-3; 4. CL-4; 5. CL-6; and 6. CL-8; (c) 1. $A_3(25)$; 2. $A_3(15)$; 3. $A_3(25) - A_3(15)$ (+128).

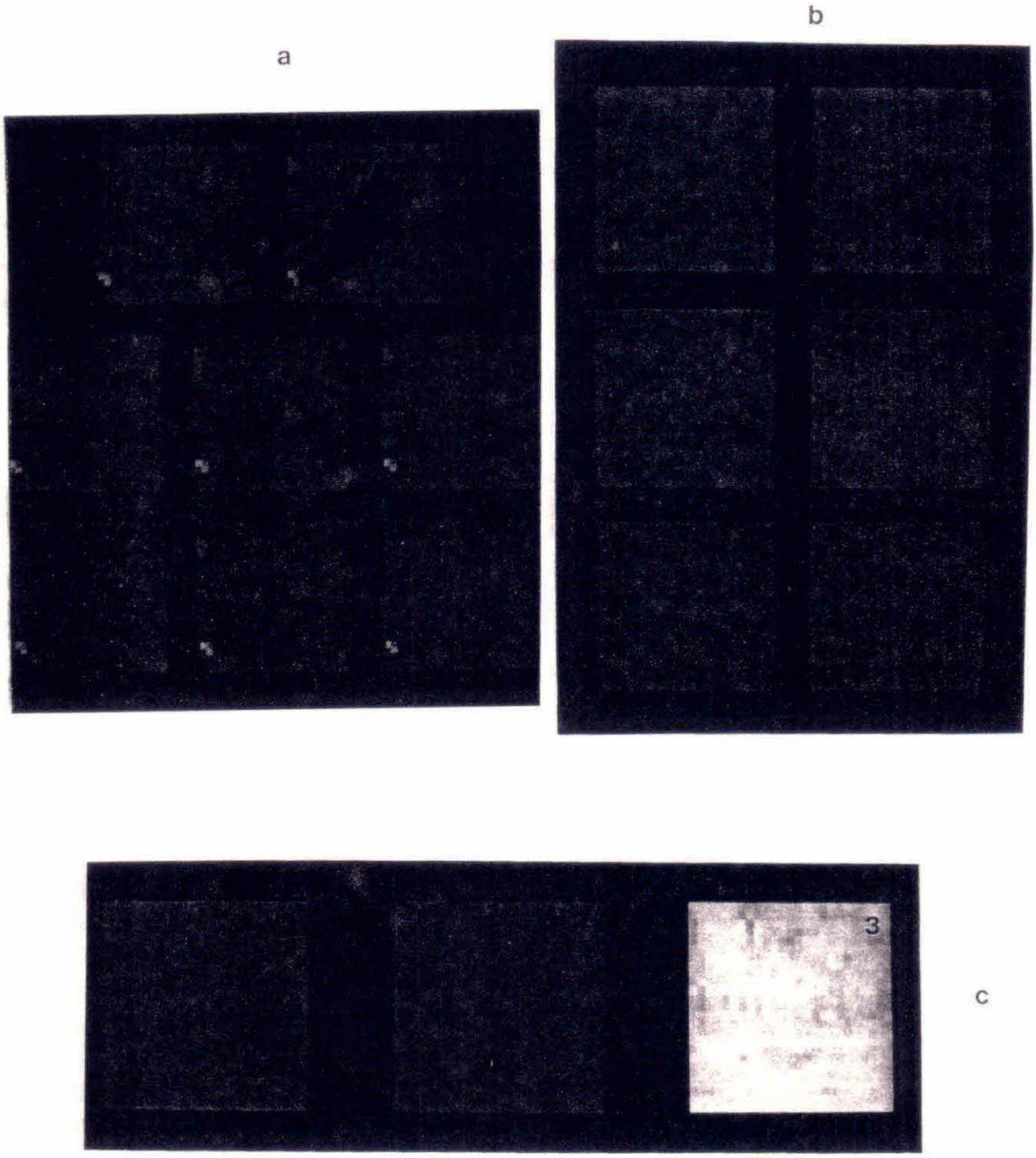

Figure 6.27: (a) Test images for area $A_3(45)$, displayed in the same order as in Figure 6.26 (a); (b) Residual images, displayed in the same order as in Figure 6.26 (b); (c) 1. $A_3(45)$; 2. $A_3(35)$; 3. $A_3(45) - A_3(35)$ (+128)

From Figure 6.26 (c) and Figure E.7 in Appendix E, it can be noted that some differences in the land cover exist between areas $A_3(15)$ (acquired at 09/09/90) and $A_3(25)$ (acquired at 08/08/90), especially between lines 20 and 25, and columns 1 to 5. This explains the greater concentration of values estimated with greater error in this area, for methods using a template date. Note that due to the similarity of the pixel values in the area bounded by the above lines and columns, the purely spatial methods are able to estimate well the missing values in the area. However, because of the dissimilarity of the information on neighbouring areas to the one indicated by the arrow in Figure 6.26 c (1) (pixels in cyan, surrounded by pixels in magenta), methods CL-1 and CL-7 to CL-10 do not estimate well the missing pixel values that occur in that small area (6 pixels).

Since the data in area $A_3(45)$ are reasonably homogeneous, and as there are few differences between areas $A_3(45)$ (acquired at 04/07/88) and $A_3(35)$ (acquired at 20/07/88) – refer to Figure E.8, all the methods estimate the missing values reasonably well. The largest (positive) residuals, for the purely spatial methods, occur in line 22. As mentioned in §6.3, in the description of this area, large variations between neighbouring pixels occur at the intersection of lines 22 and 23, with columns 1 to 5. As missing values are simulated to occur in line 22, it is expected that the purely spatial methods, especially those that use spatial modelling, do not estimate these values well. The largest residual for method CL-1 is 7, and is associated to the first missing pixel in line 22 (column 3).

6.4.4 Results for area A_4.

The values for SRMS, CCOR, ACC, and SRAN, for all methods, are given in Table 6.9, for area A_4. In the computation of ACC, the error usually assumed was ± 2 grey levels.

Table 6.10 gives the maximum likelihood estimates of β and the standard deviation, and of the function value divided by 100, respectively denoted by $\hat{\beta}$, $\hat{\sigma}$, and L.

The results in Table 6.10 indicate, again, the similar performance of the methods, with only a marginal improvement of the method using a 1p-SAR(1) model, with respect to the other methods using spatial modelling. The estimates of the parameters of the second-order surface, that is, $\hat{\alpha}_{00}$, $\hat{\alpha}_{01}$, $\hat{\alpha}_{10}$, $\hat{\alpha}_{02}$, $\hat{\alpha}_{20}$, and $\hat{\alpha}_{11}$]

Table 6.9: Values of SRMS (×100), CCOR (×100), ACC (×100), and SRAN in area A_4.

$A_4(64)$					
Method	SRMS	CCOR	ACC	SRAN	(m,M)
$CL-1$	73	27	59	3.58	$(-7,5)$
$CL-2$	63	19	51	2.98	$(-5,5)$
$CL-3$	61	19	58	2.68	$(-5,4)$
$CL-4$	68	24	49	3.88	$(-6,7)$
$CL-6$	58	17	52	2.68	$(-4,5)$
$CL-7$	60	19	47	2.98	$(-7,3)$
$CL-8$	68	22	47	3.58	$(-6,6)$
$CL-9$	63	19	50	2.98	$(-5,5)$
$CL-10$	65	21	55	2.98	$(-5,5)$

Table 6.10: L, $\hat{\beta}$, and $\hat{\sigma}$ for methods CL-7 to CL-10, in area A_4.

	$A_4(64)$		
Method	L	$\hat{\beta}$	$\hat{\sigma}$
CL-7	46.58	0.2517	1.50
CL-8	41.71	0.2356	1.23
CL-9	45.54	0.2511	1.38
CL-10	45.00	0.2513	1.33

are 39.07, -0.07, -0.52, 0.01, 0.01, and 0.01, respectively. Note again that the estimate of the parameter β, for all methods, is near the upper limit, possibly due to the heterogeneity of the data in the area, as can be observed from Figure 6.28.

The test images and the residual images for methods CL-1, to CL-6, and CL-8, are given in Figure 6.28 (a) and (b), for $A_4(45)$. The photographs are presented in the same order as those in Figure 6.26.

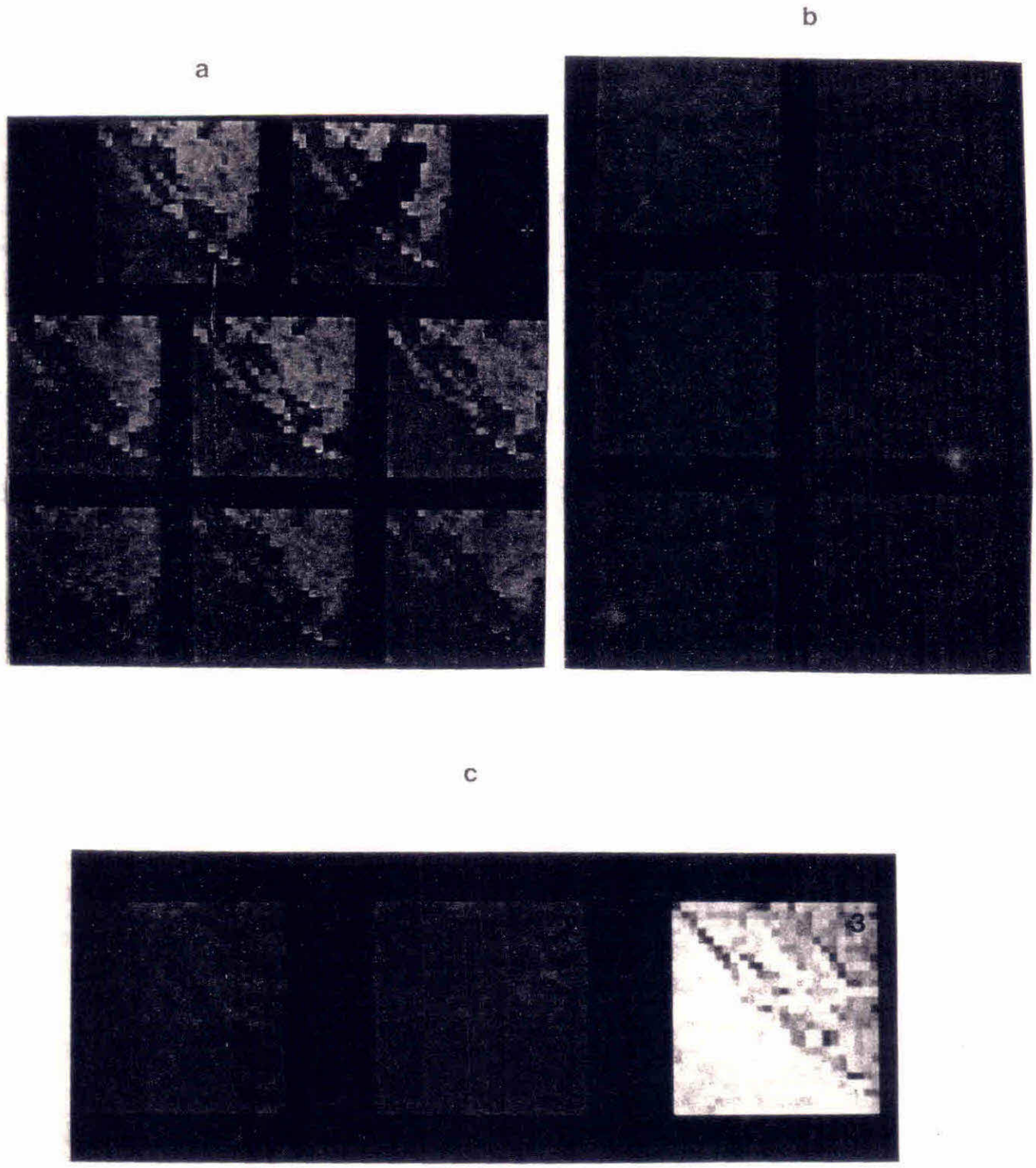

Figure 6.28: (a) Area $A_4(25)$, simulated area, and the test images for area $A_4(25)$, displayed in the same order as in Figure 6.26 (a); (b) Residual images, displayed in the same order as in Figure 6.26 (b); (c) 1. $A_4(45)$; 2. $A_4(35)$; 3. $A_4(45) - A_4(35)$ (+128)

The range of colours in Figure 6.28 (a) has been adjusted (from 24 to 56) to be approximately the same as the range of the data in the area (the minimum and maximum values are 29 and 45, respectively), to enhance the differences between the two types of ground cover in the area (see Figure 6.16). The failure of the purely spatial methods to estimate the missing values occurring at the boundary between the soil with low density vegetation, and the reforested area is very clear from this figure. The residual pixel shown in magenta, in Figure 6.28 b (1) and b (6) corresponds to the pixel indicated by the arrow, in (a) (note that the value of this pixel is not similar to any of its immediate neighbours (sites that are adjacent horizontal, vertical or diagonal to it). From Figure 6.28 (b), the association between the areas of change, and the failure of the methods that use a template date can again be observed. Although, numerically, there is not a significant improvement in the performance of the template date methods, over the purely spatial methods, at least visually they are far superior, since they preserve 'intact' the boundaries between the areas of soil and reforestation.

6.5 Summary of Results

In order to evaluate the methods, an approach similar to that used in Chapter 4 and Chapter 5 is also implemented here. Hence, ranks from 1 to 13 are assigned to each method, for each measure, on each of the 6 simulated 'clouded' areas from D_1. Similarly, ranks from 1 to 9 are formed for the methods that are applied to the areas chosen from D_2. By averaging these individual ranks, an average rank is obtained for each methods, for each measure. This average rank indicates the average performance of the method, for a given measure.

The average ranks (AR) of each method, for SRMS, CCOR, and SRAN are given in Table 6.11, for D_1 and D_2.

Table 6.11: Average ranks of the methods, for RMS, CCOR, and RAN, for the simulated areas from D_1, and D_2.

D_1					
SRMS		CCOR		SRAN	
Method	AR	Method	AR	Method	AR
CL-5	3.50	CL-5	3.75	CL-5	4.17
CL-3L	5.50	CL-6	4.83	CL-3L	4.33
CL-7	5.67	CL-3L	6.33	CL-7	5.50
CL-3H	6.00	CL-2L	6.33	CL-8	5.67
CL-9	6.25	CL-4H	7.00	CL-9	5.92
CL-10	6.42	CL-3H	7.08	CL-1	6.17
CL-8	6.50	CL-2H	7.08	CL-10	6.50
CL-6	7.17	CL-7	7.17	CL-6	6.58
CL-1	7.67	CL-8	7.42	CL-3H	7.17
CL-4H	8.00	CL-9	7.67	CL-2L	8.42
CL-2H	8.67	CL-10	7.83	CL-4L	9.83
CL-4L	9.50	CL-4L	8.67	CL-4H	10.33
CL-2L	10.17	CL-1	9.83	CL-2H	10.42

D_2					
SRMS		CCOR		SRAN	
Method	AR	Method	AR	Method	AR
CL-6	2.67	CL-7	2.50	CL-7	2.50
CL-7	2.83	CL-9	3.33	CL-9	3.50
CL-3	4.17	CL-6	3.50	CL-6	4.00
CL-9	4.83	CL-10	3.50	CL-10	4.00
CL-10	5.33	CL-3	5.50	CL-3	5.00
CL-8	5.67	CL-2	5.50	CL-2	6.33
CL-1	6.00	CL-8	6.50	CL-8	6.67
CL-4	6.33	CL-1	6.50	CL-1	6.67
CL-2	7.17	CL-4	6.83	CL-4	7.00

From the average ranks in Table 6.11 it can be noted that all methods are reasonably consistent for the 3 measures, in the second data set (the maximum difference between the average rank of any method, for any two measures, does not exceed 2.0). For the first data set, the methods in Table 6.11 are also reasonably consistent for the 3 measures. The maximum difference between the average ranks of any method, for any two measures, is 3.8.

In order to clarify the overall performance of the methods, in each data set, new ranks are formed for the methods, according to their position on Table 6.11 (rank 1 for the method at the top). These 3 new ranks (one for each measure) are then averaged, to give the results in Table 6.12, where $\bar{r}_a$ and s_{r_a} are the mean and standard deviation of the new ranks.

Table 6.12: Mean and standard deviation of the new ranks assigned to the methods, for SRMS, CCOR, and SRAN: $D_1(15)$ and $D_2(15)$.

D_1			D_2		
Method	$\bar{r}_a$	s_{r_a}	Method	$\bar{r}_a$	s_{r_a}
$CL-5$	1.00	0.00	$CL-7$	1.33	0.58
$CL-3L$	2.50	0.87	$CL-6$	2.33	1.16
$CL-7$	4.67	2.89	$CL-9$	2.67	1.16
$CL-6$	6.00	3.46	$CL-10$	4.33	0.58
$CL-3H$	6.50	2.50	$CL-3$	4.33	1.16
$CL-8$	6.67	2.52	$CL-8$	6.67	0.58
$CL-9$	6.67	2.89	$CL-2$	7.00	1.73
$CL-10$	8.00	2.65	$CL-1$	7.67	0.58
$CL-2L$	8.83	4.86	$CL-4$	8.67	0.58
$CL-4H$	9.00	3.61			
$CL-1$	9.33	3.51			
$CL-2H$	10.17	3.33			
$CL-4L$	11.67	0.58			

From the results in Tables 6.11 and 6.12 it can be seen that method CL-1 does not perform well, on average, for any of the measures. One of the reasons to justify this poor performance is the fact that most of the areas where the missing values have been simulated feature particular structures that do not favour the

purely spatial methods – refer, for instance, to Figures 6.21 and 6.28. Also, the fact that, in general, few changes occurred in the selected areas, between the passages where the missing values are simulated, and the template dates, suggest a good performance of methods that incorporate the temporal information.

It can also be noted from Table 6.12 that method CL-5 performs consistently better than the other methods, for the three measures. Since, in general, no significant changes occur between the selected areas from D_1, from one passage to another, the estimates of the parameters for this method (a_1 and a_2, in equation 6.4) are, in general, similar. Hence, the estimates of the missing values occurring in areas of change, in one template, which do not correspond to areas of change, in the second template, are 'smoothed' from the contribution of this additional template, whose data are more similar to those in the original sub-image.

As in Chapter 4, a poor performance of methods CL-2 and CL-3 (which correspond to methods TD-1 and TD-4, in that chapter, respectively) is expected when the missing values occur over areas where changes have occurred between the original sub-image and the template date. It is also expected that whenever the original sub-image and the template are not well correlated, the estimates of the missing values will closely resamble the corresponding values in the template image. This is also expected from methods CL-5, (especially if the missing values occur in areas of change in both templates), CL-4 (which uses the estimates from CL-3), and CL-6.

From the observation of the visual results presented in section 5.4, it can be seen that the purely spatial methods do not perform well in heterogenous areas, in particular at the boundaries between different types (classes) of land cover that have contrasting responses. As the estimate of a missing value, from CL-1, is obtained by averaging only the information from two of its immediate neighbours, it is very sensitive to the occurrance of 'local' changes (such as those indicated in page 218, for $A_3(45)$. As method CL-1 estimates the missing values sequentially, a 'poor' estimate of a missing value may also affect the estimates of subsequent missing values.

The results for the methods using a second- or a third-order trend surface with 1p-CAR errors are similar to those obtained for the 1p-CAR. Since the simulated missing clusters are enclosed in relatively small lattices, and since the missing values, in the first iteration of the method of maximum likelihood, are replaced

by the mean of the remaining value in the lattice, then it was not expected that these methods would have better estimates of the missing values than method 1p-CAR.

Since the methods that use spatial modelling include information from a much larger number of pixels, the effect of the occurrance of very 'local' changes may not be as pronounced as for CL-1. Note, however, that unlike in Chapter 4, when the information from the line above, and the line below the missing one, was assumed to be intact, in the case of clusters of missing, this may not be the case. Since the purely spatial methods estimate a missing value by weighting the information carried by its neighbours, it is fundamental that its value be similar to those in its neighbourhood (especially its adjacent horizontal and vertical neighbours, whose information is more heavily weighted). Since the methods using spatial modelling average the information from a larger number of pixels than CL-1, they usually perform better in homogeneous areas than CL-1, as indicated in Tables 6.3, 6.7 and 6.9).

In heterogenous areas the single band methods do not perform well, and there is not much difference in the results obtained for CL-1, or the methods that use spatial modelling. Depending on the nature of the structures on the area, the methods that incorporate information from a template date may improve the accuracy of the estimates that are obtained from these methods. Good estimates of the missing values that occur over specific permanent features in the area (such as roads, boundaries between agricultural plots, boundaries between reforested areas and other types of land use, etc.) are usually obtained from the application of methods that incorporate information from another passage. However, if the missing values occur over areas of change, from one passage to another, then better results may be obtained from single band methods.

Unfortunately, the amount and degree of change that has taken place between two passages is only known if none of the images is affected by cloud. Otherwise, this information is missing over the 'cloudy' patches, and there is no way to access if differences occurred or not, between the two dates of image acquisition. Hence, it is not possible to say if the estimates for the methods that use a template date will be better than those for the methods that use only the spatial information. For small areas of cloud cover, observation of the changes in the areas surrounding the missing cluster may be useful, and may indicate if changes occurred or not

over the clouded area.

6.6 Conclusions

This chapter concerned the estimation of missing values occurring in small clusters, as if arising from the presence of small, thick, clouds. Since the estimation of missing remotely sensed data of this nature has deserved little attention in the literature, this investigation may bring some light into the sort of results that may be expected from the application of simple methods, as well as more sophisticated ones.

Good estimates of missing values occurring in reasonably homogeneous areas can be obtained from the purely spatial methods, as large 'local' variations are not expected to occur. Also, considering the form of spatial interpolation of the methods using spatial modelling, and that of method CL-1, a better performance of the former methods may be expected. However, the estimates of the missing values in heterogenous areas, and at the boundaries between areas of contrasting response, from the single band methods proposed here, are not expected to be good. In this case, the information from another passage can be very useful and relevant, if few changes occur in the area affected by cloud, from one passage to another.

In the case of missing values from line drop, the occurrence of changes, from one passage to another, can be reasonably deduced from observation of the changes in the area neighbouring the missing lines. Then, the adequacy of the use of methods that incorporate information from another date could be assessed. However, over areas of extensive cloud cover, the differences in land cover, between the passages cannot be reasonably assessed, and it is difficult to decide if the use of template date methods is adequate or not.

The effect of the choice of the area that encloses the missing cluster, on the estimates obtained for the template date methods, and on the estimates of the parameters of the trend surface in method 1p-CART has not been investigated. However, since the results for the template date methods in Chapter 4 indicated that, in general, better estimates of the missing values are obtained using data from a neighbourhood of the missing line, instead of the data from the entire image, it seems that this will also be the case here. However, this should be

further investigated, particularly on the possible effects of different sizes of the enclosing area, on the estimates of the trend surface.

Considering again the form of spatial interpolation implied by the purely spatial methods, these methods are not expected to estimate well the missing values occurring in large, compact, clusters. The presence of some 'holes' in the configuration of large clusters of missing values may improve the estimates of the missing values. However, since the pixel values associated to pixels in the 'hole' may be contaminated by the cloud (in which case they do not reflect the true radiance value of the features on the area on the ground), it is doubtfull if their information will improve significantly the estimates of the missing values.

Chapter 7

Information Loss on the Parameters for Spatial Processes

7.1 Introduction

In this chapter, the formulae are given for the Fisher information loss on parameters for the mean and variance of a Gaussian univariate process occurring on a rectangular lattice, when there are missing values in the data.

Since there has been interest to advance statistical theory on the loss of information when some sites are unobserved (Haining *et al.*, 1989, Martin, 1989), it seems relevant to include results for processes other than the one-parameter first-order conditional autoregressive process, which has been the focus of attention in Haining *et al.* (1989), and Martin (1989).

The loss of information on the mean for the one-parameter first-order CAR when observations are missing from a regular rectangular lattice has been discussed numerically by Haining, Griffith, and Bennett (1989), assuming that the process has a constant mean. Martin (1989) has then deduced the general formulae for the loss on the mean and on the dependence parameter β for any process defined by its inverse covariance matrix. He also provides an approximate formulae for the loss for the specific case of the 1p-CAR(1) with contant mean. Some of those results are also given in Martin (1990b).

Krug & Martin (1991b) generalize the results in Martin (1989) and produce the exact as well as the approximate formulae for the loss of information on a constant mean for general conditional autoregressive and simultaneous autoregressive

processes.

The need to develop approximate formulae for the loss arises from the fact that the exact formulae generally requires the inversion of a matrix, which is only feasible algebraically for a small number of missing values. Besides, approximation formulae can also give a very useful insight into the effects of different configurations on the loss, something that would otherwise require extensive numerical evaluation to be achieved.

Some notation in introduced in section 7.2, and in sections 7.3 to 7.5 the loss of information on processes with a constant mean is considered. The material in these sections is essentially that in Krug & Martin (1991b).

As the formulae given in these sections are only valid when the missing sites are interior ones, section 7.6 investigates the appropriateness of their use when this assumption is relaxed, and some, or all the missing sites lie on the boundary of the lattice. This investigation is carried out for a 1p-CAR(1) and a 2p-CAR(2) processes. The influence of the number of missing sites on the loss of information on μ is also tackled in section 7.6. Section 7.7 discusses the loss of information on the dependence parameter β, giving results for a 1p-CAR(1) process when $m = 4$ and $m = 5$, and stationarity is assumed.

7.2 Notation

Let $I_{\phi\theta}\{S(u)\}$ denote the Fisher information on the parameters ϕ and θ from the sites $S(u)$ at which the observations u are collected.

The Fisher information on the parameters ϕ and θ is the expected value of minus the second derivative, with respect to ϕ and θ, of the log likelihood. From the inverse of the information matrix, the asymptotic covariance matrix of the maximum likelihood estimators of the parameters can be found. Mardia & Marshall (1984), and Martin (1984) give the formulae for the information loss on the parameters for the mean and variance of a Gaussian process, when data are available at all sites where observations are made.

Assume that the n observations have a constant mean μ and that the n-vector u is normally distributed $N(\mu 1_n, \mathbf{V}\sigma^2)$ where σ^2 is a scale parameter, and

$\mathbf{V} = \sigma^{-2}\text{var}(u)$ is the scaled dispersion matrix of u, which depends on the vector φ. If the vector u contains missing observations let it be reordered so that $x' = (y, z)$ where y is the $(n-m)$-vector of observed values, and z is the m-vector of non-observed values. Let $S(z)$ be the set of missing sites.

Denote by $L_\phi\{m, S(z)\}$ the loss of information on ϕ, for a given configuration of the missing sites. The loss is $I_{\phi\phi}\{S(u)\} - I_{\phi\phi}\{S(y)\}$.

Define m_k to be the number of pairs of sites in $S(z)$ that are lag k apart, with $m_0 = m$ and $m_{-k} = m_k$. A (two-step) directed (k, l) path is said to exist between sites i and j in $S(z)$ if there exists a site r in $S(z)$ such that $i + k = r$ and $r + l = j$. Denote by $p_{k,l}$ the number of directed (k, l) paths in $S(z)$. Then $p_{k,l} = p_{-l,-k}$ for any k and l, and $p_{k,-k} = m_k$.

The definitions of the lag k neighbour matrices $\mathbf{W}_k$ and $\mathbf{T}_k$ given in Chapter 5 (§5.2) are required herein. Let $(\mathbf{W}_k)_{zz}$ denote the submatrix of $\mathbf{W}_k$ corresponding to the missing sites $S(z)$. For the approximation formulae the sum of the elements in certain (z, z) submatrices is required. Now $1_m'(\mathbf{T}_k)_{zz}1_m = m_k$, $1_m'(\mathbf{T}_k)_{zz}(\mathbf{T}_l)_{zz}1_m = p_{k,l}$, and $1_m'(\mathbf{T}_k\mathbf{T}_l)_{zz}1_m = m_{k+l}$. It then follows that

$$1_m'(\mathbf{W}_k)_{zz}1_m = 2m_k \ , \tag{7.1}$$

$$1_m'(\mathbf{W}_k)_{zz}(\mathbf{W}_l)_{zz}1_m = p_{k,l} + p_{k,-l} + p_{l,k} + p_{-l,k} \ , \tag{7.2}$$

$$1_m'(\mathbf{W}_k'\mathbf{W}_l)_{zz}1_m = 2(m_{l-k} + m_{l+k}). \tag{7.3}$$

7.3 Loss of Information on μ

7.3.1 Introduction

In this section, the exact and the approximate formulae for the loss of information on μ, for the general CAR and general SAR processes are given.

The loss of information on μ due to the m missing values at sites in $S(z)$, denoted $L_\mu\{m, S(z)\}$, follows from theorem 2.1 in Martin (1989), which states that for a general process $N(\mathbf{A}\theta, \mathbf{V}\sigma^2)$ the loss of information on μ is given by

$$\begin{aligned} L_\mu\{m, S(z)\}\sigma^2 = \ & \mathbf{A}'\mathbf{V}^{-1}\mathbf{A} - \mathbf{A}_y'\mathbf{V}_{yy}^{-1}\mathbf{A}_y \\ = \ & (\mathbf{A}_z - \mathbf{V}_{zy}\mathbf{V}_{yy}^{-1}\mathbf{A}_y)'\mathbf{V}^{zz}(\mathbf{A}_z - \mathbf{V}_{zy}\mathbf{V}_{yy}^{-1}\mathbf{A}_y) \end{aligned} \tag{7.4}$$

For a process with constant mean, $\mathbf{A}\theta = \mu 1$ and equation 7.4 becomes

$$1_n^{'}\mathbf{V}^{-1}1_n - 1_{n-m}^{'}\mathbf{V}_{yy}^{-1}1_{n-m} = 1_n^{'}\mathbf{V}^{xz}(\mathbf{V}^{zz})^{-1}\mathbf{V}^{zx}1_n = c^{'}(\mathbf{V}^{zz})^{-1}c. \qquad (7.5)$$

for $c = \mathbf{V}^{zx}1_n$.

In all cases considered until §7.6, $c = \mathbf{V}^{zx}1_n = a1_m$ and

$$L_\mu\{m, S(z)\}\sigma^2 = a^2 1_m^{'}(\mathbf{V}^{zz})^{-1}1_m. \qquad (7.6)$$

Let $L_\mu^*\{m, S(z)\} = L_\mu\{m, S(z)\}\sigma^2/a^2 = 1_m^{'}(\mathbf{V}^{zz})^{-1}1_m$ be the scaled loss of information on the mean μ.

From equation 7.5 it is seen that the exact loss of information on μ requires the inversion of $\mathbf{V}^{zz}$, which is only feasible for small m. However, Martin (1989) notes that there are three situations when this inversion is not needed:

(i) when $\mathbf{V}^{zz}$ has constant row sums, so that 1_m is an eigenvector of $\mathbf{V}^{zz}$, i.e. $\mathbf{V}^{zz}1_m = e1_m$. The scaled loss is then $L_\mu^*\{m, S(z)\} = m/e$.

(ii) the missing sites can be reordered so that $\mathbf{V}^{zz}$ is block diagonal. In this case $L_\mu^*\{m, S(z)\} = \sum L_\mu^*\{m_i, S(z_i)\}$ where $S(z) = \cup_i S(z_i)$ and z_i is the component for the i^{th} group. The groups are then said to be isolated.

(iii) a recursive formula can be used to obtain the loss from the formula for a subset of $S(z)$ - see Martin (1989, p. 4634). For some configurations this method can be very useful when the subset is chosen appropriately.

When analytic inversion of $\mathbf{V}^{zz}$ is not feasible, an approximation to the loss may be useful. This can be found if an approximation to $(\mathbf{V}^{zz})^{-1}$ is available. When $\mathbf{V}^{zz}$ is of the form $\mathbf{I} - \mathbf{A}$ and g, the largest absolute value of the eigenvalues of $\mathbf{A}$, is less than one, $(\mathbf{V}^{zz})^{-1} = (\mathbf{I} - \mathbf{A})^{-1}$ can be expanded as $\mathbf{I} + \mathbf{A} + \mathbf{A}^2 + \ldots$. If g is small, $(\mathbf{V}^{zz})^{-1}$ can be approximated by the first few terms. The approximations below use $(\mathbf{V}^{zz})^{-1} \approx \mathbf{I} + \mathbf{A} + \mathbf{A}^2$.

7.3.2 Loss on μ for the general CAR process

A definition for CAR and SAR processes has been given in Chapter 5, (§5.3 to §5.5), along with their stationarity conditions.

Assume henceforth, unless otherwise stated, that the sites in $S(z)$ are all interior sites and that the stationarity conditions are satisfied. This ensures that $c = \mathbf{V}^{zx}1_n = a1_m$, where a is constant for each process, and that the results do not depend on the boundary assumptions. Another consequence is that the loss does not depend on the actual sites in $S(z)$, but only on the configuration of the missing sites. Provided the sites remain interior sites, the loss is unchanged when the missing sites are translated, or reflected horizontally or vertically.

The approximate formula for the loss for the general CAR, for low values of the $|\ \beta_k\ |$, is found using the expansion of $(\mathbf{V}^{zz})^{-1} = \{\mathbf{I}_m - \sum \beta_k(\mathbf{W}_k)_{zz}\}^{-1}$ which, restricted to terms up to second-order in the parameters is given by

$$\mathbf{I}_m + \sum \beta_k(\mathbf{W}_k)_{zz} + \sum\sum \beta_k\beta_l(\mathbf{W}_k)_{zz}(\mathbf{W}_l)_{zz}.$$

Hence, using results 7.1 and 7.2, $L_\mu\{m, S(z)\} \approx$

$$m + 2\sum_k m_k\beta_k + \sum_k 2(p_{k,k} + m_k)\beta_k^2 + \sum\sum_{l\neq k}(p_{k,l} + p_{k,-l} + p_{l,k} + p_{-l,k})\beta_k\beta_l. \quad (7.7)$$

Note that in the double summation $\beta_k\beta_l$ occurs twice. For any arbitrary ordering of the vectors in K_c, this sum can be re-expressed as $2\sum\sum_{l>k}(p_{k,l} + p_{k,-l} + p_{l,k} + p_{-l,k})\beta_k\beta_l$. A similar remark holds for equations 7.8 and 7.9.

Some examples of exact formulae are now given. Firstly, when $m = 1$, $L_\mu^*\{1, S(z)\} = 1$. Secondly, some general examples when 1_m is an eigenvector of $\mathbf{V}^{zz}$ (see 7.3.1) are:

(i) $m = 2$ and the two missing sites are lag k apart: $L_\mu^*\{2, S(z)\} = 2/(1 - \beta_k)$. Thus there are as many different values for the loss when $m = 2$, and hence as many essentially different configurations, as there are different values of β_k (including 0).

(ii) $m = 4$ and each missing site is in a corner of a rectangle with sides defined by vectors k_1 and k_2: $L_\mu^*\{4, S(z)\} = 4/(\text{row sum of } \mathbf{V}^{zz}) =$
$4/(1 - \beta_{k_1} - \beta_{k_2} - \beta_{k_1+k_2})$, for any $d \geq 2$, provided $\beta_{k_1+k_2} = \beta_{k_1-k_2}$.

(iii) $m = 8$ and each missing site is in a corner of a block with sides defined by vectors k_1, k_2, k_3: $L_\mu^*\{8, S(z)\} = 8/(\text{row sum of } \mathbf{V}^{zz})$, for any $d \geq 3$, provided $\beta_{k_i+k_j} = \beta_{k_i-k_j}$ for $i, j = 1, 2, 3$ and the $\beta_{\pm k_1 \pm k_2 \pm k_3}$ are equal.

(iv) $m = 8$, $d = 2$, and each missing site is the vertex of an octagon of sides s and $s\sqrt{2}$ and vertices, after translation, of $(0,0), (s,0), (2s,s), (2s,2s)$, $(s,3s), (0,3s), (-s,2s), (-s,s)$: $L_\mu^*\{m, S(z)\} = 8/(\text{row sum of } \mathbf{V}^{zz})$, provided the β_k occurring in $\mathbf{V}^{zz}$ only depend on the squared distance $k'k$.

7.3.3 Loss on μ for the general SAR process

The first approach to find the loss of information on μ for a SAR process comes from its corresponding CAR representation, as already introduced in §5.3 in Chapter 5.

If $\mathbf{V}^{zz}$ is taken as $b\{\mathbf{I}_m - \sum_{k \in K_s^*} \beta_k^* (\mathbf{W}_k)_{zz}\}$ and b^{-1} as approximately $1 - \sum_{k \in K_s} \beta_k^2$, then, substituting for the β_k^* in equation 7.7, and neglecting terms above second order in the β_k, gives the approximation to $L_\mu^*\{m, S(z)\}$.

Alternatively, $L_\mu^*\{m, S(z)\} = 1_m'(\mathbf{V}^{zz})^{-1} 1_m$ can be found directly from the expansion of $(\mathbf{V}^{zz})^{-1}$ which up to second-order in the parameters is

$$\mathbf{I} + \sum \beta_k (\mathbf{W}_k)_{zz} + \sum\sum \beta_k \beta_l \{(\mathbf{W}_k)_{zz}(\mathbf{W}_l)_{zz} - (\mathbf{T}_k' \mathbf{T}_l)_{zz}\}$$

for all sums ranging over K_s, and assuming that the expansion is valid.

Either method leads to $L_\mu^*\{m, S(z)\}$ being approximately

$$\begin{aligned} m + 2\sum m_k \beta_k + \sum \{2(p_{k,k} + m_k) - m\} \beta_k^2 \\ + \sum\sum_{l \neq k} \{(p_{k,l} + p_{k,-l} + p_{l,k} + p_{-l,k}) - m_{k-l}\} \beta_k \beta_l \end{aligned} \tag{7.8}$$

for low $|\ \beta_k\ |$, where all sums are over K_s.

If $m = 1$ then $L_\mu^*\{1, S(z)\} = b^{-1}$. Recall also that if 1_m is an eigenvector of $\mathbf{V}^{zz}$, then the loss can be found directly. In particular, when $m = 2$, $L_\mu^*\{2, S(z)\} = 2/(\text{row sum of } \mathbf{V}^{zz})$. Other results follow from those in subsection 7.3.2 for the CAR.

7.3.4 The case of the symmetric SAR process

For the symmetric SAR, $\mathbf{V}^{zz}$ is

$$\mathbf{I} - 2\sum \beta_k (\mathbf{W}_k)_{zz} + \sum\sum \beta_k \beta_l (\mathbf{W}_k \mathbf{W}_l)_{zz}$$

and the expansion of its inverse, to second order terms in the parameters is

$$\mathbf{I} + 2\sum \beta_k (\mathbf{W}_k)_{zz} + \sum\sum \beta_k \beta_l \{4(\mathbf{W}_k)_{zz}(\mathbf{W}_l)_{zz} - (\mathbf{W}_k \mathbf{W}_l)_{zz}\}.$$

Then, directly, using results 7.1, 7.2, and 7.3, or using equation 7.8, gives for low $\mid \beta_k \mid$ that $L_\mu^*\{m, S(z)\} \approx$

$$\begin{aligned} & m + 4\sum m_k \beta_k + 2\sum \{4(p_{k,k} + m_k) - (m + m_{2k})\}\beta_k^2 \\ & \quad + 2\sum\sum_{l \neq k} \{2(p_{k,l} + p_{k,-l} + p_{l,k} + p_{-l,k}) - (m_{k+l} + m_{k-l})\}\beta_k \beta_l. \end{aligned} \tag{7.9}$$

7.4 Application to some conditional autoregressive processes

In sections 7.4 and 7.5, some particular cases are considered when data are missing from a two-dimensional n_1 by n_2 rectangular lattice. The approximation for the loss of information on the mean μ for the cases of the two-parameter first-order and a two-parameter second-order CAR are presented in this section. The exact results and the corresponding approximations are given for the one-parameter first-order CAR when m=5, and for the two-parameter first-order CAR when m=4.

For the first- and second-order CAR processes discussed here a site i is interior if it is not in the outer layer of the rectangular lattice, i.e. if it is not in the first or last row, or in the first or last column of the lattice.

7.4.1 Notation

For simplicity, a different notation is introduced for sections 7.4 and 7.5. Some notation introduced in Chapter 5 is also used here.

Let l_{hv} denote the number of pairs of sites separated by lags $\pm h$ and $\pm v$. Then $l_{10} + l_{01}$ is equal to m_1 in Martin (1989). Also, $l_{h0} = m_k$ for $k = (h, 0)$, $l_{0v} = m_k$ for $k = (0, v)$, and $l_{hv} = m_k + m_l$ for $k = (h, v)$ and $l = (h, -v)$ when $h, v \neq 0$.

Define $p_h = p_{k,k}$ for $k = (1, 0)$ and $p_v = p_{k,k}$ for $k = (0, 1)$ as the number of non-returning paths obtained respectively from two horizontal unit links and from two vertical unit links. Let p_d be the number of paths involving one horizontal and one vertical unit link. Then $p_d = p_{k,l} + p_{k,-l} + p_{l,k} + p_{-l,k}$ for $k = (1, 0)$

and $l = (0,1)$ is the sum of the elements of the (z,z) submatrix of $\mathbf{U}_{1h}\mathbf{U}_{1v}$ - see equation 7.2. Denote by p_t the sum of p_h and p_v. Note that $p_t + p_d$ is equal to m_2 used by Martin (1989).

Let p_{dd} denote the number of paths formed by two diagonal links and let p_b be the number of paths involving one diagonal and one horizontal (or vertical) link. Then $p_{dd} = p_{k,k} + p_{k,l} + p_{k,-l} + p_{l,k} + p_{-l,k} + p_{l,l}$ where $k = (1,1)$ and $l = (-1,1)$, and p_b is the sum of the elements of the (z,z) submatrix of $\mathbf{U}_1\mathbf{U}_2$, which can be expressed in terms of the $p_{k,l}$ using equation 7.2.

Two examples, referred to in subsections 7.4.4 and 7.5.2, are given below.

Example 7.1

Consider the 'T' shaped configuration for $m = 5$, numbered $\begin{pmatrix} 123 \\ 4 \\ 5 \end{pmatrix}$. Here, $l_{10} = 2\ [1-2, 2-3]$, $l_{01} = 2\ [2-4, 4-5]$, $l_{11} = 2\ [1-4, 3-4]$,
$p_t = 2\ [1-2-3, 2-4-5]$, $p_d = 2\ [1-2-4, 3-2-4]$, $p_{dd} = 1\ [1-4-3]$
and $p_b = 6\ [1-4-5, 3-4-5, 1-4-2, 2-1-4, 2-3-4, 2-4-3]$.
Note that the configuration $\begin{pmatrix} 12 \\ 4 \end{pmatrix}$ contributes 1 to $p_d\ [1-2-4]$ and 2 to p_b $[1-4-2\ ,\ 2-1-4]$.

Example 7.2

Consider the configuration numbered $\begin{pmatrix} 123 \\ 4 \\ 56 \end{pmatrix}$.

For this configuration the number of pairs and paths are:
$l_{10} = 3\ [1-2, 2-3, 5-6]$, $l_{01} = 1\ [1-4]$, $l_{11} = 2\ [2-4, 4-5]$, $l_{20} = 1\ [1-3]$,
$l_{02} = 2\ [2-5, 3-6]$, $l_{12} = 3\ [1-5, 2-6, 3-5]$, $l_{21} = 2\ [3-4, 4-6]$,
$l_{22} = 1\ [1-6]$, $p_t = 1\ [1-2-3]$, $p_d = 1\ [2-1-4]$, $p_{dd} = 1\ [2-4-5]$ and
$p_b = 5\ [1-4-5, 4-5-6, 3-2-4, 2-4-1, 1-2-4]$.

7.4.2 One-parameter first-order CAR

The one-parameter first-order CAR has one parameter for its horizontally and vertically adjacent neighbours. It is defined by $\mathbf{V}^{-1} = \mathbf{I}_n - \beta\mathbf{U}_1$. The stationarity condition is $|\ \beta\ | < \frac{1}{4}$, and a is $1 - 4\beta$.

For a first-order CAR, two sites i and j are isolated if j is not an adjacent horizontal or vertical neighbour of i.

The approximation for $L_\mu^*\{m, S(z)\}$ for low $\mid \beta \mid$ was given in Martin (1989), and is $m+2(l_{10}+l_{01})\beta+2(p_t+p_d+l_{10}+l_{01})\beta^2$. Thus the more compact the configuration of sites in $S(z)$, the greater the loss. Martin (1989) also gave exact formulae for $m = 2,\ 3,\ 4$ for all possible configurations.

In Table 7.1 the exact and approximate values for $L_\mu^*\{5, S(z)\}$ are given in order of increasing loss for $0 < \beta < \frac{1}{4}$ for all possible different configurations of five missing values. A + denotes a missing site, and brackets denote isolated groups. The approximation is very good for low β, and still good for higher β. For example, the maximum difference between the true value and the approximation is 0.06 when $\beta = 0.1$, and 0.65 when $\beta = 0.2$.

Each configuration depicted in Table 7.1 is one of a family of configurations having the same loss. For the 5-connected case 7.1(h), for instance, the following configurations (plus their reflections and rotations) give the same loss:

$$\begin{pmatrix} + & + & + & + \\ & & & + \end{pmatrix} \quad \begin{pmatrix} + & + & + \\ & & + \\ & & + \end{pmatrix} \quad \begin{pmatrix} + & + & + \\ + & & + \end{pmatrix} \quad \begin{pmatrix} & & & + \\ + & + & + \\ + & & \end{pmatrix}$$

The formulae for cases 7.1(a) to 7.1(g), and 7.1(j) are obtained directly from results in Martin (1989). The loss $L_\mu^*\{5, (+\,+\,+)(++)\}$, for instance, is simply $L_\mu^*\{3, (+\,+\,+)\} + L_\mu^*\{2, (++)\}$.

The ranking in order of loss is constant for all $0 < \beta < \frac{1}{4}$. The loss increases as the missing points are more compacted together, and, for all configurations the loss $\mathbf{L}_\mu\{5, S(z)\}$ increases as β increases.

7.4.3 Two-parameter first-order CAR

The two-parameter first-order CAR has one parameter for horizontal neighbours and one for vertical neighbours. Its inverse covariance matrix is $\mathbf{V}^{-1} = \mathbf{I}_n - \alpha\mathbf{U}_{1h} - \beta\mathbf{U}_{1v}$. The stationarity condition is $\mid \alpha \mid + \mid \beta \mid < \frac{1}{2}$,and a is $1 - 2\alpha - 2\beta$. For an n_1 by n_1 lattice, $\mathbf{V}^{-1}$ is positive definite when $\mid \alpha \mid + \mid \beta \mid < [2cos\{\pi/(n_1+1)\}]^{-1}$. When $\alpha = \beta$ the one-parameter first-order CAR of subsection 7.4.2 results. The condition for two sites to be isolated is the same as in subsection 7.4.2. From equation 7.7, for low values of $\mid \alpha \mid$ and $\mid \beta \mid$, $L_\mu^*\{m, S(z)\}$ is approximately equal to

Table 7.1: $L_\mu^*\{5, S(z)\}$ for all different configurations of 5 missing points and a one-parameter first-order CAR.

CASE	*CONFIGURATION*	L_μ^*	*APPROXIMATION*
7.1(a)	$(+)(+)(+)(+)(+)$	5	5
7.1(b)	$(++)(+)(+)(+)$	$\frac{5-3\beta}{1-\beta}$	$5+2\beta+2\beta^2$
7.1(c)	$(++)(++)(+)$	$\frac{5-\beta}{1-\beta}$	$5+4\beta+4\beta^2$
7.1(d)	$(+++)(+)(+)$	$\frac{5+4\beta-4\beta^2}{1-2\beta^2}$	$5+4\beta+6\beta^2$
7.1(e)	$(+++)(++)$	$\frac{5+\beta-8\beta^2}{(1-2\beta^2)(1-\beta)}$	$5+6\beta+8\beta^2$
7.1(f)	$(+++)(+)$	$\frac{5+\beta-\beta^2}{1-\beta-\beta^2}$	$5+6\beta+10\beta^2$
7.1(g)	$\begin{pmatrix}+++\\+\end{pmatrix}(+)$	$\frac{5+6\beta-3\beta^2}{1-3\beta^2}$	$5+6\beta+12\beta^2$
7.1(h)	$(+++++)$	$\frac{5+8\beta-\beta^2}{1-3\beta^2}$	$5+8\beta+14\beta^2$
7.1(i)	$\begin{pmatrix}+++\\+\\+\end{pmatrix}$	$\frac{5+8\beta-4\beta^2-4\beta^3}{1-4\beta^2+2\beta^4}$	$5+8\beta+16\beta^2$
7.1(j)	$\begin{pmatrix}++\\++\end{pmatrix}$	$\frac{5-2\beta}{1-2\beta}$	$5+8\beta+16\beta^2$
7.1(k)	$\begin{pmatrix}+\\+++\\+\end{pmatrix}$	$\frac{5+8\beta}{1-4\beta^2}$	$5+8\beta+20\beta^2$
7.1(l)	$\begin{pmatrix}+++\\++\end{pmatrix}$	$\frac{5+10\beta-3\beta^2-4\beta^3}{1-5\beta^2+2\beta^4}$	$5+10\beta+22\beta^2$

$m + 2l_{10}\alpha + 2l_{01}\beta + 2(p_h + l_{10})\alpha^2 + 2(p_v + l_{01})\beta^2 + 2p_d\alpha\beta.$

Thus, for positive dependence in both directions, α, $\beta > 0$,and not too large, then the more compact the sites in $S(z)$, the greater the loss. If $\alpha > \beta$ then horizontal compactness has a higher loss than vertical compactness.

Exact formulae for all configurations when $m = 2$ and $m = 3$ can easily be obtained. All can be obtained directly from Martin (1989) except $\begin{pmatrix}+\\++\end{pmatrix}$ for which $L_\mu^*\{3, S(z)\}$ is $(3 + 2\alpha + 2\beta - \alpha^2 - \beta^2 + 2\alpha\beta)/(1 - \alpha^2 - \beta^2)$. The exact formulae and approximations for $L_\mu^*\{4, S(z)\}$ are presented in Table 7.2 for some configurations of four missing sites. Only those configurations for which results cannot be obtained immediately from Martin (1989) are presented, in increasing order of loss, for $\alpha = \beta > 0$. Note that configurations 7.2(c), 7.2(d), and 7.2(e) have a different form when rotated through 90°, the loss being found by

interchanging α and β.

Table 7.2: $L^*_\mu\{4, S(z)\}$ for some different configurations of 4 missing points and a two-parameter first-order CAR.

CASE	*CONFIGURATION*	L^*_μ	*APPROXIMATION*
7.2(a)	(++) (+ / +)	$\frac{4-2\alpha-2\beta}{(1-\alpha)(1-\beta)}$	$4+2\alpha+2\beta+2\alpha^2+2\beta^2$
7.2(b)	(+ / ++) (+)	$\frac{4+2\alpha+2\beta-2\alpha^2-2\beta^2+2\alpha\beta}{1-\alpha^2-\beta^2}$	$4+2\alpha+2\beta+2\alpha^2+2\beta^2+2\alpha\beta$
7.2(c)	(++ / ++)	$\frac{4+4\alpha+2\beta-4\alpha^2-2\beta^2+4\alpha\beta-4\alpha^3+2\alpha^2\beta}{1-2\alpha^2-\beta^2+\alpha^4}$	$4+4\alpha+2\beta+4\alpha^2+2\beta^2+4\alpha\beta$
7.2(d)	(+ / +++)	$\frac{4+4\alpha+2\beta-2\alpha^2-2\beta^2+2\alpha\beta-2\alpha\beta^2}{1-2\alpha^2-\beta^2+\alpha^2\beta^2}$	$4+4\alpha+2\beta+6\alpha^2+2\beta^2+2\alpha\beta$
7.2(e)	(+ / +++)	$\frac{4+4\alpha+2\beta-2\alpha^2-2\beta^2+4\alpha\beta}{1-2\alpha^2-\beta^2}$	$4+4\alpha+2\beta+6\alpha^2+2\beta^2+4\alpha\beta$
7.2(f)	(++ / ++)	$\frac{4}{1-\alpha-\beta}$	$4+4\alpha+4\beta+4\alpha^2+4\beta^2+8\alpha\beta$

If $\alpha, \beta > 0$, $\alpha \neq \beta$, then the larger losses occur for those configurations with the larger numbers of adjacent sites along the direction of greater weight. Hence, if $\alpha > \beta$ then $L^*_\mu\{4, (S(z)\}$ is always greater for configurations 7.2(c), 7.2(d) and 7.2(e) than for their corresponding 90° rotation. The loss for the more compact case 7.2(f) is not consistently greater than the 'T' shaped case 7.2(e) for $\alpha, \beta > 0, \alpha \neq \beta$. For small values of β (up to 0.05) associated with increasingly higher values of α ($\alpha \geq 0.11$ when β is 0.01 and $\alpha \geq 0.23$ when β is 0.05) the loss is greater for case 7.2(e) than for case 7.2(f). The approximate condition, for small α, for configuration 7.2(f) to have a smaller loss than 7.2(e) is $\beta < \alpha^2$. Under the same condition configurations 7.2(f) and 7.2(d) also interchange position. Configuration 7.2(c) has a higher loss than case 7.2(d) when $\alpha < \beta$. The order when $\beta = 0$, $\alpha > 0$ is 7.2(a) and 7.2(b), 7.2(c) and 7.2(f), 7.2(d) and 7.2(e).

7.4.4 Two-parameter second-order CAR

From equation 7.7, for low $|\alpha|$ and $|\beta|$, $L_\mu^*\{m, S(z)\} \approx$

$$m + 2(l_{10} + l_{01})\alpha + 2l_{11}\beta + 2(p_t + p_d + l_{10} + l_{01})\alpha^2 + 2(p_{dd} + l_{11})\beta^2 + 2p_b\alpha\beta.$$

If $\alpha, \beta > 0$ then the more compact the sites in $S(z)$ the greater the loss. However, positive dependence can occur with $\alpha > 0$ and $\beta < 0$ for example, the doubly-geometric process (Martin, 1979) has $\beta = -\alpha^2$, and positive correlations when $\alpha > 0$. In this case the effect of increasing compactness is less clear.

As an illustration of the use of the formula, the approximation for the scaled loss on the mean for the 'T' shaped configuration of Example 7.1 is $L_\mu^*\{5, S(z)\} \approx 5 + 8\alpha + 4\beta + 16\alpha^2 + 6\beta^2 + 12\alpha\beta$. The exact value can be found easily using a recursion, and is

$$(5 + 8\alpha + 4\beta - 4\alpha^2 - 4\beta^2 + 12\alpha\beta - 4\alpha^3)/(1 - 4\alpha^2 + 6\beta^2 - 4\alpha^2\beta + 2\alpha^4).$$

Now, consider the exact formulae when $m = 2$. There are three possible configurations, viz., isolated, horizontally or vertically adjacent, and diagonally adjacent. From §7.3.2, the scaled loss is 2 over the row sum of $\mathbf{V}^{zz}$. Thus, $L_\mu^*\{2, S(z)\}$ is 2, $2/(1-\alpha)$ and $2/(1-\beta)$ respectively.

7.5 Application to some Symmetric Simultaneous Autoregressive Processes

In this section the formulae for the approximations for the loss of information on μ for some special cases of symmetric simultaneous autoregressive processes are presented along with some exact results. The exact formulae for the loss as well as the corresponding approximation for low values of the parameters of the models are given for three missing values for the one-parameter first-order SAR.

For all SAR processes discussed in this section a site i is interior if it does not lie in the two outer layers of the rectangular lattice, i.e., if it is not a site in the first or last two rows or first or last two columns of the lattice.

7.5.1 First-order symmetric SAR

From equation 7.9, the approximation for $L_\mu^*\{m, S(z)\}$ is

$$m + 4l_{10}\alpha + 4l_{01}\beta + (8p_h + 8l_{10} - 2l_{20} - 2m)\alpha^2$$
$$+(8p_v + 8l_{01} - 2l_{02} - 2m)\beta^2 + (8p_d - 4l_{11})\alpha\beta.$$

For the one-parameter first-order SAR with $\alpha = \beta$, $\mathbf{V}^{-1}$ is $(\mathbf{I}_n - \beta\mathbf{U}_1)^2$ and the approximation for $L_\mu^*\{m, S(z)\}$ becomes $m + 4(l_{10} + l_{01})\beta + \{8p_t + 8p_d + 8(l_{10} + l_{01}) - 2(l_{20} + l_{02}) - 4l_{11} - 4m\}\beta^2$.

Thus configurations with many diagonal or lag 2 adjacencies can have smaller losses than isolated sites. Otherwise greater compactness leads to greater loss.

Exact results for the one-parameter first-order SAR when $m = 2$ can be obtained immediately from the result in subsection 7.3.3. They can also be obtained by putting $\beta = 0$ in the results in subsection 7.5.2. Table 7.3 gives the scaled loss $L_\mu^*\{3, S(z)\}$ in increasing order for $0 < \beta < \frac{1}{4}$, for all configurations when $m = 3$. Approximations up to second order in β are also given. The notation o refers to those sites for which the observation is available. The loss $L_\mu\{3, S(z)\}$ increases as β increases (for $0 < \beta < \frac{1}{4}$) and as the configuration includes more sites that are horizontal or vertical neighbours of each other.

Note that if $|\beta|$ is allowed to be large, as is possible for the non-stationary process, a slightly different order results. In this case the leading term in $L_\mu^*\{m, S(z)\}$ is $1_m'\{(\mathbf{U}_1^2)_{zz}\}^{-1}1_m\beta^{-2}$, and the largest loss is associated with those configurations which have no diagonal neighbours and no lag 2 neighbours, i.e. 7.3(g) and 7.3(j).

For the one-parameter process, if the unobserved sites form a closed chain in which each element has exactly one horizontal (or vertical) neighbour and exactly one diagonal neighbour, then 1_m is an eigenvector of $\mathbf{V}^{zz}$, and $\mathbf{L}_\mu^*\{m, S(z)\} = m/(1 - 2\beta + 6\beta^2)$. An example is the octagon mentioned in subsection 7.3.2 when $s = 1$.

Now, consider the case when $m = 2$ for the two-parameter first-order SAR. There are six different configurations, viz., 1(a) : diagonally adjacent sites, 1(b) : sites lag $(2, 0)$ apart; 1(c) : sites lag $(0, 2)$ apart; 1(d) : isolated sites; 1(e) : horizontally adjacent sites; and 1(f) : vertically adjacent sites. As noted in subsection 7.3.3, the scaled loss is 2/(row sum of $\mathbf{V}^{zz}$). Since the diagonal element of $\mathbf{V}^{zz}$ is $1 + 2\alpha^2 + 2\beta^2$, only the off-diagonal element need to be specified. These are

$2\alpha\beta$, α^2, β^2, 0, -2α, -2β for configurations $1(a)$ to $1(f)$, respectively. The approximate loss is $2 - 4\alpha^2 - 4\beta^2$ plus $-4\alpha\beta$, $-2\alpha^2$, $-2\beta^2$, 0, $4\alpha + 8\alpha^2$, and $4\beta + 8\beta^2$ respectively.

If $\alpha = \beta > 0$ then the order of increasing loss is $1(a)$, $1(b)$ and $1(c)$, $1(d)$, $1(e)$ and $1(f)$. The ranking of the configurations in increasing order of loss is not consistent if $\alpha \neq \beta$, α, $\beta > 0$. For instance, configuration $1(b)$ has smaller loss than $1(a)$ for any value of $\alpha > 2\beta$, and $1(c)$ has smaller loss than $1(a)$ for any $\beta > 2\alpha$. Also, if $\alpha > \beta$ then configuration $1(b)$ has smaller loss than $1(c)$, but configuration $1(e)$ has larger loss than $1(f)$. If $\alpha > 0$, $\beta = 0$ then $1(b)$ has smallest loss, and $1(e)$ has largest loss, with the other configurations having the same loss.

Table 7.3: $L_\mu^*\{3, S(z)\}$ for all different configurations of 3 missing points and a one-parameter first-order SAR.

CASE	*CONFIGURATION*	L_μ^*	*APPROXIMATION*
7.3(a)	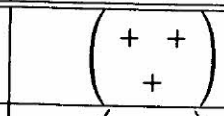	$\frac{3+5\beta^2}{1+9\beta^2+12\beta^4}$	$3-22\beta^2$
7.3(b)	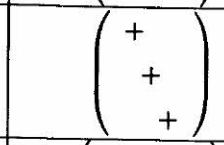	$\frac{3+4\beta^2}{1+8\beta^2+8\beta^4}$	$3-20\beta^2$
7.3(c)	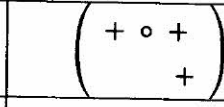	$\frac{3+18\beta^2+23\beta^4}{(1+4\beta^2)(1+8\beta^2+11\beta^4)}$	$3-18\beta^2$
7.3(d)	$(+\circ+\circ+)$	$\frac{3+8\beta^2}{1+8\beta^2+14\beta^4}$	$3-16\beta^2$
7.3(e)	$(+)$ 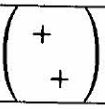	$\frac{3+14\beta^2}{(1+4\beta^2)(1+6\beta^2)}$	$3-16\beta^2$
7.3(f)	$(+)(+\ \circ\ +)$	$\frac{3+13\beta^2}{(1+4\beta^2)(1+5\beta^2)}$	$3-14\beta^2$
7.3(g)	$(+)(+)(+)$	$\frac{3}{1+4\beta^2}$	$3-12\beta^2$
7.3(h)	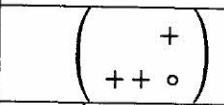	$\frac{3+4\beta+16\beta^2+8\beta^3+28\beta^4}{(1+4\beta^2)(1+4\beta^2+12\beta^4)}$	$3+4\beta-8\beta^2$
7.3(i)	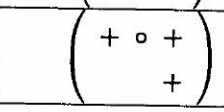	$\frac{3+4\beta+18\beta^2+12\beta^3+39\beta^4}{(1+4\beta^2)(1+4\beta^2+15\beta^4)}$	$3+4\beta-6\beta^2$
7.3(j)	$(+)(++)$	$\frac{3-2\beta+12\beta^2}{(1+4\beta^2)(1-2\beta+4\beta^2)}$	$3+4\beta-4\beta^2$
7.3(k)	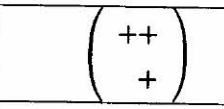	$\frac{3+8\beta+14\beta^2}{(1+2\beta^2+24\beta^4)}$	$3+8\beta+8\beta^2$
7.3(l)	$(+++)$	$\frac{3+8\beta+13\beta^2}{1+\beta^2+20\beta^4}$	$3+8\beta+10\beta^2$

7.5.2 Two-parameter second-order symmetric SAR

Two sites i and j for a second-order SAR are isolated if, besides satisfying the conditions for being isolated in subsection 7.5.1, site j is also not a lag $(\pm 1, \pm 2)$, $(\pm 2, \pm 1)$ or $(\pm 2, \pm 2)$ neighbour of site i.

From equation 7.9 the approximation for $L^*_\mu\{m, S(z)\}$, provided the values of $\mid \alpha \mid$ and $\mid \beta \mid$ are not too large, is :

$$m + 4(l_{10} + l_{01})\alpha + 4l_{11}\beta + \{8p_t + 8p_d + 8(l_{10} + l_{01}) - 2(l_{20} + l_{02}) - 4l_{11} - 4m\}\alpha^2$$
$$+\{8p_{dd} + 8l_{11} - 4(l_{20} + l_{02}) - 2l_{22} - 4m\}\beta^2 + \{8p_b - 8(l_{10} + l_{01}) - 4(l_{12} + l_{21})\}\alpha\beta.$$

As an illustration of the use of this approximate formula consider Example 7.2 given in subsection 7.4.1. For this configuration $\mathbf{L}^*_\mu\{6, S(z)\} \approx 6+16\alpha+8\beta+10\alpha^2-14\beta^2-12\alpha\beta$. The exact formula for this example is difficult to obtain.

Now consider the exact formulae when $m = 2$. Again, the scaled loss is 2 divided by the row sum of $\mathbf{V}^{zz}$. The diagonal element of $\mathbf{V}^{zz}$ is $1+4\alpha^2+4\beta^2$. There are six possible configurations: $2(a)$: diagonally adjacent sites; $2(b)$: sites at lags $(2, 0)$ or $(0, 2)$ apart; $2(c)$: sites at lags $(2, \pm 1)$ or $(1, \pm 2)$, apart; $2(d)$: sites at lag $(2, \pm 2)$ apart; $2(e)$: isolated sites, and $2(f)$: horizontally or vertically adjacent sites. The off-diagonal element of $\mathbf{V}^{zz}$ is $-2\beta + 2\alpha^2$, $\alpha^2 + 2\beta^2$, $2\alpha\beta$, β^2, 0, and $-2\alpha+4\alpha\beta$ respectively. The approximate loss is $2-8\alpha^2-8\beta^2$ plus $4\beta-4\alpha^2+8\beta^2$, $-2\alpha^2 - 4\beta^2$, $-4\alpha\beta, -2\beta^2$, 0, and $4\alpha + 8\alpha^2 - 8\alpha\beta$ respectively.

If $\alpha > 0$, $\beta = 0$ then the order of increasing loss is $2(a)$, $2(b)$, $2(c)$ and $2(d)$ and $2(e)$, $2(f)$. This order can change appreciably as β varies.

7.6 Information loss with boundary sites

The exact formulae and the approximations given in the previous sections are valid under the assumption that the missing sites are all interior ones. This section evaluates the effect of using those formulae when not all missing sites satisfy this condition. For instance, if the failure of a detector causes the first, and/or the last line on imagery to be 'defective', all the missing values along the 'defective' lines occur at sites that are not interior, when conditional autoregressive processes are considered (see §5.3). Most frequently, however, the missing

values arising from line dropout occur at sites that are interior ones. The effect of the using the formulae for the loss of information assuming that all missing sites are interior, when they are not, varies with the size of the lattice. This is also aproached in this section. The discussion is restricted to the cases of a 2p-CAR(1) and a 2p-CAR(2) processes, as defined in §5.5.2 (one parameter for the horizontal neighbours and one for vertical neighbours) and §5.5.3 (one parameter for horizontally and vertically adjacent neighbours, and one for diagonally adjacent neighbours), respectively.

Assume initially that only one line on the image is defective. This assumption is dropped latter, with results for multiple defective lines being merely an extension of the results for a single faulty line.

First the discussion is carried out for the two-parameter first-order conditional autoregressive process.

7.6.1 The case of a 2p-CAR(1) process

If the missing line is not the first or the last one, then there are only two boundary sites to consider, viz., the first and last sites in the defective line.

If all sites in $S(z)$ are interior then $\mathbf{V}^{zx}1_n$ is a vector of constant values a, $a = 1 - 2\alpha - 2\beta$, and the loss of information on μ can be evaluated from equation 7.6, that is

$$L_\mu\{m, S(z)\}\sigma^2 = a^2 1_m'(\mathbf{V}^{zz})^{-1}1_m.$$

However, when there are two boundary sites amongst the m missing, $(\mathbf{V}^{zx}1_n)' = [a^* \;\; a \;\; a \;\; a \;\; \ldots \;\; a^*]$ for a as above, and $a^* = 1 - \alpha - 2\beta$.

Let the m by m matrix$(\mathbf{V}^{zz})^{-1} = \{v^*_{k,l}\}$, $k, l = 1, \ldots, m$ be partitioned as follows:

$$\begin{bmatrix} \mathbf{V}^*_{11} & \mathbf{V}^*_{12} \\ \mathbf{V}^*_{21} & \mathbf{V}^*_{22} \end{bmatrix}$$

where

- $\mathbf{V}^*_{11}$ is a 2 by 2 matrix with elements $v^*_{1,1}$, $v^*_{1,m}$, $v^*_{m,1}$, and $v^*_{m,m}$;
- $\mathbf{V}^*_{12}$ is a 2 by $m-2$ matrix with elements $v^*_{1,l}$, and $v^*_{m,l}$, $l = 2, \ldots, m-1$; and

- $\mathbf{V}^*_{22}$ is a $m-2$ by $m-2$ matrix obtained from $(\mathbf{V}^{zz})^{-1}$ by the deletion of the first and last row, and first and last column.

The exact loss of information on μ is then given by

$$\begin{aligned} L_\mu\{m, S(z)\}\sigma^2 &= a^2 1'_{m-2}\mathbf{V}^*_{22}1_{m-2} \\ &+ a^{*2}[v^*_{11} + v^*_{1,m} + v^*_{m,1} + v^*_{m,m}] \\ &+ aa^*[\textstyle\sum_{l=2}^{m-1}(v^*_{1,l} + v^*_{m,l} + v^*_{l,1} + v^*_{l,m})] \end{aligned} \tag{7.10}$$

Equation 7.10 can be simplified as

$$\begin{aligned} L_\mu\{m, S(z)\}\sigma^2 &= a^2 1'_{m-2}\mathbf{V}^*_{22}1_{m-2} + 2a^{*2}[v^*_{1,1} + v^*_{1,m}] \\ &+ 2aa^*[\textstyle\sum_{l=2}^{m-1}(v^*_{1,l} + v^*_{m,l})]. \end{aligned} \tag{7.11}$$

Hence, if the loss of information on μ is calculated using equation 7.6 instead of equation 7.11, the difference between the exact and the approximate loss due to the m missing sites in $S(z)$ (exact loss - approximate loss), denoted $D[L_\mu\{m, S(z)\}\sigma^2]$ is

$$2\alpha(2 - 3\alpha - 4\beta)(v^*_{1,1} + v^*_{1,m}) + 2\alpha(1 - 2\alpha - 2\beta)[\sum_{l=2}^{m-1}(v^*_{1,l} + v^*_{m,l})]. \tag{7.12}$$

Note that $D[L_\mu\{m, S(z)\}\sigma^2]$ depends only on the values $v^*_{k,l}$ associated with the boundary sites. Also, as all the missing sites occur on a single line, then all the elements in matrix $\mathbf{V}^{zz}$ [and hence, in $(\mathbf{V}^{zz})^{-1}$)] have dependence only in the horizontal direction, that is, have elements that depend only on α.

Two boundary sites

The difference in loss of information on μ has been evaluated for the stationary 2p-CAR(1) process for some sets of α and β, and $m = 92$. For each set, the percentage difference in loss (PDL) is calculated as minus 100 times the ratio between the difference loss, and the loss obtained from equation 7.6, that is, $-\frac{100 \times D[L_\mu\{m,S(z)\}\sigma^2]}{L_\mu\{m,S(z)\}\sigma^2}$. The calculations are performed for $-0.25 < \alpha, \beta < 0.25$ with respective increments of 0.05 and 0.02 for α and β. The PDL for these sets of α and β are given in Figure 7.1.

From Figure 7.1 and equation 7.12, the following conclusions can be drawn:

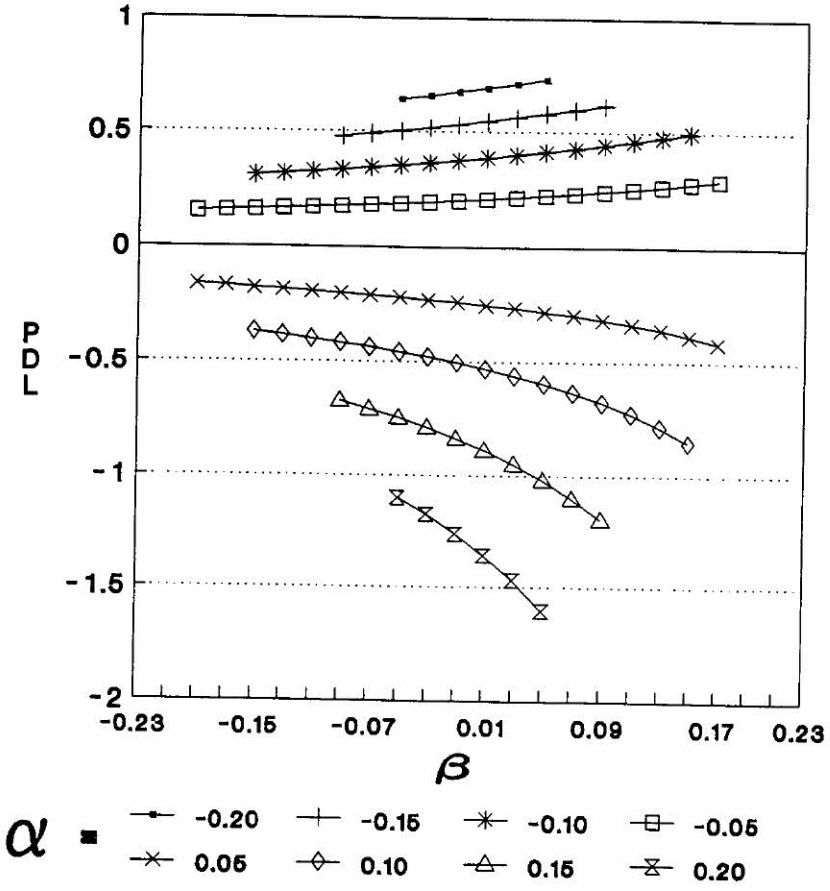

Figure 7.1: Plot of the PDL for a 2p-CAR(1) process when two of the missing sites lie on the boundary, for $m = 92$, and using different sets of α and β.

- for m=92 the percentage difference in loss is negligible. The smallest and largest absolute values of the computed PDL are 0.151 (for $\alpha = -0.05$ and $\beta = -0.19$), and 1.603 $\alpha = 0.20$ and $\beta = 0.05$.

- for $\alpha > 0$ and any β, the loss of information of μ computed via equation 7.6 always underestimates the exact loss, and becomes larger as α and β increase.

- for $\alpha < 0$ and any β, equation 7.6 always overestimates the loss. The difference becomes larger as $\mid \alpha \mid$ and β increase.

- for $\alpha = 0.0$ the difference between the exact loss and that calculated via equation 7.6 is zero. This follows directly from 7.12.

Figure 7.2 (a) and (b) gives the plot of the percentage difference in loss for several values of m, and different sets of values of α and β, assuming only two boundary sites amongst the missing; whilst in (c) and (d) it is assumed that all the missing values lie at the boundary (discussed in the next section).

From Figure 7.2 (a) and (b) it can the seen that the PDL becomes increasingly smaller as the number of missing sites increase, and that for large value of m the PDL is negligible, unlike when a small number of missing sites occur. Considering that the number of missing values in the image, arising from line-dropout is usually large, then the loss of information on μ, calculated via equation 7.6 is a very good approximation.

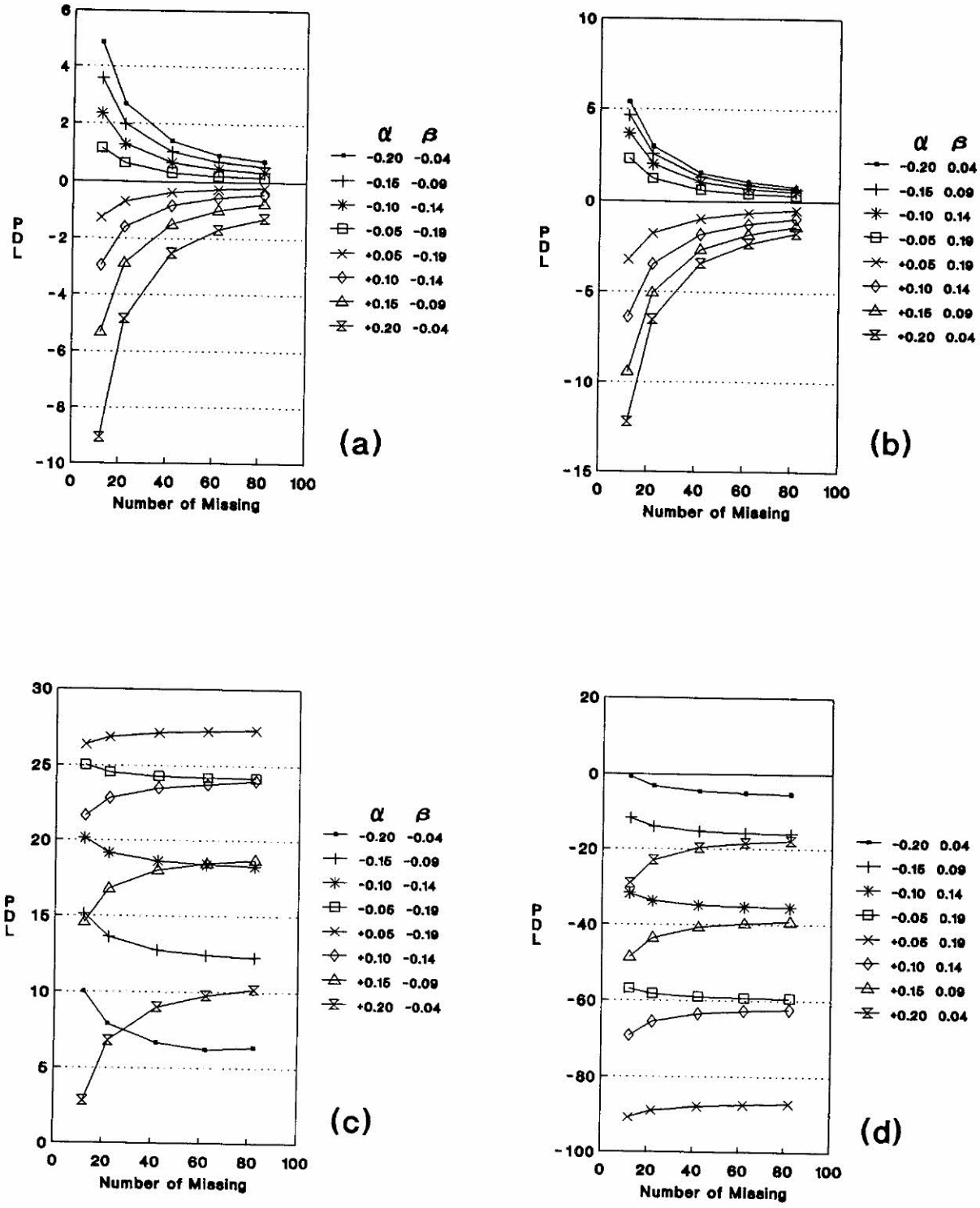

Figure 7.2: Plot of the percentage difference in loss for a 2p-CAR(1) process, for different values of m, and assuming (a) two boundary sites when $\alpha \neq 0$ and $\beta < 0$; (b) two boundary sites when $\alpha \neq 0$ and $\beta > 0$; (c) all boundary sites when $\alpha \neq 0$ and $\beta < 0$; (d) all boundary sites when $\alpha \neq 0$ and $\beta > 0$.

7.6.1.2 All missing sites on the boundary

If the 'defective' line on the image is the first, or the last one, all missing values occur at sites that are not interior. In this situation $(\mathbf{V}^{zx}1_n)' = [a_1 \;\; a_2 \;\; a_2 \;\; \ldots \;\; a_2 \;\; a_1]$ for $a_1 = 1 - \alpha - \beta$ and $a_2 = 1 - 2\alpha - \beta$.

The difference between the exact loss of information on μ and that obtained from equation 7.6 is

$$\begin{aligned} D[L_\mu\{m, S(z)\}\sigma^2] &= 2(\alpha+\beta)(2-3\alpha-3\beta)(v^*_{1,1}+v^*_{1,m}) \\ &+ \beta(2-4\alpha-3\beta)\textstyle\sum_{k=2}^{m-1}\sum_{l=2}^{m-1} v^*_{k,l} \\ &+ 2(\alpha+2\beta-2\alpha^2-5\alpha\beta-3\beta^2)\textstyle\sum_{l=2}^{m-1}(v^*_{1,l}+v^*_{m,l}). \end{aligned} \tag{7.13}$$

Unlike equation 7.11, which has only terms involving the two boundary sites, the equation for the difference in loss in 7.13 involves all elements in $(\mathbf{V}^{zz})^{-1}$. The difference in loss is not negligible, as in the case of only two boundary sites, even for large values of m. Figure 7.3 gives the plot of the percentage difference in loss for some values of $-0.20 \leq \alpha, \beta \leq 0.20$, and $m = 92$, from where it can be seen that the largest absolute value of the PDL (86 %) occurs for $\alpha = 0.05$ and $\beta = 0.19$.

From Figure 7.3 it can be seen that for any α, and small β $(-0.01 < \beta < 0.01)$, the PDL is approximately zero, and the difference between the exact loss and that calculated via equation 7.6 is negligible. From equations 7.12 and 7.13 it can be seen that the difference in loss is always greater when all sites lie on the boundary, than when there are only two boundary sites. This can also be observed in Figure 7.2 (c) and (d), which gives the plot of the PDL for some sets of α and β, and different values of m. From this figure it can be noted that unlike in the case of two boundary sites, when the PDL always decreases as the number of missing sites increases, the PDL for the case of all boundary sites increases as m increases when α and β have different signs. Otherwise, the PDL decreases with increasing m.

7.6.2 Difference in loss for the 2p-CAR(2) process

7.6.2.1 Two boundary sites

If all the missing sites are interior, then $a = 1 - 4\alpha - 4\beta$ for a two-parameter second-order CAR process. A site is said to be interior if it does not lie on the

7.6.1.2 All missing sites on the boundary

If the 'defective' line on the image is the first, or the last one, all missing values occur at sites that are not interior. In this situation $(\mathbf{V}^{zx}1_n)' = [a_1 \;\; a_2 \;\; a_2 \;\; \ldots \;\; a_2 \;\; a_1]$ for $a_1 = 1 - \alpha - \beta$ and $a_2 = 1 - 2\alpha - \beta$.

The difference between the exact loss of information on μ and that obtained from equation 7.6 is

$$\begin{aligned} D[L_\mu\{m, S(z)\}\sigma^2] &= 2(\alpha+\beta)(2-3\alpha-3\beta)(v^*_{1,1}+v^*_{1,m}) \\ &+ \beta(2-4\alpha-3\beta)\textstyle\sum_{k=2}^{m-1}\sum_{l=2}^{m-1} v^*_{k,l} \\ &+ 2(\alpha+2\beta-2\alpha^2-5\alpha\beta-3\beta^2)\textstyle\sum_{l=2}^{m-1}(v^*_{1,l}+v^*_{m,l}). \end{aligned} \tag{7.13}$$

Unlike equation 7.11, which has only terms involving the two boundary sites, the equation for the difference in loss in 7.13 involves all elements in $(\mathbf{V}^{zz})^{-1}$. The difference in loss is not negligible, as in the case of only two boundary sites, even for large values of m. Figure 7.3 gives the plot of the percentage difference in loss for some values of $-0.20 \leq \alpha, \beta \leq 0.20$, and $m = 92$, from where it can be seen that the largest absolute value of the PDL (86 %) occurs for $\alpha = 0.05$ and $\beta = 0.19$.

From Figure 7.3 it can be seen that for any α, and small β ($-0.01 < \beta < 0.01$), the PDL is approximately zero, and the difference between the exact loss and that calculated via equation 7.6 is negligible. From equations 7.12 and 7.13 it can be seen that the difference in loss is always greater when all sites lie on the boundary, than when there are only two boundary sites. This can also be observed in Figure 7.2 (c) and (d), which gives the plot of the PDL for some sets of α and β, and different values of m. From this figure it can be noted that unlike in the case of two boundary sites, when the PDL always decreases as the number of missing sites increases, the PDL for the case of all boundary sites increases as m increases when α and β have different signs. Otherwise, the PDL decreases with increasing m.

7.6.2 Difference in loss for the 2p-CAR(2) process

7.6.2.1 Two boundary sites

If all the missing sites are interior, then $a = 1 - 4\alpha - 4\beta$ for a two-parameter second-order CAR process. A site is said to be interior if it does not lie on the

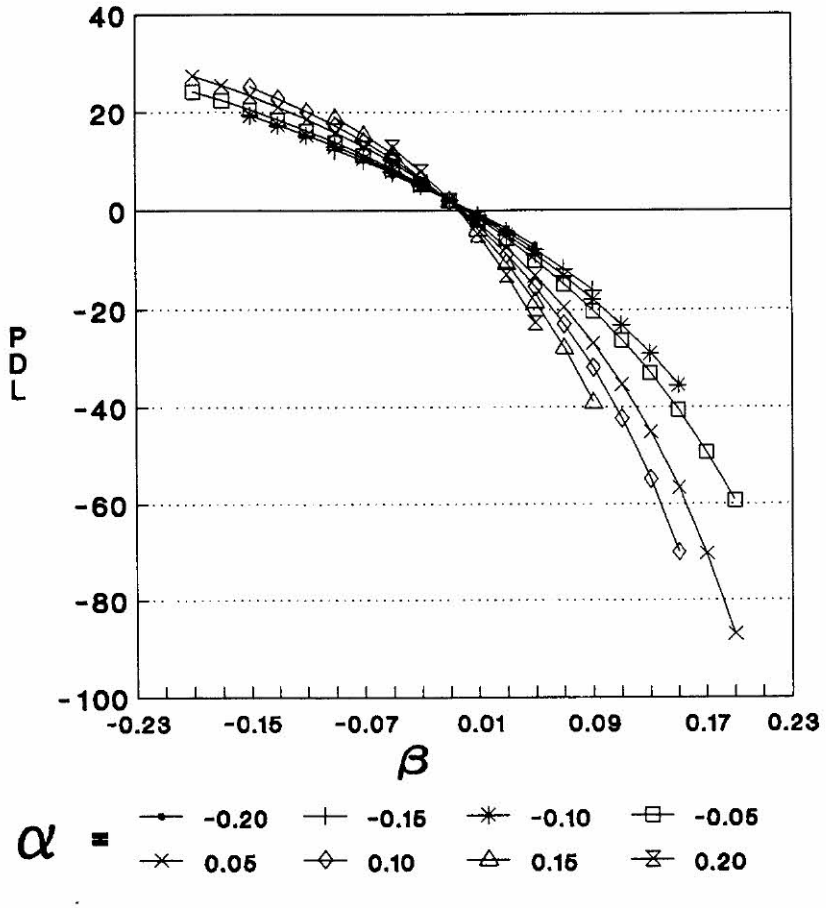

Figure 7.3: Plot of the PDL for a 2p-CAR(1) process when all the missing sites lie on the boundary, for $m = 92$, and using different sets of α and β.

first or last line, or first or last column of the lattice.

When there are two boundary sites amongst those missing, then $(\mathbf{V}^{zx}1_n)' = [a^* \;\; a \;\; a \;\; a \;\; \ldots \;\; a^*]$ for $a = 1 - 4\alpha - 4\beta$ and $a^* = 1 - 3\alpha - 2\beta$, and the difference between the exact loss and that calculated from 7.6 is

$$\begin{aligned} D[L_\mu\{m, S(z)\}\sigma^2] &= 2(\alpha + 2\beta)(2 - 7\alpha - 6\beta)(v^*_{1,1} + v^*_{1,m}) \\ &+ 2(\alpha + 2\beta)(1 - 4\alpha - 4\beta)\textstyle\sum_{i=2}^{m-1}(v^*_{i,1} + v^*_{i,m}). \end{aligned} \tag{7.14}$$

Since all the missing sites occur on a line, the elements in $\mathbf{V}^{zz}$ are either zero, or else a function of α, and are exactly as for the case of a 2p-CAR(1), in §7.6.1.

Figure 7.4 gives the plot of the percentage difference in loss obtained using equation 7.14 for a set of values α and β satisfying the stationarity condition given in Chapter 5 (§5.5.2).

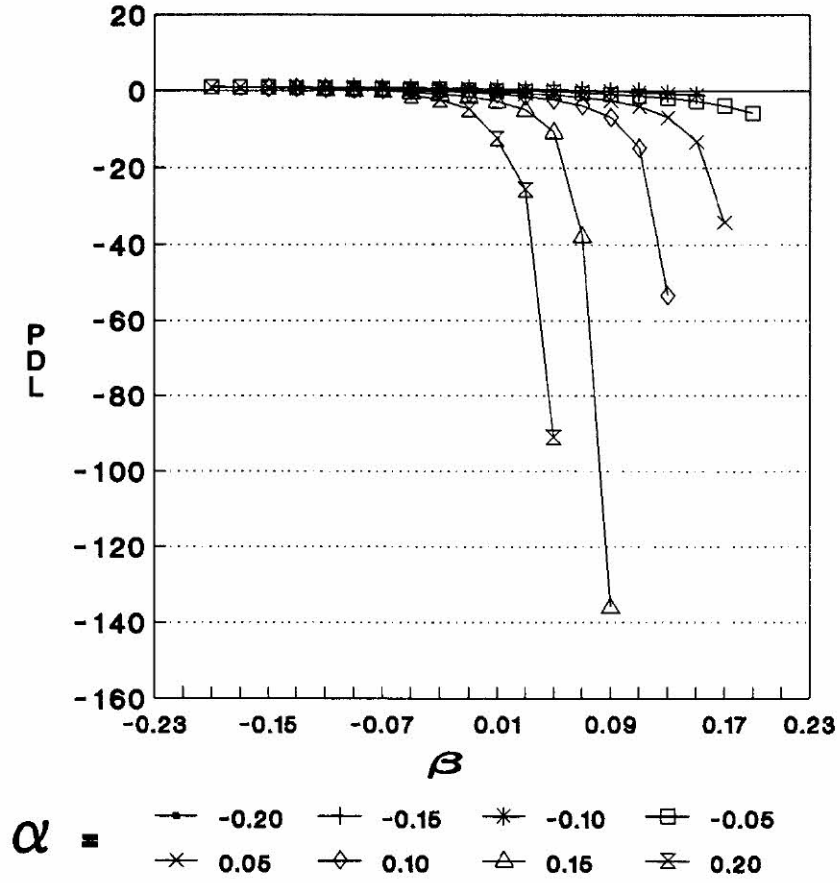

Figure 7.4: Plot of the PDL for a 2p-CAR(2) process when two of the missing sites lie on the boundary, for $m = 92$, and using different sets of α and β.

The following conclusions can be drawn from Figure 7.4 and from equation 7.13:

- for any α, and $\beta = -\alpha/2$, there is no difference between the exact loss and that obtained from equation 7.6. This follows directly from 7.14.
- for any $\alpha > 0$ and $\beta > -\alpha/2$, the absolute value of the PDL increases as α and β increase, and the exact loss is underestimated from equation 7.6.
- for $\alpha < 0$ and any β, the PDL is negligible (less than 5%).
- the PDL increases as α and β increase, but is always negligible (less than 5%) for $\beta < 0$.

7.6.2.2 All boundary sites

When all missing sites lie on the boundary of the image (either first, or last line), then for a 2p-CAR(2) process $(\mathbf{V}^{zx}1_n)' = [a_1 \quad a_2 \quad a_2 \quad \ldots a_1]$ for $a_1 = 1 - 2\alpha - \beta$, and $a_2 = 1 - 3\alpha - 2\beta$. The difference between the exact loss and the approximate loss computed from equation 7.6 with $a = 1 - 4\alpha - 4\beta$ is

$$\begin{aligned} D(L_\beta\{m, S(z)\}/\sigma^2) &= 2(4\alpha + 6\beta - 12\alpha^2 - 28\alpha\beta - 15\beta^2)(v^*_{1,1} + v^*_{1,m}) \\ &+ (2\alpha + 4\beta - 7\alpha^2 - 20\alpha\beta - 12\beta^2)\textstyle\sum_{k=2}^{m-1}\sum_{l=2}^{m-1} v^*_{k,l} \\ &+ 2(3\alpha + 5\beta - 10\alpha^2 - 25\alpha\beta - 14\beta^2)\textstyle\sum_{l=2}^{m-1}(v^*_{1,l} + v^*_{m,l}). \end{aligned} \tag{7.15}$$

Figure 7.5 gives the plot of the percentage difference in loss obtained for a 2p-CAR(2) process, using equation 7.15, and some sets of values of α and β within the stationarity range of the process. From Figure 7.5 it is seen that most conclusions drawn for the case of the 2p-CAR(2) with two boundary sites are still valid here, when all sites are boundary sites. The loss in much greater than for the case of two boundary sites, and is only negligible for any fixed α, when β is close to β^*_α, the value of β at which the PDL is zero.

Figure 7.6 (a) and (b) gives the PDL for different values of m, and for some sets of values of α and β when there are only two boundary sites. Figure 7.6 (c) and (d) gives the PDL for the same values of m and of α and β, when all missing sites lie at the boundary.

Figure 7.6 (a), (b), (c) and (d) shows that the PDL usually decreases as m increases, and is much greater when all the missing sites are boundary sites, especially when $\alpha, \beta > 0$. Note that for the case of two boundary sites [Figure 7.6 (a) and (b)] and a 2p-CAR(2) process, the difference between the approximate and exact loss when $\beta < 0$ is very small, even for small values of m, and becomes negligible as m increases. When $\alpha < 0$ and $\beta > 0$, the PDL becomes negligible as m increases, being largest (in absolute value) when $\mid \alpha \mid$ is small.

For any α and $\beta < 0$ the PDL decreases as $\mid \alpha \mid$ increases, whereas when $\beta > 0$ the PDL increases as $\mid \alpha \mid$ decreases. The approximate formulae usually overestimates the exact loss of information on μ when $\beta < 0$ and there are only two boundary sites amongst those missing.

When all missing sites are boundary sites, the largest absolute value of the PDL occurs when $\alpha, \beta > 0$. The PDL increases as α decreases, and is always

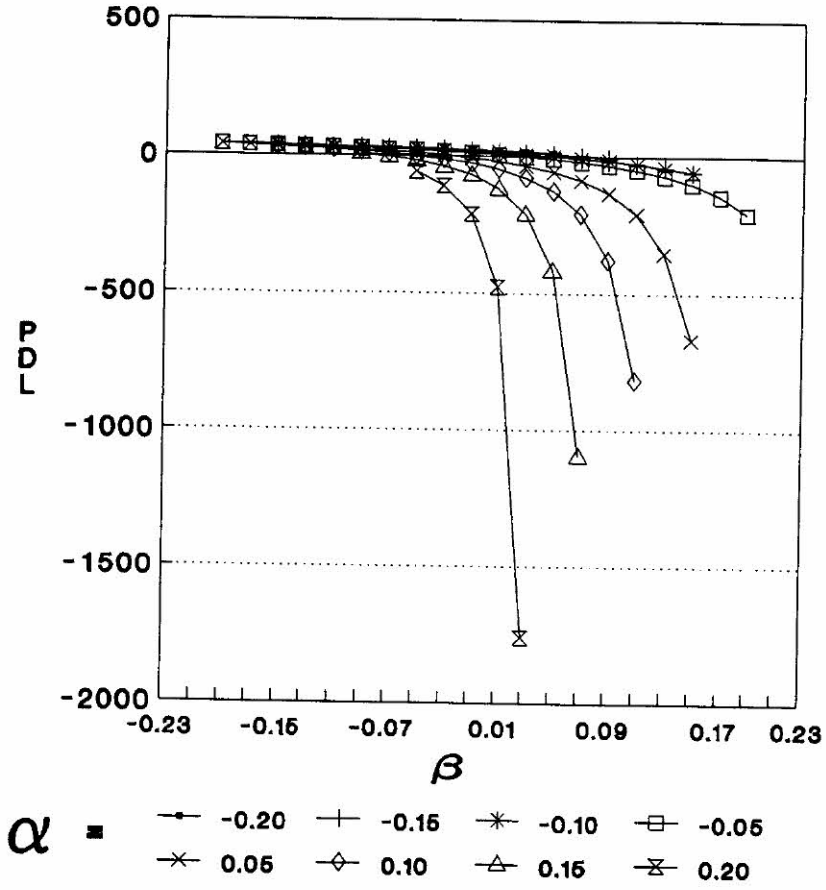

Figure 7.5: Plot of the PDL for a 2p-CAR(2) process when all the missing sites lie on the boundary, for $m = 92$, and using different sets of α and β.

negative. Thus, the approximate formulae underestimates the exact loss.

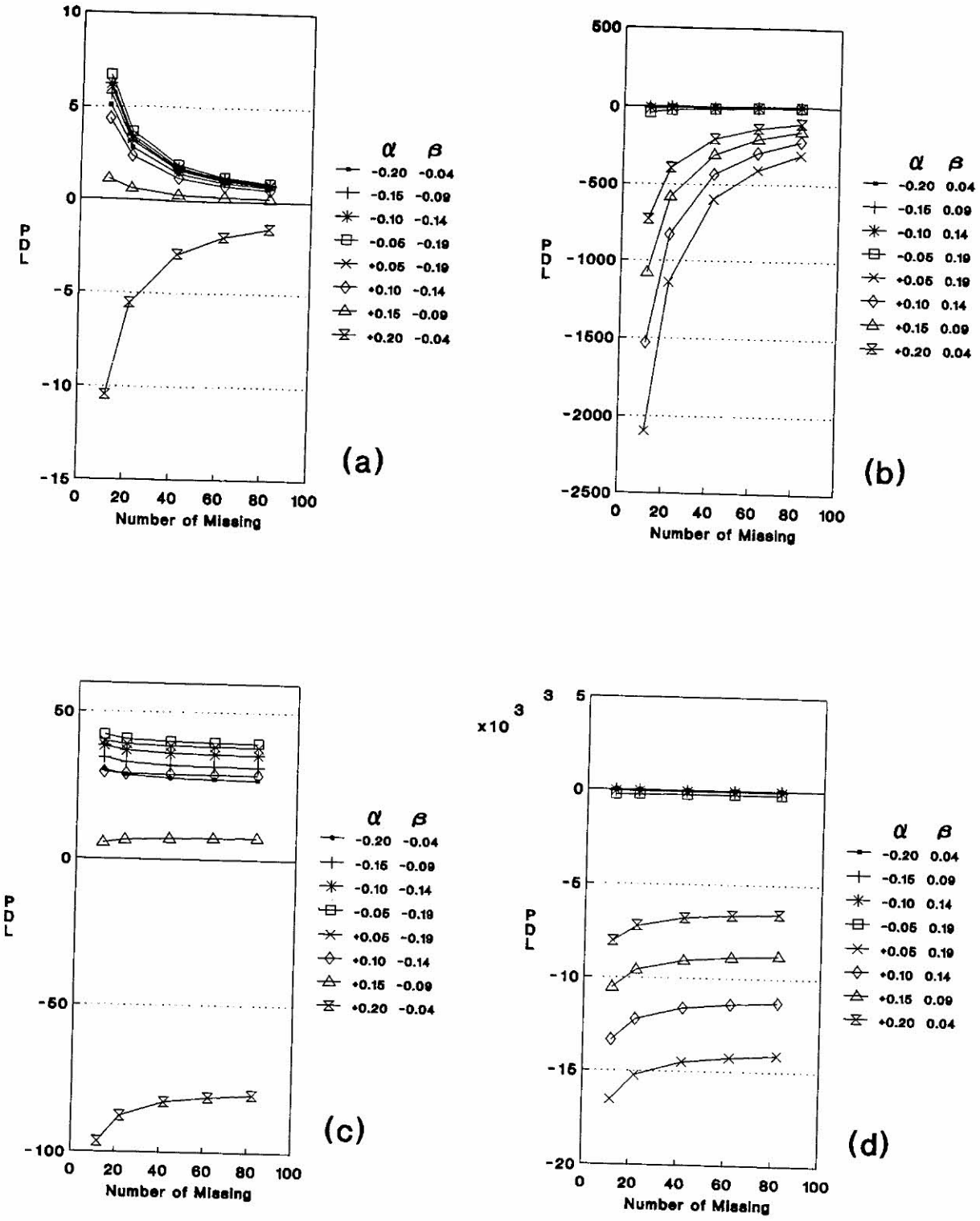

Figure 7.6: Plot of the PDL for different values of m and (a) two boundary sites when $\alpha \neq 0$ and $\beta < 0$; (b) two boundary sites when $\alpha \neq 0$ and $\beta > 0$; (c) all boundary sites when $\alpha \neq 0$ and $\beta < 0$; (d) all boundary sites when $\alpha \neq 0$ and $\beta > 0$.

Consider now the case of multiple lines missing from the failure of one detector. As every site on a defective line is isolated from any other site on another faulty line, that is, no two sites in two distinct lines are adjacent horizontal or vertical neighbours, then $\mathbf{V}^{zz}$ is block diagonal, and the loss of information on μ is simply the sum of the individual losses for a single line.

If the faulty line is not the first, or the last one on the image, then the loss of information on μ for a 2p-CAR(1) process can be computed from the approximation formulae given in subsection 7.4.3, for small values of $\mid \alpha \mid$ and $\mid \beta \mid$. If the number of missing sites per line is large, then the approximation formulae is still good even for large values of α and β, given that they are within the stationarity range of the process. This also holds for the 2p-CAR(2) process, except when $\alpha + \beta$ is close to $\frac{1}{4}$.

However, if the faulty line is the first, or the last one, then the use of formula 7.6, or of the approximation formulae for the loss on μ is not recommended for any of the processes, even for low values of α and β and m is large. The greatest discrepancy between the exact loss and that calculated via equation 7.6 occurs when $\alpha+\beta$ is close to $\frac{1}{4}$.

The difference between the exact loss on μ and that evaluated under the assumption of all missing sites being interior ones depends on the exact location of the sites in $S(z)$. The ranking of the loss is not as easily determined as when all the missing sites are interior ones.

Consider, for instance, case 7.2(a) in Table 7.2. There are several different configurations of the missing sites, all with different values for the loss on μ. Figure 7.7 shows 6 out of the 10 possible configurations of 4 missing sites, when there are two isolated groups with neighbouring sites. The loss on μ for configurations (a) to (f), for the stationary 1p-CAR(1) process, when $\beta = 0.24$ are: 0.0948, 0.1812, 0.4485, 0.4126, 0.6506, and 0.8886. The loss becomes greater as more missing sites occur at the boundary of the lattice. When all sites are interior, the loss on μ is 0.0084. As $\beta > 0$ decreases, the loss on μ increases, and for $\beta = 0.05$ it is respectively 2.7815, 2.8682, 2.9604, 3.0421, 3.1341, and 3.2261 for configurations (a) to (f) in Figure 7.7. The loss when the sites in the two isolated groups are interior ones is 2.6947. Therefore, the formulae for the loss on μ assuming that all missing sites is interior can be used as an approximation for the exact loss for clusters of missing with boundary sites, when there are few

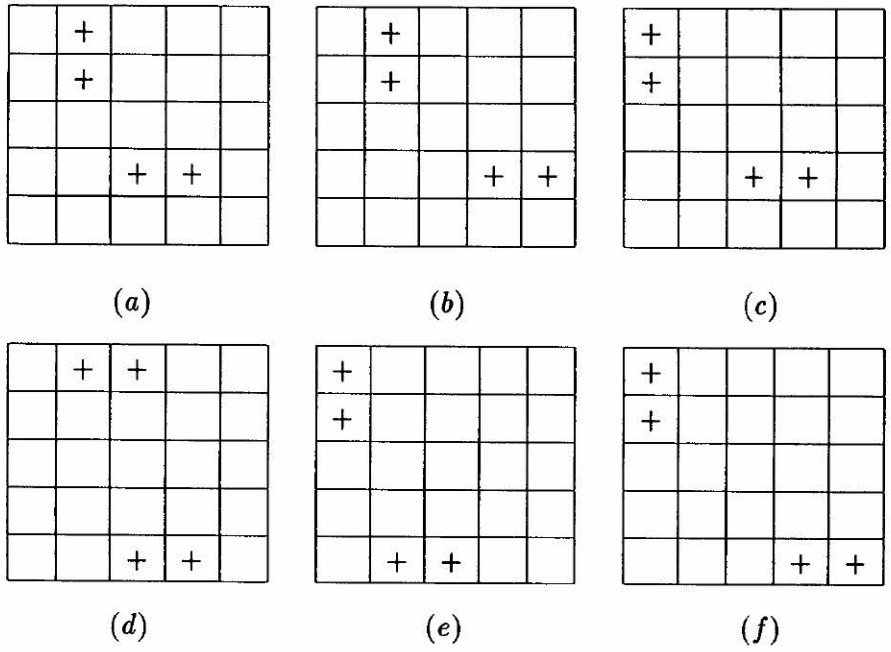

Figure 7.7: Configurations with different loss on μ when $m = 4$ and there are two isolated groups with two neighbouring sites.

boundary and edge sites. In this case the approximation formulae provided for all processes can also be used if the conditions imposed upon those approximations are satisfied.

7.7 Loss of Information on β for the stationary 1p-CAR(1) process

Let $L_\beta\{m, S(z)\}\sigma^2$ denote the loss of information on the dependence parameter β, due to m missing values at sites in $S(z)$.

The formulae for the loss of information on β are much more complicated than those provided for the loss on μ. Martin (1989) deduces the general formulae for the loss on β using the conditional distribution of $z \mid y$, and especializes to the case of a 1p-CAR(1). The expression for the loss of information on β, for this process, can be simplified to

$$L_\beta\{m, S(z)\}\sigma^2 = \beta^{-2}[tr\{(\mathbf{V}^{zz})^{-1}\mathbf{V}_{zz}\} + \tfrac{m}{2} - tr(\mathbf{V}^{zz})^{-1} - \tfrac{1}{2}tr(\mathbf{V}^{zz})^{-2}] \quad (7.16)$$

From equation 7.16 it is seen that even for the simple case of the 1p-CAR(1) process the formulae for the loss of information is complicated and requires the knowledge of $\mathbf{V}_{zz}$, which is not simple to obtain. Moreover, the loss depends not only on the value of β, but also on the size and shape of the lattice, and on the number and the actual sites $S(z)$ that are unobserved.

Martin (1989) gives the general loss of information on β for the 1p-CAR(1) when $m = 1, 2, 3$, and gives the results assuming stationarity. Thus, for instance, when $m = 2$ and the missing sites i and j are neighbours, $L_\beta\{m, (i,j) = (v_{ii} + v_{jj} + 2\beta v_{ij})/[\beta^2(1-\beta^2)] - (2-\beta^2)(1+\beta^2)/[\beta^2(1-\beta^2)^2]$. Assuming stationarity, $v_{ii}+v_{jj}+2\beta v_{ij}$ is replaced by $2f(1+\beta\rho_{10})$, where $f = var(u_{ij})/\sigma^2 = (1-4\beta\rho_{10})^{-1}$.

When $m = 4$, there are 10 cases to consider. In half of these cases the missing sites i, j, k, l are connected. In the remaining cases the configuration of the missing sites consists of disconnected groups, and as for the loss of information on μ, the loss is a sum of terms of the form $L_\beta\{m_i, S(z_i)\}$.

Unlike in the case of the loss on μ, the loss on β for a chain does depend on the shape of the chain. (apart from rotations and reflections). Thus, the losses on β for configurations $(++++)$, $\begin{pmatrix} +++ \\ + \end{pmatrix}$, and $\begin{pmatrix} + \\ ++ \\ + \end{pmatrix}$ are all different.

First, the case of 4 connected sites is investigated. The missing sites can form a connected line from i to l, and in this case the formula, assuming stationary is

$$\begin{aligned} L_\beta\{4,(++++)\}\sigma^2 &= (-4+9\beta^2-3\beta^4-9\beta^6+2\beta^8)/[\beta(1-3\beta^2+\beta^4)]^2 \\ &+\beta^{-2}\{[(4-6\beta^2)f+(6-4\beta^2)\beta f\rho_{10}+4\beta^2 f\rho_{20}+2\beta^3 f\rho_{30}]/(1-3\beta^2+\beta^4)\} \end{aligned} \tag{7.17}$$

The configuration of the four missing sites can also have a 'step' shape, in which case ρ_{20} and ρ_{30} in equation 7.17 are replaced by ρ_{11} and ρ_{12}, respectively. Since $\rho_{11} > \rho_{20}$, and $\rho_{12} > \rho_{30}$ for all $\beta > 0$, the loss for the 'step' shape is always slightly greater than for the linear case. The four sites can also form a chain with an 'L' shape. In this case equation 7.17 changes slightly, with the coefficient of ρ_{20} now being $2\beta^2$ and ρ_{30} being replaced by ρ_{12}. It also includes a term in ρ_{11}, with coefficient $2\beta^2$. The loss is slightly smaller than for the 'step' case, but slightly greater than for the linear configuration. This is due to the greater number of sites linked diagonally in the 'step' case than in the 'L' shape case. As $\rho_{11} > \rho_{20}$ for all $\beta > 0$, then the loss is expected to be slightly greater in the former case than in the latter.

Other configurations for four missing sites include the compact form $\begin{pmatrix} ++ \\ ++ \end{pmatrix}$ and $\begin{pmatrix} +++ \\ + \end{pmatrix}$.

For the compact configuration, the loss of information on β is given by

$$L_\beta\{4, \begin{pmatrix} ++ \\ ++ \end{pmatrix} \} = 4/\{\beta^2(1-4\beta^2)^2\}\{(-1+3\beta^2-4\beta^4)+(1-4\beta^2)[(1-2\beta)^2 f+2\beta f\rho_{10} + 2\beta^2 f\rho_{11}]\},$$

whilst for configuration $\begin{pmatrix} +++ \\ + \end{pmatrix}$ the loss is

$$L_\beta\{4, \begin{pmatrix} +++ \\ + \end{pmatrix} \} = \{[\beta^2(1-3\beta^2)^2]\}^{-1}\{(-4+9\beta^2-9\beta^4)+(1-3\beta^2)(4-6\beta^2)f+6\beta f\rho_{10}+2\beta^2 f\rho_{20}+4\beta^2 f\rho_{1,1}]\}$$

Table 7.4 gives the loss on β for the stationary 1p-CAR(1) process for some values of $\beta > 0$, and $m = 4$. The results in the table are found using equation 7.16, and the values of v_{gh} obtained from the inversion of $\mathbf{V}^{-1} = \mathbf{I} - \beta\mathbf{U}_1$, using a 9 by 9 torus lattice. These values are an approximation which is good for low values of β, but less good for $\beta = 0.24$. The values of v_{gh}, for sites separated by lags (g,h) are given below, for some values of g and h. The loss of information on β, for configurations 7.4 (f) to 7.4 (j) in Table 7.4 are found by summation. For instance, the loss on β for configuration 7.4 (f) is $L_\beta\{4, \ (+++)(+) \ \} = L_\beta\{3, \ (+++) \ \} + L_\beta\{1, \ (+) \ \}$.

	β				
(g,h)	0.05	0.10	0.15	0.20	0.24
(0,0)	1.01023	1.04405	1.11456	1.27047	1.76737
(0,1)	0.05115	0.11014	0.19094	0.33808	0.79935
(0,2)	0.00260	0.01186	0.03435	0.09920	0.43890
(0,3)	0.00013	0.00130	0.00649	0.03222	0.28573
(0,4)	0.00000	0.00016	0.00149	0.01369	0.22592
(1,1)	0.00515	0.02274	0.06202	0.16038	0.56217
(1,2)	0.00039	0.00358	0.01579	0.06287	0.37183
(1,3)	0.00002	0.00051	0.00371	0.02405	0.26284
(2,2)	0.00003	0.00074	0.00518	0.03071	0.28539

Table 7.4: Loss on β for the stationary 1p-CAR(1) process.

CASE	CONFIGURATION	β				
		0.05	0.10	0.15	0.20	0.24
7.4(a)	$\begin{pmatrix} ++ \\ ++ \end{pmatrix}$	12.56	14.51	19.06	31.15	83.08
7.4(b)	(+ + + +)	13.53	15.35	19.45	29.87	72.50
7.4(c)	$\begin{pmatrix} + \\ +++ \end{pmatrix}$	13.53	15.37	19.51	30.02	72.85
7.4(e)	$\begin{pmatrix} +++ \\ + \end{pmatrix}$	13.53	15.36	19.52	30.21	74.40
7.4(d)	$\begin{pmatrix} + \\ ++ \\ + \end{pmatrix}$	13.54	15.39	19.57	30.16	73.15
7.4(f)	(+ + +)(+)	14.48	16.17	19.77	28.89	65.44
7.4(g)	$\begin{pmatrix} + \\ ++ \end{pmatrix}$(+)	14.48	16.19	19.83	29.02	65.72
7.4(h)	(+ +)(+ +)	14.49	16.15	19.81	28.79	64.06
7.4(i)	(+ +)(+)(+)	15.43	16.99	20.09	27.92	58.67
7.4(j)	(+)(+)(+)(+)	16.37	17.84	20.37	27.05	53.29

From Table 7.4 it can be noted that for low values of β (β<0.15), the loss of information on β is greater for the case of isolated sites, whereas the converse is true for larger values of β.

The loss of information on β has also been calculated for $m = 5$. There are 23 possible cases to consider. In 12 of these cases, all the sites are connected. For some of the configurations of the missing sites, the formulae for the loss of information on β are similar. For instance, for configurations (+++++) , $\begin{pmatrix} +++ \\ + \\ + \end{pmatrix}$, $\begin{pmatrix} +++ \\ + \ + \end{pmatrix}$, $\begin{pmatrix} ++++ \\ + \end{pmatrix}$, $\begin{pmatrix} ++ \\ ++ \\ + \end{pmatrix}$, $\begin{pmatrix} + \\ +++ \\ + \end{pmatrix}$ and $\begin{pmatrix} + \\ ++ \\ + \\ + \end{pmatrix}$ the loss of information on β is

$L_\beta\{5, S(z)\}\sigma^2 = [\beta^2(1-3\beta^2)^2(1-\beta^2)^2]^{-1}(-5+20\beta^2-20\beta^4-12\beta^6+9\beta^8) +$ $[\beta^2(1-3\beta^2)(1-\beta^2)]^{-1}\{(5-12\beta^2+3\beta^4)f + 4\beta(2-3\beta^2)f\rho_{10}$ + additional terms which are indicated below, along with the respective coefficients $\}$.

Configuration	$f\rho_{20}$	$f\rho_{30}$	$f\rho_{40}$	$f\rho_{11}$	$f\rho_{12}$	$f\rho_{13}$	$f\rho_{22}$
(+ + + + +)	**a**	**b**	**c**	--	--	--	--
++ ++ +	--	--	--	**a**	**b**	--	**c**
+ + ++ +	**d**	**h**	--	**g**	**h**	**c**	--
+ + + + +	**e**	--	--	**f**	**b**	--	**c**
+ + + + +	**f**	--	--	**e**	**b**	--	**c**
+ ++ + +	**g**	--	--	**d**	**b**	**c**	--
+ + + + +	**i**	--	--	**j**	**b**	--	--

where **a, b, c, d, e, f, g, h** are as follows:

a $= \beta^2(6-4\beta^2)$;

b $= 4\beta^3$;

c $= 2\beta^4$;

d $= \beta^2(4-2\beta^2)$;

e $= 2\beta^2$;

f $= 4\beta^2(1-\beta^2)$;

g $= 2\beta^2(1-\beta^2)$;

h $= 2\beta^3$;

i $= 2\beta^2(1+\beta^2)$; and

j $= 4\beta^2(1-\beta^2)$.

For configurations $\begin{pmatrix} ++++ \\ + \end{pmatrix}$, $\begin{pmatrix} ++ \\ ++ \\ + \end{pmatrix}$, $\begin{pmatrix} +++ \\ + \\ + \end{pmatrix}$,the expression for the loss of information on β is

$L_\beta\{5, S(z)\}\sigma^2 = [\beta^2(1-4\beta^2+2\beta^4)^2]^{-1}(-5+20\beta^2-24\beta^4-8\beta^6+4\beta^8)+[\beta^2(1-4\beta^2+2\beta^4)]^{-1}\{(5-12\beta^2+2\beta^4)f+8\beta(1-\beta^2)f\rho_{10}+$ additional terms as indicated below, along with the respective coefficients $\}$

Configuration	$f\rho_{20}$	$f\rho_{30}$	$f\rho_{11}$	$f\rho_{12}$
$\begin{pmatrix} ++++ \\ + \end{pmatrix}$	**k**	**l**	**m**	**n**
$\begin{pmatrix} ++ \\ ++ \\ + \end{pmatrix}$	**o**	$--$	**p**	**q**
$\begin{pmatrix} +++ \\ + \\ + \end{pmatrix}$	**m**	$--$	**k**	**q**

where:

$\mathbf{k} = 4\beta^2$;

$\mathbf{l} = 2\beta^3$;

$\mathbf{m} = \beta^2(4-2\beta^2)$;

$\mathbf{n} = 2\beta^3$;

$\mathbf{o} = 2\beta^2$;

$\mathbf{p} = \beta^2(6-2\beta^2)$;

$\mathbf{q} = 4\beta^3$.

Finally,

$L_\mu\{5, \begin{pmatrix} ++ \\ +++ \end{pmatrix}\}\,\sigma^2 = [\beta^2(1-5\beta^2+2\beta^4)^2]^{-1}(-5+25\beta^2-42\beta^4-10\beta^6+4\beta^8)+[\beta^2(1-5\beta+2\beta^4)]^{-1}\{(5-15\beta^2+2\beta^4)f+2\beta(5-4\beta^2)f\rho_{10}+2\beta^2 f\rho_{02}+2\beta^2(5-\beta^2)f\rho_{11}+4\beta^3 f\rho_{12}\}$

and

$L_\mu\{5, \begin{pmatrix} & + & \\ + & + & + \\ & + & \end{pmatrix}\} \sigma^2 = [\beta^2(1-4\beta^2)^2]^{-1}(-5+20\beta^2-32\beta^4) + [\beta^2(1-4\beta^2)]^{-1}\{(5-12\beta^2)f + 8\beta f\rho_{01} + 4\beta^2 f\rho_{0,2} + 8\beta^2 f\rho_{11}\}$

Table 7.5 gives the loss of information on β for some values of β and 23 possible configurations of missing sites, when $m = 5$. The ranking of the loss for the configurations displayed in Table 7.5 depends on the value of $\beta > 0$, as can be observed from Figure 7.8, which shows the plot of the loss of information on β for some configurations of 5 missing sites. Note that for small $\beta > 0$, the configuration with all isolated sites gives the largest loss, whilst for larger values of β, the largest loss is associated with the more compact configuration.

Table 7.5: Loss of information on β, for different configurations of 5 missing sites.

CASE	CONFIGURATION	β				
		0.05	0.10	0.15	0.20	0.24
7.5(a)	$\begin{pmatrix} + + \\ + + + \end{pmatrix}$	15.69	18.13	23.83	39.15	106.12
7.5(b)	$\begin{pmatrix} + \\ + + + \\ + \end{pmatrix}$	16.66	18.97	24.29	38.33	98.63
7.5(c)	$\begin{pmatrix} ++ \\ ++ \end{pmatrix}(+)$	16.65	18.97	24.15	37.91	96.40
7.5(d)	$\begin{pmatrix} + \\ + + + \\ + \end{pmatrix}$	16.68	19.01	24.35	38.15	95.57
7.5(e)	$\begin{pmatrix} + + + \\ + \\ + \end{pmatrix}$	16.67	18.99	24.29	37.96	95.28
7.5(f)	$\begin{pmatrix} + + ++ \\ + \end{pmatrix}$	16.67	18.99	24.29	37.99	95.20
7.5(g)	$\begin{pmatrix} ++ \\ ++ \\ + \end{pmatrix}$	16.68	19.05	24.40	38.07	93.99
7.5(h)	$\begin{pmatrix} + + + \\ + \quad + \end{pmatrix}$	16.68	19.03	24.34	37.93	93.69
7.5(i)	$\begin{pmatrix} + \\ ++ \\ + \\ + \end{pmatrix}$	16.68	19.03	24.35	37.93	93.68
7.5(j)	$\begin{pmatrix} + \\ + + + \\ + \end{pmatrix}$	16.68	19.03	24.34	37.92	93.67
7.5(k)	$\begin{pmatrix} + + + \\ + \\ + \end{pmatrix}$	16.67	19.00	24.29	37.79	93.39
7.5(l)	$\begin{pmatrix} + + ++ \\ + \end{pmatrix}$	16.68	19.00	24.28	37.77	93.32
7.5(m)	$(+ + + + +)$	16.67	18.98	24.22	37.56	92.96
7.5(n)	$\begin{pmatrix} + + + \\ + \end{pmatrix}(+)$	17.62	19.82	24.61	36.97	87.72
7.5(o)	$\begin{pmatrix} + \\ ++ \\ + \end{pmatrix}(+)$	17.63	19.85	24.66	36.92	86.47
7.5(p)	$\begin{pmatrix} + \\ + + + \end{pmatrix}(+)$	17.63	19.83	24.60	36.78	86.17
7.5(q)	$(\ + + ++\ )(+)$	17.62	19.81	24.54	33.63	85.82
7.5(r)	$\begin{pmatrix} + \\ ++ \end{pmatrix}(++)$	17.63	19.81	24.64	36.66	84.42
7.5(s)	$(+ + +)(++)$	17.63	19.79	24.59	36.52	84.14
7.5(t)	$\begin{pmatrix} + \\ ++ \end{pmatrix}(+)(+)$	18.57	20.65	24.92	35.78	79.04
7.5(u)	$(+ + +)(+)(+)$	18.57	20.63	24.86	35.65	78.76
7.5(v)	$(++)(++)(+)$	18.58	20.61	24.91	35.56	77.38
7.5(w)	$(++)(+)(+)(+)$	19.52	21.46	25.18	34.68	71.99
7.5(x)	$(+)(+)(+)(+)(+)$	20.46	22.30	25.46	33.81	66.61

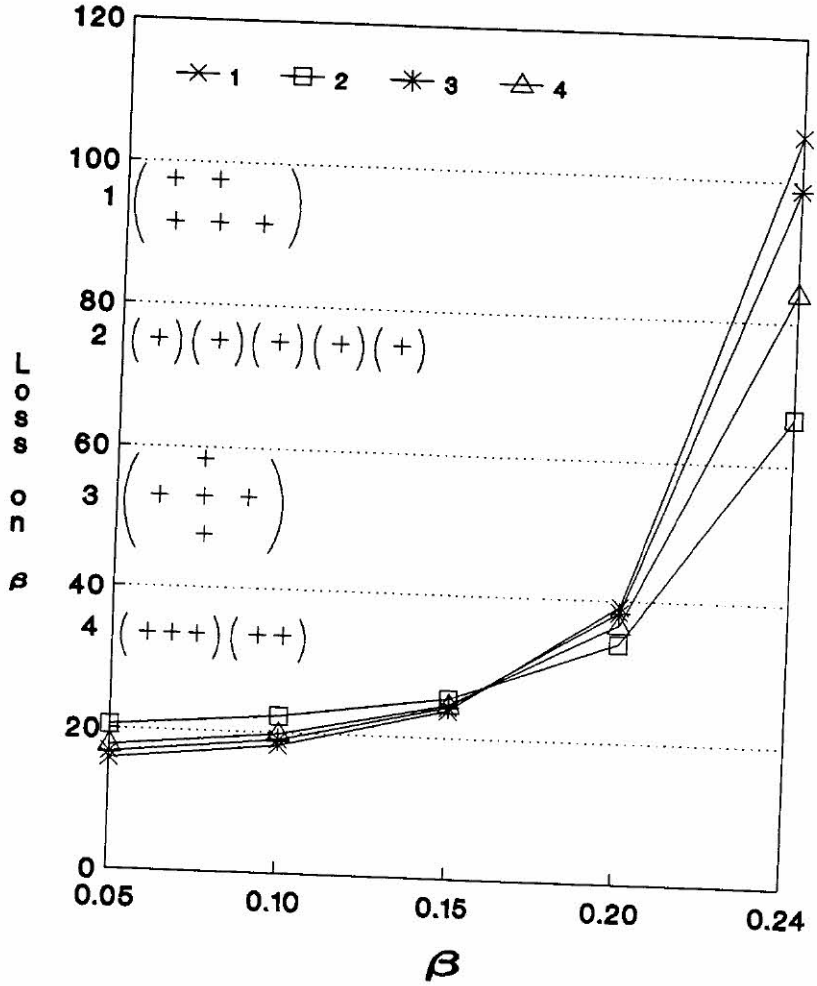

Figure 7.8: Exact loss of information on β for some configurations when $m = 5$, and some values of $\beta > 0$.

Martin (1989) also gives an approximate formulae for the loss on information on β, for the stationary 1p-CAR(1) process for general m, when β is small. The formula can be expressed as

$$(4m - m_1) + (36m + 23m_1 - 6m_2 - 4m_3 + 4l_{11} + 2l_{20})\beta^2 \qquad (7.18)$$

where m_3 is the number of 4-circuits of the type $\begin{pmatrix} ++ \\ ++ \end{pmatrix}$.

Figure 7.9 gives the plot of the exact and the approximate loss of information on β, for $\beta = 0.10$, for all configurations in Table 7.5. In this figure, configuration 1 refers to case 7.5(a) in Table 7.5, 2 to case 7.5(b), and so on. From this plot it is can be noted that the approximation is very good for $\beta = 0.10$. It has been observed that the approximate formulae for the loss is reasonable even for $\beta = 0.15$.

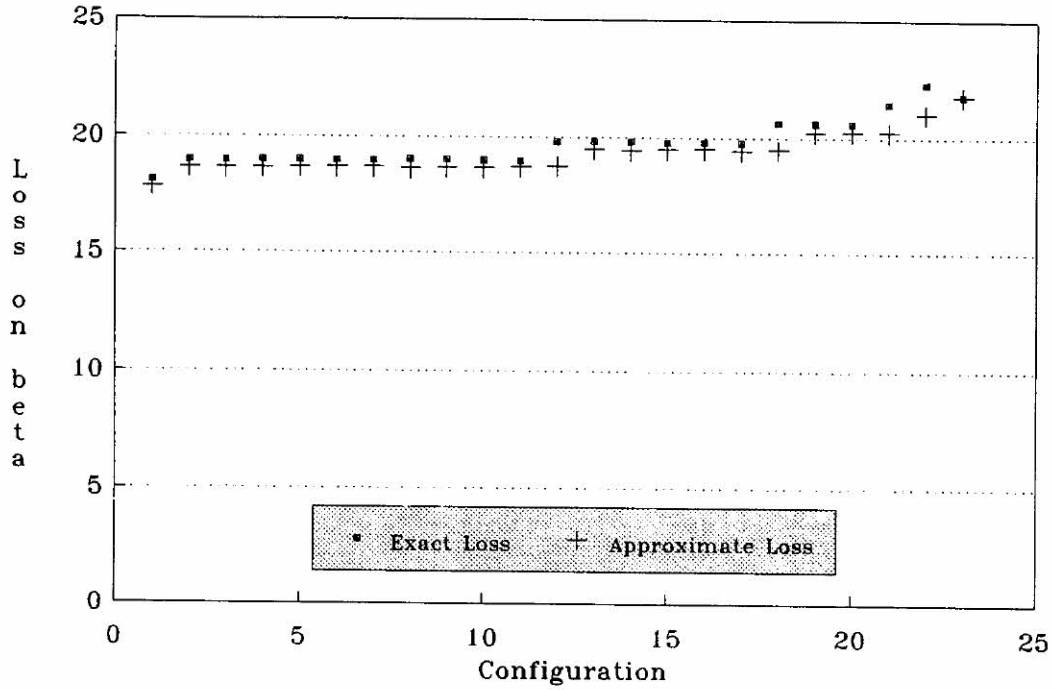

Figure 7.9: Exact versus approximate loss of information on β for the configurations in Table 7.5, and $\beta = 0.10$.

Chapter 8

Conclusions

This study concerned the estimation of missing values arising in remotely sensed data, due to line dropout, or from the presence of small cloud cover.

Although only two relatively small TM-Landsat sub-images have been used, and only a few bands were made available, the investigation allowed the identification of the methods that work usually well, and the conditions under which better estimates of the missing values can be obtained.

In the case of missing values arising from line-dropout, good estimates of the missing values can be obtained from very simple methods, such as linear interpolation, and the use of more sophisticated methods may not be warranted. This is particularly the case when the estimates of the missing values are used only to visually correct the image (cosmetic purpose), and no further analyses of the data is envisaged. Since better results are always expected from linear interpolation than from the method of adjacent line replacement, and considering the small computational effort that is required to implement the former method, it is recommended that this method be routinely used to estimate the missing values from line-dropout, during the pre-processing stage of image processing. Furthermore, since the method of linear interpolation allows the identification of the lines that have been replaced (as in the case of adjacent line replacement), it is always possible to apply other methods *a posteriori*, if more accurate estimates of the missing are required. This may not be easily achieved if other methods, such as those using multispectral and/or multitemporal data, are used.

In this investigation it has been shown that data from other passages is an important source of information that should not be neglected, especially in the

case of missing values arising from cloud cover, when multispectral information is not available. In the case of missing values arising from line drop, the information in the neighbourhood of the 'defective' lines, in the original sub-image and the template image, may indicate the amount, and degree, of changes that occurred between the passages, and the quality of the estimates from template date methods can be reasonably inferred. However, in the case of large clusters of missing values, it is not possible to access the extent of the changes that occurred from one passage to another, thus making it difficult to foresee the kind of results that the template date methods will have.

The facts that remotely sensed imagery usually contains a diversity of land covers, and that different methods perform well under different situations, makes it reasonable to expect that better estimates of the missing values are obtained from the use of a 'switching' method, which explores the individual potential of each method, for the specific data at hand. The main difficulties of this approach are the choice of the methods to be used, and the definition of which switching rule to apply. In the present study a reasonable 'switching' method could not be identified, which would consistently have better numerical results than the method of linear interpolation alone. As mentioned in Chapter 4, further research in this area is warranted. Although the use of 'switching' methods seem more appropriate in the estimation of missing values arising from line dropout (due to the availability of the information in the 'local' neighbourhood of the missing lines), they can also be reasonable alternatives as methods to estimate missing values arising from cloud cover, if it is believed that different passages may contain pieces of information that are individually more appropriate for the template date methods being considered.

It is important to realize, however, that the development of a 'switching' method should be specific for the characteristics of the image where the missing values occur, and involves the analysis of the data in this passage, as well as in other passages acquired in different bands, and/or different dates. The results in Chapter 4 are important to rule out the application of methods which do not perform well generally.

Although the methods that use spatial modelling may have better estimates of the missing values occurring over reasonably homogeneous areas, the estimates are usually not significantly better than those obtained for the method of linear

interpolation (in the case of the missing values arising from line-drop), or possibly for other methods which use a reasonable form of spatial interpolation (in the case of clusters of missing values). Moreover, the methods that use spatial modelling have several drawbacks that need to be taken into consideration. They are much more computing demanding than other simpler methods, and may not be easily implemented, if the number of missing values is large. It has been pointed out that some simplification can be achieved if a fixed value for the dependence parameter β is assumed, as usually the maximum likelihood estimates for this parameter, for most of the situations investigated here, are near the boundary (upper limit). This, however, does not completely ameliorate the problem when the number of missing values is large.

Another problem in the application of methods that use spatial modelling is the fact that these methods are expected to work well for data that are reasonably homogeneous, or when the non-homogeneity of the data is adequately accounted for. The methods using trend surface analyses in this study have not been adequate to remove the heterogeneity of the data. It is possible that the application of methods that use a 'step function', for instance, to account for the non-stationarity on the mean, due to the presence of different types of land cover in the imagery, may improve the estimates of the missing values for methods using spatial modelling. This is another area which needs to be further explored.

In the case of missing values occurring in large clusters, it is not expected that single band methods should perform well, unless the missing values occur in areas which are very homogeneous. The form of spatial interpolation implied by the methods that use spatial modelling studied here requires that the data in the neighbourhood of the missing values be 'relatively' similar to those that are missing, if good estimates are desired. Since it is not always reasonable to assume that remotely sensed data are homogeneous, particularly if data from the entire image is considered, then other methods of estimation may be more adequate than the single band methods studied here. It is important to bear in mind the undue difficulties in obtaining sensible estimates of missing values occurring in large clusters, due both to the 'natural' heterogeneity of the data, and the likelihood of changes in land cover occurring between the passages, over more extensive areas. Still, an overall better performance of the template date methods than the single band methods can possibly be expected, in this case.

The examples provided for some specific cases of conditional autoregressive, and simultaneous autoregressive processes show that the loss of information on the mean, for low values of the parameters of the models, can be quickly and efficiently computed using the approximate formulae, which does not involve the analytic inversion of a matrix, which is only feasible for a small number of missing values. Besides, from the approximate formulae, it is possible to have a good insight into which configurations of the missing sites lead to larger loss. The results show that under positive dependence, for a given number of missing sites, a cluster of missing sites (as that occurring from cloud cover) is more serious than a missing line (as that occurring from line dropout). Although the approximation formulae were restricted to second-order terms in the parameters, higher order terms could be included, which would involve longer paths in $S(z)$. Also, although it has been assumed that the processes have a constant mean, it is possible to allow the mean to include trend and other fixed effects. It is also possible to obtaine results for other processes, such as multivariate and spatial-temporal processes, and more results on the loss of information on the model parameters, β_k. Exact formulae for the loss on μ, for higher order CAR and SAR processes, and for a larger number of missing values can also be obtained. All these possibilities are open for further research.

Appendix A

Tables for Chapter 3

Table A.1: Sample autocorrelations $r_{g,h}$ for $g = 0, \ldots, 19$, and $h = -6, \ldots, 6$ and ± 19: $D_1(13)$.

LAG	0	1	2	3	4	5	6	7	8	9
−19	0.141	0.141	0.150	0.158	0.176	0.177	0.182	0.180	0.172	0.157
⋮				⋮			⋮			
−6	0.414	0.420	0.411	0.398	0.374	0.357	0.338	0.325	0.308	0.281
−5	0.475	0.464	0.452	0.431	0.409	0.387	0.362	0.344	0.327	0.300
−4	0.545	0.521	0.490	0.459	0.437	0.419	0.390	0.365	0.343	0.316
−3	0.626	0.591	0.534	0.489	0.461	0.448	0.419	0.387	0.358	0.331
−2	0.729	0.676	0.598	0.536	0.491	0.467	0.441	0.405	0.372	0.341
−1	0.872	0.777	0.669	0.579	0.516	0.474	0.445	0.408	0.374	0.340
0	1.000	0.842	0.703	0.591	0.521	0.465	0.432	0.395	0.360	0.327
1	0.872	0.803	0.687	0.584	0.509	0.454	0.420	0.384	0.351	0.316
2	0.729	0.709	0.634	0.558	0.491	0.441	0.404	0.372	0.341	0.307
3	0.626	0.613	0.569	0.517	0.465	0.421	0.385	0.357	0.329	0.299
4	0.545	0.528	0.503	0.470	0.430	0.392	0.361	0.336	0.313	0.288
5	0.475	0.455	0.435	0.418	0.395	0.363	0.339	0.315	0.295	0.276
6	0.414	0.392	0.370	0.363	0.354	0.338	0.315	0.296	0.281	0.270
⋮				⋮			⋮			
19	0.141	0.139	0.153	0.167	0.175	0.179	0.173	0.151	0.135	0.132

LAG	10	11	12	13	14	15	16	17	18	19
−19	0.151	0.145	0.141	0.127	0.117	0.096	0.072	0.047	0.027	0.007
⋮				⋮			⋮			
−6	0.250	0.222	0.193	0.178	0.167	0.158	0.150	0.134	0.118	0.106
−5	0.266	0.239	0.211	0.192	0.183	0.169	0.156	0.135	0.119	0.108
−4	0.281	0.252	0.225	0.206	0.192	0.174	0.152	0.135	0.118	0.109
−3	0.297	0.265	0.238	0.218	0.200	0.178	0.153	0.137	0.121	0.114
−2	0.307	0.274	0.244	0.219	0.203	0.182	0.159	0.138	0.126	0.118
−1	0.304	0.270	0.239	0.212	0.197	0.177	0.161	0.142	0.129	0.120
0	0.294	0.261	0.231	0.205	0.188	0.168	0.157	0.149	0.137	0.127
1	0.284	0.253	0.226	0.203	0.182	0.168	0.156	0.154	0.148	0.142
2	0.276	0.246	0.220	0.203	0.184	0.170	0.158	0.156	0.154	0.150
3	0.273	0.245	0.221	0.200	0.186	0.171	0.162	0.157	0.158	0.155
4	0.266	0.245	0.227	0.207	0.192	0.175	0.168	0.160	0.160	0.154
5	0.263	0.247	0.234	0.219	0.203	0.185	0.173	0.164	0.157	0.149
6	0.259	0.246	0.237	0.229	0.216	0.199	0.181	0.172	0.163	0.152
⋮				⋮			⋮			
19	0.142	0.152	0.158	0.152	0.154	0.158	0.171	0.171	0.169	0.167

Table A.2: Sample autocorrelations $r_{g,h}$ for $g = 0, \ldots, 19$, and $h = -6, \ldots, 6$ and ± 19: $D_1(14)$.

LAG	0	1	2	3	4	5	6	7	8	9
−19	0.197	0.201	0.204	0.209	0.212	0.214	0.207	0.197	0.190	0.179
⋮				⋮			⋮			
−6	0.545	0.536	0.526	0.511	0.488	0.458	0.425	0.392	0.359	0.327
−5	0.599	0.584	0.564	0.544	0.517	0.485	0.450	0.417	0.384	0.346
−4	0.657	0.638	0.608	0.577	0.548	0.516	0.481	0.444	0.406	0.365
−3	0.727	0.698	0.657	0.615	0.578	0.547	0.511	0.470	0.426	0.384
−2	0.810	0.764	0.712	0.660	0.610	0.570	0.531	0.488	0.441	0.396
−1	0.919	0.837	0.761	0.695	0.634	0.583	0.538	0.494	0.449	0.404
0	1.000	0.894	0.788	0.708	0.643	0.586	0.537	0.491	0.447	0.407
1	0.919	0.884	0.792	0.710	0.646	0.586	0.534	0.489	0.446	0.408
2	0.810	0.825	0.774	0.698	0.633	0.574	0.521	0.477	0.437	0.400
3	0.727	0.748	0.735	0.676	0.612	0.558	0.506	0.461	0.423	0.385
4	0.657	0.672	0.679	0.649	0.591	0.538	0.489	0.445	0.408	0.372
5	0.599	0.606	0.614	0.609	0.573	0.523	0.475	0.432	0.394	0.360
6	0.545	0.548	0.554	0.558	0.550	0.511	0.464	0.422	0.385	0.349
⋮				⋮			⋮			
19	0.197	0.197	0.201	0.206	0.211	0.218	0.227	0.232	0.236	0.240

LAG	10	11	12	13	14	15	16	17	18	19
−19	0.168	0.156	0.141	0.118	0.095	0.073	0.054	0.040	0.027	0.017
⋮				⋮			⋮			
−6	0.300	0.278	0.259	0.235	0.202	0.173	0.147	0.123	0.104	0.085
−5	0.314	0.290	0.269	0.246	0.215	0.183	0.154	0.129	0.108	0.094
−4	0.327	0.299	0.275	0.250	0.223	0.191	0.158	0.134	0.113	0.100
−3	0.343	0.309	0.281	0.253	0.226	0.198	0.163	0.137	0.117	0.104
−2	0.355	0.319	0.287	0.257	0.229	0.202	0.171	0.140	0.119	0.106
−1	0.364	0.328	0.291	0.260	0.230	0.202	0.174	0.144	0.121	0.107
0	0.367	0.333	0.294	0.261	0.230	0.199	0.169	0.143	0.120	0.104
1	0.373	0.339	0.301	0.264	0.229	0.196	0.163	0.139	0.118	0.101
2	0.368	0.335	0.299	0.262	0.223	0.188	0.155	0.131	0.114	0.096
3	0.353	0.323	0.288	0.251	0.214	0.178	0.147	0.121	0.104	0.088
4	0.337	0.309	0.277	0.241	0.205	0.167	0.138	0.116	0.098	0.086
5	0.326	0.296	0.266	0.234	0.197	0.159	0.131	0.115	0.100	0.088
6	0.317	0.285	0.254	0.225	0.192	0.157	0.129	0.115	0.104	0.092
⋮				⋮			⋮			
19	0.251	0.263	0.255	0.230	0.212	0.199	0.182	0.163	0.141	0.117

Table A.3: Sample autocorrelations $r_{g,h}$ for $g = 0, \ldots, 19$, and $h = -6, \ldots, 6$ and ± 19: $D_1(15)$.

LAG	0	1	2	3	4	5	6	7	8	9
−19	0.116	0.119	0.124	0.130	0.135	0.141	0.139	0.134	0.127	0.115
⋮				⋮			⋮			
−6	0.584	0.587	0.587	0.577	0.556	0.535	0.509	0.483	0.455	0.421
−5	0.640	0.633	0.622	0.611	0.590	0.565	0.536	0.508	0.479	0.445
−4	0.697	0.683	0.659	0.640	0.616	0.591	0.558	0.527	0.497	0.461
−3	0.758	0.738	0.700	0.668	0.638	0.610	0.577	0.540	0.508	0.473
−2	0.828	0.797	0.749	0.702	0.661	0.626	0.594	0.556	0.522	0.487
−1	0.923	0.868	0.802	0.738	0.682	0.638	0.604	0.568	0.534	0.496
0	1.000	0.915	0.825	0.751	0.688	0.638	0.599	0.564	0.531	0.495
1	0.923	0.889	0.811	0.740	0.679	0.627	0.586	0.553	0.524	0.492
2	0.828	0.824	0.780	0.720	0.663	0.613	0.572	0.540	0.512	0.482
3	0.758	0.758	0.737	0.693	0.642	0.594	0.552	0.520	0.494	0.467
4	0.697	0.697	0.685	0.655	0.611	0.566	0.525	0.496	0.471	0.445
5	0.640	0.636	0.621	0.605	0.573	0.537	0.502	0.472	0.448	0.424
6	0.584	0.576	0.562	0.550	0.533	0.506	0.477	0.449	0.425	0.402
⋮				⋮			⋮			
19	0.116	0.121	0.130	0.144	0.146	0.144	0.138	0.131	0.124	0.119

LAG	10	11	12	13	14	15	16	17	18	19
−19	0.104	0.097	0.085	0.073	0.054	0.035	0.017	−0.003	−0.023	−0.042
⋮				⋮			⋮			
−6	0.390	0.358	0.325	0.300	0.276	0.255	0.240	0.224	0.212	0.197
−5	0.411	0.379	0.344	0.318	0.294	0.271	0.254	0.235	0.219	0.203
−4	0.426	0.393	0.359	0.331	0.307	0.282	0.260	0.239	0.221	0.205
−3	0.438	0.405	0.373	0.344	0.316	0.288	0.264	0.243	0.226	0.211
−2	0.454	0.419	0.386	0.355	0.324	0.296	0.272	0.252	0.235	0.219
−1	0.463	0.427	0.390	0.359	0.328	0.297	0.274	0.256	0.240	0.224
0	0.461	0.427	0.391	0.357	0.326	0.295	0.273	0.257	0.242	0.227
1	0.458	0.424	0.391	0.358	0.327	0.297	0.273	0.257	0.244	0.227
2	0.453	0.420	0.385	0.353	0.321	0.293	0.269	0.252	0.241	0.227
3	0.439	0.407	0.372	0.340	0.308	0.280	0.258	0.242	0.233	0.222
4	0.419	0.390	0.358	0.328	0.298	0.270	0.251	0.238	0.229	0.218
5	0.402	0.376	0.347	0.318	0.292	0.267	0.249	0.238	0.228	0.219
6	0.383	0.358	0.333	0.309	0.285	0.264	0.247	0.237	0.230	0.223
⋮				⋮			⋮			
19	0.121	0.126	0.130	0.137	0.147	0.157	0.169	0.178	0.186	0.196

Table A.4: Sample autocorrelations $r_{g,h}$ for $g = 0, \ldots, 19$, and $h = -6, \ldots, 6$ and ± 19: $D_2(14)$.

LAG	0	1	2	3	4	5	6	7	8	9
−19	0.132	0.132	0.132	0.131	0.130	0.127	0.121	0.116	0.110	0.104
⋮				⋮			⋮			
−6	0.546	0.530	0.501	0.462	0.418	0.375	0.333	0.293	0.260	0.233
−5	0.610	0.589	0.554	0.509	0.460	0.412	0.367	0.325	0.289	0.259
−4	0.678	0.652	0.607	0.555	0.501	0.450	0.401	0.357	0.317	0.283
−3	0.750	0.719	0.665	0.603	0.546	0.490	0.438	0.391	0.346	0.307
−2	0.831	0.791	0.726	0.656	0.593	0.533	0.476	0.425	0.378	0.337
−1	0.926	0.868	0.788	0.709	0.640	0.575	0.514	0.460	0.412	0.370
0	1.000	0.928	0.838	0.754	0.680	0.611	0.546	0.489	0.439	0.396
1	0.926	0.891	0.827	0.756	0.688	0.619	0.555	0.499	0.450	0.406
2	0.831	0.821	0.785	0.735	0.679	0.619	0.560	0.507	0.459	0.417
3	0.750	0.751	0.732	0.698	0.655	0.605	0.555	0.507	0.464	0.425
4	0.678	0.683	0.674	0.650	0.617	0.579	0.536	0.495	0.456	0.421
5	0.610	0.616	0.613	0.596	0.572	0.545	0.511	0.476	0.442	0.412
6	0.546	0.552	0.551	0.541	0.525	0.504	0.477	0.448	0.419	0.395
⋮				⋮			⋮			
19	0.132	0.129	0.123	0.116	0.107	0.098	0.093	0.089	0.088	0.090

LAG	10	11	12	13	14	15	16	17	18	19
−19	0.098	0.090	0.080	0.069	0.057	0.044	0.031	0.020	0.011	0.009
⋮				⋮			⋮			
−6	0.210	0.188	0.166	0.144	0.123	0.102	0.079	0.055	0.028	0.005
−5	0.232	0.207	0.181	0.154	0.131	0.109	0.084	0.059	0.031	0.007
−4	0.255	0.228	0.200	0.169	0.141	0.116	0.091	0.064	0.037	0.013
−3	0.276	0.246	0.217	0.185	0.152	0.123	0.096	0.069	0.042	0.019
−2	0.303	0.271	0.239	0.206	0.170	0.138	0.108	0.079	0.052	0.026
−1	0.333	0.298	0.263	0.226	0.190	0.157	0.124	0.091	0.060	0.032
0	0.356	0.320	0.282	0.240	0.204	0.169	0.136	0.101	0.066	0.035
1	0.365	0.327	0.288	0.247	0.211	0.176	0.141	0.105	0.069	0.037
2	0.377	0.337	0.298	0.259	0.224	0.187	0.148	0.111	0.076	0.044
3	0.387	0.350	0.313	0.275	0.239	0.200	0.160	0.120	0.084	0.051
4	0.388	0.354	0.321	0.286	0.250	0.211	0.170	0.130	0.092	0.057
5	0.384	0.354	0.325	0.293	0.259	0.221	0.181	0.141	0.103	0.065
6	0.372	0.346	0.318	0.289	0.259	0.225	0.186	0.147	0.109	0.069
⋮				⋮			⋮			
19	0.099	0.109	0.117	0.120	0.119	0.115	0.106	0.091	0.074	0.054

Table A.5: Sample autocorrelations $r_{g,h}$ for $g = 0, \ldots, 19$, and $h = -6, \ldots, 6$ and ± 19: $D_2(15)$.

LAG	0	1	2	3	4	5	6	7	8	9
−19	0.262	0.275	0.283	0.279	0.273	0.267	0.258	0.232	0.188	0.144
⋮				⋮			⋮			
−6	0.675	0.670	0.645	0.597	0.538	0.478	0.421	0.368	0.320	0.274
−5	0.729	0.721	0.687	0.631	0.568	0.507	0.448	0.393	0.343	0.298
−4	0.785	0.773	0.727	0.664	0.599	0.536	0.475	0.420	0.369	0.321
−3	0.842	0.823	0.766	0.698	0.630	0.565	0.503	0.447	0.395	0.346
−2	0.900	0.869	0.804	0.732	0.662	0.596	0.533	0.475	0.421	0.371
−1	0.960	0.915	0.842	0.768	0.697	0.629	0.565	0.505	0.450	0.397
0	1.000	0.948	0.874	0.800	0.729	0.661	0.596	0.534	0.477	0.422
1	0.960	0.932	0.878	0.816	0.751	0.687	0.622	0.560	0.502	0.447
2	0.900	0.883	0.850	0.806	0.754	0.699	0.640	0.581	0.525	0.471
3	0.842	0.828	0.803	0.772	0.735	0.691	0.642	0.590	0.539	0.488
4	0.785	0.772	0.751	0.726	0.699	0.666	0.626	0.583	0.539	0.494
5	0.729	0.715	0.697	0.676	0.654	0.629	0.598	0.563	0.525	0.488
6	0.675	0.660	0.643	0.625	0.606	0.584	0.558	0.530	0.501	0.470
⋮				⋮			⋮			
19	0.262	0.242	0.221	0.198	0.175	0.153	0.131	0.112	0.099	0.090

LAG	10	11	12	13	14	15	16	17	18	19
−19	0.102	0.061	0.023	−0.015	−0.050	−0.080	−0.104	−0.123	−0.138	−0.147
⋮				⋮			⋮			
−6	0.228	0.184	0.145	0.110	0.080	0.053	0.027	0.006	−0.009	−0.022
−5	0.250	0.206	0.166	0.131	0.100	0.073	0.048	0.028	0.013	0.000
−4	0.273	0.229	0.189	0.153	0.121	0.093	0.069	0.049	0.034	0.021
−3	0.297	0.253	0.213	0.176	0.143	0.115	0.093	0.073	0.058	0.044
−2	0.322	0.278	0.237	0.200	0.167	0.139	0.117	0.098	0.083	0.067
−1	0.347	0.302	0.261	0.223	0.190	0.164	0.141	0.121	0.106	0.090
0	0.371	0.326	0.284	0.246	0.213	0.187	0.165	0.145	0.129	0.114
1	0.396	0.349	0.307	0.269	0.238	0.213	0.191	0.173	0.156	0.140
2	0.420	0.373	0.330	0.293	0.263	0.240	0.219	0.200	0.183	0.167
3	0.440	0.394	0.352	0.317	0.289	0.267	0.246	0.227	0.210	0.193
4	0.450	0.407	0.368	0.337	0.311	0.290	0.272	0.253	0.235	0.217
5	0.449	0.411	0.377	0.349	0.328	0.309	0.293	0.276	0.260	0.242
6	0.438	0.406	0.378	0.355	0.337	0.322	0.309	0.295	0.281	0.263
7	0.417	0.391	0.369	0.352	0.339	0.327	0.318	0.308	0.296	0.279
⋮				⋮			⋮			
19	0.083	0.079	0.079	0.082	0.087	0.095	0.103	0.107	0.108	0.107

Appendix B

Tables for Chapter 4

Table B.1: Values for SRMS (×100): D_1.

OT	TEMPLATE BAND												
	LR	LI	CSP	TB-1	TB-2	TB-3	TB-4	TB-5	TB-6	TB-7	TB-8	TB-9	TB-10
$D_1(13)(14)$	54	40	41	133	49	100	98	90	43	49	60	70	58
$D_1(23)(24)$	56	42	43	140	52	104	100	90	46	51	66	70	64
$D_1(33)(34)$	53	38	41	148	44	118	100	89	44	49	63	65	59
$D_1(13)(15)$	54	40	41	73	41	58	69	64	39	41	50	70	58
$D_1(23)(25)$	56	42	43	76	44	60	70	64	42	43	54	70	64
$D_1(33)(35)$	53	38	41	69	40	55	65	59	40	41	51	65	59
$D_1(14)(13)$	46	32	33	133	49	99	98	84	36	43	55	99	76
$D_1(24)(23)$	48	34	33	140	52	102	100	86	38	46	59	99	78
$D_1(34)(33)$	51	36	37	148	53	113	100	83	41	48	61	99	77
$D_1(14)(15)$	46	32	33	130	44	97	99	83	40	49	55	99	76
$D_1(24)(25)$	48	34	33	141	45	106	100	81	42	56	56	99	78
$D_1(34)(35)$	51	36	37	149	46	113	99	77	48	56	61	99	77
$D_1(15)(13)$	41	29	29	74	41	56	69	63	34	35	35	69	58
$D_1(25)(23)$	41	29	30	76	45	57	71	65	36	46	38	71	59
$D_1(35)(33)$	40	28	29	69	42	53	65	59	34	35	35	65	53
$D_1(15)(14)$	41	29	29	130	44	97	99	87	32	39	46	69	58
$D_1(25)(24)$	41	29	30	141	45	106	100	85	35	41	46	71	59
$D_1(35)(34)$	40	28	29	149	47	113	99	82	35	42	46	65	53

OT	TEMPLATE DATE												
	LR	LI	CSP	TD-1	TD-2	TD-3	TD-4	TD-5	TD-6	TD-7	TD-8	TD-9	TD-10
$D_1(13)(23)$	54	40	41	50	45	41	49	47	41	40	43	49	47
$D_1(23)(13)$	56	42	43	50	46	42	49	46	42	41	44	44	42
$D_1(33)(23)$	53	38	41	61	48	46	57	53	45	43	46	57	51
$D_1(14)(24)$	46	32	33	57	33	46	54	49	30	30	33	55	46
$D_1(24)(14)$	48	34	33	57	32	45	54	47	31	33	35	41	37
$D_1(34)(24)$	51	36	37	54	38	43	52	48	37	37	41	52	46
$D_1(15)(25)$	41	29	29	35	32	28	35	32	32	31	31	32	31
$D_1(25)(15)$	41	29	30	35	32	28	35	32	32	31	32	31	31
$D_1(35)(25)$	40	28	29	40	33	32	39	37	33	33	33	36	35

Table B.2: Values for CCOR (×100): D_1.

OT	TEMPLATE BAND												
	LR	LI	CSP	TB-1	TB-2	TB-3	TB-4	TB-5	TB-6	TB-7	TB-8	TB-9	TB-10
$D_1(13)(14)$	151	85	90	918	122	624	918	575	98	125	194	280	198
$D_1(23)(24)$	157	92	98	988	141	686	988	582	112	136	215	294	223
$D_1(33)(34)$	136	79	86	874	106	822	874	559	102	125	195	239	192
$D_1(13)(15)$	151	85	90	280	90	183	280	230	84	88	131	280	198
$D_1(23)(25)$	157	92	98	295	102	193	295	238	94	98	144	294	223
$D_1(33)(35)$	136	79	86	240	87	152	240	201	84	85	126	239	192
$D_1(14)(13)$	107	56	56	918	117	595	918	478	70	98	154	850	358
$D_1(24)(23)$	118	62	59	988	135	653	988	497	80	112	177	964	378
$D_1(34)(33)$	133	71	70	874	141	804	874	453	90	123	188	868	357
$D_1(14)(15)$	107	56	56	854	99	555	854	439	84	121	157	850	358
$D_1(24)(25)$	118	62	59	984	105	698	984	421	92	138	165	964	378
$D_1(34)(35)$	133	71	70	878	112	802	878	377	114	159	189	868	357
$D_1(15)(13)$	87	44	43	280	83	169	280	231	59	61	62	276	181
$D_1(25)(23)$	87	44	45	295	94	176	295	244	64	105	71	294	193
$D_1(35)(33)$	83	42	43	240	82	147	240	190	59	61	62	240	154
$D_1(15)(14)$	87	44	43	854	97	561	854	514	54	78	108	276	181
$D_1(25)(24)$	87	44	45	984	101	705	984	475	61	88	112	294	193
$D_1(35)(34)$	83	42	43	878	106	807	878	431	61	90	108	240	154

OT	TEMPLATE DATE												
	LR	LI	CSP	TD-1	TD-2	TD-3	TD-4	TD-5	TD-6	TD-7	TD-8	TD-9	TD-10
$D_1(13)(23)$	151	85	90	136	99	94	136	116	90	85	96	130	117
$D_1(23)(13)$	157	92	98	136	100	91	136	107	91	86	98	102	89
$D_1(33)(23)$	136	79	86	183	117	113	183	147	102	97	112	175	138
$D_1(14)(24)$	107	56	56	166	52	113	166	131	47	48	52	166	114
$D_1(24)(14)$	118	62	59	166	53	110	166	119	51	56	61	88	70
$D_1(34)(24)$	133	71	70	147	74	97	147	124	80	74	86	147	112
$D_1(15)(25)$	87	44	43	63	51	43	63	55	51	48	48	54	48
$D_1(25)(15)$	87	44	45	63	51	41	63	54	53	49	52	50	47
$D_1(35)(25)$	83	42	43	80	55	53	80	74	55	55	58	69	60

Table B.3: Values for SRAN: D_1.

OT	TEMPLATE BAND												
	LR	LI	CSP	TB-1	TB-2	TB-3	TB-4	TB-5	TB-6	TB-7	TB-8	TB-9	TB-10
$D_1(13)(14)$	6.9	5.6	5.2	9.8	7.3	7.1	6.7	6.6	5.6	6.6	7.3	5.8	6.6
$D_1(23)(24)$	8.0	6.4	5.2	11.4	8.0	9.2	6.4	7.6	5.6	7.4	9.8	6.8	6.8
$D_1(33)(34)$	6.9	5.1	5.1	8.7	6.1	6.9	7.5	7.3	7.5	6.5	7.5	5.3	5.5
$D_1(13)(15)$	6.9	5.6	5.2	6.0	4.9	5.0	5.8	6.2	6.2	6.0	9.2	5.8	6.6
$D_1(23)(25)$	8.0	6.4	5.2	7.2	5.6	6.2	6.6	6.8	6.4	7.2	10.4	6.8	6.8
$D_1(33)(35)$	6.9	5.1	5.1	5.5	5.1	4.6	5.5	5.3	6.7	6.5	8.5	5.3	5.5
$D_1(14)(13)$	5.1	3.9	4.1	9.7	7.4	8.3	6.6	6.2	6.9	6.9	8.8	6.4	6.6
$D_1(24)(23)$	5.5	4.4	4.6	11.2	7.9	6.3	6.8	7.0	6.2	6.3	8.2	7.0	7.3
$D_1(34)(33)$	5.4	4.4	4.5	8.7	7.0	5.4	6.7	6.8	6.5	6.6	6.1	6.8	7.0
$D_1(14)(15)$	5.1	3.9	4.1	7.2	6.3	5.5	6.5	6.9	8.6	8.4	6.6	6.4	6.6
$D_1(24)(25)$	5.5	4.4	4.6	7.2	5.6	5.0	6.8	7.5	8.9	8.9	7.8	7.0	7.3
$D_1(34)(35)$	5.4	4.4	4.2	6.9	5.3	7.7	6.9	6.8	10.0	10.0	7.4	6.8	7.0
$D_1(15)(13)$	5.7	4.1	4.4	5.9	4.7	5.0	4.7	4.6	3.8	4.4	4.4	4.6	5.3
$D_1(25)(23)$	5.5	3.8	4.0	7.3	5.5	4.3	6.1	4.8	4.4	4.9	5.0	6.1	5.0
$D_1(35)(33)$	4.7	3.6	3.8	5.5	5.2	5.9	4.7	4.6	3.8	4.7	4.6	4.7	3.9
$D_1(15)(14)$	5.7	4.1	4.4	7.2	6.3	5.0	5.1	5.8	5.1	6.5	5.7	4.6	5.3
$D_1(25)(24)$	5.5	3.8	4.0	7.2	5.6	5.3	5.8	6.5	7.0	7.0	5.3	6.1	5.0
$D_1(35)(34)$	4.7	3.6	3.8	7.0	5.3	5.4	6.2	6.7	6.6	7.2	4.9	4.7	3.9

OT	TEMPLATE DATE												
	LR	LI	CSP	TD-1	TD-2	TD-3	TD-4	TD-5	TD-6	TD-7	TD-8	TD-9	TD-10
$D_1(13)(23)$	6.9	5.6	5.2	7.5	5.6	3.9	7.1	6.0	6.2	6.2	5.8	6.7	6.4
$D_1(23)(13)$	8.0	6.4	5.2	7.6	5.6	4.6	6.8	5.6	5.8	5.8	6.0	5.4	5.2
$D_1(33)(23)$	6.9	5.1	5.1	7.3	7.3	5.5	6.7	6.3	6.7	6.7	7.9	6.3	6.5
$D_1(14)(24)$	5.1	3.9	4.7	6.6	4.8	4.8	6.1	5.9	4.8	5.0	5.2	6.1	6.0
$D_1(24)(14)$	5.5	4.4	4.6	6.6	4.7	5.0	6.1	5.7	4.7	4.7	5.0	5.1	4.8
$D_1(34)(24)$	5.4	4.4	4.5	7.1	5.4	4.8	6.6	5.9	5.6	5.4	6.5	6.6	6.7
$D_1(15)(25)$	5.7	4.1	4.4	4.8	4.8	3.6	4.8	4.8	4.9	4.8	4.9	4.1	4.3
$D_1(25)(15)$	5.5	3.8	4.0	4.8	4.8	3.9	4.6	4.6	7.3	5.4	5.5	4.2	4.3
$D_1(35)(25)$	4.7	3.6	3.8	5.4	5.0	4.4	5.4	5.3	4.9	5.5	5.7	5.3	5.7

Table B.4: Values for ACC (×100): D_1.

OT	TEMPLATE BAND												
	LR	LI	CSP	TB-1	TB-2	TB-3	TB-4	TB-5	TB-6	TB-7	TB-8	TB-9	TB-10
$D_1(13)(14)$	21	12	18	74[a]	17	65	54	51	14	17	25	38	30
$D_1(23)(24)$	33	12	18	71[a]	34	72	47	43	14	13	30	37	29
$D_1(33)(34)$	17	10	16	78	13	61	42	38	12	16	23	29	24
$D_1(13)(15)$	21	12	18	44	15	35	38	34	13	33	13	38	30
$D_1(23)(25)$	33	12	18	43	15	34	37	31	13	24	14	37	29
$D_1(33)(35)$	17	10	16	35	12	22	29	25	23	10	10	29	24
$D_1(14)(13)$	12	9	7[b]	75	13	56	48	40	7	10	16	43	31
$D_1(24)(23)$	13	10	10[b]	73	15	54	50	41	8	10	18	38	33
$D_1(34)(33)$	13	11	8[b]	62	13	55	49	37	9	12	18	48	31
$D_1(14)(15)$	12	9	7[b]	70	11	60	50	37	7	16	12	43	31
$D_1(24)(25)$	13	10	10[b]	68	12	64	50	36	9	17	11	38	33
$D_1(34)(35)$	13	11	8[b]	72	11	64	48	33	17	18	22	48	31
$D_1(15)(13)$	31	12	16	89	38	77	70	72	14	26	39	59	44
$D_1(35)(33)$	18	10	15	91	22	78	63	67	21	13	23	53	41
$D_1(25)(23)$	17	10	14	88	23	77	72	63	21	26	23	47	35
$D_1(15)(14)$	31	12	16	72	25	47	55	50	18	18	17	59	44
$D_1(25)(24)$	18	10	15	69	23	44	53	48	16	17	29	53	41
$D_1(35)(34)$	17	10	14	47	21	38	47	40	15	15	15	47	35
OT	TEMPLATE DATE												
	LR	LI	CSP	TD-1	TD-2	TD-3	TD-4	TD-5	TD-6	TD-7	TD-8	TD-9	TD-10
$D_1(13)(23)$	21	12	18	33	18	19	21	19	15	13	15	20	18
$D_1(23)(13)$	33	12	18	24	14	18	18	16	13	12	14	14	12
$D_1(33)(23)$	17	10	16	10	16	19	21	18	14	13	15	20	17
$D_1(14)(24)$	12	9	7	16	5	13	11	10	4	5	5	11	10
$D_1(24)(14)$	13	10	10	17	5	13	13	11	5	6	6	10	7
$D_1(34)(24)$	13	11	8[a]	18	7	13	13	12	7	7	8	13	10
$D_1(15)(25)$	31	12	16	18	13	13	17	16	13	13	13	15	14
$D_1(25)(15)$	18	10	15	17	11	10	15	13	22	11	11	11	10
$D_1(35)(25)$	17	10	14	15	12	12	17	15	12	11	12	15	13

[a]number of pixels within the range ±5 grey levels
[b]number of pixels within the range ±8 grey levels

Table B.5: Minimum (m) and maximum (M) values for the residuals: D_1.

OT	TEMPLATE					BAND							
	LR	LI	CSP	TB-1	TB-2	$TB-3$	$TB-4$	$TB-5$	$TB-6$	$TB-7$	$TB-8$	$TB-9$	$TB-10$
	(m,M)	(m,M)	(m,M)	(m,M)	(m,M)	(m,M)	(m,M)	(m,M)	(m,M)	(m,M)	(m,M)	(m,M)	(m,M)
$D_1(13)(14)$	$(-18,19)$	$(-12,18)$	$(-13,15)$	$(-28,24)$	$(-18,21)$	$(-19,19)$	$(-15,21)$	$(-16,19)$	$(-11,19)$	$(-12,23)$	$(-20,19)$	$(-14,17)$	$(-18,17)$
$D_1(23)(24)$	$(-15,25)$	$(-13,19)$	$(-12,14)$	$(-27,30)$	$(-18,22)$	$(-21,25)$	$(-13,19)$	$(-17,21)$	$(-14,14)$	$(-14,23)$	$(-26,23)$	$(-11,23)$	$(-14,20)$
$D_1(33)(34)$	$(-15,19)$	$(-11,14)$	$(-12,13)$	$(-18,25)$	$(-15,15)$	$(-14,20)$	$(-15,22)$	$(-17,19)$	$(-14,23)$	$(-13,19)$	$(-19,18)$	$(-10,16)$	$(-11,16)$
$D_1(13)(15)$	$(-18,19)$	$(-12,18)$	$(-13,15)$	$(-14,18)$	$(-11,15)$	$(-12,15)$	$(-14,17)$	$(-15,18)$	$(-16,17)$	$(-17,15)$	$(-32,17)$	$(-14,17)$	$(-18,17)$
$D_1(23)(25)$	$(-15,25)$	$(-13,19)$	$(-12,14)$	$(-12,24)$	$(-13,15)$	$(-11,20)$	$(-11,22)$	$(-12,22)$	$(-12,20)$	$(-19,17)$	$(-36,16)$	$(-11,23)$	$(-14,20)$
$D_1(33)(35)$	$(-15,19)$	$(-11,14)$	$(-12,13)$	$(-11,16)$	$(-12,13)$	$(-09,14)$	$(-10,17)$	$(-10,16)$	$(-19,14)$	$(-18,14)$	$(-24,18)$	$(-10,16)$	$(-11,16)$
$D_1(14)(13)$	$(-29,26)$	$(-21,21)$	$(-24,20)$	$(-48,55)$	$(-43,36)$	$(-48,40)$	$(-35,35)$	$(-36,30)$	$(-42,32)$	$(-42,32)$	$(-62,32)$	$(-34,34)$	$(-36,34)$
$D_1(24)(23)$	$(-34,26)$	$(-26,22)$	$(-26,24)$	$(-65,57)$	$(-47,39)$	$(-42,27)$	$(-39,35)$	$(-39,37)$	$(-28,39)$	$(-30,39)$	$(-46,43)$	$(-40,36)$	$(-44,35)$
$D_1(34)(33)$	$(-28,28)$	$(-23,23)$	$(-24,23)$	$(-52,38)$	$(-35,38)$	$(-24,32)$	$(-44,26)$	$(-40,31)$	$(-26,41)$	$(-30,38)$	$(-37,26)$	$(-45,26)$	$(-45,28)$
$D_1(14)(15)$	$(-29,26)$	$(-21,21)$	$(-24,20)$	$(-33,44)$	$(-28,39)$	$(-29,30)$	$(-34,35)$	$(-39,35)$	$(-26,66)$	$(-27,63)$	$(-36,35)$	$(-34,34)$	$(-36,34)$
$D_1(24)(25)$	$(-34,26)$	$(-26,22)$	$(-26,24)$	$(-39,39)$	$(-32,29)$	$(-30,24)$	$(-39,35)$	$(-41,40)$	$(-33,64)$	$(-36,61)$	$(-45,40)$	$(-40,36)$	$(-44,35)$
$D_1(34)(35)$	$(-28,28)$	$(-23,23)$	$(-24,20)$	$(-41,31)$	$(-32,23)$	$(-42,38)$	$(-45,27)$	$(-43,28)$	$(-39,65)$	$(-35,69)$	$(-52,25)$	$(-45,26)$	$(-45,28)$
$D_1(15)(13)$	$(-42,59)$	$(-41,33)$	$(-42,37)$	$(-59,47)$	$(-49,35)$	$(-57,32)$	$(-49,35)$	$(-43,40)$	$(-40,29)$	$(-48,31)$	$(-48,31)$	$(-46,36)$	$(-43,52)$
$D_1(25)(23)$	$(-44,45)$	$(-29,33)$	$(-29,36)$	$(-78,40)$	$(-47,41)$	$(-41,28)$	$(-61,37)$	$(-42,36)$	$(-38,33)$	$(-42,37)$	$(-46,35)$	$(-62,36)$	$(-47,34)$
$D_1(35)(33)$	$(-38,38)$	$(-28,30)$	$(-30,32)$	$(-54,35)$	$(-44,40)$	$(-53,41)$	$(-45,30)$	$(-43,31)$	$(-36,25)$	$(-49,26)$	$(-48,26)$	$(-46,30)$	$(-35,28)$
$D_1(15)(14)$	$(-42,59)$	$(-41,33)$	$(-42,37)$	$(-74,55)$	$(-65,47)$	$(-45,45)$	$(-46,46)$	$(-62,41)$	$(-45,46)$	$(-45,71)$	$(-61,40)$	$(-46,36)$	$(-43,52)$
$D_1(25)(24)$	$(-44,45)$	$(-29,33)$	$(-29,36)$	$(-58,58)$	$(-43,47)$	$(-36,50)$	$(-50,43)$	$(-63,42)$	$(-40,73)$	$(-42,71)$	$(-46,40)$	$(-62,36)$	$(-47,34)$
$D_1(35)(34)$	$(-38,38)$	$(-28,30)$	$(-30,32)$	$(-48,64)$	$(-36,49)$	$(-36,50)$	$(-56,44)$	$(-68,39)$	$(-37,68)$	$(-42,73)$	$(-37,42)$	$(-46,30)$	$(-35,28)$

OT	TEMPLATE					DATE							
	LR	LI	CSP	TD-1	TD-2	TD-3	TD-4	TD-5	TD-6	TD-7	TD-8	TD-9	TD-10
	(m,M)	(m,M)	(m,M)	(m,M)	(m,M)	(m,M)	(m,M)	(m,M)	(m,M)	(m,M)	(m,M)	(m,M)	(m,M)
$D_1(13)(23)$	$(-18,19)$	$(-12,18)$	$(-13,15)$	$(-18,22)$	$(-15,15)$	$(-11,10)$	$(-16,22)$	$(-14,18)$	$(-18,15)$	$(-18,15)$	$(-14,17)$	$(-14,22)$	$(-13,21)$
$D_1(23)(13)$	$(-15,25)$	$(-13,19)$	$(-12,14)$	$(-21,17)$	$(-14,14)$	$(-09,14)$	$(-18,16)$	$(-11,17)$	$(-13,16)$	$(-13,16)$	$(-17,13)$	$(-12,15)$	$(-12,14)$
$D_1(33)(23)$	$(-15,19)$	$(-11,14)$	$(-12,13)$	$(-18,18)$	$(-21,15)$	$(-11,16)$	$(-15,18)$	$(-13,18)$	$(-19,14)$	$(-19,14)$	$(-24,15)$	$(-13,18)$	$(-15,17)$
$D_1(14)(24)$	$(-29,26)$	$(-21,21)$	$(-24,20)$	$(-39,31)$	$(-27,24)$	$(-30,21)$	$(-37,28)$	$(-35,28)$	$(-28,23)$	$(-27,26)$	$(-28,28)$	$(-37,28)$	$(-35,29)$
$D_1(24)(14)$	$(-34,26)$	$(-26,22)$	$(-26,24)$	$(-32,40)$	$(-24,27)$	$(-23,31)$	$(-30,36)$	$(-31,31)$	$(-25,26)$	$(-26,25)$	$(-28,26)$	$(-24,32)$	$(-26,26)$
$D_1(34)(24)$	$(-28,28)$	$(-23,23)$	$(-24,23)$	$(-40,34)$	$(-28,28)$	$(-26,24)$	$(-36,32)$	$(-31,30)$	$(-33,25)$	$(-31,25)$	$(-37,30)$	$(-36,32)$	$(-37,32)$
$D_1(15)(25)$	$(-42,59)$	$(-41,33)$	$(-42,37)$	$(-47,38)$	$(-52,34)$	$(-32,32)$	$(-47,38)$	$(-48,37)$	$(-54,33)$	$(-49,37)$	$(-50,38)$	$(-39,35)$	$(-39,38)$
$D_1(25)(15)$	$(-44,45)$	$(-29,33)$	$(-29,36)$	$(-35,43)$	$(-30,48)$	$(-25,38)$	$(-33,41)$	$(-31,43)$	$(-60,45)$	$(-44,43)$	$(-43,45)$	$(-28,40)$	$(-28,41)$
$D_1(35)(25)$	$(-38,38)$	$(-28,30)$	$(-30,32)$	$(-42,45)$	$(-40,40)$	$(-36,35)$	$(-41,45)$	$(-40,45)$	$(-42,36)$	$(-51,38)$	$(-52,39)$	$(-41,44)$	$(-47,45)$

Table B.6: Values for SRMS (×100): D_2.

OT	TEMPLATE BAND										
	LR	LI	CSP	TB-1	TB-2	TB-3	TB-4	TB-5	TB-6	TB-7	TB-8
$D_2(14)(15)$	38	25	25	92	31	68	80	71	28	34	63
$D_2(24)(25)$	46	32	33	105	37	79	90	79	35	40	70
$D_2(34)(35)$	48	34	35	116	37	87	94	79	35	40	66
$D_2(44)(45)$	46	32	32	128	36	94	98	82	34	39	67
$D_2(54)(55)$	43	31	32	119	37	87	95	83	33	38	66
$D_2(64)(65)$	42	30	31	131	37	98	98	86	32	37	65
$D_2(15)(14)$	31	19	19	92	31	68	80	76	23	29	29
$D_2(25)(24)$	29	17	16	105	36	77	90	77	21	27	30
$D_2(35)(34)$	27	16	15	116	37	83	94	85	18	23	30
$D_2(45)(44)$	29	17	16	128	37	94	98	89	17	23	32
$D_2(55)(54)$	30	19	19	119	37	85	95	83	21	26	31
$D_2(65)(64)$	32	20	20	131	38	94	98	87	21	26	34
OT	TEMPLATE DATE										
	LR	LI	CSP	TD-1	TD-2	TD-3	TD-4	TD-5	TD-6	TD-7	TD-8
$D_2(14)(24)$	38	25	25	61	31	46	58	52	28	29	34
$D_2(24)(14)$	46	32	33	61	31	48	58	55	29	32	33
$D_2(34)(44)$	48	34	35	44	37	37	42	40	35	35	37
$D_2(44)(34)$	46	32	32	44	36	36	42	40	34	35	36
$D_2(54)(64)$	43	31	32	48	38	38	46	45	37	37	40
$D_2(64)(54)$	42	30	31	48	39	37	46	42	37	37	39
$D_2(15)(25)$	31	19	19	29	16	24	29	22	17	17	18
$D_2(25)(15)$	29	17	16	29	16	22	29	22	16	16	15
$D_2(35)(45)$	27	16	15	25	17	19	25	23	17	18	18
$D_2(45)(35)$	29	17	16	25	17	20	25	23	17	19	19
$D_2(55)(65)$	30	19	19	31	23	24	31	29	22	23	24
$D_2(65)(55)$	32	20	20	31	23	23	31	29	23	24	24

Table B.7: Values for CCOR (×100): D_2.

OT	TEMPLATE BAND										
	LR	LI	CSP	TB-1	TB-2	TB-3	TB-4	TB-5	TB-6	TB-7	TB-8
$D_2(14)(15)$	72	33	32	421	51	250	421	305	42	62	179
$D_2(24)(25)$	104	53	54	559	68	347	559	385	61	87	217
$D_2(34)(35)$	113	59	66	678	74	411	678	386	66	86	211
$D_2(44)(45)$	108	53	54	828	70	510	828	449	59	83	217
$D_2(54)(55)$	93	50	53	702	71	422	702	448	59	76	196
$D_2(64)(65)$	92	48	51	862	75	571	862	501	54	72	200
$D_2(15)(14)$	49	19	19	421	50	251	421	349	29	44	45
$D_2(25)(24)$	41	15	15	559	64	337	559	365	24	38	47
$D_2(35)(34)$	39	13	12	678	69	401	678	474	17	29	47
$D_2(45)(44)$	42	15	13	828	66	535	828	555	16	28	55
$D_2(55)(54)$	48	19	18	702	68	420	702	443	23	35	53
$D_2(65)(64)$	53	22	21	862	72	537	862	521	23	35	61
OT	TEMPLATE DATE										
	LR	LI	CSP	TD-1	TD-2	TD-3	TD-4	TD-5	TD-6	TD-7	TD-8
$D_2(14)(24)$	72	33	32	190	49	110	190	153	40	45	61
$D_2(24)(14)$	104	53	54	190	51	120	190	163	47	54	56
$D_2(34)(44)$	113	59	66	97	67	67	97	86	62	63	69
$D_2(44)(34)$	108	53	54	97	67	68	97	86	61	63	66
$D_2(54)(64)$	93	50	53	113	75	76	113	105	68	70	80
$D_2(64)(54)$	92	48	51	113	75	73	113	97	68	70	74
$D_2(15)(25)$	49	19	19	44	14	30	44	26	15	15	17
$D_2(25)(15)$	41	15	15	44	14	26	44	26	13	13	12
$D_2(35)(45)$	39	13	12	32	15	20	32	28	15	17	17
$D_2(45)(35)$	42	15	13	32	15	22	32	27	16	18	18
$D_2(55)(65)$	48	19	18	49	27	31	49	44	26	28	29
$D_2(65)(55)$	53	22	21	49	27	29	49	44	27	29	30

Table B.8: Values for SRAN: D_2.

OT	TEMPLATE BAND										
	LR	LI	CSP	TB-1	TB-2	TB-3	TB-4	TB-5	TB-6	TB-7	TB-8
$D_2(14)(15)$	5.5	3.6	3.8	6.5	4.4	5.2	6.9	7.1	4.2	4.4	10.0
$D_2(24)(25)$	8.3	5.3	4.4	8.8	5.7	8.1	8.8	7.9	5.7	7.9	13.7
$D_2(34)(35)$	8.5	5.9	6.1	7.5	5.1	6.1	7.5	7.9	7.5	7.9	9.8
$D_2(44)(45)$	7.8	4.6	5.5	7.6	5.1	6.9	7.5	8.6	6.5	6.3	15.3
$D_2(54)(55)$	8.0	4.6	4.6	7.2	4.6	6.4	6.7	6.6	5.6	5.3	12.2
$D_2(64)(65)$	7.0	5.7	4.9	7.5	5.9	6.0	7.3	7.5	6.2	7.7	8.6
$D_2(15)(14)$	4.2	3.3	3.4	6.4	4.3	4.8	5.6	6.1	3.6	3.7	3.8
$D_2(25)(24)$	3.7	2.5	2.5	8.9	5.6	6.4	4.7	6.0	3.9	4.3	5.2
$D_2(35)(34)$	4.0	2.5	2.7	7.6	5.1	5.7	4.4	5.1	2.7	3.2	5.4
$D_2(45)(44)$	4.7	2.8	2.8	7.7	5.2	5.8	4.8	5.3	2.9	3.4	5.4
$D_2(55)(54)$	4.8	3.1	3.2	7.2	4.6	5.8	4.5	5.0	3.3	3.5	4.3
$D_2(65)(64)$	4.8	2.9	2.6	7.5	5.9	5.7	4.9	5.3	2.9	3.5	4.5
OT	TEMPLATE DATE										
	LR	LI	CSP	TD-1	TD-2	TD-3	TD-4	TD-5	TD-6	TD-7	TD-8
$D_2(14)(24)$	5.5	3.6	3.8	6.8	3.8	4.9	5.8	5.7	4.2	4.6	6.1
$D_2(24)(14)$	8.3	5.3	4.4	6.8	3.7	6.1	7.0	6.6	3.8	5.3	4.8
$D_2(34)(44)$	8.5	5.9	6.1	8.3	5.1	6.6	7.7	6.4	5.0	5.5	5.7
$D_2(44)(34)$	7.8	4.6	5.5	8.2	5.0	6.7	8.2	7.6	4.8	4.8	5.0
$D_2(54)(64)$	8.0	4.6	4.6	5.9	5.3	4.8	5.4	5.4	5.0	5.0	5.1
$D_2(64)(54)$	7.0	5.7	4.9	5.9	5.0	4.5	5.7	5.9	5.0	5.2	5.4
$D_2(15)(25)$	4.2	3.3	3.4	3.2	2.6	2.5	3.1	3.3	2.8	2.5	2.6
$D_2(25)(15)$	3.7	2.5	2.5	3.2	2.6	2.6	3.1	2.8	2.5	2.2	2.1
$D_2(35)(45)$	4.0	2.5	2.7	4.0	2.8	3.2	4.0	4.0	3.5	3.7	3.4
$D_2(45)(35)$	4.7	2.8	2.8	4.0	2.7	3.6	3.9	3.6	3.0	4.1	3.7
$D_2(55)(65)$	4.8	3.1	3.2	4.3	4.2	3.3	4.3	4.3	4.3	3.7	3.9
$D_2(65)(55)$	4.8	2.9	2.6	4.4	4.2	3.7	4.4	4.1	5.3	3.7	3.8

Table B.9: Values for ACC (×100): D_2.

OT	TEMPLATE BAND										
	LR	LI	CSP	TB-1	TB-2	TB-3	TB-4	TB-5	TB-6	TB-7	TB-8
$D_2(14)(15)$	16	6	10	72	11	51	68	64	9	13	34[a]
$D_2(24)(25)$	34	8	12	72	11	65	63	56	9	27	32[a]
$D_2(34)(35)$	32	9	14	72	12	47	67	61	21	25	28[a]
$D_2(44)(45)$	27	7	11	75	10	52	56	61	8	10	26[a]
$D_2(54)(55)$	26[a]	10	14	74	15	65	70	64	11	15	35[a]
$D_2(64)(65)$	31	9	14	78	15	61	74	67	10	26	33[a]
$D_2(15)(14)$	31	11	15	84	41	80	83	78	17	37	39
$D_2(25)(24)$	14	8	11	70[b]	48	80	87	81	12	30	37
$D_2(35)(34)$	22	8	11	85	45	76	92	84	9	14	33
$D_2(45)(44)$	12	5	8	85	35	80	81	80	6	11	28
$D_2(55)(54)$	23	7	10	82	43	73	81	77	9	14	20
$D_2(65)(64)$	15	8	11	83	37	75	88	78	9	13	20
OT	TEMPLATE DATE										
	LR	LI	CSP	TD-1	TD-2	TD-3	TD-4	TD-5	TD-6	TD-7	TD-8
$D_2(14)(24)$	16	6	10	50	11	25	34	31	8	10	15
$D_2(24)(14)$	34	8	12	26	8	22	25	22	7	8	9
$D_2(34)(44)$	32	9	14	33	12	11	33	14	10	10	11
$D_2(44)(34)$	27	7	11	30	10	13	30	27	9	9	9
$D_2(54)(64)$	26[a]	10	14	27	18	18	26	24	15	16	18
$D_2(64)(54)$	31	9	14	26	14	20	25	22	14	15	16
$D_2(15)(25)$	31	11	15	31	21	26	29	19	10	6	11
$D_2(25)(15)$	14	8	11	27	8	17	28	16	7	7	6
$D_2(35)(45)$	22	8	11	30	7	10	29	24	7	8	8
$D_2(45)(35)$	12	5	8	11	5	11	11	9	5	6	6
$D_2(55)(65)$	23	7	10	19	10	13	18	17	10	11	11
$D_2(65)(55)$	15	8	11	17	9	11	17	16	17	10	10

[a]number of pixels within the range ±5 grey levels
[b]number of pixels within the range ±20 grey levels

Table B.10: Minimum (m) and maximum (M) values for the residuals: D_2.

OT	TEMPLATE					BAND					
	LR	LI	CSP	TB-1	TB-2	TB-3	TB-4	TB-5	TB-6	TB-7	TB-8
	(m,M)	(m,M)	(m,M)	(m,M)	(m,M)	(m,M)	(m,M)	(m,M)	(m,M)	(m,M)	(m,M)
$D_2(14)(15)$	$(-19, 16)$	$(-10, 13)$	$(-11, 13)$	$(-18, 23)$	$(-12, 16)$	$(-15, 18)$	$(-21, 23)$	$(-24, 21)$	$(-12, 15)$	$(-13, 15)$	$(-35, 28)$
$D_2(24)(25)$	$(-20, 25)$	$(-13, 16)$	$(-12, 12)$	$(-22, 26)$	$(-14, 17)$	$(-23, 21)$	$(-24, 24)$	$(-23, 20)$	$(-14, 17)$	$(-22, 21)$	$(-47, 27)$
$D_2(34)(35)$	$(-26, 20)$	$(-20, 12)$	$(-18, 15)$	$(-16, 25)$	$(-16, 12)$	$(-13, 20)$	$(-20, 21)$	$(-22, 21)$	$(-22, 19)$	$(-22, 21)$	$(-29, 24)$
$D_2(44)(45)$	$(-19, 22)$	$(-12, 12)$	$(-14, 15)$	$(-15, 25)$	$(-12, 15)$	$(-15, 21)$	$(-14, 25)$	$(-17, 28)$	$(-15, 19)$	$(-16, 17)$	$(-60, 20)$
$D_2(54)(55)$	$(-23, 27)$	$(-15, 14)$	$(-15, 14)$	$(-20, 25)$	$(-13, 16)$	$(-19, 21)$	$(-19, 23)$	$(-20, 21)$	$(-15, 20)$	$(-15, 18)$	$(-52, 24)$
$D_2(64)(65)$	$(-24, 19)$	$(-14, 21)$	$(-13, 17)$	$(-20, 26)$	$(-15, 21)$	$(-15, 22)$	$(-22, 23)$	$(-23, 23)$	$(-15, 23)$	$(-18, 29)$	$(-31, 22)$
$D_2(15)(14)$	$(-60, 56)$	$(-34, 56)$	$(-38, 56)$	$(-98, 77)$	$(-68, 50)$	$(-70, 63)$	$(-81, 73)$	$(-94, 73)$	$(-51, 49)$	$(-61, 42)$	$(-63, 41)$
$D_2(25)(24)$	$(-47, 46)$	$(-31, 31)$	$(-31, 31)$	$(-121, 100)$	$(-77, 64)$	$(-89, 72)$	$(-64, 53)$	$(-87, 62)$	$(-61, 38)$	$(-72, 37)$	$(-73, 58)$
$D_2(35)(34)$	$(-54, 50)$	$(-32, 33)$	$(-34, 36)$	$(-119, 75)$	$(-57, 75)$	$(-88, 59)$	$(-65, 49)$	$(-72, 58)$	$(-38, 32)$	$(-48, 34)$	$(-53, 85)$
$D_2(45)(44)$	$(-45, 54)$	$(-33, 27)$	$(-28, 31)$	$(-102, 60)$	$(-60, 50)$	$(-77, 45)$	$(-51, 49)$	$(-55, 57)$	$(-35, 27)$	$(-40, 31)$	$(-55, 59)$
$D_2(55)(54)$	$(-61, 46)$	$(-31, 37)$	$(-34, 38)$	$(-89, 70)$	$(-56, 46)$	$(-71, 57)$	$(-45, 54)$	$(-56, 55)$	$(-35, 39)$	$(-39, 39)$	$(-47, 49)$
$D_2(65)(64)$	$(-50, 49)$	$(-27, 33)$	$(-27, 28)$	$(-88, 68)$	$(-70, 52)$	$(-67, 52)$	$(-44, 58)$	$(-54, 57)$	$(-28, 33)$	$(-34, 39)$	$(-56, 38)$

OT	TEMPLATE					DATE					
	LR	LI	CSP	TD-1	TD-2	TD-3	TD-4	TD-5	TD-6	TD-7	TD-8
	(m,M)	(m,M)	(m,M)	(m,M)	(m,M)	(m,M)	(m,M)	(m,M)	(m,M)	(m,M)	(m,M)
$D_2(14)(24)$	$(-19, 16)$	$(-10, 13)$	$(-11, 13)$	$(-22, 21)$	$(-12, 12)$	$(-16, 15)$	$(-17, 20)$	$(-16, 20)$	$(-16, 11)$	$(-16, 13)$	$(-22, 17)$
$D_2(24)(14)$	$(-20, 25)$	$(-13, 16)$	$(-12, 12)$	$(-18, 19)$	$(-10, 10)$	$(-17, 16)$	$(-18, 20)$	$(-18, 18)$	$(-10, 11)$	$(-14, 15)$	$(-13, 13)$
$D_2(34)(44)$	$(-26, 20)$	$(-20, 12)$	$(-18, 15)$	$(-21, 24)$	$(-15, 13)$	$(-16, 20)$	$(-19, 23)$	$(-15, 20)$	$(-15, 12)$	$(-18, 12)$	$(-18, 13)$
$D_2(44)(34)$	$(-19, 22)$	$(-12, 12)$	$(-14, 15)$	$(-23, 20)$	$(-12, 14)$	$(-18, 17)$	$(-22, 21)$	$(-20, 20)$	$(-13, 12)$	$(-12, 13)$	$(-12, 14)$
$D_2(54)(64)$	$(-23, 27)$	$(-15, 14)$	$(-15, 14)$	$(-22, 15)$	$(-16, 17)$	$(-16, 14)$	$(-19, 15)$	$(-19, 15)$	$(-16, 15)$	$(-15, 16)$	$(-16, 16)$
$D_2(64)(54)$	$(-24, 19)$	$(-14, 21)$	$(-13, 17)$	$(-15, 21)$	$(-16, 15)$	$(-12, 16)$	$(-14, 21)$	$(-15, 21)$	$(-17, 14)$	$(-17, 15)$	$(-18, 15)$
$D_2(15)(25)$	$(-60, 56)$	$(-34, 56)$	$(-38, 56)$	$(-29, 59)$	$(-33, 39)$	$(-27, 41)$	$(-30, 57)$	$(-34, 57)$	$(-37, 41)$	$(-34, 35)$	$(-34, 39)$
$D_2(25)(15)$	$(-47, 46)$	$(-31, 31)$	$(-31, 31)$	$(-54, 27)$	$(-35, 30)$	$(-41, 24)$	$(-53, 25)$	$(-45, 25)$	$(-40, 24)$	$(-31, 25)$	$(-30, 24)$
$D_2(35)(45)$	$(-54, 50)$	$(-32, 33)$	$(-34, 36)$	$(-48, 56)$	$(-33, 39)$	$(-39, 43)$	$(-48, 55)$	$(-49, 53)$	$(-51, 38)$	$(-56, 38)$	$(-49, 39)$
$D_2(45)(35)$	$(-45, 54)$	$(-33, 27)$	$(-28, 31)$	$(-45, 39)$	$(-31, 27)$	$(-40, 35)$	$(-44, 39)$	$(-37, 38)$	$(-36, 28)$	$(-51, 36)$	$(-38, 40)$
$D_2(55)(65)$	$(-61, 46)$	$(-31, 37)$	$(-34, 38)$	$(-56, 40)$	$(-54, 40)$	$(-40, 34)$	$(-55, 41)$	$(-55, 40)$	$(-59, 37)$	$(-50, 32)$	$(-54, 33)$
$D_2(65)(55)$	$(-50, 49)$	$(-27, 33)$	$(-27, 28)$	$(-38, 53)$	$(-37, 51)$	$(-38, 39)$	$(-38, 53)$	$(-35, 50)$	$(-63, 48)$	$(-36, 41)$	$(-34, 46)$

Table B.11: Values for SRMS (×100) and CCOR (×100) for methods TB/D-11 to TB/D-15: D_1.

OT	TEMPLATE BAND									
	SRMS					CCOR				
	TB-11	TB-12	TB-13	TB-14	TB-15	TB-11	TB-12	TB-13	TB-14	TB-15
$D_1(13)(14)$	40	40	40	39	40	88	86	85	84	87
$D_1(23)(24)$	42	42	42	42	43	95	93	92	92	99
$D_1(33)(34)$	40	39	38	39	40	86	81	80	81	84
$D_1(13)(15)$	40	40	40	39	39	85	85	85	80	80
$D_1(23)(25)$	42	42	42	42	42	95	94	92	91	91
$D_1(33)(35)$	38	38	38	38	38	79	80	79	78	78
$D_1(14)(13)$	34	33	33	32	33	61	58	57	55	59
$D_1(24)(23)$	34	33	37	34	36	64	60	58	61	69
$D_1(34)(33)$	39	38	33	37	38	80	76	72	72	77
$D_1(14)(15)$	34	33	34	33	33	60	56	56	57	59
$D_1(24)(25)$	35	34	37	34	35	65	63	61	61	66
$D_1(34)(35)$	39	37	37	36	38	81	72	71	71	78
$D_1(15)(13)$	30	29	29	34	33	46	45	45	59	57
$D_1(25)(23)$	30	29	29	36	35	48	46	45	65	62
$D_1(35)(33)$	30	29	29	35	34	47	45	43	61	59
$D_1(15)(14)$	30	29	29	29	30	46	45	44	46	47
$D_1(25)(24)$	30	29	28	29	31	48	45	45	44	50
$D_1(35)(34)$	31	29	32	29	31	50	44	42	43	53

OT	TEMPLATE DATE									
	SRMS					CCOR				
	TD-11	TD-12	TD-13	TD-14	TD-15	TD-11	TD-12	TD-13	TD-14	TD-15
$D_1(13)(23)$	39	39	39	41	41	83	84	84	89	88
$D_1(23)(13)$	41	41	41	42	43	88	89	91	91	92
$D_1(33)(23)$	40	39	39	44	44	83	82	81	100	100
$D_1(14)(24)$	32	32	32	30	29	54	56	56	45	44
$D_1(24)(14)$	33	34	34	34	31	58	60	61	61	50
$D_1(34)(24)$	36	37	36	36	36	70	72	71	67	66
$D_1(15)(25)$	30	29	29	29	30	46	45	45	43	47
$D_1(25)(15)$	30	29	29	31	31	47	45	44	48	48
$D_1(35)(25)$	29	29	29	32	31	44	43	43	51	50

Table B.12: Values for SRAN methods TB/D-11 to TB/D-15: D_1.

OT	TEMPLATE BAND SRAN				
	TB-11	TB-12	TB-13	TB-14	TB-15
$D_1(13)(14)$	5.6	5.6	5.6	5.6	5.6
$D_1(23)(24)$	6.4	6.4	6.4	6.4	6.6
$D_1(33)(34)$	5.1	5.1	5.1	4.8	5.3
$D_1(13)(15)$	5.6	5.6	4.7	4.7	6.0
$D_1(23)(25)$	7.0	6.4	5.6	5.6	7.0
$D_1(33)(35)$	5.1	5.1	5.3	5.3	6.7
$D_1(14)(13)$	4.4	3.9	4.2	3.8	4.5
$D_1(24)(23)$	4.9	4.8	4.7	3.8	5.0
$D_1(34)(33)$	6.3	5.4	5.1	4.5	6.3
$D_1(14)(15)$	3.9	3.9	4.0	3.9	7.6
$D_1(24)(25)$	5.9	4.4	4.7	4.4	6.2
$D_1(34)(35)$	5.1	4.4	5.0	4.5	9.2
$D_1(15)(13)$	3.9	4.1	4.0	3.8	3.9
$D_1(25)(23)$	4.2	3.8	4.6	4.5	4.4
$D_1(35)(33)$	3.9	3.9	4.2	4.4	3.9
$D_1(15)(14)$	4.1	4.1	4.0	4.2	4.7
$D_1(25)(24)$	5.1	5.1	4.1	3.8	6.7
$D_1(35)(34)$	4.0	3.6	5.3	3.9	6.1

OT	TEMPLATE DATE SRAN				
	TD-11	TD-12	TD-13	TD-14	TD-15
$D_1(13)(23)$	6.2	6.2	5.6	5.2	5.2
$D_1(23)(13)$	6.2	6.2	6.2	5.4	5.6
$D_1(33)(23)$	5.3	5.3	5.3	6.3	6.1
$D_1(14)(24)$	5.0	4.8	3.9	4.3	4.3
$D_1(24)(14)$	4.4	4.4	4.4	4.4	4.7
$D_1(34)(24)$	5.4	5.4	4.4	5.0	5.0
$D_1(15)(25)$	4.9	4.9	4.9	4.6	4.5
$D_1(25)(15)$	6.1	4.8	3.8	4.8	4.7
$D_1(35)(25)$	4.6	4.2	4.2	4.8	4.9

Table B.13: Values for SRMS (×100) and CCOR (×100) for methods TB/D-11 to TB/D-15: D_2.

OT	TEMPLATE BAND									
	SRMS					CCOR				
	TB-11	TB-12	TB-13	TB-14	TB-15	TB-11	TB-12	TB-13	TB-14	TB-15
$D_2(14)(15)$	25	25	25	27	28	34	33	33	39	41
$D_2(24)(25)$	32	32	32	33	33	54	53	53	56	59
$D_2(34)(35)$	34	34	34	34	34	60	59	59	61	61
$D_2(44)(45)$	32	32	32	32	32	54	53	53	54	54
$D_2(54)(55)$	30	30	30	32	32	53	50	50	52	54
$D_2(64)(65)$	32	31	31	30	31	49	48	48	49	51
$D_2(15)(14)$	20	19	19	24	24	21	20	20	30	30
$D_2(25)(24)$	18	17	17	22	24	17	16	16	25	29
$D_2(35)(34)$	16	16	16	19	22	14	13	13	19	25
$D_2(45)(44)$	17	17	17	18	19	15	15	15	17	19
$D_2(55)(54)$	19	19	19	21	24	19	19	19	24	30
$D_2(65)(64)$	20	20	20	21	23	22	22	22	23	27
OT	TEMPLATE DATE									
	SRMS					CCOR				
	TD-11	TD-12	TD-13	TD-14	TD-15	TD-11	TD-12	TD-13	TD-14	TD-15
$D_2(14)(24)$	25	25	25	27	29	34	34	34	39	43
$D_2(24)(14)$	32	32	32	30	34	52	53	53	47	43
$D_2(34)(44)$	33	33	33	35	34	58	57	58	62	60
$D_2(44)(34)$	31	31	31	35	34	52	51	52	61	59
$D_2(54)(64)$	30	30	29	37	36	53	51	50	54	67
$D_2(64)(54)$	32	32	31	36	35	51	48	48	67	65
$D_2(15)(25)$	19	19	19	16	17	19	19	19	14	15
$D_2(25)(15)$	17	17	17	16	16	15	16	16	14	14
$D_2(35)(45)$	16	16	16	17	17	13	13	13	15	14
$D_2(45)(35)$	17	17	17	17	17	15	15	15	15	15
$D_2(55)(65)$	20	19	19	22	21	20	19	19	25	25
$D_2(65)(55)$	21	20	20	22	24	23	22	22	26	26

Table B.14: Values for SRAN methods TB/D-11 to TB/D-15: D_2.

OT	TEMPLATE BAND				
	SRAN				
	TB-11	TB-12	TB-13	TB-14	TB-15
$D_2(14)(15)$	3.8	3.6	3.6	3.9	5.0
$D_2(24)(25)$	5.3	5.3	5.3	5.1	5.5
$D_2(34)(35)$	5.9	5.9	5.9	5.5	5.5
$D_2(44)(45)$	5.9	4.6	4.6	4.6	4.8
$D_2(54)(55)$	5.6	4.6	4.6	4.5	4.3
$D_2(64)(65)$	5.7	5.7	5.7	5.7	5.7
$D_2(15)(14)$	3.9	3.8	3.8	3.6	3.6
$D_2(25)(24)$	3.1	2.5	2.5	3.1	3.8
$D_2(35)(34)$	2.6	2.5	2.5	2.7	3.5
$D_2(45)(44)$	2.9	2.9	2.9	2.6	2.5
$D_2(55)(54)$	3.0	3.0	3.1	3.3	3.5
$D_2(65)(64)$	2.9	2.9	2.9	2.9	3.3
OT	TEMPLATE DATE				
	SRAN				
	TD-11	TD-12	TD-13	TD-14	TD-15
$D_2(14)(24)$	4.6	4.6	4.6	3.3	3.6
$D_2(24)(14)$	4.6	5.3	5.3	3.7	4.2
$D_2(34)(44)$	4.2	4.4	5.3	4.8	4.6
$D_2(44)(34)$	4.8	4.8	4.8	4.6	4.2
$D_2(54)(64)$	4.8	4.6	4.6	3.8	4.8
$D_2(64)(54)$	5.0	4.4	5.7	4.9	4.7
$D_2(15)(25)$	3.2	3.3	3.3	2.6	2.7
$D_2(25)(15)$	2.8	2.8	2.8	2.5	2.9
$D_2(35)(45)$	2.7	2.5	2.5	2.7	2.7
$D_2(45)(35)$	2.9	2.8	2.8	2.7	2.8
$D_2(55)(65)$	3.8	3.1	3.1	4.2	4.2
$D_2(65)(55)$	4.4	3.5	2.9	4.1	4.0

Appendix C

Tables for Chapter 5

Table C.1: Values for SRMS (×100) for the single band, template band, and template date methods for the simulated missing lines in sub-image $D_1(15)$.

TEMPLATE BAND													
Line	LR	LI	CSP	TB-1	TB-2	TB-3	TB-4	TB-5	TB-6	TB-7	TB-8	TB-9	TB-10
11/*H*	26	16	21	54	29	39	45	40	23	22	22	50	32
11/*L*				144	38	107	115	114	21	22	33		
27/*H*	56	41	42	58	48	49	63	58	41	43	44	66	52
27/*L*				157	47	118	112	83	39	42	47		
43/*H*	21	22	23	66	27	53	65	65	23	22	24	67	64
43/*L*				132	26	99	92	82	20	19	31		
59/*H*	48	37	38	95	43	72	82	78	39	37	37	83	79
59/*L*				140	56	106	108	106	42	44	55		
75/*H*	32	23	25	108	47	81	97	86	34	36	38	89	65
75/*L*				120	32	88	108	98	25	29	34		
91/*H*	63	43	--	82	56	--	67	64	49	49	50	64	62
91/*L*			--	171	65	--	93	85	45	45	62		

TEMPLATE DATE													
Line	LR	LI	CSP	TD-1	TD-2	TD-3	TD-4	TD-5	TD-6	TD-7	TD-8	TD-9	TD-10
11/*H*	26	16	21	22	19	19	19	18	18	17	17	18	15
11/*L*				42	30	31	38	32	27	29	30		
27/*H*	56	41	42	33	30	33	32	31	31	33	32	34	35
27/*L*				64	50	54	60	57	50	54	53		
43/*H*	21	22	23	25	23	25	24	24	22	19	19	22	21
43/*L*				37	27	28	35	35	24	24	24		
59/*H*	48	37	38	40	33	36	39	39	34	32	31	39	38
59/*L*				78	43	61	75	70	44	48	47		
75/*H*	32	23	25	41	24	38	42	56	23	26	25	40	36
75/*L*				51	34	43	53	48	34	34	34		
91/*H*	63	43	--	45	51	--	44	45	53	53	50	47	50
91/*L*			--	71	51	--	71	14	51	51	51		

Table C.2: Values for CCOR (×100) for the single band, template band, and template date methods for the simulated missing lines in sub-image $D_1(15)$.

				TEMPLATE BAND									
Line	LR	LI	CS	TB-1	TB-2	TB-3	TB-4	TB-5	TB-6	TB-7	TB-8	TB-9	TB-10
11/*H*	25	11	17	66	33	40	66	66	21	19	20	88	42
11/*L*				985	56	600	985	985	16	18	42		
27/*H*	182	84	95	205	108	136	205	205	86	97	105	250	160
27/*L*				507	116	821	507	507	83	101	123		
43/*H*	31	27	34	348	51	207	348	348	38	35	40	374	335
43/*L*				732	48	905	732	732	27	25	68		
59/*H*	102	59	67	316	79	209	316	316	66	60	61	316	320
59/*L*				801	124	592	801	801	76	82	126		
75/*H*	43	25	26	405	84	255	405	405	46	52	55	351	206
75/*L*				607	46	380	607	607	27	37	57		
91/*H*	237	130	–	321	178	––	321	321	149	149	145	305	305
91/*L*				779	270	––	779	779	143	143	59		
				TEMPLATE DATE									
Line	LR	LI	CS	TD-1	TD-2	TD-3	TD-4	TD-5	TD-6	TD-7	TD-8	TD-9	TD-10
11/*H*	25	11	17	14	14	11	14	14	13	11	11	9	9
11/*L*				41	29	24	41	41	28	27	28		
27/*H*	182	84	95	56	50	60	56	56	53	60	55	62	69
27/*L*				184	126	147	184	184	133	153	149		
43/*H*	31	27	34	41	37	39	41	41	34	24	25	33	33
43/*L*				86	44	54	86	86	40	31	33		
59/*H*	102	59	67	69	50	56	69	69	51	44	43	103	70
59/*L*				244	74	166	244	244	83	94	93		
75/*H*	43	25	26	72	26	57	72	72	24	31	29	59	59
75/*L*				106	45	74	106	106	49	47	47		
91/*H*	237	130	––	143	162	––	143	143	174	174	148	161	179
91/*L*				413	178	–	413	413	172	172	178		

Table C.3: Values for SRAN for the single band, template band, and template date methods for the simulated missing lines in sub-image $D_1(15)$.

TEMPLATE BAND													
Line	LR	LI	CSP	TB-1	TB-2	TB-3	TB-4	TB-5	TB-6	TB-7	TB-8	TB-9	TB-10
11/*H*	1.5	0.8	0.9	2.3	2.2	1.7	1.8	1.8	1.5	1.6	1.5	1.9	1.3
11/*L*				4.4	2.1	3.3	3.5	3.6	1.1	1.0	2.0		
27/*H*	5.4	3.2	3.4	2.7	2.9	3.7	2.7	2.6	2.8	3.1	3.3	2.7	3.0
27/*L*				4.9	4.5	3.6	3.6	4.8	3.3	2.9	3.8		
43/*H*	1.1	1.1	1.2	3.2	1.6	2.5	2.9	2.9	1.2	1.2	1.5	2.7	3.3
43/*L*				4.2	1.9	3.2	2.9	3.8	1.1	1.2	2.2		
59/*H*	2.8	2.3	2.2	3.3	2.4	2.7	2.8	2.7	2.2	1.9	1.9	2.7	2.8
59/*L*				3.8	2.9	3.0	3.1	3.1	2.6	2.5	3.0		
75/*H*	1.8	1.6	1.4	3.5	2.4	2.5	2.8	3.1	1.8	2.2	2.2	2.9	2.6
75/*L*				5.1	1.7	3.8	3.8	3.9	1.7	2.0	1.7		
91/*H*	3.6	2.8	--	3.4	2.9	--	2.8	2.7	2.2	2.8	2.9	2.8	2.8
91/*L*				6.2	3.7	--	3.1	3.6	2.7	2.7	3.0		
TEMPLATE DATE													
Line	LR	LI	CSp	TB-1	TD-2	TD-3	TD-4	TD-5	TD-6	TD-7	TD-8	TD-9	TD-10
11/*H*	1.5	0.8	0.9	1.4	1.1	1.1	1.2	1.1	1.0	0.9	0.9	0.9	0.9
11/*L*				1.8	1.6	1.2	1.7	1.7	1.8	1.6	1.7		
27/*H*	5.4	3.2	3.4	2.3	2.0	2.5	2.3	2.3	2.2	2.0	1.9	2.6	2.8
27/*L*				5.7	4.5	4.6	5.4	5.0	4.5	4.8	4.7		
43/*H*	1.1	1.1	1.2	1.5	1.2	1.6	1.4	1.4	1.1	1.0	.9	1.4	1.4
43/*L*				2.8	1.4	5.0	2.5	2.4	1.4	1.5	1.5		
59/*H*	2.8	2.3	2.2	2.0	1.7	1.8	1.9	1.9	1.8	1.6	1.7	2.2	1.9
59/*L*				3.1	2.2	2.8	2.9	2.7	2.3	2.5	2.4		
75/*H*	1.8	1.6	1.4	2.2	1.3	1.8	2.2	2.2	1.2	2.0	1.8	1.8	1.8
75/*L*				2.4	1.9	2.0	2.4	2.4	2.3	2.2	2.2		
91/*H*	3.6	2.8	--	2.4	3.3	--	2.3	2.2	3.5	3.5	3.1	2.2	2.2
91/*L*				2.8	3.4	--	2.7	2.7	3.3	3.3	3.3		

Table C.4: Values for SRMS (×100) for the single band, template band, and template date methods for the simulated missing lines in sub-image $D_2(15)$.

TEMPLATE BAND											
Line	LR	LI	CSP	TB-1	TB-2	TB-3	TB-4	TB-5	TB-6	TB-7	TB-8
07	11	8	9	96	13	73	92	92	10	12	12
23	23	15	13	84	23	62	81	79	18	25	25
39	43	28	26	82	37	66	71	72	30	38	39
45	29	19	19	67	31	50	87	67	24	31	30
61	22	13	12	116	23	86	113	93	18	21	23
77	24	16	15	86	34	71	71	66	24	28	29
93	23	24	24	76	35	56	57	57	27	34	30

TEMPLATE DATE											
Line	LR	LI	CSP	TD-1	TD-2	TD-3	TD-4	TD-5	TD-6	TD-7	TD-8
07	11	8	9	25	7	19	27	15	8	8	8
23	23	15	13	35	19	23	36	29	30	20	24
39	43	28	26	25	17	25	25	23	19	17	16
45	29	19	19	20	16	17	20	19	19	15	17
61	22	13	12	34	20	26	32	25	24	18	21
77	24	16	15	30	18	31	26	22	21	16	18
93	23	24	24	31	19	24	30	28	29	19	22

Table C.5: Values for CCOR (×100) for the single band, template band, and template date methods for the simulated missing lines in sub-image $D_2(15)$.

				TEMPLATE BAND							
Line	LR	LI	CSP	TB-1	TB-2	TB-3	TB-4	TB-5	TB-6	TB-7	TB-8
07	7	4	4	618	9	310	618	618	6	7	7
23	27	12	8	418	29	228	418	418	17	33	33
39	115	41	38	363	74	268	363	363	51	86	90
45	30	12	13	138	34	76	138	138	20	33	32
61	21	7	7	498	23	217	498	498	14	20	20
77	31	14	12	275	58	208	275	275	32	43	46
93	30	34	28	205	65	124	205	205	42	68	56
				TEMPLATE DATE							
Line	LR	LI	CSP	TD-1	TD-2	TD-3	TD-4	TD-5	TD-6	TD-7	TD-8
07	7	4	4	12	2	7	12	12	4	3	14
23	27	12	8	47	20	17	47	47	46	21	40
39	115	41	38	32	17	32	32	32	21	16	16
45	30	12	13	14	9	11	14	14	12	9	10
61	21	7	7	27	18	18	27	27	27	14	20
77	31	14	12	28	14	34	28	28	19	13	16
93	30	34	28	48	21	28	48	48	47	21	29

Table C.6: Values for SRAN for the single band, template band, and template date methods for the simulated missing lines in sub-image $D_2(15)$.

TEMPLATE BAND											
Line	LR	LI	CS	TB-1	TB-2	TB-3	TB-4	TB-5	TB-6	TB-7	TB-8
07	0.6	0.4	0.4	3.6	0.7	2.7	3.2	3.2	0.5	0.5	0.6
23	1.9	0.8	0.6	3.8	1.2	3.1	3.5	3.6	0.9	1.6	1.6
39	2.6	1.6	1.4	3.8	2.0	3.1	3.4	3.4	1.5	2.0	2.2
45	2.0	1.5	1.5	2.7	2.0	2.1	2.5	2.5	1.7	1.8	1.7
61	1.9	0.9	0.6	5.2	1.8	3.9	4.8	4.8	1.4	1.7	1.9
77	1.5	0.7	0.8	5.0	1.7	4.1	3.1	3.0	1.3	1.5	1.5
93	1.9	1.9	1.6	5.2	2.2	4.2	3.7	3.7	1.9	2.4	2.0
TEMPLATE DATE											
Line	LR	LI	CS	TD-1	TD-2	TD-3	TD-4	TD-5	TD-6	TD-7	TD-8
07	0.6	0.4	0.4	0.8	0.3	0.7	0.9	0.8	0.4	0.4	0.4
23	1.9	0.8	0.6	2.5	1.6	1.5	2.5	2.6	2.5	1.7	2.1
39	2.6	1.6	1.4	1.2	0.8	1.2	1.2	1.2	0.8	0.8	0.7
45	2.0	1.5	1.5	1.1	0.9	0.9	1.1	1.1	1.2	0.8	0.8
61	1.9	0.9	0.6	1.4	1.3	0.7	1.4	1.4	1.7	1.1	1.6
77	1.5	0.7	0.8	1.3	1.1	1.5	1.3	1.2	1.3	0.7	1.1
93	1.9	1.9	1.6	1.4	1.1	1.1	1.3	1.3	1.9	1.1	1.4

Table C.7: Values for SRMS (×100), CCOR (×100), and SRAN, for methods TB-14 and TD-14.

$D_1(15)$					
Line	Template	SRMS	CCOR	SRAN	(m,M)
11	$D_1(13)$	25	24	1.8	$(-15, 19)$
	$D_1(14)$	17	11	0.7	$(-8, 6)$
	$D_1(23)$	18	13	0.9	$(-7, 10)$
	$D_1(24)$	28	24	1.4	$(-18, 8)$
27	$D_1(13)$	47	103	3.1	$(-32, 20)$
	$D_1(14)$	44	109	3.7	$(-34, 28)$
	$D_1(23)$	30	47	2.1	$(-15, 20)$
	$D_1(24)$	47	112	4.3	$(-30, 43)$
43	$D_1(13)$	25	43	1.6	$(-12, 14)$
	$D_1(14)$	21	30	1.2	$(-10, 9)$
	$D_1(23)$	23	35	1.4	$(-11, 11)$
	$D_1(24)$	26	39	1.6	$(-15, 10)$
59	$D_1(13)$	30	58	2.7	$(-20, 19)$
	$D_1(14)$	30	59	2.7	$(-25, 15)$
	$D_1(23)$	26	47	2.1	$(-16, 15)$
	$D_1(24)$	32	64	2.7	$(-21, 18)$
75	$D_1(13)$	33	45	1.5	$(-11, 16)$
	$D_1(14)$	24	25	1.3	$(-12, 12)$
	$D_1(23)$	24	25	1.3	$(-12, 12)$
	$D_1(24)$	34	45	1.8	$(-20, 14)$
91	$D_1(13)$	44	131	2.8	$(-24, 23)$
	$D_1(14)$	43	126	2.8	$(-17, 31)$
	$D_1(23)$	49	151	3.4	$(-27, 30)$
	$D_1(24)$	50	170	3.5	$(-28, 32)$
$D_2(15)$					
Line	Template	SRMS	CCOR	SRAN	(m,M)
07	$D_2(14)$	14	6	0.5	$(-9, 10)$
	$D_2(25)$	10	3	0.4	$(-8, 6)$
23	$D_2(14)$	22	21	1.0	$(-14, 17)$
	$D_2(25)$	25	26	1.9	$(-24, 32)$
39	$D_2(14)$	31	50	1.5	$(-20, 22)$
	$D_2(25)$	18	17	0.8	$(-10, 13)$
45	$D_2(14)$	27	28	1.9	$(-26, 22)$
	$D_2(25)$	15	9	0.9	$(-12, 12)$
61	$D_2(14)$	13	13	1.3	$(-10, 16)$
	$D_2(25)$	15	17	1.3	$(-16, 11)$
77	$D_2(14)$	21	29	1.2	$(-12, 17)$
	$D_2(25)$	15	12	0.9	$(-9, 14)$
93	$D_2(14)$	21	43	2.0	$(-22, 19)$
	$D_2(25)$	14	18	0.9	$(-10, 9)$

Appendix D

Fit of different models to Haining's data

The 11 by 11 data set used by Haining *et al.* (1989) has been kindly provided by Bob Haining, from the Geography Department. The data are a subset of reflectance values from an aerial survey monitoring marine pollution levels off the south coast of England, and are given in Table D.1 below.

Table D.1: Original data used by Haining *et al* (1989).

24	4	0	0	23	46	65	43	34	38	2
32	34	6	35	39	40	30	58	52	49	40
32	35	36	37	38	47	34	35	31	51	38
38	39	43	41	55	42	38	34	37	41	36
50	62	46	39	55	37	40	32	28	20	36
45	50	43	33	24	38	44	42	39	23	36
40	36	16	18	31	37	52	30	24	15	18
37	14	10	21	26	30	35	41	19	23	12
10	12	5	12	17	18	20	24	23	7	7
50	62	19	6	14	17	17	5	6	4	6
46	35	0	4	5	5	6	0	0	0	3

Table D.2 gives the mean, median, and variance of the data in each line and each column of the original data, where NL denotes the line number (NL=1 for

the first line at the top), and NC denotes the column number (NC=1 for the first column at the left), in Table D.1.

Table D.2: Line and column means, medians, and variances, for the data in Table E.1.

Line				Column			
NL	Mean	Median	Variance	NC	Mean	Median	Variance
1	25.3	24.0	484.00	1	36.7	38.0	144.00
2	37.7	39.0	187.42	2	34.8	35.0	363.28
3	37.6	36.0	37.21	3	20.4	16.0	332.70
4	40.4	38.0	30.80	4	22.4	21.0	234.40
5	40.4	39.0	147.62	5	29.7	26.0	254.72
6	37.9	39.0	72.08	6	32.5	37.0	182.25
7	28.8	30.0	139.95	7	34.6	35.0	271.92
8	24.4	23.0	109.20	8	31.3	34.0	280.56
9	14.1	12.0	44.49	9	26.6	28.0	219.34
10	18.7	14.0	377.14	10	24.6	23.0	319.69
11	9.5	4.0	246.80	11	21.3	18.0	252.17

From observation of the line, and column means in Table D.2, a trend in both directions (along the lines and along the columns) can be deduced. Some attempts to remove the non-stationarity of the data was to apply the exploratory data analysis technique known as *median polishing*, proposed by Tukey (1977). The algorithm successively sweeps medians out of rows (and/or columns), leaving behind the table of residuals (Cressie, 1983).

Another approach was to apply *between column differencing* to the original data, which consisted of subtracting data in adjacent columns, so that $d(i,j)$, the value at site (i,j), obtained from differencing, is simply $u(i,j+1) - u(i,j)$, $i = 1,\ldots,11$, $j = 1,\ldots,10$, where $u(i,j)$ is the original value at site (i,j), $i,j = 1,\ldots,11$. A similar approach, consisting of *between line differencing*, was also applied to the original data.

Different spatial models have been fitted to the following sets of data:

1. original;

2. residuals obtained from line median polishing;

3. residuals obtained from column median polishing;

4. residuals obtained from line differencing;

5. residuals obtained from column differencing.

The following models have been fitted:

1. a 1p-CAR(1) as defined in §5.5.1;

2. a 2p-CAR(1) as defined in §5.5.2;

3. a 3p-CAR(2) as defined in §5.5.3, but using α for the horizontal neighbours, β for the vertical neighbours, and γ for the diagonal neighbours;

4. a 1p-SAR(1) as defined in §5.5.4;

5. a 2p-SAR(1) as defined in §5.5.4;

6. a 3p-SAR(2) as defined in §5.5.5, but using α, β, and γ for the adjacent horizontal, vertical and diagonal neighbours, respectively.

Table D.3 (a) to () gives the sample autocorrelations to lags (g, h), $g = -4, \ldots, 4$, $h = 0, \ldots, 4$, for the data in each of the data sets.

Table D.3: Sample autocorrelations, $r_{g,h}$, $g = -4, \ldots, 4$, $h = 0, \ldots, 4$, for the data in the different data sets.

Original Data					
	h				
g	0	1	2	3	4
−4	−0.144	−0.123	−0.114	−0.057	0.083
−3	0.018	0.024	0.009	0.168	0.265
−2	0.247	0.240	0.242	0.301	0.302
−1	0.519	0.502	0.380	0.278	0.289
0	1.000	0.719	0.467	0.299	0.247
1	0.519	0.444	0.317	0.229	0.213
2	0.247	0.256	0.167	0.158	0.207
3	0.018	−0.018	−0.140	−0.106	−0.106
4	−0.144	−0.207	−0.331	−0.347	−0.346
Column Median Polishing					
	h				
g	0	1	2	3	4
−4	−0.200	−0.164	−0.054	−0.017	0.044
−3	−0.050	−0.078	0.064	0.164	0.227
−2	0.223	0.234	0.279	0.308	0.288
−1	0.499	0.516	0.443	0.311	0.263
0	1.000	0.719	0.545	0.373	0.276
1	0.499	0.445	0.369	0.269	0.264
2	0.223	0.237	0.231	0.236	0.286
3	−0.050	−0.040	−0.065	−0.029	−0.015
4	−0.200	−0.235	−0.246	−0.253	−0.234
Column Differencing					
	h				
g	0	1	2	3	4
−4	0.044	0.136	−0.252	−0.042	0.028
−3	0.136	−0.107	0.045	0.036	0.053
−2	−0.023	0.082	0.044	0.041	−0.091
−1	−0.007	0.219	0.201	−0.011	−0.154
0	1.000	−0.092	−0.096	−0.067	0.089
1	−0.007	0.097	−0.077	0.096	−0.012
2	−0.023	0.094	0.048	0.084	0.154
3	0.136	−0.031	0.211	−0.014	−0.056
4	0.044	0.039	−0.026	0.182	−0.145

Line Median Polishing					
	h				
g	0	1	2	3	4
−4	−0.007	−0.055	−0.192	−0.199	−0.014
−3	−0.021	−0.176	−0.201	−0.023	0.127
−2	0.012	−0.043	−0.089	−0.004	0.019
−1	0.380	0.296	0.015	−0.187	−0.184
0	1.000	0.478	0.030	−0.227	−0.295
1	0.380	0.225	0.017	−0.090	−0.089
2	0.012	0.027	−0.068	−0.082	−0.036
3	−0.021	−0.025	−0.109	−0.029	−0.040
4	−0.007	−0.041	−0.063	−0.045	0.013
Line Differencing					
	h				
g	0	1	2	3	4
−4	−0.077	0.124	0.188	0.051	0.197
−3	0.081	0.139	−0.044	0.089	0.239
−2	0.110	0.177	0.071	0.186	−0.054
−1	0.135	0.243	−0.007	−0.011	0.053
0	1.000	0.364	0.057	0.120	0.100
1	0.135	−0.086	0.121	0.193	0.068
2	0.110	0.083	−0.025	0.062	0.021
3	0.081	−0.141	−0.201	−0.046	−0.082
4	−0.077	−0.186	0.051	−0.204	−0.388

From Table D.3 it can be seen that the original data are highly spatially correlated, and shows some form of anisotropy, characterized by larger values of the sample autocorrelation in the east-west direction, than in the north-south direction. For instance, $r_{0,1} = 0.719$ and $r_{1,0} = 0.519$; $r_{0,2} = 0.467$ and $r_{2,0} = 0.247$; $r_{1,1} = 0.444$ and $r_{-1,1} = 0.502$. The sample autocorrelations for the residuals obtained from column median polishing, given in Table D.3, also shows high spatial correlation, and the same form of anisotropy as the data in the original data set. For example, $r_{0,1} = 0.719$ and $r_{1,0} = 0.499$; $r_{0,2} = 0.545$ and $r_{2,0} = 0.2237$; $r_{1,1} = 0.445$ and $r_{-1,1} = 0.499$. The sample autocorrelations for the residuals obtained from line median polishing, from line differencing, and from column differencing, in Table D.3, indicate that the data are not as highly spatially correlated, and the negative sample autocorrelations for the residuals from column differencing suggest over differencing.

The results obtained from the several spatial models are given in Table D.4, D.5, D.6, D.7 and D.8, for the original data, and for the residuals obtained from line median polishing, column median polishing, line differencing, and column differencing, respectively. The results include the maximum likelihood estimates of the model parameters, and the value of the function, L.

Table D.4: Estimates of the parameters of the spatial models applied to the original data, and the function value.

Model	$\hat{\alpha}$	$\hat{\beta}$	$\hat{\gamma}$	L
$1p - CAR(1)$	0.2572	--	--	1172.76
$2p - CAR(1)$	0.3853	0.1275	--	1167.57
$3p - CAR(2)$	0.3930	0.1219	−0.0014	1167.56
$1p - SAR(1)$	0.2230	--	--	1166.79
$2p - SAR(1)$	0.2878	0.1493	--	1162.46
$3p - SAR(2)$	0.2636	0.1048	0.0448	1160.62

From Tables D.4 and D.5 it can be noted that maximum likelihood estimates of the model parameters, for the original data, and the residuals obtained from column median polishing are close to the boundary (upper limit) (suggesting a possible trend in the data). That is not the case, however, for the residuals

Table D.5: Estimates of the parameters of the spatial models applied to the residuals obtained from line median polishing, and the function value.

Model	$\hat{\alpha}$	$\hat{\beta}$	$\hat{\gamma}$	L
$1p - CAR(1)$	0.2451	--	--	1154.93
$2p - CAR(1)$	0.3017	0.1881	--	1153.95
$3p - CAR(2)$	0.3091	0.1935	−0.0078	1153.80
$1p - SAR(1)$	0.1868	--	--	1149.45
$2p - SAR(1)$	0.2197	0.1534	--	1148.52
$3p - SAR(2)$	0.1987	0.1219	0.0443	1147.01

Table D.6: Estimates of the parameters of the spatial models applied to the residuals obtained from column median polishing, and the function value.

Model	$\hat{\alpha}$	$\hat{\beta}$	$\hat{\gamma}$	L
$1p - CAR(1)$	0.2572	--	--	1163.40
$2p - CAR(1)$	0.3928	0.1200	--	1157.35
$3p - CAR(2)$	0.3937	0.1215	−0.0013	1157.34
$1p - SAR(1)$	0.2148	--	--	1163.22
$2p - SAR(1)$	0.2770	0.1419	--	1159.13
$3p - SAR(2)$	0.2435	0.0858	0.0612	1155.53

obtained from line median polishing, and from line, and column, differencing. The similar values of the maximum likelihood function, obtained for all methods indicate only a slight gain in the application of higher-order models.

Results for the simultaneous autoregressive models have also been obtained when assuming that the data is a realization of a process occurring on a torus lattice (a lattice formed conceptually from a rectangular lattice by joining up its opposite edges so that rows become row circles and the columns, column circles). These results are presented in Tables D.9.

The larger values of the maximum likelihood function, in Table D.9, compared to the values in Tables D.4, D.5, D.6 and D.7, for the SAR processes, indicate a poorer fit from the models assumed to occur on a torus lattice, than on a

Table D.7: Estimates of the parameters of the spatial models applied to the residuals obtained from line differencing, and the function value.

Model	$\hat{\alpha}$	$\hat{\beta}$	$\hat{\gamma}$	L
$1p - CAR(1)$	0.1270	--	--	1198.13
$2p - CAR(1)$	0.3459	−0.0795	--	1180.71
$3p - CAR(2)$	0.3307	−0.1063	0.0424	1078.22
$1p - SAR(1)$	0.0638	--	--	1103.97
$2p - SAR(1)$	0.2149	−0.0891	--	1077.98
$3p - SAR(2)$	0.2279	−0.1445	0.0761	1070.60

Table D.8: Estimates of the parameters of the spatial models applied to the residuals obtained from column differencing, and the function value.

Model	$\hat{\alpha}$	$\hat{\beta}$	$\hat{\gamma}$	L
$1p - CAR(1)$	0.0327	--	--	1070.22
$2p - CAR(1)$	−0.1085	0.1736	--	1065.38
$3p - CAR(2)$	−0.1497	0.1918	0.0923	1062.29
$1p - SAR(1)$	0.0158	--	--	1070.22
$2p - SAR(1)$	−0.0729	0.1050	--	1064.45
$3p - SAR(2)$	−0.1084	0.1301	0.0794	1060.37

rectangular lattice.

The models applied to the original data, and to residuals obtained from line, and column median polishing, and from line, and column differencing, were assumed to have constant mean. In order to account for non-stationarity in the mean, a model using a second-order trend surface with CAR errors, and SAR errors, was also fitted to the original data. This model has also been fitted to the data obtained from the replacement of the values in line 5, by the values obtained from linear interpolation (average of the corresponding values in the lines 4 and 6); and to the data obtained by replacing the 3 by 3 cluster in the centre of the lattice, by the average of the observed neighbouring values. The data is shown

Table D.9: Estimates of the parameters of the simultaneous autoregressive models applied to the original data, and to the residuals obtained from line median polishing, column median polishing, and from line differencing: torus assumption.

Model	$\hat{\alpha}$	$\hat{\beta}$	$\hat{\gamma}$	L
Original Data				
$1p - SAR(1)$	0.2084	--	--	1173.26
$2p - SAR(1)$	0.2741	0.1416	--	1167.94
$3p - SAR(2)$	0.2717	0.1368	0.0046	1167.91
Residuals from line median polishing				
$1p - SAR(1)$	0.1692	--	--	1158.15
$2p - SAR(1)$	0.2034	0.1363	--	1157.00
$3p - SAR(2)$	0.2037	0.1364	0.0000	1157.00
Residuals from column median polishing				
$1p - SAR(1)$	0.2654	--	--	1174.72
$2p - SAR(1)$	0.3216	0.0774	--	1168.95
$3p - SAR(2)$	0.2556	0.1024	0.0207	1168.44
Residuals from line differencing				
$1p - SAR(1)$	0.0837	--	--	1095.12
$2p - SAR(1)$	0.1460	0.0258	--	1091.84
$3p - SAR(2)$	0.1451	0.0191	0.0109	1091.74

below, where the values in bold are those that have been replaced.

24	4	0	0	23	46	65	43	34	38	2
32	34	6	35	39	40	30	58	52	49	40
32	35	36	37	38	47	34	35	31	51	38
38	39	43	41	55	42	38	34	37	41	36
50	62	46	39	**47**	**42**	**35**	32	28	20	36
45	50	43	33	**33**	**36.7**	**42**	42	39	23	36
40	36	16	18	**22**	**30**	**32.5**	30	24	15	18
37	14	10	21	26	30	35	41	19	23	12
10	12	5	12	17	18	20	24	23	7	7
50	62	19	6	14	17	17	5	6	4	6
46	35	0	4	5	5	6	0	0	0	3

Table D.10: Results from the fit of a second-order trend surface models with CAR, and SAR errors of different orders: original data set.

Model	$\hat{\alpha}$	$\hat{\beta}$	$\hat{\gamma}$	L
$1p - CAR(1)$	0.2453	--	--	1150.61
$2p - CAR(1)$	0.3594	0.1373	--	1146.60
$3p - CAR(2)$	0.3560	0.1265	0.0077	1146.58
$1p - SAR(1)$	0.1727	--	--	1148.47
$2p - SAR(1)$	0.2373	0.1108	--	1145.02
$3p - SAR(2)$	0.2266	0.1265	0.0440	1143.63

Table D.11: Results from the fit of a second-order trend surface models with CAR, and SAR errors of different orders: original data set with line 5 altered.

Model	$\hat{\alpha}$	$\hat{\beta}$	$\hat{\gamma}$	L
$1p - CAR(1)$	0.2488	--	--	1146.13
$2p - CAR(1)$	0.3367	0.1644	--	1143.84
$3p - CAR(2)$	0.3379	0.1709	−0.0046	1143.76
$1p - SAR(1)$	0.1852	--	--	1142.72
$2p - SAR(1)$	0.2298	0.1424	--	1141.03
$3p - SAR(2)$	0.2209	0.1265	0.0223	1140.66

The estimates of the model parameters, in Tables D.10, D.11, and D.12, seems to suggest that the trend in the data could not be completely accounted for. Moreover, the similar values of the maximum likelihood function, obtained for the methods, indicate that only a slight gain is achieved by using higher-order models.

Table D.12: Results from the fit of a second-order trend surface models with CAR, and SAR errors of different orders: original data set with the centre values altered.

Model	$\hat{\alpha}$	$\hat{\beta}$	$\hat{\gamma}$	L
$1p - CAR(1)$	0.2470	$--$	$--$	1144.17
$2p - CAR(1)$	0.3800	0.1206	$--$	1138.33
$3p - CAR(2)$	0.3811	0.1275	-0.0046	1138.31
$1p - SAR(1)$	0.1792	$--$	$--$	1141.24
$2p - SAR(1)$	0.2552	0.1069	$--$	1136.23
$3p - SAR(2)$	0.2485	0.0818	0.0303	1135.58

Appendix E

Figures for Chapter 6

Figure E.1: Plot of the data in areas: (a) $A_1(13)$ and $A_1(23)$; (b) $A_1(13)$ and $A_1(33)$.

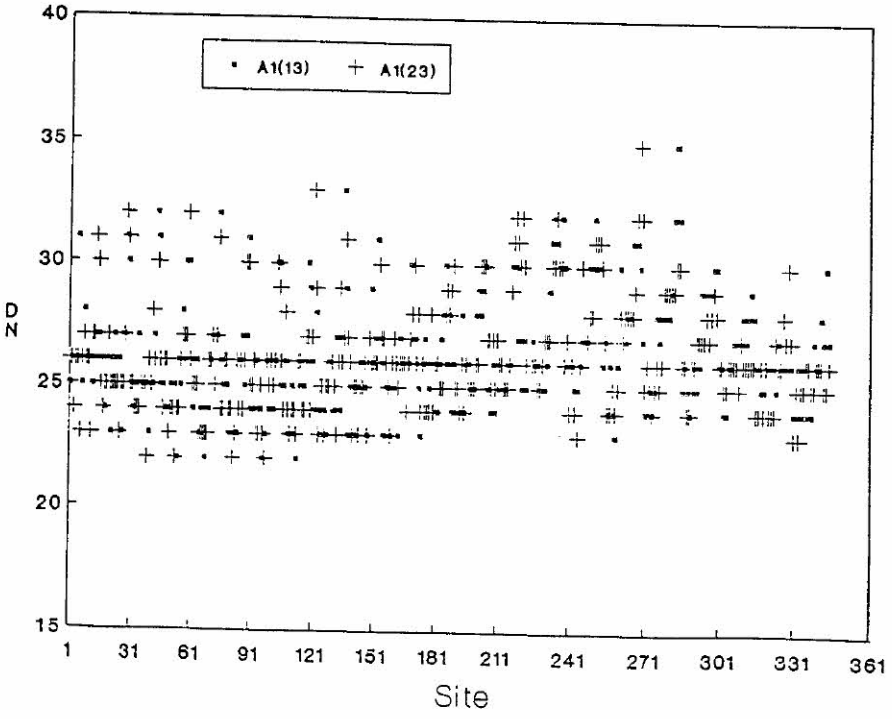

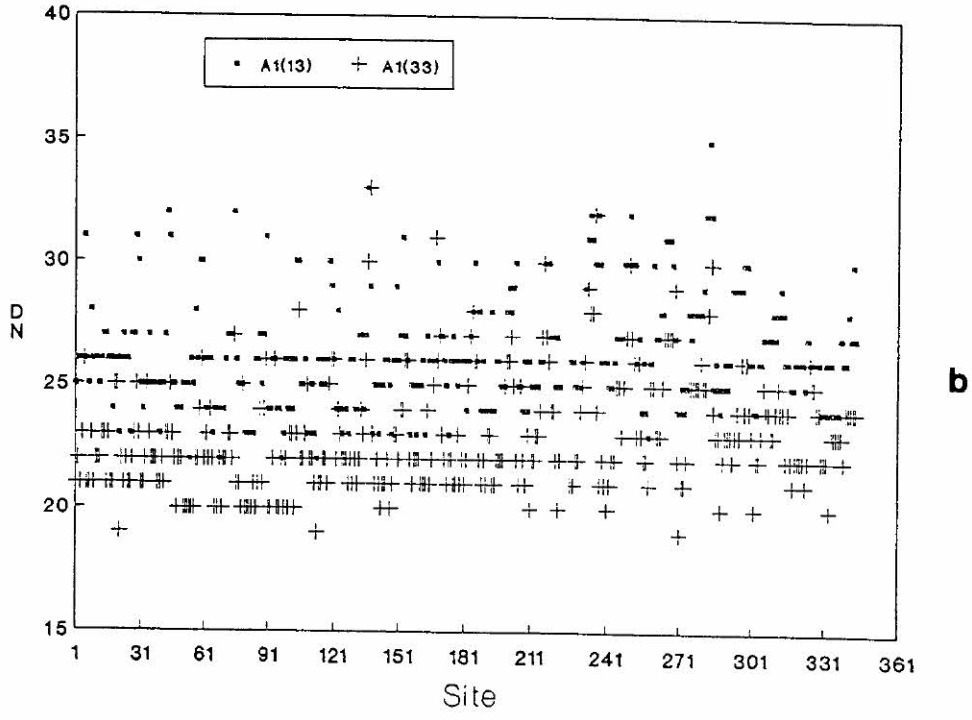

Figure E.2: Plot of the data in areas (a) $A_1(14)$ and $A_1(24)$; (b) $A_1(14)$ and $A_1(34)$.

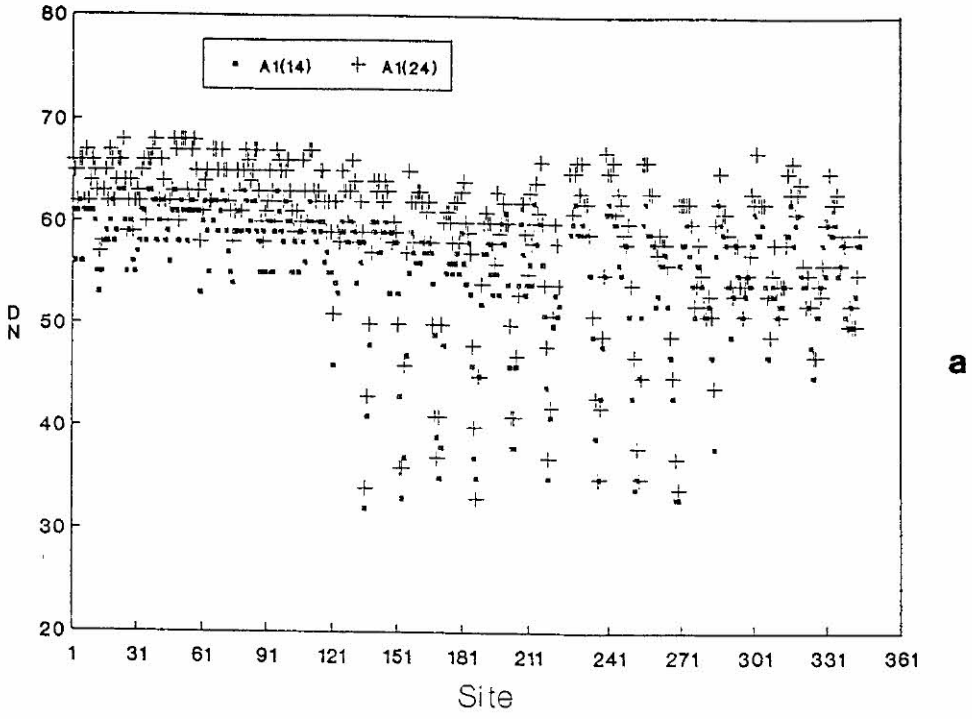

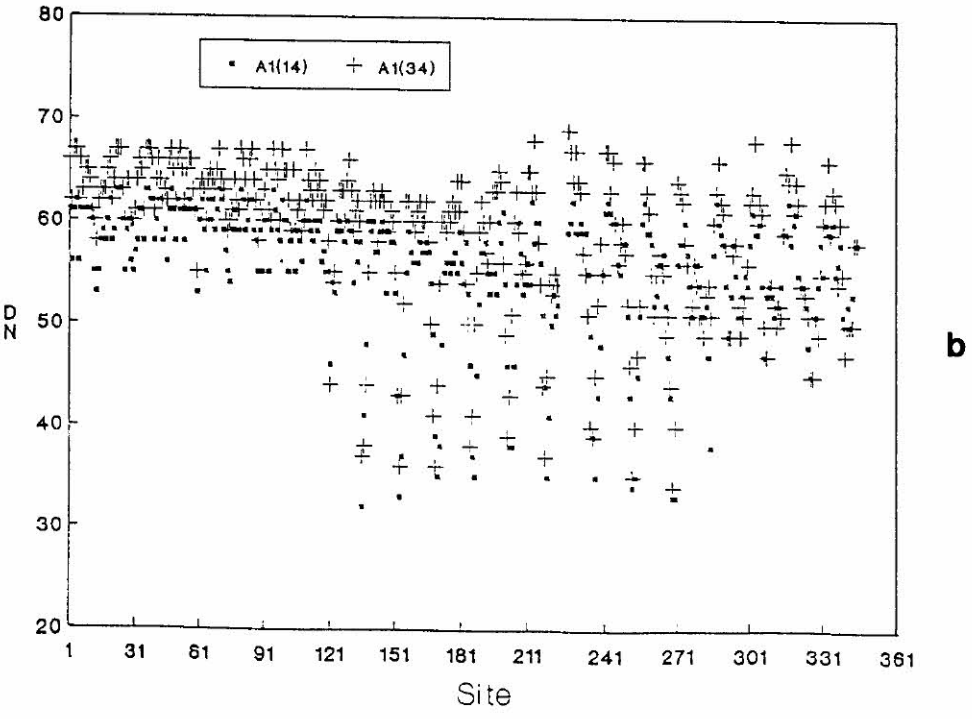

Figure E.3: Plot of the data in areas (a) $A_1(15)$ and $A_1(25)$; (b) $A_1(15)$ and $A_1(35)$.

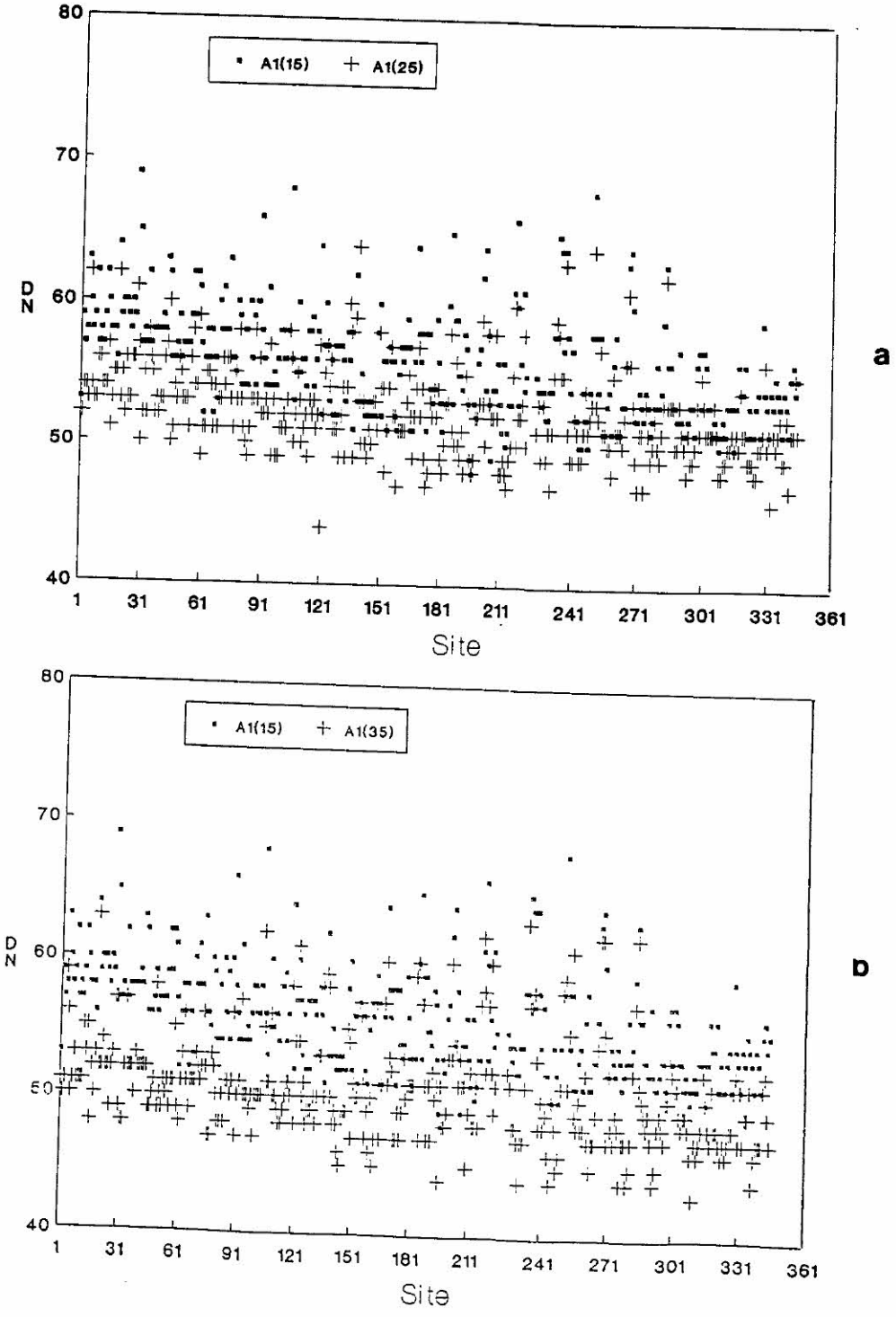

Figure E.4: Plot of the data in areas (a) $A_1(25)$ and $A_1(15)$; (b) $A_1(25)$ and $A_1(35)$.

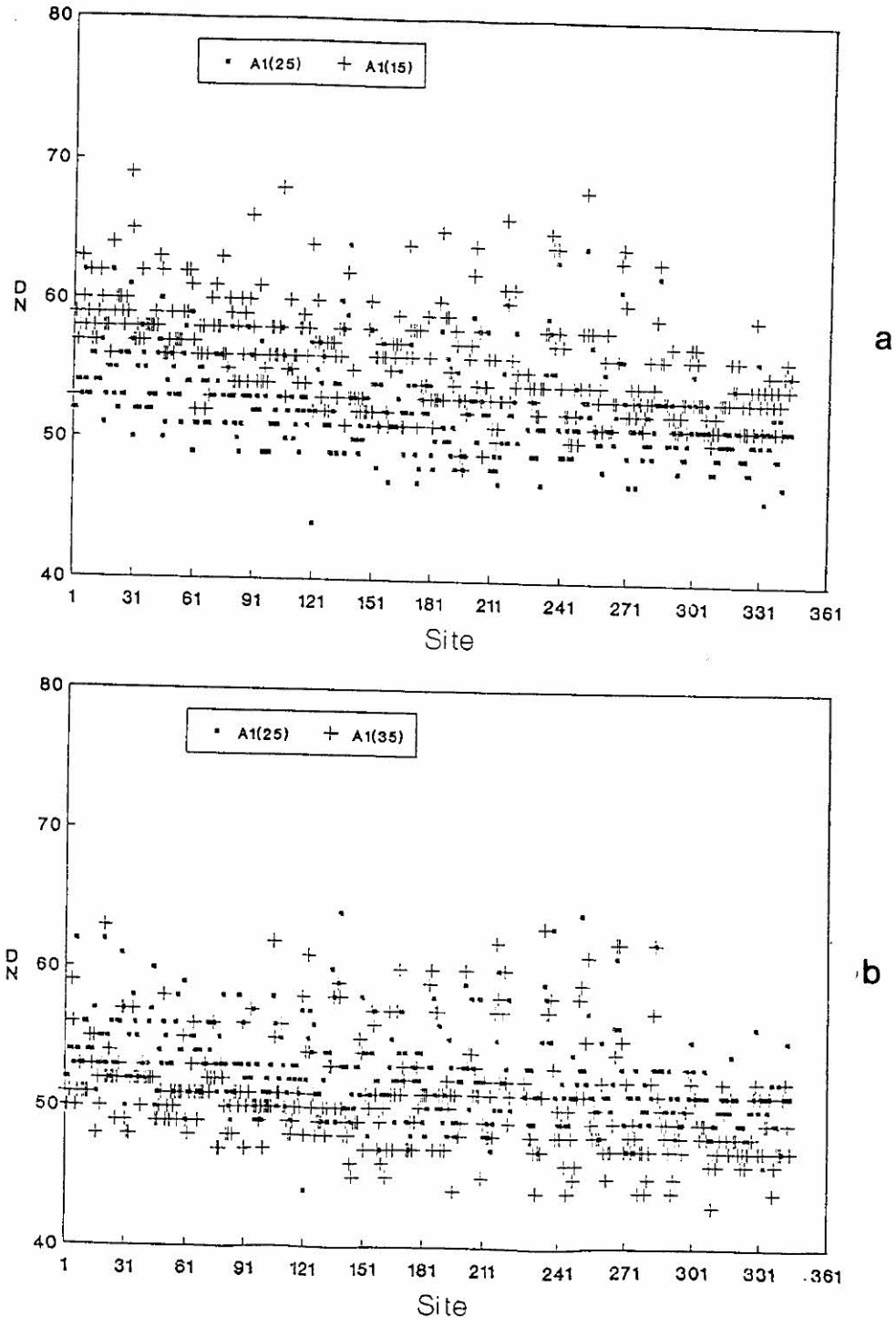

Figure E.5: Plot of the data in areas (a) $A_2(14)$ and $A_2(24)$; (b) $A_2(14)$ and $A_2(34)$.

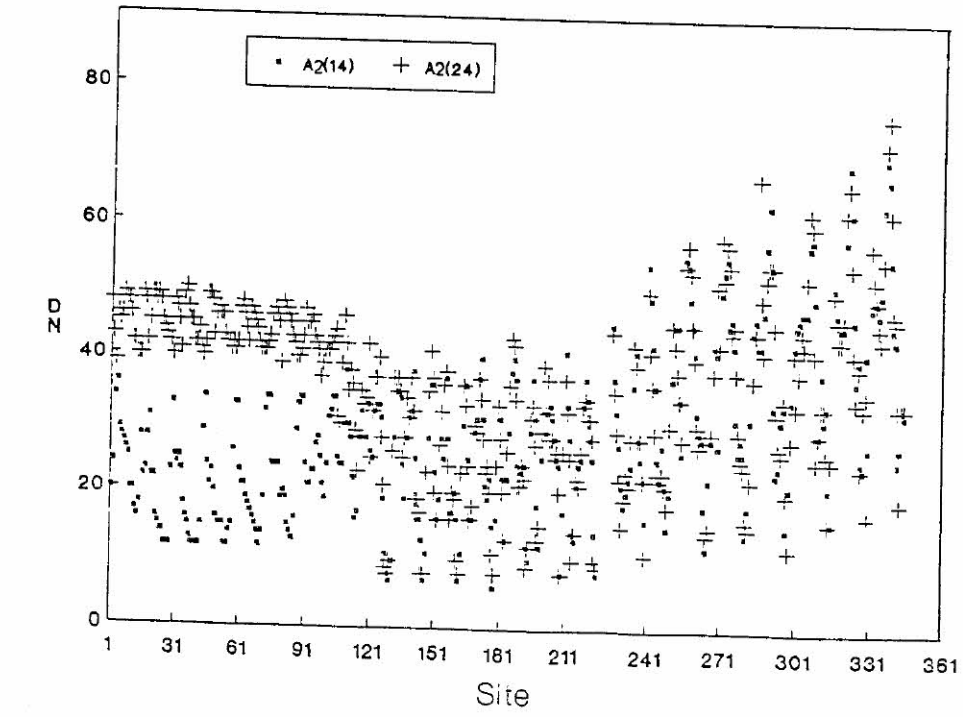

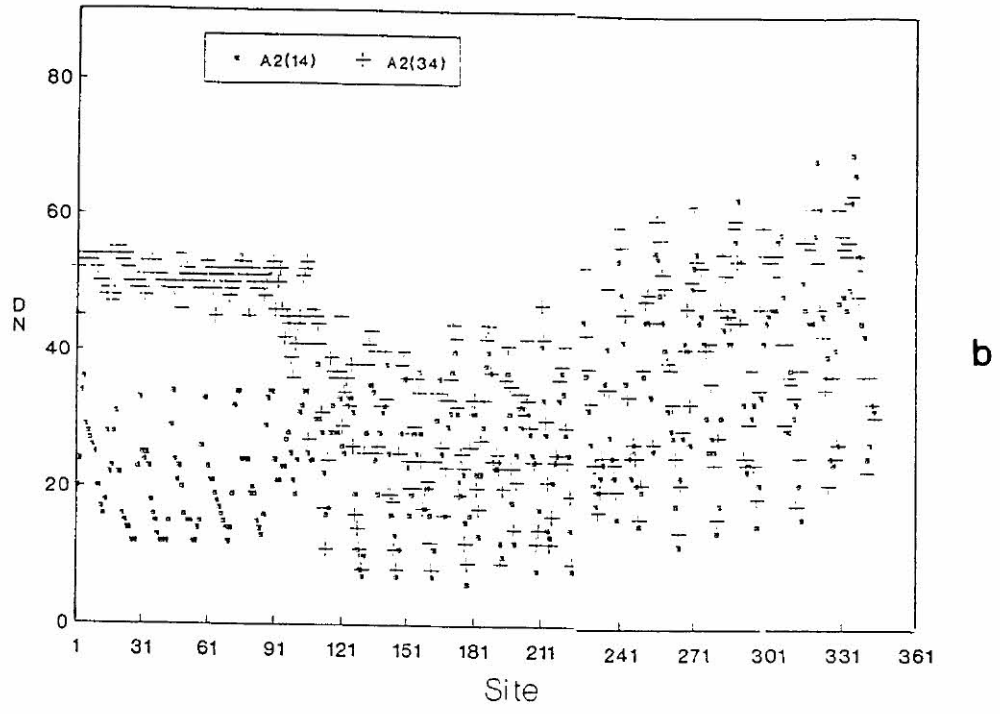

Figure E.6: Plot of the data in areas (a) $A_2(15)$ and $A_2(25)$; (b) $A_2(15)$ and $A_2(35)$.

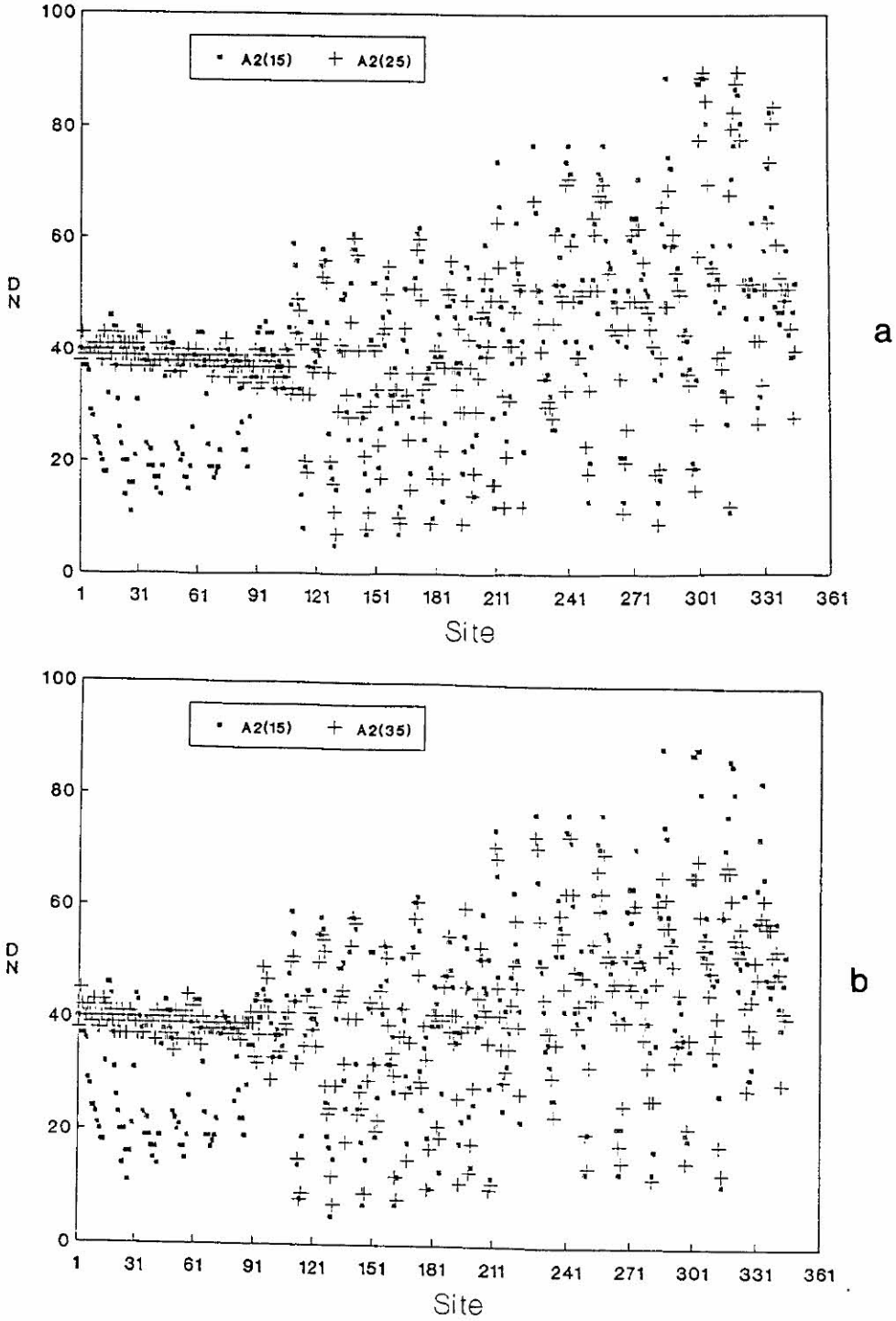

Figure E.7: Plot of the data in areas (a) $A_3(15)$ and $A_3(25)$.

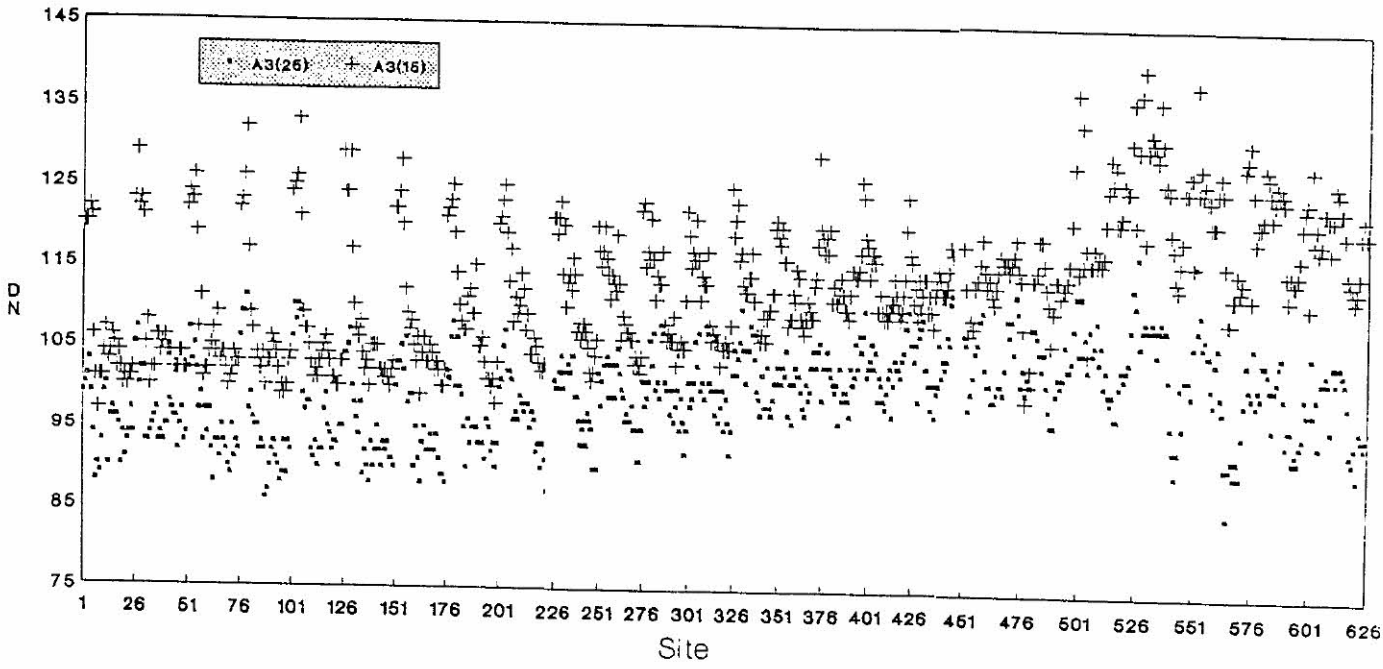

Figure E.8: Plot of the data in areas (a) $A_3(35)$ and $A_3(45)$.

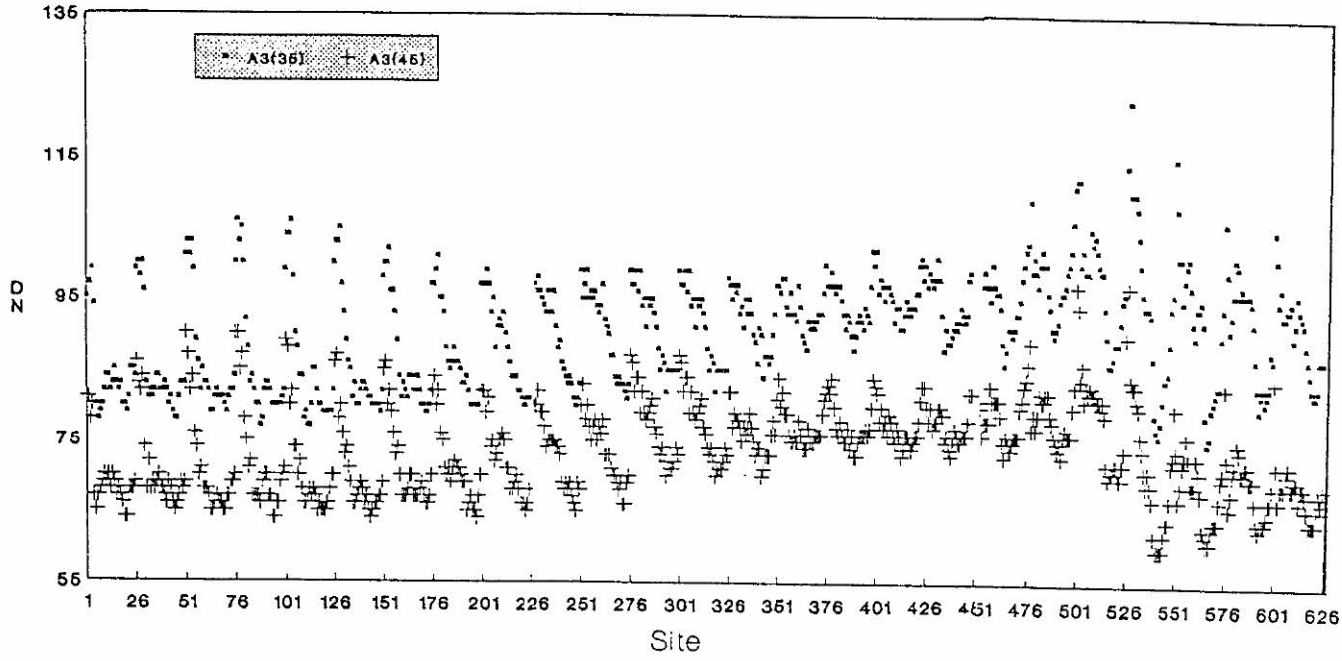

Figure E.9: Plot of the data in areas (a) $A_4(54)$ and $A_4(64)$.

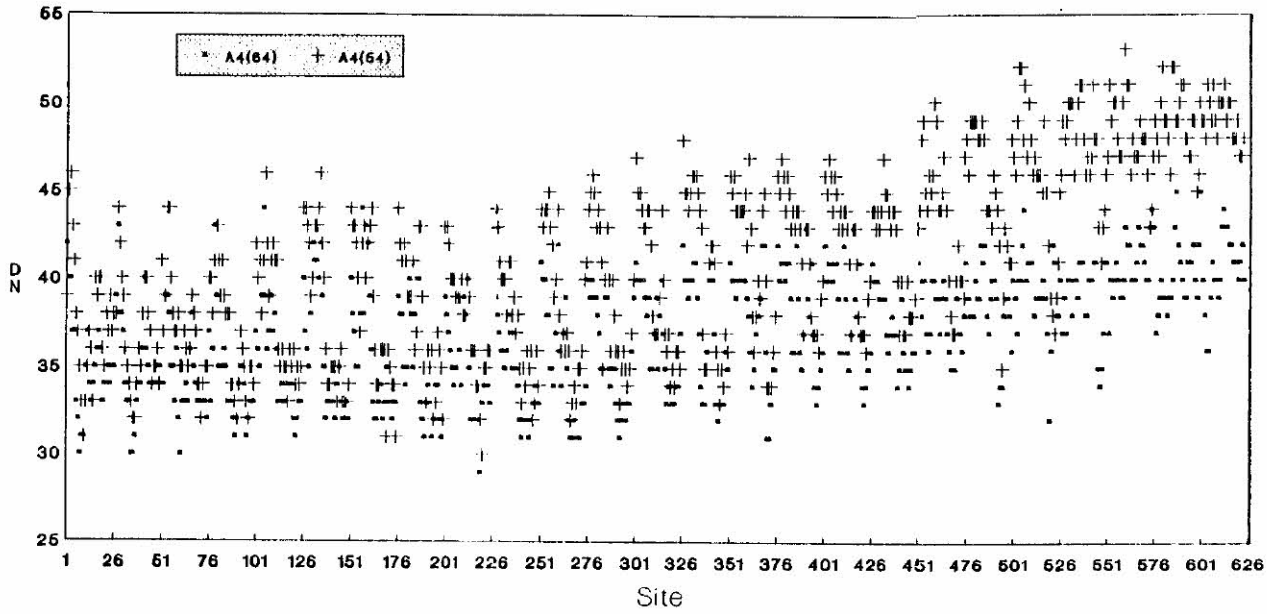

Bibliography

[1] Ali, M. M. (1979). Analysis of stationary spatial-temporal processes: estimation and prediction. *Biometrika*, **66**, 513-518.

[2] Bernstein, R., Colby, C., Murphey S. W. and Snyder, J. P. (1983). Image geometry and rectification. In Manual of Remote Sensing, Vol I, 2^{nd} ed., R. N. Colwell (Ed.). American Society of Photogrammetry, Falls Church, Va., 873-922.

[3] Bernstein, R., Lotspiech, J. B., Myers H. J., Kolsky, H. G. and Lees, R. D. (1984). Analysis and processing of LANDSAT-4 sensor data using advanced image processing techniques and technologies. *IEEE Transactions on Geoscience and Remote Sensing*, **22**, 192-221.

[4] Besag, J. (1974). Spatial interaction and the statistical analysis of lattice systems. *Journal of the Royal Statistics Society*, **B 36**, 192-236.

[5] Besag, J. (1975). Statistical analysis of non-lattice data. *The Statistician*, **24**, 179-195.

[6] Chanda, B. and Majumder, D. D. (1991). An iterative algorithm for removing the effect of thin cloud from Landsat imagery. *Mathematical Geology*, **23**, 853-860.

[7] Cliff, A. D. and Ord, J. K. (1975). Space-time modelling with an application to regional forecasting. *Transactions of the Institute of British Geography*, **64**, 119-128.

[8] Combettes, P. L. and Trussel, H. J. (1989). Methods for digital restoration of signals degraded by a stochastic impulse response. *IEEE Transactions on Acoustics, Speech, and Signal Processing*, **37**, 393-401.

[9] Cressie, N. (1984). Towards resistant geostatistics. In *Geostatistics for Natural Resources Characterization.* Eds. G. Verly, M. David, A. G. Journel and A. Marechal, Reidel, Dordrecht, 21-44.

[10] Curran, P. J. (1985). *Principles of Remote Sensing.* Longman Scientific & Technical, London.

[11] Frieden, B. R. (1980). Statistical models for the image restoration problem. *Computer Graphics and Image Processing*, **12**, 40-59.

[12] Fusco, L. and Trevese, D. (1985). On the reconstruction of lost data of more than one band. *International Journal of Remote Sensing*, **6**, 1535-1544.

[13] Gleeson, A. C. and McGilchrist, C. A. (1980). Bilateral processes on a rectangular lattice. *Australian Journal of Statistics*, **22**, 197-206.

[14] Graybill, F. A. (1969). *Introduction to Matrices with Applications in Statistics.*. Wadsworth Publishing, Belmont, California.

[15] Guindon, B. (1984). Algorithms for the estimation of failed detector data. *Proceedings, Machine Processing of Remotely Sensed Data Symposium*, Laboratory for the Applications of Remote Sensing, West Lafayette, Indiana, 39-46.

[16] Gurney, C. M. (1982). The use of contextual information to detect cumulus clouds and cloud shadows in Landsat data. *International Journal of Remote Sensing*, **3**, 51-62.

[17] Haining, R., Griffith, D. and Bennett. R. (1989). Maximum likelihood estimation with missing spatial data and with an application to remotely sensed data. *Communications in Statistics -Theory and Methods*, **18**, 1875-1911.

[18] Haralick, R. M. and Fu, King-Sun (1983). Pattern recognition and classification. In Manual of Remote Sensing, Vol I, 2^{nd} ed., R. N. Colwell (Ed.). American Society of Photogrammetry, Falls Church, Va., 793-804.

[19] Harris, R. (1980). Spectral and spatial image processing for remote sensing. *International Journal of Remote Sensing*, **1**, 361-376.

[20] Hord, R. M. (1982). *Digital image processing of remotely sensed data.* Academic Press, New York.

[21] Horn, B. K. P. and Woodham, R. J. (1979). Destriping Landsat MSS images by histogram modification. *Computer Graphics and Image Processing*, **10**, 69-83.

[22] Jewell, N. (1989). An evaluation of multi-data SPOT data for agriculture and land use mapping in the United Kingdom. *International Journal of Remote Sensing*, **10**, 939-951.

[23] Kiiveri, H. T. and Campbell, N. A. (1989). Covariance models for lattice data. *Australian Journal of Statistics*, **31**, 62-77.

[24] Krug, T. and Martin, R. J. (1990). Efficient methods for coping with missing information in remotely sensed data. Research Report No. 371/90. Dept. of Probability and Statistics, University of Sheffield.

[25] Krug, T. and Martin, R. J. (1991a). Efficient methods for coping with missing information in remotely sensed data. Preprint.

[26] Krug, T. and Martin, R. J. (1991b). Information loss on the mean for spatial processes when some values are missing. *Communications in Statistics -Theory and Methods*, **20**, 2169-2194.

[27] Künsch, H. R. (1987). Intrinsic autoregressions and related models on the two-dimensional lattice. *Biometrika*, **74**, 517-524.

[28] Labovitz, M. L., Toll, D. L. and Kennard, R. E. (1982). Preliminary evidence for the influence of physiography and scale upon the autocorrelation function of remotely sensed data. *International Journal of Remote Sensing*, **3**, 13-30.

[29] Legg, C. A. (1988). Operational remote sensing in the United Kingdom: problems of image acquisition. *Proceedings of IGARSS'88 Symposium*, Edinburgh, U.K., 1457-1461.

[30] Legg, C. A. (1991) A review of Landsat MSS image acquisition over the United Kingdom, 1976-1988, and the implications for operational remote sensing. *International Journal of Remote Sensing*, **12**, 93-106.

[31] Lillesand, T. M. and Kiefer, R. W. (1987). *Remote Sensing and Image Interpretation.* John Wiley & Sons, New York.

[32] Liu, Z. K. and Hunt, B. R. (1984). A new approach to remove cloud cover from satellite imagery. *Computer Vision, Graphics, and Image Processing,* **25**, 252-256.

[33] Liu, Z. and Caelli, T. (1988). A sequential adaptative recursive filter for image restoration. *Computer Vision, Graphics, and Image Processing,* **44**, 332-349.

[34] Mardia, K. V. and Marshall, R. J. (1984). Maximum likelihood estimation of models for residual covariance in spatial regression. *Biometrika,* **71**, 135-146.

[35] Mardia, K. V. (1990). Maximum likelihood estimation for spatial models. In *Spatial Statistics: Past, Present and Future.* Ed. D. A. Griffith, 203-252. Inst. Math. Geog.: Ann Arbor.

[36] Martin, R. J. (1979). A subclass of lattice processes applied to a problem in planar sampling. *Biometrika,* **66**, 209-217.

[37] Martin, R. J. (1984). Exact maximum likelihood for incomplete data from a correlated Gaussian process. *Communications in Statistics -Theory and Methods,* **13**, 1275-1288.

[38] Martin, R. J. (1989). Information loss due to incomplete data from a spatial Gaussian one-oarameter first-order conditional process. *Communications in Statistics -Theory and Methods,* **18**, 4631-4645.

[39] Martin, R. J. (1990a). The use of time-series models and methods in the analysis of agricultural field trials. *Communications in Statistics -Theory and Methods,* **19**, 55-81.

[40] Martin, R. J. (1990b). The role of spatial statistical processes in geographic modelling.In *Spatial Statistics: Past, Present and Future.* Ed. D. A. Griffith, 109-128. Inst. Math. Geog.: Ann Arbor.

[41] Mather, P. M. (1987). *Computer Processing of Remotely-Sensed Images – an Introduction.* John Wiley & Sons, Chichester.

[54] Thomas, I. L. (1987). *Classification of remotely sensed images.* IOP Publishing Limited, Bristol, England.

[55] Tukey, J. (1977). *Exploratory Data Analysis.* Addison-Wesley, Reading, Massachusetts.

[56] Ulaby, F. T., Moore, R. K. and Fung, A. K. (1986). *Microwave Remote Sensing: Active and Passive.* Vol. 3, Artech House, Inc., Dedhem, Massachusetts.

[57] Whittle, P. (1954). On stationary processes in the plane. *Biometrika*, **41**, 434-449.

[58] Woods, J. W., Dravida, S. and Mediavilla, R. (1987). Image estimation using doubly stochastic gaussian random field models. *IEEE Transactions on Pattern Analysis and Machine Intelligence*, PAMI-9, 245-253.

[59] Wrigley, R. C., Hlavka, C. A. and Card, D. A. (1985). Evaluation of thematic mapper interband registration and noise characteristics. *Photogrammetric Engineering and Remote Sensing*, **51**, 1417-1425.

[42] Mead, R. (1967). A mathematical model for the estimation of inter-plant competition. *Biometrics*, **23**, 189-205.

[43] Mitchell, O. R., Delp, III, E. J. and Chen, P. L. (1977). Filtering to remove cloud cover in satellite imagery. *IEEE Transactions on Geoscience Electronic*, **GE-15**, 137-141.

[44] Moik, J. G. (1980). *Digital processing of remotely sensed images.* NASA SP-431, U. S. Govt. Printing Office, Washington, D.C.

[45] Nelder, J. A. and Mead, R. (1965). A simplex method for function minimization. *Computer Journal*, **7**, 308-313.

[46] Novo, E. M. L. M. and Braga, C. Z. F. (1991). Relatório do Projeto 'Sensoriamento Remoto de Sistemas Aquáticos'. Instituto Nacional de Pesquisas Espaciais, São José dos Campos, Brazil.

[47] O' Neill, R. (1971). Function minimization using a simplex procedure. *Applied Statistics*, **20**, Algorithm AS 47.

[48] Ord, K. (1975). Estimation methods for models of spatial interaction. *Journal of the American Statistical Association*, **70**, 120-126.

[49] Press, W. H., Flannery, B. P., Teukolsky, S. A. and Vetterling, W. T. (1988). *Numerical Recipes in C: The Art of Scientific Computing.* Cambridge University Press, Cambridge.

[50] Rees, W. G. (1990). *Physical Principles of Remote Sensing.* Cambridge University Press, Cambridge.

[51] Ripley, B. D. (1981). *Spatial Statistics.* John Wiley & Sons, New York.

[52] Ripley, B. D. (1988). *Statistical Inference for Spatial Processes.* Cambridge University Press, Cambridge.

[53] Rudorff, B. F. T. and Batista, G. T. (1989). Relatório da Fase II do Projeto Estima - Dados Landsat-TM e Agrometeorológicos na Estimativa da Produtividade da Cultura do Trigo ao Nível de Propriedades Rurais. Internal Report INPE-4782-RPE/582. Instituto Nacional de Pesquisas Espaciais, São José dos Campos, Brazil.